S(RM 2023

TECHNISCHE UNIVERSITÄT DARMSTADT

Fraunhofer LBF

PROCEEDINGS OF

SIRM 2023

The 15th European Conference on Rotordynamics

Picture: Thomas Ott

Editors

Prof.-Dr. Stephan Rinderknecht
Benedikt Schüßler, M.Sc.
Sarah Schwarz, M.Sc.

22nd -24th February 2023
Darmstadt, Germany

MASCHINENBAU We engineer future IMS

PROCEEDINGS OF

SIRM 2023

The 15th European Conference on Rotordynamics

Darmstadt, Germany, 22nd -24th February 2023

Organized & edited by

Institute of Mechatronic Systems in Mechanical Engineering (IMS)
Technische Universität Darmstadt, Darmstadt, Germany

&

Institute of Applied Dynamics (AD)
Technische Universität Darmstadt, Darmstadt, Germany

&

Fraunhofer Institute for Structural Durability and System Reliability (LBF)

Darmstadt, Germany

Proceedings of SIRM 2023: The 15th European Conference on Rotordynamics

Created by
Technische Universität Darmstadt
Institute for Mechatronic Systems in Mechanical Engineering
Otto-Berndt-Straße 2
64293 Darmstadt
Germany

The cover image is provided by Thomas Ott/Technische Universität Darmstadt.

1st Edition, July, 2023

Scientific Board	Local Committee
H. Ecker, TU Wien	S. Rinderknecht, TU Darmstadt
R. Liebich, TU Berlin	B. Schüßler, TU Darmstadt
R. Markert, TU Darmstadt	S. Schwarz, TU Darmstadt
R. Nordmann, TU Darmstadt	R. Markert, TU Darmstadt
J. Strackeljan, University of Magdeburg	R. Nordmann, TU Darmstadt
T. Szolc, IPPT PAN Warsaw	S. Schweizer, TU Darmstadt
I. Santos, DTU Copenhagen	S. Herold, Fraunhofer LBF

Scientific Committee

M. Arghir, Univ. Poitiers
N. Bachschmid, Politecnico Milan
S. Braut, RITEH Univ. Rijeka
A. Chasalevris, NTU Athens
R. Dufour, INSA Lyon
H. Ecker, TU Wien
K. Ellermann, TU Graz
E. Egusquiza, UPC Barcelona
F. Heitmeir, TU Graz
S. Herold, Fraunhofer LBF
T. Holopainen, ABB Helsinki
P. Keogh, Univ. Bath
E. Knopf, GE Power Baden
R. Liebich, TU Berlin
R. Markert, TU Darmstadt
R. Nordmann, TU Darmstadt
P. Pennacchi, Politecnico Milan
L. Pesek, CAS Prague
T. Pumhössel, Univ. Linz
S. Rinderknecht, TU Darmstadt
I.F. Santos, DTU Copenhagen
J. Schmied, Delta JS Zurich
B. Schweizer, TU Darmstadt
J. Strackeljan, Univ. Magdeburg
T. Szolc, IPPT PAN Warsaw
J. Wallaschek, Univ. Hannover
E. Woschke, Univ. Magdeburg
J. Zapomel, CAS Prague
G. Żywica, IMP PAN Gdansk

Organizing Team

B. Schüßler, TU Darmstadt, IMS
S. Schwarz, TU Darmstadt, IMS
S. Backhaus, TU Darmstadt, IMS
S. Rinderknecht, TU Darmstadt, IMS

Sponsors

BorgWarner
Kleyerstraße 20
64295 Darmstadt, Germany
www.borgwarner.com

Continental Automotive Technologies GmbH
Guerickestraße 7
60488 Frankfurt/M., Germany
www.continental-automotive.com

DELTA JS AG
Technoparkstrasse 1
8005 Zürich, Swiss
www.delta-js.ch/en/

ebm-papst Mulfingen GmbH & Co. KG
Abt. E15 HighSpeed
Bachmühle
74673 Mulfingen, Germany
www.ebmpapst.com

Hofmann Mess- und Auswuchttechnik GmbH & Co. KG
Werner-von-Siemens-Straße 21
73479 Pfungstadt, Germany
www.hofmann-global.com

KSB SE & Co. KG
Johann-Klein-Straße 9
67227 Frankenthal, Germany
www.ksb.com

SCHENK RoTec GmbH
Landwehrstraße 55
64293 Darmstadt, Germany
www.schenck-rotec.de

Siemens Industry Software NV
Interleuvenlaan 68
3001 Haverlee, Berlgium
www.plm.automation.siemens.com

J.M. Voith SE & Co. KG |VTA
Voithstraße 1
74564 Crailsheim, Germany
www.voith.com

Wölfel Engineering GmbH + Co. KG
Max-Planck-Straße 15
97204 Höchberg, Germany
www.woelfel.de

Preface

It was our great honor and pleasure to host the SIRM Conference after 2003 and 2011 for the third time in Darmstadt. Rotordynamics covers a huge variety of different applications and challenges which are all in the scope of this conference. The conference was opened with a keynote lecture given by Rainer Nordmann, one of the three founders of SIRM “Schwingungen in rotierenden Maschinen”. In total 53 papers passed our strict review process and were presented. This impressively shows that rotordynamics is relevant as ever. These contributions cover a very wide spectrum of session topics: fluid bearings and seals; air foil bearings; magnetic bearings; rotor blade interaction; rotor fluid interactions; unbalance and balancing; vibrations in turbomachines; vibration control; instability; electrical machines; monitoring, identification and diagnosis; advanced numerical tools and nonlinearities as well as general rotordynamics.

The international character of the conference has been significantly enhanced by the Scientific Board since the 14th SIRM resulting on one hand in an expanded Scientific Committee which meanwhile consists of 31 members from 13 different European countries and on the other hand in the new name “European Conference on Rotordynamics”. This new international profile has also been emphasized by participants of the 15th SIRM coming from 17 different countries out of three continents.

We experienced a vital discussion and dialogue between industry and academia at the conference where roughly one third of the papers were presented by industry and two thirds by academia being an excellent basis to follow a bidirectional transfer what we call *xchange* at Technical University of Darmstadt. At this point we also want to give our special thanks to the eleven industry sponsors for their great support of the conference.

On behalf of the Darmstadt Local Committee I welcome you to read the papers of the 15th SIRM giving you further insight into the topics and presentations.

Darmstadt, Germany, May 2023

Stephan Rinderknecht

Table of Contents

Vibration Control

Instability

Unbalance and Balancing

Rotor Blade Interaction

Rotor Fluid Interactions

Fluid Bearings and Seals

Air Foil Bearings

Magnetic Bearings

Electrical Machines

Monitoring, Identification and Diagnosis

Advanced Numerical Tools and Nonlinearities

Proposed for publication in the following journals:
*[1] BPASTS – Bulletin of the Polish Academy of Sciences: Technical Sciences - PAS journals,
*[2] ACM – Applied and Computational Mechanics, an open access international journal

15th SIRM – European Conference on Rotordynamics,
Darmstadt, Germany, 22nd – 24th February 2023

Rotor dynamic excitation due to non-axisymmetric static load

Angel Martinez Aja [1]

[1] Head of Mechanical Technology, Structural Analysis Fellow, Industria de Turbopropulsores S.A.U. (ITP Aero), 48170, Zamudio (Bizkaia), Spain, angel.martinez@itpaero.com

Abstract

This paper defines methodology to perform modal and frequency response analysis of a structural system composed of static parts and different rotors (i.e. whole engine model), in a *stationary system*, subjected to rotor non-axisymmetric static load.

One example of non-axisymmetric static load is a non-axisymmetric inlet pressure on an engine fan in a cross-wind environment (see Figure 1). Although this load is static from a stationary observer point of view, each fan blade, due to its rotation, is being excited by an alternating pressure that is promoting a dynamic excitation. This type of loading is designated as 0EO (zero engine order) in a stationary frame. Another example of non-axisymmetric static load is the gravity load: weight load of a rotor blade is, again, an alternating load due to blade rotation.

1 Introduction

RotRed methodology [1] has been applied to perform rotor model reduction from a rotor cyclic symmetry 3D model. This methodology incorporates all rotating effects of a rotor model (gyroscopic effect, stress stiffening and spin softening) in *stationary system*, that allows incorporation of other rotors at different speeds and static parts in the same whole engine model. RotRed methodology presents a clear step forward to model and reduce flexible rotors with regard to commercial software [3][4][5][6] as shown in Ref. [1].

Normally, excitation type, considered in whole engine model, is out of balance on each rotor that corresponds to a 1EO excitation type. In this paper, it is shown how RotRed reduced rotor model matrices can be used to perform 0EO modal and frequency response analysis, in a stationary system, of a complete whole engine model subjected to a non-axisymmetric static load type (see Figure 1). In a stationary system Campbell diagram, 0EO excitation line corresponds to horizontal line axis. Thus, whole engine models that have backward modes crossing abscissa line will have resonances that can be excited by 0EO excitation type (see Figure 2).

With current software capabilities [3][4][5][6], this type of 0EO excitation can be considered only in *rotating system*, as a rotating load, but, with the known restriction of applicability to a *single rotor model* with axi-symmetric boundary conditions. Relevant effects in the solution like non-axisymmetric stiffness support (statics) or dynamics of other rotors, can not be represented up to now.

In conclusion, this methodology can be used to obtain dynamic response (displacements and stresses) of a whole engine model when subjected to non-axisymmetric static load (i.e. non axisymmetric inlet pressure in fans), taking into account dynamic amplification factor if resonances are within running range or if maximum speed is approaching first resonance.

Backward mode crossing with abscissa axis, in a stationary system Campbell diagram, is present in different examples in bibliography: rotating disk [7], three-bladed wind turbine [8], rotor-bearing system [9] and flexible bladed rotor (fan) [10].

A very relevant example of a backward mode crossing abscissa line was experimentally observed in ARES test rig at Imperial College (London), excited by a non-axisymmetric static load (gravity), in the same context of this paper, and was reported in [11] by Valentina Ruffini.

0EO excitation nomenclature has been used also as the excitation type that excites zero nodal diameter modes, like in the series of papers by Rzadkowski & Maurin [12] about coupling of disk stages in bladed-disk-shaft assemblies. 0EO excitation, within the context of this paper, refers to a load of zero frequency (non axi-symmetric static load) and corresponds to a straight line excitation that is coincident to abscissa axis (see Figure 2).

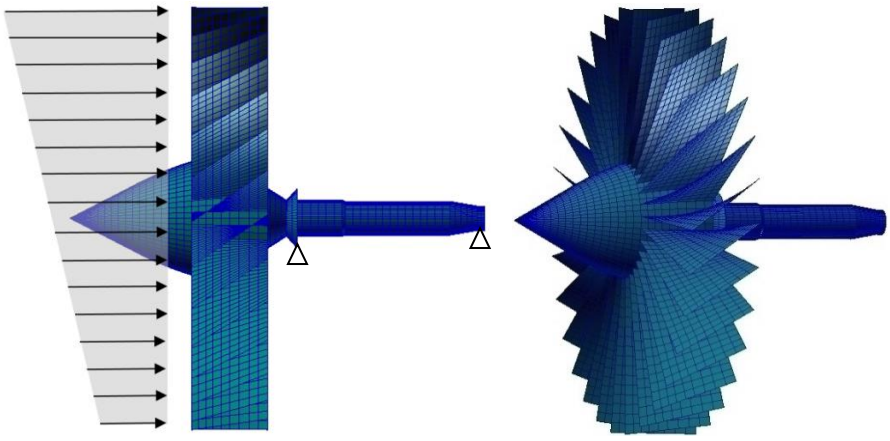

Figure 1: Non-axisymmetric static inlet pressure in a fan rotor model.

2 Single rotor 0EO modal analysis.

Equation used for an asynchronous undamped modal analysis [1], within RotRed methodology, in a *stationary system*, for a rotor model rotating at speed Ω is:

$$[-w^2\boldsymbol{M_{lin}} + iw \cdot \Omega \boldsymbol{b_{sta}} + (\boldsymbol{K_{lin}} + \Omega^2 \boldsymbol{k_{sta}})]\{\delta\} = \{0\} \quad (1)$$

Being:

$\boldsymbol{M_{lin}}$	linear mass matrix
$\boldsymbol{K_{lin}}$	linear stiffness matrix
$\boldsymbol{b_{sta}}$	fixed system gyroscopic matrix for unit rotation speed
$\boldsymbol{k_{sta}}$	fixed system speed dependent stiffness for unit rotation speed
w	excitation frequency
Ω	rotation speed

Considering fan rotor model of Figure 1, the following Campbell diagram can be constructed with eigenvalues obtained from equation (1), considering different rotation speeds:

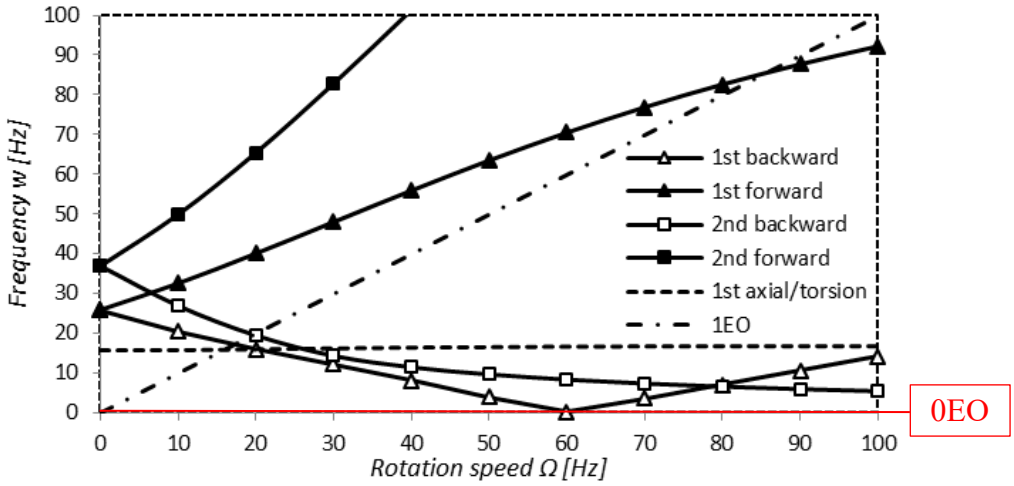

Figure 2: Fan rotor model Campbell diagram in stationary system.

As load, to be considered, is stationary in time, its excitation frequency is zero ($w = 0$) with regard to a stationary system. Considering this condition, equation (1) is simplified to the following expression:

$$[\boldsymbol{K_{lin}} + \Omega^2 \boldsymbol{k_{sta}}]\{\delta\} = \{0\} \quad (2)$$

Note that condition $w = 0$ or 0EO excitation corresponds to abscissa axis of Campbell diagram in Figure 2. Above equation (2) represents another eigenvalue analysis considering now Ω as "frequency" variable. Eigenvalue results from (2) will be those rotation speeds that correspond to the crosses of Campbell diagram modal curves with abscissa axis. In Figure 2, it can be observed graphically that first eigenvalue will be close to 60 Hz.

Equation [2] can be replaced by:

$$\left[\boldsymbol{K_{lin}} - \Omega^2 \boldsymbol{M_{f0}}\right]\{\delta\} = \{0\} \tag{3}$$

Being $\boldsymbol{M_{f0}} = -\boldsymbol{k_{sta}}$ a pseudo mass matrix of rotor.

With MSC Nastran [2], equation (3) can be solved using solution 107, inputting pseudo mass matrix with M2PP case control card and linear stiffness matrix with K2GG card. These matrices have been output previously with RotRed tool in a punch file with DMIG format. Note that all rotor mass definition needs to be removed from model (i.e. no M2GG card) because "frequency" variable has changed to rotation speed Ω.

```
SOL 107
CEND
echo=none
spc=1
MPC=1
DISP=ALL
CMETHOD=100
K2GG=KLIN
$ n=0; 0EO
$ M2GG=MLIN (NO mass matrix)
M2PP=(-1.,0.)*KSTA
```

Figure 3: Case control deck for 0EO modal analysis.

MSC Nastran solution 107 gives two eigenvalues below 300 Hz at 60.38 Hz and 234.19 Hz with mode shapes shown in Figure 4.

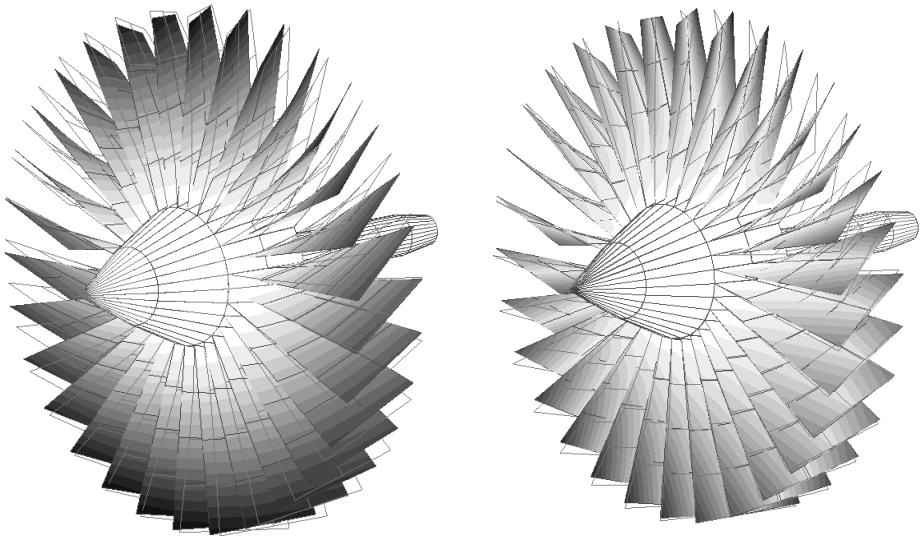

Figure 4: Modal shapes for 60.38 Hz (left: blade 1st flap mode) and 234.19 Hz (right: blade 1st torsion mode).

First mode is an harmonic 1 blade flap mode and second mode is an harmonic 1 blade torsion mode. Main characteristic of these modes is that they do not have whirling motion. In fact, as $\boldsymbol{K_{lin}}$ and $\boldsymbol{k_{sta}}$ matrices are real, then, eigenvalues and eigenvectors results from equation (3) are also real.

3 Single rotor 0EO frequency response analysis.

Best suited damping definition for 0EO excitation is via equivalent viscous damping. Equivalent viscous damping matrix [2] is defined, in the *rotating frame*, as:

$$\boldsymbol{B_{vd}} = \frac{G}{w_e}\boldsymbol{K_{lin}} = \frac{G}{2\pi f_e}\boldsymbol{K_{lin}} \tag{4}$$

Being: G equivalent structural damping
w_e main frequency [rad/s], or f_e in [Hz]

Considering equivalent viscous damping terms in *stationary system*, equation (1) becomes, in its forced version:

$$[-w^2\boldsymbol{M_{lin}} + iw(\Omega\boldsymbol{b_{sta}} + \boldsymbol{B_{vd}}) + (\boldsymbol{K_{lin}} + \Omega\boldsymbol{B_{vd}^c} + \Omega^2\boldsymbol{k_{sta}})]\{\delta\} = \{F\} \tag{5}$$

Being: $\boldsymbol{B_{vd}^c}$ circulation of equivalent viscous damping matrix (see reference [3])

Considering again 0EO excitation with condition $w = 0$, equation (5) becomes:

$$[\boldsymbol{K_{lin}} + \Omega \boldsymbol{B^c_{vd}} + \Omega^2 \boldsymbol{k_{sta}}]\{\delta\} = \{F\} \tag{6}$$

Note here that displacement results $\{\delta\}$, again, are going to be real, in stationary system, because all matrices of equation (6) are also real. These real displacements $\{\delta\}$ can be converted to rotating system to obtain physical displacements of rotor points, that are now pulsating at frequency Ω, as expected:

$$\{\delta\}_{\boldsymbol{rot}} = \boldsymbol{T}\{\delta\} \tag{7}$$

Being $\boldsymbol{T}$ transformation matrix from stationary to rotating system [3] that is dependent on rotation speed Ω.

Noting also that "frequency" variable is Ω, equation (6) can be transformed to allow an easy identification of stiffness, damping and pseudo-mass matrices terms:

$$[\boldsymbol{K_{lin}} + i\Omega \cdot (-i)\boldsymbol{B^c_{vd}} - \Omega^2(-\boldsymbol{k_{sta}})]\{\delta\} = \{F\} \tag{8}$$

Solution to this equation can be performed with MSC Nastran [2] using SOL 108 with the following cards in case control deck to input rotor matrices, previously generated by RotRed tool:

```
K2GG=KLIN      $ linear stifness matrix
$ n=0; 0EO
$ M2GG=MLIN (NO MASS MATRIX!)
B2PP=(0.,-1.)*BVDC $ damping matrix
M2PP=(-1.,0.)*KSTA $ pseudo-mass matrix
```

Figure 5: Case control deck cards for 0EO frequency response analysis.

Consider now, in the proposed example, an applied harmonic 1 static loading over fan rotor model as defined in Figure 6. This load of 10 KN is distributed over blade tip front nodes in Y direction of stationary system. Equivalent viscous damping has been defined with structural damping $G = 0.05$ at frequency $w_e = 2\pi 60$. This will result in 5% of structural damping just at 60 Hz.

A central node is defined, with number 1012, connecting loaded peripheral nodes with a RBE3 element. This central node represents the average displacement of these peripheral nodes. Radial displacement of central node 1012, as function of rotation speed, can be obtained through frequency response analysis (SOL108) directly in stationary system (see Figure 6), and using (7), it can be converted to rotating system:

Stationary system: $\delta_{rad,sta} = \sqrt{\delta^2_{y,sta} + \delta^2_{z,sta}} = A$ (9)

Rotating system: $\delta_{rad,rot} = A\cos(\Omega t + \varphi)$ (10)

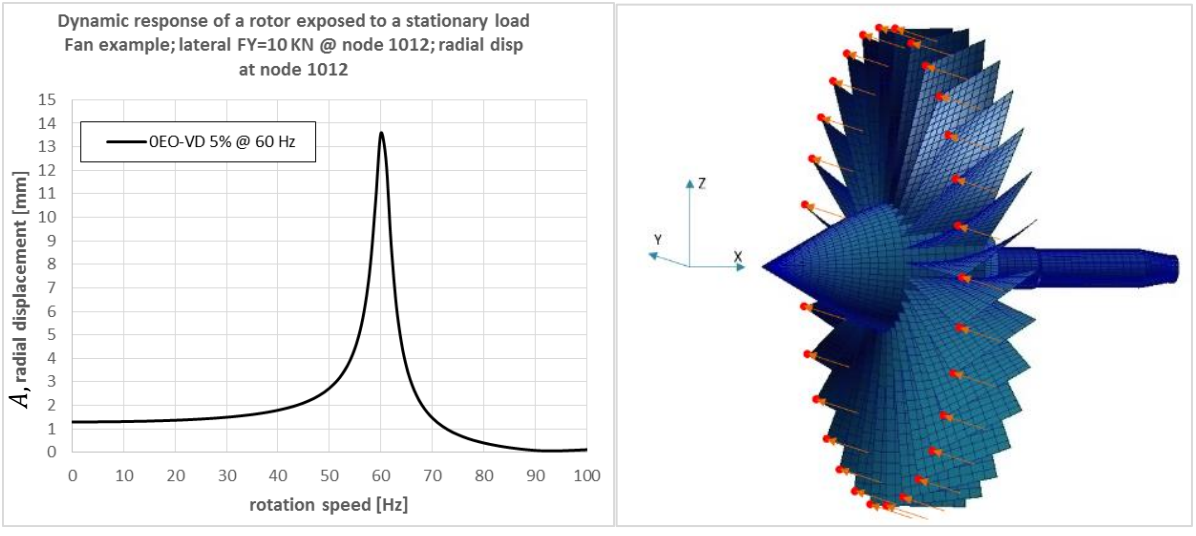

Figure 6: Frequency response of a static load over fan rotor model.

As expected, at low frequencies, node 1012 displacement is equal to the static response but has an amplification factor when rotation speed approaches first resonance at 60.38 Hz.

Figure 7 shows a contour plot of displacement magnitude of all nodes in fan rotor reduced model for speeds $\Omega = 0\ Hz$ and at resonance $\Omega = 60\ Hz$. It can be observed that node with maximum displacement turns 90 degrees comparing deformed plot at $\Omega = 0\ Hz$ (point A with 2.24 mm) and at $\Omega = 60\ Hz$ (point B with 27.38 mm).

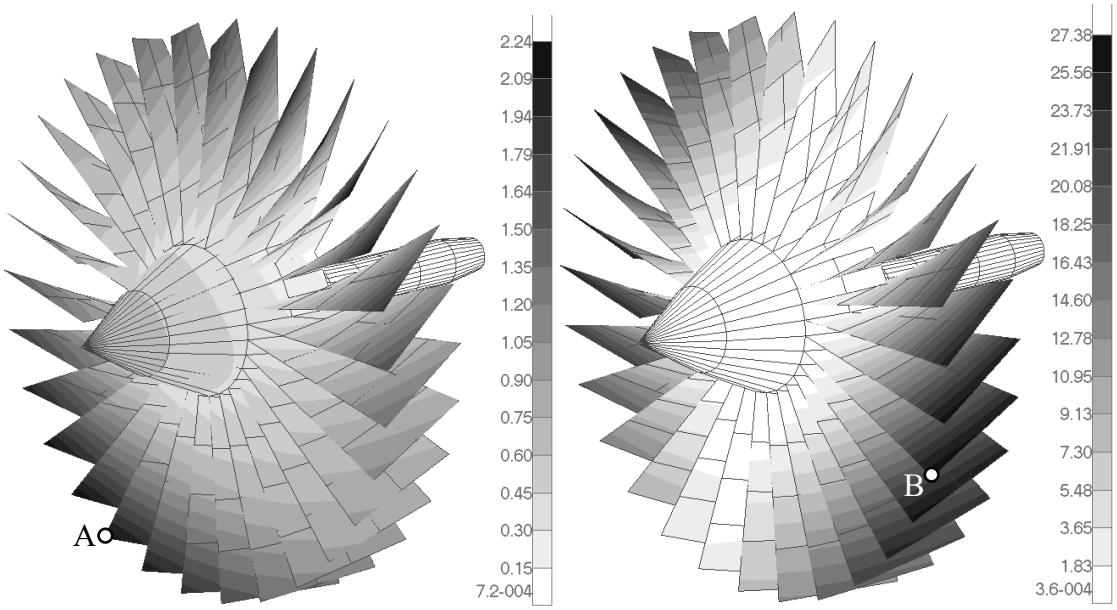

Figure 7: Nodal displacements at $\Omega = 0\ Hz$ (left) and at resonance of 60 Hz (right).

4 0EO excitation in a whole engine model with multiple rotors and static parts.

In this section, dynamic equations, particularized to 0EO excitation, are going to be developed for static parts, reference rotors and non-reference rotors that belongs to a complex system like a whole engine model.

Recalling again dynamic analysis equation (6) for forced vibrations with viscous damping of a rotor with speed Ω and for a 0EO excitation:

$$[\boldsymbol{K_{lin}} + \Omega \boldsymbol{B_{vd}^{c}} + \Omega^2 \boldsymbol{k_{sta}}]\{\delta\} = \{F\} \tag{11}$$

For a *static part*, where $\Omega = 0$, only its linear stiffness matrix $\boldsymbol{K_{lin}}$ needs to be considered in modal or frequency response analysis when excitation is 0EO, as this static part is subjected only to static load. In this particular case of 0EO excitation, when standard frequency parameter w has been changed to rotation speed Ω, frequency response standard solution of a commercial software can be used turning off mass content of static parts.

Now, the definition of *multiple rotors* is outlined. One of these rotors must be labelled as *reference rotor* and must be the one that is receiving the static load input. Suppose a *non-reference rotor*, rotating at speed Ω', that can be related to *reference rotor* speed Ω by piece-wise linear segments as shown in Figure 8:

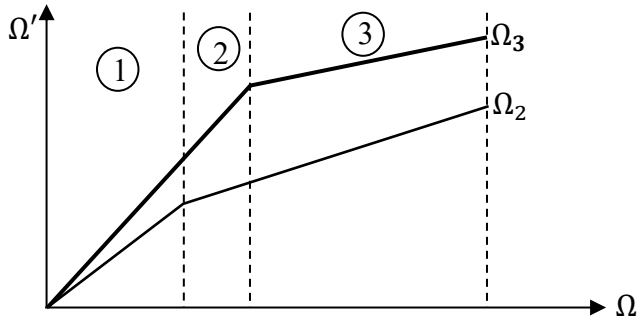

Figure 8: Piece-wise linear speed relationship of other rotors wrt reference rotor speed.

On each segment, *non-reference rotor* speeds can be approximated by a linear relationship: $\Omega' = p\Omega + q$, where p and q are constant values.

For a *non-reference rotor* with speed Ω', dynamic equation for 0EO (11) becomes:

$$[\boldsymbol{K_{lin}} + (p\Omega + q)\boldsymbol{B_{vd}^{c}} + (p\Omega + q)^2 \boldsymbol{k_{sta}}]\{\delta\} = \{F\} \tag{12}$$

Note again that all matrices and coefficients in equation (12) are real, so displacement results will be also real. Reordering terms in (12):

$$[(\boldsymbol{K_{lin}} + q\boldsymbol{B_{vd}^{c}} + q^2 \boldsymbol{k_{sta}}) + i\Omega(-i)(p\boldsymbol{B_{vd}^{c}} + 2pq\boldsymbol{k_{sta}}) - \Omega^2(-p^2 \boldsymbol{k_{sta}})]\{\delta\} = \{F\} \tag{13}$$

Equation (13) can be compared with classical formula:

$$[\boldsymbol{K} + i\Omega\boldsymbol{B} - \Omega^2\boldsymbol{M}]\{\delta\} = \{F\} \tag{14}$$

And then, *non-reference rotor* matrices are clearly identified as:

$$\begin{aligned} &\text{Stiffness:} && K = \boldsymbol{K_{lin}} + q\boldsymbol{B^c_{vd}} + q^2\boldsymbol{k_{sta}} \\ &\text{Damping:} && B = -i(p\boldsymbol{B^c_{vd}} + 2pq\boldsymbol{k_{sta}}) \\ &\text{Mass:} && M = -p^2\boldsymbol{k_{sta}} \end{aligned} \tag{15}$$

Matrices involved in a whole engine model with static parts and different rotors (reference and non-reference rotors) within a "segment", are summarized in Table 1.

Table 1: Matrices of static part and different rotors in an engine model for 0EO excitation.

pseudo-matrix	reference rotor (R)	static (S)	Non-reference rotor (Ri)
stiffness	$\boldsymbol{K_{lin}}^R$	$\boldsymbol{K_{lin}}^S$	$\boldsymbol{K_{lin}}^{Ri} + q\boldsymbol{B^c_{vd}}^{Ri} + q^2\boldsymbol{k_{sta}}^{Ri}$
damping	$-i\boldsymbol{B^c_{vd}}^R$		$-i(p\boldsymbol{B^c_{vd}}^{Ri} + 2pq\boldsymbol{k_{sta}}^{Ri})$
mass	$-\boldsymbol{k_{sta}}^R$		$-p^2\boldsymbol{k_{sta}}^{Ri}$

Matrices from Table 1 can be input through X2GG and X2PP case control cards in a MSC Nastran solution 108 to perform a frequency response analysis where the frequency variable is the speed Ω of reference rotor.

For undamped modal analysis (SOL 107), all matrices from Table 1 need to be considered except $\boldsymbol{B^c_{vd}}^x$ matrices, that are related to equivalent viscous damping.

Consider an example of a whole engine model with static parts and two rotors: (LP) Low pressure and (HP) High pressure.

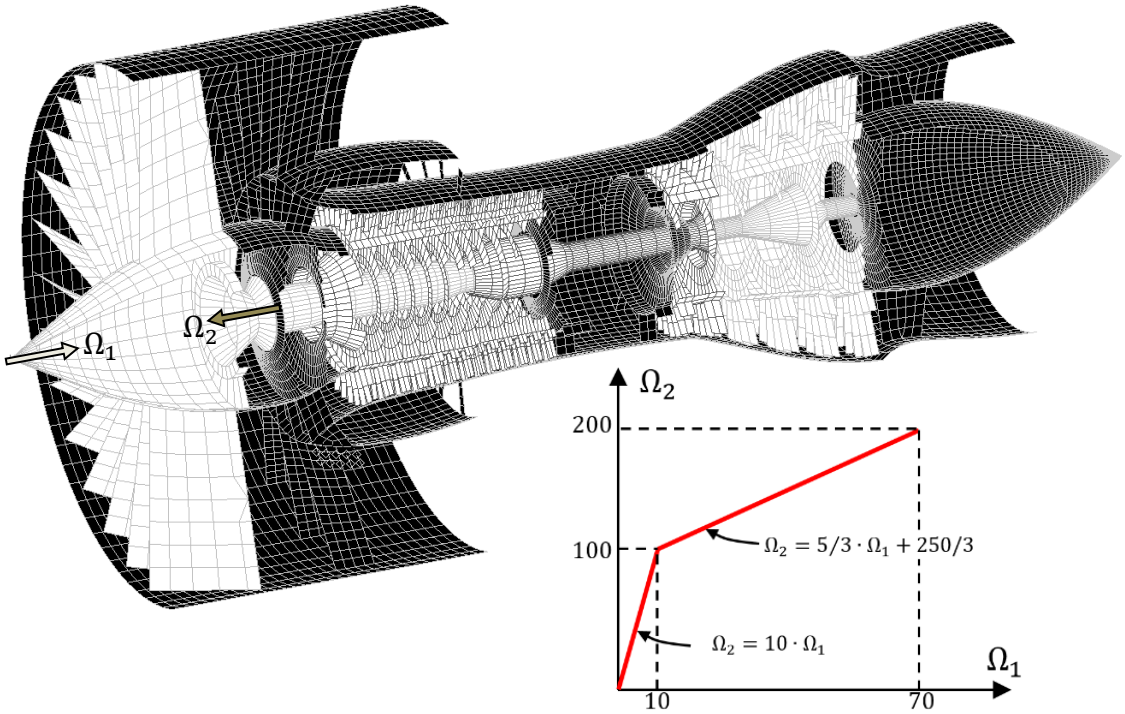

Figure 9: Whole engine model schematic view and spool speeds.

Rotor speed relationship of LP (rotor 1) and HP (rotor 2) is defined in the graph of Figure 9, where two linear segments can be identified. LP and HP spools are counter-rotating as shown also in model of Figure 9.

These two linear segment have the following p and q parameters:

Table 2: p and q parameters definition on each segment.

segment	p	q
1	10	0
2	5/3	250/3

Using contributions of LP (reference) rotor, HP (non-reference) rotor and static part from Table 1, and considering p,q constants for the two segments identified in Figure 9, asynchronous modal analyses have been run from N1=0 Hz to N1=70 Hz in steps of 5Hz.

Frequency results of these asynchronous modal analyses are shown in Figure 10, where bubble size represents fan rotor strain energy percentual. Strain energy backward content is shown with bubble filled with white colour, whilst forward content is shown with black fill. At it can be observed in Figure 10, there is a backward mode crossing abscissa axis approximately at 60 Hz that, after crossing, its strain energy turns to forward content. Modal shape of this mode is shown in Figure 11.

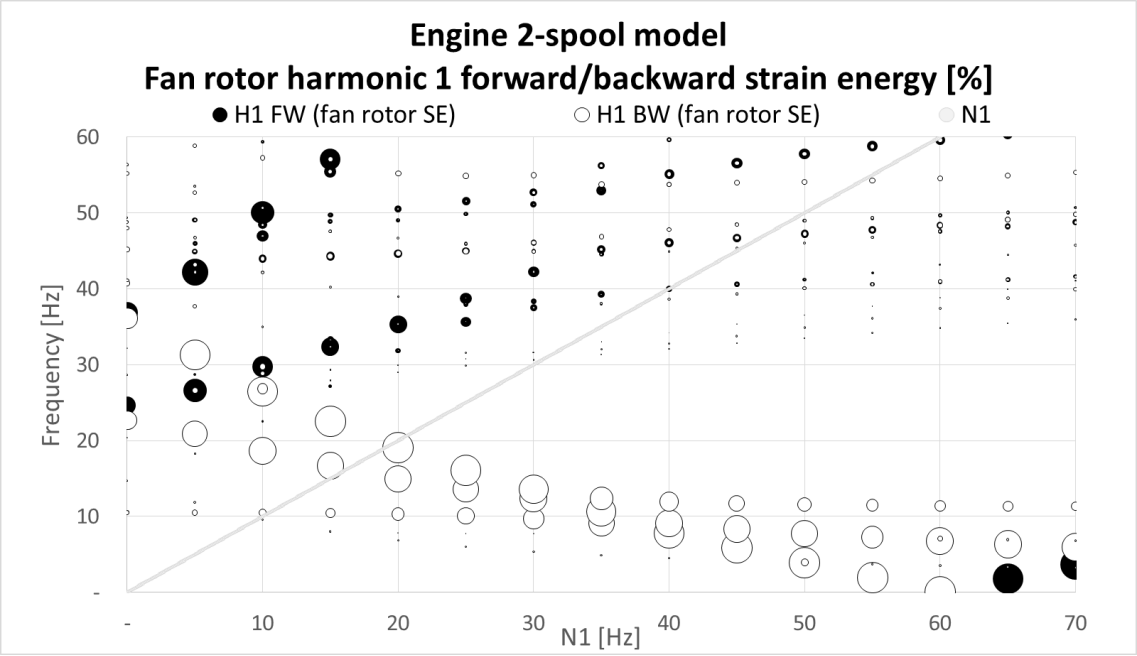

Figure 10: Whole engine model Campbell diagram. Fan rotor relevant modes.

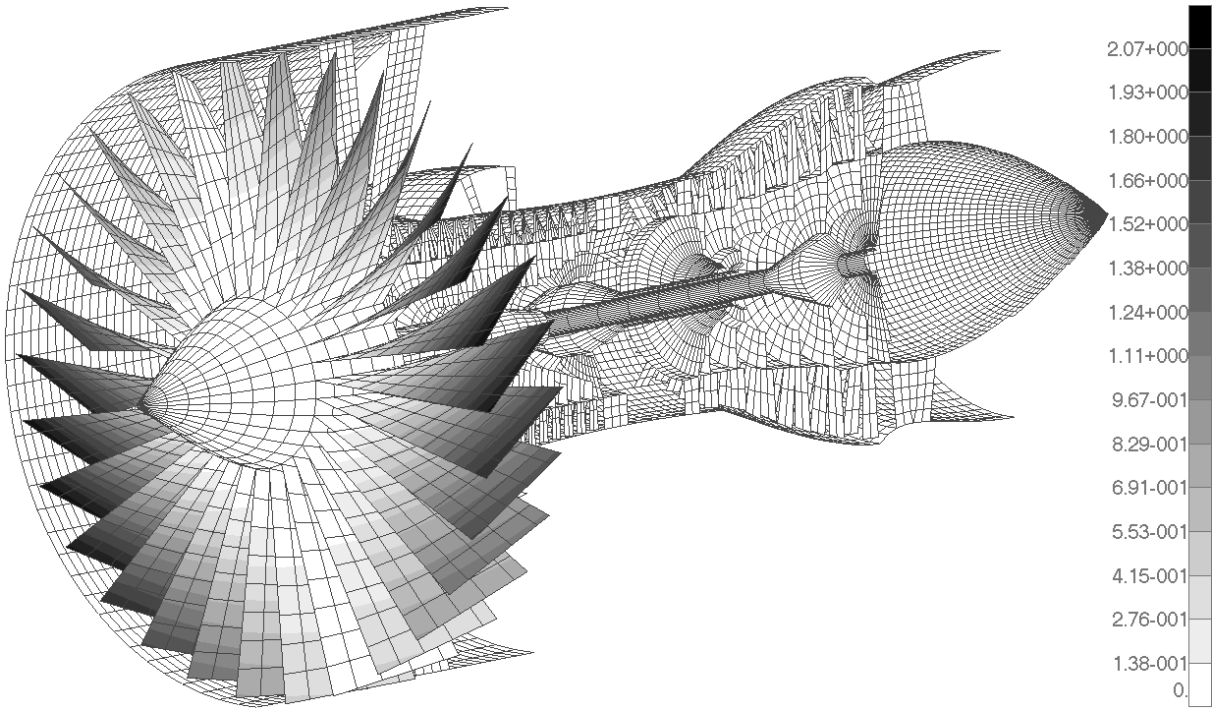

Figure 11: 1st Modal shape at 60.124 Hz from 0EO modal analysis.

Exact value of N1 speed that corresponds to crossing of this backward mode with abscissa axis can be found performing a 0EO undamped modal analysis using matrices from Table 1, except $\boldsymbol{B_{vd}^{c}}^{x}$ matrices. Resultant first eigenvalue is found exactly at N1=60.124 Hz.

As commented before, in single rotor 0EO modal analysis, this crossing mode is real and has no whirling motion content. In this case, mode is more relevant in fan blade, showing a flap mode type motion (see Figure 11).

Now, 0EO frequency response analysis results are going to be obtained using a non axi-symmetric static pressure, as shown in Figure 12, composed on harmonic 0 and 1 components.

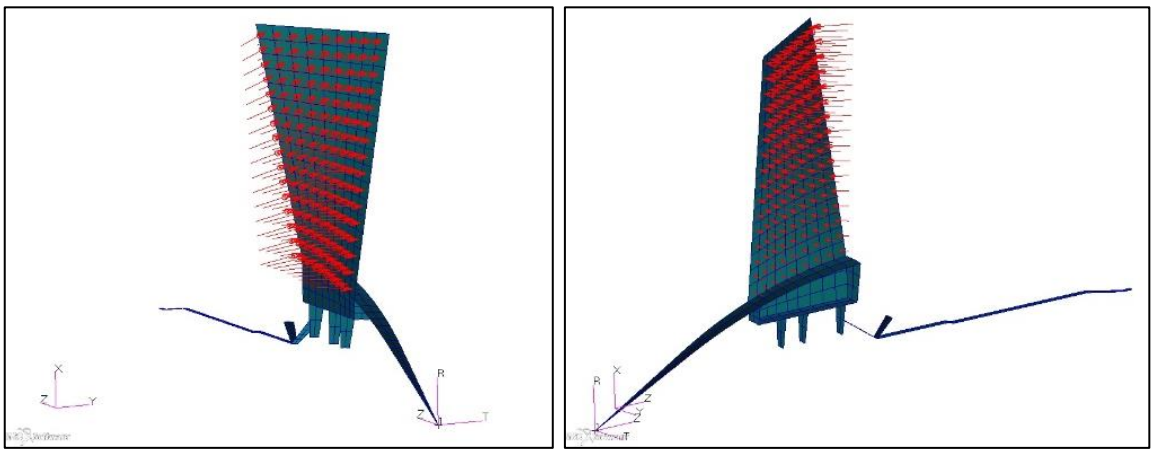

Figure 12: Harmonic 0 (left) and harmonic 1 (right) fan blade static pressure distributions.

Displacements results for N1=0 Hz are shown in Figure 13 (top). Maximum fan blade displacement occurs at Bottom Depth Centre (BDC) blade (see point A in Figure 13-top), where static pressure is maximum (maximum harmonic 1 pressure with the same sign than harmonic 0).

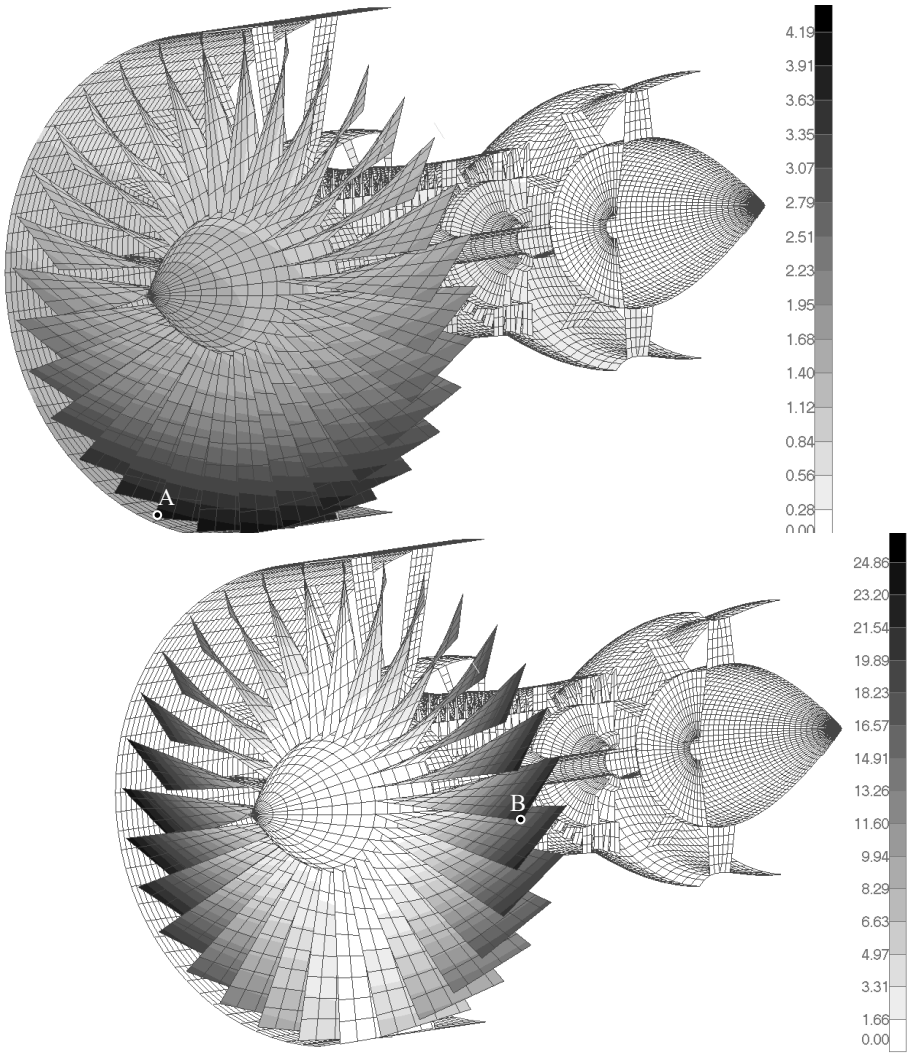

Figure 13: Displacements at N1=0 Hz (top) and at first resonance N1=60Hz (bottom).

0EO frequency response analysis is conducted, considering contributions of LP rotor, HP rotor and static parts, per Table 1, of this engine model. Equivalent viscous damping has been introduced with an equivalent structural damping coefficient $G = 0.05$ (5%) for a main frequency $f_e = 60\ Hz$. Displacement contour plot at resonance (N1=60 Hz) is shown in Figure 13 (bottom).

It can be observed in Figure 13 (bottom), in comparison with Figure 13 (top), that maximum displacement has been amplified: from a maximum displacement of 4.19 mm at point A at Bottom Depth Centre (BDC) blade for 0Hz, to 24.86 mm at point B at 3 o'clock blade for 60 Hz. Maximum displacement, within these blades, occurs at blade tip front (points A and B).

Displacement evolution of blade front tip points A (BDC) and B (3 o'clock) is shown in Figure 14.

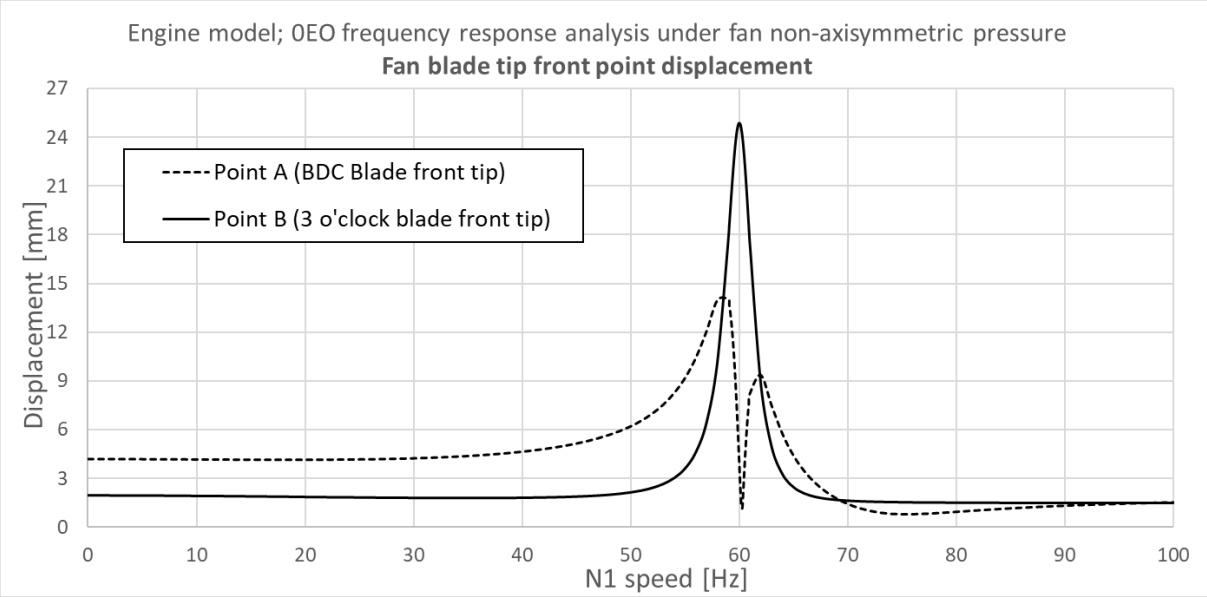

Figure 14: Displacements evolution of Points A and B with N1 speed.

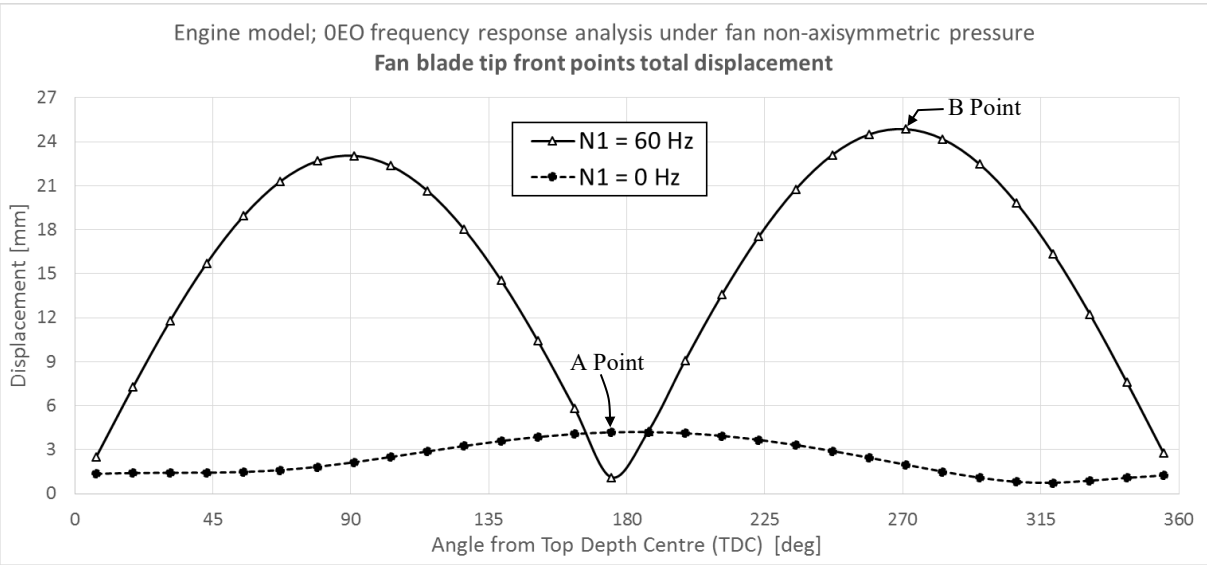

Figure 15: Blade front tip points displacements circumferential distribution at N1=0 and N1=60 Hz.

An interesting aspect to note is that Point B is dephased 90 physical degrees versus point A (see Figure 13). Typical resonance "time dephase" of 90 degrees equals here to 90 physical degrees because resonance frequency is the rotation speed of fan. This change in the displacement field with rotation speed can be easily seen if blade tip front displacements of points A and B, are plotted against circumferential angle (origin at Top Depth Centre TDC), as shown in Figure 15.

It can be noted that curves in Figure 15 are not perfectly symmetric against BDC (180 deg). This asymmetry comes from blade turning angle that results in a global geometry that is not symmetrical against an engine vertical meridional plane.

It is important to note that, as a resultant from generic equation (13), solution from frequency response analysis, under 0EO excitation, is static or constant for a stationary observer. This means that the displacement of a point that belongs to a static part will be static or constant in time for a given speed regime in engine rotors. In the same way, the displacement of a point that belongs to a rotor will be the same when it passes through a given circumferential position. In other words, all fan blade tip front points will have the same displacement when these points pass through a given circumferential position (i.e. 3 o'clock position).

But, also, a particular rotor point will have different values of displacements when this point passes through the different circumferential positions, hence suffering a vibrating motion. Displacement solution for particular rotor points can be obtained, as shown, using equation (7).

When rotor speed reaches a 0EO resonance, although response is static from a stationary observer, it will have a dynamic response amplification, and rotor deformed shape will rotate circumferentially 90 degrees, opposite to rotation speed sense, with regard to deformed shape at zero speed (see Figure 13).

5 Conclusions.

RotRed is a methodology to consider all rotating effects (stress stiffening, spin softening and Coriolis effect) on dynamics of a rotor in a fixed or stationary system. RotRed represents a clear step forward, with regard to current commercial rotordynamics software, in the simulation of dynamics of whole engine models in which several rotors are combined with static parts and, specially, when these rotors are flexible.

In this paper, it has been shown how a static non-axisymmetric pressure or load can generate a dynamic excitation in a rotating component when using a *stationary system*. Harmonic 1 content of this static load can promote a dynamic amplification of a backward mode that is crossing abscissa axis in stationary system Campbell diagram. This type of loading is named 0EO excitation.

Also, 0EO excitation has been applied to a rotor of a whole engine model, in *stationary system*, where different rotors and static part are presented. 0EO modal analysis and frequency response analysis have been outlined for these complex systems. To maintain solution in the real domain, equivalent viscous damping has been selected as the method to introduce damping in the system.

Acknowledgement

I would like to express my deepest appreciation to my company, ITP Aero, and its encouraged motivation to invest in the research of rotordynamics technology. This paper is one of the products of this effort that ITP Aero has allowed me to publish in this conference.

All models referenced in this paper, and their derived results, do not represent real proprietary engine parts. They are dummy models generated to show applicability of 0EO dynamic excitation methodology.

References

[1] Martinez Aja, A., Exposito, I. (2016): *Multi-rotor dynamics in fixed system with all steady state rotation effects*, Vibrations in Rotating Machinery, VIRM11, Manchester.

[2] MSC.Software Corporation (2013): *MSC Nastran 2013 Dynamic Analysis User's Guide*.

[3] MSC.Software Corporation (2018): *Rotordynamics User's Guide*, Chapter 4, Damping circulation matrix, MSC Nastran 2018.

[4] Siemens (2016): *Rotordynamics User's Guide*, NX Nastran 10.

[5] Ansys Incl. (2009): *Rotordynamics Analysis Guide*, Release 12.0.

[6] LMS Samtech: *SAMCEF for Rotors User's Guide,* Siemens PLM Software.

[7] B.Kirchgäßner (2016): *Finite Elements in Rotordynamics*, Procedia Engineering 144 736-750

[8] Malcolm, D.J. (2018): *On the structural response of two- and three-bladed vertical axis wind turbines*, Wind Energy, John Wiley & Sons, Ltd.

[9] Zhiguo Wan, Yu Wang, Binqiang Chen, Yihua Dou, Xinjuan Wei (2020): *The Vibration of a Transversely Cracked Rotor Supported by Anisotropic Journal Bearings with Speed-Dependent Characteristic*, Applied Sciences, 10(16):5617.

[10] Lesaffre, N., Sinou, J.J., Thouverez, F. (2006): *Model and stability analysis of a flexible bladed rotor*, Int. Journal of Rotating Machinery, 2006, ID 63756, 1-16.

[11] C.W.Schwingshackl, L.Muscutt, M.Szydlowski, A.Haslam, G.Tuzzi, V.Ruffini, M.Price, A.Rix, J.Green (2020): *Asynchronous rotor excitation system (ARES)–A new rotor dynamic test facility at Imperial College London*, VIRM12, Liverpool.

[12] Rzadkowski, R., Maurin, A. (2015): *Forced Vibration of Eight Mistuned Bladed Disks on a Solid Shaft—Excitation of the First Compressor Bladed Disc*, Vibration Eng. and Technology of Machinery 349–361.

15th SIRM – European Conference on Rotordynamics,
Darmstadt, Germany, 22nd – 24th February 2023

Vibratory response of planetary gear sets housing by a spectral iterative approach – Modulation effects induced by carrier rotation

Jessica Neufond [1], **Joël Perret-Liaudet** [2], **Emmanuel Rigaud** [2], **Pascal Bouvet** [1]

[1] Vibratec SA, 69130, Ecully, France, jessica.neufond@vibratec.fr
[2] Laboratoire de Tribologie et Dynamique des Systèmes (LTDS), UMR CNRS 5513, Ecole Centrale de Lyon, Université de Lyon, 36 Avenue Guy de Collongue, F69134 ECULLY cedex, France

Abstract

The main source of excitation at the origin of the vibratory response of gear system is generated by the meshing process, leading to the variation of the mesh stiffness and deviation between the ideal input/output transmission law and the real one. In planetary gear, these phenomena are amplified due to the presence of multiple meshes. Moreover, in operating, the varying relative position between the planets gears and the ring gear is at the origin of a modulation in the temporal response measured on a fixed point on the ring gear housing. The aim of this work is to present a novel method to investigate the dynamic behaviour of a planetary gear set. This method is a complete procedure for a planetary gear system whining noise computation induced by the multi-mesh excitations. This procedure is divided in three main steps. First, the parametrical internal excitations are simultaneously characterized by considering all contacts at the multiple gear meshings. Secondly, the coupled equations of motion are projected onto the modal basis and the stationary dynamic response is computed using an iterative spectral method. Finally, the modulated response of the planetary gear housing (ring gear) is evaluated. Numerical results are discussed and compared with experimental observations.

1 Introduction

Over the wide range of geared systems, the planetary gear sets are distinguished by their capacity to provide high gear ratio in a compact package. Indeed, a single stage planetary gear is composed of a central gear, called the sun, which meshes with N gears called planets, which mesh with a peripheral gear (with internal teeth) called the ring gear, while a carrier drives the axis of the planets. Thus, the sun, the ring gear and the carrier are three coaxial solids. Planetary gear sets are used for example in automatic gearboxes, transmissions for hybrid vehicles, energy production systems such as wind turbines, home automation applications such as shutters or blinds. However, contrary to cylindrical gears with fixed and parallel axes, whining noise prediction and control remains a difficult problem because of the coupling between the multiple gear meshes and the mobility of the planets axes.

It is well know that the gear whining noise is generated by the mesh process [1]. The problem posed is multi-scale in nature. Indeed, the overall dynamic and vibroacoustic behaviour of geared systems (on the scale of a meter) depends on the local micro-geometry of the teeth (on the scale of a micron), associated with the transmission error. Moreover, the problem is parametric in nature, due to the periodic fluctuation of the mesh stiffness, and non-linear, due to the presence of functional clearance and close contacts between teeth and bearings. These parametric internal excitations generate dynamic mesh forces which are transmitted to the housing through wheel bodies, shafts and bearings. In the end, the radiated noise is directly related tot he vibratory state [2, 3, 4].
In the case of planetary gear sets, housing vibratory state prediction is challenging. In many applications, the carrier rotation modulates the housing vibration response at its rotational frequency [5, 6], as a consequence of the successive passage of the planets. The iterative spectral method allows the solving of linear parametric equations of motion, in the carrier reference frame, in the spectral domain, with short computational time [7, 8]. The dynamic response at meshes is hence fully characterized and the short computational time allows parametric investigation. However, the computation of the dynamic response of any point on the ring gear requires an additional step. Even if many works deal with ring gear modulated dynamic response [9] [10], further work is required to include modal behaviour contribution of the ring gear. Indeed, these existing methods propose a simplified formulation based on the use of Hanning window functions to simulate the growth/decay of the vibratory amplitude as one planet

approaches or moves away from the measured point. Though these approach give good correlation with experiments at low frequencies, the coincidence between mesh frequencies and housing modes at higher frequencies is less discussed. Thus, a novel approach is proposed by taking into account the modulation effects induced by the relative rotation between the observation point (fixed point located on the ring gear) and the meshes (attached to the carrier reference frame). Numerical results are analysed and compared with experimental data.

Figure 1: Example of modulated housing vibratory response of a planetary gear with three planets, computed using Hanning and Heaviside functions [9]

2 Numerical model

This paper proposes a novel approach to predict the vibroacoustic behaviour of planetary gear sets, from evaluation to the internal parametric excitations and their coupling to the housing vibratory state. The focus is set on how to calculate the modulation effects due to the relative motion between the axis of the planets and the ring gear, using a finite element approach and a spectral iterative method. This procedure can be divided into three main steps. First, static transmission error and mesh stiffness fluctuation at each meshes are computing through the solving of contact equations. Next, the computation of the dynamic response of the drive train is performed through an iterative spectral method. Finally, the dynamic response of the housing is computing through the relative rotation between the observation point (fixed point located on the housing) and the meshes (attached to the carrier rotating reference frame).

2.1 Static transmission error and mesh stiffnesses fluctuation

Assuming infinitely rigid and geometrically perfect gears, their circular involute profile offers a constant instantaneous transmission ratio. However, these undeformable and geometrical assumptions are never met. Geometrical errors or tooth corrections as well as deformation under torque, induce a fluctuation of the instantaneous reduction ratio around its theoretical value. This fluctuation results in the so-called static transmission error (STE). It is defined as the deviation between the actual position of the output shaft and its theoretical position [1, 2]. The calculation of the STE is well mastered. It is based on the resolution of the equations describing the static contact between the gear teeth (see for example Tavakoli et al. [11] and Rigaud et al. ([12]). For each position θ of the driving gear, the contact between the teeth are established based on a kinematic analysis which assumes a geometrically perfect and infinitely rigid mechanism, leading to the theoretical contact line on the tooth surfaces. The resolution of the contact equations leads to the evaluation of STE $\delta(\theta)$ and load distribution $\mathbf{P}$ along the contact line.

In the case of planetary gears, equations of contact are solved taking account of all the meshes simultaneously [13]. First, a planet gear is defined as reference. Contact points for the other gears are deduced for each successive angular position of the reference gear, by taking into account planets mesh phasing condition [14], which depends on the number of planets and the number of tooth of the sun gear.

With knowledge of contacts lines location between the sun and the planets, the contacts lines between ring and planets occur is deduced from geometrical construction. For each angular position θ of the driving wheel, a kinematic analysis allows the resolution of contact equations of each meshes $j = 1 : 2N$:

$$\begin{cases} \mathbf{H_j P_j} = \delta_j(\theta)\mathbf{1} - e_j \\ \mathbf{P_j} = F_j \end{cases} \tag{1}$$

At each contact, the constraints are:

$$\begin{cases} -\mathbf{H_j P_j} + \delta_j(\theta)\mathbf{1} \leq e_j \\ \mathbf{P_j} \geq F_j \end{cases} \tag{2}$$

With $\mathbf{H_j}$ the compliance matrix of contact j, $\mathbf{P_j}$ the vector of the load distribution on the contact line j. δ_j is the STE at mesh j, which correspond to a linear displacement of the gear related to the pinion along the line of action. $\mathbf{e_j}$ is the vector of the initial gaps between the contact surfaces determined from tooth modifications and manufacturing errors, F_j is the static load oriented along the line of action, induced by the input torque, and $\mathbf{1}$ is a unitary vector used for dimensional consideration.

In the case of a planetary gear train with N planets, the contact equations are solved by taking into account the $2N$ meshes simultaneously. For each planets, the overall STE Δ is introduced from the sum of the local sun-planet δ_n and planet-ring gear $\delta_{n'}$ STE:

$$\Delta = \delta_n + \delta_{n'} \tag{3}$$

Unlike cylindrical gears with fixed axes for which the static force transmitted by the teeth is an initial input data of the problem, the distribution of the driving torque between the teeth of the planetary gear sets (and thus of the force transmitted by each gear) is an unknown of the problem. This distribution depends on the flexibility of the elements in contact, on the initial distances between the teeth induced by the microgeometrical gaps, and on the phase conditions between the gears: in out of phase systems, the contact can be established between two pairs of teeth for a gear (sun-planet or planet-ring), whereas it is established between a single pair of teeth for another gear of the same nature. Thus, complementary constraint are added, acting that the total force is transmitted by the sun to the three planets and from the three planets to the ring, and all the force received by a planet from the sun are transmitted to the ring, so:

$$F_T = \sum_{n=1}^{N} F_n = \sum_{n'=N+1}^{2N} F'_n, \qquad F_n = F'_n \tag{4}$$

Furthermore, the instantaneous local mesh stiffness is defined from the derivative of the force transmitted by the mesh, in relation to the static transmission error, for each angular position θ_s of the driving gear and for each meshes:

$$k_j(\theta_s) = \frac{\partial F_j}{\partial \delta_j}(\theta_s) \tag{5}$$

2.2 Dynamic response of the kinematic chain by a spectral iterative method

The numerical procedure proposed in this paper is based on several main assumptions. The ring gear is assumed to be axisymmetric. Thus, the modal basis is independent of the angular position of the planets. As a result, one modal basis is enough for solving equations at each angular position. Futhermore, the equations of motion are first solved in a reference frame associated with the carrier, which is equivalent to considering that the ring gear is moving in this reference frame. In practice, the modal basis is computed, considering the carrier fixed. Indeed, the maximum relative speed of the ring gear to the carrier is about 12 m/s. This represents about 0.2% of the pressure wave propagation speed of 5200 rpm. Except for very high speed applications, gyroscopic and centrifugal effects can be neglected. This assumption is verified by the complex modal basis calculation (see equations detailed Cooley and Parker [15]), here performed for a carrier rotational [0-120] rad/s speed range. The results obtained show a negligible impact of gyroscopic effects. Less than 1% difference in eigenfrequencies is observed. Mode shapes are almost identical.

The dynamic model chosen is based on a finite element discretisation of the transmission. The dynamic response of the kinematic chain (i.e. dynamic transmission errors and teeth dynamic loads) can directly be computed in the carrier reference frame. Thus, the equations of motion are expressed from the linearised gear force:

$$\mathbf{M}_{EF}\ddot{x} + \mathbf{C}_{EF}\dot{x} + \mathbf{K}_{EF}x + \sum_{j=1}^{2N} k_j(t)\mathbf{R}_j\mathbf{R}_j^T x = \sum_{j=1}^{2N} k_j(t)\mathbf{R}_j\mathbf{R}_j^T x_s(t) \tag{6}$$

With $\mathbf{M}_{EF}$ and $\mathbf{K}_{EF}$ respectively the mass and stiffness matrix from the finite element model and $\mathbf{C}$ the damping matrix taken into account a posteriori with the modal decoupling hypothesis, through an equivalent viscous damping coefficient for each mode. The elastic coupling between gears is introduced via the periodic mesh stiffnesses $k_j(t)$, which results from the limited development of the first-order of tooth dynamic load. This coupling, which acts along the lines of action, involves vectors of geometrical structure $\mathbf{R}_j$. The vector x_s corresponds to the static response generated by the driving and brake torque, assumed constant. $\mathbf{R}_j^T x$ is the dynamic transmission error and $\mathbf{R}_j^T x_s$ the static transmission error.

The finite element model of the planetary gear is presented in Figure 2. The housing (with ring gear directly manufactured on), gears, input and output shafts and the carrier are modelled using 3D elements. The bearings are modelled using axial and radial spring elements. Inertia are used to model the presence of a motor and a break. These boundary inertia are connected to the input and output shafts with torsional stiffnesses, modelling the flexible couplings on test bench. Mesh stiffnesses mean values are included in the finite elements model for elastic coupling of the gears.

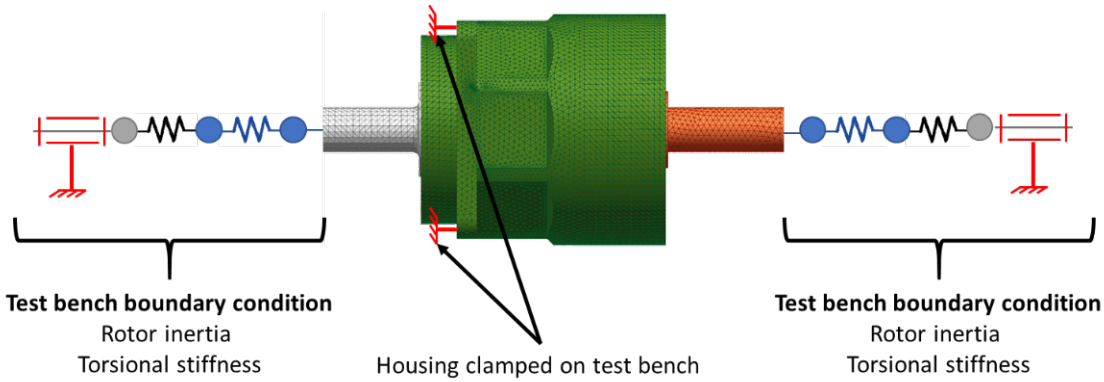

Figure 2: Finite elements model of the planetary gear

Time discretization methods lead to prohibitive calculation times. Low frequencies require long time period. High frequencies require fine time sampling. Hence, parametric equations of motions are solved using the spectral iterative method. The method is described in details in [7].It is based on the direct computation of the solutions in the spectral domain [7]. To this end, the matrix equation **??** is rewritten in the mean modal basis with $\mathbf{B}$, deduced from the eigenvalues problem $(\mathbf{K}_{EF} + \sum_{j=1}^{2N} k_j(t)\mathbf{R}_j\mathbf{R}_j^T) - \omega^2\mathbf{M}_{EF}$. By introducing the vector of modal coordinates $\mathbf{z}$ such as $\mathbf{x} = \mathbf{B}\,\mathbf{z}$, and thanks to the orthogonality property of the eigenmodes, equations in the modal basis can be written under the following index form:

$$\ddot{z}_k + 2\zeta_k\omega_k\dot{z}_k + \omega_k^2 z_k + \sum_{j=1}^{2N} g_j(t) r_{jk} \sum_{l=1}^{L} r_{jl} z_l = \sum_{j=1}^{2N} k_j(t) r_{jk} \delta_j^{(s)}(t) \tag{7}$$

In this equation, ζ_k is the equivalent viscous damping ratio of mode k, the term $r_{jk} = \mathbf{V}_k^T\mathbf{R}_j$ is the projected geometric structure vector in the modal basis and ωk is the k^{th} eigenvalues of the system. One should note that equations 7 remains coupled.

The first step of the iterative spectral method is based on solving the coupled equations of motion 7 in the spectral domain, retaining only the stationary part of the forced response of the system. Indeed, the parametric instabilities are characterised by an exponentially increasing free response. It is assumed that the viscous damping is sufficient to lie outside these regions of parametric instabilities and that it leads to an exponentially decreasing free response (asymptotic stability). Thus one can write:

$$Z_k(\omega) + H_k(\omega) \sum_{j=1}^{2N} G_j(\omega) r_{jk} \otimes \sum_{l=1}^{L} r_{jl} Z_l(\omega) = H_k(\omega) \sum_{j=1}^{2N} K_j(\omega) \otimes r_{jk} E_j^{(s)}(\omega) \tag{8}$$

where $Z_k(\omega)$, $G_j(\omega)$, $K_j(\omega)$ et $E_j^{(s)}(\omega)$ are respectively the Fourier transform of $z_k(t)$, $g_j(t)$, $k_j(t)$ et $\delta_j^{(s)}(t)$. The operator $\otimes$ represents the convolution product and $H_k(\omega)$ represents the complex frequency response function of the k mode, i.e.:

$$H_k(\omega) = \frac{1}{(\omega_k^2 - \omega^2 + 2i\zeta_k\omega_k\omega)} \tag{9}$$

After several judicious transformations, the iterative process can be written as follows:

$$E_i^{n+1}(\omega) = S_i(\omega) - \sum_{j=1}^{2N} T_{ij}(\omega) \cdot \left[G_j \otimes E_j^n \right](\omega) \tag{10}$$

with:

$$E_i^{(1)}(\omega) = S_i(\omega) \tag{11}$$

The stopping criterion is based on the relative difference between two iterations which is compared to a very small real ϵ, i.e. $\epsilon = 10^{-6}$:

$$\frac{||E_i^{n+1}(\omega) - E_i^n(\omega)||}{||E_i^{n+1}(\omega)||} < \epsilon \tag{12}$$

With the spectral iterative method, large systems of periodic differential equations can be solved, with minimal calculation times. Previous studies have demonstrated the validity of this method for multi-meshings systems [4], like planetary gear sets [16, 8].

2.3 Vibroacoustic response of the planetary gear housing

The dynamic response computation with the spectral iterative method allows to describe the vibratory state of any point of the finite element model. Even if this approach allows to directly compute the planetary gear chain dynamic response, one more step is needed to compute the response of any point on the ring gear. The carrier rotation modulates this response, as well as its rotational frequency [9]. The modulation is considered at posteriori, by taking into account the effect induced by the relative rotation between the observation point (fixed point located on the ring gear) and the meshes (attached to the carrier reference frame, as schematized in Figure 3.

The radial dynamic response of the cylindrical ring gear node n is noted $\tilde{u}_n(R, \psi_n, z, t)$, with R the external radius of the ring gear, z its axial position and t the time. The angular position of the observation point is noted ψ_n and in the carrier reference frame $(\overrightarrow{X}_c, \overrightarrow{Y_c}, \overrightarrow{Z_c})$ and φ_n in the housing frame $(\overrightarrow{X}_r, \overrightarrow{Y}_r, \overrightarrow{Z}_r)$. The dynamic responses are computed by considering the system under load, without any relative movement between the ring gear and the carrier. In practice, the dynamic response $u_n(r, \varphi_n, z, t)$ of a fixed point on the ring gear (in relative motion to the carrier) is measured.

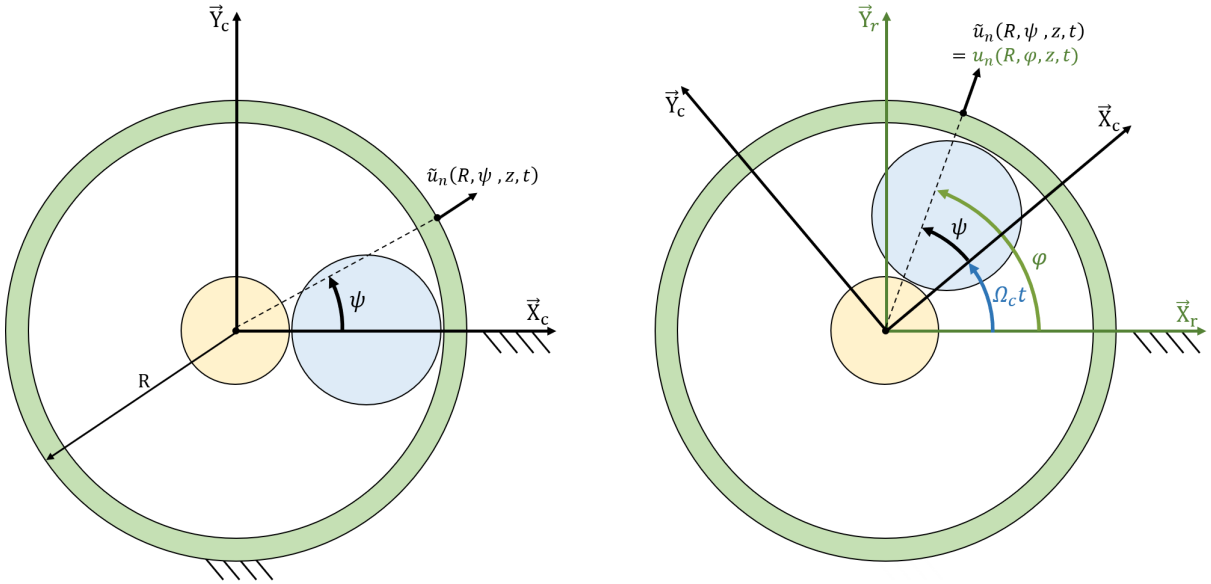

Figure 3: Model for the calculation of the dynamic response of a housing point

By properly choosing the initial position of the carrier at $t = 0$, one can write:

$$u_n(R,\varphi,z,t) = \tilde{u}_n(R,\psi,z,t) = \tilde{u}_n(R,\varphi_n - \Omega_c t,z,t) \tag{13}$$

Therefore, a point $B(R,\varphi_B,z_B)$ on the ring gear has a dynamic response out of phase from point $A(R,\varphi_A < \varphi_B, z_A = z_B)$ with a delay of:

$$t_B - t_A = -\frac{\varphi_B - \varphi_A}{\Omega_c} \tag{14}$$

With Ω_c the carrier angular rotational speed. Based on this description, we proposed to access the dynamic response $u_n(R,\varphi_n,z,t)$, a linear temporal interpolation between the responses $\tilde{u}_n(R,\psi_i,z,t)$ is build. This interpolation is based on the main assumptions previously described in this paper, and more particularly one on those stating on the axisymmetric condition of the ring gear and the invariability of the modal basis whatever the position of the planet axis. On the time interval $t_i \leq t \leq t_{i+1}$, the following linear time interpolation scheme can be written:

$$u_n(R,\varphi_n,z,t) = \frac{\tilde{u}_n(R,\varphi_n - \Omega_c t_i,z,t)(t_{i+1} - t) + \tilde{u}_n(R,\varphi_n - \Omega_c t_{i+1},z,t)(t - t_i)}{(t_{i+1} - t_i)} \tag{15}$$

From a practical point a view, the iterative spectral method gives access to the answers in discrete nodes of the ring gear $\tilde{u}_i(R,\psi = \psi_i,z,t)$, $i = 1$ à P (54 points considered in our application). Thus, the answer $u_n(R,\varphi_n,z,t))$ is evaluated at the node of the model identified by $\varphi_k = 2k\pi/P$ $(k = 0,1,...,P-1)$. By properly choose time interval and ring gear discretization, and by considering that all the nodes on a peripheral circle of the ring gear have an identical response to within one phase, the dynamics response of the node identified by the angle $\varphi_k = 0$ at time t is equal to:

$$\begin{aligned} u_n(R,0,z,t) = \Omega_{kc} \sum_{i=0}^{P-1} \left[\tilde{u}_i(R,\frac{2\pi(P-i)}{P},z,t)(t_{i+1} - t) + \tilde{u}_i(R,\frac{2\pi(P-1-i)}{P},z,t)(t - t_i) \right] \\ \times \mathrm{H}(t - t_{i+1})\mathrm{H}(t_i - t) \end{aligned} \tag{16}$$

with H the Heaviside function.

3 Numerical results

The studied planetary gear set has the sun as its input and the carrier as the output, so that the ring gear remains fixed. Its main characteristic are given in Table 1.

Table 1: Main characteristics of the studied planetary gear set

	Sun	Planets	Ring
Number of planets N	3		
Number of teeth Z	27	40	108
Module m_o	1.5		
Pressure angle α (°)	20		
Helix angle β (°)	0		
Transmission ratio 1	5		

Based on the gear module, the maximum permissible input torque is 156 Nm, i.e. a breaking torque of $780\ Nm$. The nominal input operating speed of the planetary gear is $1500\ rpm$, with a maximum operating speed of $3500\ rpm$. A test bench is instrumented to allow the vibratory and acoustical characterization of planetary gear sets, such as instantaneous rotational speed of input and output gearbox shafts, the radial acceleration of planetary gear housing and the radiated noise. This allows direct comparison with numerical results at each computational step [17]. In this paper, the focus will be on the radial acceleration of planetary gear housing to validated the capacity of the proposed method to access housing modulated vibratory response.
In this application, the applied motor torque is equal of $100\ Nm$ and the excitation spectra (STE and mesh stiffnesses fluctuations) include the first six harmonics of the mesh frequency. The modal equivalent modal damping rate is chosen to be uniform across all modes and is equal to 5%. Finally, the ring gear is supposed to be perfectly cylindrical (and so perfectly axisymmetric). Indeed, the small variation of ring gear thickness observed on the real system induced negligible deviation in modal basis and dynamic response.
Two test cases will be discussed. First, the dynamic response at low speed ($250\ rpm$) is computed, when the harmonics of the mesh frequency are lower than the eigenfrequencies of the system. Then, the dynamic response at high speed ($3100\,rpm$) is computed, when the harmonics of the mesh frequency may coincide with frequencies for which the ring gear exhibits significant operational dynamic deformation. Hight speed measurement result are finally discussed to evaluate the relevance of the proposal numerical model. For both results, special attention is given to modulation shape of the radial acceleration of housing (ring gear) over a complete carrier rotational period T_c.

3.1 Dynamic response of the ring gear at low speed

The dynamic response of the ring gear is evaluated for a sun rotation speed of $250\,rpm$. The mesh frequency is then equal to $f_m = 90\ Hz$. At low rotational speeds, the first harmonics of the mesh frequency are lower than the natural frequencies of the system, thus the ring gear responds on its static deformation, i.e. the static contribution of the modes. This static deformation is calculated by considering unitary forces directed along the lines of action, as shown on Figure 4(a). This induced a deformation composed of six lobes, that can be express as a function A_s describing the amplitude of the static deformation in polar coordinate, as shown in Figure 4(b).Figure 4(c, d) show temporal response of the radial acceleration of the ring gear dynamic response for a complete carrier rotation T_c, for purely harmonic excitation at the mesh frequency H_{108}, and its associated spectrum, plotted as a function of the output frequency order (carrier frequency) around the range of order from 100 to 116. If the model was perfectly axisymmetric, one would observed a periodic temporal response with a period equal to $T_c/3$, corresponding to the periodic passage of the three planets. In our application test case, ones can observed a slightly different behaviour because the system isn't perfectly axisymmetric. The spectrum has a moderate amplitude at the mesh frequency f_m. The dominant lines are the sidebands at $f_m \pm N$, where N is the number of planets. Ones also observe that the envelope of the temporal response has six lobes, reflecting the amplitude modulation phenomena. Detailed analysis of the time response envelope for this operating regime allows a link to be established between

its amplitude and the static deformation of the ring gear. This result shows a different behaviour from those usually found in the literature with simplified formulation, when the modulated signal is only considered as a growth/decay of the vibratory amplitude as one planet approaches or moves away, which would lead for our application case to a three-lobe signal [9].

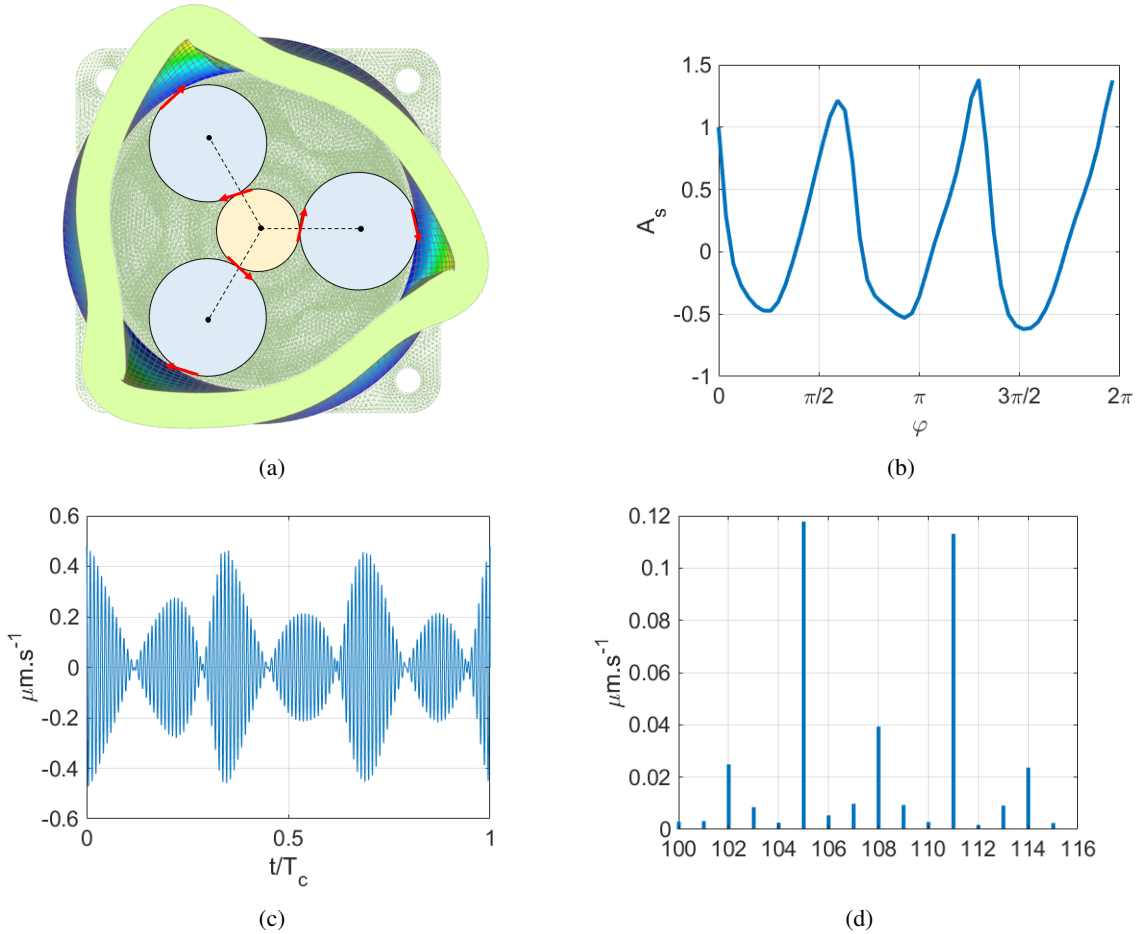

Figure 4: (a) Static deformation of the ring gear induced by unitary force oriented along the line of action. (b) Adimensionnal amplitude of the static deformation in polar coordinate. (c) Temporal response of the radial acceleration of the ring gear dynamic response for a complete carrier rotation. (d) Amplitude spectra in function of the mesh frequency order.

3.2 Dynamic response of the ring gear at high speed

For high operating regimes, the higher order harmonics of the mesh frequency are high enough to coincide with the eigenmodes of the system. The dynamic response of the ring gear is considered for a sun rotation speed equal to $3100\ rpm$. The mesh frequency is then equal to $1116\ Hz$.

Figure 5(a) shows the time evolution of the modulated dynamic response of the ring gear and figure 5(d) the amplitude spectrum, plotted as a function of the carrier frequency order. An amplification of the fifth and sixth harmonics of the mesh frequency is observed, corresponding to an excitation of the modes around 5580 and $6695\ Hz$. We propose to analyse the dynamic response extracted around these two harmonics. Figures 5(b, c) show the corresponding temporal evolutions. Figures 5(e, f) show the amplitude spectra associated, plotted as a function of the output frequency order (carrier frequency) around the order range from 532 to 548 on one hand, and from 640 to 656 on the other hand. As with the low-speed dynamic response, the amplitude of the harmonics of the mesh frequency H_{540} and H_{648} are lower than that of the sidebands at $H_{108}i \pm NH_1$ and $H_{108}i \pm kH_1$, with N the number of planets and k an integer. The shape of the envelope of the temporal dynamic responses is complex and

depends on the frequency of observation, and so on the modes exited. Futhermore, the number of lobes seems to be driven by the difference between the two most significant sidebands. For example, we observe six lobes for the dynamic response around the fifth harmonic (driven by the sidebands $H_{537}$and H_{543}), while we observe four lobes for the dynamic response around the sixth harmonic (driven by the sidebands H_{645} andH_{649}). Moreover, one should observed that the periodic temporal response with a period equal to $T_c/3$ observed at low speed is no longer representative of the modulated signal. Here again, numerical results show a behaviour far to be representative to a three lobe temporal evolution of the ring gear radial acceleration.

In order to validate the relevance of the numerical results from the new method proposed in this paper, experimental results for hight rotational speed are analysed. Here, the complexity lies in the quality of the tunning of the numerical model compared to measurement. Indeed, a frequency shift of the modes, a poorly estimated modal damping or geometrical simplifications of the numerical model make it difficult to choose the rotational speed which would give us exactly the same operational deformation shape both in simulation and in measurement. In the present paper, numerical rotational speed and measurement one are choose to give a qualitative comparison of the phenomena that drive the modulated vibratory response of a planetary gearbox without trying an quantitative comparison.

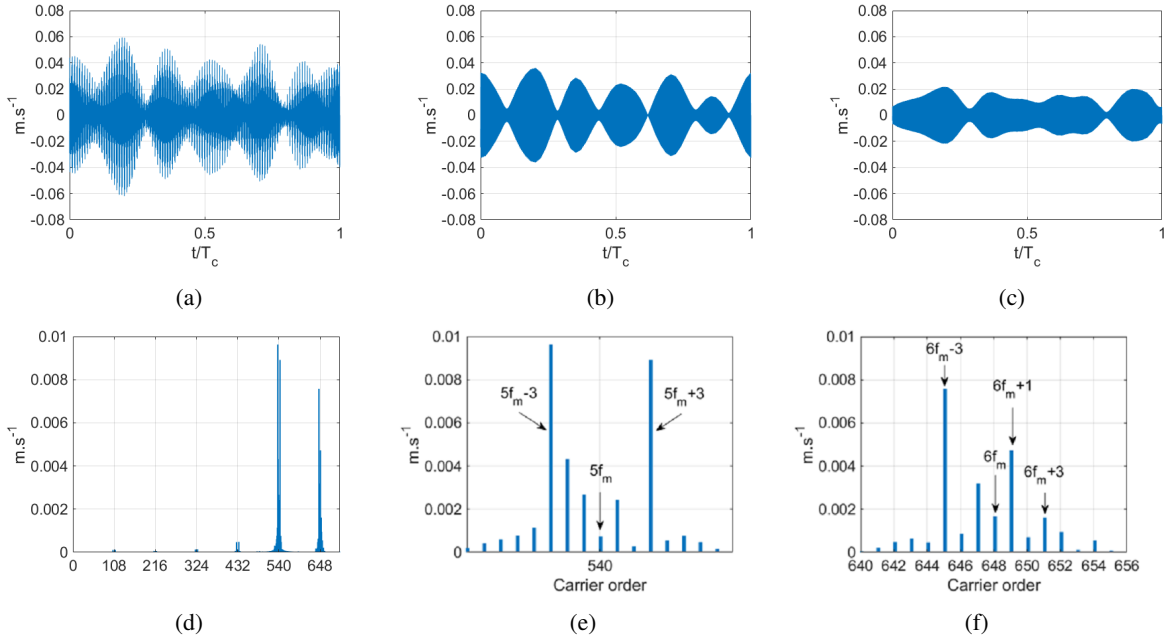

Figure 5: (a) Temporal evolution of the overall ring gear dynamic response. (b) Temporal evolution of the ring gear dynamic response on the order range [532 548]. (c) Temporal evolution of the ring gear dynamic response on the order range [640 656]. (d) Amplitude spectra of the overall ring gear dynamic response. (e) Amplitude spectra of the ring gear dynamic response on the order range [532 548]. (f) Amplitude spectra of the ring gear dynamic response on the order range [640 656].

The quasi-axisymmetric boundary conditions of the ring gear are experimentally well verified. Thus, the experimental results presented below are the algebraic mean value of the levels measured by the different accelerometers. The global level measured experimentally includes phenomena not considered in the numerical model (friction, assembly errors, etc.). For the comparison between computation and measurement, the dynamic responses are extracted around the first four harmonic of the mesh frequency, included sidebands induced by carrier rotation.
As an example, the experimental dynamic response measured at 800 and at $2200\,rpm$ is presented in Figure 6(a, b) retaining only the frequency contributions on the order band $H_{108}i \pm NH_1$, (i=1, 2, ...6), N being the number of planets. We observe a signal with a complex modulation, with a high number of sidebands at the mesh frequency. Qualitatively, one observes 6 lobes at 800 and $2200\,rpm$. The zero crossing of the dynamic response is only visible when the dynamic response is plotted by only retaining an order band around a particular harmonic (see 6(c, d)). It is also observed in this figure that the dynamic response at 800 rpm, retaining only the frequency contributions on

the order band $H_{216} \pm 3H_1$, shows a number of lobes equal to 5, whereas at 2 200, by retaining only the frequency contributions on the order band $H_{432} \pm 3H_1$, we observe 6 lobes. The experimental observations are qualitatively consistent with what is observed numerically (see the digital application).

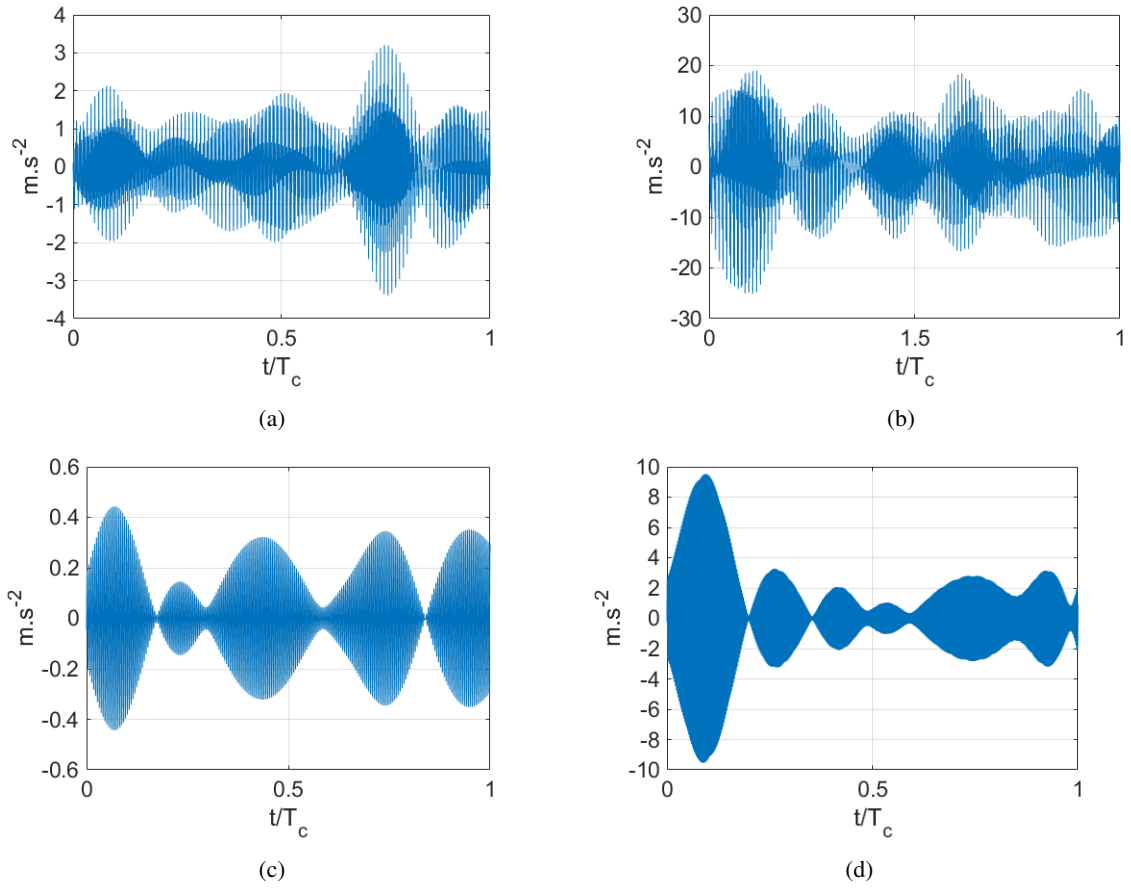

Figure 6: (a) Ring gear dynamic response measured at 800 rpm. (b) Ring gear dynamic response measured at 2200 rpm. (c) Ring gear dynamic response measured at 800 rpm, order 2 of the mesh frequency. (d) Ring gear dynamic response measured at 2200 rpm, order 4 of the mesh frequency

The observation of number of lobes performed here illustrated than conventional simplified analytical formulation to modulate the dynamic response of the ring gear failed to be representative of the complexity of this phenomena. By integrating modal behaviour in the modulation numerical model, based on non-modulated initial signal, one can reach a richer dynamic response, where an acoustic transcription of which would be closer to the real sound of the planetary gearbox.

4 Conclusion

The modulated dynamic response of the ring gear of the planetary gear is evaluated using an original approach which considers its operational deformation for each operating regime. Analysis of numerical and experimental results is based one observation of the number of lobes over a complete carrier rotational period. If this analysis don't statued on the quantitative capability of the propose model, it shows how taking into account the modal behaviour of the system during converting a non-modulated signal to a modulated one can reach a more complex dynamic response, correlated to experimental observation.
The numerical results show that for low sun rotation speeds, the envelope of the dynamic response of the ring gear is driven by the static deformation of the planetary gear. At higher rotational speeds, when the harmonics of the mesh frequency are high enough to coincide with the eigenmodes of the system, the envelope of the modulated dynamic response is driven by the operational deformation of the ring gear. Measurement investigations confirm that the modulated dynamic response of the ring gear can presented more lobes than the number of planet.

The used of the spectral iterative method offer low computational time and give the opportunity to extract the dynamic response at several points to construct a refine modulated response. It also offer the opportunity to performed parametrical simulation, key of a better understanding of ring gear modulation dynamic responses effects and improving numerical model.

Acknowledgment

References

[1] D. B. Welbourn, "FUNDAMENTAL KNOWLEDGE OF GEAR NOISE: A SURVEY," 1979.

[2] S. L. Harris, "Dynamic Loads on the Teeth of Spur Gears," *Proceedings of the Institution of Mechanical Engineers*, vol. 172, pp. 87–112, June 1958.

[3] E. Rigaud and J. Sabot, "Effect of Elasticity of Shafts, Bearings, Casing and Couplings on the Critical Rotational Speeds of a Gearbox," Jan. 2007. arXiv:physics/0701038.

[4] A. Carbonelli, E. Rigaud, and J. Perret-Liaudet, "Vibro-Acoustic Analysis of Geared Systems—Predicting and Controlling the Whining Noise," in *Automotive NVH Technology* (A. Fuchs, E. Nijman, and H.-H. Priebsch, eds.), pp. 63–79, Cham: Springer International Publishing, 2016. Series Title: SpringerBriefs in Applied Sciences and Technology.

[5] P. D. McFadden and J. D. Smith, "An Explanation for the Asymmetry of the Modulation Sidebands about the Tooth Meshing Frequency in Epicyclic Gear Vibration," *Proceedings of the Institution of Mechanical Engineers, Part C: Journal of Mechanical Engineering Science*, vol. 199, pp. 65–70, Jan. 1985.

[6] J. McNames, "Fourier Series Analysis of Epicyclic Gearbox Vibration," *Journal of Vibration and Acoustics*, vol. 124, pp. 150–153, Jan. 2002.

[7] J. Perret-Liaudet, "AN ORIGINAL METHOD FOR COMPUTING THE RESPONSE OF A PARAMETRICALLY EXCITED FORCED SYSTEM," *Journal of Sound and Vibration*, vol. 196, pp. 165–177, Sept. 1996.

[8] J. Neufond, E. Denimal, E. Rigaud, J. Perret-Liaudet, and A. Carbonelli, "Whining noise computation of a planetary gear set induced by the multi-mesh excitations," *Proceedings of the Institution of Mechanical Engineers, Part C: Journal of Mechanical Engineering Science*, vol. 233, pp. 7236–7245, Nov. 2019.

[9] M. Inalpolat and A. Kahraman, "A theoretical and experimental investigation of modulation sidebands of planetary gear sets," *Journal of Sound and Vibration*, vol. 323, pp. 677–696, June 2009.

[10] D. F. Plöger, C. Fischer, and S. Rinderknecht, "Linking the modulation of gear mesh vibration in planetary gearboxes to manufacturing deviations," *Mechanical Systems and Signal Processing*, vol. 155, p. 107554, June 2021.

[11] M. S. Tavakoli and D. R. Houser, "Optimum Profile Modifications for the Minimization of Static Transmission Errors of Spur Gears," *Journal of Mechanisms, Transmissions, and Automation in Design*, vol. 108, pp. 86–94, Mar. 1986.

[12] E. Rigaud and D. Barday, "Modelling and Analysis of Static Transmission Error. Effect of Wheel Body Deformation and Interactions between Adjacent Loaded Teeth," 1999.

[13] S.-J. Tsai, G.-L. Huang, and S.-Y. Ye, "Gear meshing analysis of planetary gear sets with a floating sun gear," *Mechanism and Machine Theory*, vol. 84, pp. 145–163, Feb. 2015.

[14] R. G. Parker and J. Lin, "Mesh Phasing Relationships in Planetary and Epicyclic Gears," *ASME*, vol. 2003, pp. 525–534, 2003.

[15] C. G. Cooley and R. G. Parker, "Vibration Properties of High-Speed Planetary Gears With Gyroscopic Effects," *Journal of Vibration and Acoustics*, vol. 134, p. 061014, Oct. 2012.

[16] J. Neufond, Y. Xu, J. Perret-Liaudet, and E. Rigaud, "The iterative spectral method for computing the planetary gear dynamic response," in *International Conference on Gears 2017* (VDI Wissensforum GmbH, ed.), pp. 209–218, VDI Verlag, 2017.

[17] J. Neufond, E. Rigaud, J. Perret-Liaudet, and A. Carbonelli, "Influence of tooth profile modifications on the dynamic behavior of a planetary gear set – Experimental investigation and numerical validation for different amplitudes of tooth profile modifications," in *International Conference on Gears 2019* (VDI Wissensforum GmbH, ed.), pp. 765–776, VDI Verlag, 2019.

15th SIRM – European Conference on Rotordynamics,
Darmstadt, Germany, 22nd – 24th February 2023

Thrust collar induced vibrations of a pinion shaft in an integral gear unit

Bastian Pfau [1]

[1] VOITH Turbo, 74564, Crailsheim, Germany, bastian.pfau@voith.com

Abstract

Thrust collars are an established machine element in integral gear units to transmit axial forces between wheel and pinion shaft(s).

In this paper it is shown that the design of the thrust collar – especially the clearance – can cause a resonance phenomenon, at which the axial and/or yaw motion of the gear wheel is coupled with the lateral motion of a pinion shaft. An excitation of this specific motion can for example be induced by an axial run-out of the thrust collars contact face. As a result, unwanted lateral vibrations are observed, at first in the mechanical running test of the gear unit.

For the investigations in this paper, a multi-body simulation model is used. In addition to the simulation, a phenomenological comparison with results from the mechanical running test is made.

1 Introduction

Thrust collars are widely used in integral gear units. They transmit axial forces, which arise due to thrust forces of impellers as well as due to helical gearings, from the pinion shaft(s) to the wheel shaft via a thin lubrication film. This lubrication film arises due to the rotation of the shafts. In comparison to a design with conventional thrust bearings, thrust collars generate less power loss due to significant lower difference speeds in the lubrication area. Thus, they lead to a higher efficiency of the gear box. Figure 1 shows both technical solutions.

Various authors made investigations on the operating characteristics of thrust collars using different model depths, for example SIMON [11], THODEN [12], HESS and LOHRENGEL [7] and SAN ANDRÉS, et. al. [10]. In the latter one, which is using a thermal-mechanical approach, also stiffness and damping coefficients were derived. CABLE et al. investigated in [1], on the base of the model presented in [10], the influence of shaft misalignment on pressure distribution as well as on stiffness and damping coefficients.

There are also some few investigations on the dynamics of thrust collars in integral gear units from the recent years. CHILDS and CRANDALL showed in [2], that the bull gear run-out can lead to subsynchronous vibrations of a pinion shaft. For this, they developed an analytical model of a simple rotor and showed, that the thrust collars oil film couples the motion of bull gear and pinion shaft. Meshing forces are not considered in this model.

HEINRICH and LOHRENGEL investigated in [6], experimentally and theoretically, a thrust collar in a parallel shaft gear box with focus on improved acoustics. In their mechanical model, also meshing forces are considered.

Taking into account the dates of publication, this short literature study shows that the dynamic behavior of systems with thrust collars is an upcoming topic in the research of turbomachinery/gear boxes.

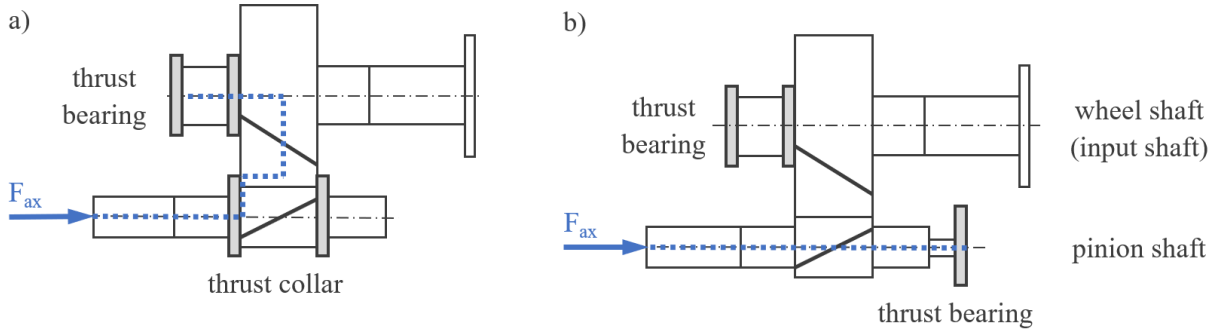

Figure 1: a) thrust collar design and b) conventional thrust bearing design

see also figure 2. The rotational frequency of the pinion shaft itself is in the range of 240 Hz, so the observed phenomenon is a kind of subsynchronous vibration. Even if the amplitudes of these frequency components are relatively low, they have still a potential for improvement. In the present case, the thrust collar and its characteristics played a crucial role for the presence of these vibrations.

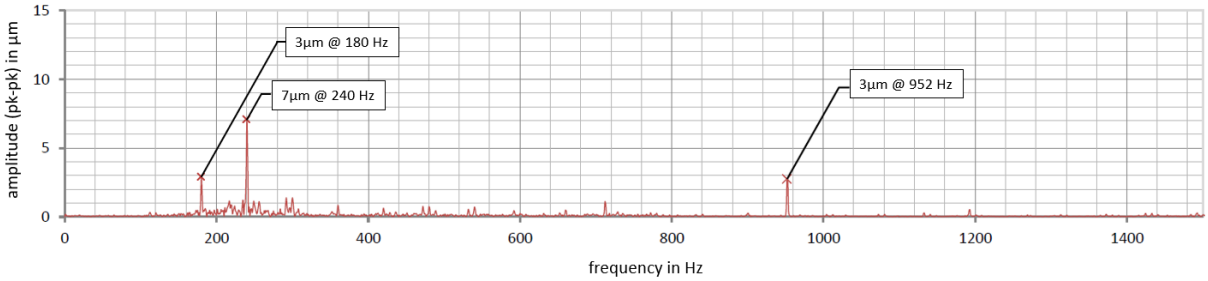

Figure 2: FFT of measured lateral vibrations at one of the pinion shafts with dominant components at 180 Hz and 240 Hz (3x and 4x of the wheel shafts rotational speed)

2 Simulation Model

For a better understanding of the observed phenomenon of subsynchronous vibrations, a simulation model is set up. Here, a multi-body simulation tool (Dassault Systèmes/Simpack [3]) is used. In this manner, a general investigation of the dynamical behavior of the gear box can be made and forces between different bodies, which are often a crucial point, can be easily modelled with different levels of complexity.

The simulation model is shown in figure 3. It consists mainly of three bodies: one wheel shaft in the centre of the gear box and two pinion shafts, which are at the left respectively right side of the wheel shaft. The housing, which is shown as transparent in figure 3, is modelled as rigid body with a fixed support. Thus, it has no influence on the simulation results. It has the purpose for a better overview here.

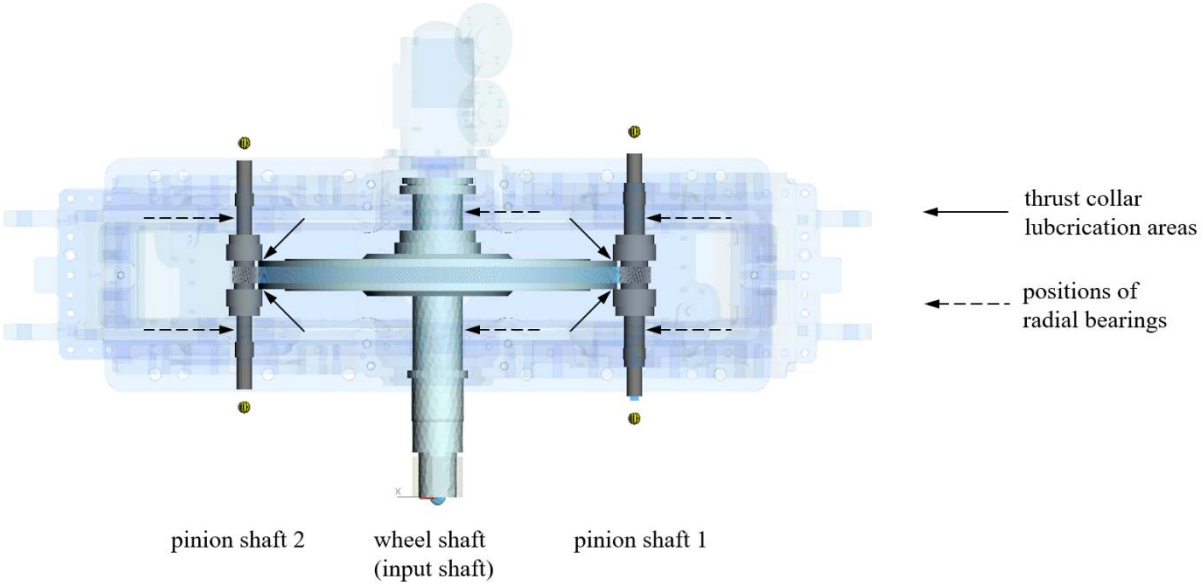

Figure 3: Simulation model (top view)

For all shafts, the rigid body motion is not constrained. So, they can move completely free in space. Further degrees of freedom arise due to modelling of the pinion shafts as flexible bodies. Here, all modes up to a frequency of $1.5 \cdot 240$ Hz are considered in the model. This is realized by the use of a substructuring technique implemented in SIMPACK. The wheel shaft is modelled as rigid body.

The shafts are running in fluid film bearings. A connection between wheel shaft and pinion shafts is given due to the toothing as well as due to the thrust collars. The related models for all these forces are described separately in the following sections. The system is driven by a torque acting at the front end of the wheel shaft.

2.1 Thrust collar

The forces in the thrust collar are modelled by solving the REYNOLDS equation of lubrication theory in every time step. This is a comfortable way, to also consider a tilting motion of the concerned shafts and to take into account possibly present non-linear effects.

Due to the contact angle of the thrust collar faces, see also figure 4 a), a converging lubrication gap $h(x, y)$ is present, so that a pressure build-up takes place. The characteristics of a thrust collar are similar to a journal bearing. They depend mainly on geometry, oil viscosity of the lubricant, load, circumferential speeds and especially on the clearance between pinion shaft and wheel shaft, here denoted as h_0.

In the investigations here it is assumed, that the viscosity of the oil is constant in the lubrication gap. As a consequence, the REYNOLDS equation is not coupled with the thermal energy transport equation and can be solved stand-alone. Furthermore, it is assumed that always a sufficient oil flow at the entry of the lubrication gap is present. In the gear box, this is ensured by a spray bar. Figure 4 b) shows an exemplary pressure distribution as a solution of the REYNOLDS equation.

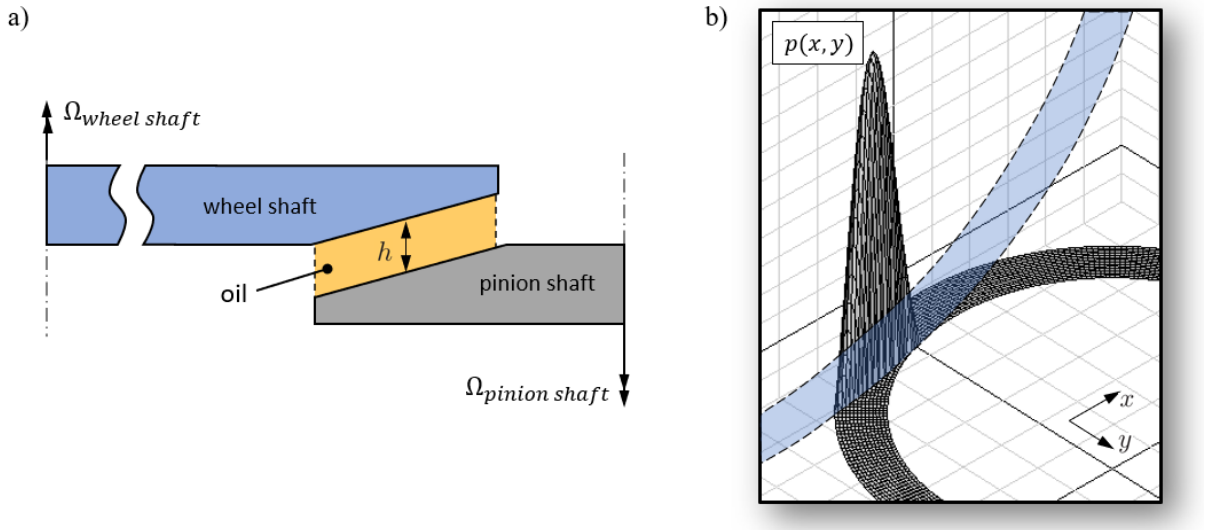

Figure 4: a) schematic sketch of the lubrication zone and b) exemplary pressure distribution

2.2 Gear mesh

For all gear meshing forces a linear spring-dashpot model is used. The values for stiffness and damping coefficients are calculated a priori. The stiffness coefficient, usually denoted as c_γ, is calculated on base of ISO 6336, [8]. For the damping coefficient the model from GERBER is used, [4].

2.3 Bearings

The gear box contains six radial bearings, which are all fluid film bearings. The bearings of the wheel shaft are fixed geometry bearings, while the bearings for the pinion shafts are tilting pad journal bearings, what is typical for these kind of gear boxes. Furthermore, one thrust bearing supports the wheel shaft in the axial direction.

For all these bearings a linear approach using stiffness and damping matrices, respectively scalar values for the thrust bearing, is applied. For the calculation of the related coefficients the software COMBROS R/A is used, [5,9].

3 Simulation Results

3.1 Systematic investigation of the system behavior

For a better understanding of the system dynamics, a calculation of the transmission behavior is performed. Due to the observance of frequency components, which are related to the rotational frequency of the wheel shaft, this body is used to apply an excitation $p(t)$. For this purpose, the axial motion of the driven end of the wheel shaft

Because of manufacturing tolerances, the thrust collar clearance h_0 fluctuates in a certain range, what influences the dynamical behavior of the system significantly. Figure 5 shows the magnitude of $H(\Omega)$ for different clearances $h_{0,i}$. Following circumstance is to observe: For $h_{0,1}$, thus a relatively low thrust collar clearance, a resonance phenomenon in the region around 220 Hz is present. And the larger the thrust collar clearance is, the lower is the related resonance frequency. In addition, the maximum of $|H(\Omega)|$ is lower. The reason for these effects is the change of the lubrication films stiffness and damping characteristic in dependence of the clearance.

The simulation shows that the lateral motion the pinion shaft is coupled with the axial motion of the wheel shaft. The reason for this is, that the force acting on the thrust collar of the pinion shaft has a lever arm around the shaft's centre of mass. This leads to a tilting motion of the pinion shaft, what is registered by the displacement sensors. Even if the "amplification" is below the value of 1: If an excitation is present, it can lead to the vibration phenomenon shown in figure 2.

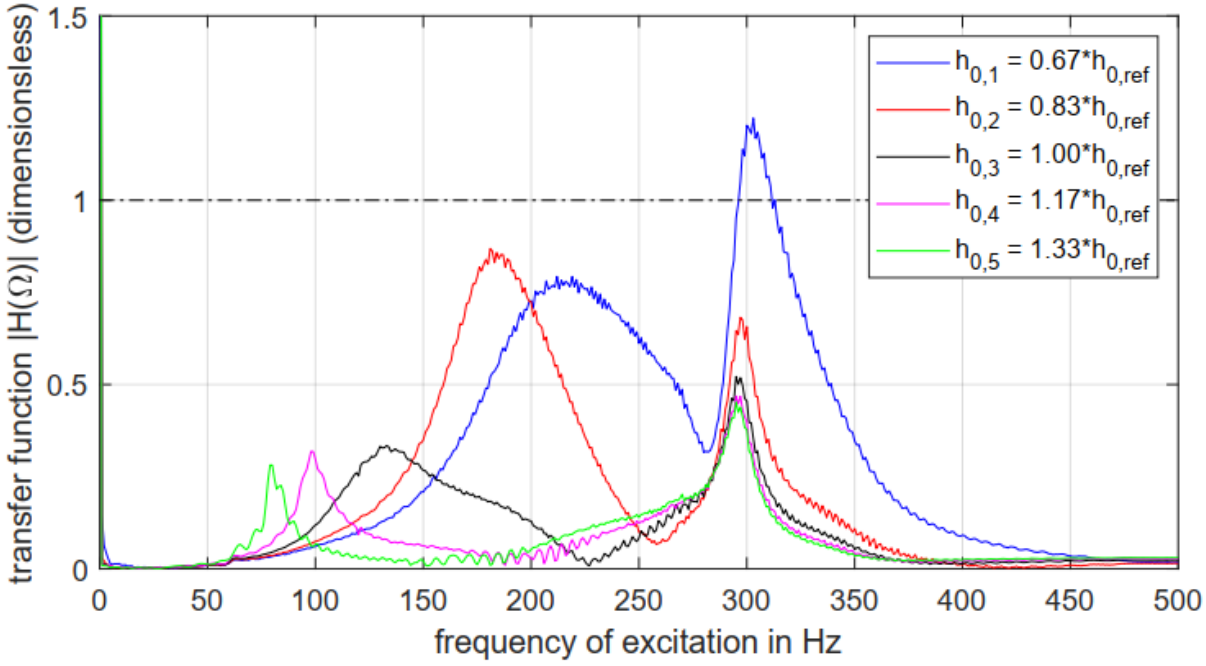

Figure 5: transmission behavior between axial motion of the wheel shaft and radial motion of pinion shaft 2 in dependence of the thrust collar clearance

The resonance in the vicinity of 300 Hz, whose frequency is practically not changing in dependence of the thrust collar clearance, belongs to a bend-critical speed and was not excited during the mechanical running test.

3.2 Exemplary result for a gear wheel with a manufacturing defect at the thrust collars face

In chapter 3.1. it is shown that an axial motion of the gear wheel can lead to a lateral motion of the pinion shaft. In the gear box, a similar excitation is present, when the thrust collars face at the gear wheel has an axial run-out or more precisely: a flatness imperfection. Such imperfections can arise in the manufacturing process and can have specific orders.

As an exemplary calculation a gear wheel with different flatness imperfections from first to fourth order, each with a magnitude of 15µm (pk-pk) at one side of the gear wheel only, is simulated. Figure 6 shows as an example a flatness imperfection of third order. For the simulations, a clearance of $h_{0,1}$ (see also figure 5) is used.

An evaluation of the simulations results is made by analysing the system's response when a steady-state condition is reached. Like in section 3.1, the deflection of pinion shaft 2 near the motor side bearing is used for the analysis. The simulations yield, that the system is responding only with the related frequency of the excited order (60 Hz at 1st order, 120 Hz at 2nd order, etc.). In other words: The system behaves linear regarding this point.

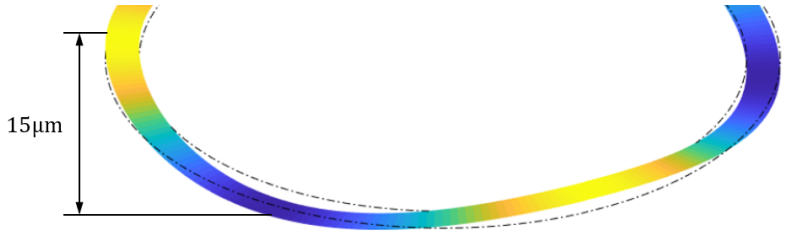

Figure 6: Illustration of a flatness imperfection of third order

Table 1 is listing the response amplitudes. As expected from figure 5, the response amplitudes at 180 Hz and 240 Hz are the two largest ones.

Table 1: Simulation results with different orders of flatness imperfection

Order of flatness imperfection	Response at pinion shaft 2 @ related frequency
1st	0.1 µm (pk-pk) @ 60 Hz
2nd	0.4 µm (pk-pk) @ 120 Hz
3rd	3.1 µm (pk-pk) @ 180 Hz
4th	5.2 µm (pk-pk) @ 240 Hz

This shows that a flatness imperfection of the gear wheel's thrust collar face can excite lateral vibrations of a pinion shaft. However, in these simulations an imperfection was admitted only to one side of the gear wheel. If both sides have an imperfection, the response amplitude can be higher or lower, according to the particular magnitudes and the relative phases of the imperfections. And looking at a manufactured gear wheel, flatness imperfections of all orders will be present, more or less in magnitude. The system will response accordingly to that excitation, see also figure 2.

4 Conclusion

This paper shows with the use of a multi-body simulation model a coupled vibration phenomenon between wheel and pinion shaft in an integral gear unit. The crucial role hereby plays the thrust collar and its design parameters – especially the clearance – which can lead to a resonance phenomenon. An axial run-out of the thrust collars face can then act as excitation. The resulting subsynchronous vibration can for example be lowered by a rework of the wheel shaft's thrust collar face. This leads to two positive effects: The manufacturing defect – and therewith the excitation – is brought to a lower level. Furthermore, the thrust collar clearance is increased, leading to an improved dynamical behavior.

However, there are under circumstances more mechanism of excitation, e.g. due to pitch errors of the toothing. This can be a topic for investigations in the future.

Acknowledgement

The author likes to thank Mr Axel Vötterl for the fruitful discussions on this topic. Equally important is the role of the VOITH company, giving the possibility for this work.

References

[1] Cable T.A., San Andrés, L., Wygant, K. (2016): On the Predicted Effect of Angular Misalignment on the Performance of Oil Lubricated Thrust Collars in Integrally Geared Compressors. *J. of Engineering for Gas Turbines and Power* 139(4), pp. 042503-1-11.

[2] Childs, D., Crandall, A. (2018): A Simple (1-Flexible Rotor) Model That Shows Bull Gear Runout As a Source of Subsynchronous, Lateral, Vibration in Integrally Geared Compressor (IGC) Pinions. *Proceedings of ASME Turbo Expo*.

[3] Dassault Systèmes: SIMPACK 2021.1 Documentation.

[4] Gerber, H. (1984): *Innere dynamische Zusatzkräfte bei Stirnradgetrieben.* Dissertation, TU München.

Ingenieurwes. (86), pp. 161–172.

[7] Heß, M., Lohrengel, A. (2017): Thrust cone bearings provide increased efficiency for helical gear units at moderate speed levels. *Forsch. Ingenieurwes.* (81), pp. 135–143.

[8] ISO 6336-1 (1996): Calculation of load capacity of spur and helical gears.

[9] Kraft, C. (2012): Verbesserte Axialgleitlagerberechnung: Hochbelastete, schnelllaufende Axialgleitlager in einfacher und doppeltwirkender Anordnung unter Berücksichtigung statischer Spurscheibenverkantung. *FVV*, 1019 – 2013.

[10] San Andrés, L., Cable T.A., Wygant, K., Morton, A. (2015): On the Predicted Performance of Oil Lubricated Thrust Collars in Integrally Geared Compressors. *J. Eng. Gas Turbines Power*, 137(5).

[11] Simon, V. (1984): Thermal Elastohydrodynamic Lubrication of Rider Rings, *ASME Journal of Tribology*, 106, pp. 492-498.

[12] Thoden, D. (2006): Elasto-hydrodynamische Schmierung von Druckkämmen. *Mitteilungen aus dem Institut für Maschinenwesen der TU Clausthal*, 31, pp. 23-26.

15th SIRM – European Conference on Rotordynamics,
Darmstadt, Germany, 22nd – 24th February 2023

Coupled torsional–bending vibration analysis of the ship's propulsion shaft with a residual shaft bow

Sanjin Braut [1], Alen Marijančević [1], Roberto Žigulić [1], Ante Skoblar [1]

[1] Faculty of Engineering, University of Rijeka, HR-51000, Rijeka, Croatia,
sbraut@riteh.hr, alen.marijancevic@riteh.hr, zigulic@riteh.hr, askoblar@riteh.hr

Abstract

The paper describes a coupled torsional-bending vibration model of a ship's propulsion shaft system with a residual shaft bow. The developed model presents an extension of the Jeffcott rotor model. In order to test the numerical model and determine the coupled torsional-bending vibrations, several cases were analyzed. First, a reference case corresponding to a fully axisymmetric ship propulsion system is set up. Then a shaft bow was introduced, and the influence of the constant radial force in the vertical direction at the position of the stern bearing was analyzed. Such conditions exist when a ship navigates on a calm sea under a partial or fully loaded hull. Finally, the case of sailing on a rough sea is analyzed when the propeller racing occurs due to the stern lifting out of the sea. Based on the results of numerical analysis, it was found that the proposed model well describes the coupling of torsional and bending vibrations of the propulsion shaft system with residual shaft bow. The aim of the research is to prepare input data for estimating the fatigue life of the propulsion shafting system of ships sailing at slow steaming speed for low carbon shipping.

1 Introduction

The ship's propulsion system suffers various complex loads during operation. The shaft line is usually loaded externally due to combination of radial forces that represent reactions in the bearings and the torque variations caused by the torsional vibration applicable for continuous operation, basically due to engine firing pulses [1, 2].

A proper consideration of the single and coupled vibration modes of the propeller shaft, including torsional, longitudinal, and transverse vibrations is important to ensure safe ship propulsion and navigation at sea, [3, 4].

The weather conditions under which the ship sails can also have a impact on the shaft line loadings since the rough sea can cause periodical emerging and immersion from the sea, causing a propeller racing phenomenon, [5, 6].

Due to mentioned loads the torsional and transverse vibrations of a shaft line are expected, having the influence on fatigue [7-9] as well as fractural [10,11] behavior of shaft line system.

Additionally, due to always present shaft unbalance and bow [12,13], the conditions for appearance of coupled torsional – transverse vibrations, are met.

This paper presents a contribution in terms of explaining the coupling between torsional and bending vibrations of the shaft line with a residual shaft bow when the ship is navigating on calm and rough seas.

2 Mathematical and numerical model for coupled torsional–bending vibration analysis of the ship's propulsion shaft with a residual shaft bow

In this paper mathematical model based on the modified model of the Jeffcott rotor is used, Figure 1. The propulsion shaft, subjected to both torsional as well as bending vibrations is modelled as rigid disc characterized with inertial parameters such as mass m and mass moment of inertia *J*. Propulsion shaft is also subjected to cross – section eccentricity due to unbalance *e*. The equations of motion for the disc due to planar motion are

$$x = x(t),\ \ y = y(t),\ \ \varphi = \varphi(t) = \theta(t) + \omega t \tag{1}$$

In the previous equation, the total rotational angle φ of disc is a sum of rotational angle due to shaft rotation with constant rotational speed ω and torsional vibrations angle θ. The unknown displacement vector, as function of time t, consists of two translational displacements and one rotational angular displacement:

$$\{u(t)\} = \{x(t), y(t), \theta(t)\}^T \tag{2}$$

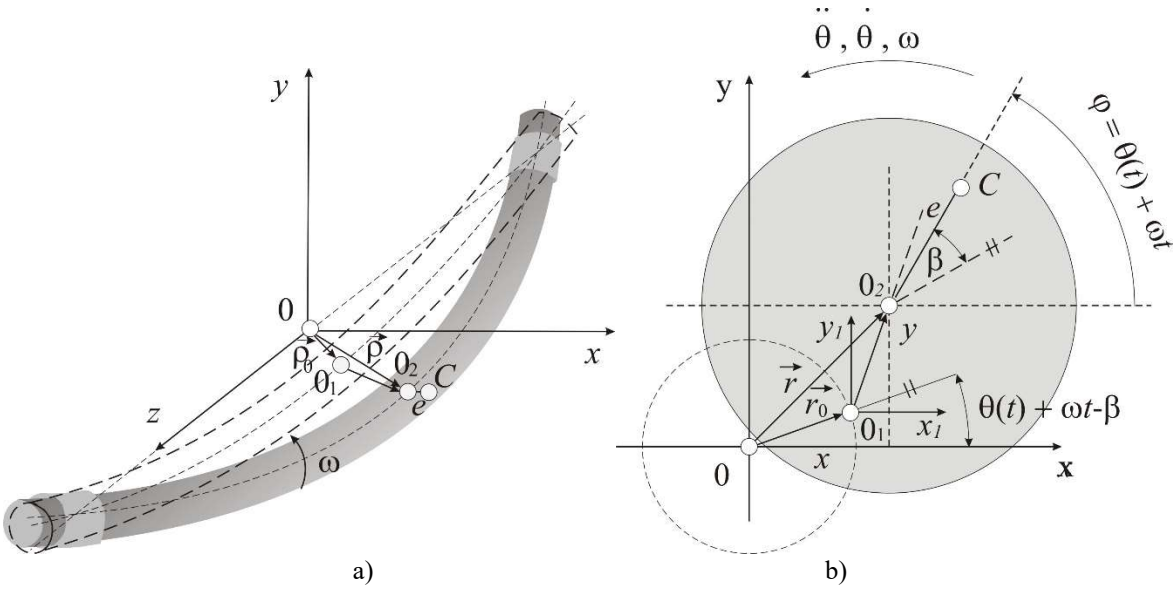

Figure 1: Shaft with a residual shaft bow.

Coordinates of geometrical center of the disc O_2 are defined with expressions

$$x = x_1 + r_0 \cos(\omega t + \theta(t) - \beta)$$
$$y = y_1 + r_0 \sin(\omega t + \theta(t) - \beta) \tag{3}$$

where r_0 is the initial bow, β is the initial angle between initial bow and mass eccentricity, θ is torsional angle and x_1 and y_1 are coordinates of coordinate system which rotates with rotors angular speed ω and which define distance from geometrical disc center O_2 and it's initial position O_1.

Coordinates of mass center of the disc C are defined with

$$x_c = x + e\cos\big(\omega t + \theta(t)\big)$$
$$y_c = y + e\sin\big(\omega t + \theta(t)\big) \tag{4}$$

The displacement of the geometrical center O_2, during its whirling motion, is defined with the expression:

$$\delta = \sqrt{x^2 + y^2} \tag{5}$$

The disc is assumed to be a rigid body; thus, the strain energy of the rotor system comes from the elastic deformation of the rotor and its mass is neglected. Radial stiffness is defined from the expression:

$$F_r = k_r\delta_1 + \alpha\delta_1^3 \tag{6}$$

where k_r is the equivalent radial linear stiffness coefficient, α is the equivalent nonlinear stiffness coefficient [13] and δ_1 is displacement of geometrical center O_2 from its initial position O_1 which is defined with expressions

$$k_r = EI\frac{\pi^4}{2l^3}$$
$$\alpha = EA\frac{3\pi^4}{16l^3} \tag{7}$$
$$\delta_1 = \sqrt{x_1^2 + y_1^2}$$

where E is modulus of elasticity of rotor material, I is second moment of rotor's cross section, A is the area of rotor cross section and l is the rotor's length.

Torsional stiffness is defined with expression

$$M_{rot} = k_\theta\theta \tag{8}$$

where k_θ is the equivalent rotational stiffness coefficient.

Given that rotor torsion is also taken into account, 3 degrees of freedom (x,y,θ) are needed to define motion of the disc mass as it is shown in the Figure 1. Kinetic energy of the disc is defined with the expression

$$T = \frac{1}{2}m\dot{x}_c^2 + \frac{1}{2}m\dot{y}_c^2 + \frac{1}{2}J\left(\omega + \dot{\theta}\right)^2 \tag{9}$$

while the dissipated energy of the rotor system caused by viscous structural damping is expressed as

$$D = \frac{1}{2}c_x\dot{x}^2 + \frac{1}{2}c_x\dot{y}^2 + \frac{1}{2}c_\theta\dot{\theta}^2 \tag{10}$$

where c_x, c_y and c_θ denotes the viscous damping of the flexible massless rotor.

The strain energy of the rotor system can be defined as

$$V = \int_0^{\delta_1} F_r\, d\delta_1 + \int_0^{\theta} M_{rot}\, d\theta = \frac{1}{2}k_r\delta_1^2 + \frac{1}{4}\alpha\delta_1^4 + \frac{1}{2}k_\theta\theta^2 \tag{11}$$

With the use of Lagrange equations of the second kind, the vibrational equation of the dynamic model with three degrees of freedom can be obtained as follows

$$\begin{aligned} &m\ddot{x} + c_x\dot{x} + k_x^*x + F_x^{**} \\ &\quad = em\omega^2cos\left(\omega t + \theta(t)\right) + 2em\omega cos\left(\omega t + \theta(t)\right)\dot{\theta} + emcos\left(\omega t + \theta(t)\right)\dot{\theta}^2 \\ &\quad + emsin\left(\omega t + \theta(t)\right)\ddot{\theta} + F_x^* \\ &m\ddot{y} + c_y\dot{y} + k_y^*y + F_y^{**} \\ &\quad = em\omega^2sin\left(\omega t + \theta(t)\right) + 2em\omega\, sin\left(\omega t + \theta(t)\right)\dot{\theta} + em\, sin\left(\omega t + \theta(t)\right)\dot{\theta}^2 \\ &\quad - em\, cos\left(\omega t + \theta(t)\right)\ddot{\theta} + F_y^* \\ &(J + me^2)\ddot{\theta} + c_\theta\dot{\theta} + k_\theta\theta + M_\theta^{**} = me\ddot{x}sin(\omega t) - me\ddot{y}cos(\omega t) + M_\theta^* \end{aligned} \tag{12}$$

where F_x^{**}, F_y^{**} and M_θ^{**} is defined as

$$\begin{aligned} F_x^{**} &= \alpha x^3 + \alpha r_0^2 sin\left(2\left(\omega t + \theta(t)\right) - 2\beta\right)y - \alpha r_0 cos(\omega t + \theta(t) - \beta)x^2 \\ &\quad - \alpha r_0 cos(\omega t + \theta(t) - \beta)y^2 - \alpha x^2 2r_0 cos(\omega t + \theta(t) - \beta) \\ &\quad - 2\alpha r_0 xysin(\omega t + \theta(t) - \beta) + \alpha xy^2 \\ F_y^{**} &= \alpha y^3 + \alpha r_0^2 sin\left(2\left(\omega t + \theta(t)\right) - 2\beta\right)x - \alpha r_0 sin(\omega t + \theta(t) - \beta)x^2 \\ &\quad - \alpha r_0 sin(\omega t + \theta(t) - \beta)y^2 - \alpha y^2 2r_0 sin(\omega t + \theta(t) - \beta) \\ &\quad - 2\alpha r_0 xycos(\omega t + \theta(t) - \beta) + \alpha yx^2 \\ M_\theta^{**} &= 2\alpha r_0^2 cos^2\left(2\left(\omega t + \theta(t)\right) - 2\beta\right)xy - \alpha r_0 cos(\omega t + \theta(t) - \beta)y^3 + \alpha r_0^2 sin\left(2\left(\omega t + \theta(t)\right) - 2\beta\right)y^2 \\ &\quad - \alpha r_0 cos(\omega t + \theta(t) - \beta)yx^2 + k_z r_0 sin(\omega t + \theta(t) - \beta)x - k_z r_0 cos(\omega t + \theta(t) - \beta)y \\ &\quad + \alpha r_0^3 sin(\omega t + \theta(t) - \beta)x - \alpha r_0^2 sin\left(2\left(\omega t + \theta(t)\right) - 2\beta\right)x^2 + \alpha r_0 sin(\omega t + \theta(t) - \beta)x^3 \\ &\quad + \alpha r_0 sin(\omega t + \theta(t) - \beta)xy^2 - \alpha r_0^3 cos^3(\omega t + \theta(t) - \beta)y \end{aligned} \tag{13}$$

The total equivalent linear stiffness of the rotor system is

$$\begin{aligned} k_x^* &= k_r + \alpha r_0^2 + 2\alpha r_0^2 cos^2(\omega t + \theta(t) - \beta) \\ k_y^* &= k_r + \alpha r_0^2 + 2\alpha r_0^2 sin^2(\omega t + \theta(t) - \beta) \end{aligned} \tag{14}$$

Moreover, the initial bow and geometrical nonlinearity can lead to additional loads [13], which can be expressed as

$$\begin{aligned} F_x^* &= k_r r_0 cos(\omega t + \theta(t) - \beta) + \alpha r_0^3 cos(\omega t + \theta(t) - \beta) \\ F_y^* &= k_r r_0 sin(\omega t + \theta(t) - \beta) + \alpha r_0^3 sin(\omega t + \theta(t) - \beta) \\ M_\theta^* &= \alpha r_0^3 cos(\omega t + \theta(t) - \beta)sin^2(\omega t + \theta(t) - \beta) \end{aligned} \tag{15}$$

System of differential equations of motion, defined by Equation (12), is translated to ODE equation and solved by Runge Kutta 4th order [14].

2.1 External forces and torsional torque

External loadings on the shaft line can be simply defined as a combination of radial forces that represent reactions in the bearings and the torque caused by the propulsion torque load. Two cases are considered in the paper. The first case represents the shaft line response to loads when the ship is and the other one represents the shaft line response to loads when the ship is navigating on rough seas.

In the first case, different hull structure deflections and their impact on propulsion shaft line are assumed regarding different ship service load conditions, Figure 2. It is assumed that ship hull structure has constant deflections when navigating at the same service load condition. Therefore, three subcases are considered, F_x = 0; 0; 0, F_y = 0; 300; 600 N and $M_\theta = M_{\theta 0}\sin(\omega_s t)$, where F_x and F_y are external radial forces, M_θ is external torque on propulsion shaft and $\omega_s = 2\pi/T$ ($f_s = 1/T$) is shaft rotational frequency.

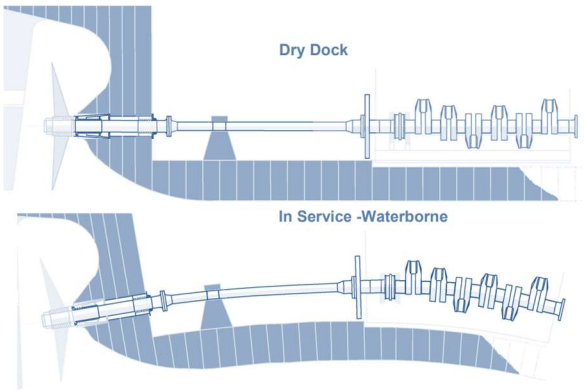

Figure 2: Hull structure deflections and their impact on propulsion shaft line, [15]

In the second case it is assumed that rough sea causes a propeller racing, Figure 3. This phenomenon happens when a ship pitches and heaves heavily. Due to these motions, the stern lifts out of the sea periodically exposing part of the propeller and causing instant increase of propeller speed as well as instant drop of propeller load, Figure 4. It is assumed that wave period T which causes propeller racing is equal to 6 s. To simulate rough sea beside the parameters used for calm sea the following conditions are additionally set: $F_x = 0$, $F_{yr} = F_{yr0}$ $(0.5 + 0.5\sin(\omega_r t))$ and $M_{\theta r} = M_{\theta r0}$ $(0.6 + 0.4\sin(\omega_r t))$, where $\omega_r = 2\pi/T$ $(f_r = 1/T)$ is wave rotational frequency and $M_{\theta r0}$ is torque amplitude due to static propeller torque drop caused by propeller racing. Table 1 presents Torque and transverse force loads used in numerical analysis.

Table 1: Torque and transverse force loads used in numerical analysis

Case No.	f_s, Hz	F_y , N	$M_{\theta 0}$, Nm	f_r, Hz	F_{yr0} , N	$M_{\theta r0}$, Nm
1	1.67	0	0.06	0	0	0
2	1.67	300	0.06	0	0	0
3	1.67	600	0.06	0	0	0
4	1.67	0	0.06	0.167	600	1

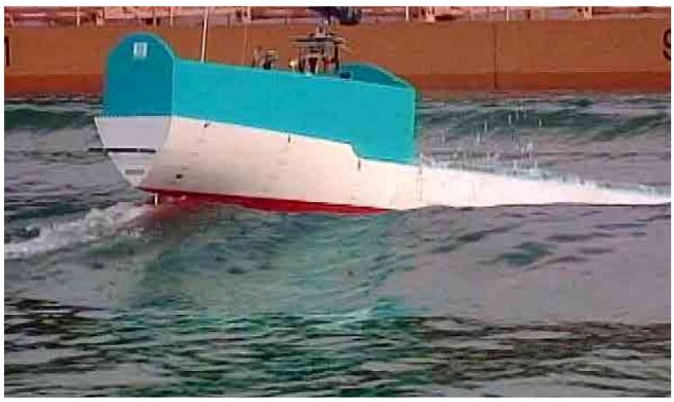

Figure 3: Propeller racing [6]

Figure 4: The emergence of the stern at the rough sea [2].

3 Numerical simulation

To investigate the coupling effect between torsional and bending vibration, propulsion shaft with following parameters was used: shaft density ρ = 7800 kg/m^3, Poisson's ratio ν = 0.3, Young's modulus, E = 206 GPa, shear

modulus, G = 77 GPa, shaft length, L = 2.665 m, shaft diameter, D = 0.086 m, rotational speed n = 100 rpm, stiffness of system $k_x = k_y = 2.847\times10^6$ N/m, $k_\theta = 1.7\times10^5$ N·m/rad, damping of system, $c_x = c_y = 60$ N·s/m and $c_\theta = 0.08$ N·m·s/rad.

Equation (6) was solved by using of Newmark's time stepping method. Time step in each simulation case was 1×10^{-3} s whereas the initial conditions of displacements x_0, y_0, θ_0 were set to zero.

The first three cases of simulation, according to Table 1, correspond to the conditions of navigation on calm seas while the fourth simulation corresponds to the conditions of navigation on rough seas. The total simulation time was equal to 30 s. Results are presented as displacements in time domain, frequency domain as well as in the form of Short time Fourier transform – STFT spectrograms. Figure 5 presents the response of the propulsion shaft displacements in horizontal, vertical direction and torsional angles for case 1 in time and frequency domain. Likewise, Figures 6 and 7 show the frequency responses of shaft displacements in horizontal, vertical direction and torsional angles for cases 2, 3 and 4. In order to gain a more detailed insight into what happens to the vibrations of the shaft line when navigating rough seas, the spectrograms for case 4 are additionally presented in Fig. 8.

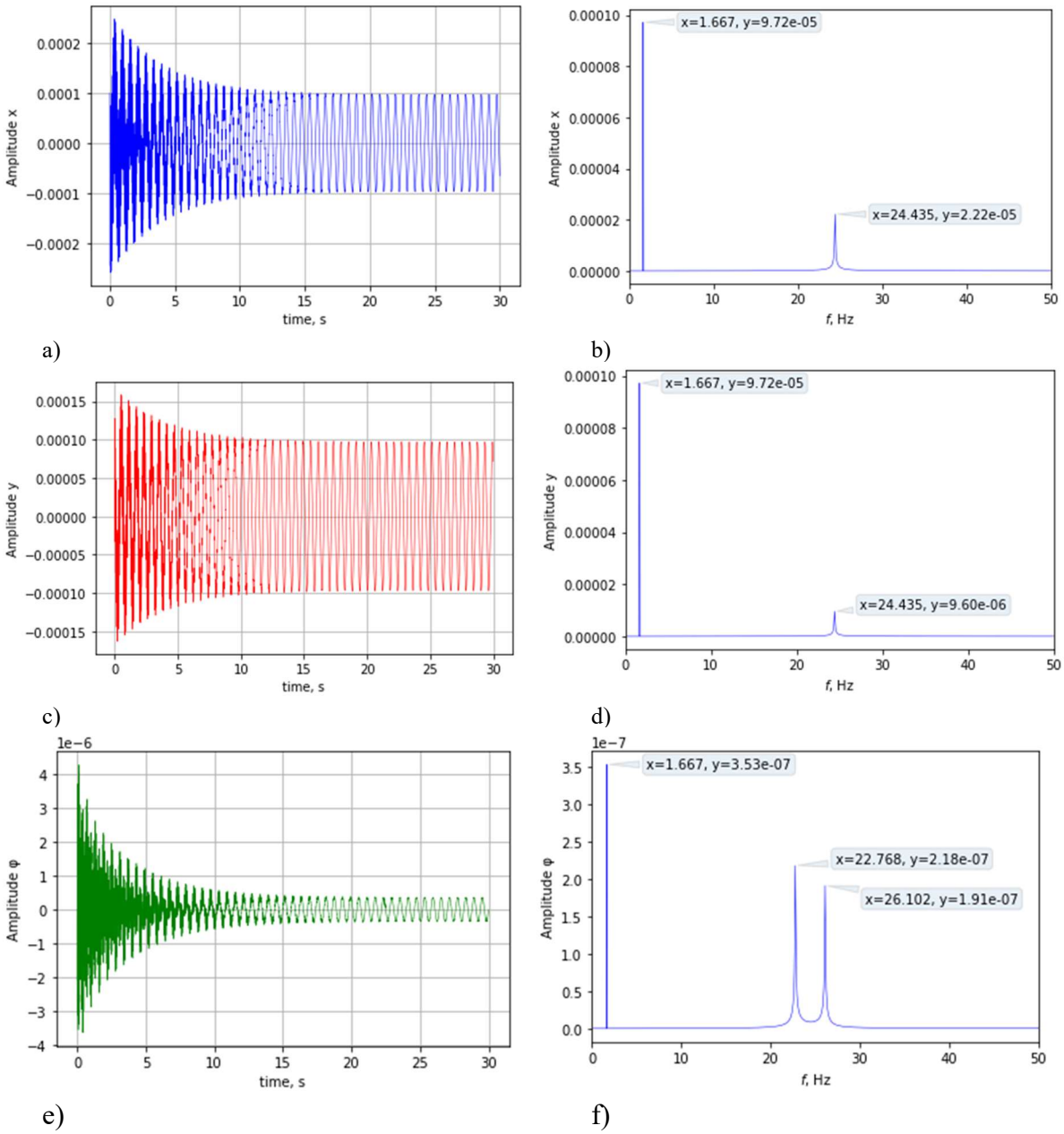

Figure 5: Response of the propulsion shaft displacements in horizontal, vertical and torsional angles for case 1, a) $x(t)$, b) frequency spectrum of $x(t)$, c) $y(t)$, d) frequency spectrum of $y(t)$, e) $\theta(t)$, f) Frequency spectrum of $\theta(t)$

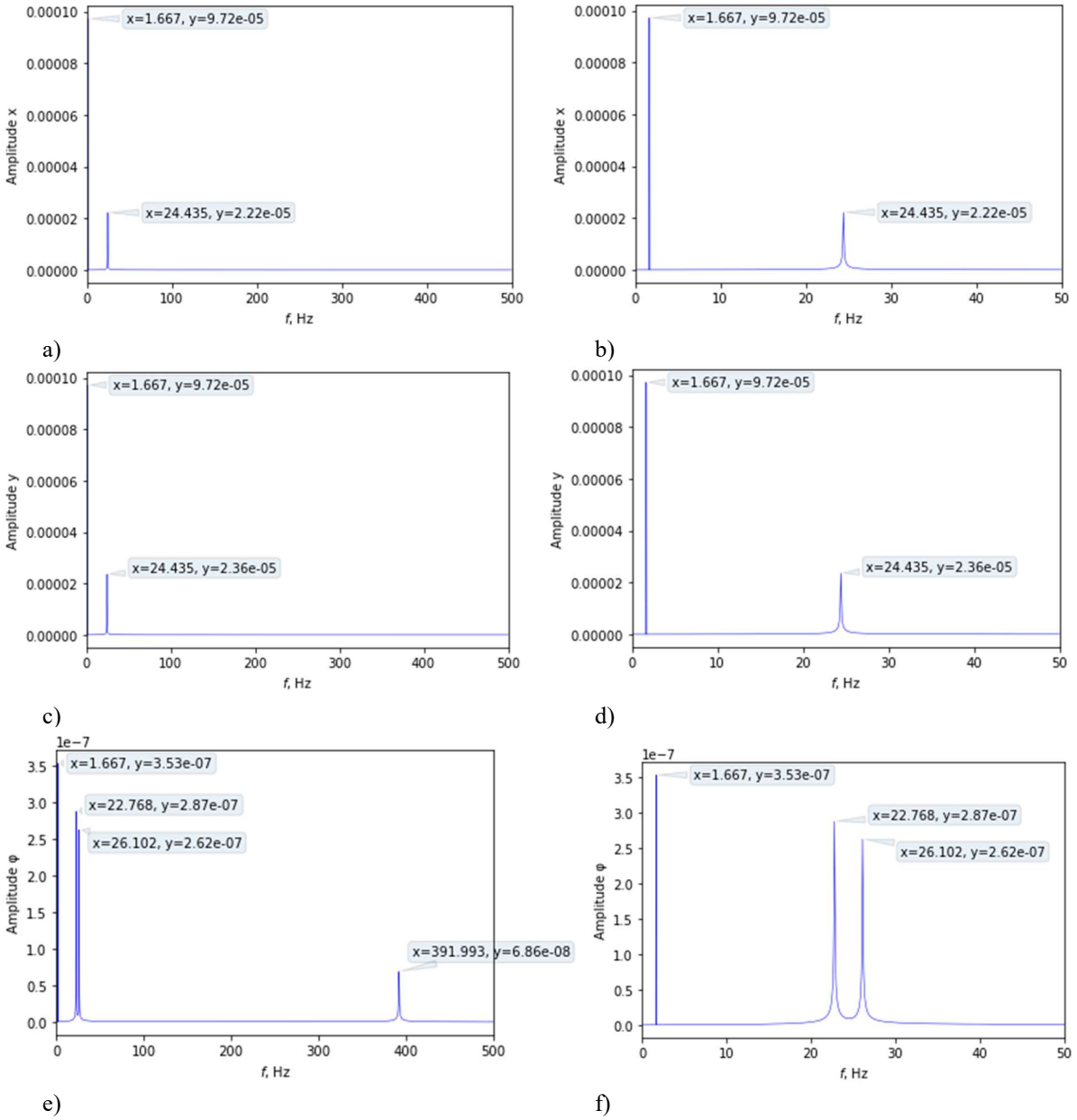

Figure 6: Response of the propulsion shaft displacements in horizontal, vertical and torsional angles for case 2, a) FFT of $x(t)$, b) FFT of $x(t)$ 0-50 Hz, c) FFT of $y(t)$, d) FFT of $y(t)$ 0-50 Hz, e) FFT of $\theta(t)$, f) FFT of $\theta(t)$ 0-50 Hz

Figure 6e shows the frequency responses of the torsional angles of shaft in frequency range 0-500 Hz for case 2. It is important to note that 1 natural torsional frequency has a value of f_t = 391.99 Hz, i.e. the frequency components that are visible on the zoom display (Figure 6f) do not actually have anything to do with the torsional free vibrations of the propulsion shaft.

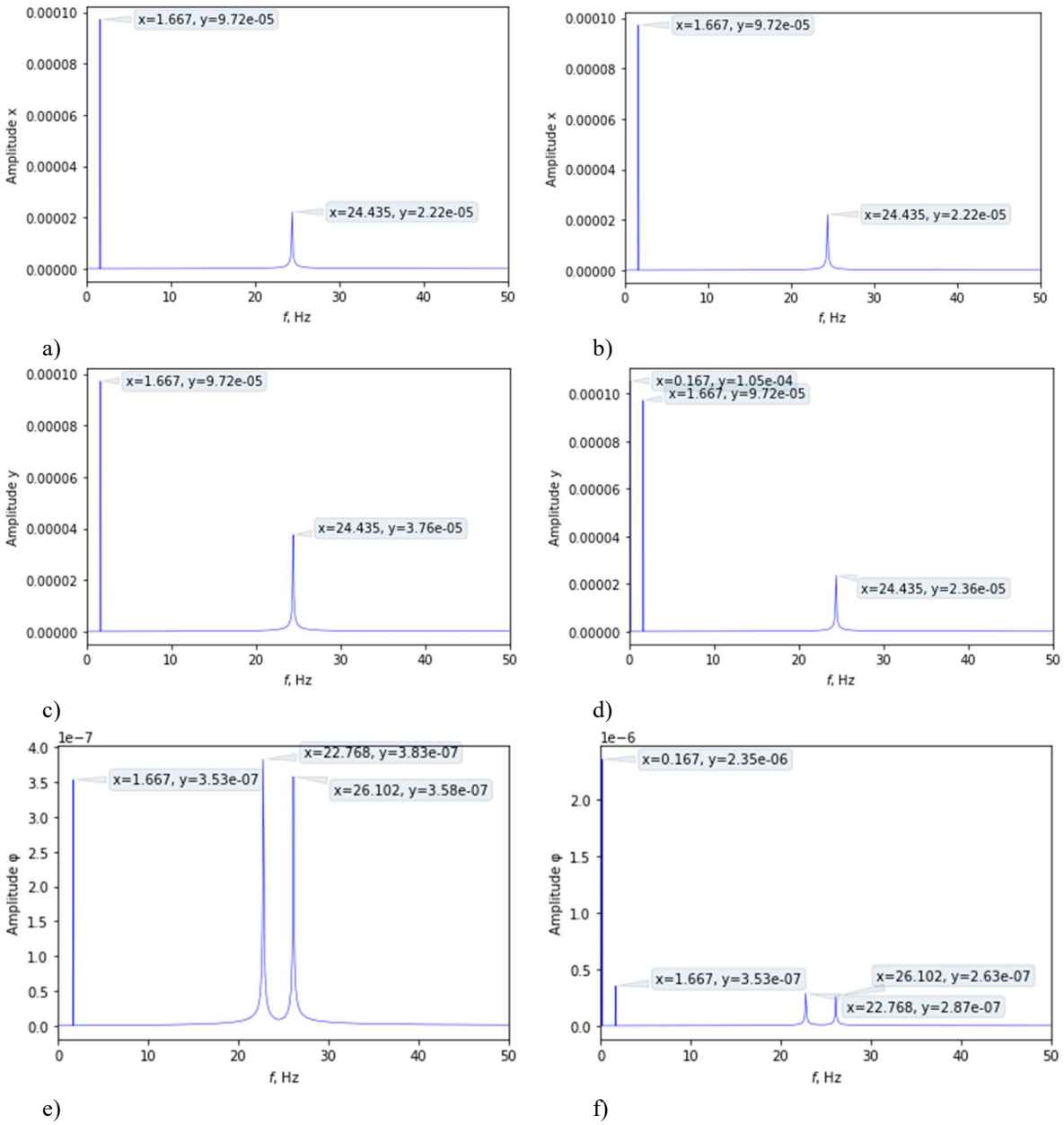

Figure 7: Response of the propulsion shaft displacements in horizontal, vertical and torsional angles for cases 3 and 4, a) c3 FFT of $x(t)$, b) c4 FFT of $x(t)$, c) c3 FFT of $y(t)$, d) c4 FFT of $y(t)$, e) c3 FFT of $\theta(t)$, f) c4 FFT of $\theta(t)$

As the first natural bending frequency of the shaft is at f_b = 24.4 Hz, the frequency components, visible in Figures 6f, 7e, 7f and 8c, actually represent the modulated frequencies $f_b \pm f_s$ = 22.8; 26.1 Hz and thus prove the coupling between the bending and torsional vibrations of the propulsion shaft.

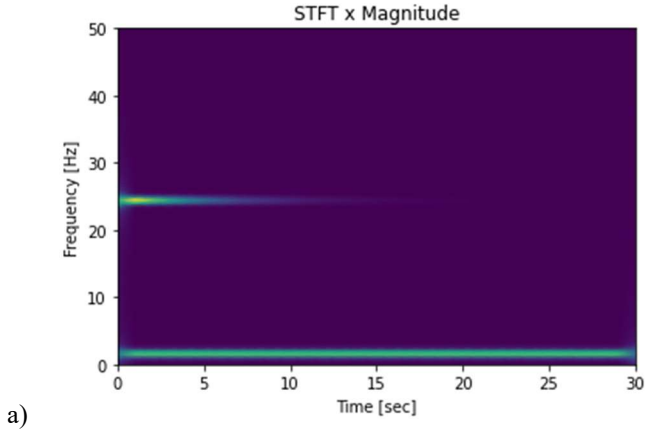

a)

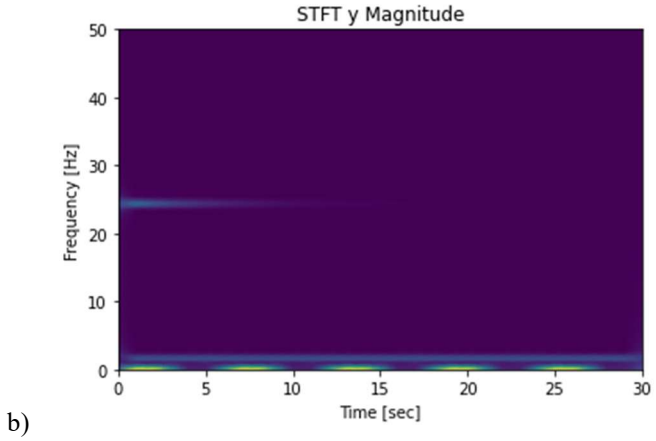

b)

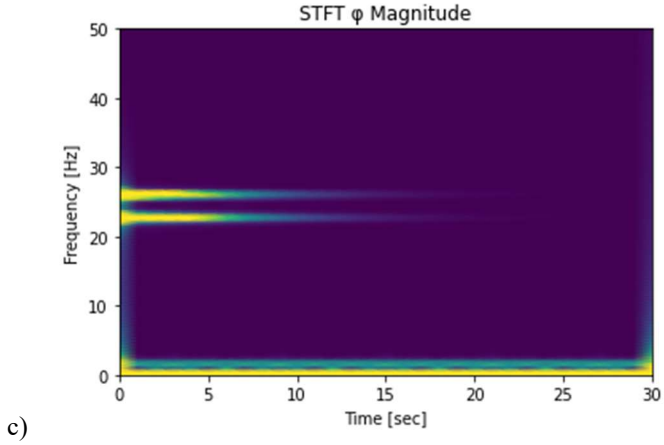

c)

Figure 8: Response of the propulsion shaft displacements in horizontal, vertical and torsional angles for case 4, a) STFT of $x(t)$, b) STFT of $y(t)$, c) STFT of $\theta(t)$

7 Conclusion

A coupled torsional-bending vibration model of ship's propulsion shaft with a residual shaft bow is considered in this paper. This model is based on the modified Jeffcott rotor model. Four cases are considered. First three cases, when the ship is navigating on calm seas and fourth, when navigating on rough seas. Coupling between bending and torsional vibration was observed in each of analyzed cases. It is manifested by the appearance of modulated frequency components ($f_b \pm f_s$) in the torsional domain even though modulation occurs around a bending natural frequency.

Coupling is minimal in the first case when the lateral force is equal to zero but it increases with increasing amplitude of the lateral force. In the STFT spectrogram of the 4th case the wave beating in vertical direction at 0.167 Hz is more intense than speed frequency harmonic at 1.667 Hz.

Acknowledgement

This study has been supported by the Croatian Science Foundation under the project IP-2020-02-8568 and in part by the University of Rijeka under the project number uniri-tehnic-18-225.

References

[1] DNVGL-CG-0038, CLASS GUIDELINE (2015): *Calculation of shafts in marine applications*.

[2] Radan, D. (2004): *Uvod u hidrodinamiku broda*, Sveučilište u Dubrovniku.

[3] Huang, Q., Yan, X., Wang, Y., Zhang, C., Wang, Z. (2017): *Numerical modeling and experimental analysis on coupled torsional-longitudinal vibrations of a ship's propeller shaft*, Ocean Engineering, ELSEVIER.

[4] Halilbese, A.N., Zhang, C., Özsoysal, O.A. (2021): *Effect of Coupled Torsional and Transverse Vibrations of the Marine Propulsion Shaft System*, Journal of Marine Science and Application, Springer.

[5] JOURNÉE, J.M.J., MASSIE, W.W.(2001): *Offshore Hydromechanics*, Delft University of Technology.

[6] JAPAN P&I CLUB (2019): *Marine Weather Ship Handling in Rough Sea*, The Japan Ship Owners' Mutual Protection & Indemnity Association Loss Prevention and Ship Inspection Department.

[7] Cazin, D.; Braut, S.; Božić, Ž.; Žigulić, R.(2020): *Low cycle fatigue life prediction of the demining tiller tool*, Engineering failure analysis, 111, 104457, 14 doi:10.1016/j.engfailanal.2020.104457.

[8] Braut, S.; Sikanen, E.; Nerg, J.; Sopanen, J.; Božić, Ž. (2021): *Fatigue life prediction of Electric RaceAbout (ERA) traction motor rotor*, Procedia structural integrity 31 (2021), 45-50.

[9] Braut, S.; Tevčić, M.; Butković, M.; Božić, Ž.; Žigulić, R.(2021), *Application of modified Locati method in fatigue strength testing of a turbo compressor blade*, Procedia Structural Integrity 31, 33-37.

[10] Pantazopoulos, G., Papaefthymiou, S. (2015), *Failure and Fracture Analysis of Austenitic Stainless Steel Marine Propeller Shaft*, J Fail. Anal. and Preven. 15:762–767, DOI 10.1007/s11668-015-0024-7.

[11] Braut, S.; Tevčić, M.; Butković, M.; Božić, Ž.; Žigulić, R.(2021), *Application of modified Locati method in fatigue strength testing of a turbo compressor blade*, Procedia Structural Integrity 31, 33-37.

[12] Braut, S.; Žigulić, R.; Butković, M. (2008) *Numerical and experimental analysis of a shaft bow influence on a rotor to stator contact dynamics*, Strojniški vestnik, 54, 10; 693-706.

[13] Yang, Y., Yang, Y., Ouyang, H. et al. (2019) *Dynamic performance of a rotor system with an initial bow and coupling faults of imbalance-rub during whirling motion*. J Mech Sci Technol 33, 4645–4657. https://doi.org/10.1007/s12206-019-0908-7

[14] Rajasekaran, S.(2009): *Free and forced vibration of a continuous system in relation to structural dynamics during earthquakes*, Structural Dynamics of Earthquake Engineering; Theory and Application Using Mathematica and Matlab, Woodhead Publishing.

[15] Leontopoulos, C.: *Shaft Alignment and Powertrain Vibration*, ABS 2011.

15th SIRM – European Conference on Rotordynamics,
Darmstadt, Germany, 22nd – 24th February 2023

Methods to experimentally identify relevant drive train vibration modes for tonality mitigation of wind turbines

Philipp Zech [1], **Oliver Eichelhard** [1], **Jonnhy Tchuindjang** [1], **Manuel Eckstein** [1]

[1] Wölfel Engineering GmbH, 97204, Höchberg, Germany, zech@woelfel.de

Abstract

Acoustic tonalities which exceed legal regulations may lead to restricted wind turbine operations and thus reduce yield. They arise for example from gear mesh vibration of planetary gearboxes, which are used in many wind turbine drive train designs. Passive or active vibration control measures at the drive train can be applied to reduce acoustic tonalities. The key to success of such mitigation measures is to understand which vibration modes of the drive train need to be reduced in order to achieve acoustic reductions. This paper proposes two experimental approaches to identify acoustic-relevant drive train vibration modes. The approaches are described in detail and their characteristic advantages and efforts are discussed.

1 Introduction

To reduce CO_2 emissions there is a trend in many countries towards renewable energy production. In 2021 approximately 40% of the energy in germany was produced from renewable energy sources. Wind energy was the most important renewable energy source with a market share of almost 50%. Although there are plans for the construction of further offshore wind parks in the North Sea, currently the onshore wind energy production capacity in germany is much bigger than offshore. Building onshore wind turbines is in general less cost-intensive than offshore-turbines. However in most countries onshore turbines must be build relatively close to residential areas, due to space constraints. Acoustic emissions produced by wind turbines are one of the most important disturbing factors for residents living nearby. For this reason wind turbine manufacturers are constantly developing towards more quiet designs. For the acoustic compliance of a wind turbine on one hand the overall sound power level must not exceed the maximum allowed level defined in the respective national legislation. On the other hand so called tonalities must not exceed a threshold which is also legally regulated. Tonality is defined as one or multiple distinct harmonic tones being audible in the acoustic spectrum of the wind turbine. Tonality problems (tone amplitudes above legally allowed limit) can have severe economic impacts, because wind farm operators can be forced by public authorities to operate their wind turbines in a noise-reduced operation mode which significantly reduces the energy yield.
Multi-stage planetary gearboxes are used to adapt torque and speed between blades and generator in many drive train designs. The gear mesh excitation is one of the most important vibration source which leads to acoustic tonalities. It is likely that challenges with respect to tonalities will increase in the coming years due to the following reasons:

1. Wind turbine sizes are ever-growing. Blades and tower are the acoustic main radiators. Acoustic emissions are expected to increase with the size of these central components.
2. There is a trend towards higher energy (torque) densities in the drive trains. Higher torque densities will most probably lead to an increase in gear mesh vibration excitation.
3. Due to limited space it will be necessary to build wind farms closer to residential areas. Acoustic emissions will thus be more relevant.
4. Improvements in the aeroacoustic-design of the turbine blades reduce the masking background noise.

In order to reduce acoustic tonalities of wind turbines it is necessary to first understand the drive train dynamics. The gear mesh excitation is the vibration source which excites drive train vibrations. Finally blades and tower are excited and radiate acoustically. In order to develop countermeasures it is thus important to understand which drive

train vibration mode is causing the acoustic emission of tones. This paper proposes methods of how to approach this problem experimentally. Advantages and drawbacks of the methods are discussed.

2 State of the art

Acoustic tonality measurements of wind turbines must be performed and analysed according to the standard IEC 61400-11 in many countries. The standard defines details for the measurement (microphone position & distance to the turbine) and the analysis (clustering of 10s averaged data into wind bins, detection & assessment of tones, assessment of masking background noise). The advantage of the standard is the clear guideline on how to assure reproducible measurement results. However the deduction of tonality countermeasures is out of scope of this standard. Furthermore for a detailed understanding of the vibroacoustic problem the measurement result, mean tonality over 0.5 m/s wind speed steps, is to inaccurate. Neither a correlation to the exact turbine speed nor the drive train torque is possible. For this reason it must be concluded that IEC 61400-11 is well suited to assess the severity of the tonality problem. However it is not suitable for problem solving.
The review paper [6] mentions tonal audibilities as one of multiple acoustic emissions of wind turbines. Passive tuned mass dampers are proposed as countermeasure. However no method on how to design or where to place the devices is described. Another review paper [8] mentions that a shielding of the nacelle or use of sound-absorbing materials would be good, without going into further details. Manufacturers are continuously developing towards quieter design [2], [7]. One standard design to reduce tonalities is to mount the gearbox using elastomer springs to the nacelle structure. The intention is to isolate the nacelle from the gearbox vibration. A drawback of the approach is that these elastomer mounts must support the differential torque of the gearbox. These very high loads can lead to wear of the elastomers and can make a regular replacement necessary.
To date there is no procedure on how to measure and assess the drive train vibration in a standardized way. Furthermore there is no standardized method to identify which drive train vibration modes are driving the acoustic radiation of tonalities. [5] describes the use of an operational transfer path analysis to identify the relevant transfer paths between gear mesh excitation and acoustic radiators (blades, tower). However [5] uses a multi-body-simulation model of a wind turbine, it is not directly obvious how to apply the method to a real wind turbine. Furthermore the knowledge of transfer paths alone is not sufficient, the excitation must also be known and additionally the paper is only looking at structural transfer paths and not the acoustic transfer paths.
Generally there are the following possibilities to reduce tonalities:

- Passive vibration control (Tuned mass dampers at drive train)
- Semi-active vibration control (Tuned mass dampers with adaptable eigenfrequency at drive train)
- Active vibration control (Closed loop control with vibration sensors and vibration actuators, suppressing gear mesh vibrations at drive trains)
- Reduction of vibration excitation (Gear tooth corrections)

Tuned mass dampers are the least expensive solution, but also have lowest potential. They work only for a limited frequency range around their tuning frequency. Active vibration control has higher system complexity but also the potential to reduce vibrations over a wide frequency range. Tonalities often occur over wider operating speeds and often it is not a resonant vibration problem, but forced vibrations which excite the acoustic radiators.
The research question of this paper is: Which drive train vibration mode drives the acoustic tonality?
This paper proposes experimental approaches. The reason for this is the fact that vibro acoustic models of whole wind turbines are normally not available before start of production of new turbine designs. Furthermore very high effort is related to model validation. For this reason a purely model-based approach seems not reasonable.

3 Problem description and basics

Figure 1 depicts a wind turbine structure with the planetary gearbox as the vibration source in the nacelle. The gear mesh vibrations are transferred to the tower and the blades, which are acoustic radiators. Finally the acoustic sound pressure p can be measured using a microphone outside of the wind turbine. The multistage planetary gearbox is necessary to adapt torque and speed of the main shaft which is connected to the hub such that the electric generator can be driven. The gearbox has an overall transmission ratio which is defined as

$$i = \frac{\dot{\varphi}_1}{\dot{\varphi}_2} \tag{1}$$

where $\dot{\varphi}_1$ and $\dot{\varphi}_2$ are the speeds of input shaft and output shaft respectively as defined in Figure 1. The gearbox housing must be mounted to the nacelle structure in order to support the very high differential torque between input

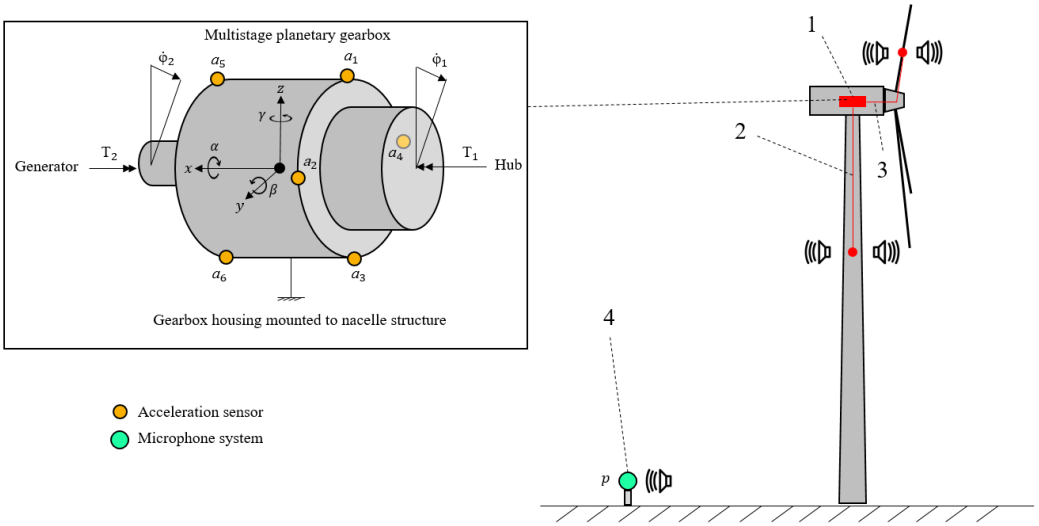

Figure 1: Right: Wind turbine structure with drive train in nacelle (1), transfer path to the tower (2), transfer path the blades (3). Acoustic tonalities can be measured with a microphone in the field (4). Left: Coordinate system definition for the multistage planetary gearbox.

torque T_1 and output torque T_2

$$\mathrm{T}_{\text{diff}} = \mathrm{T}_1 - \mathrm{T}_2. \tag{2}$$

The mathematical analysis of the vibration excitation in planetary gearboxes has been investigated by multiple authors and different models have been proposed. Often these models are used to predict complicated frequency spectrum structure which is produced by modulations within the gearbox [1], [3], [4]. Without going into detail on the modulation mechanisms there is a consensus in the literature that the vibration excitation $d(t)$ by a planetary gearbox is deterministic and can in general be described as a fourier series

$$d(t) = \frac{a_0}{2} + \sum_{k=1}^{\infty} a_k \cos(k\varphi(t)) + b_k \sin(k\varphi(t)) \tag{3}$$

where $\varphi(t) = \Omega t$ denotes the instantaneous planet carrier angle, Ω denotes the angular velocity of the planet carrier. Planetary gearbox vibration consists of frequency components which are integer multiples k of the planet carrier rotation frequency. While in other industries such as aerospace the so called sideband frequencies are subject of studies, this is not the case for wind turbines gearboxes. To the knowledge of the authors there are no strong frequency modulation effects observed within wind turbine gearboxes and the resulting vibration excitation is dominated by the nominal gear mesh order, where k is equal to the number of teeth at the ring gear Z_{Ring}. To summarize the accelerations at the gearbox housing a_i (compare acceleration sensors as depicted in Figure 1) and the sound pressure p can be described as

$$a_i(t) = A_i(\Omega, \mathrm{T}_1) \cos(Z_{\text{Ring}}\Omega t) + B_i(\Omega, \mathrm{T}_1) \sin(Z_{\text{Ring}}\Omega t) \tag{4}$$

$$p(t) = C(\Omega, \mathrm{T}_1) \cos(Z_{\text{Ring}}\Omega t) + D(\Omega, \mathrm{T}_1) \sin(Z_{\text{Ring}}\Omega t) \tag{5}$$

where i denotes the number of the acceleration measurement channel and $A_i(\Omega, \mathrm{T}_1)$, $B_i(\Omega, \mathrm{T}_1)$, $C(\Omega, \mathrm{T}_1)$, $D(\Omega, \mathrm{T}_1)$ denote the speed and load dependent amplitudes. To summarize both structural vibrations as well as the acoustics are dominated by the gear mesh order which is basically a harmonic excitation with load and speed dependent amplitude and phase. Due to the vibroacoustic transfer function between gear mesh excitation and the microphone

the amplitude coefficients $A_i(\Omega, \mathrm{T}_1)$ and $B_i(\Omega, \mathrm{T}_1)$ on the structure are different from the acoustic amplitude coefficients $C(\Omega, \mathrm{T}_1)$ and $D(\Omega, \mathrm{T}_1)$. The basic research question is how the acoustic response is linked to the structural vibrations and thus to understand the transfer function between structural and acoustic amplitudes and phases. In the following section different methods to identify this correlation are described.

4 Proposal of approaches

4.1 Method A: State of the art - Identify acceleration channels with highest vibration amplitudes

The first method is a very simple one and consists of the following steps:

1. Collect acceleration and microphone data during normal operation of the wind turbine as well as the turbine speed.
2. For turbine speed ranges where acoustic tonalities occur analyze all acceleration channels and identify those with the highest acceleration amplitudes.
3. It is assumed that the acceleration channels (consisting of acceleration sensor position and sensing direction) with the highest acceleration amplitudes have the highest correlation with the acoustics.

This approach is often used in the wind industry, however to the experience of the authors it is too simple. Due to complex structural dynamics it is easily possible that high acceleration components or directions at the gearbox have a comparably low contribution to the overall acoustics. Furthermore by just looking at individual acceleration channels it is impossible to understand the gearbox operational deflection shapes. Additionally, isolation effects (e.g. due to materials like elastomers) are not taken into account appropriately.

4.2 Method B: New proposed - Compare curve shape of structural and acoustic order cuts from operational measurements

The second approach is proposed by the authors and consists of the following steps:

1. Collect acceleration and microphone data during normal operation of the wind turbine as well as the turbine speed.
2. Calculate the acoustic order cut which corresponds to the gear mesh order. For this it is normally necessary to average over a large number of data points per turbine speed interval.
3. Calculate the acceleration order cuts of the gearbox which correspond to the gear mesh order. For this it is normally necessary to average over a large number of data points per turbine speed interval.
4. Plot both acoustic and structural order cuts in one figure. If there is a similarity in the curve observable between the acoustic and one of the structural order cuts, it is assumed that the particular degree of freedom or sensor channel is driving the acoustic problem. Even more insights are gained by combining multiple acceleration channels in order to analyze the correlation between particular operational deflection shape (components) and the acoustic.

This approach is more elaborated as the previously described method. In particular because the operational deflection shapes in which the gearbox is vibrating can be taken into account. Furthermore a correlation between structural and acoustic order cut curve shapes is performed. Using the sensor positions as depicted in Figure 1 one can calculate the gearbox accelerations.

4.3 Method C: New proposed - Experimental measurement of vibroacoustic transfer functions

A third approach is also proposed by the authors and uses multiple active vibration actuators as shakers at the drive train to excite isolated drive train modes and measures the acoustic response outside the turbine using a synchronized microphone. The method consists of the following steps:

1. Put the wind turbine into very slow rotation (idling).
2. Install vibration actuators at the gearbox such that drive train vibration modes can be excited.
3. Sequentially excite drive train modes which are controllable with a white noise or sine sweep excitation in the relevant frequency range.
4. Measure both the structural excitation (acceleration) at the gearbox housing as well as the acoustic response at the external microphone simultaneously with one synchronized measurement system.
5. Calculate the vibroacoustic transfer functions between excitation and acoustics using for example the $\mathbf{H}_1$ estimator.
6. In the next step measure the operational acceleration and calculate structural order cuts, based on normal operation vibration data from the turbine.

7. Multiply the individual acceleration order cuts with their respective vibroacoustic transfer functions to estimate the contribution to the acoustic response. Acceleration channels or their combinations with highest estimated acoustic response are assumed to drive the acoustic problem.

Compared with the two other described methods it has the highest efforts because vibration actuators must be dimensioned and electrically and mechanically installed at the gearbox housing. As a wind turbine gearbox for an up to date turbine design has a mass of multiple ten tons, a very high force actuator system is required to realize enough excitation such that an acoustic response is measurable. Furthermore a synchronized measurement of acoustic and acceleration is necessary to get good quality transfer function estimations. Compared to the other methods this method is the most systematic one and allows more detailed insights into the transfer path properties.

5 Conclusion

Tonality is an important aspect with respect to both the acceptance of wind turbines near residential areas as well as compliance to legal regulation. In order to implement mitigation measures such as passive or active vibration control, it is crucial to understand the link between the gear mesh excitation, the drive train vibration mode(s) and the acoustic response. After describing the state of the art and the problem definition, the paper proposes and discusses three methods, how the relation between structural vibrations and the acoustic response could be analyzed. The following table summarizes the properties of the proposed methods:

	Method A	**Method B**	**Method C**
Effort	Lowest	Higher	Highest
Analysis tools required	Order cut extraction for individual sensor channels, Identify channels with highest amplitudes	Combination of acceleration sensor channels, Order cut extraction, visual comparison of acoustic and structural order cut curves	Combination of acceleration sensor channels, Order cut extraction, calculation of transfer functions
Measurement setup	Acceleration sensors at drive train, external microphone	Acceleration sensors at drive train, external microphone	Acceleration sensors at drive train, external microphone, vibration actuators
Turbine operation	Normal operation	Normal operation	Normal operation + Idling
Expected insight into vibroacoustic transfer function	None	Indirect	Direct

The new proposed methods B and C are assumed to give better results if the main drive train components are vibrating as a rigid body. If internal flexibility of main drive train components cannot be neglected in the frequency range of interest, then more sophisticated methods must be developed.

References

[1] Inalpolat, M. (2009): A theoretical and experimental investigation of modulation sidebands of planetary gear sets. *JSV*, **323**(3), pp. 677–696.

[2] Gupta, M. (2019): Advancements in continuous learning for tonality free turbine design. *Proceedings of the 8th International Conference on Wind Turbine Noise*.

[3] McFadden, P.D. (2009): An Explanation for the Asymmetry of the Modulation Sidebands about the Tooth Meshing Frequency in Epicyclic Gear Vibration. *Proceedings of the Institution of Mechanical Engineers, Part C: Journal of Mechanical Engineering Science*, **199**(1), pp. 65–70.

[4] McNames, J. (2001): Fourier Series Analysis of Epicyclic Gearbox Vibration. *Journal of Vibration and Acoustics*, **124**(1), pp. 150–153.

[5] Schünemann, W. (2009): Identification of relevant acoustic transfer paths for WT drivetrains with an operational transfer path analysis. *Forschung im Ingenieurwesen*, **85**(2), pp. 345–351.

[6] Hansen, C. (2020): Recent Advances in Wind Turbine Noise Research. *Acoustics*, **2**(1), pp. 171–205.

[7] Marmo, B. (2017): Tonal noise mitigation on wind turbines. *Proceedings of the 7th International Conference on Wind Turbine Noise*.

[8] Deshmukh, S. (2019): Wind turbine noise and its mitigation techniques: A review. *2nd International Conference on Energy and Power*, **160**, pp. 633–640.

SIRM 2023 – 15th International Conference on Dynamics of Rotating Machines, Darmstadt, Germany, 22nd – 24th February 2023

Vibration Reduction on a Sewage Pump

Jochen Hartmann [1]

[1]Structural Mechanics, KSB SE & Co. KGaA, 67227, Frankenthal, Germany, jochen.hartmann@ksb.com

Abstract

This document shows the challenge of speed-controlled pumps and the associated possible increased casing vibrations. Furthermore, it is shown that increased vibrations must not only come from the pump, but also the directly adjacent environment, e.g. foundation, make a decisive contribution to the measured vibration speeds.

During commissioning, increased housing vibrations at sewage pumps occurred at certain speeds and/or flow rates, which had to be reduced. To analyze the causes of the increased vibrations, a wide variety of measurements were carried out on site and then evaluated. For example, bump tests were carried out to determine the natural frequencies. In addition, housing vibrations and shaft measurements were carried out during operation in order to determine possible excitation mechanisms. Since the measurement evaluations did not provide a clear picture, a finite element model of the pump with the adjacent components, pipeline and concrete block below the pump, was also created and a wide variety of dynamic analyzes were carried out.

The two optimizations on the pump side already reduced the housing vibrations to an acceptable level. However, since no changes could be made to the cast concrete block, the housing vibrations could not be reduced to a low level. An alternative control program had to be developed and implemented to bypass the resonance area of the overall structure.

1 Introduction

The sewage pump is also known as a dirty water pump and enables the pumping of coarsely polluted water, which often contains solid components of various organic, inorganic or mineral origins. Sewage pumps are preferably built as a single stage and are generally not self-priming.

6 variable speed pump sets (pump + coupling + motor) were supplied to pump wastewater from a storage tunnel to the local sewage treatment plant. The pumps have an operating speed range from n = 150 rpm to 326 rpm, with flow rates between Q = 1.95 m³/s to 3.8 m³/s. The motor drive is located at a different level on a separate platform. The connection between pump and motor is managed via a flexible coupling. The rotor is support by two roller bearings. At the top, drive end side, an axial, radial bearing is positioned and next to the impeller, non-drive end side, a double row radial bearing is installed. The pump and the general arrangement can be seen in Figure 1 and Figure 2.

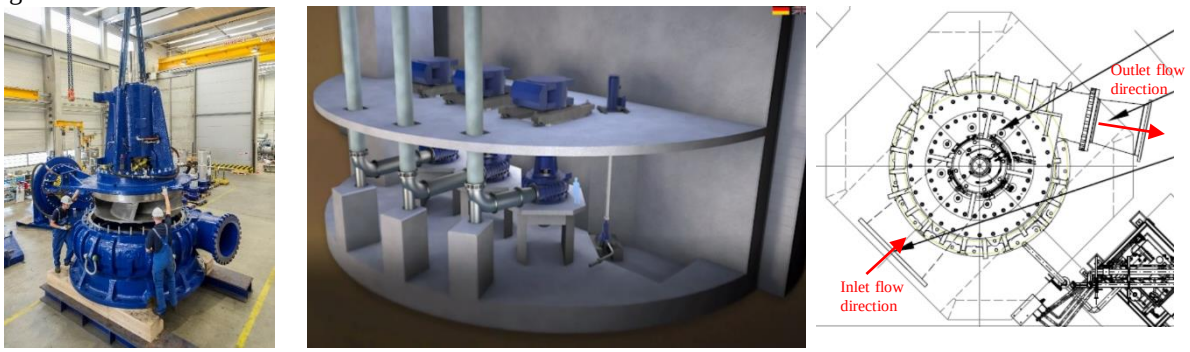

Figure 1: Sewage pump and general arrangement

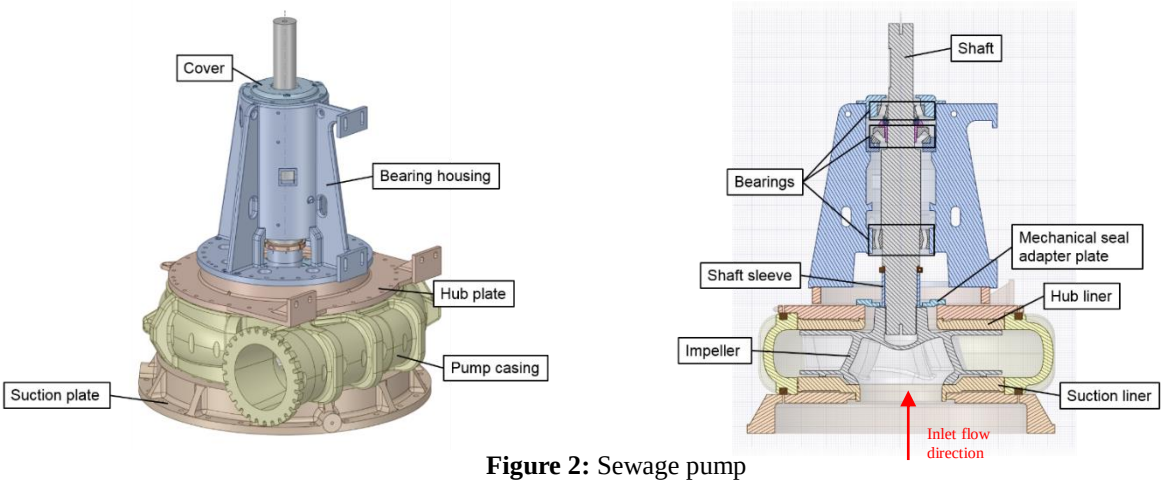

Figure 2: Sewage pump

During commissioning, increased housing vibrations occurred at certain speeds and/or flow rates, which had to be reduced. The vibrations exceeded the maximum permissible vibration speeds according to [1]. To analyze the causes of the increased vibrations, a wide variety of measurements were carried out on site and then evaluated. For example, bump tests were carried out to determine the natural frequencies. In addition, housing vibrations and shaft measurements were measured during operation in order to determine possible excitation mechanisms. Since the measurement evaluations did not provide a clear picture, a finite element model of the pump with the adjacent components, pipeline and concrete block below the pump, was also created in ANSYS [2] and a wide variety of dynamic analyzes were carried out. By comparing the measurement and the calculation, it was found that different mechanisms were responsible for the increased vibrations on the machine.

2 Measurements at Site

During operation of the pumps at site higher housing vibrations at different flows and rotational speeds occurred. A typical time history of the housing vibrational velocities over the speed can be seen in Figure 3. The sensors have been positioned at the top and bottom of the bearing housing in two perpendicular radial directions. The directions parallel to suction line and perpendicular to suction line can be explained with Figure 1. The used measurement equipment was:

Software: Famos Analyser: imc CS-7008-N Sensors: Prueftechnik Vib 6.172

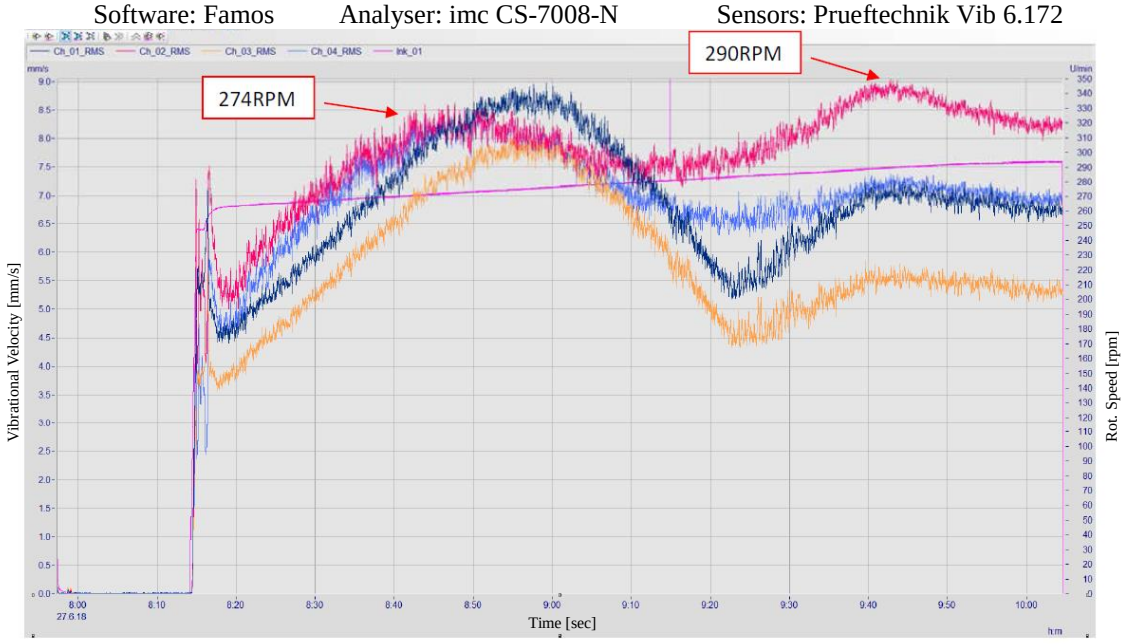

Figure 3: Typical time history of the housing vibrational velocities

To find out the source of the higher vibrations several measurements and evaluations have been conducted:

1. Bump tests at different assembly stages of the aggregate
2. Housing and shaft vibrations

2.1 Bump Test Measurements and Their Recalculation

To investigate if resonances are the source of these higher vibrations, bump tests on 3 pumps on site have been performed. To get a clear picture of the dynamic behavior of the complete system several sensors have to be placed on the structure (pump and plinth) at the same time, see Figure 4. The response has been measured with amplitude and phase angle at the same time for all sensors.

Furthermore, with these bump tests a calibrated finite-element-model can be derived. All important components are included in the FE-model. Volume elements were used for the modeling stationary components. Rotating components are modeled with beam elements. Additional masses (e.g. impeller) were modelled with mass point elements. For the radial bearings 2-D bearing spring elements were used.

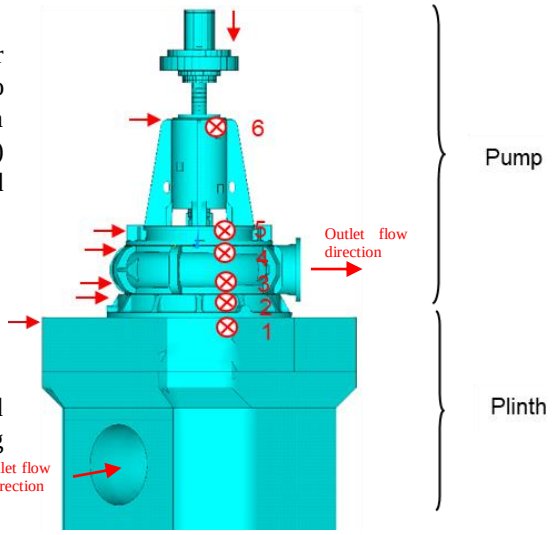

Figure 4: Positions of the sensors

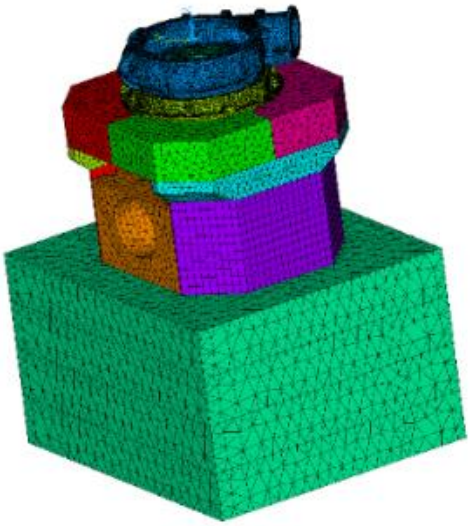

In such complex pumps there are many uncertainties. The pumps have many connections between the different system components. Usually it is difficult to model such connections. If the different parts are rigidly connected the FE Modelling can be performed on this assumption. However, if the connecting parts are flexible and movements are possible in the connecting areas stiffness and damping elements have to be introduced which are difficult to identify and to model. This is particularly the case if the connections have nonlinear character. The fixation of the entire aggregate is simulated at the concrete floor, see green block. Here all translational directions of all areas, except the top area where the plinth is poured on, are fixed. The connection between bearing housing and hub plate was simulated with linear springs with a stiffness of the associated M36 (length=140mm) connecting bolts. The remaining stationary components have surface contact. There, the preload force is sufficient to ensure that there is no relative movement of the components.

Figure 5: Finite-element-model for recalculation of bump test with plinth + suction ring + pump volute

The bump tests have also been conducted at several assembly stages of the aggregate. The first bump test was conducted only with plinth + suction ring + pump volute, see Figure 5. The corresponding bode plot parallel and perpendicular to suction line are shown in Figure 6 and Figure 7. The natural frequencies of plinth + suction ring + pump volute were measured with f = 47 / 48 Hz (perpendicular / in direction of suction line) on site. These natural frequencies have been recalculated with f = 46.14 / 47.44 Hz (perpendicular / in direction of suction line) which is a good correlation between measurement and recalculation.

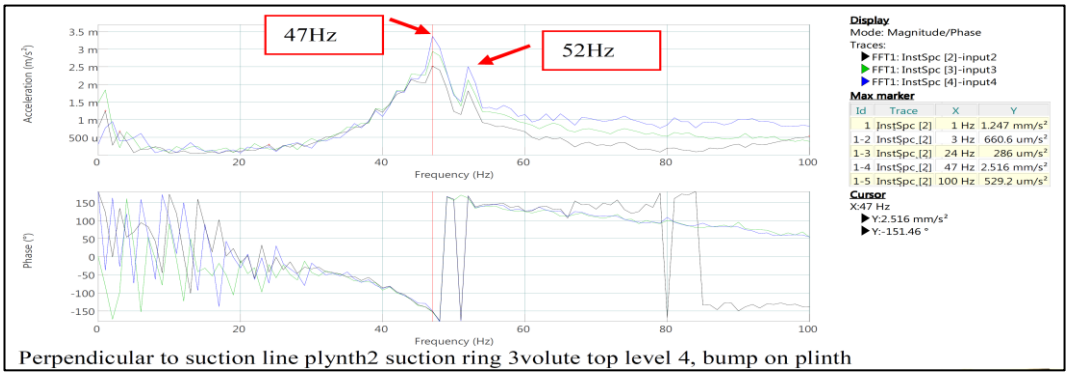

Figure 6: Measured FFT parallel to suction line with plinth + suction ring + pump volute

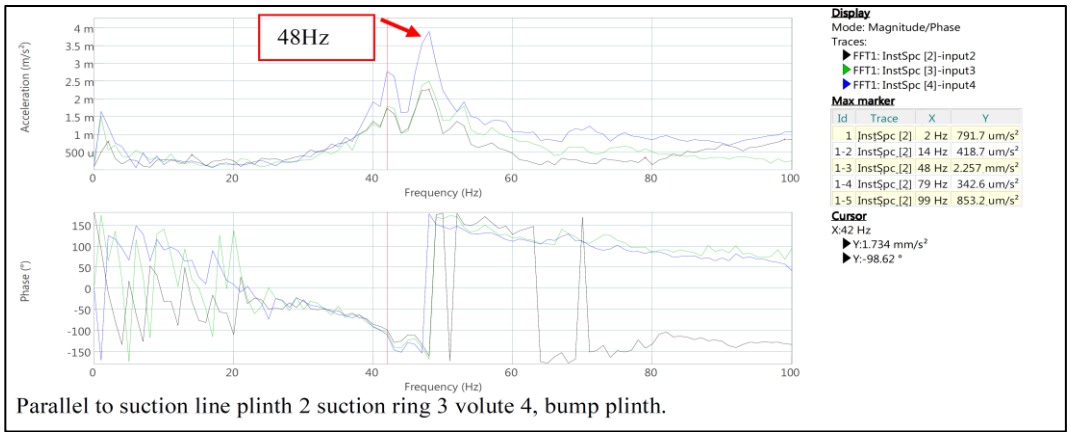

Figure 7: Measured FFT perpendicular to suction line with plinth + suction ring + pump volute

Afterwards bump tests of the complete assembled aggregate has been performed, see Figure 8. This assembly state corresponded to the completely installed unit, which was ready for operation. Compared to the previous impact test, the complete rotor has now been installed and coupled to the motor shaft. Furthermore, all missing stationary components, such as hub plate or bearing housings were installed. This assembly state also means that the pump was filled with water, which was taken into account in the calculation by increasing the density. The connected discharge pipeline, which leads about 90m vertically upwards and was screwed directly to the discharge flange, was taken into account with the help of an additional mass points. The finite element model contains about 400,000 elements with almost 1 million nodes. With this fine meshing, the complex structure and its stiffness, damping and mass behavior could be mapped well.

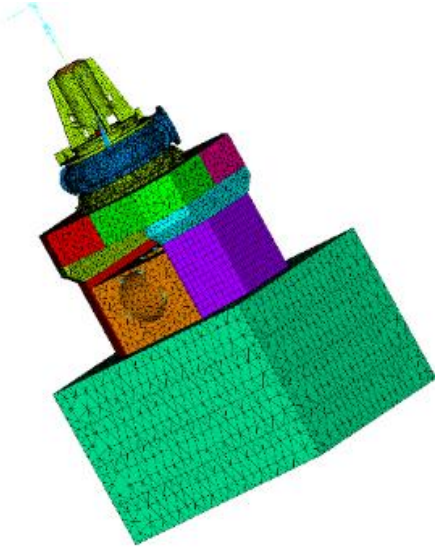

Figure 8: Complete assembled aggregate

The corresponding bode plots parallel and perpendicular to suction line are shown in Figure 9 and Figure 10.

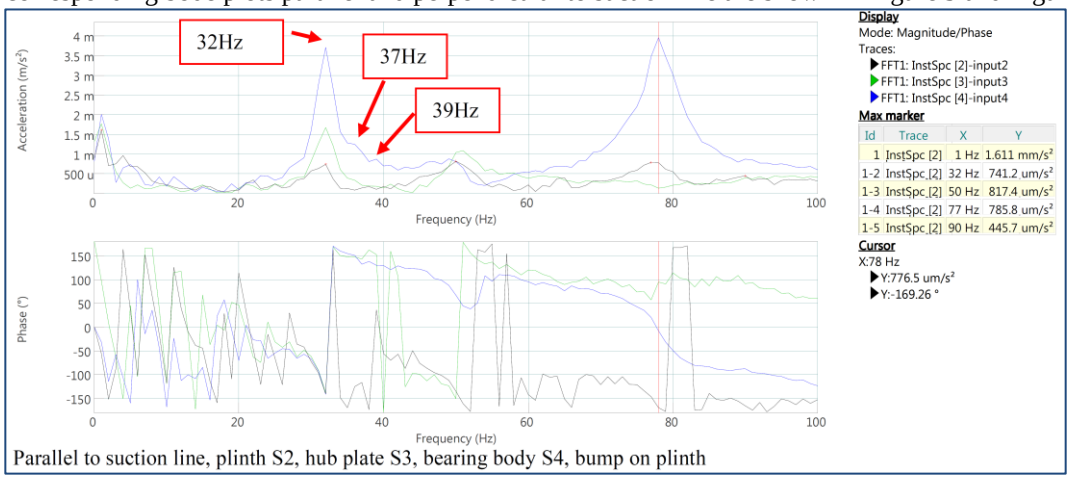

Figure 9: Measured FFT parallel to suction line of complete aggregate

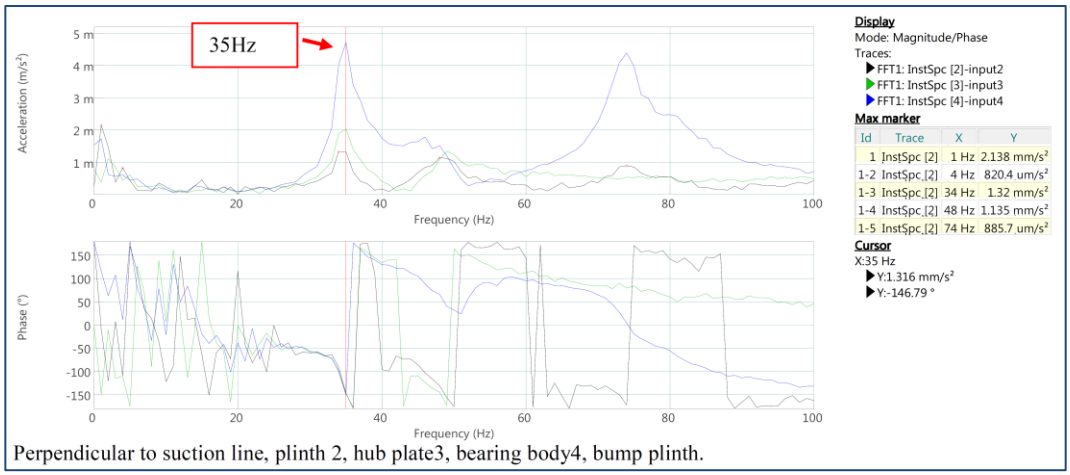

Figure 10: Measured FFT perpendicular to suction line of complete aggregate

The measurements and their recalculation showed the following results:

- The connection between plinth and pump is stiff which is evaluated by the measured phase angle.
- The results showed a rotor natural frequency at f = 25 – 26 Hz. The combined plinth – pump aggregate natural frequencies decreases to f = 37 – 40 Hz due to the higher mass of the complete aggregate compared to the previous bump test. The recalculation and measurement shows a difference in natural frequencies of $\Delta f \approx 5\%$.
- The discharge pipework has an influence on the natural frequencies of the complete system and with that on the vibration velocities. This is evaluated by comparison of the bump tests with and without connected discharge pipework. In the finite-element-model this pipework has been modeled with additional mass points at discharge piping system.
- All calculated natural frequencies shows an inverse pendulum of the combined plinth – pump aggregate with the highest deflection at the top of the pump aggregate which is as expected. A calculation variant analysis with a stiff plinth shows an increase in pendulum natural frequency of the pump of f = 55 Hz and higher. Thus the plinth is not a rigid fixation for the pump.

Additional evaluations of the bump tests in form of Frequency Response Functions (FRFs) were created. The FRF's were recalculated with harmonic response analyses using the finite element model adapted to the measured natural frequencies, see Figure 11. The figure shows the measured FRF for the two directions at the DE Bearing in continuous lines. The corresponding calculated FRFs are presented in dashed and dotted lines.

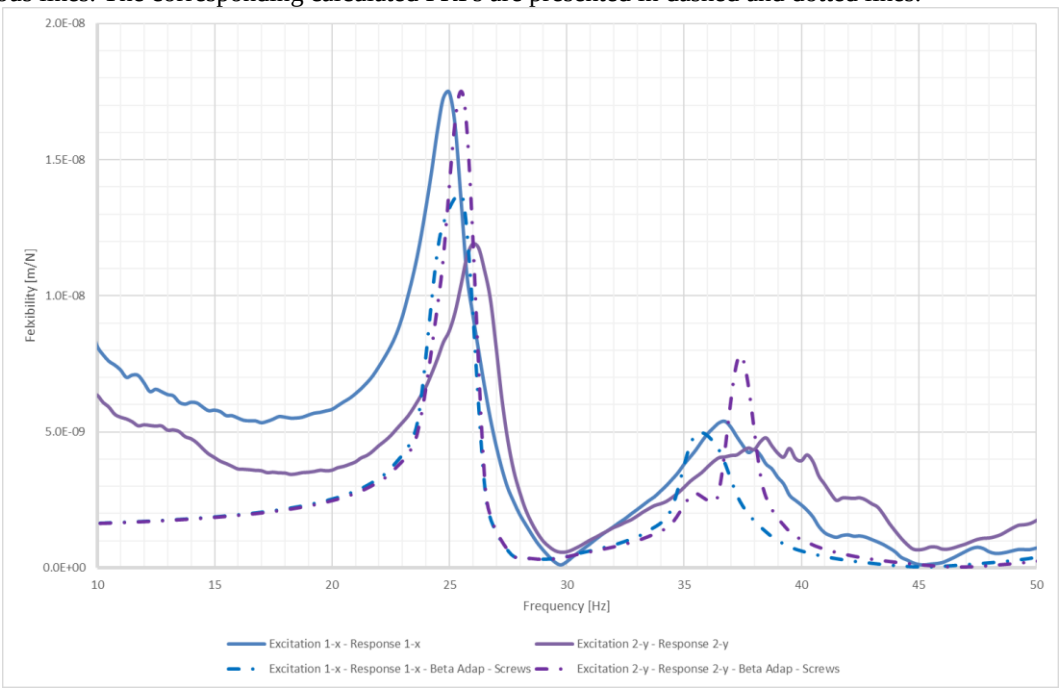

Figure 11: Measured and Calculated Frequency Response Functions (FRF)

In the following Figure 12 the measured and calculated deflection at the resonance of f = 25Hz are shown. The correlation between bump test measurement and recalculation is in terms of resonance frequencies, mode shapes and deflections quite good for a rotational speed n = 0rpm.

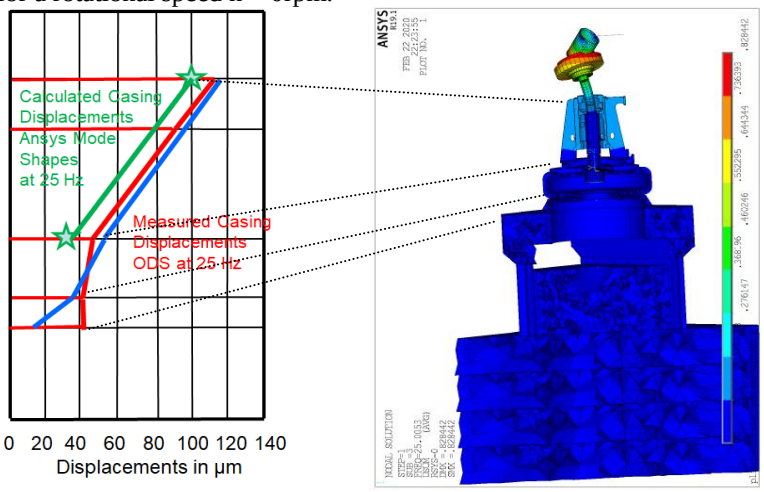

Figure 12: Measured and calculated deflections

2.2 Housing Vibration Measurements and Their Recalculation

2.2.1 Housing Vibration Measurement

Measured housing vibrations are the vibration response x(t) of excitations F(t) of a vibrational system.

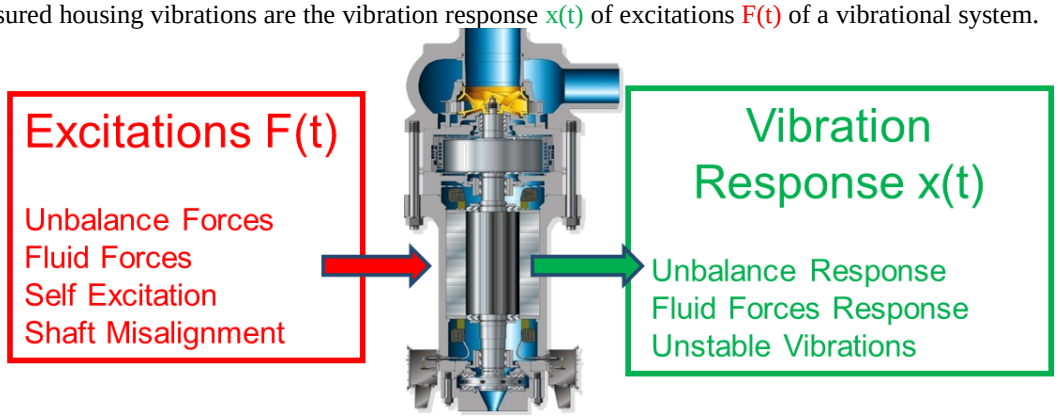

This can be expressed by the equation of motion which includes mass M, damping D, gyroscopic G and stiffness C effects.

$$M\ddot{x}(t) + (D(\Omega) + G(\Omega))\dot{x}(t) + C(\Omega)x(t) = F(t) \quad (1)$$

The pump is operated with a variable speed drive (VFD). In Table 1 an overview of possible excitations frequency components is given. From this table can be seen that a wide frequency range from 2.5Hz – 43.07Hz can excite the pump.

Table 1: Operating speed range

Rot. Speed [rpm]	1*n [Hz]	4*n [Hz]	8*n [Hz]
150	2.50	10.00	20.00
323	5.38	21.53	43.07

A typical time history of the housing vibrations is shown in Figure 3. The housing vibrations were recorded in two perpendicular directions at the bottom and top of the bearing housing. Order related waterfall plots and color maps of time related frequency spectra, see exemplarily Figure 13, have shown that:

- The 1*n frequency component (unbalance excitation) is on a low level
- The 2*n frequency component (shaft misalignment) is also on a low level.
- The dominating frequency components are 4*n and 8*n.
- The higher the rotational speed the higher the 4*n and 8*n frequency component.

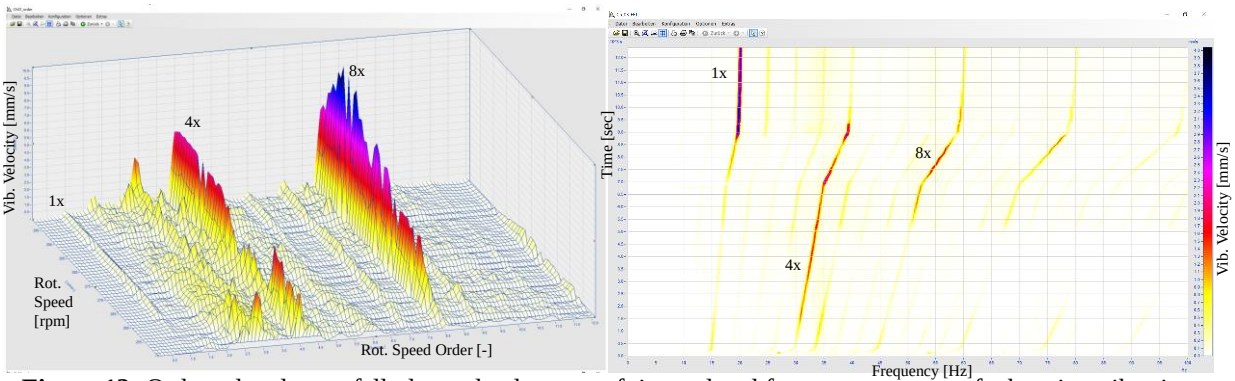

Figure 13: Order related waterfall plot and color map of time related frequency spectra of a housing vibration

Based on these evaluations resonance like vibrations could be detected at frequencies of about 19.5Hz, 35 Hz and 37Hz during operation. These frequencies are excited by 4*n and 8*n. Shaft vibration measurements next to the DE and NDE-Bearing were also conducted. The evaluation of the shaft measurement showed that the orbital shape, see Figure 14, is mainly determined by the 4*n excitation (blade pass). All other frequency components are on a low level. Furthermore, it was found that the vibrations at the lower, NDE bearing were much higher than at the DE bearing.

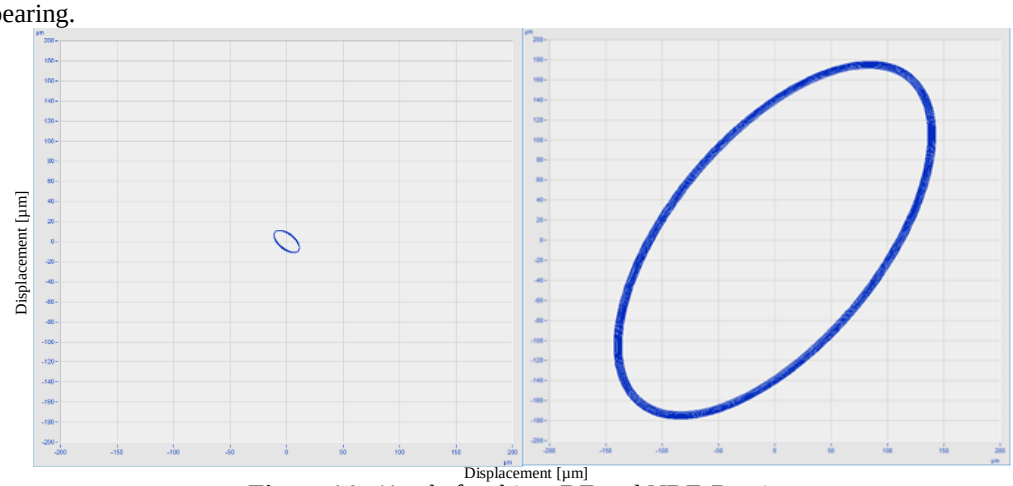

Figure 14: 4*n shaft orbit at DE and NDE-Bearing

2.2.2 Recalculation

In chapter 2.1 it is shown that a FE-Model was derived to recalculate the natural frequencies as well as the mode shapes of the complete aggregate including pipework and support structure (plinth) during standstill. But for the case „pump in operation “the model has to be extended:

- Gyroscopic effects have now been included in the FE-Model.
- Due to the static (F_{av}) and dynamic ($\Delta Fr = F_{r\ max} - F_{r\ min}$) impeller fluid forces mainly the NDE-Bearings are loaded. As in the impeller itself the NDE-Bearing force has also a static force and a dynamic force part, see Figure 15. The dynamic component of the radial thrust is determined by 4*n (number of impeller blades). The static and dynamic hydraulic forces have been calculated with the aid of CFD.

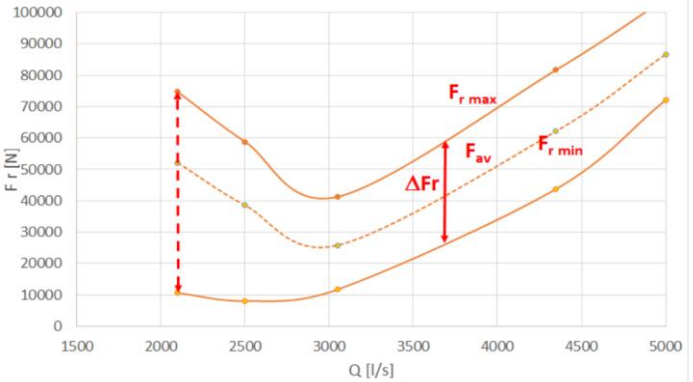

Figure 15: Hydraulic forces for different flows calculated with CFD

- The static NDE-Bearing force determines the static equilibrium position and the corresponding NDE-stiffness values. These stiffness values, expressed in the 4x4 NDE-Stiffness matrix, have now to be included in the FE-Model. The translational and bending stiffness values for different static bearing forces are shown in Figure 16 and are calculated with [3].

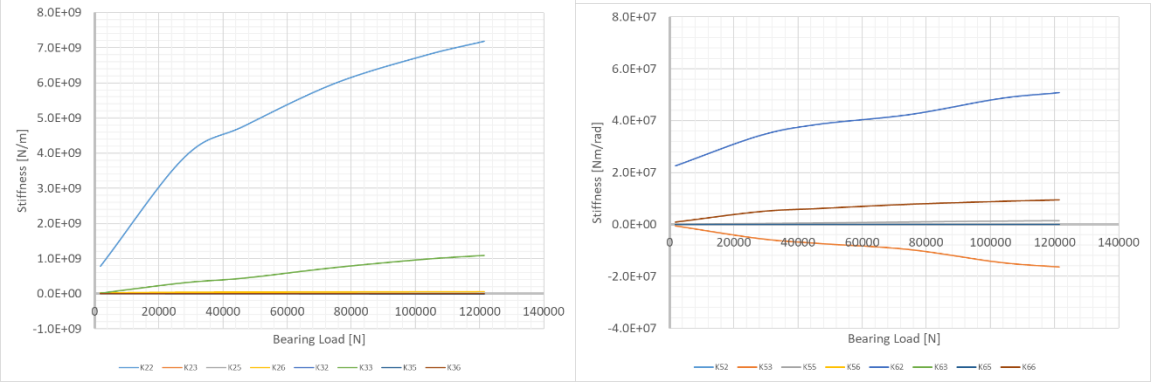

Figure 16: Linear and bending stiffness of the NDE-Bearing

With this extended FE-Model the natural frequencies have been analyzed. The calculated natural frequencies are listed in Table 2 and shown in form of a Campbell-Diagram in Figure 17. The results show that the increased vibration velocities on the housing can be linked to resonances. From this table can be seen that there are 4 natural frequencies related to rotor. These natural frequencies increase a little bit with increased rotational speed since with that also the static hydraulic radial thrust increases with rotational speed, see Figure 15. The natural frequency no. 5 and 6 remain the same for different rotational speeds and belong therefore to stationary parts such as plinth.

Table 2: Calculated natural frequencies

No.	Frequency [Hz]				
	150rpm	200rpm	250rpm	295rpm	323rpm
1	8.05	10.25	11.72	12.11	12.25
2	18.54	18.93	19.14	19.17	19.18
3	21.76	22.04	22.33	22.54	22.71
4	25.66	26.63	27.38	27.82	28.09
5	35.05	35.06	35.08	35.08	35.08
6	36.05	36.10	36.16	36.22	36.27

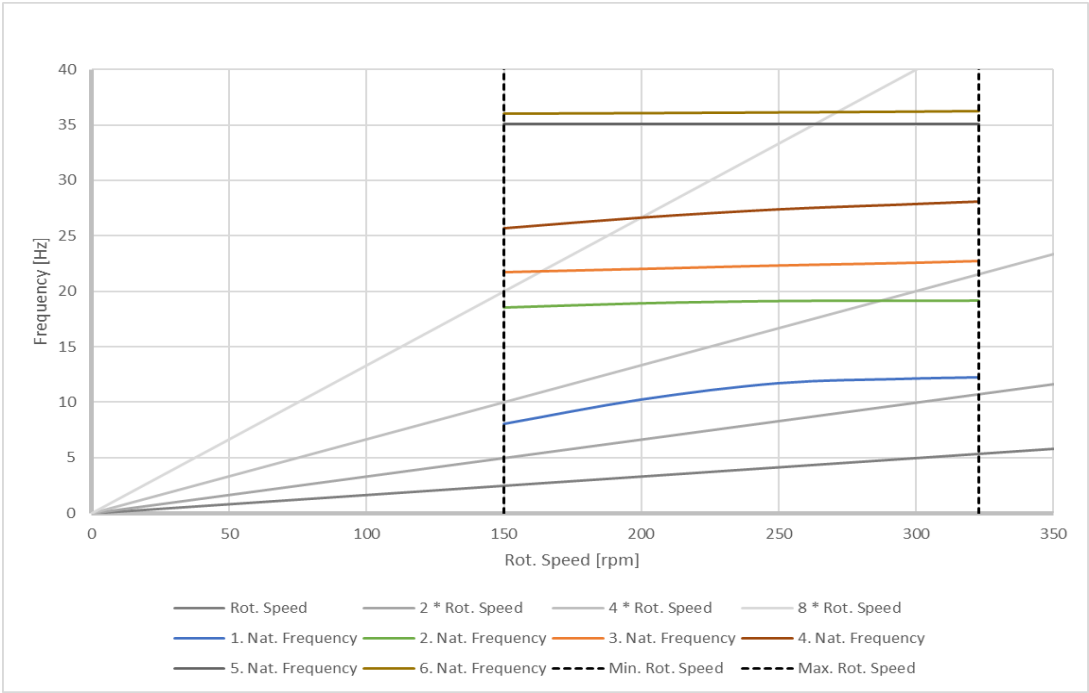

Figure 17: Campbell-Diagram

3 Optimizations based on the Recalculation of Measurements

In chapter 2 it is shown that the derived FE-Model the dynamic behavior of the complete aggregate can be recalculated. Based on the equation of motion, various optimization options are now possible to reduce the vibrational velocities. On the one hand, these are the reduction of the exciting forces F(t) and, on the other hand, a dynamic change in the vibration system M, D(Ω), G(Ω), C(Ω). Experience has shown that it is meaningful to reduce increased vibrations not only with one optimization, but also to optimize several components at the same time. Due to design reason installation of additional mass was not possible, as well as a change in the damping and gyroscopic effect. So it was decided to:

- Develop a new hydraulic design to decrease the excitation at blade passing frequency
- Install a single row type of NDE-Bearing to reduce the bearing clearance, to reduce the minimum required preload on the bearing and increase in bearing stiffness.

The new hydraulic design has been recalculated with CFD. The resulting radial forces F_r for this new design are shown in Figure 18. By comparison of these new hydraulic radial forces with the original ones, see Figure 15, can be seen that the static part F_{av} remains the same. However, the dynamic part ΔFr is reduced by approximately 30% which directly influences the 4*n and 8*n vibrational component.

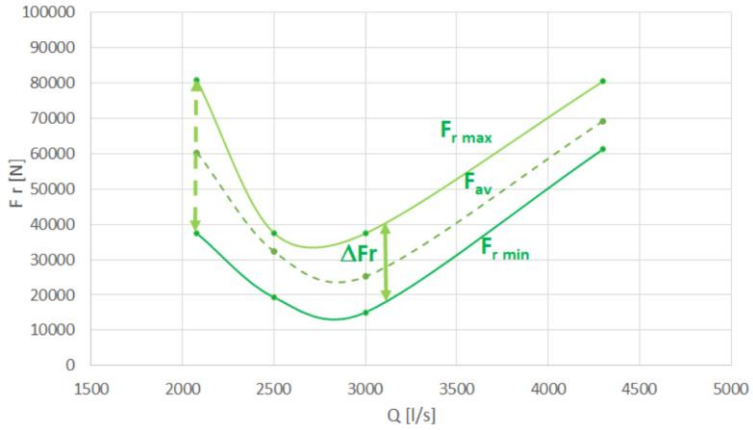

Figure 18: New hydraulic radial forces for different flows

The calculated natural frequencies with the optimized NDE-Bearing for the most interesting rotational speed at n = 295rpm are listed in Table 3.

Table 3: Calculated natural frequencies with optimized NDE-Bearing

No	Frequency [Hz]
1	11.09
2	21.64
3	27.05
4	28.60
5	35.41
6	36.27

By comparison of Table 2 and Table 3 can be seen that the second natural frequency increased from f = 19.17Hz to f = 21.64Hz. This is not a huge improvement but it is a little larger separation margin to 4*n excitation (= 19.66Hz). Additionally, this new bearing has a smaller gap clearance and with that the rotor can rotate only on a smaller orbit which directly influences the vibrational velocity. The natural frequencies of the complete aggregate remain the same at frequencies of f ≈ 35Hz and 36Hz. This variant analysis confirms that these two natural frequencies are determined by stationary parts such as plinth.

After installation of the new impeller design and the NDE-Bearing at site the vibrational velocities during operation have been measured. The reduced vibrational velocities are shown in Figure 19. By comparison of these new vibrational velocities with the original ones, see Figure 3, it can be seen that the there is a decrease of about 45% in the height for the 8*n excitation (= 274rpm). These new vibrational velocities are now in an acceptable range. Higher vibrations still occur around the rotational speed of n = 297rpm, which are still not acceptable. In this speed range a reduction of about 17% could be achieved with the previously described optimizations. The calculation with the optimized bearings predicted an increase in the originally measured resonance at approx. 290rpm (= 19.3Hz) to approx. 325rpm (= 21.46Hz). During the many on-site investigations, it could not be

determined whether there were other components with a resonance at around 290rpm. Therefore, it was agreed with the customer to develop an alternative control program. This alternative control program excludes the operation of the pump in the area of this rotational speed.

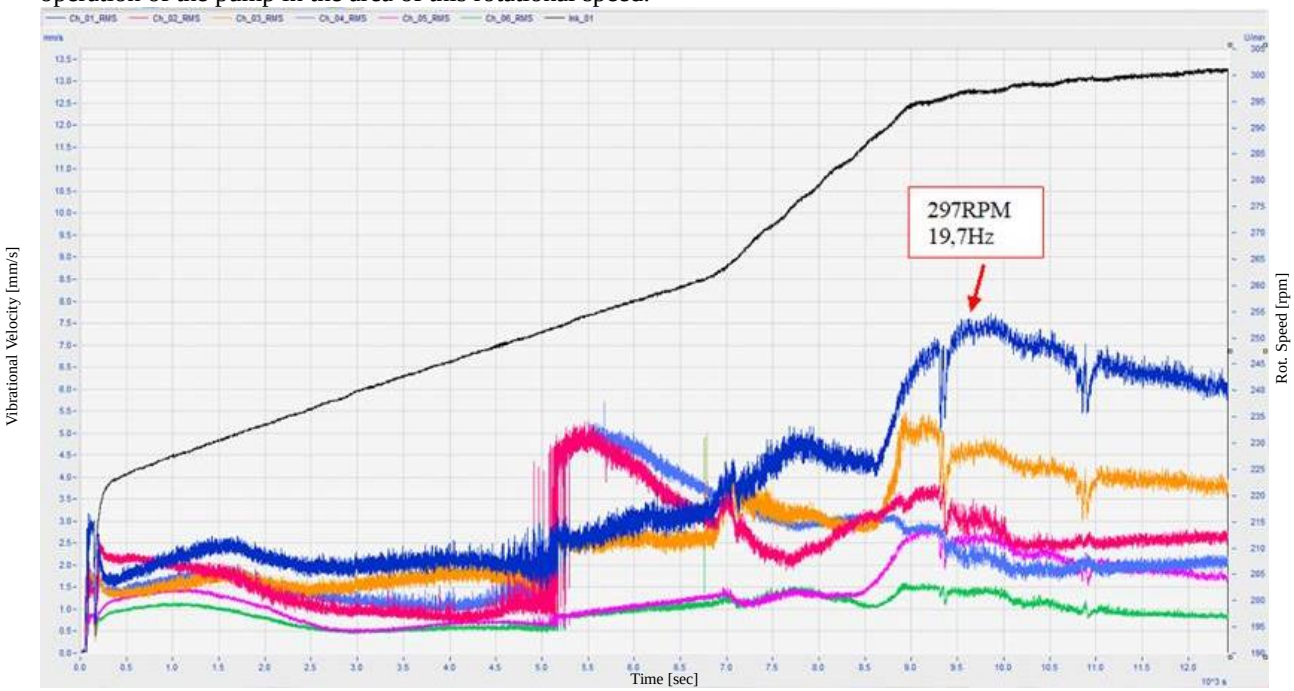

Figure 19: Vibrational velocities at site after optimization

4 Conclusion

This document shows how a finite element model can be adapted to measurements in order to then carry out optimization analyses. These analyses showed that two causes of the higher vibrational velocities were found within the pump and one with the system. The concrete block below the pump was not dimensioned to be sufficiently stiff, so that it caused the entire structure to resonate in the operating speed range. Pump-side optimization measures were defined based on the modal results using finite element analyses. A new impeller design was developed, which produces lower hydraulic excitations with the large flow rate range. Furthermore, a more suitable roller bearing for the prevailing radial bearing loads was installed.

The two optimizations on the pump side already reduced the housing vibrations to an acceptable level, except for one rotational speed. However, since no changes could be made to the cast concrete block, the housing vibrations could not be reduced to a low level in the complete operating speed range. Variant analyzes with the plinth showed a clear dependence of the natural frequencies at 8*n on the rigidity of this substructure. An alternative control program had to be developed and implemented to bypass the resonance area of the overall structure. This shows that the surrounding structure can have a major impact on the overall vibration behavior of the pump, especially in the case of speed-controlled pumps. Therefore, a holistic view of the pump and the environment will become increasingly important in the future.

Acknowledgement

Thanks go to the colleagues at KSB and to Prof. R. Nordmann for the good technical discussions, which helped to find a solution.

References

[1] DIN ISO 10816-7: *Mechanical vibration – Evaluation of machine vibration by measurements on non-rotating parts – Part 7: Rotor dynamic pumps for industrial applications, including measurements on rotating shafts.*

[2] ANSYS: *URL:www.ANSYS.com, Retrieval on November 21st, 2022*

[3] MESYS Software for mechanical engineering: *www.mesys.ag, Retrieval on November 21st, 2022*

15th SIRM – European Conference on Rotordynamics,
Darmstadt, Germany, 22nd – 24th February 2023

Turbocharger Rotors on Wire Mesh Dampers: Sensitivity and Optimization Analysis in Dynamic Design

Alexios Chatzistavris, Athanasios Chasalevris

National Technical University of Athens, 15780, Athens, Greece, {mc14347, chasalevris}@mail.ntua.gr

Abstract

This paper implements sensitivity and optimization analysis in an 8-DOF rotor-bearing system, consisting of two identical semi-floating ring bearings integrated with ring-shaped wire mesh dampers (WMDs), and a rotor carrying a disc mass at both ends, representing the compressor and turbine wheels. While the realistic geometric characteristics of the rigid rotor are fixed, the variation of WMD design variables and of operating conditions (oil temperature and unbalance phase) compose a Design of Experiment (DoE) process. The unique source of nonlinearity in the system is the bearing impedance forces, which are a combination of nonlinear oil film forces and of nonlinear WMD forces due to the varying stiffness and damping of the WMD throughout its operation (deformation). The considered WMD key design variables are the radial thickness, the relative density, the radial interference and the wire diameter, and they are methodically preselected, in order to cover a wide range of encountered WMD designs. The results show significant alternation in the synchronous and sub-synchronous dynamic response of the rotor and of the bearing rings, in the rotating speed range up to approximately 170 kRPM; this leads to a narrow acceptable design range. Furthermore, after conducting various statistical tests to the collected response data, significant correlation was presented between the maximum relative eccentricity ratio and three of the WMD design variables.

1 Introduction

In order to tackle the problem of sub synchronous vibrations in high-speed turbomachinery systems, the installation of bearings of specific design is of utmost importance. The role of the bearings is to suppress the vibrations of the rotor during its operation and more specifically, in high-speed systems, to avoid self-excited vibrations which normally lead to high response amplitudes. Hence, the need to create a bearing system with proper stiffness and damping properties, as well as sufficient life span, has been raised. In order to address the aforementioned need in high-speed rotating systems, foil bearings (FB) where developed in 1950s, and later, in 1970s, WMD Bearings [7] (see Figure 1 and 2) where presented as a potential solution among others, e.g. full/semi-floating-ring bearings. WMDs present high structural damping, resulting from the micro-slip that takes place at metal wire junctions [2], ideal for reducing synchronous and sub-synchronous instability caused by high cross-coupling stiffness [9]. Since 1980s, WMDs were implemented in series with roller bearings, and were considered as a potential solution for replacing squeeze film dampers (SFD) in aircraft engines [4]. Zarzour M. J. (1999) [17] showed that WMD's equivalent viscous damping can match that of oil-lubricated SFDs in various operating conditions, such as balanced or unbalanced rotor, high temperature and, surprisingly, in oil-lubricated environment, indicating that WMDs do not only provide damping through dry friction, but also through material hysteresis. Al-Khateeb (2002) [3] carried out thorough research on the applicability of WMDs, denoting the ability to overcome SFDs drawbacks concerning their performance under high temperatures and limitation of small displacements, with the implementation of inexpensive and readily available WMDs.

On the contrary to the previous research, which mainly studied the stiffness and damping properties of the WMD component in varying operating conditions, the present work focuses on the design of two identical WMD components supporting the oil bearings of a turbocharger rotor, to establish a stable operation (bifurcation-free) in a specific rotating speed range.

2 Analytical model of the rotor on semi-floating ring bearings with WMD

The physical model of the oil lubricated semi floating WMD bearing is constructed by three different parts; following the outer surface towards the center, these three parts include the bearing housing (rigid shell), the WMD component, and the rigid ring (semi-floating ring), as shown in Figure 1.

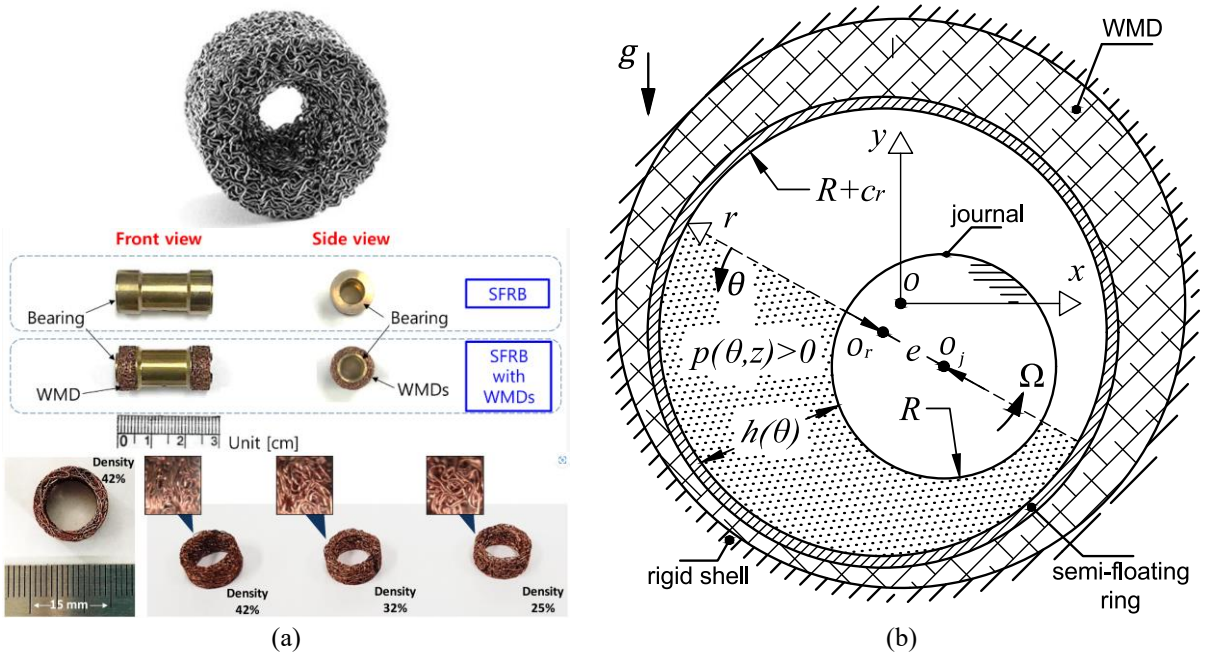

Figure 1: a) typical WMD configuration for automotive turbocharger applications, b) schematic representation of the physical model of the WMD semi-floating ring bearing.

In Fig. 1b, the journal center $O_j\left(x_j, y_j\right)$ defines an eccentricity e_j with respect to the bearing center $O(0,0)$, while the ring center $O_r\left(x_r, y_r\right)$ defines an eccentricity e_r with respect to $O(0,0)$. The effective journal eccentricity e which establishes the hydrodynamic lubrication is then defined in Eq. (1) together with its rate of change during the whirling motion of the journal and the ring. The journal may execute general plane motion with $e < c_r$, while the semi-floating ring can execute only transfer motion. Attitude angle rate of change $\dot{\phi}$ is defined in Eq. (2).

$$e = \left(\left(x_j - x_r\right)^2 + \left(y_j - y_r\right)^2\right)^{1/2},\ \dot{e} = \left(\left(x_j - x_r\right)\left(\dot{x}_j - \dot{x}_r\right) + \left(y_j - y_r\right)\left(\dot{y}_j - \dot{y}_r\right)\right)/e$$
$$\varepsilon = e / c_r,\ \dot{\varepsilon} = \dot{e} / c_r \tag{1}$$

$$\dot{\phi} = \frac{\left(x_j - x_r\right)\left(\dot{y}_j - \dot{y}_r\right) - \left(y_j - y_r\right)\left(\dot{x}_j - \dot{x}_r\right)}{e^2} \tag{2}$$

For a random position of the journal and the ring, the oil film pressure distribution can be obtained by the short-bearing approximation [1,12]. This assumption is valid in such applications as the $L_b/(2R)$ ratio is less than 0.5. Simple geometry for the ring is assumed in this work, meaning that no grooves or oil inlet holes are considered. The oil pressure distribution is then defined in Eq. (3) [12,15] where pressure values in the cavitated area are assumed zero. The resulting oil film forces applied from the ring to the journal and vice-versa are then defined in Eq. (4) [12] in the colinear and normal direction of eccentricity e. The oil film thickness h is approximated as $h(\theta) = c_r - \left(x_j - x_r\right)\cos(\theta) - \left(y_j - y_r\right)\sin(\theta)$. The dynamic viscosity μ of the lubricant is assumed constant in the entire lubricated area, and in this work two values are considered in the continue, one for hot and one for cold oil conditions.

$$p(\theta,z)=\begin{cases}\dfrac{3\mu\left(\Omega h_\theta+2\dot{h}\right)}{h^3}\left(z^2-\dfrac{L_b^2}{4}\right) & ,0\le\theta\le\pi \text{ and } -\dfrac{L_b}{2}\le z\le\dfrac{L_b}{2}\\ 0 & ,\text{other}\end{cases} \tag{3}$$

$$F_r=\frac{1}{2}\mu\left(\frac{R_r}{c_r}\right)^2\frac{L_b^3}{R_r}\left(\frac{2\varepsilon^2\left(\omega+2\dot{\phi}\right)}{\left(1-\varepsilon^2\right)^2}+\frac{\pi\dot{\varepsilon}\left(1+2\varepsilon^2\right)}{\left(1-\varepsilon^2\right)^{5/2}}\right)$$

$$F_t=\frac{1}{2}\mu\left(\frac{R_r}{c_r}\right)^2\frac{L_b^3}{R_r}\left(\frac{\pi\varepsilon\left(\omega+2\dot{\phi}\right)}{2\left(1-\varepsilon^2\right)^{3/2}}+\frac{4\varepsilon\dot{\varepsilon}}{\left(1-\varepsilon^2\right)^2}\right) \tag{4}$$

$$F_x^B=F_r\frac{\left(x_j-x_r\right)}{e}+F_t\frac{\left(y_j-y_r\right)}{e},\quad F_y^B=F_r\frac{\left(y_j-y_r\right)}{e}-F_t\frac{\left(x_j-x_r\right)}{e} \tag{5}$$

Considering the model of the wire mesh damper (WMD), copper or stainless-steel wires are meticulously knitted together producing uniform layers of wire or metal mesh (MM) (see Figure 2a), consisting of numerous microelements (see Figure 2b). Then, the designer defines the appropriate amount of the layers that will be compressed together and, therefore, the WMD's relative density, thickness, inner and outer radius and width are determined. Each set of characteristics of a WMD defines its final stiffness and damping properties.

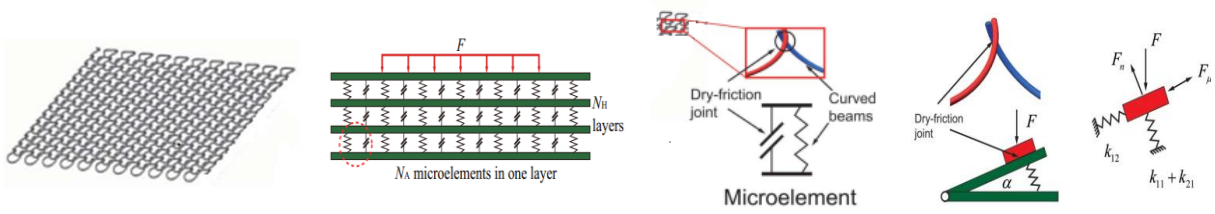

(a) (b) (c) (d)

Figure 2: a) knitted layer of MM, b) equivalent of MM component, c) equivalent model of a microelement, and d) equivalent stiffness of a microelement [8,10]

The MM component consists of N identical microelements which are distributed to N_H layers of N_A microelements in each layer, see Fig. 2b. Each microelement, see Fig. 2c, contains its own equivalent stiffness, see Fig. 2d.

The equivalent stiffness coefficient and the equivalent viscous damping coefficient of the entire MM component can be calculated in Eq. (6), where $\lambda=A/H$ is the ratio of the sectional area to thickness, and the term $2\rho_m/\pi^2d^2nR_c$ is defined by the raw material characteristics. The $K_{L/U}$ is the loading and unloading stiffness coefficients of one microelement and ΔW is the energy dissipation in period of loading and unloading. The WMD force is then given in Eq. (7), see Fig. 3c, and 3d.

$$K_{MM(L/U)}=\lambda\left(\frac{2\rho_m}{\pi^2d^2nR_c}\right)^{1/3}K_{L/U},\quad \Delta W=C_m\pi\omega u_0^2 \tag{6}$$

$$F_x^W=K_{MM(L/U)}x_r+C_m\dot{x}_r,\quad F_y^W=K_{MM(L/U)}y_r+C_m\dot{y}_r \tag{7}$$

The rotor-bearing system model consists of a rigid shaft supported on two WMD semi-floating ring bearings, see Fig. 3 and 1b. The position of the rotor and of the rings at any given time instant can be described by a 2nd-order 8×8 system of ordinary differential equations (ODEs), four of which derive from the displacement of the journals #1 and #2 along the x and y direction, see Eqs. (8-11), and the remaining four derive from the displacement of the rings #1 and #2 along the same directions, see Eq. (12). The definition of all parameters included in Eqs. (7-11) is presented in Table 1. The unbalance force acting at each unbalance plane is defined in Eq. (13) for rotating motion with constant acceleration γ. The rotor in this model is considered rigid for the reason that at the specific geometric and physical properties of the system the low flexibility would have a minor influence in the response of the system. Normally, models of automotive turbochargers operating at higher speeds (e.g. 300kRPM) include flexible rotor models; at such cases, the rotor response and the respective speeds

where self excited oscillations are triggered, have some influence, still minor though. Including a flexible rotor would render another natural mode in the system, and the time integration would be even slower at some range of rotating speed, depended also from the WMD design. In this work, it is preferable to sacrifice some accuracy in the dynamic response in order to gain higher computational efficiency.

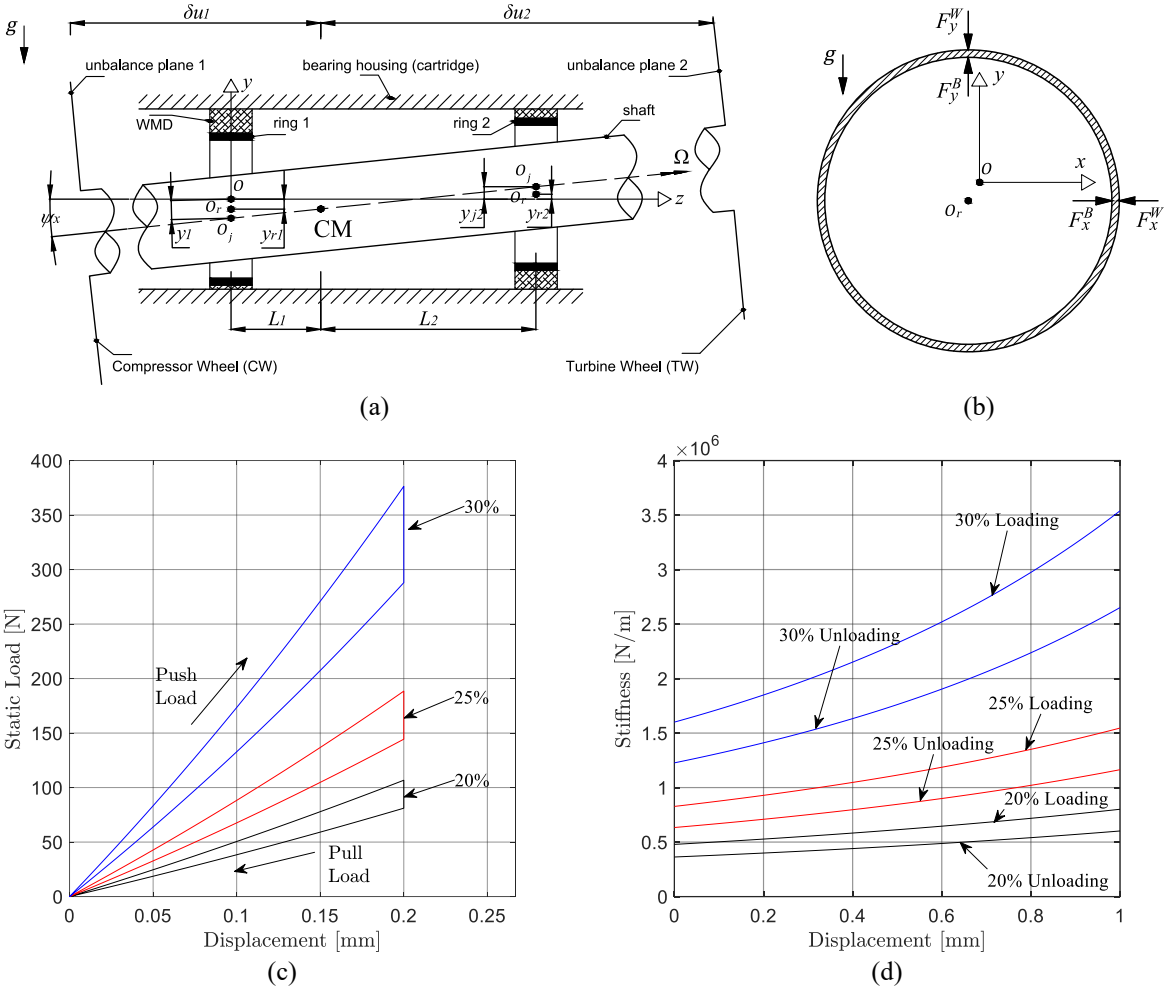

Figure 3: representation of a) rotor bearing layout with key design properties, and b) of rigid ring with loading. typical quality of the WMD c) static load, and d) stiffness, for different relative density.

The nonlinear nature of the WMD resulting forces is depicted in Figs 3c and 3d. In Fig. 3a, the displacement of the rigid ring inside the WMD takes place after a static radial load is applied. Different relative density of the wire mesh is considered. The static load acts as pull or push load for the wire mesh. Push load brings the knitted layers closer, while the pull load makes the knitted layers sparser in the radial direction. In Fig. 3c, one may notice the characteristic jump in the static load when this is changed from pull to push load and vice versa. The change in the slope of load-displacement curves in Fig. 3c is depicted in Fig. 3b where the WMD radial stiffness is evaluated for a wide range of displacement. The variation of radial stiffness is another source of nonlinearity in WMD forces together with the jump phenomenon in Fig. 3c and the relatively similar progress of damping coefficient, not depicted in Fig. 3.

$$\ddot{y}_{j,1} = \frac{L_1 + L_2}{ML_2}\left(F_1^G + F_2^G + F_{y,1}^B + F_{y,2}^B + F_{y,1}^U + F_{y,2}^U\right) - \frac{L_1}{L_2}\ddot{y}_{j,2} \tag{8}$$

$$\ddot{x}_{j,1} = \frac{L_1 + L_2}{ML_2}\left(F_{x,1}^B + F_{x,2}^B + F_{x,1}^U + F_{x,2}^U\right) - \frac{L_1}{L_2}\ddot{x}_{j,2} \tag{9}$$

$$\ddot{y}_{j,2} = -\frac{L_1 + L_2}{J_T}\left(F_{y,1}^B L_1 - F_{y,2}^B L_2 + F_{y,1}^U \delta u_1 + F_{y,2}^U \delta u_2\right) + \frac{J_P \Omega}{J_T}\left(\dot{x}_{j,1} - \dot{x}_{j,2}\right) + \ddot{y}_{j,1} \tag{10}$$

$$\ddot{x}_{j,2} = -\frac{L_1 + L_2}{J_T}\left(F_{x,1}^B L_1 - F_{x,2}^B L_2 - F_{x,1}^U \delta u_1 - F_{x,2}^U \delta u_2\right) - \frac{J_P \Omega}{J_T}\left(\dot{y}_{j,1} - \dot{y}_{j,2}\right) + \ddot{x}_{j,1} \tag{11}$$

$$m_1 \ddot{y}_{r,1} = F_{y,1}^W - F_{y,1}^B - m_1 g\,, \quad m_1 \ddot{x}_{r,1} = F_{x,1}^W - F_{x,1}^B\,, \quad m_2 \ddot{y}_{r,2} = F_{y,2}^W - F_{y,2}^B - m_2 g\,, \quad m_2 \ddot{x}_{r,2} = F_{x,2}^W - F_{x,2}^B \tag{12}$$

Table 1: definition of parameters in equations of motion

M :	rotor mass	$F_{i,j}^{G}$:	gravity force, $=-MgL_{j,i}/(L_1+L_2)$
J_P :	rotor mass polar moment of inertia	F^{B} :	bearing force, see Eq. (5)
J_T :	rotor diametral mass moment of inertia	F^{U} :	unbalance force, see Eq. (13)
m_i :	mass of the ring i	F^{W} :	WMD force, see Eq. (7)

$$F_x^U = U\left(\Omega^2\cos\left(0.5\gamma t^2\right)+\gamma\sin\left(0.5\gamma t^2\right)\right), \quad F_y^U = U\left(\Omega^2\sin\left(0.5\gamma t^2\right)-\gamma\cos\left(0.5\gamma t^2\right)\right) \tag{13}$$

The equations of motion are converted into state space equations and time integration is applied for the evaluation of time response. The Ordinary Differential Equations - ODE set is a nonlinear set of equations due to the bearing forces and the WMD forces. The ODE set is stiff in specific operating conditions and the MATLAB solvers ode15s and ode23s [16] are preferred in this case.

3 Design of experiment (DoE) and statistical analysis

The design of experiment (DoE) is a process of choosing specific design variables and operating conditions of a system in a preselected range of interest. The number of the design variables and their individual values define the total number of configurations included in the DoE.

The DoE of the present work, examines various WMD designs with the purpose of defining the design range which renders an acceptable rotor operation in the entire rotating speed range, in four different operating conditions. To determine the acceptance or not of a WMD design, the maximum relative eccentricity ratio at both journals must be less than 0.7, meaning $\varepsilon_1 < 0.7$ and $\varepsilon_2 < 0.7$, see Eq. (1). The four selected WMD design variables and their respective values are defined in Table 2.

Table 2: WMD design variables and their individual values

WMD Design Variable	1st Value	2nd Value	3rd Value	4th Value
Radial thickness $H[mm]$	6	9	12	–
Relative density ρ $[mm]$	20	30	35	–
Radial interference R_{interf} $[mm]$	0.15	0.3	0.45	0.6
Wire diameter d $[mm]$	0.15	0.2	0.3	–

In order to provide a more suitable design range of the WMD, four Cases are integrated, corresponding to the four different operating conditions of the system (see Table 3). Two temperature conditions (hot and cold), and two unbalance configurations (single and pair) are considered.

Table 3: operating conditions

Operational Variable	Case A	Case B	Case C	Case D
Oil temperature $T[^oC]$	90	150	90	150
Initial unbalance phase φ_0 $[^o]$	0	0	180	180

Indicatively, as shown in Fig. 4 and Fig. 5, two multidimensional diagrams depicting the maximum relative eccentricity ratio and the loading stiffness are presented. The scope of further extracting information on the design of the WMD component, requires a series of statistical tests. Including the sensitivity analysis and the calculation of the coefficient of importance, additional insight is gained upon the impact that each design variable has to the dynamic response of the system.

The objective of the sensitivity analysis is to quantify the influence that each selected variable has on the desired set of responses [11,13]. First, linear regression is conducted on the matrix of responses, utilizing the matrix of variables, in which a standardization is performed, as shown in Eq. (14); $\mathbf{V_{st}}$ is the standardized matrix of variables, $\mathbf{V_{V(i,j)}}$ is the specific value of the variable, μ_{mean} is the mean value, and σ is the standard deviation.

$$\mathbf{V_{st}} = \frac{\mathbf{V_{V(i,j)}} - \mu_{mean}}{\sigma} \tag{14}$$

First, the linear regression is conducted as shown in Eq. (15), where $i = 1,2$ stands for the desired responses, $k = 1,2,\ldots,108$ is the total number of configurations, $m = 4$ is the total number of design variables, $\mathbf{R_{r,i}}$ is the

individual desired response matrix, $\mathbf{q_i}$ is the individual regression coefficient matrix, and $\mathbf{e_i}$ is the error matrix, which in the present work is considered equal to zero.

$$\underbrace{\begin{bmatrix} r_1 \\ r_2 \\ \vdots \\ r_k \end{bmatrix}}_{\mathbf{R_{r,i}}} = \underbrace{\begin{bmatrix} 1\, v_{11}\; v_{12} \cdots v_{1m} \\ 1\, v_{21}\; v_{22} \cdots v_{2m} \\ \vdots\;\vdots\;\vdots\;\ddots\;\vdots \\ 1\, v_{k1}\; v_{k2} \cdots v_{km} \end{bmatrix}}_{\mathbf{V_{st}}} \underbrace{\begin{bmatrix} q_0 \\ q_1 \\ \vdots \\ q_m \end{bmatrix}}_{\mathbf{q_i}} + \underbrace{\begin{bmatrix} e_1 \\ e_2 \\ \vdots \\ e_k \end{bmatrix}}_{\mathbf{e_i}} \tag{15}$$

$$\mathbf{q_i} = \left(\mathbf{V_{st}^T V_{st}}\right)^{-1} \mathbf{V_{st}^T R_{r,i}}$$

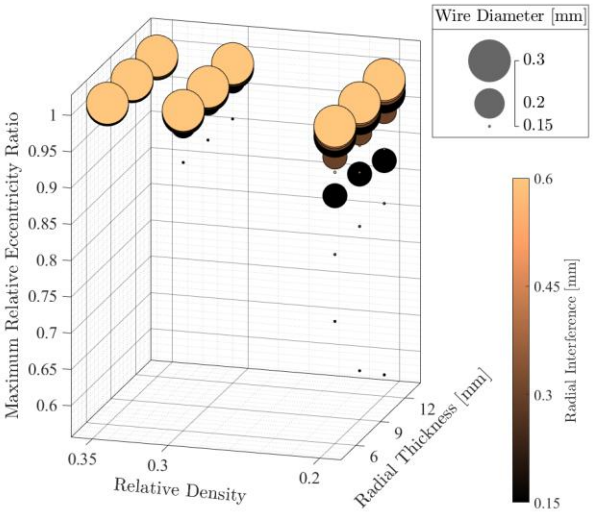

Figure 4: maximum relative eccentricity vs WMD's design variables of bearing #1 for DoE case A

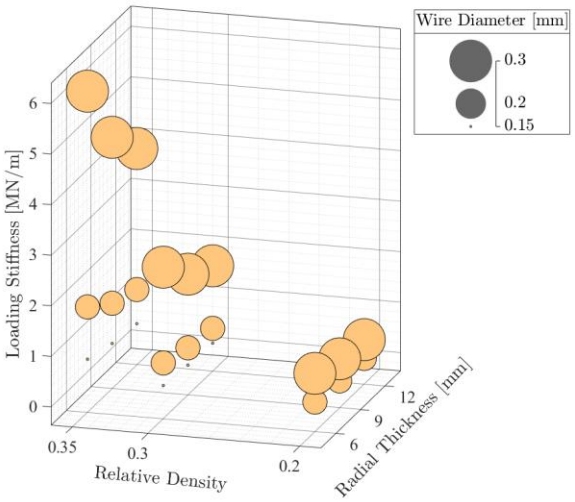

Figure 5: WMD's loading stiffness vs its design variables

Secondly, a standard Principal Component Analysis [11] is conducted on the approximate regression coefficient matrix $\mathbf{Q}$, consisting of all the individual regression coefficients matrices $\mathbf{q_i}$, after neglecting the q_0 value, in Eq. (16).

$$\mathbf{Q} = \begin{bmatrix} \mathbf{q_1} & \mathbf{q_2} & \cdots & \mathbf{q_n} \end{bmatrix} \in \mathbb{R}^{m \times n} \tag{16}$$

Additionally, the global sensitivity coefficients, accumulated in matrix $\mathbf{G}$, are obtained through the calculation of the Euclidean norm of each row vector $\hat{\boldsymbol{q}}_i$, of the approximate regression coefficient matrix $\mathbf{Q}$, in Eq. (17).

$$\mathbf{G} = \begin{bmatrix} \|\hat{\boldsymbol{q}}_1\| & \|\hat{\boldsymbol{q}}_2\| & \cdots & \|\hat{\boldsymbol{q}}_j\| \end{bmatrix}^T \in \mathbb{R}^{m \times 1}, \quad j = 1,2,\ldots,m \tag{17}$$

Finally, the calculation of the coefficient of importance (CoI) denotes the influence of single variable, among all design variables, on a single response, and ranges between 0 (negligible dependency) and 100 (complete dependency) [14]. In order to compute the CoI, the $CoI_{j,s}$ element considering a single design variable x_s and the associated response $y_{r,j}$ has to be computed in Eq. (18), where $j = 1,2$ is the desired response, $s = 1,2,3,4$ is the design variable, and $m = 4$ is the total number of design variables.

$$R_j^2 = \frac{\left\| \hat{y}_{r,j}\left(x_1,\ldots,x_s,\ldots,x_m\right) - \bar{\hat{y}}_{r,j} \right\|^2}{\left\| y_{r,j}\left(x_1,\ldots,x_s,\ldots,x_m\right) - \bar{y}_{r,j} \right\|^2}, \quad R_{j,s}^2 = \frac{\left\| \hat{y}_{r,j,s}\left(x_1,\ldots,x_{s-1},x_{s+1},\ldots,x_m\right) - \bar{\hat{y}}_{r,j} \right\|^2}{\left\| y_{r,j}\left(x_1,\ldots,x_s,\ldots,x_m\right) - \bar{y}_{r,j} \right\|^2}$$
$$CoI_{j,s} = R_j^2 - R_{j,s}^2 \tag{18}$$

The final matrix containing all the CoI is obtained in Eq. (19).

$$\mathbf{CoI} = \begin{bmatrix} CoI_{1,1} & CoI_{1,2} & \cdots & CoI_{1,s} \\ CoI_{2,1} & CoI_{2,2} & \cdots & CoI_{2,s} \\ \vdots & \vdots & \ddots & \vdots \\ CoI_{j,1} & CoI_{j,2} & \cdots & CoI_{j,s} \end{bmatrix} \tag{19}$$

4 Results

A typical quality of time response of the system with random WMD design properties is presented in Fig. 11. The relative eccentricity exceeds the acceptable value and this design is rejected as this will render excessive rub between journal and ring.

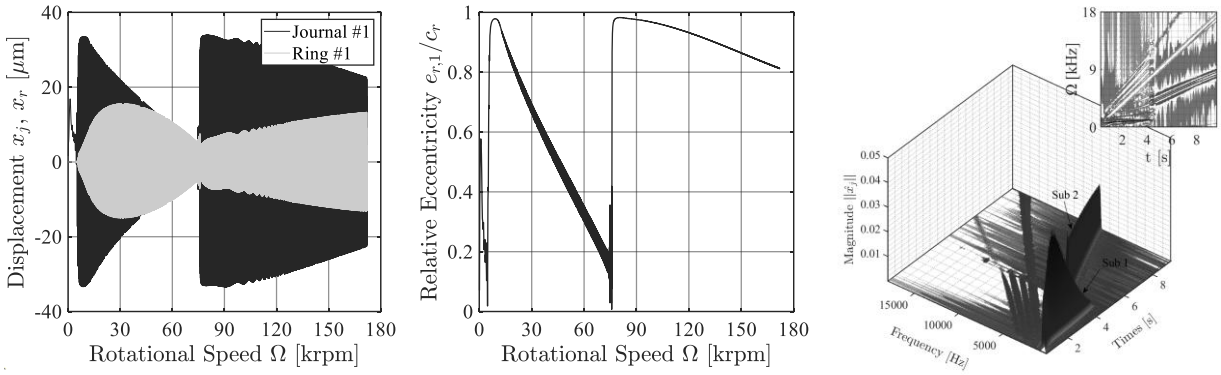

(a) (b) (c)

Figure 11: typical rejected dynamic design. a) time response, b) relative eccentricity, c) frequency content, during run up of the turbocharger.

The WMD configuration with the most favorable dynamic response, regarding the maximum relative eccentricity ratio for both journals is presented in Figure 12.

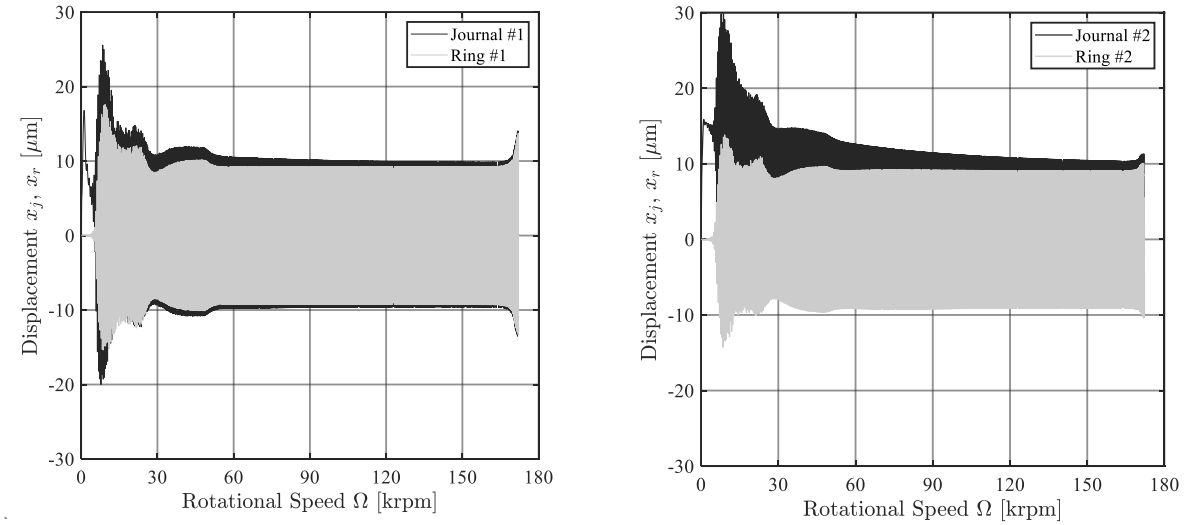

(a) (b)

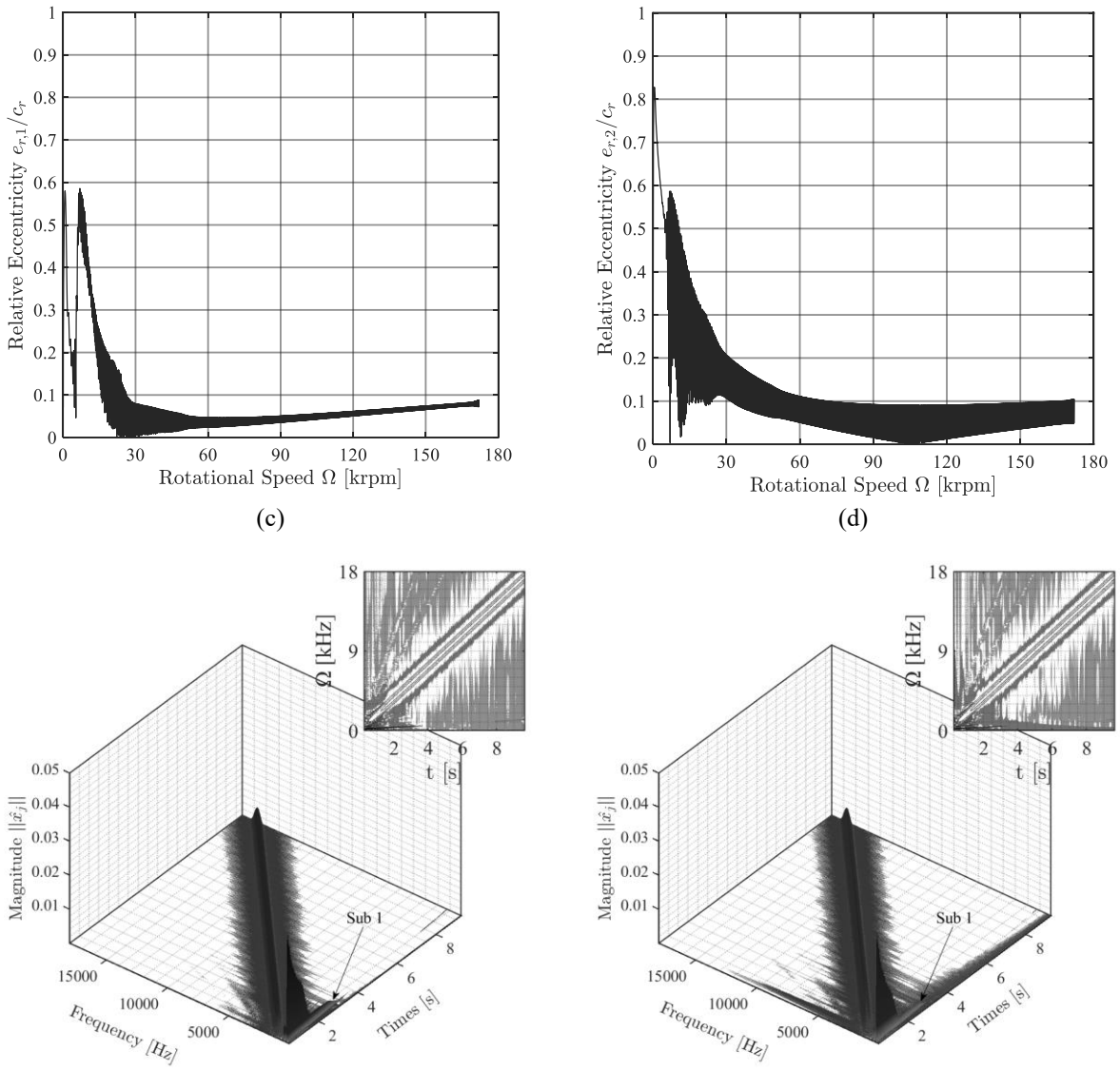

Figure 12: left and right column represent bearing #1 and #2, respectively. (a) and (b) Journal & ring transient response, (c) and (d) relative eccentricity vs Rotational speed, (e) and (f) waterfall diagram and contour plot (top-right corner) of journal's horizontal displacement x_j .

The results of the sensitivity analysis for each case of operating condition, as well as for all the cases simultaneously (global) are shown in Figure 13. Important clarification is that the absolute sensitivity percentage sum of the four variables, equals 100%. The CoI values of the four design variables for each case of operating conditions for both bearings, and the global CoI values for both bearings, are presented in Figure 14.

Further analysis into the four cases, signified the importance of maintaining relatively low oil temperature, as well as the need to contain the difference between the initial unbalance phases of the compressor and the turbine close to zero. In the results obtained with configurations of different initial unbalance phase, the first instability maintained low oscillating amplitudes and was adequately suppressed; a second more violent instability leading to high amplitude oscillations occurred due to oil whip. Hence, the respective WMD designs where proved unsuitable.

The statistical analysis implemented on the results of time response highlighted the effect that each WMD design variable had upon the system's maximum relative eccentricity ratio. Relative density, radial interference, and wire diameter, are design variables with greater than 25% global sensitivity. Relative density is a design variable of most influence, while radial thickness is the one of least influence, representing only 3% of the global sensitivity.

Additional data on the WMD design are required for a wider range of WMD variables and for different rotor and bearing geometric characteristics, in order to define reliably the appropriate design range for each rotor

support, and the influence of each design variable on the system's overall performance. Supplementary research on WMDs design in accordance with other bearing types, such as roller and gas foil bearings belong to future work of the authors.

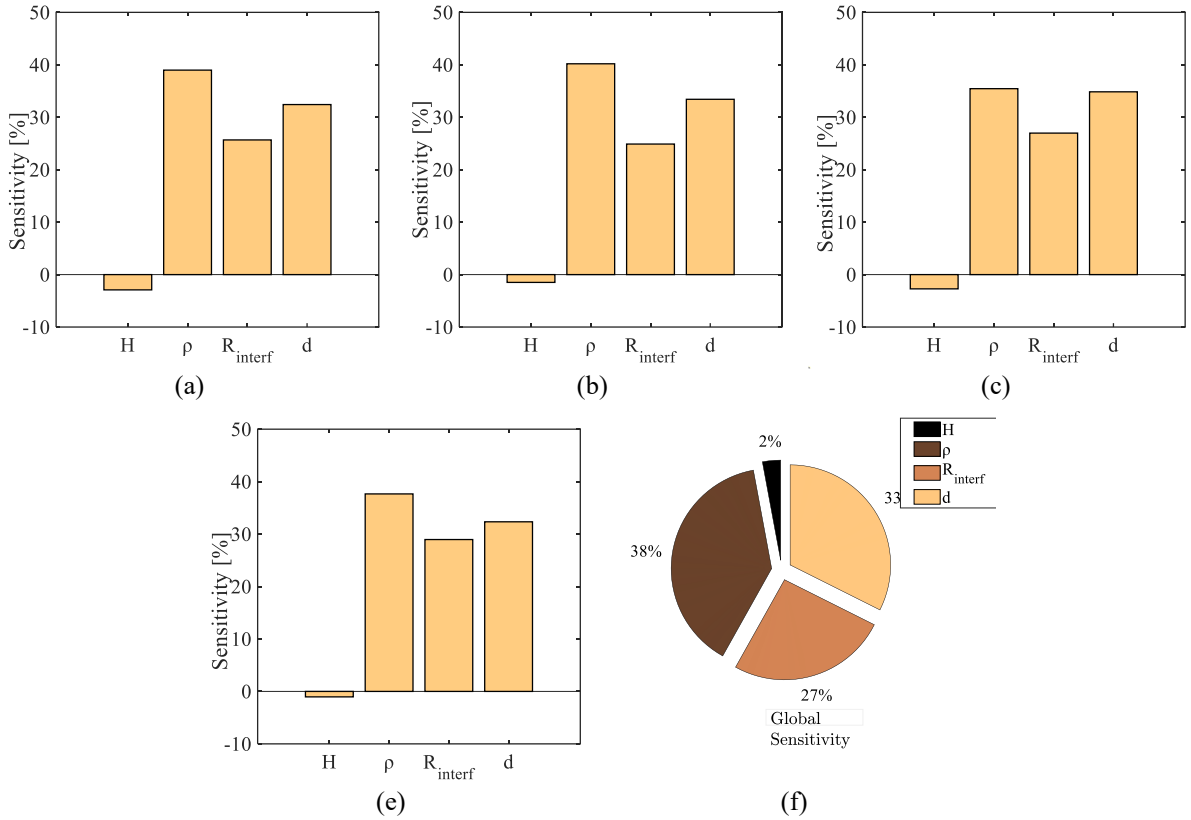

Figure 13: measurement of the sensitivity of maximum relative eccentricity ratio for each WMD design variable. (a) Case A, (b) Case B, (c) Case C, (d) Case D, (e) Global sensitivity.

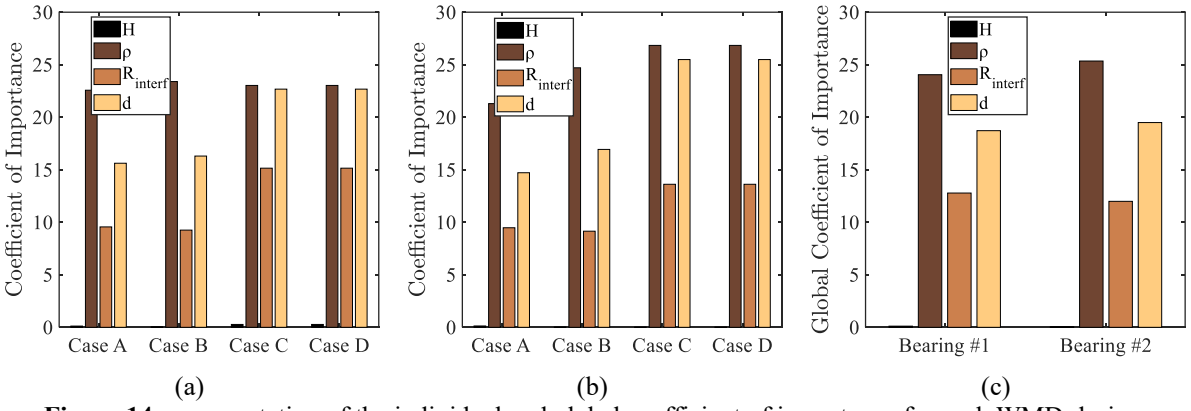

Figure 14: representation of the individual and global coefficient of importance for each WMD design variable. (a) All cases for bearing #1, (b) all cases for bearing #2, (c) global coefficient of importance for both bearings.

5 Conclusions

The present work implements statistical analysis and design optimization on the dynamics of automotive turbocharger rotors on WMD bearings. Different WMD designs and different operational conditions are applied to the system which executes a virtual run-up up to high ending speed. Each configuration was studied on its influence upon the system's overall performance and simultaneously, the system's sensitivity on each WMD design variable considering the maximum relative eccentricity ratio, was evaluated.

Total of 432 configurations (1 DoE process, 4 cases of operating conditions, with 108 configurations each), depicted considerable variance of dynamic responses, the majority of which, showed a low-speed instability resulting in a violent transition of the rotor to high amplitude oscillations, while only a few design sets resulted

in acceptable amplitude levels. Nearly all cases exhibited significant reduction of the self-excited vibration amplitude, noting the ability of WMDs to add damping in the system.

Acknowledgments

The authors would like to acknowledge Dr. Panagiotis Koutsovasilis, BorgWarner Turbosystems GmbH, Germany, for the several discussions during the preparation of this work.

References

[1] Adiletta G., Guido A., Rossi C. (1996): Chaotic motions of a rigid rotor in short journal bearings. *Nonlinear Dynamics*, 10(3), pp. 251-269.

[2] Agrawal G. (1997): Foil Air/Gas Bearing Technology - An Overview. International Gas Turbine & Aeroengine Congress & Exhibition Orlando, Florida, ASME.

[3] Al-Khateeb E. M. (2002): Design, Modeling and Experimental Investigation of Wire Mesh Vibration Dampers. *Doctor of Philosophy*, Texas A&M University.

[4] Ao H., Jiang H., Wei W., Ulanov A. (2005): Study on the Damping Characteristics of MR Damper in Flexible Supporting of Turbo-Pump Rotor for Engine.

[5] Blok H., Van Rossum J. (1953): The Foil Bearing-A New Departure in Hydrodynamic Lubrication. *ASLE J. Lubr. Eng*, 9, pp. 346-330.

[6] Chasalevris A. (2016): An Investigation on the Dynamics of High-Speed Systems Using Nonlinear Analytical Floating Ring Bearing Models. *International Journal of Rotating Machinery*, 2016, pp. 1-22.

[7] Childs D. (1978): The Space Shuttle Main Engine High-Pressure Fuel Turbopump Rotordynamic Instability Problem. *Journal of Engineering for Power*, 100(1), pp. 48-57.

[8] Feng K., Liu W., Zhang Z., Zhang T. (2016): Theoretical model of flexure pivot tilting pad gas bearings with metal mesh dampers in parallel. *Tribology International*, 94, pp. 26-38.

[9] Feng K., Liu Y., Zhao X., Liu W. (2016): Experimental Evaluation of the Structure Characterization of a Novel Hybrid Bump-Metal Mesh Foil Bearing. *Journal of Tribology*, 138(2).

[10] Feng K., Zhao X., Zhang Z., Zhang T. (2016): Numerical and Compact Model of Metal Mesh Foil Bearings. *Tribology Transactions*, 59(3), pp. 480-490.

[11] Golub G., Van Loan C. (2013): *Matrix Computations 4th Edition*, The Johns Hopkins University Press, Maryland.

[12] Ishida Y., Yamamoto T. (2012): *Linear and Nonlinear Rotordynamics: A Modern Treatment with Applications*. Wiley-VCH Verlag & Co. KGaA, Germany.

[13] Koutsovasilis P., Driot N. (2015): Turbocharger rotors with oil-film bearings: sensitivity and optimization analysis in virtual prototyping. *11th International Conference on Vibrations in Rotating Machines*, Magdeburg, Germany.

[14] Koutsovasilis P., Driot N., Lu D., Schweizer B. (2014): Quantification of sub-synchronous vibrations for turbocharger rotors with full-floating ring bearings. *Archive of Applied Mechanics*, 85(4), pp. 481-502.

[15] Muszynska A. (1988): Alford and the destabilizing forces that lead to fluid whirl/whip, 19(3), pp. 29-31.

[16] Shampine L., Reichelt M. (1997): The MATLAB ODE Suite. *SIAM Journal on Scientific Computing*, 18(1), pp. 1-22.

[17] Zarzour M. (1999): Experimental Evaluation of a Metal Mesh Bearing Damper. *International Gas Turnine & Aeroengine Congress & Exhibition*, Indianapolis, Indiana, Transactions of the ASME.

15th SIRM – European Conference on Rotordynamics,
Darmstadt, Germany, 22nd – 24th February 2023

Advancements in the rotor dynamic optimization of heavy duty gas turbines – handling complexity in the industrial practice

Eric Knopf [1], Mateusz Golebiowski [2], David Stacy [3], Daryl Collins [4]

[1] Chief Consulting Engineer, GE Vernova, 5400, Baden, Switzerland, eric.knopf@ge.com
[2] Manager Power Train Dynamics , GE Vernova, 5400, Baden, Switzerland, mateusz.golebiowski@ge.com
[3] Principal Engineer, GE Vernova, 29615, Greenville SC, US, david.stacy@ge.com
[4] Senior Engineer, GE Vernova, 29615, Greenville SC, US, daryl.collins@ge.com

Abstract

Modern Gas Turbine require a detailed and precise rotor dynamic design. As the engine size, power output and shaft length increase, the requirements related to vibration magnitude and dynamic behaviour are getting more and more challenging. A key pre-requisite to have an excellent prediction of the operational behaviour of the shaft train (especially in early design stages), is a) to have good numerical model which includes all relevant interfaces and substructures and b) to know the most sensitive parameters and components that determine and influence the overall dynamic behaviour of the complete shaft train.

This paper presents an overview of various approaches with the objective to identify the most significant parameters and subcomponents of the powertrain, which have the highest impact on damping and eigenfrequencies of the powertrain using DOE statistical methods. The effort is based on a detailed mixed 3D/1D numerical model including all significant interfaces and subcomponents. The modelling approach goes beyond today's typical industrial practices. The rotating part is based on standard 1-D models for rotors, blades and journal bearings. The stationary substructures, e.g. Gas Turbine and Generator stator and support, the concrete foundation and the soil and piles underneath the foundation, have been modelled using a 3D FE approach. Special attention has been paid regarding accurate and detailed representation of the interfaces, like foundation bolting, bearing connection, etc..

The 3D models have been reduced and attached to the rotating part using substructuring methods. This allows a very economic throughput time without losing accuracy. To minimize the number of calculation cases and to extract the dominating parameters (direct and interactions), statistical DOE methods have been applied extensively. The results of this study enable a robust rotor dynamic design of the shaft trains already in early development stages. The results enable as well to separate between important design parameters, i.e. need to be specified with tight tolerances and unimportant contributors, that allow a loose tolerance, which at the end reduces cost and risk.

1 Introduction

The rotor dynamic behaviour of large turbomachinery can be described by the shaftline geometrical and material properties, by the excitation forces and by interactions. This paper focusses on the methodological description of the interactions, especially between rotating and stationary parts and their implementation and usage in the industrial practice. The second focus of this paper is on the experience the authors gained by using DOE techniques to understand the impact of subcomponents on the overall system behaviour and to optimise them.

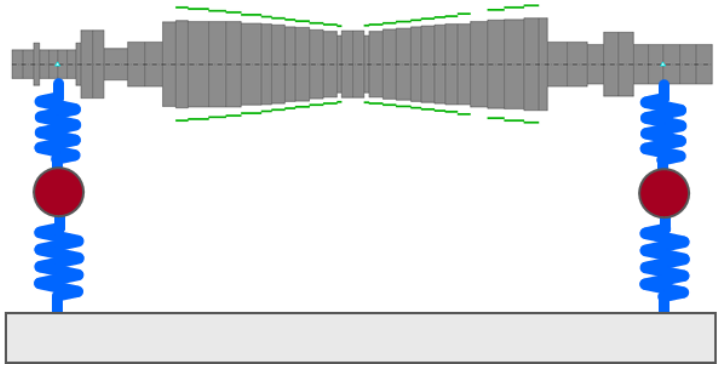

Figure 1: Schematic rotor supported on oilfilm bearings and pedestals

Historically, the turbomachinery rotors have been modelled as 1D beam elements and even

in the times of very advanced 3D FE codes and automated meshing, this is still state of the art in a lot of applications.

With the increasing power output, interactions of the rotor with the supporting structures became more and more important to describe the overall vibrations behaviour. A very simple, but tremendously important interaction diagram is shown in figure 2 [1]. The diagram shows the expected eigenfrequencies of the coupled rotor casing system, based on individual rotor and casing eigenfrequencies and mass ratios. The diagram enables a quick estimation of system eigenfrequencies, if only component eigenfrequencies are available, e.g. in early design stages. As an example, assuming a (modal) mass ratio of 2 and an eigenfrequency ratio f_{casing}/f_{rotor}= 1.2 (modal damping of 1% applied), the coupled system will split up into "new eigenfrequencies at 0.79 and 1.52 x the original rotor eigenfrequency (see also Figure 3).

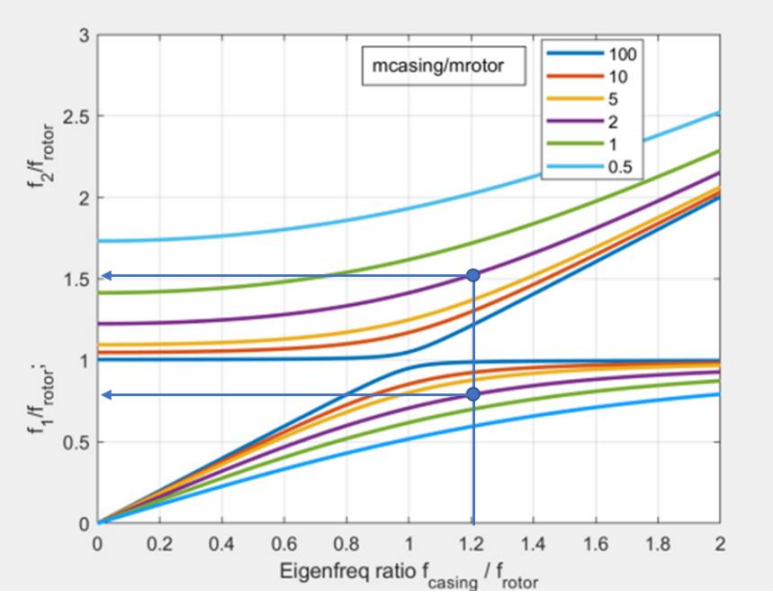

Figure 2: Generalized Rotor-Casing Interaction Diagram

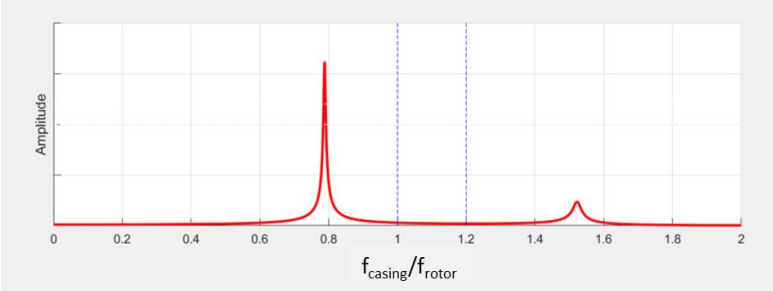

Figure 3: Harmonic response of the coupled system (vertical lines show original rotor and casing eigenfrequencies; f_{casing}/f_{rotor} =1.2; m_{casing}/m_{rotor}=2

With the evolution of the gas turbines, powerful methods and tools have been developed and applied to encounter for the complex dynamics of the support structure. Today's casing models are very sophisticated and based on 3D finite element models. Typically, they are generated by the individual component owners or even by third party (e.g. concrete foundation models). The casing submodels themselves consist of many (and for the rotordynamic analysis unnecessary) details and a huge number of DoFs. The model size itself still makes a direct use of full-sized 3D models in rotor dynamics very time consuming and not efficient. The submodels need to be reduced in size, while retaining the relevant dynamic characteristics. GE is using Component Mode Synthesis [2], [3], [4] approaches as well as a state space based modal approaches [5]. The basis for both of these approaches is always a 3D component/ system model. The main goal of these efforts is to describe the operational behaviour as precise as possible, from early design stages to field feedback, while still keeping computational time comparably low.

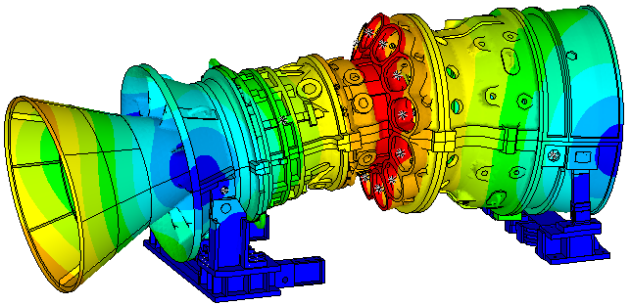

Figure 4: 3D FE model of a GT casing including the support structure, showing first bending mode of the casing

Now, the dynamic behaviour of the gas turbine alone is not sufficient to describe the behaviour of the overall shaft train as a system.
The following chapter describes an approach where all flexible substructures, including foundation and soil properties, have been integrated in the model. This was done with the intention to identify the most dominating parameter, which drive the dynamic behaviour of the rotor system. Once the important parameters are known, this knowledge can be used to optimise the dynamic behaviour, especially in early design stages. On the other hand, the information of the non-significant parameters offers opportunities for less strict tolerances or wider specification bands.

For this study, the following substructures have been integrated, based on 3d FE models

- Shaftline, consisting of gas turbine, intermediate shaft and generator rotors
- Gas Turbine Casing
- Generator Casing
- Concrete Pedestals and foundation
- Soil and foundation pillars

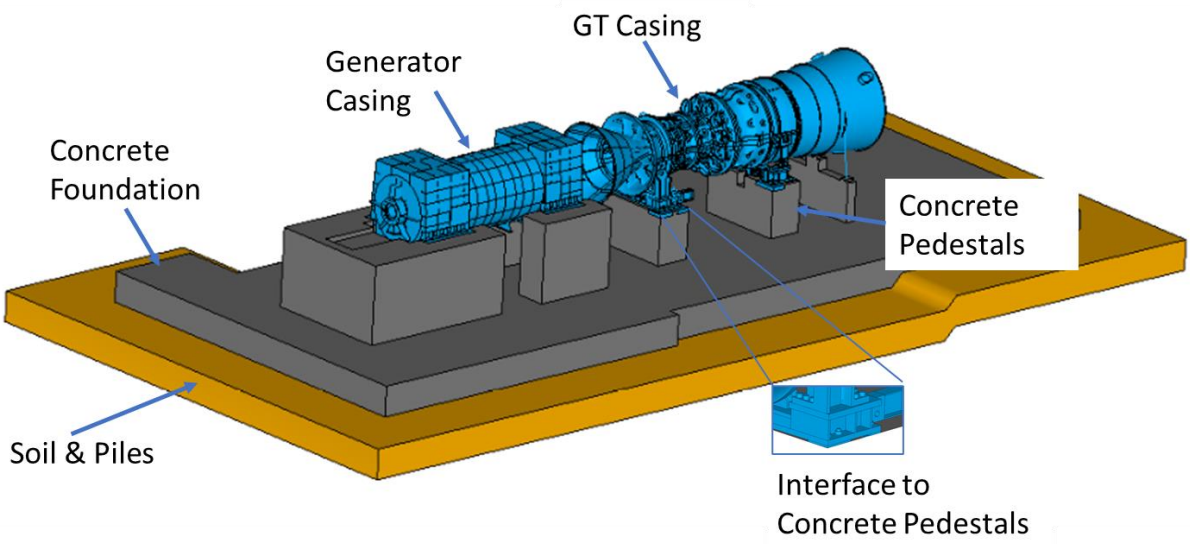

Figure 5: System Model consisting of the various subcomponents

The gas turbine and generator rotors have been modelled following the standard 1D beam approach including gyroscopic effects and shear deformation. The hydrodynamic bearings are modelled via speed dependent stiffness and damping coefficients. The spring and damper elements are representing the interface of the rotor to the stationary structure. The concrete foundation has been modelled following the material properties derived from civil engineering. The soil and pile subsystem can differ from site to site. The soil and pile stiffness and damping properties have been developed from GE specifications and following the elastic half-space approach [6].

2 Reduction Techniques – Craig-Bampton and State Space Representation

In order to make efficient use of DOE strategies, the “big” FE models need to be reduced. Secondly, sub-structuring methods like CMS offer a very efficient way to connect submodels at interface DOFs *b* from different origins or even different FE software. Keep in mind, that the gas turbine models, the generator models and the foundation models are typically generated by different departments across the organization.
Craig Bampton and states space representation are both based on a modal representation of the substructures.

2.1 Craig-Bampton Reduction

Starting with the equation of Motion the degrees of freedom are re-arranged to interior DoFs $\boldsymbol{q_i}$ and boundary DoFs $\boldsymbol{q_b}$. The boundary DoFs are representing the interfaces to the adjacent substructure (e.g. rotor)

$$\begin{bmatrix} m_{ii} & m_{ib} \\ m_{ib} & m_{bb} \end{bmatrix} \cdot \begin{bmatrix} \ddot{q}_i \\ \ddot{q}_b \end{bmatrix} + \begin{bmatrix} k_{ii} & k_{ib} \\ k_{ib} & k_{bb} \end{bmatrix} \cdot \begin{bmatrix} q_i \\ q_b \end{bmatrix} = \begin{bmatrix} F_i \\ F_b \end{bmatrix} \tag{1}$$

The boundary DoFs $\boldsymbol{q_b}$. are kept physical, whereas the interior DoFs $\boldsymbol{q_i}$ are transformed to modal DoFs using modal transformation:

$$\begin{bmatrix} q_1 \\ \vdots \\ q_i \\ \hline \boldsymbol{q_b} \end{bmatrix} = \underbrace{\left[\begin{array}{cccc|c} \vdots & \vdots & \vdots & \vdots & \boldsymbol{\psi_1^T} \\ \boldsymbol{\varphi_1} & \boldsymbol{\varphi_2} & \cdots & \boldsymbol{\varphi_i} & \vdots \\ \vdots & \vdots & \vdots & \vdots & \boldsymbol{\psi_{1b}^T} \\ \hline \multicolumn{4}{c|}{\boldsymbol{0}} & \boldsymbol{1} \end{array}\right]}_{\boldsymbol{T_{CB}}} \begin{bmatrix} \eta_1 \\ \vdots \\ \eta_i \\ \hline \boldsymbol{q_b} \end{bmatrix} \tag{2}$$

$\boldsymbol{\varphi_1 \ldots \varphi_i}$ are the elastic eigenmodes of the substructure, $\psi_1 .. \psi_b$ are static constraint modes [6].
The reduction is achieved as only the first n eigenvectors $\boldsymbol{\varphi_1 \ldots \varphi_n}$ (with n <<i) are used in $\boldsymbol{T_{CB,\,red}}$. This leads to to the equation of motion with reduced mass and stiffness matrices $\boldsymbol{M_{red}}$ and $\boldsymbol{K_{red}}$:

$$\underbrace{T_{CB,red}^T \cdot \begin{bmatrix} m_{ii} & m_{ib} \\ m_{ib} & m_{bb} \end{bmatrix} \cdot T_{CB,red}}_{\boldsymbol{M_{red}}} \cdot \begin{bmatrix} \ddot{\eta}_{1..n} \\ \ddot{q}_b \end{bmatrix} + \underbrace{T_{CB,red}^T \cdot \begin{bmatrix} k_{ii} & k_{ib} \\ k_{ib} & k_{bb} \end{bmatrix} \cdot T_{CB,red}}_{\boldsymbol{K_{red}}} \cdot \begin{bmatrix} \eta_{1..n} \\ q_b \end{bmatrix} = \underbrace{T_{CB,red}^T \cdot \begin{bmatrix} \mathrm{Z}_{1..n} \\ F_b \end{bmatrix}}_{\boldsymbol{F_{red}}} \tag{3}$$

The reduction of the DOFs is achieved in $\boldsymbol{T_{CB,red}}$ by truncation of high frequency modes, as they do not contribute significantly to the vibrations in the interesting speed range.

2.2 State Space Representation

The state space representation follows a similar approach. Re-writing the equation of motion in state space representation:

$$\begin{bmatrix} \dot{\boldsymbol{q}} \\ \ddot{\boldsymbol{q}} \end{bmatrix} = \begin{bmatrix} \mathbf{0} & \mathbf{1} \\ -\mathrm{M}^{-1}\mathrm{K} & -\mathrm{M}^{-1}\mathrm{D} \end{bmatrix} \begin{bmatrix} \boldsymbol{q} \\ \dot{\boldsymbol{q}} \end{bmatrix} + \begin{bmatrix} \mathbf{0} \\ \mathrm{M}^{-1} \end{bmatrix} \boldsymbol{F} \tag{4}$$

$$[\, \boldsymbol{q} \,] = [\quad \mathbf{1} \qquad \mathbf{0} \quad] \begin{bmatrix} \boldsymbol{q} \\ \dot{\boldsymbol{q}} \end{bmatrix} + [\quad \mathbf{0} \quad] \boldsymbol{F}$$

Applying a modal transformation and normalization leads to

$$\begin{aligned} \boldsymbol{\Phi}^T \mathrm{M}\, \boldsymbol{\Phi}\ \ddot{\boldsymbol{p}} \ + \ \boldsymbol{\Phi}^T \mathbf{D}\, \boldsymbol{\Phi}\ \dot{\boldsymbol{p}} \ + \ \boldsymbol{\Phi}^T \mathrm{K}\, \boldsymbol{\Phi}\ \boldsymbol{p} \ &= \ \boldsymbol{\Phi}^T \boldsymbol{F} \\ \mathbf{1} \quad \ddot{\boldsymbol{p}} \ + \quad \tilde{\mathbf{D}} \quad \dot{\boldsymbol{p}} \ + \quad \tilde{\boldsymbol{\Omega}}_0 \quad \boldsymbol{p} \ &= \ \boldsymbol{\Phi}^T \boldsymbol{F} \end{aligned} \tag{5}$$

And finally to the modal representation of the substructure

$$\begin{bmatrix} \dot{\boldsymbol{p}} \\ \ddot{\boldsymbol{p}} \end{bmatrix} = \begin{bmatrix} \mathbf{0} & \mathbf{1} \\ -\tilde{\boldsymbol{\Omega}}_0 & -\tilde{\mathbf{D}} \end{bmatrix} \begin{bmatrix} \boldsymbol{p} \\ \dot{\boldsymbol{p}} \end{bmatrix} + \begin{bmatrix} \mathbf{0} \\ \boldsymbol{\Phi}^T \end{bmatrix} \boldsymbol{F} \tag{6}$$

$$[\, \boldsymbol{q} \,] = [\quad \boldsymbol{\Phi} \qquad \mathbf{0} \quad] \begin{bmatrix} \boldsymbol{p} \\ \dot{\boldsymbol{p}} \end{bmatrix} + [\quad \mathbf{0} \quad] \boldsymbol{F}$$

The vector $\boldsymbol{q}$ is representing the physical DoFs, the vector $\boldsymbol{p}$ is representing modal displacements. The reduction is again achieved by truncating the modal matrix $\boldsymbol{\Phi}$. One main advantage of the state space representation is, that modal coordinates are used internally, while external displacements and forces are kept physical.

Both methods are mathematically equivalent, and both are extensively used in rotordynamic assessment of GE´s gas turbines.

3 Design of Experiment (DOE) Framework

With an increasing demand of a shorter design cycle and competition in performance, cost, footprint and safety, the probabilistic approach is gaining an important role in the power train design process. The main challenge arises with the size of the design space (see Figure 5) and complexity of its mapping onto multiple objective functions and criteria which are defined for different machines.

In the context of rotordynamics, a number of authors have extended the deterministic rotor model to account for uncertainties in physical and geometrical parameters. Various methods were used, such as Polynomial Chaos Expansion technique [8] and Karhunen-Loève (KL) decomposition [9]. Another approach, as shown in [10], used a Latin Hypercube sampling method followed by Kriging modeling to approximate the response of a 8 staged compressor rotor. Becker [11] also showed a stochastic rotordynamic simulation in a gas turbine, with the aid of an optimizer, to understand the robustness of a rotor design using the Monte-Carlo simulation and Surface Response Methods.
The use of statistical methods to explore (screening Design of Experiment) and understand (Response Surface Methods) the design space of the rotating equipment leads to a quicker definition of a turbo-generator's arrangement. Further statistical analyses are carried out to quantify the robustness of the chosen design against future modifications as well as parameters' uncertainties.
Several statistical methods are being deployed to deliver these answers. In the following sections of this article the basic outline of the used techniques, main assumptions regarding the design space, evaluation and optimization criteria are given.

3.1 Screening analysis

In many applications, the number of factors that potentially affect the rotordynamic characteristic of the system is too great to study all factors in detail. The usual goal of a screening design is to identify the most important ones. After screening experiments, optimization experiments are performed that provide more detail on the relationships among the most important factors and the response variables.

The most commonly used type of screening DoE is a full factorial or fractional factorial design. A factorial design (Figure 6) is type of designed experiment that allows studying of the effects that several factors can have on a response. When conducting an experiment, varying the levels of all factors at the same time instead of one at a time enables exploring the interactions between the factors.

A fractional design is a design in which experimenters conduct only a selected subset or "fraction" of the runs in the full factorial design.

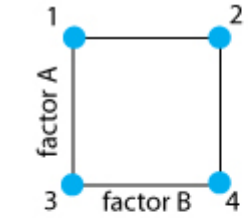

factor levels

trial	A	B
1	+	−
2	+	+
3	−	−
4	−	+

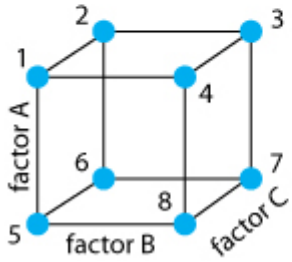

factor levels

trial	A	B	C
1	+	−	−
2	+	−	+
3	+	+	+
4	+	+	−
5	−	−	−
6	−	−	+
7	−	+	+

Figure 6: Full factorial design: levels distribution, runs/trial table (+/- denotes high/low settings of the individual factors)

3.2 Response Surface Methods (RSM)

A response surface design is a set of advanced DOE techniques that help better understand and optimize system's response [12],[13]. Response surface design methodology is often used to refine models after the important factors have been determined using screening designs or factorial designs; especially if a curvature in the response surface is expected.

The difference between a response surface equation and the equation for a factorial design is the addition of the squared (or quadratic) terms that enables modeling of curvature in the response, making them useful for:

- Understanding or mapping a region of a response surface. Response surface equations model how changes in variables affect a response of interest.
- Finding the levels of variables that optimize a response.
- Selecting the operating conditions to meet desired rotordynamic criteria.

There are two main types of response surface designs:

- **Central Composite designs**

Central Composite designs can fit a full quadratic model. They are often used when the design plan calls for sequential experimentation because these designs can include information from a correctly planned factorial experiment.

- **Box-Behnken designs**

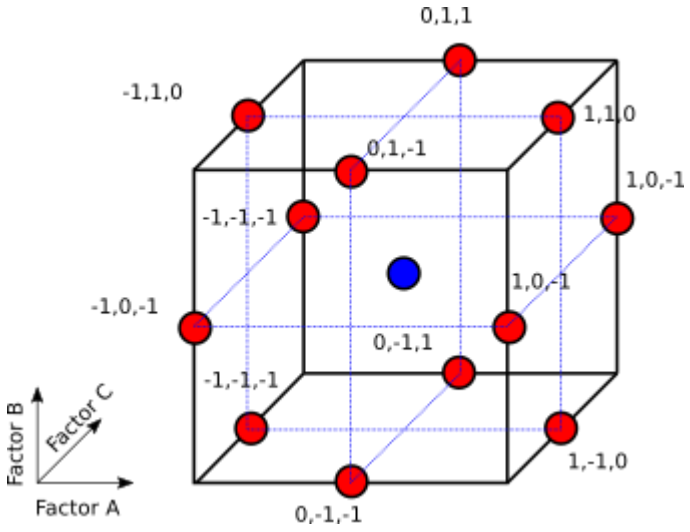

Figure 7: Box-Behnken Factor Level Distribution

Box-Behnken designs (Figure 7) usually have fewer design points than central composite designs, thus, they are less expensive to run with the same number of factors. They can efficiently estimate the first- and second-order coefficients; however, they can't include runs from a factorial experiment. Box-Behnken designs always have 3 levels per factor, unlike central composite designs which can have up to 5. Unlike central composite designs, Box-Behnken designs never include runs where all factors are at their extreme setting, such as all of the low settings.

Both RSM methods have their advantages and disadvantages. Box Behnken is typically chosen by the authors because for engineering practice, the GT shaft arrangement it is very unlikely to be at the vertices of the design space, and this method gives a better approximation in the more practical range.

3.3. Why are we doing all this?

The requirements towards vibrations are extremely stringent and challenging to any OEM. The inherent complexity of the rotordynamic simulation of the future GT engines becomes difficult when the increasing pressure of design cycle time and cost reduction challenges the classic approach to the design iterations. The ability of providing quick answers with reduced effort becomes critical in the preliminary design phases of the power train development in the today industrial practice [12]. A good prediction of the field vibrational behaviour is absolutely necessary to reduce the risk of late design changes or field problems and to ensure a robust dynamic behaviour, insensitive to operational parameters. The focus of the rotordynamic investigations lie on the prediction of vibration amplitudes (plus stresses, moments etc.) a) at rated speed and b) at prediction of criticals speed amplitudes and damping during runup. The identification of the most significant parameters gives the opportunity to define target values to the individual component owners. In addition, the vibrational behaviour needs to be insensitive to external structures, like concrete foundation or soil and pile properties.

For all these cases, the rotor stator interaction can be significant and impacts the resulting vibration amplitudes at rated speed, means under off-resonance conditions, as well as critical speed amplitudes during runup and shutdown.

4 Case study

In the following chapter, a case study and selected results and findings are presented. The intention of this study was to identify relevant and non-significant system parameters, for both runup (critical speeds) and steady state operation. The system is as shown Figure 5.
Figure 8 shows the factors, which have been considered in the DOE study.

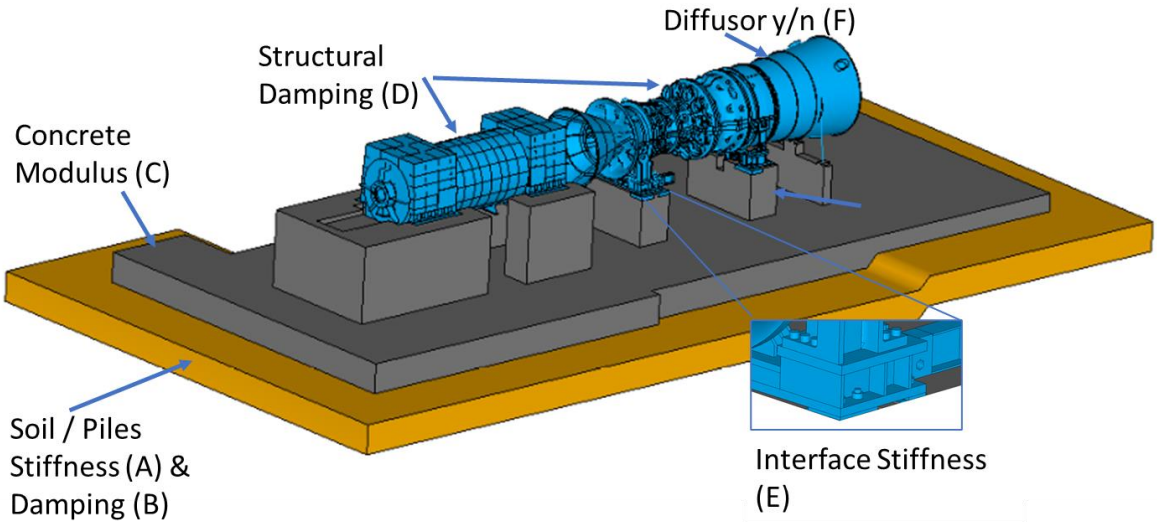

Figure 8: System models with according DOE Factors (Variations)

Figure 9 shows the DoE screening results (Pareto charts). The figures clearly highlight the main significant and insignificant parameters for critical speeds. It shows that structural damping is a main contributor to critical speed damping, besides oilfilm damping (not investigated here) of course. The pareto charts also show the importance of interactions (marked as factor combinations). Another significant factor is the interface stiffness with respect to critical speed frequency.

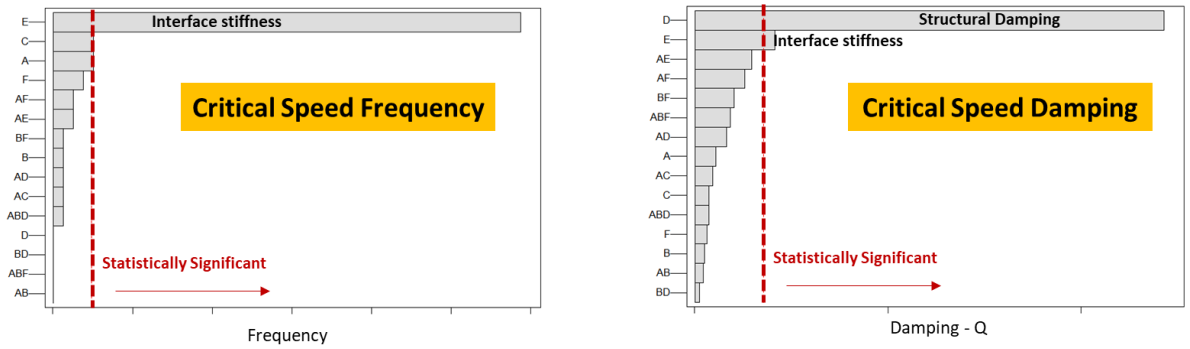

Figure 9: Pareto Chart of Screening Results (Critical Speed), see also Figure 8 for DOE Factors

Following figure gives another illustration of main effects and interactions between factors from the DoE screening result. The plots show a coded range of each parameter, and how the mean response changes as the parameter goes from low to high level. Because the experiment design is based on a 2-level fractional factorial, the mean response is assumed to be linear with the design space.

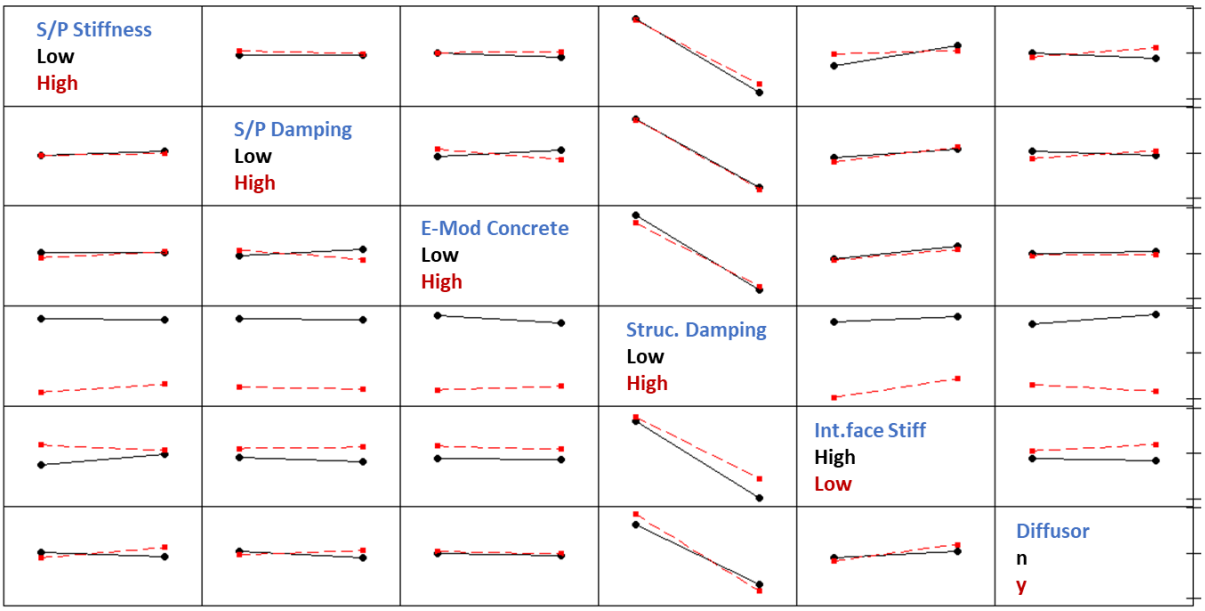

Figure 10: Response Surface Model / Interaction Plot

The response surface model (Figure 10) gives an overview of the whole design space rather than limiting the focus to the tuning of a single component. This gives a great advantage in the GT design process where the rotordynamic characteristics can be driven by the interaction between practically all interfacing subsystems.
Figure 11 shows a practical application of the metamodel developed for this case. It enables defining the targets for each subsystem component that are required to obtain a desired characteristic of the GT rotor mode. In addition to this, it gives the opportunity to quickly tune the model to field test results, e.g. in order to detect any deviations from the nominal parameters.

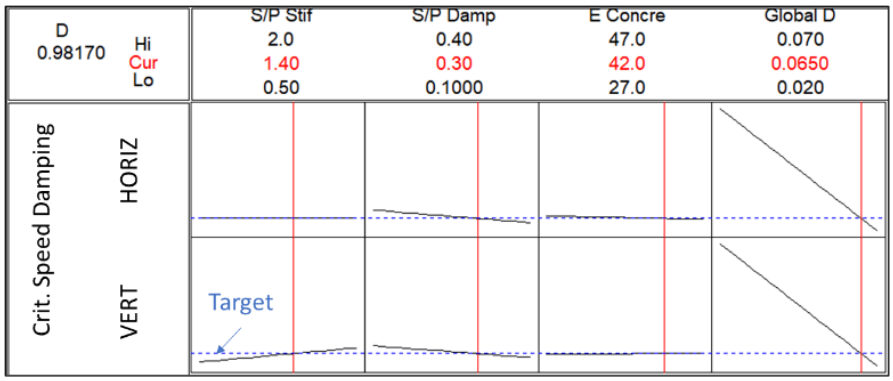

Figure 11: Multiple Response Optimizer – Damping

5 Conclusions

The intention of this paper was to highlight the importance of rotor-structure interaction on the dynamic behaviour of heavy – duty gas turbine power trains. It showed that the system to consider might be larger, than "just" the gas turbine or generator casings. Powerful reduction techniques are available and often integrated in commercial software packages. This enables the integration of the complex substructure dynamics into rotordynamic assessment, while keeping the throughput time on an acceptable level. DOE techniques offer a great opportunity to explore the available design space especially in early design stages. DOE studies give the necessary information on which system parameters it needs to be focussed and which ones are less important for the overall performance.

References

[1] Krämer, E. (1993): *Dynamics of Rotors and Foundations* . Springer Verlag, ISBN: 978-3-662-02798-1.

[2] Bathe, J-D, Dong, J. (2014): *Component mode synthesis with subspace iterations for controlled accuracy of frequency and mode shape solutions* . Journal Computers & Structures

[3] Dohnal, F., Nordmann, F., Knopf, E., (2015): *Modal component mode synthesis in torsional vibration analysis: rotor-blade interaction*, 11th International Conference on Vibrations in Rotating Machines – SIRM 2015, Magdeburg

[4] Hurty, W. C. (1965): *Dynamic analysis of structural systems using component modes*. AIAA Journal 3, pp. 678–682..

[5] Krueger, T.; Liberatore, S.; Knopf, E.; Clark, A.: *Consideration of complex support structure dynamics in rotordynamic assessments*; Proceedings of ASME Turbo Expo, San Antonio TX, 2013

[6] Schönhoff, U., Eisenträger,P., Nordmann, R.: *Reduction of finite element models of flexible structures for controller design and integrated modelling*. – Invited Paper to the International Conference on Noise and Vibration Engineering, ISMA25. Leuven, Belgium: 2000

[7] Gasch, R.; Nordmann, R.; Pfützner: Rotordynamik, 2nd edition; Springer Verlag; ISBN 354007046-X

[8] Rémond, D., Faverjon, B. and Sinou, J.J., 2011, *Analysing the Dynamic Response of a Rotor System under Uncertain Parameters Polynomial Chaos Expansion*, Journal of Vibration and Control, Vol. 18, pp. 712-732.

[9] Koroishi, E.H, Cavalini, A., de Lima, A.M.G. and Steffen, V., *Stochastic Modeling of Flexible Rotors*, J. of the Braz. Soc. of Mech. Sci. & Eng, Special Issue 2, 2012, Vol. XXXIV / 575

[10] Stocki, R., Szolc, T., Tauzowski, P., and Knabel, J., *Robust design optimization of the vibrating rotor shaft system subjected to selected dynamic constraints*, Mechanical Systems and Signal Processing, Vol. 29, May 2012, Pg 34-44

[11] Becker, K., *Rotordynamics and Uncertainty of Variables in Gas Turbine*, ISROMAC12-2008, P.18

[12] Golebiowski, M., Ling J., Knopf, E., Niedermeyer, A.: *Torsional Robustness of the Combined Cycle Powertrain Arrangement – Application of statistical Methods to accelerate Shaft Line Design Cycles*, Journal of Engineering for Gas Turbines and Power, 2017

[13] Diurno T., Fondelli T., Nettis L., Maceli N., Arcangeli L., Andreini A., Facchini B. *Numerical Investigation on the Aerodynamic Performance of a Low-Pressure Steam Turbine Exhaust Hood Using DOE Analysis* GT2020-15993 Proceedings of ASME Turbo Expo 2020

SIRM 2023 – 15th International Conference on Dynamics of Rotating Machines,
Darmstadt, Germany, 22nd – 24th February 2023

Finite element rotordynamics design of gas turbine with a slim spoke frame stator

Zhiqiang Meng [1], Richard Bluck [1], Caroline Raick [2]

[1] Siemens Energy Industrial Turbomachinery Ltd, Lincoln, UK,
david.meng@siemens-energy.com, richard.bluck@siemens-energy.com
[2] Siemens Digital Industries Software, Liège, Belgium, caroline.raick@siemens.com

Abstract

A method to quickly assess the stator support structure dynamic stiffness using the FE simulated frequency response functions (FRF) data is introduced. Using this method, the dynamic support stiffness of a newly designed power turbine (PT) with a slim spoke frame stator is estimated on the requirement of API standard [11]. The derived support dynamic stiffness is directly applied to the unbalance response analysis of the PT rotor incorporating the bearing characteristics. The unbalance response of the rotor with support dynamic stiffness shows that the effect of the flexible support and the critical speeds induced by support structure resonance are well captured. A full rotor/stator FE model with CMS based superelement modal reduction is developed to cross validate the model of the rotor with FRF representation of support structure. The comparison of the unbalance response shows that the rotor with FRF representation of stator structure and the full FE model with superelement are very well cross validated. The superelement based on CMS are used on both rotor and stator FE models to enable high-fidelity FE analysis and fast computation. Finally, the rotordynamic analysis of the rotor / stator model shows that with the slim spoke frame, the PT still meets all the API requirements.

NOMENCLATURE

uu	normalized displacement unit
fr	normalized frequency or speed unit
ff	normalized force unit
umb	normalized unbalance unit
MCS	maximum continuous speed
CMS	component mode synthesis
X	displacement
$\mathbf{H}(\omega)$	transfer function matrix
ζ	damping ratio
h	element of the transfer function matrix
F	force
K_{sd}	dynamic stiffness matrix
K_b	bearing stiffness coefficient
C_b	bearing damping coefficient
API	American Petroleum Institute
FE	finite element
FRF	frequency response functions
DOF	degree of freedom

1. INTRODUCTION

Lighter casing and stator are favourable features for a gas turbine product design improving cost competitiveness and manufacturability. It is particularly important for turbomachinery in the oil & gas industry. A lighter structure with smaller struts also offers opportunity to reduce loses and provide higher overall turbine efficiency. However, a light and very flexible stator leads to challenging rotor dynamics due to rotor and flexible support interaction. The operational margin to the critical speeds and the stability maybe compromised by the flexible support of the stator structure [1]. The stator bearing support structures are conveniently and often modelled with constant stiffness and damping coefficients over the entire speed range [2, 3]. Particularly the support stiffness is based on experimental or analytical static deflections and force.

Nicolas and Whalen et al. [4] used experimental forced response function (FRF) data to represent the bearing support structure. The supports are modelled as two single degree of freedoms (SDOFs) systems. The resulting dynamic compliance [5] incorporated with bearing coefficients was developed for expressions of equivalent

stiffness and damping coefficients. The advantage of using FRF data to represent the support structure is that the resulting dynamic stiffness as a function of excitation frequencies not only includes the support stiffness and damping, it also implicitly includes the support mass. Vazquez and Barrett et al. [6] used polynomial transfer functions from the FRF compliance to model the flexible bearing support. The transfer function approach enable modelling multi-degree-of-freedom (MDOF) support structure can be used for both unbalance response and stability analysis [7,8,9]. Krüger, Liberatore and Knopf [8] presented the comparison of rotordynamic analysis between MDOF and SDOF modelling of the support structure. The comparison showed that the MDOF model much better represents the complex dynamic behaviour of the support structure.

DE Santiago and Abraham [7] compared the response results between a rotor model with FRF representation of support structure and a full FE model and only showed an approximate match in trend. There were significant differences in structure resonance induced critical speed peaks and amplitudes at those peaks.

Apart from using FRFs data to represent the support structure, there are very few reported works that use the component mode synthesis (CMS) technique and finite element (FE) analysis of the full model of support structure and rotor. Reference [10] provides one example of the large industrial engine model. The method showed high fidelity and fast computation.

Until recently the turbomachinery industry preferred using the FRFs data and transfer function method to model the flexible support structure [8, 9,16] rather than use full FE model of rotor and support structure. This may be because the full FE model would add more complexity to the modelling and hence the modelling and solving time would be greater. Most of the applications mentioned above use experimental FRFs data. However, the FRFs data from the modal test have some limitation. From the authors experience for the high speed (up to 15krpm) machine, the hammer test may not be accurate enough. On the other hand, for the bearing house bore diameter less than 200mm, it is difficult to put a shaker at the suitable position. Also, for the new design of machine a similar stator may not be available for the modal test. Therefore, the FE simulation of the FRFs data is a good resource for estimation of the dynamic stiffness of the stator.

This paper introduces a quick method to assess the support structure dynamic stiffness using the FE simulated FRFs data. The derived support dynamic stiffness is directly applied to the unbalance response of the power turbine (PT) rotor incorporating the bearing stiffness and damping coefficients.

A full rotor/stator FE model with CMS based superelement modal reduction is developed to cross validate the model of the rotor with FRF representation of support structure. The superelement based on the CMS approach is used on both rotor and the stator FE models to enable the high-fidelity FE analysis and fast computation. The methods used are deployed in the Simcenter 3D Rotor Dynamic package [18].

2. THE SPOKE FRAME STATOR

2.1 FRFs of the stator

A slim spoke frame stator for the power turbine (PT) of a newly designed industrial gas turbine was proposed for the aero performance and optimisation of cost and manufacturability. The API standard [11] recommends the dynamic stiffness of the bearing support should be 3.5 times greater than the bearing stiffness in the range from 0% to 150 % of MCS. Otherwise, the structure characteristics shall be incorporated as an adequate dynamic system model with calculated frequency dependent structure stiffness and damping values derived from modal or other testing.

The dynamic stiffness of the stator can be derived from experimental FRFs data [4,14]. However, in the design stage the spoke frame stator is not available. The dynamic stiffness of the stator bearing support is assessed by the FE simulated FRFs in this paper.

For the stator structure, when the excitation force applies on the front and rear bearing supports, the response at the bearing support can be solved at the limited local DOF. The frequency responses to the excitation force are expressed as:

$$\begin{matrix} X_{x1} \\ X_{y1} \\ X_{x2} \\ X_{y2} \end{matrix} = \begin{vmatrix} h_{x1x1} & h_{x1y1} & h_{x1x2} & h_{x1y2} \\ h_{y1x1} & h_{y1y1} & h_{y1x2} & h_{y1y2} \\ h_{x2x1} & h_{x2y1} & h_{x2x2} & h_{x2y2} \\ h_{y2x1} & h_{y2y1} & h_{y2x2} & h_{y2y2} \end{vmatrix} \begin{matrix} F_{x1} \\ F_{y1} \\ F_{x2} \\ F_{y2} \end{matrix} \quad \text{or} \quad \boldsymbol{X} = \boldsymbol{H}(\omega)\boldsymbol{F} \qquad (1)$$

While the $\mathbf{H}(\omega)$ is the transfer function matrix (TFM). The TFM is a complex matrix as the functions of frequency.

Re-write Eq. (1) as

$$\mathbf{F} = \mathbf{H}(\omega)^{-1}\,\mathbf{X} = \mathbf{K}_{sd}\,\mathbf{X} \qquad (2)$$

$\mathbf{K}_{sd}$ is the dynamic stiffness matrix of the bearing support of the stator and $\mathbf{K}_{sd} = \mathbf{H}(\omega)^{-1}$. The real part of the dynamic stiffness represents the stiffness and the inertia terms, the imaginary part stands for the damping of the bearing supports. The TFM can be derived from the measured FRFs data from the modal test. For example, applying a sweeping frequency force in x direction on the front bearing support, the first column of H(ω) can be achieved from measuring the FRFs data in x, y directions and front, rear support respectively.

$$h_{imin} = \frac{X_{imin}}{F_{in}} \ , (i = x, y \ , j = x, y \ \ directions, m = 1{,}2, n = 1{,}2 \ supports) \qquad (3)$$

FRFs in one direction at one support due to a force of same direction at same support is the principal FRF, e.g., X_{x1x1}. The FRFs in one direction due to a force in the other direction at same support are the cross coupling FRFs, e.g., X_{y1x1}. The FRFs at one support due to a force applied at the other support are designated cross talk FRF e.g., X_{x2x1}. The FRF modal test is simulated by FE analysis and performed by the harmonic analysis for the static parts [19]. The PT stator consists of the spoke frame, exhaust and bearing house. The stator is made of steel and cast iron. The 3D stator FE model comprises 4 node tetrahedral 3D elements. In the stator model, the two central nodes of bearing diameters are connected to the nodes on the bearing house bore diameter (ID) surface with RBE2 connection 1D elements. The RBE2 connection element is a rigid connection between nodes to transfer DOFs. Therefore, the displacement of the two central nodes represents the resultant displacements of the two bearing supports respectively. The full FE model of the stator has a huge number of DOF and direct FRFs simulation is very time consuming. The superelement (SE) reduction based on CMS approach [12] is used for the 3D stator FE model to save solving time. The SE reduction condenses the FE model to its mass, stiffness and damping matrices at specified retained nodes. Since the force applied and the response solution needed are only at the two bearing supports, the two central nodes of bearing diameters are configured as the retaining nodes. Shown in Figure 1(a) is the FE model of the spoke frame stator and a variable frequency force in horizontal (x) direction applied at the front support. Figure 1(b) is the schematic SE model and the retaining nodes.

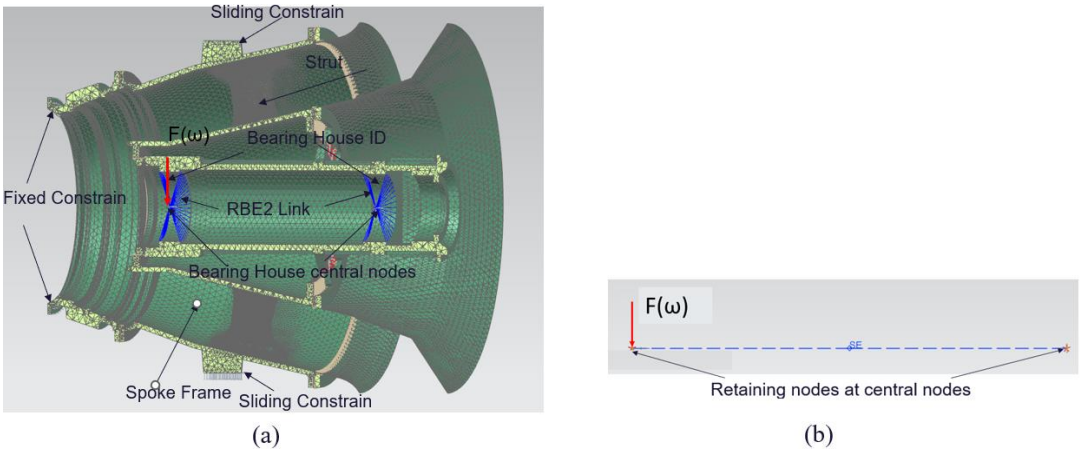

Figure 1: Stator 3D FE model and schematic SE model with load

For the FRF simulation, a unit force with a sweeping frequency 1 fr to 12 fr is applied on the front central node in x and y directions respectively. The FRFs correspond to the first two columns of TRM in Eq. (2). A modal damping ζ of 2% is applied in the stator SE model to simulate the equivalent viscous damping. Shown in Figure 2 are the amplitudes of principal (a) and cross coupling, cross talk FRFs (b)

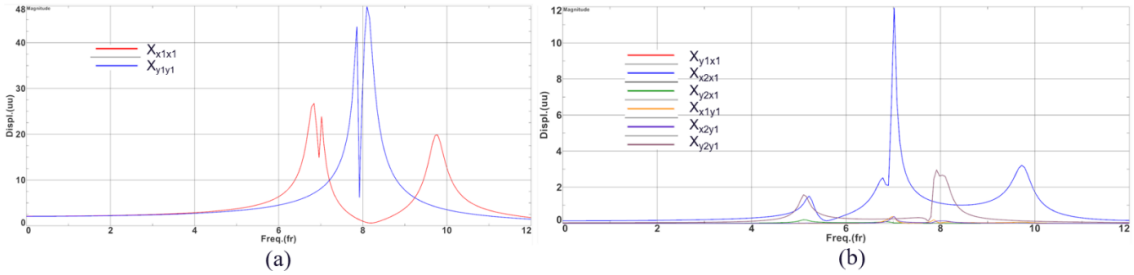

Figure 2: Amplitudes of the principal (a) and of cross couple and the cross talk (b) FRFs

It is seen from Figure 2 that the cross coupling and cross talk FRFs are an order less than the principal FRFs. It is noted that there are structure resonances at circa 6.9 fr, 7.8 fr and 9.8 fr identified by the FRFs in x and y directions.

In industrial practice [4,13], only the principal FRFs are kept for the TFM. The dynamic stiffness matrix becomes de-coupled and each bearing support can be simplified to two SDOFs. For each support, the complex dynamic stiffness can be written as:

$$K_{sdxx} = \frac{F_x}{X_{xx}} = K_{sx} - m_s\omega^2 + i\omega C_{sx} \ ;$$

$$K_{sdyy} = \frac{F_y}{X_{yy}} = K_{sy} - m_s\omega^2 + i\omega C_{sy} \qquad (4)$$

While K_{sd} is the dynamic stiffness, K_s, C_s and m_s are the support stiffness, damping and mass.

The real part of the dynamic stiffness is the direct dynamic stiffness. The imaginary part is referred as quadrature stiffness, which represent the support damping. Shown in Figure 3 are the complex principal FRFs at front bearing support (a) and rear bearing support (b) which are directly used to calculate the front support dynamic stiffness.

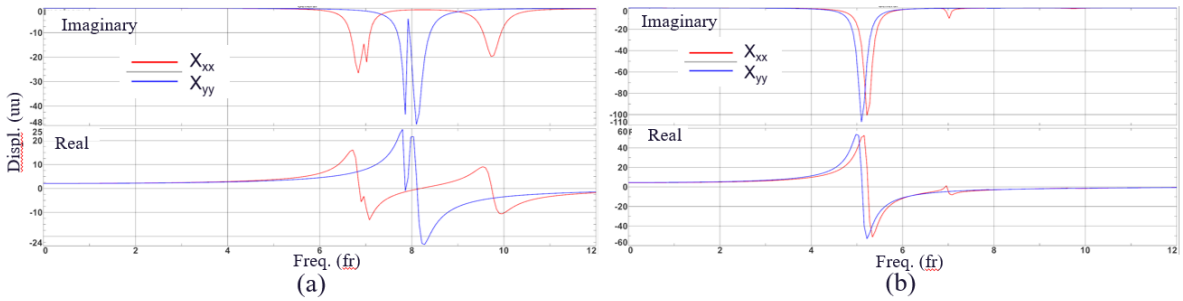

Figure 3: The principal FRFs at front (a) and rear (b) bearing supports

2.2 Tilting pad bearings

The PT rotor is supported by a front (PT side) bearing and a rear (drive side) bearing. The two bearings comprise of 5 tilting pad journal modules and load between the bottom 2 pads. For the rotordynamic analysis in this paper, the bearing stiffness and damping coefficients versus the rotating speed are analysed by hydrodynamic bearing software COMBROS [17]. For the tilting pad bearings, the cross-coupling stiffness and damping coefficients are very small comparing to the principal stiffness and damping coefficients. This property of tilting pad bearing improves the bearing stability.

2.3 Dynamic stiffness of bearing support

The dynamic stiffnesses of the front and rear bearing support are calculated by Eq. (4). Shown in Figure 4 (a) are the calculated direct stiffness (real part). The 3.5 times of the bearing principal stiffness coefficients as the functions of the rotational speed are also shown in Figure 4 (a) for comparison. Shown in Figure 4 (b) are the quadrature stiffness (imaginary part) or the support damping versus the excitation frequency.

It is noted from Figure 4 (a) that since the dynamic stiffness includes the mass of the support structure, they can be positive or negative. At the resonance frequency, the direct dynamic stiffness crosses the zero. According to the API standard [11], “For machines whose dynamic structural stiffness values are less than or equal to three and a half times the bearing stiffness values in the range from 0% to 150% of MCS, the structure characteristics shall be incorporated as an adequate dynamic system model, calculated frequency dependent structure stiffness and damping values (impedances)”. It is seen from Figure 4 (a), that for the front bearing frequency range of 0 - 12 fr and for the rear bearing 5-12 fr, the direct dynamic support stiffness in the horizontal (x) and vertical directions (y) are not in compliance with API standard. That is, these 3.5 times bearing stiffness values exceed the dynamic stiffness of the stator. Therefore, it is concluded that for the new designed PT, the stator should be included in the rotodynamic analysis via dynamic structural stiffness to be in compliance with the API standard.

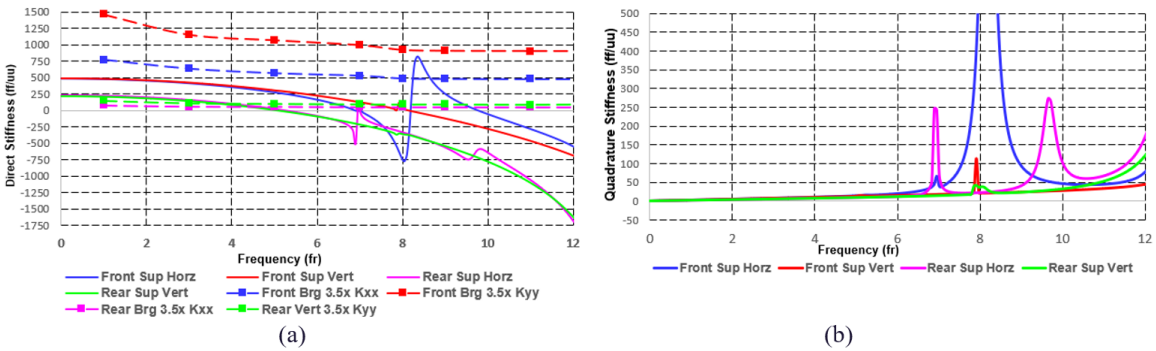

Figure 4: The dynamic direct stiffnesses(a) and quadrature stiffness (b) of the front and rear bearing support

The dynamic stiffness not only includes the support stiffness and damping but also includes the support mass. In Eq. (4) the K_s, C_s and m_s do not need to be identified to be used in the rotordynamic analysis. The direct and quadrature dynamic stiffness can be directly used in the rotordynamic analysis to represent the support structure. The equivalent stiffness and damping [4], which incorporate support dynamic stiffness and bearing stiffness and damping coefficients can be derived by

$$K_{eqii} = \frac{K_{dsii}K_{bii}(K_{dsii}+K_{bii})+\omega^2(K_{bii}C_{sii}{}^2+K_{dsii}C_{bii}{}^2)}{(K_{dsii}+K_{bii})^2+\omega^2(C_{sii}+C_{bii})^2} \quad (5)$$

$$C_{eqii} = \frac{K_{bii}^2 C_{sii} + K_{sii}^2 C_{bii} + \omega^2 C_{sii} C_{bii}(C_{sii}+C_{bii})}{(K_{dsii}+K_{bii})^2 + \omega^2 (C_{sii}+C_{bii})^2} \qquad (6)$$

While $K_{dsii} = K_{sii} - m_s\omega^2$ *(ii=xx, yy)*

The resulting equivalent stiffness and damping coefficients are directly used in the following unbalance response analysis to include the support structure effect.

3. 2D axisymmetric Fourier multi-harmonic rotor and rotating superelement

The PT rotor consists of two bladed turbine discs connected to the shaft with multi-bolt curvic coupling. The PT1 and PT2 disc are made of nickel based alloy and connected with a steel shaft. The rotor is modelled with 2D axisymmetric Fourier multi-harmonic [15] elements. A Fourier expansion of the displacement field in the circumferential direction is performed. It can be written as

$$\begin{aligned} X_r(r,\theta,z) &= \sum_{n=0}^{\infty} X_{nr}(r,z)\cos(n\theta) + \sum_{n=1}^{\infty} X_{-nr}(r,z)\sin(n\theta) \\ X_\theta(r,\theta,z) &= \sum_{n=1}^{\infty} X_{n\theta}(r,z)\sin(n\theta) + \sum_{n=0}^{\infty} X_{-n\theta}(r,z)\cos(n\theta) \\ X_z(r,\theta,z) &= \sum_{n=0}^{\infty} X_{nz}(r,z)\cos(n\theta) + \sum_{n=1}^{\infty} X_{-nz}(r,z)\sin(n\theta) \end{aligned} \qquad (7)$$

In Eq. (7), *n* is the wave number of Fourier harmonics. Harmonic 0 allows the description of axial and torsional behaviors and Harmonic 1 is related to bending (lateral analyses). In this case only the harmonics 0 and 1 are used.

Shown in Figure 5 (a) is the 2D axisymmetric Fourier multi-harmonic PT rotor model. It is created with different boundary conditions (e.g bearings, lumped masses and unbalance masses). The PT1 and PT2 blades are modeled as lumped masses at the axis nodes of the PT discs. The half mass of the flexible coupling which connects the driven machine is also modeled as lumped mass at an axial location. The tilting pad bearings are modeled using 1D connection elements. The connection elements are modeled by the bearing characteristics (e.g. the stiffness and damping coefficients). The PT1and PT2 discs are connected by a curvic coupling and same between PT2 disc and the shaft. The Fourier nodes on each side of curvic coupling are connected by the 1D coupling element (FOU3 and CLINK) [18] at axis of rotor. This configuration enables the load on the curvic coupling output to be provided in the mechnical design. This is paticularly important when verifying the strength of curvic coupling under some special case e.g. resonance under high unbalance induced by blade off.

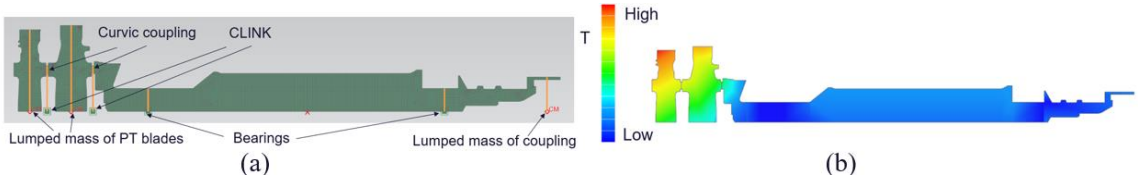

Figure 5: PT rotor FE model (a) and the temperature distribution (b)

The high temperature of PT rotor will affect the rotordynamic performance. The estimated temperature distribution is mapped onto the rotor model and the temperature dependent material properties is input in the FE analysis. Thus the temperature effect on the rotordynamics are considered. Shown in Figure 5 (b) is the estimated temperature distribution on the PT rotor.

The rotating superelement (SE) model of the PT rotor is created for saving computation time with very little loss of accuracy. The CMS based SE for the rotating part condenses a rotor to its mass, stiffness, damping, and gyroscopic matrices at specified retained nodes. For the PT rotor SE model, the retaining nodes are associated with the bearings, lumped mass, and at curvic coupling for output the bending moment. The undamped critical speed analysis for the SE and full 2D FE model (NSE) of the PT rotor are carried out respectively. Shown in Table 1 are the first six undamped critical speeds from SE and NSE respectively.

Table 1: Comparisons of critical speeds between the NSE and SE

Mode	Property	NSE (fr)	SE (fr)	Diff (%)
1	conical(BW)	1.7853	1.7854	0.006
2	conical (FW)	2.0222	2.0223	0.005
3	bounce(BW)	3.3377	3.3376	-0.003
4	bounce (FW)	3.5036	3.5036	0
5	1st bending (BW)	7.2348	7.2339	-0.012
6	1st bending (FW)	13.266	13.273	0.05

BW-backward mode FW- forward mode

It is seen from Table 1 that the SE results of the undamped critical speeds are almost identical to the NSE results. The maximum difference is only 0.05%, which is negligible. This comparison validates the accuracy of the SE model.

The unbalance response analyses are carried out for the SE and NSE model respectively. Both analyses have 141 frequency steps. Calculating in the same computer the computational times are 235 minutes and less than 2 minutes respectively for the NSE and SE model. The comparisons evidently show that the SE model greatly saves the solving time but without loss of accuracy.

The bearing coefficients and the equivalent stiffness and damping coefficients from Eq. (5) and (6) are used in the unbalance response analyses. The unbalance of 17 umb and 3.06 umb are applied at the middle of PT1 disc and the coupling flange on the drive end of PT respectively, at which the retaining nodes for the lumped masses are located. The unbalance values are just over the 2 times of the API standard [11] allowable residual unbalance. To sufficiently excite the mode of natural frequencies the unbalance is applied in-phase (static) and 180º out-of-phase (couple) respectively. Shown in Figure 6 are the unbalance responses at front and rear bearings under static (a) and couple (b) unbalance cases respectively using the equivalent stiffness and damping coefficients from the FRFs (KeqFRFs). For the comparison, the unbalance response with rigid bearing support and bearing stiffness and damping coefficients only (Kbrg) are also shown in figure 6. The unbalance response is peak to peak on the major axis of the orbit.

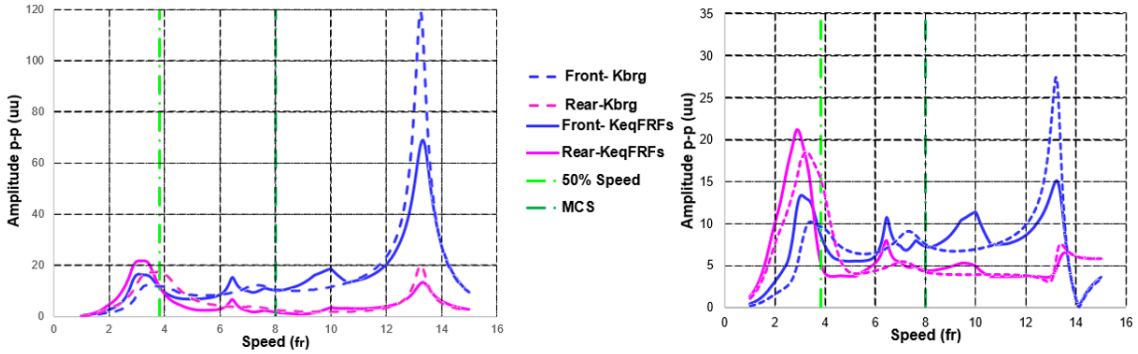

(a) (b)

Figure 6: Static unbalance (a) and couple unbalance (b) response comparison between KeqFRFs and Kbrg

Shown in Table 2 are the identified unbalance response peaks corresponding to the critical speeds for the cases of KeqFRFs and Kbrg.

Table 2: Identified critical speeds for the cases of KeqFRFs and Kbrg by unbalance response

KeqFRFs			Kbrg				
critical speed (fr)	amplitude (uu)	bearing location	critical speed (fr)	amplitude (uu)	bearing location	unbalance case	mode property
2.95	12.9	rear	3.25	18.6	rear	couple	conical (FW)
3.10	21.6	rear	3.75	17.4	rear	static	bounce (FW)
6.45	15.3	front	7.30	12.2	front	static	bending (BW)
7.60	11.0	front	-	-	-	static	structure
10.10	18.7	front	-	-	-	static	structure
13.35	69.0	front	13.3	119	front	static	bending (FW)

It is seen that with rigid bearing support there are amplitude peaks at 3.25 fr, 3.75 fr, 7.3 fr and 13.3 fr corresponding to the critical speeds of rigid body forward conical and bouncing mode, backward bending and forward bend mode respectively. On the other hand, with FRF representation of equivalent stiffness (KeqFRFs), the amplitude peaks appear at 2.95 fr, 3.1 fr, 6.45 fr, 7.6 fr, 10.1 fr and 13.35 fr. Within these critical speeds the

2.95 fr, 3.1 fr, 6.45 fr and 13.35 fr correspond to the same modes as observed from plots of the rigid bearing support. But the first 3 critical speeds are significantly less than those of the rigid bearing support because of the effect of the flexible stator. It is noted that the stator damping effect leads to much lower amplitude peak of the forward first bending critical speed (13.3) for the KeqFRFs than that for Kbrg. The critical speeds of 7.6 fr and 10.1 fr correspond to the stator structure resonances. Therefore, using the FRF structure equivalent stiffness can identify the critical speeds accounting for the effects of stator structure stiffness, damping and also the structure resonances. This evidently shows that with the equivalent stiffness and damping coefficients, the effects of the support structure are captured.

4. Full FE model of the rotor in the stator

A full rotor/stator FE model was developed to perform the rotor/stator rotordynamic design in terms of critical speeds, amplitude and stability according to the API standard requirement. Also, the unbalance response of the full FE model is compared with those of FRFs represented support structure to cross validate between the two methods. Shown in Figure 7 is schematic plot of the PT rotor in the 3D stator (a) and the retaining nodes of the SE model of the rotor and stator (b).

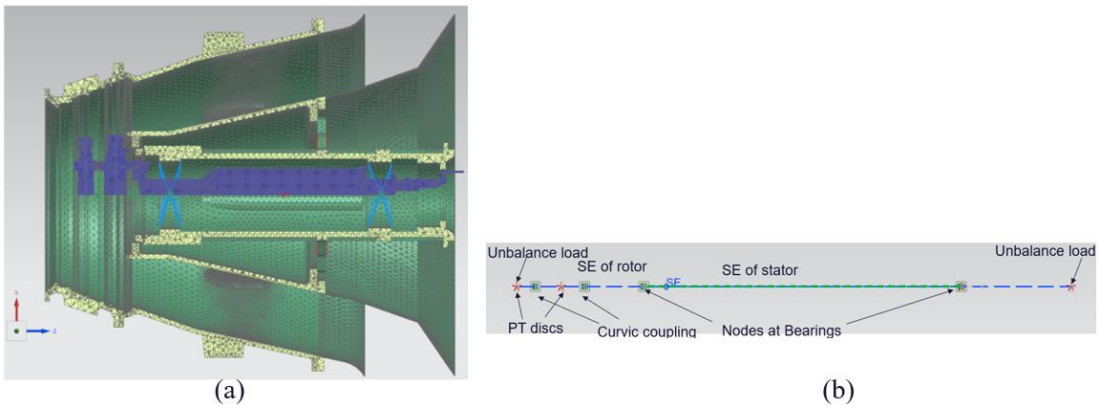

Figure 7: 2D PT rotor in the 3D stator(a) and the schematic retaining nodes of the SE model(b)

The rotor connects the stator at the front and rear bearing locations with the bearing elements. The bearing stiffness and damping coefficients as the function of the rotational speed are used to model the tilting pad bearings. The SE models for the 2D axisymmetric rotor and the 3D spoke frame stator created in previous sections are imported into the assembly to replace the full FE model of the rotor and stator. Again, the modal damping ζ of 2% is applied in the stator SE but no damping is assumed in the rotor SE. The SE model enables fast analysis and obtaining accurate results.

4.1 Unbalance response

The unbalance responses of the full FE model are performed. The results are used to check the critical speeds and amplitudes against the criteria of the API standard. Also, the results are compared with the results from FRFs representation of the bearing support. Since the vibration probes are usually mounted on the bearing housing to monitor shaft displacement, the relative responses are used for the rotordynamic validation.

The unbalances applied are the same as the ones used in section 3, in accordance with the API standard. Shown in Figure 8 are the unbalance response relative amplitudes in major axis for peak-to-peak (uu) at the front and rear bearings for the 2 cases of static (a) and couple (b) unbalance. Also shown is the maximum and minimum operating speed range. The unbalance response results from FRFs representation of bearing support are compared and superimposed in the plot.

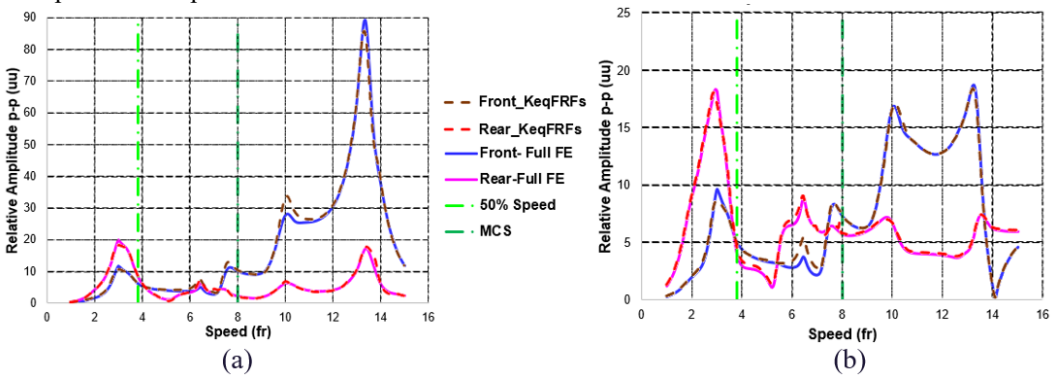

Figure 8: Relative amplitude response to static (a) and couple (b) unbalance

It is noted from Figure 8 that the unbalance response with the FRFs representing the bearing support comply very well with that from the full FE model in terms of the predicted critical speeds, structural resonances and amplitude. More specifically the structural resonances at 7.65 fr and 10.1 fr are accurately predicted by the response from the FRFs representing the bearing support. This comparison shows as quite different from the results of Ref [7], which also compared the response results between rotor model with FRF representation of the support structure and the full FE model. Ref [7] showed approximate match in trend between FRF representation and full FE model of rotor and structure. However, the transfer function approach in [7] did not show all of the peaks predicted by the full rotor-structure FEA model. There were significant differences in structure resonance induced critical speed peaks and amplitudes at those peaks.

The comparison of the unbalance response results shows that the rotor with FRF representation of the support structure and the full FE model with CMS model reduction can be very well cross validated. The FRFs representation of a support structure is a quick and accurate approach to assess the dynamic stiffness of the stator support structure. In summary, results of Figure 6 and Figure 8, FRF structure dynamic stiffness is equivalent to full FE model of rotor-stator in terms of representing support structure in the unbalance response analysis. The advantage of using FRF structure dynamic stiffness is that it enables quick assessment the dynamic properties of the support structure and can be used in traditional rotordynamic software. The drawback is that comparing to the full FE model, using FRF structure dynamic stiffness neglects the cross coupling and cross talk term of TFM. This may lead to less accuracy in stability analysis.

According to API standard, the corrected static and couple unbalance response for front and rear bearings are shown respectively in Figure 9. The 75% of the minimum design running clearance limit is also shown in the plot. In this case the diametral clearance of the bearings is taken as minimum design running clearance.

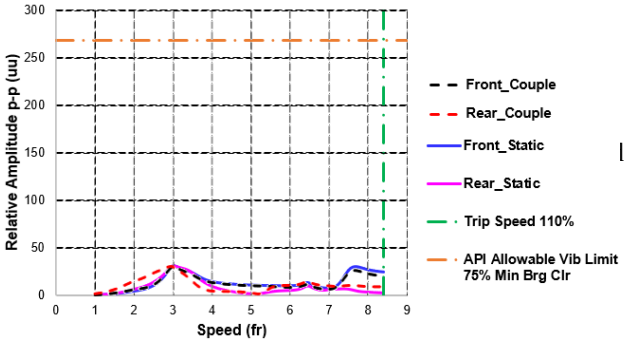

Figure 9: The corrected amplitudes are well within the limit of 75% running clearance in speed range 0 to trip speed (110% full speed).

From the unbalance response shown in Figure 8 and the corrected unbalance response for front and rear bearings in Figure 9, it is seen that PT rotor with the slim spoke frame meets the API requirements in terms of separation margin to the critical speeds and the criteria for the limit of corrected response amplitude.

4.2 Damped modal analysis and stability

The eigenvalue analysis of the full FE model with SE is applied for the stability analysis. Shown in Figure 10 are the Campbell plot and log dec of each natural frequencies plot respectively.

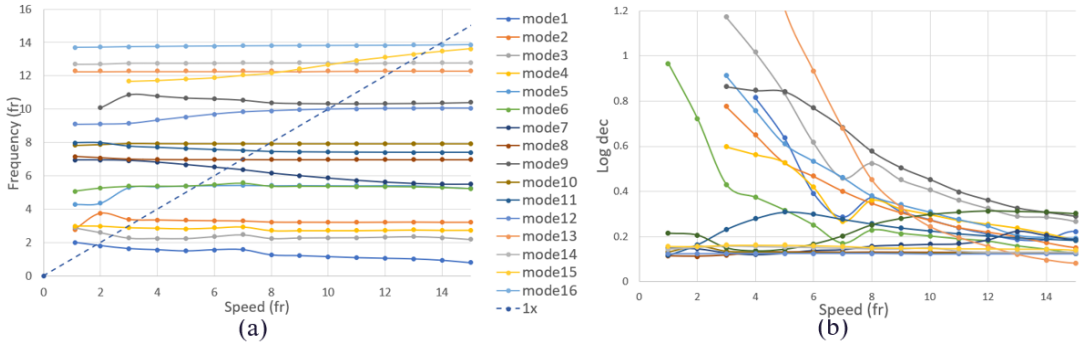

Figure 10: Campbell diagram (a) and log dec (b) for each mode of damped natural frequencies

In Figure 10 (a), the intersections between the curve of eigen frequencies and 1x excitation line correspond to the critical speeds and the resonances of stator. Also, it can be seen from the Campbell diagram that there are a lot of stator frequencies in which the curves are flat. Shown Table 3 are the result of critical speeds and ζ, the strain energy distribution. From the strain energy distribution, the mode property can be identified. It is noted that for

the stator mode or rotor-stator mixed mode ζ are close to 2% since modal damping ζ of 2% is applied in the stator SE.

Table 3: Damped critical speeds and properties

Mode	critical speeds (fr)	ζ %	strain energy distribution			mode property
			bearings %	rotor %	stator %	
1	1.84	29.45	76.5	10.2	13.2	conical (BW)
2	2.43	24.20	62.2	14.1	23.7	conical (FW)
3	2.91	10.50	57.3	17.1	25.6	bounce (BW)
4	3.38	11.50	43.5	19.8	36.7	bounce (FW)
5	5.42	9.20	17.1	0.6	82.3	stator mixed
6	5.43	4.60	8.5	0.3	91.1	stator mixed
7	6.45	2.28	5.6	57.5	36.8	bending (BW)
8	6.98	2.07	0.4	0.4	99.1	stator
9	7.49	4.28	12.5	8.6	78.9	stator mixed
10	7.91	2.03	0	0.2	99.7	Stator
11	9.99	4.75	17.2	12.4	70.3	stator mixed
12	10.34	6.90	27.4	7.1	65.5	stator mixed
13	12.29	2.00	0	0	100	stator
14	12.78	2.07	0.6	1.5	97.8	stator
15	13.66	2.31	2.6	6.7	90.7	bending (FW)
16	13.85	2.03	0.1	0	99.9	stator

It is shown in Figure 10 (b) that in the speed rang 0 to MCS of 8.06 fr, all log decs exceed 0.1, which is the requirement of API standard for the stability. Therefore, the rotor with the slim spoke fame stator system is stable.

5. CONCLUSION

A method to quickly assess the stator support structure dynamic stiffness using the FE simulated frequency response functions (FRF) data is introduced. Using this method, the dynamic support stiffness of a newly designed slim spoke frame stator of a PT is estimated against the requirement of API standard [11].

The derived support dynamic stiffness is directly applied to the unbalance response analysis of the PT rotor incorporating the bearing characteristics. The results are compared with the unbalance responses with the rigid supported bearing and the full FE model of rotor/stator respectively. The comparison shows that the effect of the flexible support and the critical speeds induced by support structure resonance are well captured. It is evidently demonstrated that the dynamic stiffness assessment for the slim spoke frame stator using the FE simulated FRFs data is a quick and accurate approach.

A full rotor/stator FE model is developed using superelement reduction for the rotating and static parts. The full FE model enables the capture of all the dynamics of the rotor-bearing-stator system. The superelement based on the CMS approach used on both rotor and stator FE model enable the high-fidelity FE analysis and fast computation. The analysis shows that with the slim spoke frame stator the newly designed PT satisfies all the API standard requirements in terms of critical speeds, amplitude and stability.

ACKNOWLEDGEMENTS

Authors would like to thank Siemens Energy for allowing the publication of this research, Paul Stephens, Senthil Krishnababu and Roger Wells for their support and comments.

REFERENCES

[1] Nicholas, J. C., and Barrett, L. E., "The Effect of BearingSupport Flexibility on Critical Speed Prediction," ASLE 'Itansactions, Vol.29 No.3 (1986):pp.329-338.

[2] Lund, J. W., "The Stability of an Elastic Rotor in Journal Bearings with Flexible, Damped Supports," ASME Journal of Applied Mechanics, Vol.87, Series E (1965): pp. 911-920.

[3] Hashish, E. and Sankar, T. C., "Finite Element and Modal Analyses of Rotor-Bearing Systems Under Stochastic Loading Conditions," ASME Journal of Vibration, Acoustics, Stress, and Reliability in Design, Vol.106 No.1 (1984), pp. 80-89.
[4] Nicholas, J. C., Whalen, J. K. and Franklin, S. D., "Improving Critical Speed Calculations Using Flexible Bearing Support FRF Compliance Data," Proceedings of the Fifteenth Turbomachinery Symposium, pp. 69-78. Texas A&M University, College Station, Texas, 1986.
[5] Ewins, D. J., Modal Testing: Theory, Practice and Application, Letchworth, Hertfordshire, England: Research Studies Press, (1984).
[6] Vazquez, Josi A., Barrett, Lloyd E., et al. "Flexible Bearing Supports, Using Experimental Data," ASME Turbo Expo 2000, 2000-GT-0404.
[7] De Santiago, O., Abraham, E. , "Rotordynamic Analysis of a Power Turbine Including Support Flexibility Effects," Proc. of ASME Turbo Expo 2008: Power for Land, Sea and Air, Berlin, Germany, GT2008-50900.
[8] Krüger, T., Liberatore, S., Knopf, E., "Complex Substructures And Their Impact On Rotordynamics," 10th International Conference on Vibrations in Rotating Machines, SIRM 2013.
[9] Ehehalt, U., Luneburg, B. et al., "Methods to Incorporate Foundation Elasticities in Rotordynamic Calculations," 8th Internat. Conf. on Vibrations in Rotating Machines. Vienna, Austria, SIRM 2009.
[10] Kumar, D., Juethner, K. and Fournier, Y., "Efficient Rotordynamic Analysis Using The Superelement Approach For An Aircraft Engine". Proc. of ASME Turbo Expo 2017, GT2017-64954.
[11] API Standard 616, Gas turbines for the petroleum, chemical and gas industry services, Fifth edition, 2011.
[12] Craig, R. R., and Bampton, M. C. C., "Coupling of substructures for dynamic analyses.". AIAA Journal, Vol.6 No.7 (1968), pp. 1313–1319.
[13] Vazquez,Josi, A., Barrett, Lloyd E., et al. "Including the Effects of Flexible Bearing Supports in Rotating Machinery," International Journal of Rotating Machinery, Vol. 7, No. 4 (2001), pp. 223-236.
[14] API Recommended Practice 684, Rotordynamic Tutorial: Lateral Critical Speeds, Unbalance Response, Stability, Train Torsionals, and otor Balancing, 2nd edition, 2010.
[15] Geradin, M. and Kill, N., "A new approach to finite element modelling of flexible rotors", Engineering Computations, Vol. 1 No. 1 (1984): pp. 52 – 64.
[16] Nordmann, R. and Knopf, E., "Scientific Mehtods and Tools in rotordynamics for the design process of high performance turbomahcinery," Vibrations in Rotating Machinery- VIRM(11), 2016, September.
[17] Hagemann, T. and Schwarze, H., 2016, "Documentation Journal bearing simulation software COMBROS R, Version 1.3 – Part 1: Theoretical descriptions, basics of modeling and selected guidances for calculation procedures ", FVV/FVA Frankfurt am Main, Germany
[18] Simcenter 3D, v.2206, 2022 June, https://www.plm.automation.siemens.com/global/en/products/simcenter/simcenter-3d.html

15th SIRM – European Conference on Rotordynamics,
Darmstadt, Germany, 22nd – 24th February 2023

Bearing Damage Manifested by Extremely High Half-Speed Subharmonic Vibration on a Steam Turbine Generator

John J. Yu [1], Nicolas Péton [2]
[1] Bently Nevada, Baker Hughes, Atlanta, USA, john.yu@bakerhuges.com
[2] Bently Nevada, Baker Hughes, Nantes, France, nicolas.peton@bakerhuges.com

Abstract

Parametric excitation can occur on a rotor-bearing system with subharmonic or fractional frequency vibration response if the stiffness has a sudden change over a fraction of its orbit. This can be explained from the Jeffcott rotor model, simplified into the standard Mathieu Equation. This paper focus on the exactly half-speed subharmonic vibration phenomenon. A corresponding real case of fluid film bearing damage is then presented on a steam turbine generator. Vibration reached over full scale of 508 microns (20 mil pp) at generator drive end bearing and therefore tripped the machine. The major vibration component that tripped the unit was exactly half-speed subharmonic frequency at a level of over 500 microns. The root-cause was found to be due to bearing damage. Why the half-speed subharmonic vibration occurred at such a high level that tripped the machine is fully explained in this paper. Other vibration plots including orbit, spectrum, and shaft centreline are also presented for vibration diagnostics. Rubs occurred but were not believed to be the root-cause of half-speed subharmonic vibration.

Keywords

Parametric excitation, Half-speed subharmonic vibration, Fractional frequency vibration, Vibration diagnostics, Shaft centreline, Orbit, Rub

Nomenclature

x = rotor lateral deflection in horizontal direction
y = rotor lateral deflection in vertical direction
M = rotor mass
D = damping of the rotor-bearing system
$K(\Omega t)$ = time-varying stiffness of the rotor-bearing system
K_0 = original stiffness
ΔK = increased or decreased stiffness during part of vibration cycle
α = range where ΔK occurs
k = any positive integer
m = unbalance mass
r = radius of unbalance mass
φ = phase lag of unbalance mass
Ω = rotor speed
t = time

τ = dimensionless time variable

a_n = Fourier coefficient of cosine term

b_n = Fourier coefficient of sine term

δ = coefficient in Mathieu Equation

ε = coefficient in Mathieu Equation (same sign as ΔK in this paper)

ω_n = original natural frequency of the rotor-bearing system

1 Introduction

Sub-synchronous vibration can sometimes be difficult in finding its root-cause. Amplitude of sub-synchronous vibration that occurs due to an instability issue can often go beyond the danger level to trip the machine.

Sub-synchronous vibration at a frequency of around one-half of the rotational speed or typically below is sometimes called half-frequency whirl [1] due to fluid-induced instability in bearings or seals. Muszynska [2] demonstrated whirl frequency of around but just below ½X through both analytical and experimental approaches. Many analytical and experimental results such as those by Crandall [3] and Childs [4] in addition to reference [1] do not support the notion of exact ½X whirl due to fluid-induced instability. It is believed that the exact ½X vibration is caused by parametric excitation due to non-linear or step-changing stiffness within the shaft orbit. Ehrich [5] published his observation of ½X vibration in an aircraft gas turbine engine and called it as subharmonic vibration to distinguish it from general sub-synchronous vibrations. Bently in [6] demonstrated his experimental results of this fractional frequency and named "normal-tight" and "normal-loose" conditions. Childs in [7] published some analytical work to explain Bently's work. Muszynska [8] presented partial rub experimental results with shaft orbit shape "8" containing the ½X component. Yu [9] presented three cases of ½X vibration.

This paper first demonstrates theoretically how subharmonic ½X is possible from a simple Jeffcott rotor model. Then a real case of ½X subharmonic vibration on a steam turbine generator is presented. Vibration plots including orbit, spectrum, and shaft centreline are illustrated for vibration diagnostics to help diagnose the malfunction.

2 Theory

The Jeffcott rotor model as shown in Figure 1 is employed to drive parametric excitation solution of ½X subharmonic vibration. Flexible bearing supports, represented by an asymmetric spring and dashpot array, are combined with a lumped mass. To simplify the solution, only one directional motion (in the horizontal direction) is described in terms of displacement *x*.

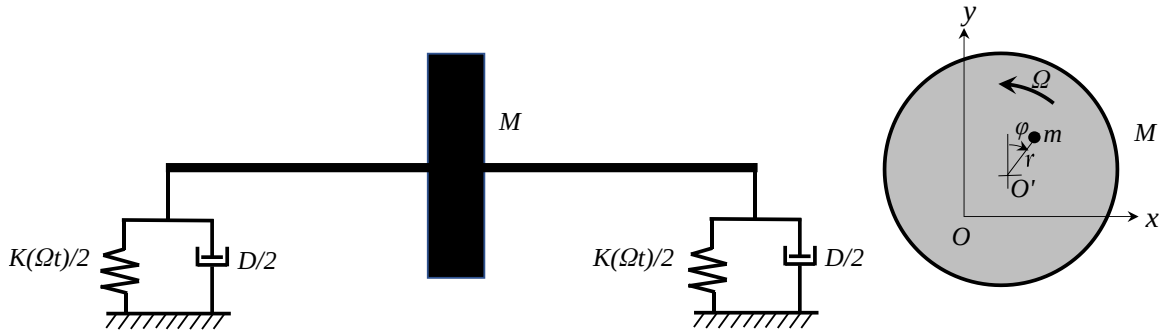

Figure 1: Jeffcort Rotor on flexible bearing supports

The rotor with lumped mass *M* and rigid shaft is supported by flexible bearings with stiffness *K(Ωt)* and damping *D*. Ω is the rotor speed, and *t* is time. The movement of the disk centre *O'* is described by displacement in horizontal and vertical displacements *x* and *y* in the fixed reference frame *Oxy*. Mass unbalance is expressed by *m* with radius *r* and phase lag φ relative to the top dead center.

Let us only consider the motion in the y-direction. The equation of motion of the Jeffcott rotor model in the y-direction as shown in Figure 1 can be given by

$$M\frac{d^2y}{dt^2}+D\frac{dy}{dt}+K(\Omega t)y=mr\Omega^2\cos(\Omega t-\varphi) \tag{1}$$

In some circumstance, stiffness changes within each vibration cycle. It could be decreased (normal-loose) or increased (normal-tight) for part of synchronous 1X vibration cycle. To reflect this change of stiffness, as shown in Figure 2, $K(\Omega t)$ can be modelled by the following periodic step-function:

$$K\left(\Omega t\right)=\begin{cases}K_0, & \text{for } 2\left(k-1\right)\pi\le\Omega t<2k\pi-\alpha\\ K_0+\Delta K, & \text{for } 2k\pi-\alpha\le\Omega t\le 2k\pi\end{cases} \tag{2}$$

where K_0 is original stiffness, ΔK is the change of stiffness, α is the range corresponding to the change of ΔK, and k can be any positive integer. Equation (2) can be expressed as Fourier series in the following:

$$K\left(\Omega t\right)=\frac{a_0}{2}+\sum_{n=1}^{\infty}\left(a_n\cos n\Omega t+b_n\sin n\Omega t\right) \tag{3}$$

where

$$a_n=\frac{1}{\pi}\int_0^{2\pi}K\left(\Omega t\right)\cos n\Omega t\ d\left(\Omega t\right)$$

$$b_n=\frac{1}{\pi}\int_0^{2\pi}K\left(\Omega t\right)\sin n\Omega t\ d\left(\Omega t\right)$$

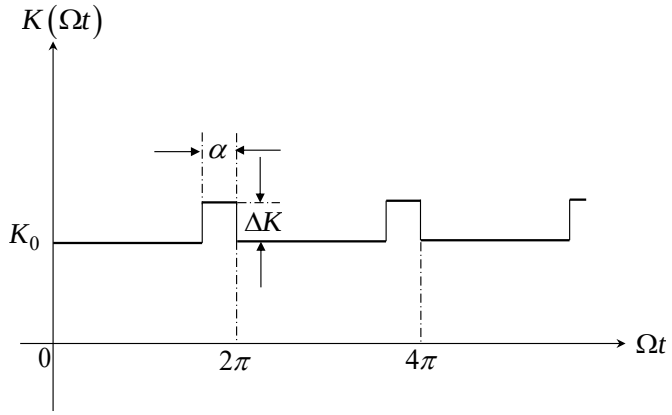

Figure 2: Time-dependent stiffness varying within each synchronous 1X vibration cycle

Thus time-dependent stiffness $K(\Omega t)$ can be given by

$$K\left(\Omega t\right)=K_0+\frac{\alpha\Delta K}{2\pi}+\frac{2\Delta K}{\pi}\sum_{n=1}^{\infty}\frac{\sin\frac{n\alpha}{2}}{n}\cos\left(n\Omega t+\frac{n\alpha}{2}\right) \tag{4}$$

A dimensionless time variable τ is introduced as follows:

$$\tau=\frac{1}{2}\Omega t+\frac{1}{4}\alpha \tag{5}$$

Since the homogenous solution of Eq. (A1) is of interest only to examine instability issues, the unbalance force term is neglected. To examine possible ½X parametric excitation due to time-dependent stiffness, case $n=1$ in Equation (4) is considered. Inserting Equation (4) with $n=1$ and Equation (5) into Equation (1) yields

$$\frac{d^2x}{d\tau^2}+\frac{2D}{M\Omega}\frac{dx}{d\tau}+\left(\delta+2\varepsilon\cos 2\tau\right)x=0 \tag{6}$$

where

$$\delta=\frac{1}{\left(\frac{1}{2}\Omega\right)^2}\frac{K_0+\frac{\alpha\Delta K}{2\pi}}{M} \tag{7}$$

$$\varepsilon=\frac{1}{\left(\frac{1}{2}\Omega\right)^2}\frac{\Delta K\sin\frac{\alpha}{2}}{\pi M} \tag{8}$$

To obtain approximate solution of instability region and frequency, the damping term in Equation (6) is neglected. Thus, Eq. (A6) is simplified into the standard Mathieu Equation [10] as follows:

$$\frac{d^2x}{d\tau^2}+\left(\delta+2\varepsilon\cos 2\tau\right)x=0 \tag{9}$$

The principal instability region is approximately determined by

$$\left|\delta-1\right|<\left|\varepsilon\right| \tag{10}$$

and the unstable solution is dominantly composed of $\cos\tau$ and $\sin\tau$ terms. As indicated in Equation (5), this is exactly the ½X vibration.

Assume that α is small. Thus $\sin\frac{\alpha}{2}\approx\frac{\alpha}{2}$. From Equation (10), unstable speed region due to step-changing stiffness is determined by

$$2\omega_n<\Omega<2\omega_n\sqrt{1+\frac{\alpha\Delta K}{\pi K_0}},\quad \text{for } \Delta K>0 \tag{11}$$

and

$$2\omega_n\sqrt{1+\frac{\alpha\Delta K}{\pi K_0}}<\Omega<2\omega_n,\quad \text{for } \Delta K<0 \tag{12}$$

where

$$\omega_n=\sqrt{\frac{K_0}{M}}$$

is obviously the original natural frequency of the rotor-bearing system. Equations (11) and (12) can be regarded as normal-tight and normal loose cases, respectively.

3 Real Case

This is a cross-compound steam turbine generator unit with HP turbine (3600 rpm) and LP turbine (1800 rpm), as shown in Figure 3. Its rated power output is 775 MW. High vibration excursion occurred on the generator of the HP section. It consists of HP and IP rotors along with the hydrogen-cooled generator.

Figure 3: cross-compound steam turbine generator

The radial vibration probes are mounted at 45° left (Y-probe) and 45° right (X-probe) relative to the top dead center (TDC). There is also a dual-probe setup at each bearing at 30 degrees right, which takes both shaft relative and seismic data to generate shaft absolute readings. They are numbered in order from turbine to generator. The Keyphasor® probe is located at about 90 degrees right relative to the TDC when looking from the turbine to the generator.

After a scheduled outage, startup vibration data was monitored and obtained by using Bently Nevada ADRE® Sxp software and 408 DSPi Data Acquisition System.

3.1 ½X vibration excursion

When the HP generator was brought up to a constant warmup speed of 1800 rpm (half speed of rated 3600 rpm), vibration reached over 508 μm pp (20 mil pp) at the generator drive end bearing (Brg#5 as shown in Figure 4) and therefore tripped the unit.

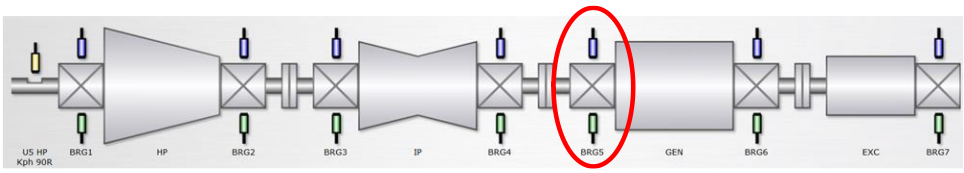

Figure 4: HP generator machine train diagram

Figure 5 is a vibration trend plot containing direct (broad-band frequency), 1X, ½X, and 2X components measured from Brg#5 X-probe. During initial 5 minutes at 1800 rpm, vibration was very low and stable. Then the 1X synchronous vibration started to change with amplitude being up and down. After 2 hours and 20 minutes, the ½X suddenly appeared with amplitude up to 518 μm pp, causing the unit to trip.

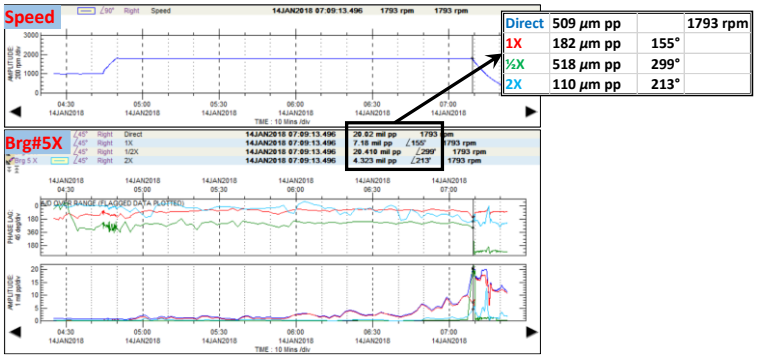

Figure 5: Direct, 1X, ½X, and 2X vibration trend plot at 1800 rpm with ½X up to 518 μm pp

Figure 6 shows orbit plots at 1800 rpm from low to high vibration amplitude in red color. The first 5 orbits were mainly due to the 1X vibration. Then the ½ X vibration occurred and tripped the unit. The last orbit in green color was at 1780 rpm during shutdown after the trip. Since the full scale was set at 508 um pp (20 mil pp) in ADRE configuration, amplitude over that level was truncated. It had not been expected that vibration amplitude would exceed this level.

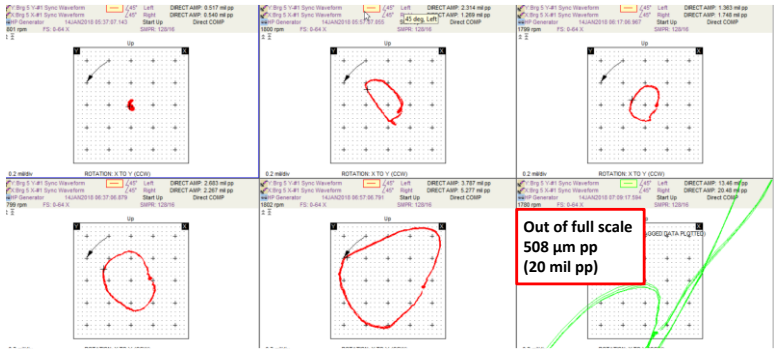

Figure 6: Orbit plots at Brg#5 during vibration excursion at 1800 rpm followed by trip at 1780 rpm

Figure 7 shows full-spectrum waterfall plot during the run. When the 1X vibration was dominating, vibration amplitude was low. Then the abnormal ½ X vibration occurred, accompanied by its multiples 1X, ³⁄₂ X, 2X, etc.

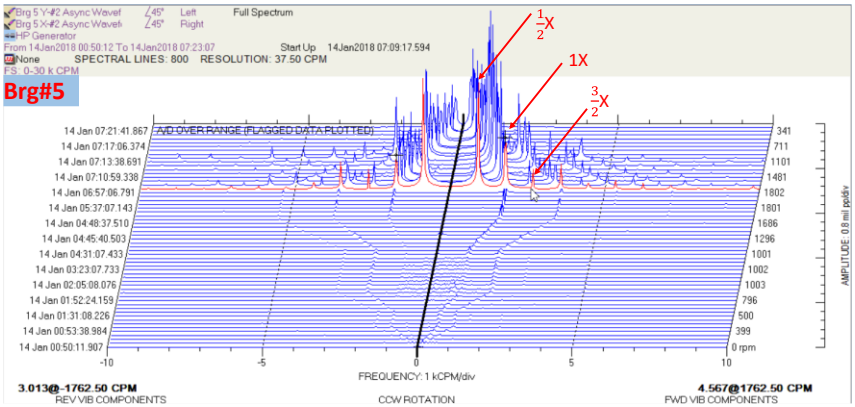

Figure 7: Waterfall plot at Brg#5 during the run

3.2 Diagnostics of the ½X vibration excursion

The root-cause of the abnormal ½ X vibration needed to be found out before the unit could safely start again. Whether it was exactly ½ X or close to ½ X would make a big difference in malfunction diagnostics. Figure 8 shows the orbit/timebase plot at Brg#5 at 1780 rpm. Though X directional amplitude was beyond the 508 μm pp (20 mil pp) full scale, Keyphasor dots were available on the plot plus Y directional amplitude was not affected. These Keyphasor dots were clearly locked at the same location in the orbit and timebase. Therefore, the sub-synchronous vibration was exactly ½ X subharmonics, not close to 0.5X.

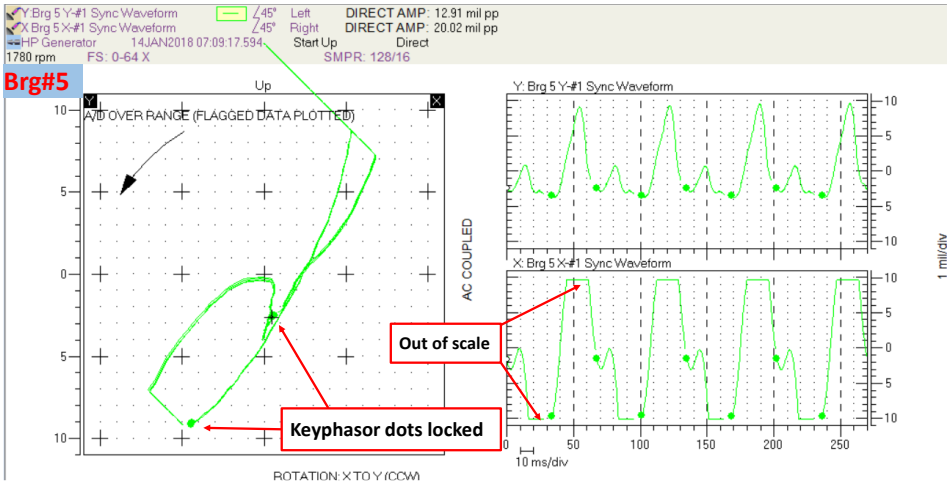

Figure 8 Evidence of exactly ½ X subharmonics from Keyphasor dots

As to whether it was a normal-tight or normal loose case as shown in Equation (11) or (12), the natural frequency of the generator rotor-bearing system would need to be examined. Figure 9 presents Bode plots measured by 4 proximity probes on the generator DE and NDE bearings. The first critical speed was 991 rpm as shown in Figure 9, which can be interpreted as the natural frequency of the generator rotor-bearing system ω_n.

The ½X subharmonics occurred at 1631 to 1800 rpm during shutdown. Therefore, this situation fits the normal-loose condition described in Equation (11), i.e.,

$$2\times 991\sqrt{1-\frac{\alpha|\Delta K|}{\pi K_0}} < \Omega < 2\times 991 \text{ rpm}$$

where $\Delta K < 0$, and $\Omega = 1631-1800$ rpm . The value of the left term is obviously around 1631 rpm. Certainly there is no need to evaluate the exact values of α and ΔK.

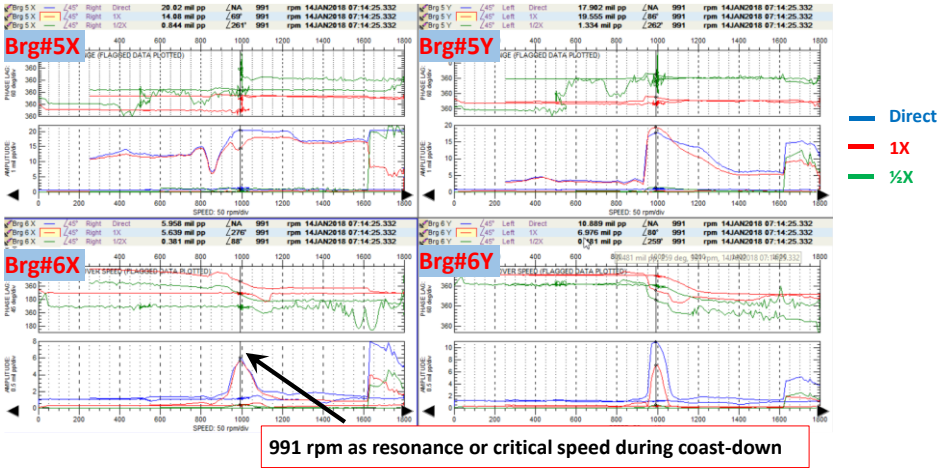

Figure 9: Bode plots measured by 4 proximity probes at generator bearings during coastdown

As to the root- cause of the normal-loose condition, shaft centerline plots were examined to see journal positions relative to the bearing walls. It was surprised to observe that shaft centerline position at Brg#5 moved well beyond its bearing clearance wall, based on the startup reference point taken during the startup. During the outage, the as-left bearing diametral clearance in the vertical direction was measured as 0.610 mm (24 mils). However, the current position appeared that the bearing clearance had significantly increased by approximately 1 mm (40 mils). Therefore, bearing damage was strongly suspected. Normally bearing wipe-up can be easily detected via bearing metal temperature spiking. At that time, unfortunately bearing metal temperature reading was invalid, and therefore only vibration data could be used to diagnose any possible malfunctions.

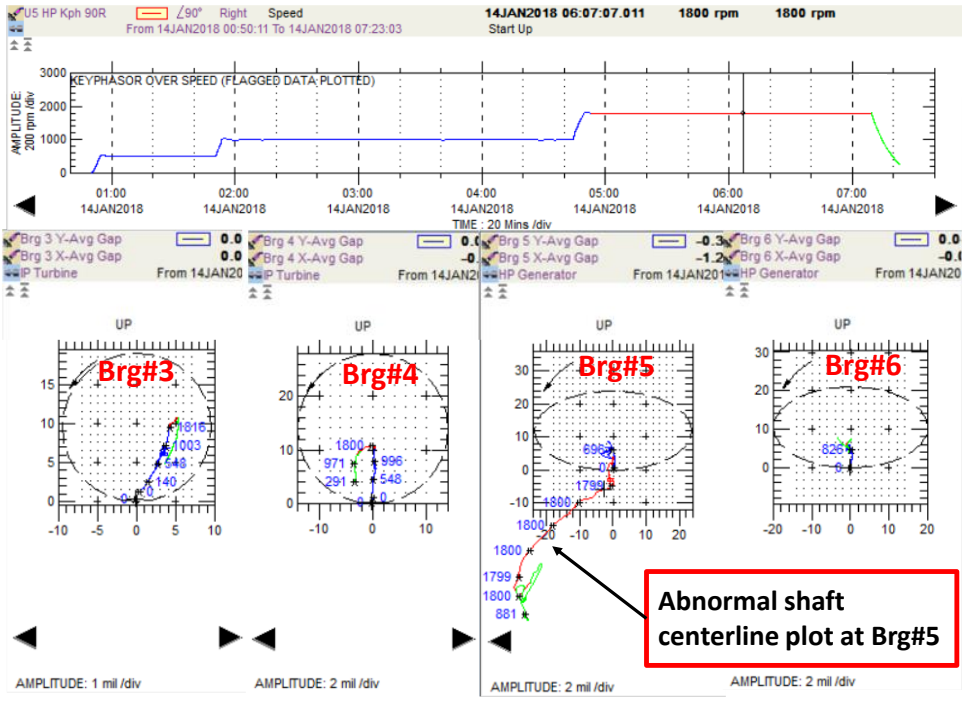

Figure 10: Shaft centerline plots from Brg#3 to Brg#6

One thing regarding changing 1X vibration prior to the onset of ½ X subharmonic vibration remained unexplainable in the very beginning. Later further in-depth data review pinpointed a possibility of rub events. Figure 11 shows 1X trend and polar plots measured by Brg#5 X probe. The 1X vector increased against shaft rotation, behaving as the Newkirk effect. The other evidence of rub was the high 1X amplitude of over 254 μm pp (10 mil pp) measured by Brg#5 X probe from 750 rpm to 250 rpm during shutdown, as shown in Figure 9, indicative of strong shaft bow resulted from rubs.

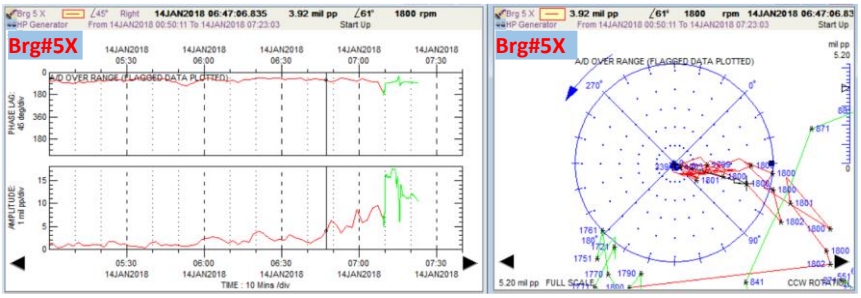

Figure 11: 1X vibration excursions prior to the onset of ½ X subharmonic measured by Brg#5 X probe

3.3 Inspection and findings

An inspection was requested to open the machine near Brg#5 area. The bearing was found to be indeed wiped at the left bottom, as shown in Figure 12, with additional 1.067 mm (42 mils) clearance due to wear beyond as-left clearance of 0.610 mm (24 mils) in the vertical direction, matching the diagnosis. Obviously, the wear was due to the journal rubbing against the babbitt surface.

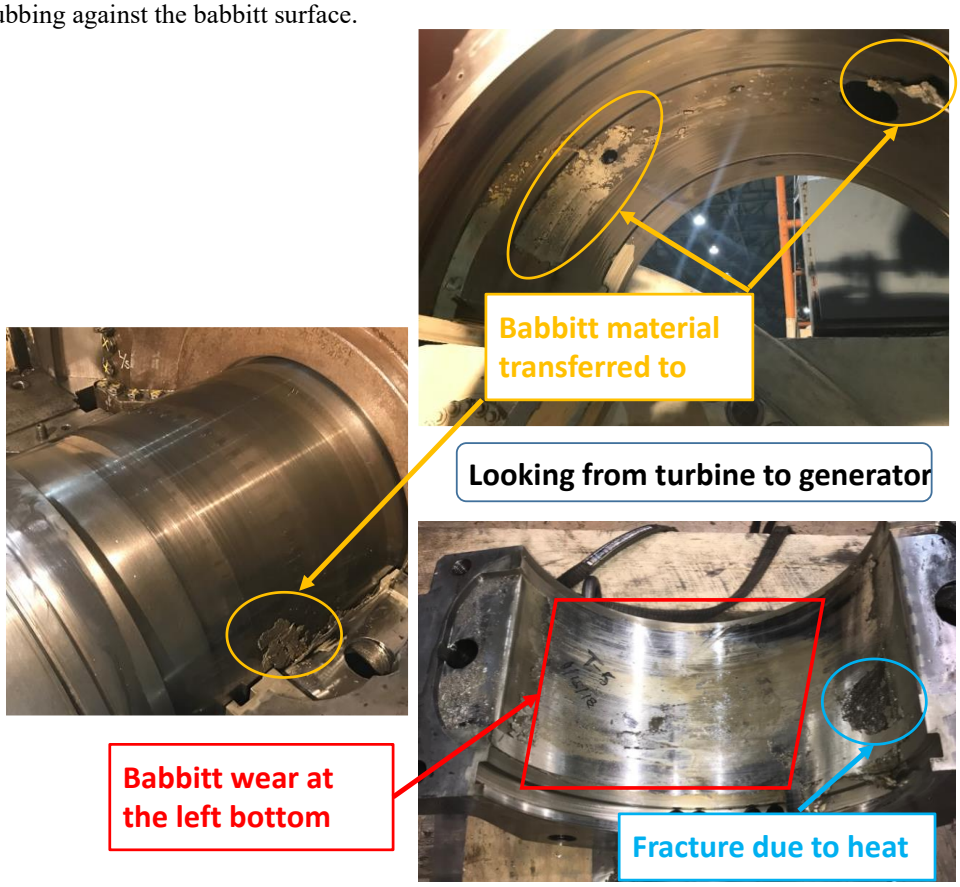

Figure 12: Bearing damages found during an inspection

It was found that a fine strainer was mistakenly left in place, causing oil reduction and starvation, and finally wiping up the bearing. This was believed to be the root-cause. The bearing was shipped offsite to be re-spun.

It appeared that rubs had occurred on inner and outer oil deflectors at Brg #5 as well as that at the adjacent Brg #4 generator side. All these three oil deflectors were shipped offsite for teeth replacement.

It also seemed that Brg#5 hydrogen seal casing oil deflector had been rubbed, which was then replaced with new one.

The clearance and alignment condition were found to be acceptable at the adjacent Brg #4 turbine side oil deflector.

3.4 Resolution and final vibration results

The bearing was repaired by refurbishing its babbitt and re-installed correctly. Several damaged oil deflectors were replaced with new ones. The bearing lube oil system was ensured to function normally.

The unit was then restarted successfully with acceptable vibration level without any abnormal vibration behavior. Figure 13 shows a normal full-spectrum waterfall plot measured by Brg#5 X and Y probes. Note that a seemingly ½ X in a very low level was not due to its own HP rotor vibration. It was the 1X LP (1800 cpm at rated speed) vibration transmitted from the same foundation.

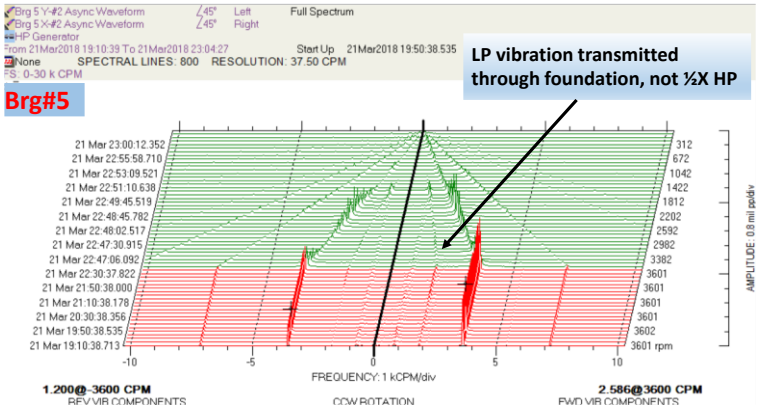

Figure 13: Normall full-spectrum waterfall plot at Brg#5

The corresponding shaft centerline plot also became normal. The journal position was moving within the normal range, as shown in Figure 14.

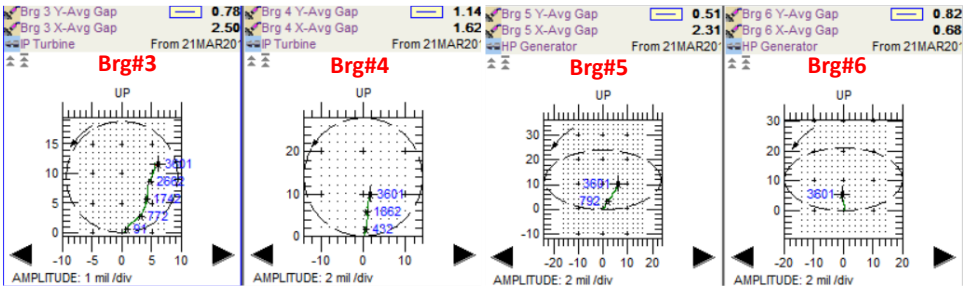

Figure 14: Normal shaft centerline plot at Brg#5 and adjacent bearings

4 Discussion and Conclusions

Parametric excitation analysis on why ½X vibration can occur is presented, which includes unstable speed region by using the Jeffcott rotor model. Step-changing nonlinear stiffness function is modelled and expanded into Fourier series. The homogeneous equation of the Jeffcott rotor model is then simplified into the well-known Mathieu Equation, which yields the solution of instability.

Two conditions are needed to make this unstable ½X vibration possible. First, stiffness would need a step-change within a cycle or orbit of synchronous 1X vibration. In the real case presented here, the bearing surface damage resulted in the large clearance within the fluid bearing. Thus, the bearing stiffness had a step-change likely at the top right of the orbit. In other words, on part of the orbit trajectory at the top right, oil film support could not be provided and bearing stiffness had a sudden decrease from K_0 to $K_0 + \Delta K$, where $\Delta K < 0$. Secondly, rotor speed would have to be approximately at twice the natural frequency of the rotor-bearing system. For the current case, when speed Ω is between 1631 to 1800 rpm, close but slightly lower than 2 times the natural frequency of 991 rpm.

Rubs occurred in this case, but it was manifested by 1X synchronous vibration excursion. In other words, it was not the root-cause of the ½X subharmonic vibration. Had the natural frequency been 815 rpm or below, the ½X subharmonic vibration would have been resulted from rubs as ΔK could be considered as positive due to rub contact leading to a step-increase in stiffness.

In addition to correct determination if sub-synchronous vibration is exactly ½ X subharmonics or close to 0.5X sub-synchronous vibration, review of shaft centerline plot is very important to help diagnose the root-cause of the vibration.

References

[1] Ehrich, F.F., 1999, Handbook of Rotordynamics, Krieger Publishing Company, Malabar, FL.

[2] Muszynska, A., 1986, "Whirl and Whip – Rotor/Bearing Stability Problems," J. Sound Vib., 110, pp.443-462.

[3] Crandall, S., 1990, "From Whirl to Whip in Rotordynamics," IFToMM 3rd Int. Conf. on Rotordynamics, Lyon, France, pp. 19-26.

[4] Childs, C., 1993, Turbomachinery Rotordynamics: Phenomena, Modeling, and Analysis, John Wiley & Sons, New York.

[5] Ehrich, F.F., 1966, "Subharmonic Vibration of Rotors in Bearing Clearance," ASME Paper No. 66-MD-1.

[6] Bently, D.E., 1974, "Forced Subrotative Speed Dynamic Action of Rotating Machinery," ASME Paper No. 74-Pet-16.

[7] Childs, C., 1982, "Fractional Frequency Rotor Motion Due to Non-Symmetric Clearance Effects," ASME J. Eng. Power, pp. 533-541.

[8] Muszynska, A., 1984, "Partial Lateral Rotor to Stator Rubs," Proceedings of the 3rd Int. Conf., Vibration in Rotating Machinery, IMechE, C281/84, York, UK, pp227-236.

[9] Yu, J. J., 2010, "Onset of 1/2X Vibration and Its Prevention", Transactions of the American Society of Mechanical Engineers, Journal of Engineering for Gas Turbines and Power, Vol. 132, 022502.

[10] Meirovitch, L. 1975, Elements of Vibration Analysis, McGraw-Hill, New York.

15th SIRM – European Conference on Rotordynamics,
Darmstadt, Germany, 22nd – 24th February 2023

Experimental dynamic characteristics of a gas microturbine with a supercritical rotor supported by a hybrid bearing system

Grzegorz Żywica [1], Paweł Bagiński [2], Artur Andrearczyk [3]

[1] Department of Turbine Dynamics and Diagnostics, Institute of Fluid-Flow Machinery, Polish Academy of Sciences, 80-231, Gdańsk, Poland, gzywica@imp.gda.pl
[2] Department of Turbine Dynamics and Diagnostics, Institute of Fluid-Flow Machinery, Polish Academy of Sciences, 80-231, Gdańsk, Poland, pbaginski@imp.gda.pl
[3] Department of Turbine Dynamics and Diagnostics, Institute of Fluid-Flow Machinery, Polish Academy of Sciences, 80-231, Gdańsk, Poland, aandrearczyk@imp.gda.pl

Abstract

This paper presents the results of experimental tests carried out on a 30-kilowatt prototype gas microturbine. An unconventional bearing system, which consists of two super-precision ball bearings and a single gas bump-type foil bearing, was used to support the rotor of this machine. The function of the foil bearing is to support the overhung end of the shaft where the rotor disc of the gas microturbine and compressor is located. The experimental examination of the microturbine prototype was conducted under laboratory conditions and included several start-up tests, a test carried out at constant speed, and rotor rundowns. The vibration level of the casing and the temperature of the selected components were monitored during the tests. Based on the obtained characteristics, the dynamic state of the machine was evaluated and some modifications to the bearing system were proposed. The analysis of the vibrations that occur in the resonance area has shown that an additional foil bearing significantly reduces the vibration level, as well as the risk of damage to the machine as it passes through critical speeds. The results presented in this paper may be of interest to other researchers and engineers who are involved in the development of high-speed turbomachines, especially gas microturbines.

1 Introduction

The rotors of modern turbomachines, such as microturbines and turbocompressors, operate at very high rotational speeds. This is beneficial in terms of the flow system and allows high efficiency to be achieved, but at the same time high speeds can cause dynamic problems and advanced bearing systems must be used. The mechanical, thermal, and electrical loads that act on the rotating systems of such machines require very detailed analyses, because, at high speeds, some components must operate slightly below the limits of their technical capacities. As the speed increases, new dynamic problems may also arise due to the occurrence of critical speeds. This applies to long, flexible rotors, including, in particular, rotors with a significant overhang. Therefore, a lot of attention is paid to the design of rotating machines, where the high-speed rotor of the generator and the disc of the turbine rotor are mounted on the same shaft. In a low-speed machine, such a rotor can be driven by a coupling [7] or a gear, but it is typical of micro-power machines that their generator and rotor disc share the same shaft [2], [4]. Thanks to this, it is possible to achieve high efficiency and a more compact and reliable structure. In the case of vapour microturbines, the use of a single shaft without coupling between the turbine and the generator makes it possible to build oil-free turbogenerators [4]. In order to reduce the vibration level of turbomachinery, much attention is also paid to high-speed balancing [9]. Accurate balancing of a rotor reduces not only the dynamic forces acting on the rotor and bearings but also the impact of the machine on the environment [10]. Rotor unbalance can also increase during operation, for example as a result of the deposition of debris on rotating parts [23].

In machines with overhung rotors, one end of the shaft is not supported by any bearing. When passing through resonant speeds, the vibrations of the overhanging part are not limited and dampened by the bearing, which can lead to significant shaft bending. In this type of rotors, the gyroscopic effect, which affects the massive disc located at the end of the shaft, is also important. For many years now, these problems have been the

subject of numerous scientific publications. In the paper by Shende [17], an analytical method applied to a flexible overhung rotor with a squeeze film damper mounted in the bearing support is presented. In the next paper [16], the effect of various combinations of unbalance and disc skew on the amplitude and phase angle response was analysed. The authors show that it is impossible to balance the overhung rotor at all speeds by single-plane balancing, even if three correction planes are used. It was also noted that a rotor that might appear to be well balanced at a particular speed may be considerably unbalanced at other speeds due to the effects of shaft deflection and disc skew. A balancing analysis carried out on high-speed overhung rotors is also presented in [8]. The proposed method is based on determining the influence coefficient of the rotor overhang, which changes the natural frequencies. The authors of this paper noticed that the standard balancing procedure is ineffective for such rotors. In the paper published in 2010 [12], a practical computer model and analysis of an overhung rotor, taking into account the design changes related to the increase in the output power of a machine, are presented. Different design alternatives were considered and finally the bearing diameter was changed to obtain satisfactory vibration characteristics. In the next paper [13], the same author numerically examines an overhung rotor with hysteretic dynamic behaviour and compares these results with the results of experimental tests. A numerical model of an overhung rotor with rolling element bearings is presented in [6]. The authors used a multi-body system model of a ball bearing to calculate the dynamic behaviour and resonance characteristics of the rotating system. A test rig was also designed and built to validate the theoretical model using experimental data. The model was capable of representing the modal characteristics with satisfactory accuracy.

The dynamic forced response analysis, using a simple two-degree-of-freedom model of an unbalanced overhung rotor subjected to intermittent annular rubs, is presented in [22]. It was found that, for sufficiently high levels of transient energy in the rotor, there exists the possibility to jump into a stable limit cycle characterised by the synchronous response frequency. Nonlinear forced vibration analysis of overhung rotors is also presented in [14]. Unbalance forces resulting from eccentricity and disc skew were considered. It is shown that large-amplitude rotor vibrations led to nonlinearities in curvature and inertia. Static deflection creates second-order nonlinearity. Because gravity decreases the hardening effect, the nonlinear system tends to become a linear system. Paper [1] presents a numerical analysis of an overhung rotor with snubbing contact. It is shown that incorporating the couple of snubbing moments into the equations of motion yields a piecewise and strongly nonlinear system. Three cases were analysed to investigate the effect of isotropy and anisotropy of the stiffness of the support. The whirl response and the full-spectrum analysis have confirmed the excitation of post-resonance backward whirl zones of rotational speeds for all these cases. A rotating system consisting of a massless viscoelastic shaft supported by rolling bearings with a rigid massive disc mounted on the overhung shaft end is considered in [15]. It is shown that the disc can be stabilized and its bifurcating self-excited vibration can be effectively reduced and modified by contactless radial magnetic actuators acting as external dampers.

In the literature, one can find many examples of experimental studies of different types of energy microturbines. The authors of these studies mainly focus on energy issues and usually determine power and efficiency as a function of rotational speed [3], [5], [19]. Although gas microturbines with an external combustion chamber can be supplied with low-quality fuels [4], the number of papers that focus on experimental studies of such machines is low in the available literature. One such study is presented in [18] concerning an 80 kW gas microturbine with an external combustor. An experimental evaluation of the output power of a 100 kW gas microturbine with an external heat exchanger is presented in [20]. Much less attention is paid to operational and diagnostic issues. Examples of such tests are presented in publications [21], [24], where the vibrations of energy microturbines have been studied in relation to various operating parameters. These studies, however, did not concern gas microturbines with an external combustion chamber. Therefore, based on the literature review, it can be concluded that publications devoted to experimental studies of the dynamic properties of microturbines with an external combustion chamber can be sought by other researchers. Such publications allow, for example, the verification of computational models and the comparison of microturbines of different designs.

This paper discusses the results of an experimental study conducted on a prototype gas microturbine with a nominal power of 30 kW. This microturbine uses a high-speed overhung rotor supported by an uncommon bearing system consisting of rolling bearings and a foil bearing. The research was carried out under laboratory conditions, in several stages. Each stage of the research provided new results that allowed the design of the rotating system to be improved and higher speeds to be achieved. Much of the attention has been focused on accessing the effect of rotational speed on the vibration level of the microturbine and on identifying resonant speeds. The following part of the paper discusses in detail the object of the research and the design of the rotating system. Then, several stages of the experimental study are discussed and selected measurement results are presented. At the end of the paper, the results obtained are summarised and further directions for the research and development of the gas microturbine are indicated.

2 Characteristics of the gas microturbine

The research object is the prototype of a gas microturbine that will be used in a cogeneration system with a so-called external combustion chamber. The machine in question comprises an air compressor, a gas turbine and an electric generator. The compressor is used to increase the pressure of air and force its flow to the flue gas–air heat exchanger. The exhaust gases flow there from the boiler. Then, the compressed and heated air flows through the turbine that drives the shaft, including the compressor disc and the electric generator. The designed machine has a nominal electric power of 30 kW, which is achieved at 100,000 rpm. A picture of the prototype mounted on the test rig is shown in Fig. 1.

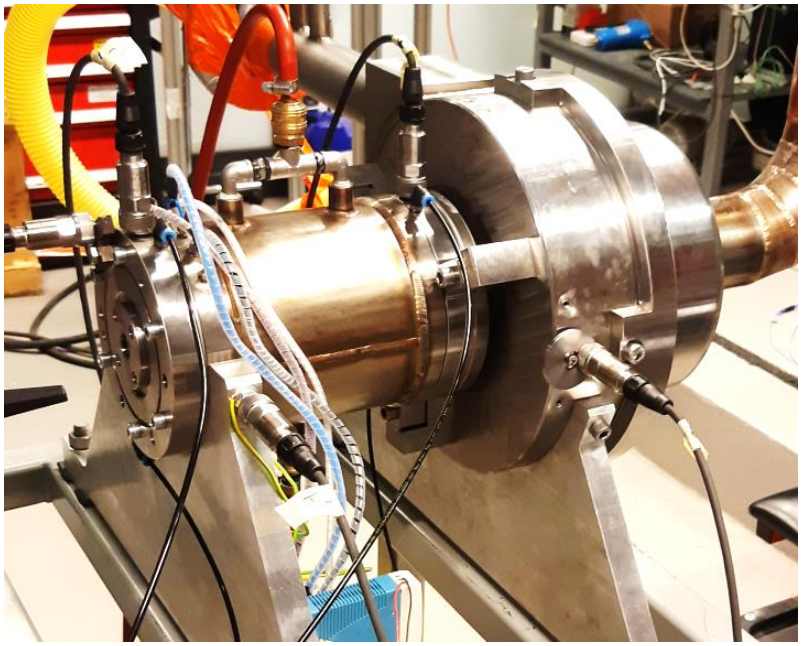

Figure 1: Prototype of a 30 kW gas microturbine.

At the nominal operating point, the temperature of the hot air flowing through the turbine reaches 850°C. In the immediate vicinity of the turbine rotor disc, the operating conditions can be very difficult, making it impossible for a bearing node to be installed at this location. Therefore, in the first version of a rotating system, only two bearings were used to support the rotor in the turbocompressor prototype. They were placed in an area where the temperature is much lower—on both sides of the electric generator [25]. In the second version of the prototype, a third bearing was used between the gas turbine disc and the compressor disc. Due to very difficult operating conditions (high rotational speed and high temperature), it was decided to use a foil bearing in this place. A 3D model of a rotating system with three bearings is shown in Fig. 2. The rotor has a total length of 418 mm and a shaft diameter of 25 mm between the generator and the compressor rotor disc. The outer diameter of the rotor disc of the turbine and compressor is 108 mm. The weight of the complete rotor (including the generator sleeve, compressor disc and turbine disc) is approximately 3.6 kg.

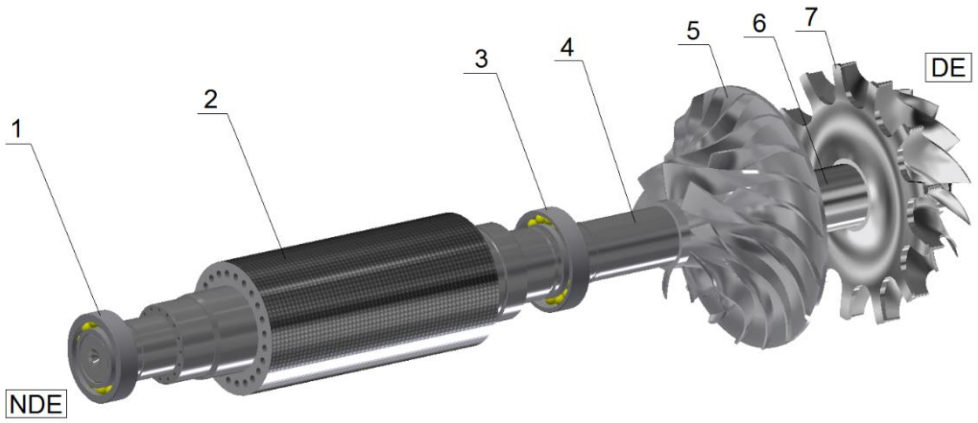

Figure 2: Rotating system of the 30 kW gas microturbine (1 – NDE ball bearing, 2 – generator rotor, 3 – DE ball bearing, 4 – shaft, 5 – compressor disc, 6 – foil bearing, 7 – turbine disc, NDE – non-drive end, DE – drive end).

The bearing systems of such machines must withstand high rotational speeds, low- and high-frequency dynamic loads that act on the shaft as well as high thermal loads. In addition, in this case, the bearings must be able to withstand certain axial forces, as this is necessary to maintain the correct position of the rotor in the casing. Initially, the possibility of using different types of bearings was considered, but due to the harsh operating conditions, the number of possible solutions gradually decreased. That is why the scope of research also included unconventional bearing systems such as foil bearings [11] and gas bearings lubricated with uncommon lubricants [23]. However, the key issue when selecting bearings lies in the rotor design, which determines the requirements and operating conditions of each bearing node. That is why high-speed, super-precision rolling bearings (with a nominal bore diameter of 20 mm at the non-driven end and 25 mm at the driven end) were used in the first version of the gas microturbine. Bearings of this type have ceramic rolling elements, so that they can operate at very high speeds even under poor lubricating conditions. In order for the bearings to be able to withstand the axial loads occurring in the machine, a decision was made to use angular bearings in the X arrangement. One of the important reasons for choosing these bearings was the fact that the turbocompressor is a prototype that must undergo extensive testing under laboratory conditions before it is put into service. Preloaded rolling bearings are characterised by a fairly high stiffness, which can be an advantage for a rotor with a significant overhang. On the other hand, the low damping of the rolling bearings will not be advantageous because of the possibility of the occurrence of large vibrations when the system passes through resonant speeds. Preliminary experimental tests confirmed that very high vibrations of the machine had occurred around resonant speeds. Therefore, in the target design, a decision was made to use an additional bearing to support the overhung end of the shaft. As mentioned earlier, due to the operating conditions, an in-house developed gas foil bearing was chosen in this case. The effect of using such a bearing on the vibration level of the microturbine is presented in the following sections of this article.

3 Results of experimental tests

Experimental research on the prototype gas microturbine was carried out in a laboratory of the Institute of Fluid-Flow Machinery in Gdańsk (IMP PAN). Subsequent stages of the research allowed the characteristics of the actual machine to be determined, thus providing the basis for the improvement of the bearing system. Since this article focuses on the dynamic characteristics of the microturbine, the following subsections discuss the results of vibration measurements. Vibrations were measured on the machine casing using uniaxial accelerometers with magnetic feet. Two accelerometers were mounted near each rolling bearing to measure vibrations in the horizontal (X) and vertical (Y) directions. The root-mean-square (V_{rms}) and zero-to-peak ($V_{0\text{-}P}$) values of vibration velocity, determined over a frequency range of 1 Hz to 1,600 Hz, were used as a measure of vibration level. Apart from vibrations, the rotational speed of the rotor and the temperature of the rolling bearing located closer to the driven end of the shaft (marked as DE) were also measured. In addition, thermodynamic parameters such as inlet and outlet air temperature and pressure, as well as mass flow rate, were measured during the study of the hot air driven microturbine. Before each series of measurements, the microturbine rotor was precisely balanced so that the residual unbalance was less than the value permitted by the balancing grade G2.5, according to the ISO 1940 standard.

3.1 Preliminary test of the microturbine with two ball bearings

Preliminary tests were carried out at room temperature using an electric drive for the rotor. During these tests, the electric generator operated as an electric motor, which allowed precise control of the rotational speed. In the first configuration of the machine, the rotor was supported by only two ball bearings, located on two sides of the generator (Fig. 2). The end of the shaft, on which the rotor disc of the turbine and compressor was located, was not supported by any bearing. Such a rotor was characterised by a significant overhang.

Prior to the experimental tests, simulation calculations were performed to estimate the resonant speeds of the rotor. These calculations included both a modal analysis and a forced vibration analysis of the unbalanced rotor [24]. Based on numerical analyses, the successive resonant speeds associated with the bending vibrations of the shaft with two bearings were estimated to be around 12,000 rpm, 33,000 rpm and 73,000 rpm.

The experimental tests consisted of gradually increasing the rotational speed of the rotor (in steps of 2,000 rpm) and monitoring the vibration level of the microturbine casing and the temperature of the rolling bearing. During these tests, the vibration level of the microturbine was very low, but only up to a speed of about 11,000 rpm. When the speed was increased to 12,000 rpm, a significant increase in vibration velocity (V_{rms}) was observed, from about 0.5 mm/s to about 4 mm/s. An increase in speed above 12,000 rpm resulted in a further increase in vibration level. At 14,000 rpm, the vibration velocity (V_{rms}) was approximately 10 mm/s. The results of the vibration velocity measurements (V_{rms} and $V_{0\text{-}P}$) are shown in Fig. 3. These results were obtained for the bearing node located closer to the turbine (DE), in the vertical direction. Similar increases in vibration levels occurred at other measurement points.

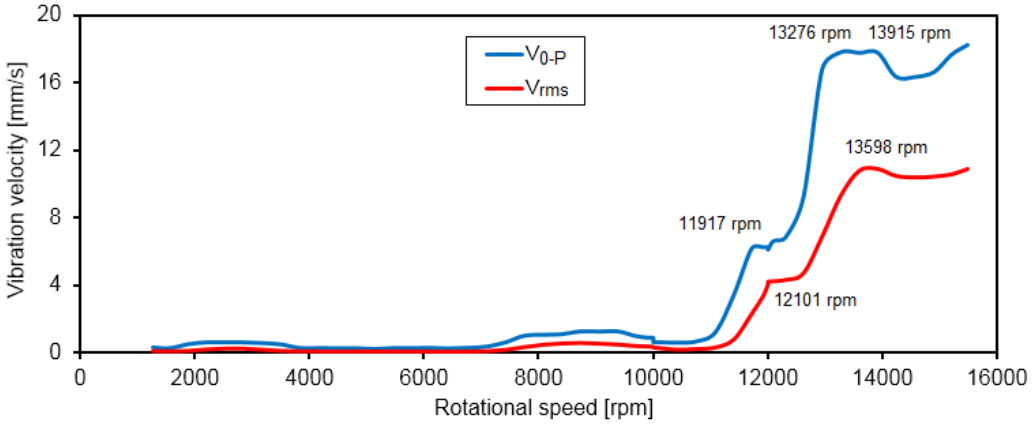

Figure 3: Vibration velocities (V_{rms} and $V_{0\text{-}P}$) measured in the vertical direction near the DE ball bearing versus rotational speed.

Attempts to achieve higher speeds of the rotor with two bearings have been unsuccessful. The vibration level was so high that it prevented the safe operation of the machine. Rotor vibrations interfered with the operation of the generator and bearings, and the free end of the shaft with the turbine rotor disc rubbed against the casing. Therefore, despite several attempts, it was not possible to achieve stable operation of the machine at speeds exceeding 15,000 rpm. The results of this study have shown that it is necessary to modify the rotating system.

3.2 Test of the microturbine at room temperature

Based on the preliminary study discussed above, the bearing system of the gas microturbine rotor has been modified. To additionally support the overhanging part of the shaft, a gas foil bearing was used between the rotor disc of the turbine and the compressor. This was an in-house developed foil bearing with a nominal diameter of 26 mm, which was made of heat-resistant materials that can withstand temperatures above 500°C. In addition, the preload of the rolling bearings had been adjusted to the actual axial force acting on the shaft during machine operation at different speeds. The microturbine thus prepared was subjected to further tests, which consisted of gradually increasing the speed of the rotor to 32,000 rpm. During these tests, an electric generator operating in motor mode was again used as the rotor drive, and room-temperature air (collected from the laboratory space) flowed through the compressor and turbine.

The test results in the form of vibration waveforms in the horizontal and vertical directions are shown in Figs. 4 and 5. When these graphs are compared to the results presented in Subsection 3.1, it can be concluded that the modifications made to the bearing system significantly reduced vibration levels. Up to a speed of 15,000 rpm, the maximum vibration level (V_{rms}) in the vertical direction at the DE bearing decreased from about 10 mm/s to 3 mm/s (Fig. 4). The peak vibration level occurred at 13,050 rpm. Even at higher speeds, the vibration level near this bearing in the vertical direction did not exceed 3 mm/s. In the horizontal direction, the highest vibration level was about 4 mm/s and occurred at 25,300 rpm. Based on the vibration measurements performed on the NDE bearing, it can be concluded that in the horizontal direction, the highest V_{rms} values occurred at 11,050 rpm (approx. 3.5 mm/s) and 25,750 rpm (approx. 9 mm/s). In the vertical direction, the highest vibration levels occurred at 12,950 rpm and 28,150 rpm, and over the entire range, the level of these vibrations did not exceed 5 mm/s. The aforementioned increases in vibration levels had to do with the resonant speeds of the rotor. In the remaining speed range, the machine's vibration was much lower, reaching a maximum level of about 2 mm/s. The differences between the vibration levels in the horizontal and vertical directions at the same rotational speeds can be explained by the anisotropic properties of the support of the microturbine casing. The casing was bolted to the steel frame by two supports (Fig. 2), which did not provide the same support stiffness in the horizontal and vertical directions. The microturbine support structure itself also has different stiffness in the horizontal and vertical directions, which is reflected in the vibration waveforms measured on the microturbine casing.

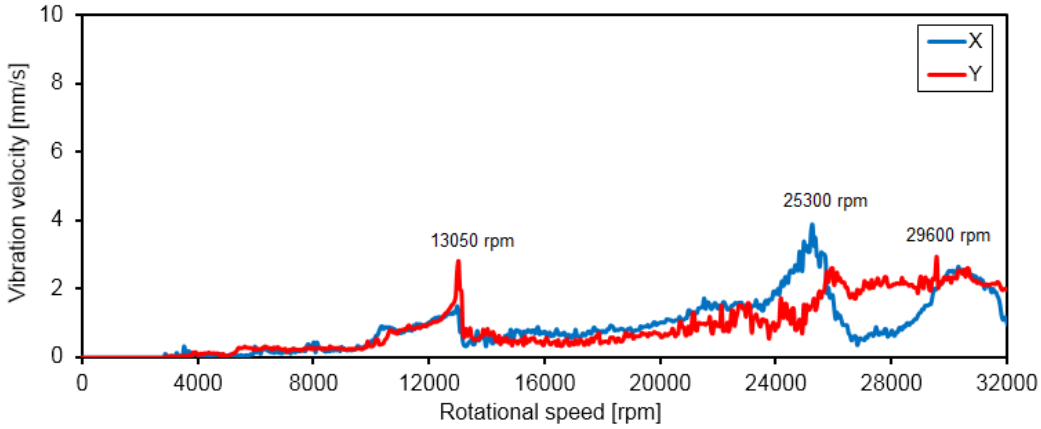

Figure 4: Vibration velocity (V_{rms}) measured on the microturbine casing close to the rolling bearing (DE) versus rotational speed (X – horizontal direction, Y – vertical direction).

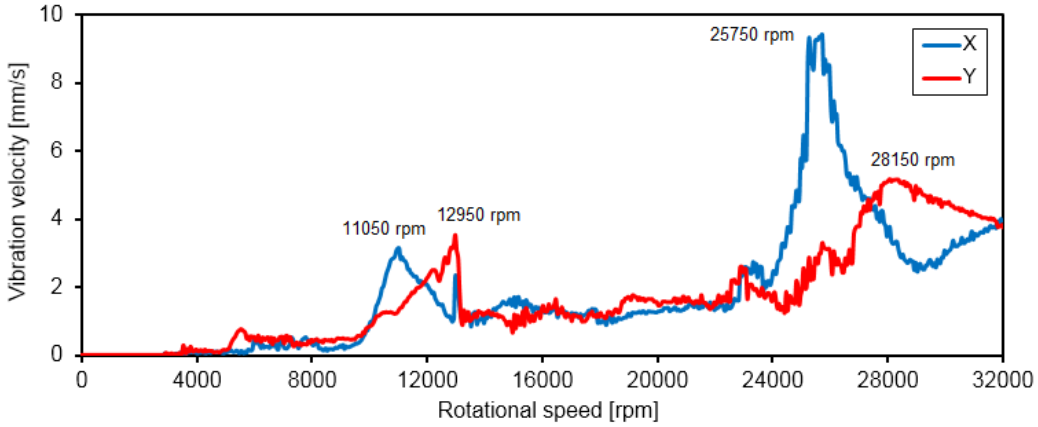

Figure 5: Vibration velocity (V_{rms}) measured on the microturbine casing close to the rolling bearing (NDE) versus rotational speed (X – horizontal direction, Y – vertical direction).

In order to fully evaluate the dynamic characteristics of the microturbine at selected speeds, vibration velocity spectra were determined. Although at lower speeds (up to about 20,000 rpm), no components other than that corresponding to the rotational frequency were observed, superharmonic components were present at higher speeds. The frequencies of these components corresponded to multiples of the rotational speed (2n, 3n and so on). Examples of such frequency distributions are shown in Figs. 6 and 7. Such vibration spectra could indicate, for example, misalignment of the bearing supports in which the rolling bearings were embedded. During these tests, the temperature of the DE rolling bearing did not exceed 45°C.

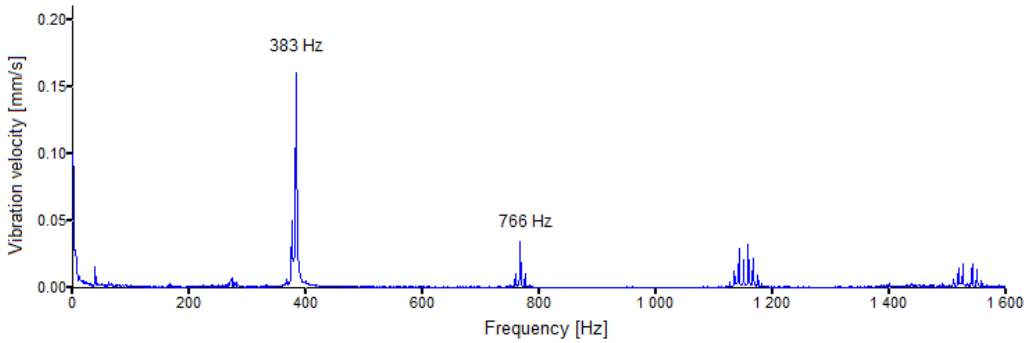

Figure 6: Vibration velocity spectrum recorded on the microturbine casing in the vertical direction close to the DE bearing at a speed of 22,980 rpm.

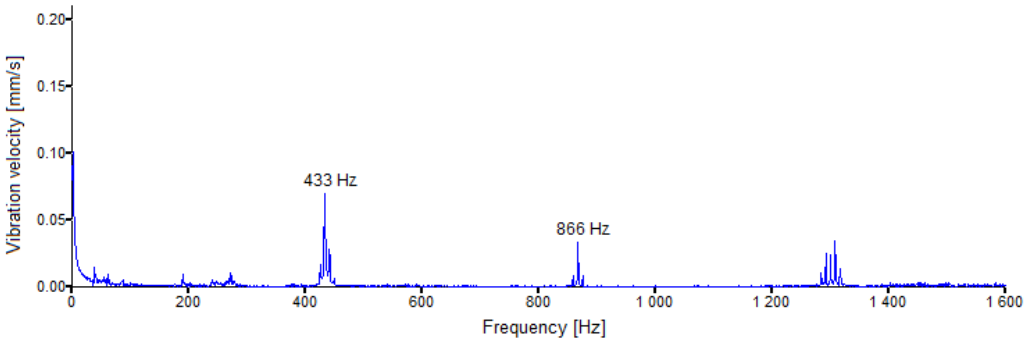

Figure 7: Vibration velocity spectrum recorded on the microturbine casing in the vertical direction close to the DE bearing at a speed of 25,980 rpm.

3.3 Test of the microturbine at elevated temperature

Tests of the prototype gas microturbine with cold air confirmed its proper operation at speeds up to 32,000 rpm. Unacceptable increases in vibration levels were observed only within the resonant speed range. Using this knowledge, it was possible to plan further experimental studies in such a way that the operation of the microturbine at these speeds would be as short as possible. Based on a previous study, it was determined that the following speed ranges should be avoided: 10,500–13,500 rpm and 24,000–31,000 rpm. A prolonged operation of the machine at these speeds could result in accelerated wear or damage to the bearings or even rubbing of the rotating system components against the casing.

The next stage of the experimental study of the microturbine involved testing it under conditions similar to real operating conditions. Therefore, the microturbine was connected to the boiler so that the pressurised air supplied by the compressor would be heated in a heat exchanger and then used to power the gas turbine. The vibration waveforms (V_{rms}) as a function of rotational speed, obtained during these tests, are presented in Figs. 9 and 10. During these tests, the maximum rotor speed almost reached 60,000 rpm, but in the graphs shown here, the speed has been reduced to 50,000 rpm due to unstable measurement results at the highest speeds. Near the DE bearing, the highest vibration level of about 11 mm/s (V_{rms}) was recorded at 34,713 rpm in the vertical direction (Fig. 9). In the horizontal direction, the highest vibration level of about 8 mm/s occurred at 32,043 rpm. Near the NDE bearing (Fig. 10), the highest V_{rms} value was approximately 18 mm/s and occurred in the vertical direction at 13,227 rpm. High vibration levels were also observed at 34,052 rpm (about 10 mm/s) in the vertical direction and at 46,872 rpm (about 9 mm/s) in the horizontal direction. At other speeds, the vibration level of the microturbine casing was significantly lower. Up to a speed of 30,000 rpm, it did not exceed 4 mm/s, and at higher speeds, it was higher, but in some speed ranges, it also did not exceed the value given earlier (4 mm/s). The different vibration levels in the horizontal and vertical directions were due, among other things, to the difference in the stiffness of the microturbine support in the two directions. In the speed range of 12,000 to 15,000 rpm, the significant increase in the vibration level near the NDE bearing may have been due to the modification of the foundation of the test rig with the microturbine. During the earlier laboratory tests, the test rig was placed on a concrete floor, while the elevated temperature tests were conducted in a container with a floor made of wooden plates. This may have had a significant impact on the stiffness of the support of the entire test rig, which manifested itself mainly on the side of the microturbine casing that was not connected by pipes to the remaining components of the cogeneration installation.

During the tests, which lasted several hours in total, the temperature of the DE bearing did not exceed 50°C. Considering the fact that the temperature of the air supplied to the turbine was above 600°C, which also caused the shaft and casing to heat up, maintaining such a low temperature of the bearing can be considered a very good result. Since the temperature of the individual parts of the microturbine, including the shaft, was not accurately measured during the study in question, the effect of this parameter on the dynamic characteristics of the rotating system was not analysed in detail. Although it was possible to keep the temperature of the rolling bearings low throughout the study, the foil bearing, which operated in close proximity to the rotor disc of the microturbine supplied with hot air, was exposed to high temperatures. The dynamic properties of the rotating system were also significantly affected by the temperature increase of the shaft end on which the microturbine rotor disc was mounted. An increase in temperature causes a change in material properties, including a decrease in Young's modulus, among others. A thorough analysis of the effect of temperature on the dynamic characteristics of the tested microturbine would require a more extensive study in which additional measurement points would have to be taken into account.

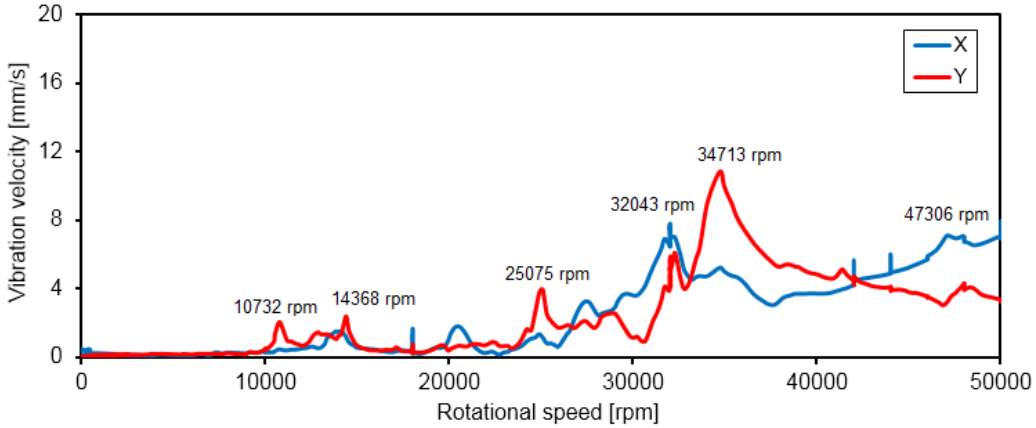

Figure 9: Vibration velocity (V_{rms}) measured on the microturbine casing close to the DE bearing versus rotational speed (X – horizontal direction, Y – vertical direction).

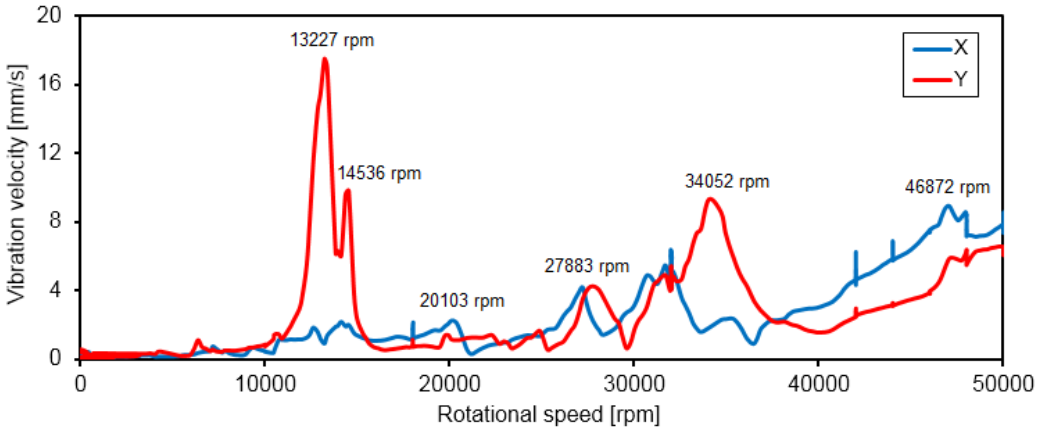

Figure 10: Vibration velocity (V_{rms}) measured on the microturbine casing close to the NDE bearing versus rotational speed (X – horizontal direction, Y – vertical direction).

4 Conclusions

This paper discusses an experimental study of a prototype gas microturbine with a nominal power of 30 kW, designed to operate in a cogeneration system. The research focused on vibration measurements and the evaluation of the dynamic properties of the machine. Based on the tests performed, the following conclusions can be drawn:

- The results of preliminary research conducted on the microturbine with two bearings showed that to reduce the vibration level of the rotor in the area around resonant speeds, it was necessary to use an additional bearing supporting the overhung end of the shaft. Due to the difficult operating conditions, a gas foil bearing was used.
- Tests carried out on the gas microturbine with a modified bearing system at speeds up to 32,000 rpm have confirmed that, with the exception of selected speed ranges associated with resonant speeds, the vibration level of the machine was acceptable during operation. According to the ISO 10816:1 standard, it is recommended that the vibration level (V_{rms}) for the long-term operation of such machines should not exceed 2.8 mm/s. During the tests, this condition was met in almost the entire speed range.
- The study carried out on the microturbine supplied with hot air showed that under such operating conditions, at certain speeds, the vibration level was very high, reaching 18 mm/s. Such high vibrations were related to the occurrence of a resonant speed of the rotor. Except for the resonant speeds, the vibration levels measured on the microturbine casing were much lower and acceptable. The tests carried out showed that it was necessary to improve the rotating system of the microturbine, paying particular attention to the balancing of the shaft operating in the resonant speed range. At this stage of the research, due to the high vibration level observed above a speed of 50,000 rpm, it was not yet possible to achieve a nominal speed of 100,000 rpm.

All in all, it can be concluded that the study carried out provided very valuable information on the actual dynamic properties of the new microturbine. Based on these results, further research and development work will be carried out to prepare the developed microturbine for long-term operation at higher speeds.

Acknowledgement

This research was supported by the National Centre for Research and Development in Poland [the research grant No. POIR.04.01.04-00-0014/17 entitled “A versatile gas turbine micro CHP system”].

References

[1] AL-Shudeifat, M.A., Friswell, M., Shiryayev, O., Nataraj, C. (2020): On post-resonance backward whirl in an overhung rotor with snubbing contact. *Nonlinear Dynamics*, 101, pp. 741–754.

[2] Arroyo, A., McLorn, M., Fabian, M., White, M., Sayma, A. I. (2016): Rotor-dynamics of different shaft configurations for a 6 kW micro gas turbine for concentrated solar power. *Proceedings of the ASME Turbo Expo 2016*, June 13–17, Seoul, South Korea, GT2016-56479.

[3] Badami, M., Ferrero, M., Portoraro, A. (2012): Experimental tests of a small-scale microturbine with a liquid desiccant cooling system. *International Journal of Energy Research*, 37(9), pp. 1069–1078.

[4] Barbarelli, S., Berardi, E., Amelio, M., Scornaienchi, N.M. (2019): An externally fired micro combined-cycle, with largely adjustable steam turbine, in a CHP system, *Procedia Manufacturing*, 42, pp. 532–537.

[5] Cagnano, A., De Tuglie, E. (2018): On-line identification of simplified dynamic models: Simulations andexperimental tests on the Capstone C30 microturbine. *Electric Power Systems Research*, 157, pp. 145–156.

[6] Cakmak, O., Sanliturk, K.Y. (2011): A dynamic model of an overhung rotor with ball bearings. Proc. *ImechE Part K: J. Multi-body Dynamics*, 225, pp. 310–321.

[7] Feng, S., Geng, H., Yu, L. (2015): Rotordynamics analysis of a quill-shaft coupling-rotor-bearing system. Proceedings of the Institution of Mechanical Engineers. *Part C: Journal of Mechanical Engineering Science*, 229(8), pp. 1385–1398.

[8] Hidalgo, J., Dhingra, A. (2006): High-speed balancing of rotors with overhangs: when is overhang likely to cause problems? *Journal of Testing and Evaluation*, 34(3), pp. 218–223.

[9] Hong, D.-K., Joo, D.-S., Woo, B.-C., Koo, D.-H., Ahn, C.-W. (2014): Unbalance response analysis and experimental validation of an ultra high speed motor-generator for microturbine generators considering balancing. *Sensors*, 14, pp. 16117–16127.

[10] Kaczmarczyk, T.Z., Żywica, G., Ihnatowicz, E. (2016): Vibroacoustic diagnostics of a radial microturbine and a scroll expander operating in the organic Rankine cycle installation. *Journal of Vibroengineering*, 18(6), pp. 4130-4147.

[11] Kicinski, J., Zywica, G. (2012): The numerical analysis of the steam microturbine rotor supported on foil bearings. *Advances in Vibration Engineering*, 11(2), pp. 113-119.

[12] Marin, M.A. (2010): Practical uses of advanced rotor dynamic tools to ensure trouble free operation of an overhung turbo-expander rotor. *Proceedings of ASME Turbo Expo 2010*, June 14-18, Glasgow, UK, GT2010-22147.

[13] Marin, M.A. (2012): Rotor dynamics of overhung rotors: hysteretic dynamic behavior. *Proceedings of ASME Turbo Expo 2012*, June 11-15, Copenhagen, Denmark, GT2012-68285.

[14] Moradi Tiaki, M., Hosseini, S.A.A., Zamanian, M. (2016): Nonlinear forced vibrations analysis of overhung rotors with unbalanced disk. *Arch Appl Mech*, 86, pp. 797–817.

[15] Przybylowicz, P.M., Kurnik, W. (2020): Stability and Bifurcation Analysis of an Overhung Rotor with Electromagnetic Actuators. *Journal of Theoretical and Applied Mechanics*, 58(2), pp. 525–539.

[16] Salamone, D.J., Gunter, E.J. (1980): Synchronous unbalance response of an overhung rotor with disk skew. *Journal of Engineering for Gas Turbines and Power*, 102, pp. 749–755.

[17] Shende, R.W. (1997): Synchronous steady state response of an overhung rotor with squeeze film damping. *Mechanism and Machine Theory*, 12, pp. 281–291.

[18] Traverso, A., Massardo, A.F., Scarpellini, R. (2006): Externally Fired micro-Gas Turbine: Modelling and experimental performance. *Applied Thermal Engineering*, 26, pp. 1935–1941.

[19] Wlodarski, W. (2018): Experimental investigations and simulations of the microturbine unit with permanent magnet generator. *Energy*, 158, pp. 59–71.

[20] Xu, Z., Lu, Y., Wang B. et al. (2019): Experimental evaluation of 100 kW grade micro humid air turbine cycles converted from a microturbine, *Energy*, 175, pp. 687–693.

[21] Zhang, B., Qi, S., Feng, S. et al. (2018): An experimental investigation of a microturbine simulated rotor supported on multileaf gas foil bearings with backing bump foils. *Proc IMechE Part J: J Engineering Tribology*, 223(9), pp. 1169–1180.

[22] Zilli, A., Williams, R.J., Ewins, D.J. (2015): Nonlinear dynamics of a simplified model of an overhung rotor subjected to intermittent annular rubs. *J. Eng. Gas Turbines Power.*,137(6), 065001.

[23] Żywica, G., Kaczmarczyk, T.Z. (2019): Experimental evaluation of the dynamic properties of an energy microturbine with defects in the rotating system. *Maintenance and Reliability*, 21(4), pp. 670–678.

[24] Żywica, G., Kaczmarczyk, T.Z., Breńkacz, Ł., et al. (2020): Investigation of dynamic properties of the microturbine with a maximum rotational speed of 120 krpm –predictions and experimental tests. *Journal of Vibroengineering*, 22(2), pp. 298–312

[25] Żywica, G., Zych, P., Bogulicz, M. (2021): Dynamic characteristics of a high-speed supercritical rotor with a significant overhang. *Proceedings of SIRM 2021 Conference*, February 17–19, Gdańsk, Poland, Paper ID-15.

15th SIRM – European Conference on Rotordynamics,
Darmstadt, Germany, 22nd – 24th February 2023

Semi-Active Foundation Stiffness Control for Rotor Resonance Avoidance

Sampo S. Laine [1], **Sampo A. Haikonen** [2], **Raine A. Viitala** [3]

[1],[2],[3] Department of mechanical engineering, Aalto University, 02150, Espoo, Finland, sampo.laine@aalto.fi

Abstract

The operating speed range of large rotating systems is often limited by vibrations caused by subcritical resonances. In this paper, a semi-active control method based on control of the foundation stiffness is presented. Modification in the foundation stiffness of the rotor system results in a corresponding change in the natural frequencies. This principle is used in the developed method to choose an optimal foundation stiffness for each rotating speed of the rotor system. The presented method is validated with a rotor model based on experimental dimensions. The vibration response of the model employing the foundation stiffness optimization is evaluated in the subcritical speed region. With the optimal foundation stiffness, the subcritical resonances caused by multiple rotor bending modes can be avoided in a given speed range. The extent of the resonance-free range depends on the control range of the foundation stiffness. In the light of the presented results, the proposed semi-active foundation stiffness control can be applied to reduce the total vibration levels in rotating systems. The presented method can be applied in any rotating system where it is possible to modify the foundation stiffness during operation.

1 Introduction

Mitigating vibrations is important for the operation of large flexible rotors. In industries such as paper and steel production, large rolls are used to work the material. Excess vibration of these rolls can cause quality problems in the end-product. In worst cases, the vibration may even lead to unscheduled maintenance or component failure. Subcritical vibrations are always present in rotating systems which operate at speeds lower than the critical speed. Subcritical resonances occur when the operating speed coincides with an integer fraction of a natural frequency. Avoiding the subcritical resonances is important for reducing vibrations in rotating machines [5]. Roller element bearings are also known for causing vibrations in frequencies which are not harmonics of the operating speed, i.e., integer multiples of the rotating speed [9]. These vibrations originating from the bearing frequencies have however been left out of the scope of this study for a simplified interpretation of the results.

Vibration suppression of rotating systems is often done using various forms of active, passive, or semi-active dampers. Passive dampers rely on the dissipation of the vibration energy through a physical process, such as fluid friction or eddy current loss. Active dampers use external energy to counteract vibrations through various actuators, such as active magnetic bearings [8, 1] or magnetorheological fluid controlled by electromagnets [18]. Semi-active dampers usually have one adjustable characteristic which can be used to alter the vibration response indirectly, increasing or decreasing the system damping based on the predominant conditions. As the damping of the system is increased through passive or active means, the overall vibration levels can be decreased [3].

In almost all rotating machinery, at least the resonance conditions due to critical speeds are avoided through operating region selection. Such an operating speed range is defined, where major excitations do not cross the natural frequency of the rotor. In supercritical applications, the critical speed is crossed with rapid acceleration to limit the vibrations to a short time. In advanced applications and larger rotor systems, also the subcritical resonances can be avoided [12]. Estimating the critical speeds and unbalance response is a basic component of rotor dynamic analyses.

Circumventing the resonance speeds is called resonance avoidance. This is an alternate mean to mitigate vibrations, which does not rely on modifying the damping properties of the system. Resonance avoidance can be achieved through operating speed limitations or altering the natural frequencies of the system based on predominant excitations. The goal is simply to minimize the operating time of the rotating system in resonant conditions. The duration of resonance can be minimized by adjusting or switching the stiffness properties of the system, or increasing acceleration rate during crossing over the resonance speeds [19].

The asymmetry of the foundation stiffness in vertical and horizontal directions is known to cause separation of the first bending modes [7]. It is common for large rotating machinery to have two separate first bending modes, one in both principal directions. The principal directions are typically denoted as vertical and horizontal. The extent of the separation depends on the asymmetry of the supporting structure. For this reason, it is important to separately model the vertical and horizontal properties of the rotor foundations i.e., the stiffness and damping of the bearings and their supports.

Foundation stiffness is a parameter which is challenging to estimate in the design phase of rotor systems. If the estimated design value for foundation stiffness varies from the actual stiffness, erroneous results can be expected from rotordynamic analyses [7]. Experimental frequency response identification can be used to determine the influence of foundation stiffness on rotor systems [2]. Moreover, adaptive foundation stiffness can be used to alter natural frequencies of rotor systems, enabling the avoidance of resonant conditions. These problems have called for rotor system designs with adjustable foundation stiffness. The operating principle of a device which can be used to adjust the foundation stiffness to the extent that is described in this paper is based on stiffness provided by an external adjustible-length beam. The referenced device is presented in detail in an earlier study [13].

Variable stiffness can be used in semi-active vibration isolators to produce zero stiffness [16, 15, 14]. Vibration isolators are used in a wide range of applications, such as car suspension [17]. Adjustable stiffness can be achieved using continuous or switching devices. Devices to modify foundation stiffness have been developed for seismic protection [10]. Methods used in foundation stiffness modeling were recently compared by [6].

The methods available in the present literature mostly focus on vibration control strategies relying on vibration dampers or narrow-band control of stiffness. Multiple methods have been presented to actively alter the foundation stiffness, but methods for choosing an optimal foundation stiffness seem to be missing.

In this paper, a method based on semi-active control is presented. The resonant conditions are avoided by altering the dynamic properties of the rotor system, namely, the horizontal foundation stiffness. In this method, the natural frequencies of the system are chosen for the operating speed, instead of choosing the operating speed for natural frequencies. The presented strategy does not significantly alter the damping of the system, but the natural frequencies of the machine are actively modified to avoid subcritical resonances. The developed method is validated with calculated responses of a rotordynamic model. The dimensions and foundation stiffness parameters of the rotor are based on a physical rotor and foundation stiffness adjustment device persented in an earlier study [13].

2 Methods

As this paper deals only with the horizontal dynamics of the rotor, in rest of the paper, the horizontal foundation stiffness is referred to as the foundation stiffness, and the horizontal modes and natural frequencies are referred to as the modes and natural frequencies of the rotor. The abbreviations 1x, 2x, .. refer to the excitation frequencies which are integer multiples of the fundamental frequency. The rotor and foundation model used in the analysis is presented in the following section. After that, the optimization procedure developed for the semi-active vibration control is presented.

2.1 Rotor model

A rotor model consisting of 22 Timoshenko beam elements with 8 degrees-of-freedom was created to analyze the foundation stiffness effects. The model was developed on a modified version of an open-source rotor dynamic library [11]. The dimensions of the applied model are based on those of an actual paper machine roll used in laboratory tests. The main dimensions of the roll are presented in Figure 1. The rotor itself is symmetric, but the foundation stiffness is asymmetric in horizontal and vertical directions. The support stiffness is modeled as additional spring elements at the bearing locations, which are nodes 1 and 21 in the model. Due to the support asymmetry, the vertical and horizontal bending modes of the system separate. Point masses located at the same nodes as the bearings are used to model the inertia of the supports.

The foundations are modeled as equivalent stiffness and damping at the bearing locations. The equivalent stiffness and damping values for the horizontal and vertical foundations are identical in both ends of the rotor. The equivalent support stiffness of the model consists of two components, the stiffness of the roller-element bearings and the stiffness of the supporting structure. These two stiffness components are modeled as two linear springs in series. The stiffness of the foundations is based on previous experimental results [13].

Modifying the foundation stiffness is observed as a shift in the horizontal natural frequency. The relationship between the foundation stiffness and frequencies of the two lowest bending modes of the model is presented in Figure 2. In the model, the first natural frequency can be controlled in a range of 9.29 Hz to 20.69 Hz. The second natural frequency is simultaneously shifted in the range of 12.32 Hz to 31.02 Hz. These shifts in the natural

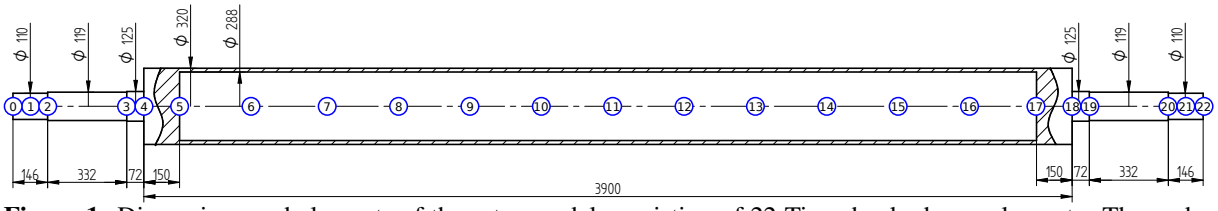

Figure 1: Dimensions and elements of the rotor model consisting of 22 Timoshenko beam elements. The nodes umbered from 0 to 22 mark the edges of the beam elements. The equivalent stiffness, damping and weight of the supporting structures are added to nodes 1 and 21, positioned at 60 mm from the ends of the rotor. All dimensions are in mm.

frequencies are achieved by altering the foundation stiffness values at the bearing locations from 2.04 MN/m to 18.3 MN/m. This natural frequency range produced by the model is similar to previous experimental results [13]. The natural frequencies are calculated from the eigenvalues of the system matrix of the model. The corresponding vertical natural frequencies remain constant at 21.76 Hz and 33.38 Hz.

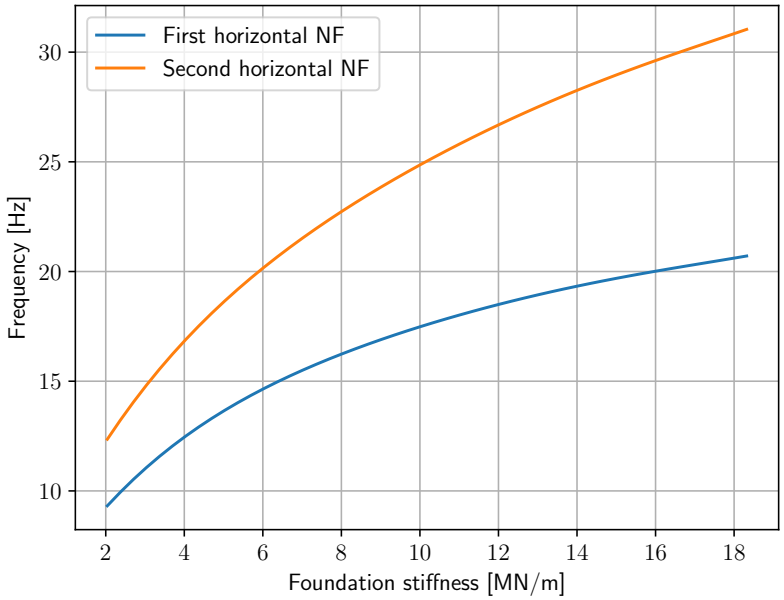

Figure 2: Effect of the foundation stiffness adjustment on the first two damped horizontal natural frequencies (NF)

The material properties used in the model are presented in Table 1. Comparison to previous experimental results shows a good agreement between the modeled and the measured natural frequencies of the system [4]. For the present analysis the accuracy of the model is sufficient, but for a more detailed analysis impulse responses should be used to further tune the stiffness and damping properties of the model.

Table 1: Material parameters used in the rotor model

Parameter	ρ [kg/m^3]	E [GPa]	ν [-]
Value	7764	209	0.3

In order to estimate the vibration response, an excitation force at integer multiples of the rotor rotation frequency is designed. The harmonics of the excitation force can be thought to originate from, for example, unbalance (1x), bending stiffness variation (2x), or bearing excitations (2x, 3x, 4x,...). The response is calculated for each harmonic component, and summed to get the total response. Amplitude of the excitation force at fundamental

frequency is based on an unbalance mass of 250 grams at 10 cm distance from the axis of rotation at node 15 the roll model. The amplitudes of the subsequent harmonics are fractions of this amplitude. The input node is purposely chosen to be offset from the center in order to excite bending modes which have a node in the middle of the rotor. The complex valued excitation force comprising of the unbalance force and the three subsequent harmonics defined proportionally to it are defined as follows

$$F(t) = \sum_{k=1}^{4} (F_k \sin k\omega t + jF_k \cos k\omega t), \tag{1}$$

$$F_1 = Ae^{j\phi_1}, \quad F_k = \frac{A}{k}e^{j\phi_1}, \quad A = m\varepsilon\omega^2 \tag{2}$$

where F is the unbalance force, A is the amplitude of the unbalance vibrations, m is the unbalance mass, ε is the distance of the unbalance mass from the centre-point of the rotor, ϕ is the phase of the unbalance mass, and ω is the rotating angular frequency. The unbalance force acts on the horizontal and vertical axes at an 90 degree phase shift. Thus the forcing vector acting on the i$^{\text{th}}$ node where the unbalance is located at is

$$\mathbf{F}_i = \begin{bmatrix} F_i & -jF_i & 0 & 0 \end{bmatrix}^{\mathrm{T}}. \tag{3}$$

This is a simple way to implement the forcing vector for the purposes of this study. In real rotor systems, the higher order harmonic forces acting on the rotor are not due to the unbalance, but various complex phenomena such as bending stiffness variation, bearing forces, gear meshing error and modal unbalances. Nevertheless this approximation provides a sufficient means of analyzing the effects of the vibrations occurring at integer multiples of the rotating frequency without needless increase of the modeling complexity.

The vibration response of the system is calculated by solving the global system of equations

$$\mathbf{M}\ddot{\boldsymbol{q}} + (\mathbf{C} + \omega\mathbf{G})\dot{\boldsymbol{q}} + K\boldsymbol{q} = \mathbf{F} \tag{4}$$

where **M**, **C**, **G**, and **K** are the global mass, damping, gyroscopic and stiffness matrices of the rotor system, respectively. $\boldsymbol{q}$ is the vector of the free variables. The harmonic solution to this system of equations is calculated using the well-known receptance matrix approach [5]. The response is calculated separately at each rotating speed for each harmonic component of the excitation force, and the total response at each rotating speed is the sum of the individual responses.

It should be noted, that the amplitudes of the vibration response may greatly vary from ones that would be experimentally measured due to the presented modeling assumptions. The modeling choices are justified, because the absolute vibration amplitudes are not relevant for this paper, as the results are interpreted by the relative change of vibration amplitudes.

2.2 Optimization procedure

The operating principle of the optimization is to cross the subcritical resonance frequencies at the lowest possible operating speeds. The foundation stiffness is thus kept at minimum value until the operating region is reached. In this controllable region, an optimal foundation stiffness value is calculated for each rotating speed. The distance from the 2x excitation to the two lowest natural frequencies should be equal to maximize the separation margin to the resonance. A boundary term is added if the natural frequency equals the 2x excitation or crosses it. A visual reference to the optimization procedure is shown in Figure 3.

The optimization problem can be defined at one rotating speed as follows

$$\begin{aligned} \min_{k} \quad & |f_{\text{ex}}(\omega) - \lambda_1(k,\omega)| - |f_{\text{ex}}(\omega) - \lambda_2(k,\omega)| \\ \text{s.t.} \quad & f_{\text{ex}}(\omega) - \lambda_1(k,\omega) > 0, \\ & f_{\text{ex}}(\omega) - \lambda_2(k,\omega) < 0, \\ & k_{\text{min}} \leq k \leq k_{\text{max}} \end{aligned} \tag{5}$$

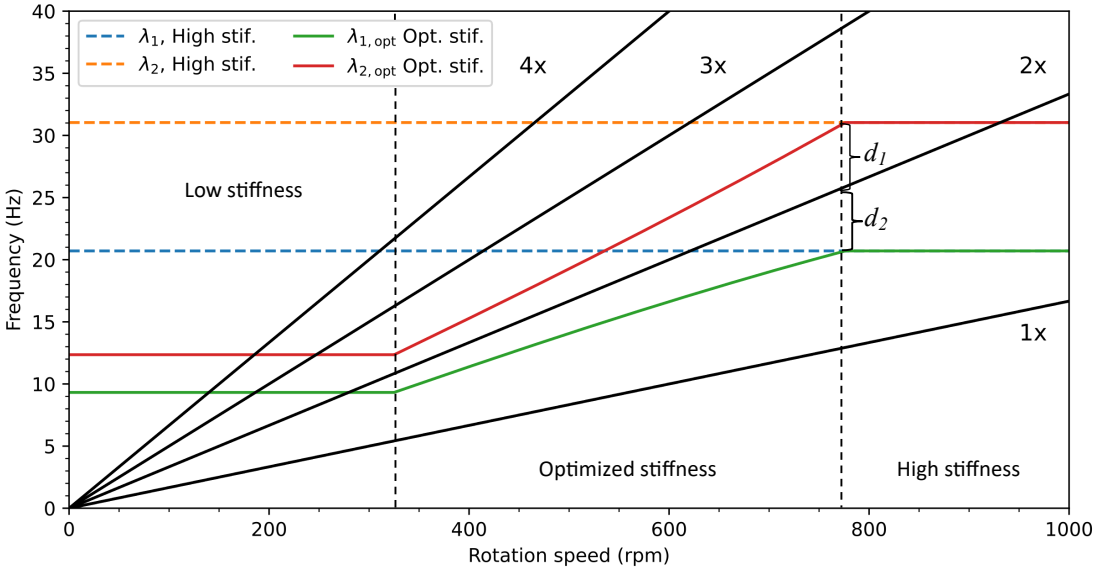

Figure 3 : An optimal foundation stiffness is chosen for each rotating speed to prevent subcritical resonances in the operating speed region. Variables d_1 and d_2 denote the distance from the natural frequency to the 2x excitation. In the proposed method, the optimal foundation stiffness is achieved when the two distances are equal.

where λ_1 and λ_2 are the first and second damped natural frequencies of the rotor system, k is the foundation stiffness at each bearing, f_{ex} is the 2x excitation frequency and ω is the rotating speed. The optimization procedure is repeated for each rotating speed in the optimization range. The values used in the following analyzes for the foundation stiffness represent those of a device presented in an earlier study [13].

3 Results and discussion

Dynamic response calculations are performed to analyze the developed method. The excitation force defined in Equation 1 is applied to the rotor model presented in Section 2. The excitation force is applied to node 15 of the model which contains 23 nodes. The calculated vibration response is the acceleration at the tending end bearing location e.g., node 1.

The vibration response is calculated at rotation speeds 50-1000 rpm. This corresponds to the actual operating speed range for which the modeled rotor is designed for. Two different test cases were calculated. In the first case, the foundation stiffness is fixed to the maximum value of the adjustment range. This case corresponds to a rotor in normal operation, without any stiffness adjustment. It is customary in the industry to maximize foundation stiffness to avoid vibrations. If a significantly lower foundation stiffness was chosen, the rotor would reach critical speed.

In the second test case, the stiffness is kept at the minimum value, until the first natural frequency crosses the 2x rotating speed frequency. An optimal foundation stiffness is chosen at each rotating speed as described by the optimization problem defined in Equation 5 and applied to the model. The optimal foundation stiffness curve is displayed in Figure 4. A visual explanation of the control method is presented in Figure 3.

Figure 5 displays the calculated acceleration response in the two aforementioned cases. The crossing of the six subcritical resonance speeds due to the 2-4x excitation frequencies are visible in both experiments. In the constant stiffness case, the crossing of the resonance speeds occur at higher frequencies, and their amplitudes are consequently higher when compared to those in the optimized stiffness case. When the optimized lower stiffness is applied, the resonances shift to lower rotating speeds, causing their relative amplitude to drop. In the higher rotating speed range, the required optimal stiffness is out of the control range, thus causing the response to be equal in both of the cases.

In addition to the six subcritical resonances, vertical resonance speeds are observed as peaks in the calculated responses. These peaks are visible at approximately 500 rpm, 670 rpm and 865 rpm, which correspond to the subcritical resonances of the two first vertical bending modes. The reason for the visibility of the vertical modes in the horizontal response is unknown. Furthermore, a resonance is present in the results at approximately 845 rpm. The resonance peak corresponds to the intersection of the 4x excitation and the 3rd horizontal natural frequency of the rotor system which lies at 56.25 Hz when the maximum stiffness is reached. These resonances are excluded

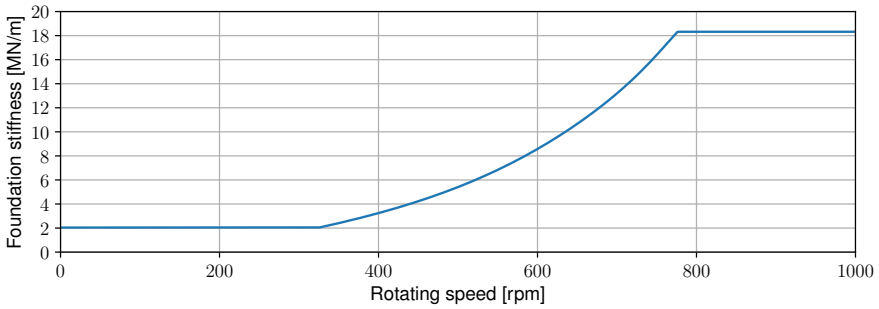

Figure 4: Optimal stiffness is calculated for each rotating speed and applied to the model.

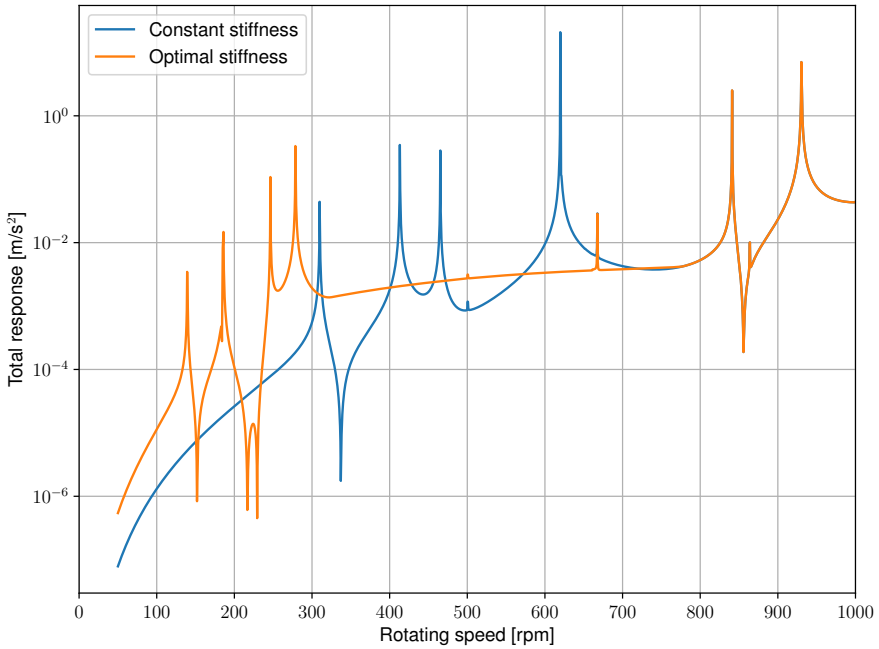

Figure 5: Calculated total horizontal vibration response at one of the bearing nodes of the rotor model. The maximum stiffness is reached at 776 rpm, after which the responses are equal. Applying the optimal stiffness significantly decreases the vibration response of the rotor in the mid-speed region. The response is consequently increased in lower rotating speeds due to the decreased stiffness.

from the Campbell diagram in Figure 3, as this paper focuses on the two lowest natural frequencies.

Due to the modeling limitations, the absolute amplitude of the calculated response would likely differ from experimental measurements. This does not however greatly limit the interpretation of these results, as the presented method aims to lower the relative vibration response of subcritical resonances in selected operating speed ranges.

4 Conclusion

Foundation stiffness can greatly influence the natural frequencies of a rotor system. Consequently, the subcritical resonance speeds are altered by the foundation stiffness. If the foundation stiffness of the rotor system can be controlled, a semi-active control based on an optimization procedure can be used to create a resonance free operating speed region. The subcritical resonances can never be entirely avoided, but shifting them to lower rotating speeds can significantly reduce the total vibrations in higher rotating speeds. The proposed method is especially useful in applications, where the varying rotating speed causes multiple crosses of the subcritical speeds. Moreover, the method could be extended to control in supercritical applications. In future research the method will be applied to actual rotor system and the results will be experimentally verified.

Acknowledgment

This research was funded in part by Business Finland (GOOD Future electrified mobile machinery for harsh conditions), under grant 3014/31/2021 and in part by the Academy of Finland (centre of excellence in high speed electromechanical energy conversion systems), under grant number 346443.

References

[1] Ł. Breńkacz, Ł. Witanowski, M. Drosińska-Komor, and N. Szewczuk-Krypa, "Research and applications of active bearings: A state-of-the-art review," *Mechanical Systems and Signal Processing*, vol. 151, p. 107 423, 2021, ISSN: 0888-3270. DOI: https://doi.org/10.1016/j.ymssp.2020.107423.

[2] K. Cavalca, P. Cavalcante, and E. Okabe, "An investigation on the influence of the supporting structure on the dynamics of the rotor system," *Mechanical Systems and Signal Processing*, vol. 19, no. 1, pp. 157–174, 2005, ISSN: 0888-3270. DOI: https://doi.org/10.1016/j.ymssp.2004.04.001.

[3] W. Chen and E. Gunter, *Introduction to Dynamics of Rotor-bearing Systems*. Trafford, 2007, ISBN: 9781412051903.

[4] T. Choudhury, E. Kurvinen, R. Viitala, and J. Sopanen, "Development and verification of frequency domain solution methods for rotor-bearing system responses caused by rolling element bearing waviness," *Mechanical Systems and Signal Processing*, vol. 163, p. 108 117, 2022, ISSN: 0888-3270. DOI: https://doi.org/10.1016/j.ymssp.2021.108117.

[5] M. Friswell, J. Penny, S. Garvey, and A. Lees, *Dynamics of Rotating Machines*, ser. Cambridge Aerospace Series. Cambridge University Press, 2010, ISBN: 9780521850162.

[6] M. Hajžman, M. Balda, P. Polcar, and P. Polach, "Turbine rotor dynamics models considering foundation and stator effects," *Machines*, vol. 10, no. 2, 2022, ISSN: 2075-1702. DOI: 10.3390/machines10020077.

[7] E. Krämer, *Dynamics of Rotors and Foundations*. Springer Berlin Heidelberg, 2013, ISBN: 9783662027981.

[8] N. A. Saeed and A. Kandil, "Lateral vibration control and stabilization of the quasiperiodic oscillations for rotor-active magnetic bearings system," en, *Nonlinear Dyn.*, vol. 98, no. 2, pp. 1191–1218, Oct. 2019.

[9] A. Slocum, *Precision Machine Design*. Society of Manufacturing Engineers, 1992, ISBN: 9780872634923.

[10] C. Sun and S. Nagarajaiah, "Study of a novel adaptive passive stiffness device and its application for seismic protection," *Journal of Sound and Vibration*, vol. 443, pp. 559–575, 2019, ISSN: 0022-460X. DOI: https://doi.org/10.1016/j.jsv.2018.12.015.

[11] R. Timbó *et al.*, "Ross - rotordynamic open source software," *Journal of Open Source Software*, vol. 5, no. 48, p. 2120, 2020. DOI: 10.21105/joss.02120.

[12] R. Viitala, "Minimizing the bearing inner ring roundness error with installation shaft 3D grinding to reduce rotor subcritical response," English, *CIRP Journal of Manufacturing Science and Technology*, p. 9, 2020, ISSN: 1755-5817. DOI: 10.1016/j.cirpj.2020.05.002.

[13] R. Viitala and R. Viitala, "Method and device to investigate the behavior of large rotors under continuously adjustable foundation stiffness," *Journal of Vibroengineering*, vol. 22, pp. 1037–1054, Aug. 2020. DOI: 10.21595/jve.2020.21107.

[14] S. Wang and Z. Wang, "Curved surface-based vibration isolation mechanism with designable stiffness: Modeling, simulation, and applications," *Mechanical Systems and Signal Processing*, vol. 181, p. 109 489, 2022, ISSN: 0888-3270. DOI: https://doi.org/10.1016/j.ymssp.2022.109489.

[15] Y.-S. Wu and C.-C. Lan, "Linear Variable-Stiffness Mechanisms Based on Preloaded Curved Beams," *Journal of Mechanical Design*, vol. 136, no. 12, Oct. 2014, 122302, ISSN: 1050-0472. DOI: 10.1115/1.4028705. eprint: https://asmedigitalcollection.asme.org/mechanicaldesign/article-pdf/136/12/122302/6225367/md_136_12_122302.pdf.

[16] T.-H. Wu and C.-C. Lan, "A wide-range variable stiffness mechanism for semi-active vibration systems," *Journal of Sound and Vibration*, vol. 363, pp. 18–32, 2016, ISSN: 0022-460X. DOI: https://doi.org/10.1016/j.jsv.2015.10.024.

[17] I. Youn and A. Hać, "Semi-active suspensions with adaptive capability," *Journal of Sound and Vibration*, vol. 180, no. 3, pp. 475–492, 1995, ISSN: 0022-460X. DOI: https://doi.org/10.1006/jsvi.1995.0091.

[18] J. Yu, X. Dong, X. Su, and S. Qi, "Development and characterization of a novel rotary magnetorheological fluid damper with variable damping and stiffness," *Mechanical Systems and Signal Processing*, vol. 165, p. 108 320, 2022, ISSN: 0888-3270. DOI: https://doi.org/10.1016/j.ymssp.2021.108320.

[19] J. Zapoměl and P. Ferfecki, "A computational investigation on the reducing lateral vibration of rotors with rolling-element bearings passing through critical speeds by means of tuning the stiffness of the system supports," *Mechanism and Machine Theory*, vol. 46, no. 5, pp. 707–724, 2011, ISSN: 0094-114X. DOI: https://doi.org/10.1016/j.mechmachtheory.2010.12.006.

15th SIRM – European Conference on Rotordynamics,
Darmstadt, Germany, 22nd – 24th February 2023

Effectivity of particle dampers with granular filling under rotating conditions

Christian Daniel [1], **Elmar Woschke**[1], **Braj Bhushan Prasad** [1], **Fabian Duvigneau**[1]

[1] Institute of Mechanics, Otto-von-Guericke University Magdeburg , 39106, Magdeburg, Germany
{christian.daniel}{ elmar.woschke}{braj.prasad}{fabian.duvigneau}@ovgu.de

Abstract

The reduction of noise or more general vibration amplitudes as one major issue in large structures can be achieved with different methods. Preferable passive systems are used due to the reduced costs and easy application. Besides conventional concepts like viscous dampers or tuned mass dampers, particle dampers offer a broadband damping behaviour combined with a small increase of the overall mass of the system. The working principle of particle dampers is based on energy dissipation induced by frictional contacts between the particles themselves as well as particle and the surrounding structure. Several parameters influence the damping characteristic and thus allow for an optimization of the system. In the case of granular materials at least the filling ratio, the particle size and the particle shape define the frequency range, in which the damper works effective, and the amount of dissipated energy. As the usage in rotating systems superimpose centrifugal forces on the particle dampers the setup and chosen parameters for the usage in blades of a wind turbine or similar systems is quite different to non rotating applications. Due to the centrifugal force the positioning of the granular materials in a damper cavity is affected and the resulting contact behaviour varies. In this contribution the influence of the centrifugal force on the damping behaviour of a granular particle damper in a blade structure is investigated. The vibration is measured with a laser scanning vibrometer and a derotator, which is a special device to measure vibrations on rotating objects. This method can be used to determine the vibration modes of the rotating blades in a body-fixed reference frame.

1 Introduction

Control of noise and structural vibration is a crucial step in the development process of any mechanical system that is subjected to dynamic loads. Principally, two different damping mechanisms are used - [1] [2]. Vibration can be a reason for excessive stresses and strains in the machine component, which can lead to fatigue failure. For instance, several catastrophic failures can occur if the rotating velocity of a rotating machine component reaches a system resonance frequency. Therefore, it is necessary to pay detailed attention to reducing the vibration and sound emissions of a mechanical structure in the conceptual design phase. The determination of the damping can be done with different methods: active vibration control (AVC) and passive vibration control (PVC). However, the application of the PVC technique is preferable in comparison to the AVC technique because of its conceptual simplicity, cost-effectiveness, low maintenance, and robustness in nature. Furthermore, the implementation of PVC requires no external power supply to operate as it is in AVC, which makes PVC technology more favorable for real-world applications. There are several methods for passive damping, like viscoelastic damper, viscous damper, friction damper, and tuned mass damper. Nevertheless, the performance of these damping methods is extremely sensitive to temperature, pressure, material selection, and other factors. For instance, the tuned mass damper is designed to reduce the vibration amplitude of the specific vibration mode of a structure. On the other hand, the performance of viscoelastic dampers can degrade at very low or high temperatures. To overcome the drawbacks of the conventional PVC techniques particle damping technology can be used for vibration attenuation. Particle dampers utilize the damping properties of granular materials to reduce or suppress the vibration amplitude of a structure. Generally, a container is partially filled with granular materials and is attached to a vibrating structure whose vibration amplitude needs to be reduced. The vibrational energy of the primary structure is transferred to the granular materials through the container walls due to which inelastic collision between the particles and the cavity walls takes place. This phenomenon leads to friction-based energy dissipation. A schematic illustration of energy dissipation in a particle damper can be seen in Figure 1. The simple, inexpensive and robust design of a particle damper along with its broadband damping efficiency makes this technique more attractive for real-world applications. Moreover, depending on the granular materials the particle damper can be reused. In the

current contribution, the waste of automotive tires is used to design the particle damper. In our previous works, the particle damping technique has been successfully used to reduce the vibration amplitude of an automotive engine oil pan [3, 4] and wind turbine components [5, 6].

In the current contribution, the focus is on analyzing the performance of particle dampers exposed to centrifugal loads. For this purpose, a scaled wind turbine blade structure has been chosen. Although for the experimental study the wind turbine blade structure is used, the obtained results can be used in any kind of rotating machine components.

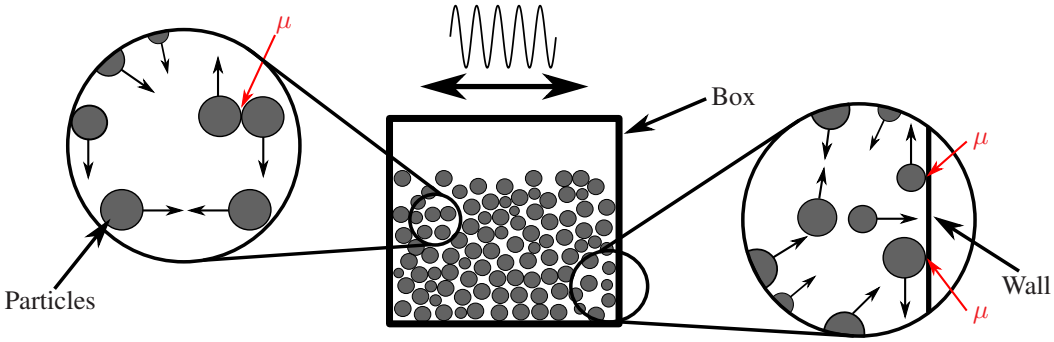

Figure 1: Schematic representation of the particle damper mechanisms [7].

2 Particle damper

Sandanshiv et al. [8] have studied the performance of particle damper on a rotating wind turbine blade model. For their experimental investigation, they used three blades of 1525 mm in length. For particle damper design they have used steel balls of 9 mm diameter which are enclosed in a polypropylene container. The authors have investigated three different positions of the particle dampers on the blade, namely 300 mm, 600 mm, 900 mm, and 1200 mm from the tip of the wind turbine blade. Furthermore, they have also studied the influence of particle damper efficiency on three different rotational speeds 60 rpm, 70 rpm, and 80 rpm. The experimental investigation has shown that the rotational speed of 60 rpm and particle damper position at 1200 mm from the wind turbine tip is optimal for damping the primary structure. This corresponds to a centrifugal acceleration of 84 $\mathrm{m/s^2}$. For real blades of a wind turbine the centrifugal acceleration can reach up to 170 $\mathrm{m/s^2}$ in the mid position of the blade (96 m length, rot. speed 0.3 Hz).

$$a_{blade} = R_{cav} \cdot \Omega^2 = 96\, m/2 \cdot (0.3\, Hz \cdot 2\pi)^2 = 170\, m/s^2 \tag{1}$$

However, the use of metallic particles to design a particle damper for wind turbine blades can be difficult because of the lightning strike concern [6]. Furthermore, the additional mass of the granular material is a major concern while implementing the particle damping technique to wind turbine blades. Therefore, it is necessary to use lightweight granular materials, like rubber granulate, to design a particle damper [6]. Els [9] has studied the effect of centrifugal force on the efficiency of particle damper. For his experimental investigation, he used a rotating cantilever beam with a particle damper attached to its tip. His study shows that the centrifugal load can influence the damping efficiency of a particle damper of steel balls of three different diameters. Michon et al. [10] have studied particle damper efficiency for space applications. They have used soft hollow particles instead of classical hard particles to maintain the additional mass of the granular materials low. It should be noted that in their experimental investigation the honeycomb cantilever beam, which is partially filled with hollow particles shows no damping for the first vibration mode. The application of particle damper in reducing the vibration and noise of a bank note machine can be seen in the work of Xu et al. [11]. They have embedded the tungsten particles of 0.5 mm diameter in the cam-shaft and folk-shaft of the banknote processing machine. According to their experimental investigation, it has been found that the particle damper is highly effective in the frequency range of 4000-6000 Hz and can reduce the vibration amplitude of the primary structure up to 40 dB. However, for the frequency range of 0-2000 Hz, the tungsten particles show moderate damping capabilities. Furthermore, 6 dB(A) of noise reduction has been also achieved. Hollkamp et al. [12] attempt to study the influence of five

different materials on vibration attenuation. The experimental investigation shows that the damping efficiency of stainless steel, titanium, and tungsten are similar to each other. However, the damping performance of aluminum was poor. Furthermore, the authors have examined the effect of particle size on damping. For this purpose, they used glass beads of three different sizes. The studies show that the vibration attenuation increases as the particle size increases. Xiao et al. [13] shows that the stainless steel balls of radius 3 mm as particle damper embedded in the gear cavity reduces the vibration and sound emission of the gear system under centrifugal load. They found that the optimal packing ratio of the particles depends on the centrifugal load, i.e. on the angular velocity of the gear. Veeramuthuvel et al. [14] have successfully applied particle-damping techniques in the spacecraft industry. They have attached a capsule-shaped particle damper on a printed circuit board, which experiences an enormous amount of vibration during launch time. Authors have studied the influence of tungsten carbide, stainless steel, and aluminium alloy on the vibration attenuation of the printed circuit board. In their investigation, it has been observed that materials with higher densities are more efficient for vibration attenuation. Authors have found the packing ratio of 60% effective for vibration suppression for all the materials they have investigated. Furthermore, they have observed that irrespective of granular materials, the packing ratio of 100% is not effective for reducing the vibration amplitude. A very similar effect has been also observed in our previous work [4]. Another application of particle dampers in the aerospace industry can be seen in the work of Simonian [15]. He has experimentally investigated the effectiveness of particle dampers to reduce the vibration amplitude from spacecraft cantilever beam-type appendages. For this purpose, he has attached a small cavity box containing 30 g of lead shot to the main structure at the position with the highest deflection during flight. The study has shown a significant reduction in the vibration amplitude of the primary structure under random vibration. He has concluded that in comparison to conventional damping materials like viscoelastic materials or viscous fluids, particle dampers are more suitable for spacecraft applications due to their immense damping performance for higher vibration amplitude and also for their insensitive nature towards extreme temperature. From the above discussion, it can be summarized that most of the particle damper experimental investigation is done for the steady state or transient state [16]. Practical experiments on the effect of particle dampers under centrifugal load are very limited [17]. Therefore, the interest of the current work is to experimentally investigate the influence of particle dampers efficiency subjected to centrifugal load.

3 Dynamic behaviour of the blade structure

For this investigation, a replacement structure is used to measure a particle damper under rotating condition. The propeller of the test rig is made of composite materials using long glass fibers with a Nylon matrix with a diameter of 533 mm and a mass of 115 gram. To reach a similar centrifugal acceleration as in the real blade a rotational speed of 368 rpm is necessary. The cavity is placed near the mid position at a radius of 11.5 cm.

$$a_{prop} = R_{cav} \cdot \Omega^2 = 11.5\ cm/2 \cdot (368\ rpm \cdot 2\pi)^2 = 170\ m/s^2. \tag{2}$$

To measure the natural frequencies and the corresponding damping the propeller was directly excited by a shaker Fig. (2). The transfer function was calculated from the reference point on the propeller hub to the surface of the blades

$$H_i(\omega) = \frac{v_i(\omega)}{v_{ref}(\omega)}. \tag{3}$$

This is useful to have the same reference later in the rotating system. Typically, the transfer function is formed between vibration and applied force, but this is very challenging when measuring in the rotating system.

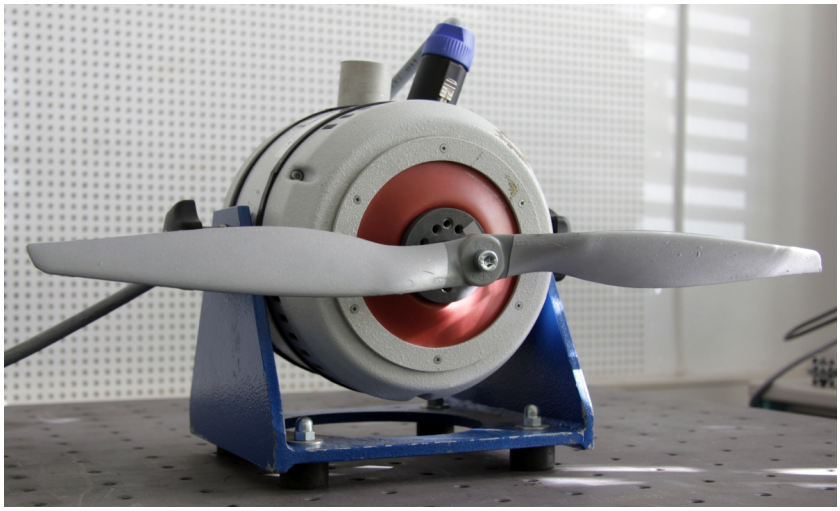

Figure 2: Propeller on an electrodynamic shaker for the non-rotating measurement

The test rig Fig. (2) was used to determine the transfer functions for the propeller with and without the particle damper. The application of the damper on the propeller will be discussed in the next section. Fig. (3) shows the potential of amplitude reduction using the particle damper with rubber granulate.

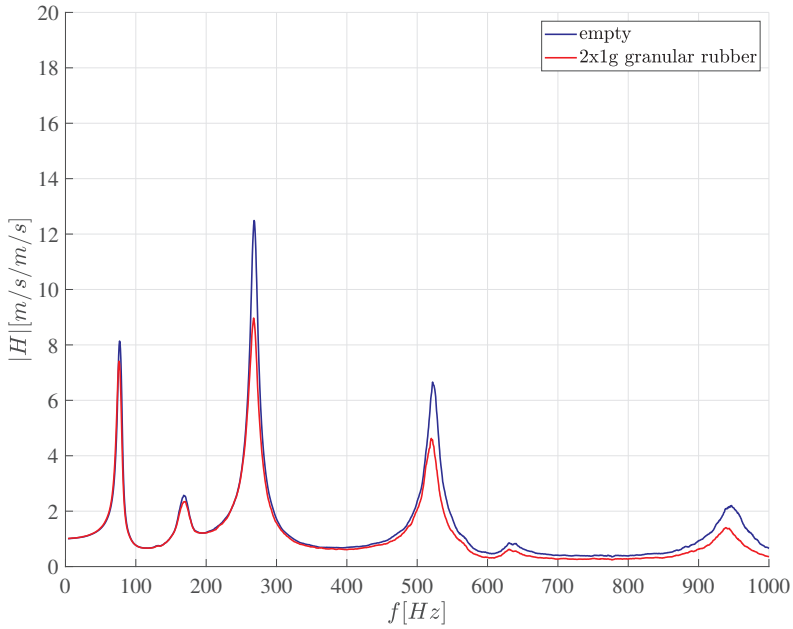

Figure 3: Frequency response of the non-rotating measurement - only propeller (see Fig. (2))

The corresponding mode shapes of the first 4 eigenfrequencies are all symmetric (see Fig. (4)) due to the excitation in the center position of the propeller.

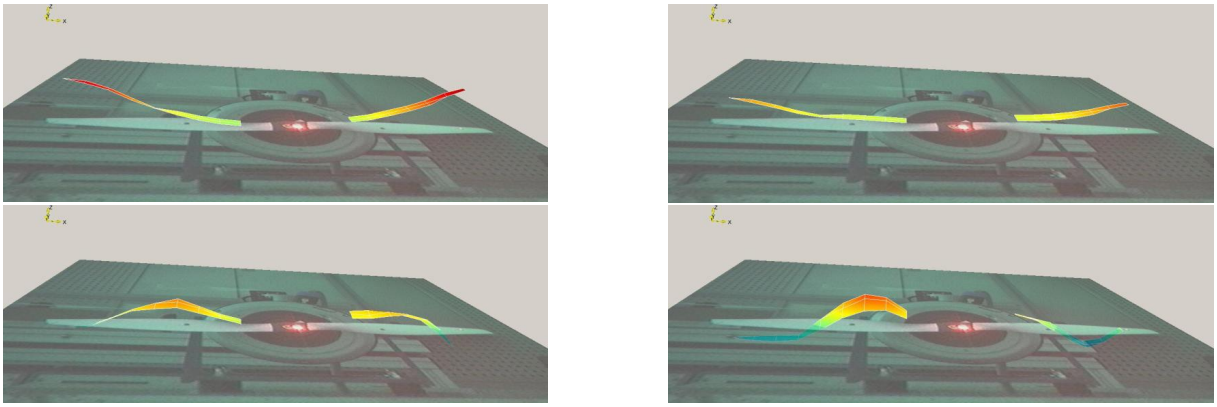

Figure 4: Mode shapes of the propeller (75 Hz, 168 Hz, 267 Hz, 519 Hz)

4 Application of the particle damper on the blade

In order to attach the particle damper to the rotor blade, a cavity was created which contains the particles and connects them to the surface of the blade. The cavity is screwed against the blade surface with a screw to close the cavity so that no particles escape due to centrifugal force - Fig. (5). To reduce the imbalance caused by the cavities and the filling, the cavities are only used empty or filled in pairs. The filling is only 1 gram, but on the radius of 11.5 cm the propeller would otherwise be very unbalanced. Rubber granulate with an average particle size of 1.7 mm has been chosen as a filling material. The rubber granulate used in this study is manufactured by recycling automotive tires. In previous work, it has been shown that the rough and textured surfaces and high non-linear behavior of rubber particles can show exceptional damping behavior in comparison to other conventional granular materials, like steel balls, which are generally used to design a particle damper [7]. Moreover, The lightweight property and because of lightning safety requirements, the application of rubber granulate to design a particle damper for the rotor blade of a wind turbine is favorable.

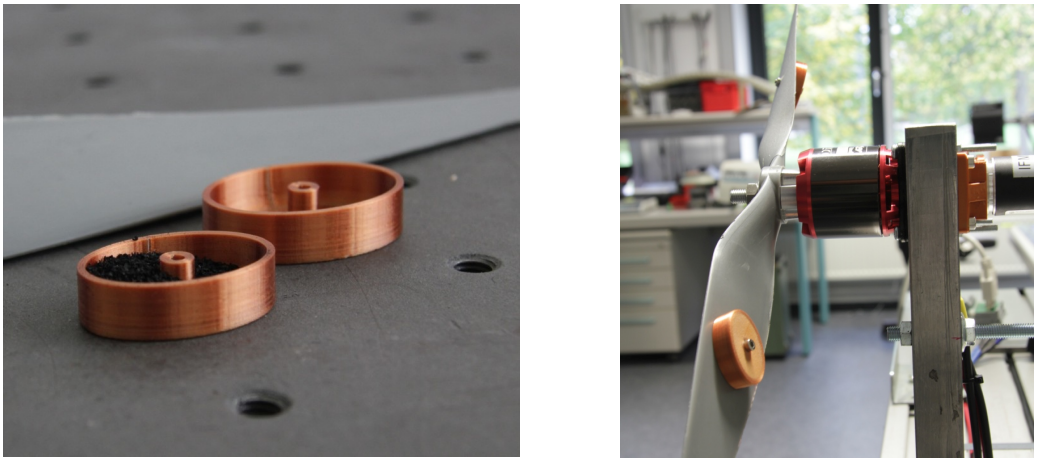

Figure 5: Particle damper - cavity with rubber particles (left), cavities mounted on propeller (right)

5 Measurement of the damping behaviour in a rotating system

To measure the blade vibrations during rotation, a derotator unit is used with a laser scanning vibrometer - Fig. (6). The derotator is an optical unit with a rotating prisma wich redirects the laser beam of the laser scanning vibrometer and the second beam of the reference vibrometer on the object. The rotational speed of the prisma is synchronised with the propeller speed through the use of an incremental encoder which is connected to the motor on the back side. In order for the derotator to track the target, the axis of rotation must be aligned very precisely. An offset leads to an eccentricity and a misalignment leads to a wobbling of the object. In both cases, the laser beam would not keep the measuring point constant and measures the movement as an additional component. Fig. (7)

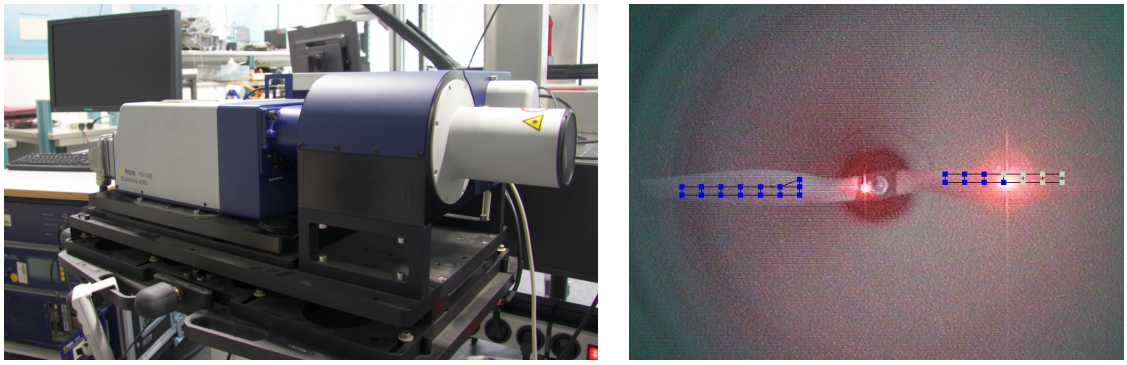

Figure 6: Laser scanning vibrometer with derotator unit (left), view with laser scanning vibrometer on rotating object (right)

shows the test rig during rotation. The inner laser beam points on the hub an measures the reference in order to get a correct phase information of the blade vibration. The second laser beam measures several points on the surface of the blade. The measurement process involves scanning all measurement points (visible in Fig. (6) (right)) on the blade surface, using 5 complex averages per point to compensate for variations in the object due to imperfect synchronisation.

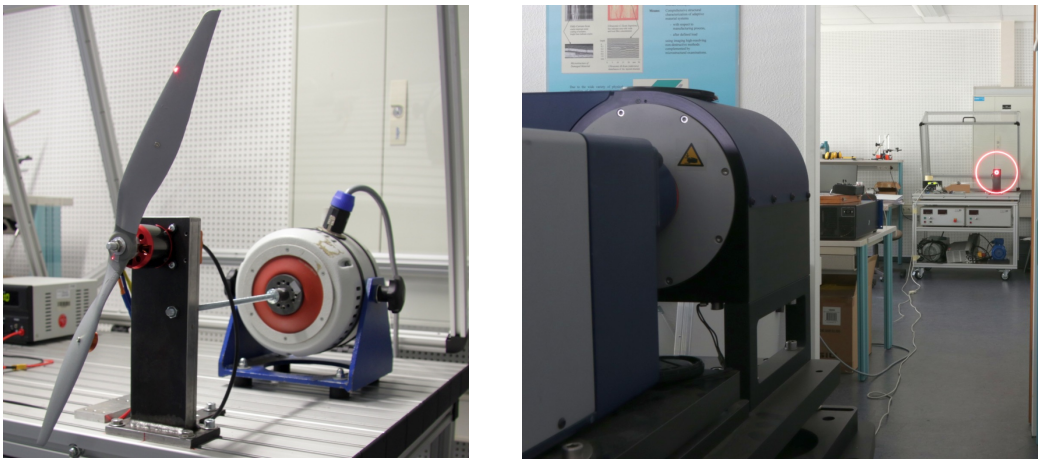

Figure 7: Propeller with motor and shaker (left) , measurement during rotation (right)

Before the transfer function is determined from the measurement signals, the frequency up to which the excitation takes place must be checked. The reference in this case is the vibration at the rotor hub. Fig. (8) shows the vibration velocity of the reference $v_{ref}(\omega)$ and the mean velocity of the surface $v_{mean}(\omega)$. Two different cases are shown, with and without excitation with the shaker connected with the motor mount. Without shaker excitation the vibration at the blade hub is not sufficient to excite all natural frequencies. The usage of the shaker with a pseudo random signal generates a sufficient excitation up to 300 Hz, above this frequency the transfer function could not be proper calculated because of the limited resolution of the AD converter in the scanning vibrometer.

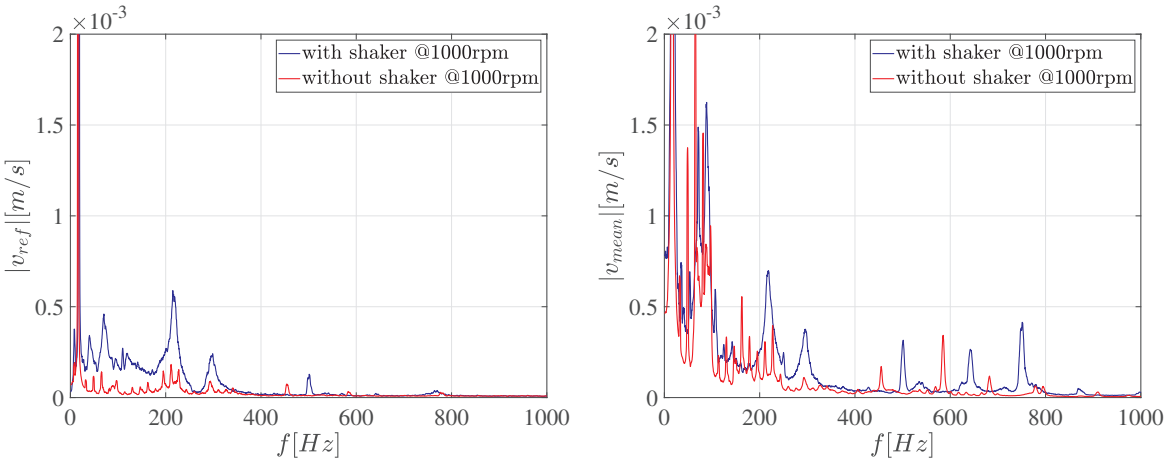

Figure 8: Reference (left) and mean vibration (right) velocity at 1000 rpm

Due to the lack of excitation above 300 Hz, all measured transfer functions are shown limited up to this frequency. The response was measured for different rotational speeds between 120 rpm and 1000 rpm. The limit speed to reach the same centrifugal acceleration as in a real wind turbine is 368 rpm so that the measured operating points are below and above the practically relevant boundary condition. The first stage at 120 rpm (Fig. (9)) shows hardly a difference between the vibration with and without granular filling. Due to 1 gram more mass at the blade, there is a frequency shift downwards for the 268 Hz peak.

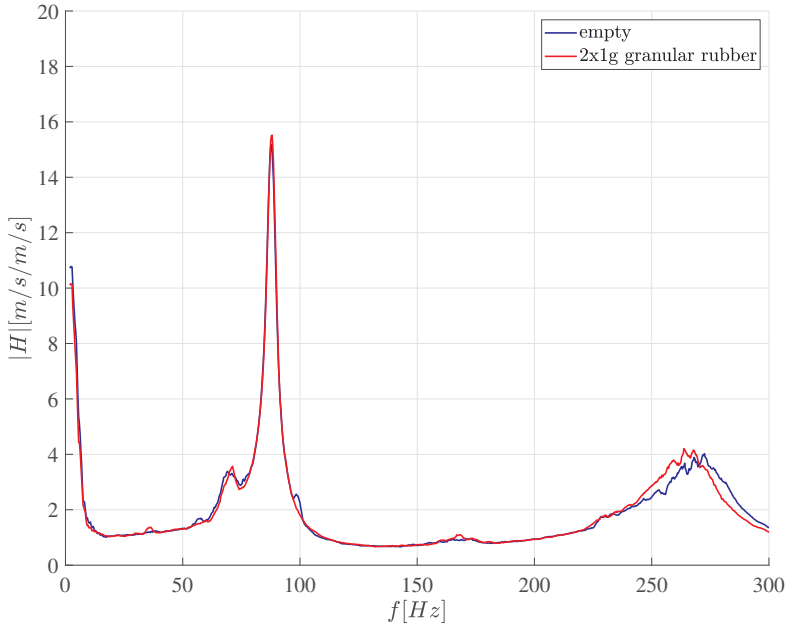

Figure 9: Frequency response at 120 rpm

At the 180 rpm operating point, on the other hand, an amplitude reduction for the peak at approx. 80 Hz is noticeable - Fig. (10).

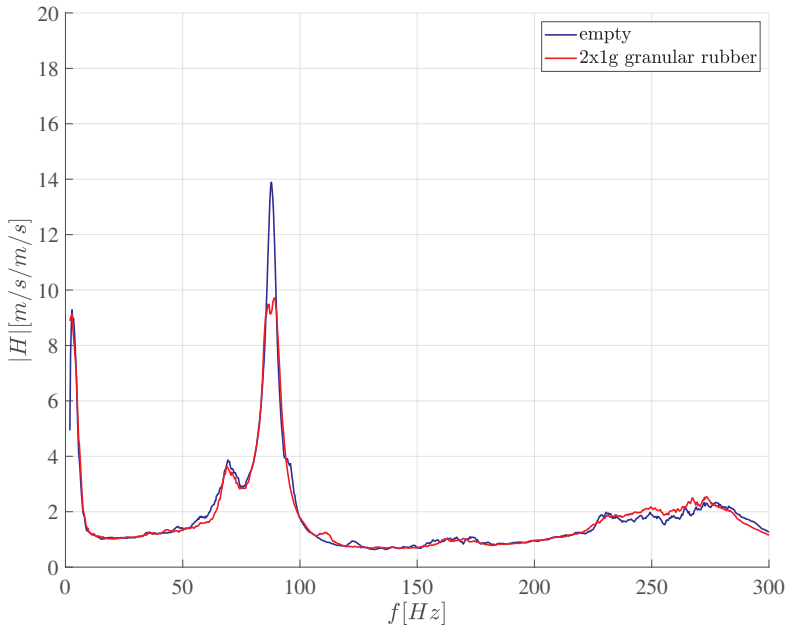

Figure 10: Frequency response at 180 rpm

For the operating points at higher speeds, there is no amplitude reduction noticeable. On the contrary, some natural frequencies are damped more weakly. Such negative damping effects due to internal damping in rotating structures are known from rotor dynamics. Both stages Fig. (11) and Fig. (12) show higher peaks with particle damper at 270 Hz than without filling.

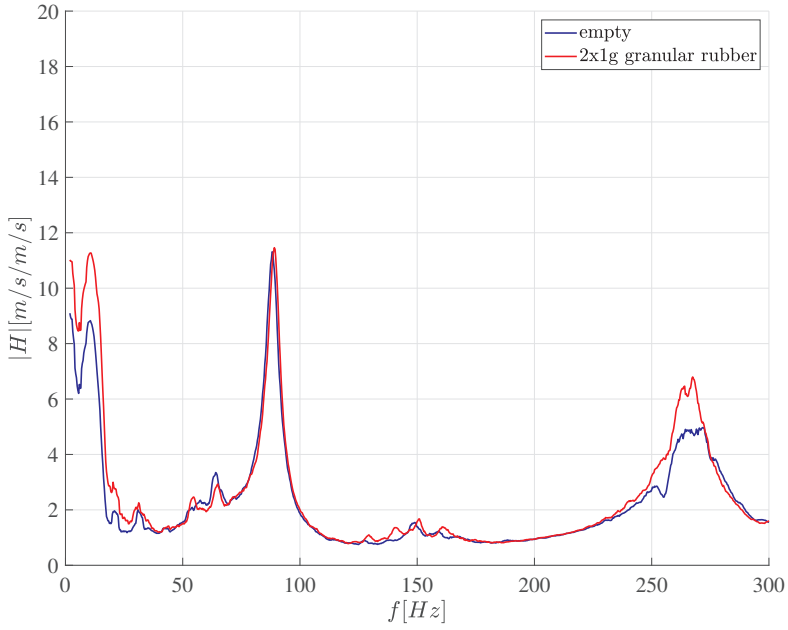

Figure 11: Frequency response at 660 rpm

Figure 12: Frequency response at 1080 rpm

6 Conclusion

The particle damper can reduce the vibration of blade structures. For the non-rotating condition the damper influences all eigenfrequencies up to 1000 Hz. Under rotating condition the damping effect is reduced and not all eigenfrequencies are effected. At high speeds, the damping of some natural frequencies is reduced by the particle damper. This effect is well known as destabilization due to inner damping in rotating machines.

For further investigations the test rig should be improved, the cavity on the surface of the blade has an influence on the air flow around the blade and distort the system behaviour. To measure the transfer function of the blade while rotating a piezo actuator could be mounted on the blade if the blade would be larger. The current excitation procedure through the motor mount is not sufficient for frequencies higher than 300 Hz, which are definitively of interest.

References

[1] Duvigneau, F., Spannan, L., Gavila Lloret, M., Woschke, E. and Gabbert, U. (2018). Characterization of the frequency-dependent properties of damping materials, *PAMM* **18**(1): pp. e201800018.
URL: *https://onlinelibrary.wiley.com/doi/abs/10.1002/pamm.201800018*

[2] Spannan, L., Duvigneau, F., Gavila Lloret, M., Daniel, C. and Woschke, E. (2020). A study on harmonic excitation based experimental characterization of damping materials for acoustic simulations, *TECHNISCHE MECHANIK* **40**(2): pp. 134–148.
URL: *https://journals.ub.uni-magdeburg.de/index.php/techmech/article/view/1680*

[3] Duvigneau, F., Koch, S., Woschke, E. and Gabbert, U. (2018). An effective vibration reduction concept for automotive applications based on granular-filled cavities, *Journal of Vibration and Control* **24**(1).
URL: *https://journals.sagepub.com/doi/10.1177/1077546316632932*

[4] Koch, S., Duvigneau, F., Orszulik, R., Gabbert, U. and Woschke, E. (2017). Partial filling of a honeycomb structure by granular materials for vibration and noise reduction, *Journal of Sound and Vibration* **393**.
URL: *https://www.sciencedirect.com/science/article/pii/S0022460X1630668X*

[5] Prasad, B. B., Duvigneau, F., Juhre, D. and Woschke, E. (2022). Application of particle dampers on a scaled wind turbine generator to improve low-frequency vibro-acoustic behavior, *Applied Sciences* **12**(2).
URL: *https://www.mdpi.com/2076-3417/12/2/671*

[6] Prasad, B. B., Duvigneau, F., Juhre, D. and Woschke, E. (2021). Experimental study of particle dampers applied to wind turbine blades to reduce low-frequency sound emission, *INTER-NOISE and NOISE-CON*

Congress and Conference Proceedings, Vol. 263.
URL: *https://www.ingentaconnect.com/content/ince/incecp/2021/00000263/00000006/art00007*

[7] Prasad, B. B., Duvigneau, F., Juhre, D. and Woschke, E. (2022). Damping performance of particle dampers with different granular materials and their mixtures, *Applied Acoustics* (109059).
URL: *https://doi.org/10.1016/j.apacoust.2022.109059*

[8] Sandanshiv, S. R. and Chavan, U. S. (2019). Vibration suppression effects on rotating wind turbine blade using a particle damping method, *Vibroengineering Procedia* **29**.
URL: *https://www.extrica.com/article/20944*

[9] Els, D. N. (2011). Damping of rotating beams with particle dampers: experimental analysis, *AIAA journal* **49**(10).
URL: *https://arc.aiaa.org/doi/abs/10.2514/1.J050984?journalCode=aiaaj*

[10] Michon, G., Almajid, A. and Aridon, G. (2013). Soft hollow particle damping identification in honeycomb structures, *Journal of Sound and Vibration* **332**(3).
URL: *https://www.sciencedirect.com/science/article/pii/S0022460X12007481*

[11] Xu, Z., Wang, M. Y. and Chen, T. (2004). A particle damper for vibration and noise reduction, *Journal of Sound and Vibration* **270**(4).

[12] Hollkamp, J. J. and Gordon, R. W. (1998). Experiments with particle damping, *Smart structures and materials 1998: Passive damping and isolation*, Vol. 3327.
URL: *https://www.spiedigitallibrary.org/conference-proceedings-of-spie/3327/0000/Experiments-with-particle-damping/10.1117/12.310675.short?SSO=1*

[13] Xiao, W., Huang, Y., Jiang, H., Lin, H. and Li, J. (2016). Energy dissipation mechanism and experiment of particle dampers for gear transmission under centrifugal loads, *Particuology* **27**.
URL: *https://www.sciencedirect.com/science/article/pii/S1674200116000432*

[14] Veeramuthuvel, P., Shankar, K. and Sairajan, K. (2016). Experimental investigation of particle damper-based vibration suppression in printed circuit board for spacecraft applications, *Proceedings of the Institution of Mechanical Engineers, Part g: Journal of Aerospace Engineering* **230**(7).
URL: *https://journals.sagepub.com/doi/full/10.1177/0954410015607552*

[15] Simonian, S. (2004). Particle damping applications, *45th AIAA/ASME/ASCE/AHS/ASC Structures, Structural Dynamics & Materials Conference*.
URL: *https://arc.aiaa.org/doi/abs/10.2514/6.2004-1906*

[16] Prasad, Braj Bhushan; Duvigneau, F. W. E. J. D. (2022). Vergleich verschiedener granularer Materialien und Mixturen für die Anwendung in partikelbasierten Schwingungsdämpfern, Deutsche Gesellschaft für Akustik e.V. (DEGA), Berlin, pp. 1358–1361.

[17] Sandanshiv, S. R. and Chavan, U. S. (2019). Vibration suppression effects on rotating wind turbine blade using a particle damping method, *Vibroengineering PROCEDIA* **29**: pp. 43–48.
URL: *https://doi.org/10.21595/vp.2019.20944*

15th SIRM – European Conference on Rotordynamics,
Darmstadt, Germany, 22nd – 24th February 2023

Self-excited vibration cases in critical machinery, part 2: parametric subsynchronous vibration.

Piotr Miałkowski, PhD

Machinery Diagnostic Services of Bently Nevada, a Baker Hughes business.
Piotr.Mialkowski@BakerHughes.com

Abstract

The work is continuation of the article [8], in which an education model of fluid induced instabilities in rotating machinery and its application for solving rotordynamic problems in the industry were shown. Parametric vibrations, due to periodic changes in the rotor support stiffness caused by rubs or looseness are often wrongly diagnosed as fluid induced instabilities, so the goal of this of article is to present the educational model of such phenomena that allows correct identification in the industry conditions.

Terminology

Self-excited Vibration: Vibration of a system caused by an internal feedback mechanism converting a supply of external energy (which may or may not be oscillatory) to oscillatory force.

Forced Vibration: The vibration response of the system due to a periodic exciting force (forcing function). Typically, the response frequency is at the same frequency as the excitation frequency and due to system nonlinearities may include harmonics.

Fluid Induced Instability: Self excited rotor vibration (lateral or axial) caused by interaction between the rotor and surrounding fluid.

Parametric Subsynchronous Vibration: Forced subsynchronous response of the rotor due to periodic changes in system parameters (rotor or support stiffness).

Stability (practical): A system is stable if a transient perturbation does not result in a system response with amplitudes exceeding an acceptable level.

1 Introduction

The mechanism by which a rotor is able to develop strong subsynchronous vibration due to a rub condition was identified by Ehrich in 1966 [1] and explained by Bently in 1974 [2]. The mathematical model was introduced by Childs [3] in 1982, followed by works of many researchers to improve numeric models of contact events and improve prediction of behavior due nonlinearities on rotor response, for example Ehrich 1988 [4] and 1991 [5], Gonsalves et al 1992 [6] or Goldman and Muszynska 1993 [7]. However, in daily industrial practice use of rigid mathematical models is often prohibitive due to time and other costs required to identify parameters for highly nonlinear behavior of the machine. At the same time, the experience shows cases of incorrect identification of the malfunction, as the first and often only conclusion for subsynchronous phenomena is fluid induced instability. When numeric modelling is not possible or not practical, use of simple physical models, describing the machine behavior in terms of forces, stiffness, and vibration to explain observed vibration signal characteristics, was found, by this author's service organization, to be an effective alternative of tables of symptoms which by their nature are static and may be not detailed enough. A simple educational model is presented, based on [9] as it is used in training of the diagnostic engineers and in problem solving during industrial analyses.

2 Educational model of parametric subsynchronous vibration

A test rotor that consists of a shaft with two disks supported by sleeve bushings, installed on rubber O-rings in rigid supports is used to demonstrate phenomenon (fig. 1a). There is a rub screw, that in the sample experiment below was installed between second disk and bearing 2 (fig. 1b) in the same angular direction as X-probe (45° right from top vertical, when looking from driver to driven).

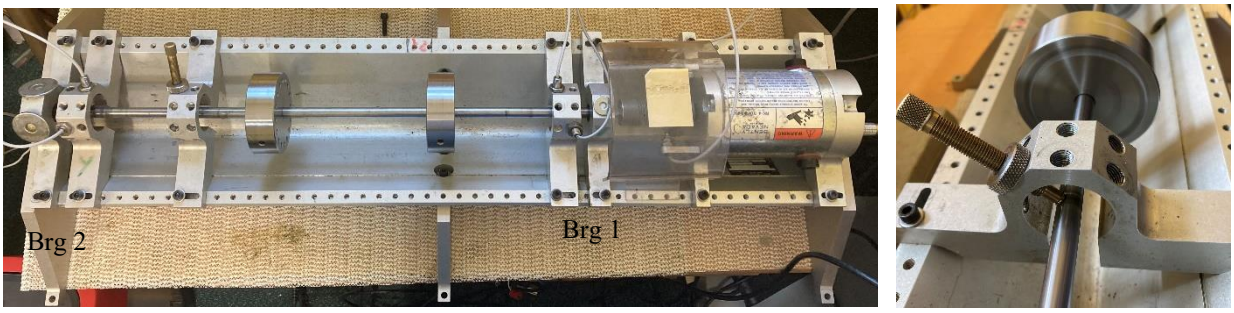

a) b)

Figure 1: a) Standard training rotor), b) rub screw detail.

Demonstration of the rub conditions show effects of deformation of orbit (rotor centerline motion trajectory), generation of higher harmonics and other classic rub symptoms but in some speed ranges there is also visible subsynchronous activity with the fractional component following the speed change, for example ½ *X* (*X* denotes rotational frequency), in fig. 2. Experiments of this type can show subharmonics $^1/_2X$, $^1/_3X$, $^1/_4X$ ... $^1/_nX$), for the speed regions slightly higher than n times any resonance speed. More difficult to present are excitations of simple integer ratios $^2/_3X$, $^3/_4X$..., $^m/_nX$) generated for the speed regions directly above *n* times the resonance speed and for *m* locations of contact.

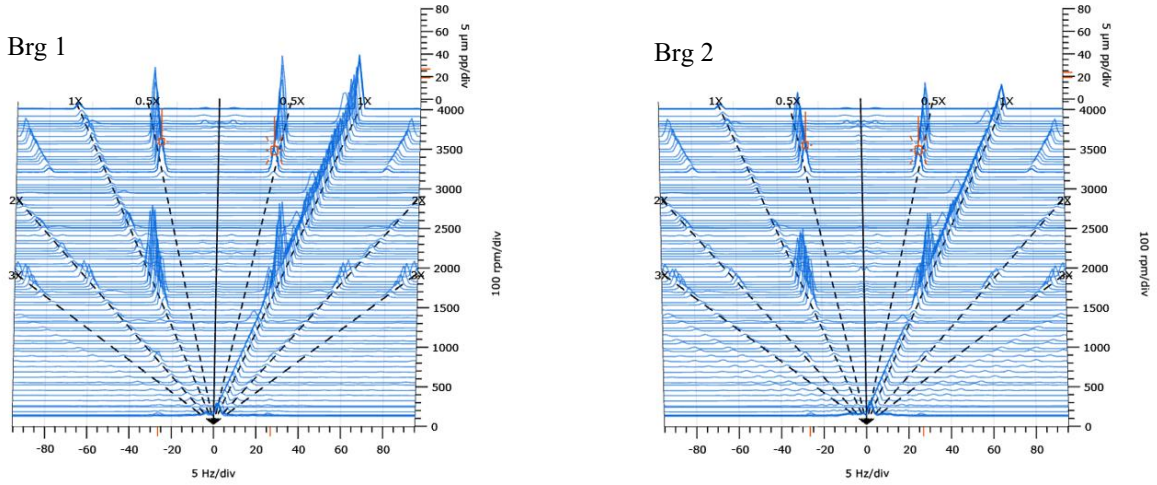

Figure 2: Full spectrum cascade plots for startup with the rub (training rotor) showing generation of ½ X component.

During the dwell time of contact in a partial rub condition, the normal impact force and tangential friction force are converting some kinetic energy of shaft rotation into shaft vibration. The vibration transferred by a single contact event will decay but if the next impulse occurs with proper timing, the next impulse will increase in amplitude. Bently [9] illustrates this by analogy of "a child on a swing": push applied at correct timing increases the amplitude of free vibration, push with incorrect timing removes the energy from system and amplitude decreases. If, for rub events there is a system resonance at the fractional speed then this fractional component of the vibration provides necessary timing: the ½ *X* component generation means the shaft operates at two times resonance speed and the energy impulse is added once per two revolutions of the shaft, the $^1/_3X$ can be generated if it is 3 times resonance speed, and so on. The orbit plots (with keyphasor, one per turn reference marks) allow demonstration of the part of the rotation cycle in which the rub impulse happens, followed by a single cycle (in case of ½ *X*) or cycles (in case of higher denominator number) of free vibration.

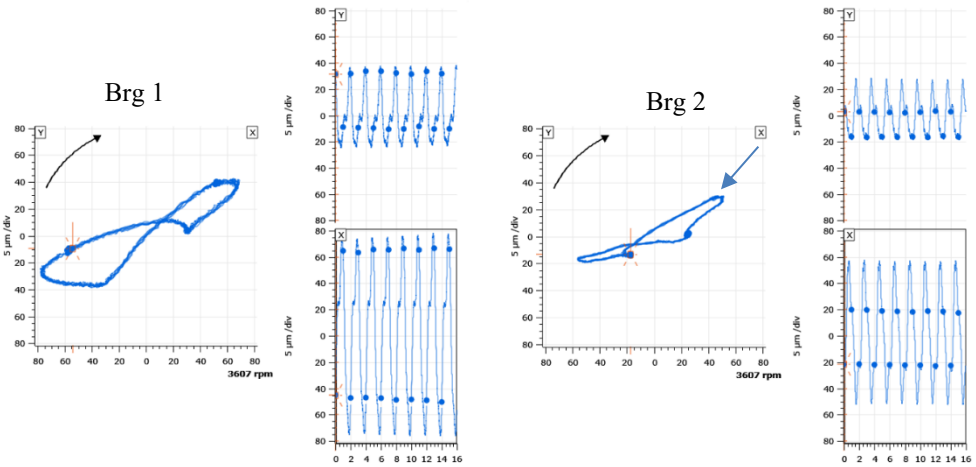

Figure 3: Sample orbits during excitation of subsynchronous component. The arrow indicates location of rub (close to bearing 2).

One of the recognized effects of the rub is modification of the system natural frequency: the contact creates additional support, increasing system stiffness and reducing modal mass. For a partial rub, the stiffness changes during the vibration cycle: it is increased during the dwell time and normal for the rest of the cycle, causing an increase of the average effective stiffness (fig. 4a). A helpful analogy is the modification of the natural frequency of a pendulum with restriction (fig. 4b).

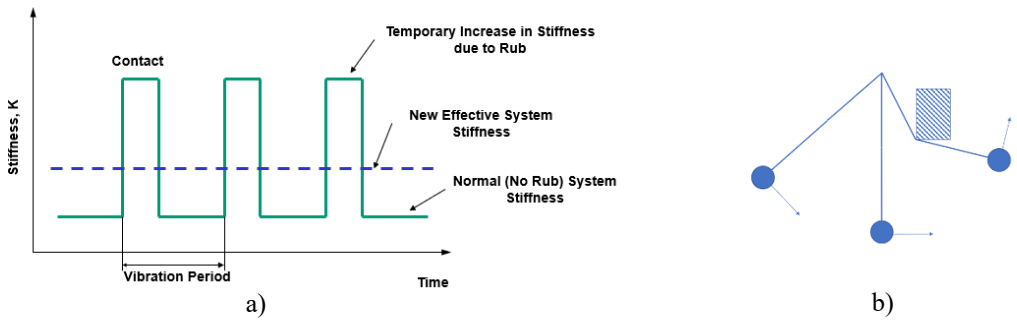

Figure 4: a) Nonlinear stiffness due partial rub events and b) nonlinear pendulum analogy.

The rub condition changes during speed change, for instance as speed increases more energy is transferred during contact, increasing vibration amplitude and leading to higher normal forces and longer dwell time, both effects increasing the effective stiffness. Thus, for a partial rub condition, the generation of $^1/_nX$ is possible for some speed range that is *above n* times the unmodified resonance speed and the subsynchronous activity will last for the range of the increased speed as long as the increase of stiffness sustains the resonance condition. In the case of machine operation with constant speed, the behavior can continue until the contact condition and subsequently the stiffness change, due to wear.

Periodic change of the system stiffness is also possible due to another type of malfunction, looseness in the supporting structures. If due to high *1X* vibration the rotor is moved *away* from the constraint then, for part of the vibration cycle, the stiffness is reduced (fig. 5). For the rotor operating in the speed region slightly *below n* times unmodified resonance speed, there is a timing condition allowing conversion of the portion of the rotational energy into vibration, with $^1/_nX$ component and exciting the rotor resonance. The rub condition, in which the effective stiffness increases is referred to as normal-tight condition. The looseness is named normal-loose condition. The speed range, in which excitation is observed (below or above n times resonance speed) allows identification of the malfunction. The other differentiator between the two phenomena is due to the need of driving force: excitation of parametric vibration due to looseness requires a significant *1X* (unbalance) component and for a partial rub, the energy is transferred both for normal and tangential components of the contact force, so subharmonic action can be generated independently of the balance condition i.e., with or without significant *1X* content.

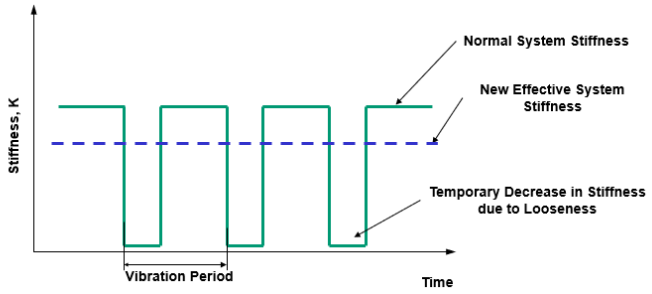

Figure 5: Nonlinear stiffness due looseness condition.

As a result of experiment and the descriptive model of the phenomena, the students are expected to acquire the following knowledge:

- Both partial rub and looseness in the support can lead to development of exact subsynchronous component (and possibly its harmonics) *if* the rotor operates in the specific speed range. The condition is a coincidence of excitation with modified (periodically changing) stiffness of the system.
- The rub condition momentarily increases system stiffness leading to higher effective stiffness, so the rotor resonance is excited by $^1/_n X$ component, for the speed range *above* n times any resonance speed.
- Looseness in the support reduces system stiffness, causing lower effective stiffness and the rotor resonance is excited by an $^1/_n X$ component, for the speed range *below* n times any resonance speed.

It can be noted that the most common situation in industrial machines is excitation of ½*X*, as many rotors are operating with speeds twice exceeding their first mode resonance but much less than three or more times.
Generating rub induced subsynchronous components on a test rotor is intentionally done with non-fluid film bearings to demonstrate that not all ½ *X* vibration is fluid induced as is assumed by many in the industry.
On two separate cases, the author was able to use such a demonstration to change the decision of a machine owner, from pursuing bearing replacement with a more expensive but technically correct option of internal alignment of turbine casing: the striking resemblance of visual patterns of orbits for the test rotor and real machine was evident even for non-experts.
Data from real machines may look differently than on the test rotor. Both rub and looseness are nonlinear and produce variety of patterns. The analysts are expected to utilize all standard formats (vibration presented in time and frequency domain, position), across the range of conditions to match them to provided models of behavior. Sample analyses are provided below.

3 Normal-tight condition in steam turbine – generator train

The case was mentioned in the first part of this article [8] as example of typical “impostor” for the fluid induced instability. Following the replacement of generator bearing in the 30MW steam turbine-generator train, the repair company asked for analysis of the data because of unstable operation of the new bearing.

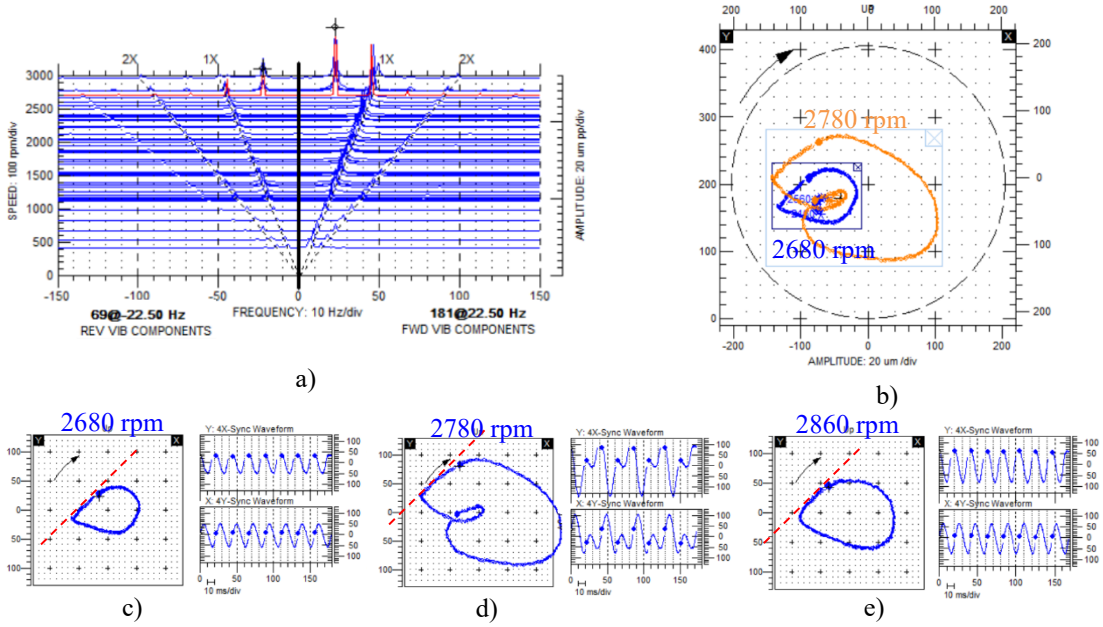

Figure 5: Re-excitation of rotor resonance by ½X component resulting from lubricated rub: a) full spectrum cascade plot, b) shaft centerline position in the clearance with overlaid orbits for stable and unstable conditions; orbit and timebase for c) speed below, d) speed at and e) speed above instable speed range. Dashed lines showing estimated location of contact.

Forward subsynchronous component close to *½X* appears in vibration when the speed exceeds 2700 rpm but ceases for speed higher than 2800 rpm (fig. 5a and 5c-e). For fluid induced instabilities, educational model in [8], the spontaneous stabilization on speed increase would not be expected, this suggests parametric vibration. The orbit timebase plots (fig. 5d) show precise timing of two separate cycles of vibration: the stationary position of keyphasor dots indicates the presence of an exact *½ X* component, the energy is delivered at the same part of the cycle in one rotation of the shaft and then the next rotation is free vibration with motion *away* from an obstacle. Orbit shape shows characteristic deformation at upper left part suggesting limitation of trajectory i.e. angular location of the rub spot. Rub symptoms are present for a wider speed range than the excitation of *½ X*. The latter is limited to the region above two times resonance speed which was identified from shutdown data to be 1280 rpm. The shaft centerline position gives no reason for the rub as the trajectory plotted around average position (fig. 5b) is still far away from the nominal clearance. The shape of the orbit is not typical for light, impact type rub but rather looks like a heavy rub, which by [9] is less likely to produce parametric vibration.
Inspection of the newly installed bearing was requested and revealed the error in manufacturing: the end section from one side of bearing was machined with eccentricity and protruded in the bore, exactly at the angular location suggested by orbit and shaft centerline plot. The rub was a lubricated one, which can explain why impact type characteristics were not seen.
The lesson learned is that with use of synchronous orbits and waveforms it is easy to recognize characteristic patterns of parametric excitation, because exact timing can be confirmed.

4 Normal-loose condition in steam turbine – generator train

The following case study data were provided by John Winterton [10]: the 300MW steam turbine generator train coming from overhaul was not able to operate with full capacity due to elevated vibrations in front generator bearing. These vibrations were present when machine was loaded to more than 50% of nominal load and characterized by an exact *¼ X* component.

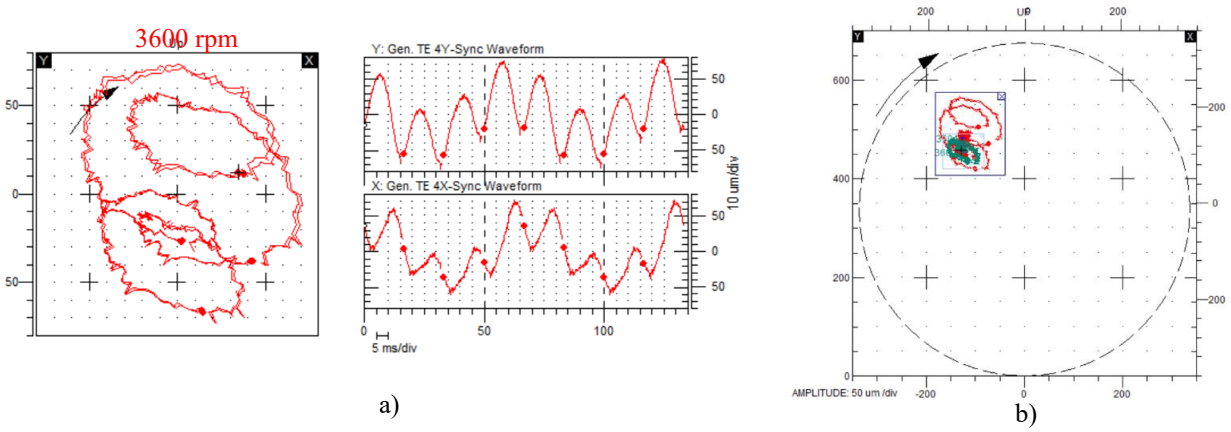

Figure 6: Re-excitation of rotor resonance by *¼ X* component: a) orbit-timebase for unstable condition b) stable and unstable orbits overlaid on shaft centerline position in the clearance.

As these types of units are starting with high gradient of speed through resonance regions, the exact value of the critical speed was unknown and speed range criterion could not be immediately applied. The shape of the orbit (fig. 6a) is not showing any clear truncation indicating rub contact. There is significant *1X* vibration, so at least the normal-loose possibility should be considered.

By comparing the stable and unstable shaft trajectories (orbits) in fig. 6b it can be also noted that free vibration cycles are higher and at bigger distance from the center of the clearance than the part of the cycle with normal stiffness. We can estimate which part of the cycle is normal stiffness because it is the same position and trajectory as stable cycle shown in green in fig. 6b. Considering that the machine is electric generator with high internal clearances, the rub is not suspected since there should not be point of contact in such direction for any condition of bearing or casing seals. The looseness theory was confirmed when operator tightened the support bolts (with unit still in operation): the subsynchronous vibration ceased, leaving *1X* almost unmodified (fig.7). The resonance speed was identified during shutdown to be 930 rpm, so at operating speed 3600 rpm the unit was below 4 times resonance speed and thus with reduction of the stiffness the re-excitation of rotor resonance by *¼ X* was possible.

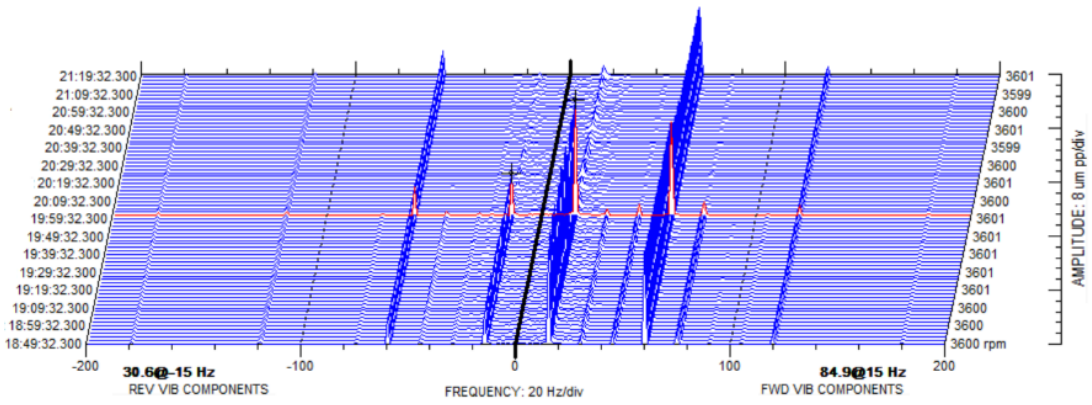

Figure 7: Full spectrum waterfall showing the ceasing of ¼ X component, following the tightening of the bearing support bolts.

The lessons learned from this case are that the diagnostic model also works for looseness condition and although statistically the rub is a much more common malfunction than looseness, the diagnostic analysis should not be driven by statistics but by verifying alternative options, if supported by model.

5. Classification of forced subsynchronous phenomena and other forms of subsynchronous parametric vibration.

By terminology used in diagnostic analyses the forced subsynchronous phenomena are often classified as instabilities. This is acceptable by definition of stability used in practical diagnostics, which is not based on strict utilization of Lyapunoff definition but rather postulates the system is stable if the transient perturbation does not result in the response amplitude increase above acceptable level. In this sense, re-excitation of natural frequency by an exact fractional component, which can lead to vibration increase well above alarm or even danger levels and thus make operation of the machine not possible, can be considered instability. However, it is not the same type of vibration as fluid induced instabilities, because it is not self-excited vibration, resulting from internal feedback mechanism converting a supply of external energy into vibration. In the case of fully developed self-excited vibration models [8] the limit for shaft vibration is the physical boundary (clearance) and once the system becomes unstable it requires significant change of parameters to stabilize (hysteresis). Rub and looseness are forced vibration phenomena, they require continuous forcing (repetitive impulses of energy from rub events or significant unbalance force for looseness) and if for some reason the forcing is removed, the vibration ceases. This required forcing is also a source of the timing of the impulses, so the amplification of vibration is only possible at exact fractional components, when they excite system resonances. On the other hand, forced vibration phenomena are typically defined as the response at the frequency of the forcing function or (due to system nonlinearities) at harmonics. From this perspective the forced subsynchronous action has indeed some characteristics from both classifications. Correct classification of observed vibration phenomenon (forced vs. self-excited) can be very useful in tracking of a root cause of vibration, which is illustrated by the case below.

6. Parametric self-excited torsional vibration of single-shaft combined cycle unit.

A newly built, single shaft combined cycle power generation unit showed high subsynchronous vibration during every startup, when operated with idle load [7]. The machine train consists of an electric generator driven from one side by gas turbine and from the other side by steam turbine. The high vibrations were present at the steam turbine bearing next to coupling to electric generator. When the load of gas turbine and generator was increased the vibration ceased (fig.8 a, b).

The vibration was caused by the repetitive excursions of shaft movement in the clearance (fig. 9 a, b) with frequency 5.5Hz, coinciding with model calculated frequency of lowest torsional vibration mode, with its nodal point in the adjacent flexible coupling. The conversion of torsional vibration into radial motion was identified to be hard contact of the teeth between the coupling diaphragm and the flange guard (fig. 10 a, b). The teeth are a design safety feature, in case of damage to or an overload of the diaphragm. In normal operating condition, steady state or transient, the teeth should not be in contact. However, their assembly position is not in the center of the clearance but with an offset to compensate for a twist of the coupling when loaded by nominal torque during operation. Therefore, when the machine operates on idle load, a relatively small load change can lead to the contact and cause the impact followed by free vibration with the torsional natural frequency. Since the observed impulses are repetitive this could be either forced or self-excited vibration. No forcing function was found at 5.5Hz and this frequency is not a natural fraction of the rotating speed so forced vibration can be excluded. The torque produced is a function of fuel consumption and the changes in the latter are leading to rotating speed change, but the fuel flow and rotating speed were showing small and non-cyclic changes driven by operation of the emission control (NOx reduction) system.

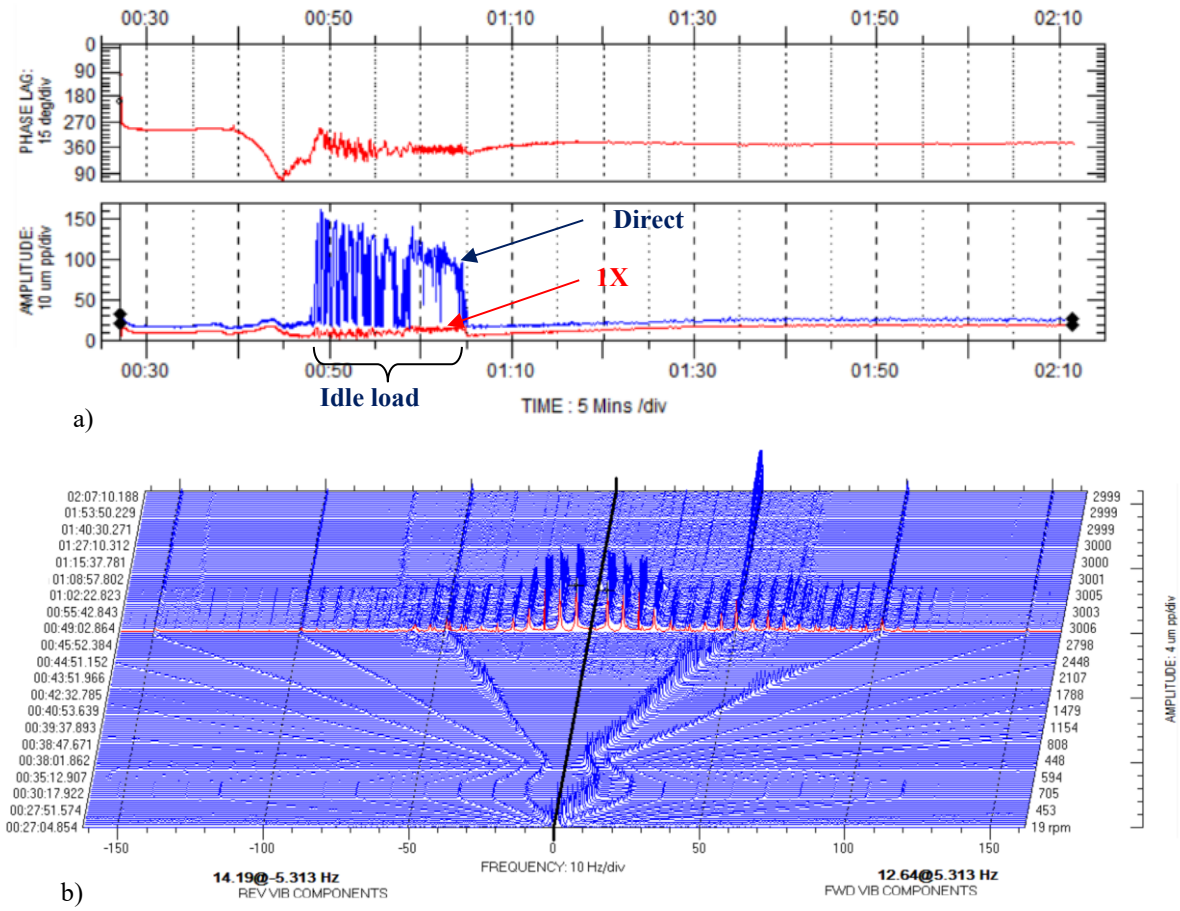

Figure 8: Subsynchronous vibration in turbine bearing, when train on idle load. a) The vibration trend showing presence of non-synchronous content and b) full-spectrum waterfall.

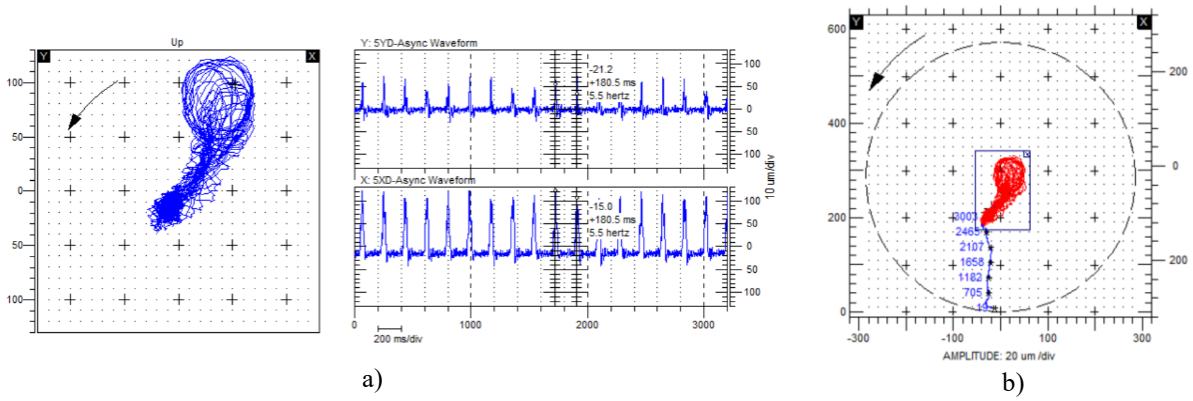

Figure 9: a) Orbit and timebase for shaft vibration during idle run and b) trajectory plotted on shaft centerline position with bearing clearance.

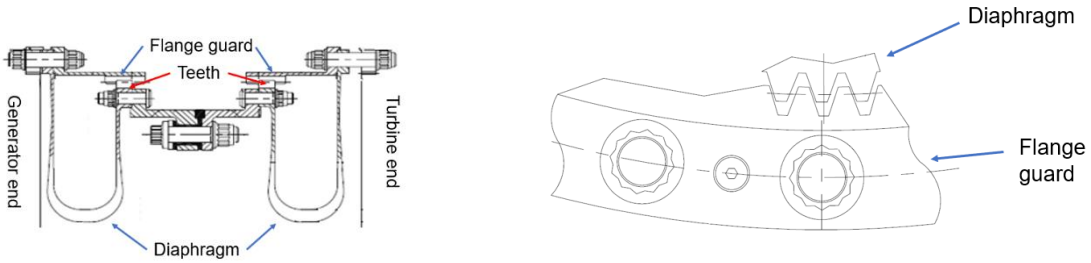

Figure 10: a) The coupling design: flexible diaphragm with protection against excessive twist b) detail of coupling design: protection teeth between diaphragm and the flange guard.

Based on the characteristics of the signal, the phenomenon was classified as parametric, self-excited vibration. The working hypothesis was that the system behaves unstable because of speed control interaction with nonlinear feedback mechanism (fig. 11). On the ground of the control system theory such a configuration can be unstable for all feedback signals exceeding the linear part of the characteristics.

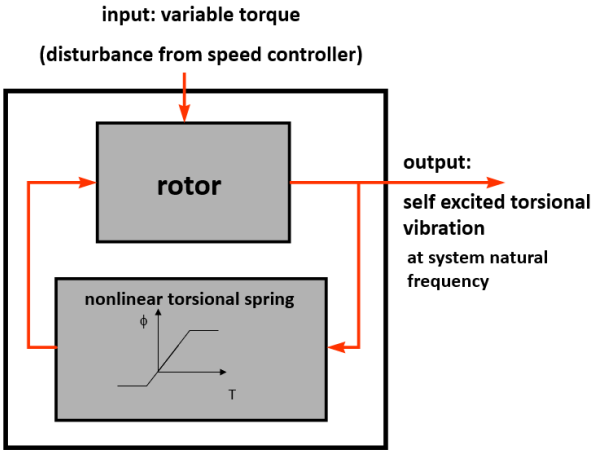

Figure 11: Postulated model of rotor behavior.

Diagnostic service made no attempt to formalize a model or identify the parameters, it was only used to conceptualize and review possible solutions. If the model is applicable, then the system can be stabilized either by removing nonlinearity or by ensuring operation is within linear part of spring characteristics. The behavior of the machine agrees with this assumed model: when the train is loaded, the coupling operates with higher twist, further from the nonlinearity but also the amplitude of perturbations is lower because of the changes in the flow of fuel due to the emission control system are small percentage of the fuel flow due to load demand. Coupling redesign would not only be expensive but would also change the dynamic behavior of the whole train, so the alternative solution was pursued. The manufacturer optimized the algorithms of the emission control system to reduce the level of perturbations. This was a significant engineering project, based on strict modelling of the system, but it is worth mentioning that diagnosis of the machine behavior was done in short time and based on simple diagnostic models applied to basic characteristics of the vibration, as outlined above.

7 Conclusion

Fluid induced instabilities are most common but not the only source of subsynchronous vibration problems in the rotating machinery. The next most common and often in practical cases wrongly recognized situation is forced subsynchronous action caused by re-excitation of rotor resonances by partial rub or by looseness in the rotor support. An educational model used in training of industry rotordynamic specialists has proven to be effective in correctly identifying the forced subsynchronous actions as well as in recognizing the situations when the behavior is not caused by one. Positive identification required analysis of shaft vibration trajectories (analysis in time domain), preferably with sampling synchronized with rotation, use of the phase reference mark (keyphasor) and analysis of the rotor position in the clearance.

References

[1] Ehrich, F. F. (1966), *Subharmonic vibrations of rotors in bearing clearance.* ASME Paper No. 66-MD-1 Design Engineering Conference and Show, Chicago, Illinois, 9-12 May.

[2] Bently, D. E. (1974): *Forced Subrotative Speed Dynamic Action of Rotating Machinery.* ASME publication 74-Pet-16.

[3] Childs, D. W. (1982): *Fractional Frequency Rotor Motion Due to Non-Symmetric Clearance Effects*, ASME J. Eng. Power. 104(3)

[4] Ehrich, F. F. (1988), *High Order Subharmonic Response of High Speed Rotors in Bearing Clearance*, Journal of Vibration, Acoustics, Stress and Reliability in Design, January 1988

[5] Ehrich, F. F. (1991), *Observations of Subcritical Superharmonic and Chaotic Response in Rotordynamics*, DE—Vol. 35, Rotating Machinery and Vehicle Dynamics, ASME, 1991

[6] Gonsalves, D., Neilson, R. D., Barr, A. D. S., *Response of a Discontinuously Nonlinear Rotor System*, Proc. of "Rotordynamic 92," Venice, Italy, 1992

[7] Goldman, P., Muszynska, A. (1993) *Chaotic Behavior of Rotor/Stator Systems with Rubs*, International Gas Turbine and Aeroengine Congress and Exposition Cincinnati, Ohio May 24-27, 1993 ASME 93-GT-387

[8] Mialkowski, P., Peton, N. (2021): *Self-excited vibration cases in critical machinery.* SIRM 2021, ID-30.

[9] Bently, D. E., Hatch C. T., Grissom, B. (2002): *Fundamentals of Rotating Machinery Diagnostics*, Bently Pressurized Bearings Press 2002

[10] Winterton, J. G. (2006); *A Study of an Exact ¼ X Component on a Hydrogen Cooled Generator*, Internal MDS Conference 17-19 Oct 2006, Minden NV

[11] Mialkowski, P., Peton, N. (2020): *Self excited torsional vibration in Single Shaft Combined Cycle Turbine Generator train*, 49th Turbomachinery and 36th Pump Symposia, Houston, TX

15th SIRM – European Conference on Rotordynamics,
Darmstadt, Germany, 22nd – 24th February 2023

Multi-Harmonic Unbalance Response of Aircraft Jet Engine Rotors on Squeeze Film Dampers

Georgios Mitsos [1], **Ioannis Chatzisavvas** [2], **Athanasios Chasalevris** [1]

[1] National Technical University of Athens, 15780, Athens, Greece
[2] MTU Aero Engines AG, 80995, Munich, Germany, ioannis.chatzisavvas@mtu.de

Abstract

Squeeze film dampers depict strong nonlinearities in the impedance forces. However, they are usually included in analytical dynamic models of jet engines as linear elements, especially in frequency domain, using linearized coefficients. In this manner, the unbalance response of the system can be evaluated with relatively low computational cost. The linearization of SFDs in aircraft engine applications is not trivial, despite the fact that SFDs are used in aircraft engines for more than 40 years. The present paper incorporates nonlinear SFDs in rotor dynamic simulations through a harmonic balance approach. The method used is in principle a general approach and can be used on any SFD type or model, as well as other types of nonlinear bearings. The method is firstly applied to a Jeffcott rotor mounted on two SFDs in order to provide insights on its accuracy and its efficiency, comparing the results to the time response of a reference model with nonlinear SFDs. It is shown that, depending on the system configuration, higher harmonics are necessary in order to capture the response of the rotor. Finally, the method is applied to a realistic jet engine model, where different unbalance and bearing configurations are applied. The method aims to offer a solution on the implementation of load and speed dependent nonlinear SFD forces for a fast frequency response analysis, which is required in the dynamic design of the machine.

1 Introduction

Typically, aircraft engine rotors are supported by rolling element bearings, mostly ball and roller bearings. Bearings operate in series with squeeze film dampers in aerospace applications, which are the main source of external damping applied on the rotor system. Moreover, they increase engine stability by isolating vibration and reducing bearing wear. Due to journal motion, oil is constantly squeezed and displaced, which leads to the generation of oil film impedance forces.

The most influential parameters for the performance of squeeze film dampers [14] are: the geometric characteristics (length, diameter and radial clearance) and the oil characteristics (viscosity). However, many other design parameters, such as seals type, cavitation profile along the oil film, supply pressure levels and fluid inertia, prove to be important, thus their effect has been studied in detail. Reinhardt and Lund [12] examine journal bearings and find out that the inclusion of the inertial term in the Reynolds equation leads to added mass coefficients that importantly affect small rotors. Moreover, the influence of fluid inertia proves to be more important to open-ended than partially sealed SFDs, while the vapor cavitation affects both configurations, especially for small Reynolds numbers [6], [7]. It is also discovered that piston-ring seals provide significantly larger damping forces than end seals and are less affected by the number of oil feeds [9]. Experiments show that piston-ring sealed SFDs restrict the lubricant leakage and, as a result, produce remarkably larger damping and added mass coefficients than open-ended SFDs [1], [3].

Bearings and SFDs are in principle speed dependent and nonlinear with rotor displacement, hence linear analysis is not feasible, unless they are introduced in the dynamic models as linear elements. Linearization methods can only be applied to bearings under the condition that they perform small perturbations about a fixed point, thus their extension to cases of large amplitude motions is likely to produce inaccurate results. The results of journal bearing unbalance response with linearized coefficients prove to be satisfying for amplitudes as large as 40% of the radial clearance [10], [13]. In [8] the linearization process of multi-bearing rotor systems is explained in detail and its results are compared to those of a nonlinear model. Another approach is presented in [11]; the separate solution of linear and nonlinear system equations.

Contrary to journal bearings, the linearization of squeeze film dampers is not well documented, although SFDs are used in aircraft applications for more than 40 years. Their linearization is only examined in [2], where dynamic stiffness coefficients are calculated based on journal orbits.

Nonlinearities often become crucial for the dynamic behaviour of the system so that linear models are not sufficient. Hence, a new multi-harmonic method is introduced in the present paper in order to solve nonlinear systems in the frequency domain. Linearized SFD forces (under short bearing approximation) consisting of higher-order harmonics are calculated based on journal orbits, through an iterative process. The method is significantly faster than transient analysis and equally accurate, at the same time.

2 Analytical Model for Squeeze Film Damper Forces

Starting from Navier-Stokes equations and making the short bearing approximation [4], the Reynolds equation for squeeze film dampers is given by (1). Inertial terms are neglected.

$$\frac{\partial}{\partial z}\left(\frac{h^3}{\mu}\cdot\frac{\partial P}{\partial z}\right)=12\frac{\partial h}{\partial t} \tag{1}$$

Oil film thickness h and its first derivative with respect to time are calculated by (2).

$$h=c_r-x\cdot\cos\theta-y\cdot\sin\theta \quad , \quad \frac{\partial h}{\partial t}=-\dot{x}\cdot\cos\theta-\dot{y}\cdot\sin\theta \tag{2}$$

(1) is integrated twice with respect to the axial direction z along the entire length L of the SFD. Open-ended squeeze film dampers are selected for the present analysis, therefore the corresponding boundary conditions arise; oil film pressure P equals to 0 at the two ends of the SFD ($z=0$ and $z=L$) for any angle θ. The final expression for film pressure along the circumferential and the axial direction is presented in (3).

$$P(\theta,z)=6\mu\cdot\frac{-\dot{x}\cdot\cos\theta-\dot{y}\cdot\sin\theta}{(c_r-x\cdot\cos\theta-y\cdot\sin\theta)^3}\cdot\left(z^2-L\cdot z\right) \tag{3}$$

Expressions for SFD oil film forces in x and y direction result from the integration of (3) with respect to θ and z as presented in (4). SFD radius is symbolized by R.

$$F_x=\int_0^L\int_{\theta_1}^{\theta_2}P(\theta,z)\cdot\cos\theta\cdot R\,d\theta\,dz \quad , \quad F_y=\int_0^L\int_{\theta_1}^{\theta_2}P(\theta,z)\cdot\sin\theta\cdot R\,d\theta\,dz \tag{4}$$

The substitution of (3) in (4) and the rearrangement of the terms leads to (5).

$$F_x=\mu\cdot R\cdot L^3\int_{\theta_1}^{\theta_2}\frac{\dot{x}\cdot\cos^2\theta+\dot{y}\cdot\sin\theta\cdot\cos\theta}{(c_r-x\cdot\cos\theta-y\cdot\sin\theta)^3}\,d\theta \quad , \quad F_y=\mu\cdot R\cdot L^3\int_{\theta_1}^{\theta_2}\frac{\dot{x}\cdot\cos\theta\cdot\sin\theta+\dot{y}\cdot\sin^2\theta}{(c_r-x\cdot\cos\theta-y\cdot\sin\theta)^3}\,d\theta \tag{5}$$

Gümbel cavitation approach is selected in order to calculate the limits of integration θ_1 and θ_2 taking into account oil cavitation. Hence, only positive pressure contributes to the calculation of oil film forces; (3) is positive in the range between θ_1 and θ_2, where:

$$\theta_1=arctan2(-\dot{x},\dot{y}) \quad , \quad \theta_2=\theta_1+\pi \tag{6}$$

The forces of (5) are also expressed by (7), as a function of nonlinear damping coefficients.

$$\begin{Bmatrix} F_x \\ F_y \end{Bmatrix} = \begin{bmatrix} c_{xx} & c_{xy} \\ c_{yx} & c_{yy} \end{bmatrix} \cdot \begin{Bmatrix} \dot{x} \\ \dot{y} \end{Bmatrix} \quad , \quad \begin{Bmatrix} c_{xx} \\ c_{xy} \\ c_{yx} \\ c_{yy} \end{Bmatrix} = \mu \cdot R \cdot L^3 \int_{\theta_1}^{\theta_2} \frac{1}{(c_r - x \cdot \cos\theta - y \cdot \sin\theta)^3} \cdot \begin{Bmatrix} \cos^2\theta \\ \sin\theta \cdot \cos\theta \\ \cos\theta \cdot \sin\theta \\ \sin^2\theta \end{Bmatrix} d\theta \quad (7)$$

The effect of journal position in x and y direction on the nonlinear damping coefficients is examined in Figure 1, where the common logarithm of the coefficients is reflected across the z-axis. Sommerfeld cavitation approach is selected (only for the present Figure), namely pressure is integrated along the entire SFD circumference, so that journal velocity does not influence the coefficients.

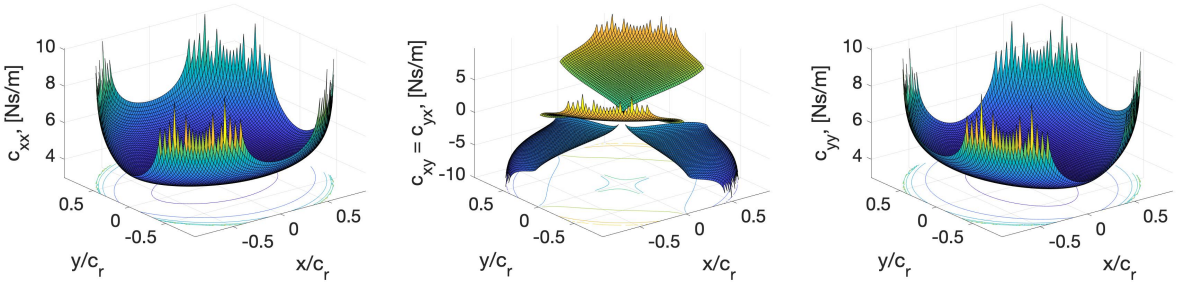

Figure 1: SFD nonlinear damping coefficients for Sommerfeld cavitation approach.

Furthermore, the effect of both journal position and velocity on the coefficients along circular orbits about bearing center under Gümbel cavitation approach is examined in Figure 2, where the common logarithm of the coefficients is reflected across the z-axis. The coefficients are constant along the circular orbits.

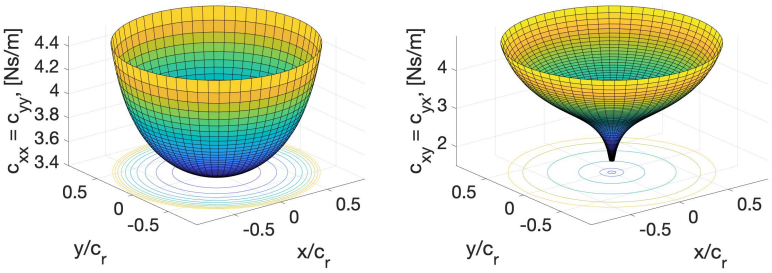

Figure 2: SFD nonlinear damping coefficients along circular orbits about bearing center for Gümbel cavitation approach.

In conclusion, SFD damping coefficients are highly nonlinear with respect to journal position and velocity, hence their substitution with constant values regardless of bearing eccentricity is not an accurate approximation. Therefore, a different approach is necessary.

3 Approximation of SFD Forces Using Discrete Fourier Transform and Solution of the System Using Multi-Harmonic Analysis

Oil film forces are calculated at P discrete points along the orbit, where P is set to 60 in this paper. The angle interval between two consecutive points is $\Delta\phi$. The forces are periodic with period $T = 1/\omega$, where ω is the whirling frequency of the journal in Hz. The approximation of forces is feasible using N harmonics, as shown in (8).

$$F_{SFD}(\phi) \approxeq c_0 + \sum_{n=1}^{N} \left[c_n \cdot e^{nj\phi}\right] = c_0 + c_1 \cdot e^{j\phi} + c_2 \cdot e^{2j\phi} + \cdots + c_N \cdot e^{Nj\phi} \quad , \quad \phi \in [0, 2\pi] \tag{8}$$

The mean value of the force is symbolized by c_0. The terms c_n, $n = 1, 2, \cdots$, N, are calculated [5] separately for each order by Discrete Fourier Transform (DFT).

$$c_0 = \frac{1}{P} \sum_{i=0}^{P-1} F(\phi_i) \quad , \quad c_n = \frac{2}{P} \sum_{i=0}^{P-1} F(\phi_i) \cdot e^{-nj\phi_i} \quad (n = 1, \cdots, N) \tag{9}$$

The number of orders N is defined according to the accuracy required for the approximation of SFD impedance forces. However, there are some general rules regarding the predefinition of the requisite orders. Firstly, the mean values of the forces in both x and y direction equal to 0 for centered circular or elliptic orbits. Moreover, in the case of circular centered orbits, the forces are described by single-harmonic sine or cosine functions, thus only the first-order harmonic is required. On the other hand, in the case of elliptic centered orbits, the forces are described by odd functions, thus even-order harmonics equal to 0 and can be omitted. Finally, in the case of off-centered orbits, no symmetry is observed and no orders can be ignored.

A dynamic system of multiple DoFs is described by (10). The rotational speed is symbolized by Ω.

$$\mathbf{M} \cdot \ddot{\underline{\mathbf{x}}} + (\Omega \mathbf{G} + \mathbf{C}) \cdot \dot{\underline{\mathbf{x}}} + \mathbf{K} \cdot \underline{\mathbf{x}} = \underline{\mathbf{f_u}} + \underline{\mathbf{f_w}} + \underline{\mathbf{f_{SFD}}} \tag{10}$$

The external forces of the system are the unbalance force $\underline{\mathbf{f_u}}$, the weight $\underline{\mathbf{f_w}}$ and the SFD impedance force $\underline{\mathbf{f_{SFD}}}$. The elements of $\underline{\mathbf{f_{SFD}}}$ that concern the DoFs of the SFD are described by (8). It is highlighted that they need to be included with a negative sign in the right-hand side of (10). Hence the right-hand side of (10) is given by (11).

$$RHS = \underline{\mathbf{f_u}} + \underline{\mathbf{f_w}} + \underline{\mathbf{f_{SFD}}} = \underline{\mathbf{f_1}} e^{j\phi} + \underline{\mathbf{f_w}} + (\underline{\mathbf{c_0}} + \underline{\mathbf{c_1}} e^{j\phi} + \underline{\mathbf{c_2}} e^{2j\phi} + \cdots + \underline{\mathbf{c_N}} e^{Nj\phi}) \tag{11}$$

Hence, the solution of (10) has the general form:

$$\underline{\mathbf{x}} = \underline{\mathbf{x_0}} + \underline{\mathbf{x_1}} e^{j\phi} + \underline{\mathbf{x_2}} e^{2j\phi} + \cdots + \underline{\mathbf{x_N}} e^{Nj\phi} \tag{12}$$

Subsequently, (11) and (12) are substituted in (10). In order to have a nontrivial solution of the system, (13) need to apply.

$$\begin{gathered} \underline{\mathbf{x_0}} = \mathbf{K}^{-1} \cdot (\underline{\mathbf{f_w}} + \underline{\mathbf{c_0}}) \qquad \underline{\mathbf{x_1}} = \left[-\Omega^2 \mathbf{M} + j\Omega (\Omega \mathbf{G} + \mathbf{C}) + \mathbf{K}\right]^{-1} \cdot (\underline{\mathbf{f_1}} + \underline{\mathbf{c_1}}) \\ \underline{\mathbf{x_n}} = \left[-n^2 \cdot \Omega^2 \mathbf{M} + jn \cdot \Omega (\Omega \mathbf{G} + \mathbf{C}) + \mathbf{K}\right]^{-1} \cdot \underline{\mathbf{c_n}} \qquad (n = 2, \cdots, N) \end{gathered} \tag{13}$$

The calculations of the multi-harmonic method are repeated at each rotational speed. The algorithm followed by the method is the following:

1. An initial estimation for the solution, which has the dimension of the number of DoFs multiplied by the number of orders used for the approximation (N), is assumed based on the solution of the previous frequencies, supposing that the calculations have converged.
2. SFD journal orbits are defined based on the initial estimation. Analytical SFD forces are calculated along the orbit by (5), afterwards, they are approximated using (8) and, finally, they are included in $\underline{\mathbf{f_{SFD}}}$ of (10).
3. It is examined if (13) are satisfied. If this is not the case, the previous steps are repeated, starting from a new estimation, until convergence.

4 The Multi-Harmonic Method for the Evaluation of Dynamic Response of Jeffcott Rotor

A Jeffcott rotor of diameter D_s supported by two bearings B_1 and B_2 is presented in Figure 3a. The rotor rotates with speed Ω and consists of a massless shaft and a disk attached to it. The Young's modulus and the density of the rotor are symbolized by E and ρ, respectively. Its total mass m_d is concentrated on the disk, which is located in half the distance between the bearings (L_s).

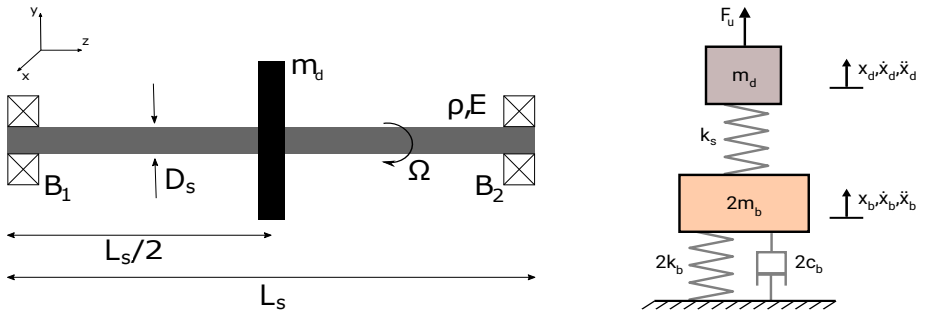

(a) (b)

Figure 3: (a) Jeffcott rotor supported by two bearings. (b) Simplified linear model of a Jeffcott rotor.

Each bearing is consisted of a rolling element bearing, a squirrel cage and a squeeze film damper. They are connected to the housing, which is modeled as rigid ground. The shaft stiffness is symbolized by k_s and its damping equals to 0. Mass unbalance force F_u acts on the disk. Two models are examined and compared to each other:

1. A **linear model**, in which each bearing is modeled as a mass (m_b) - spring (k_b) - damper (c_b) system. The mass m_b is the mass of the journal. Bearing total stiffness k_b comes from both the rolling element bearing itself and the squirrel cage, while total damping c_b comes from the rolling element bearing and the SFD. Eventually, the system is simplified in the model presented in Figure 3b, which is identical for x and y direction. The results of the linear model are deduced using linear harmonic analysis without taking the weight into account.
2. A **nonlinear model**, in which the linear damping coefficient c_b is replaced by nonlinear SFD impedance forces. In this way, anisotropy is introduced to the system, when weight is included in the simulations. The rest of the parameters remain the same. The results of the nonlinear model are deduced using the multi-harmonic method.

Time transient response evaluated by time integration of the nonlinear equations of motion including nonlinear SFD impedance forces is used as a reference for the results of the models.

The degrees of freedom of the disk are x_d and y_d. Since the system is symmetric (no tilting of the disk is assumed), the same set of DoFs (x_b and y_b) is used to describe both bearings. Moreover, their mass, damping and stiffness act parallel to each other, thus they are added together, e.g $m_{b,tot} = 2m_b$. No gyroscopic phenomena are observed because of the position of the disk.

The results of all the following figures concern the relative to the radial clearance eccentricity of the bearing in x and y direction.

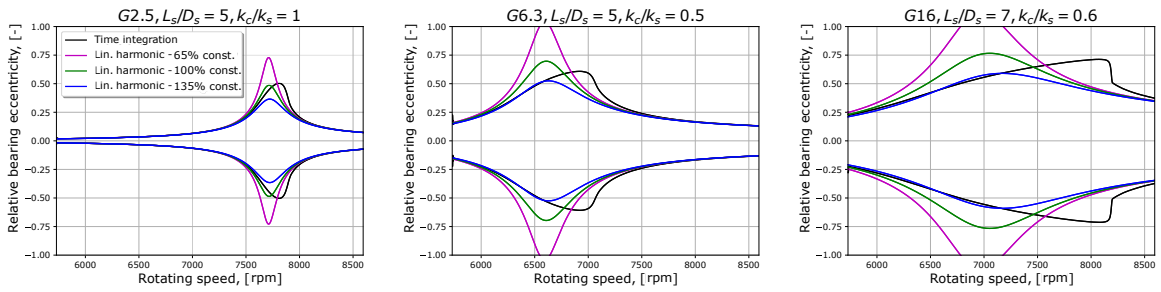

Figure 4: Comparison of the unbalance response of the linear model to the transient response.

The results of the linear model with constant damping coefficients (ranging from 65% to 135% of a typical SFD damping coefficient) fail to approximate the transient response as observed in Figure 4. In total, three cases of different G unbalance grades [15] with operating speed set at 1500 rad/s, shaft slenderness ratios (L_s/D_s) and squirrel cage to shaft stiffness ratios (k_c/k_s) are examined. Although, the results of linear harmonic analysis manage to capture decently the amplitude, they fail to predict the critical speed and the shape of the curve.

For the same three cases, the results of the nonlinear model using the multi-harmonic method are compared to the transient response in Figure 5. Since circular orbits about the centerline are examined, SFD impedance forces are described by a single-harmonic sine or cosine function and the response in the two directions is identical. Therefore, only the first-order harmonic is required to capture the transient response. The results of the method are identical to those of transient analysis. A small difference due to transient phenomena is observed in the third case.

Subsequently, three cases of elliptic centered orbits are presented in Figure 6. Nonsymmetric squirrel cages are employed in order to produce elliptic journal motions. It is reminded that only the odd-order harmonics are required for these cases. Although the first-order harmonic excellently approximates the transient response in the first and the third case, the third-order harmonic offers a significant improvement in the second case.

Finally, three cases of off-centered orbits are examined. In these cases, the squirrel cage and the shaft slenderness ratio remain constant, while G unbalance grade ranges from G1 to G6.3. The squirrel cage is symmetric in x and y direction and flexible, hence large static eccentricity ($> 70\%$ of the radial clearance) is observed. The unbalance response in y direction for the three cases is presented in Figure 6. For cases of flexible or, even, not present squirrel cage, the journal whirls close to the radial clearance. As a result, the zeroth-order response is crucial since it lifts the journal, especially at high rotational speeds. Finally, it is observed that the third-order harmonic offers a significant improvement in the approximation of the transient response in the second and, mainly, the third case.

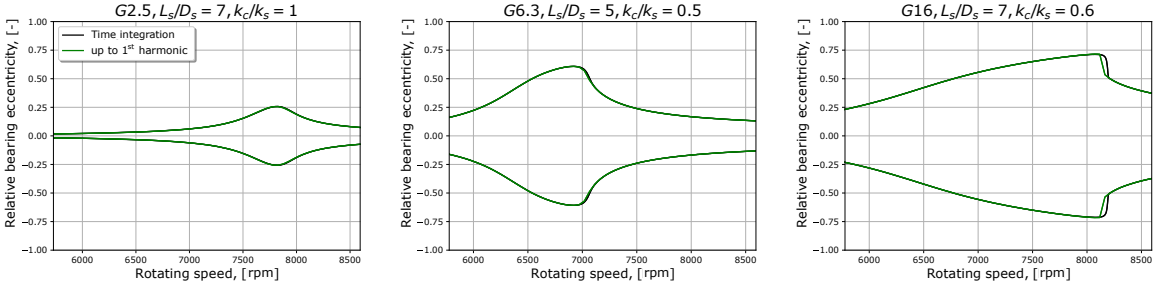

Figure 5: Comparison of the multi-harmonic method to transient analysis for circular centered orbits.

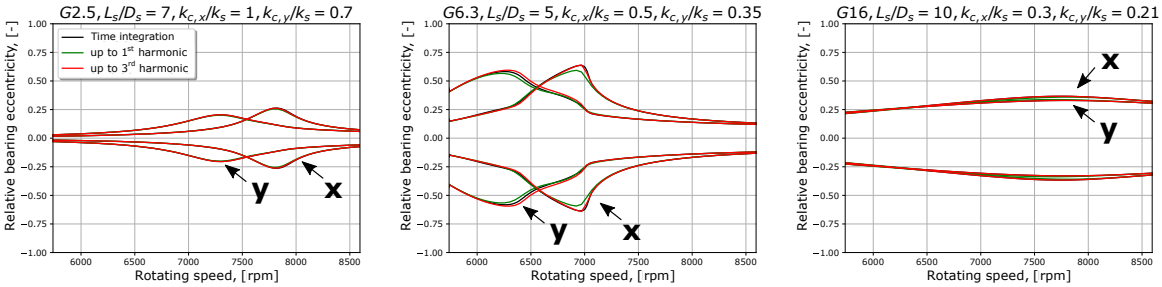

Figure 6: Comparison of the multi-harmonic method to transient analysis for elliptic centered orbits about the bearing center.

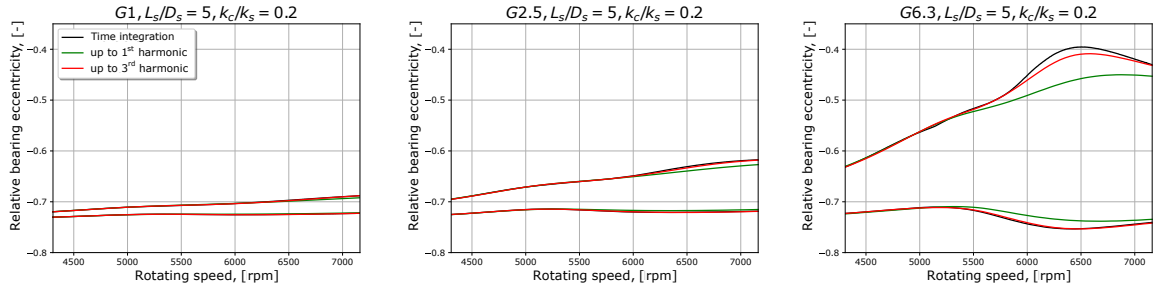

Figure 7: Comparison of the multi-harmonic method to transient analysis for off-centered orbits.

The multi-harmonic method is also validated by comparing its results to MSC Nastran nonlinear harmonic balance for a case of centered circular orbit. Hence, only the first-order harmonic is required. The two methods provide similar results, since the relative error is about 3% for both the disk and the journal response. However, this small error is due to a difference on the SFD geometry between the two models.

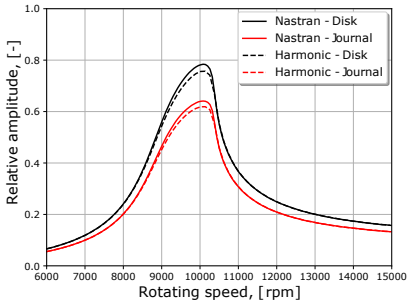

Figure 8: Comparison of the multi-harmonic method to MSC Nastran nonlinear harmonic balance.

5 Rotor Dynamic Simulations of Realistic Aircraft Engine

The simulations of the current Chapter concern the model of Figure 9. The jet engine consists of 2 counter-rotating rotors, Low Pressure (LP) rotor (in blue, yellow and magenta) and High Pressure (HP) rotor (in green), and the casing (in red). The speed ratio Ω_{HP}/Ω_{LP} equals to -1.6. There are three Low Pressure Compressor (LPC) stages and five High Pressure Compressor (HPC) stages, as well as one High Pressure Turbine (HPT) and one Low Pressure Turbine (LPT) stages. Their place is symbolized by black squares. The five bearings (B_1 - B_5) are depicted as light blue springs. The nodes where the bearings are connected to the rotor are symbolized by red squares. Finally, the grey dashed line is the centerline of the engine. Because of the symmetry about the centerline, only half the engine is depicted in Figure 9.

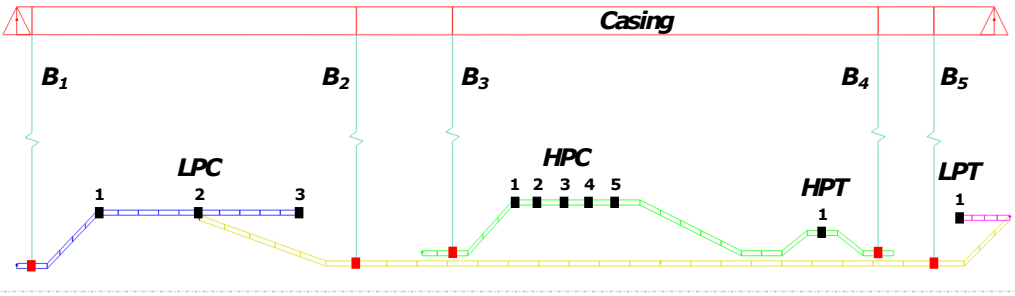

Figure 9: Realistic aircraft engine model.

The two rotors are dynamically decoupled. Henceforward, it is preferred to present results of the multi-harmonic method that concern the HP rotor, since the entire model has approximately 350 DoFs and the simulations are time-consuming, especially when multiple harmonics are used. The nonlinear multi-harmonic method is applied to the HP rotor for a variety of cases.

The parameters for the following simulations are:

1. the configuration of the bearings B_3 and B_4 that support the HP rotor. They may consist of a rigid or flexible squirrel cage and a SFD of constant or eccentricity dependent damping.
2. the weight of the rotor, that is included or not.
3. the unbalance case, either single or pair.
4. the number of orders for the multi-harmonic method.

Due to the high stiffness of the squirrel cages B_3 and B_4 and the low weight of the HP rotor, the static deflection is minimal. The maximum deflection of the rotor is 7.7% of the radial clearance and the static eccentricity of the journals B_3 and B_4 is 6.9% and 4.8%, respectively. All squirrel cages and rolling element bearings of the system are isotropic and the weight is negligible, thus the orbit is circular and the second-order harmonic, as well as higher-order harmonics, are insignificant. Hence, only the first-order harmonic is employed for the multi-harmonic method. The weight is not included in the simulations in order to compare the results of the method to those of linear harmonic analysis with constant coefficients.

Two cases are examined, one of single and one of pair unbalance. They both correspond to balance grade "G25", in order to provoke large eccentricities. For the nonlinear simulations using the multi-harmonic method, the bearing B_3 consists of a squirrel cage and a nonlinear SFD, while a squirrel cage and a SFD of constant damping are employed for the bearing B_4. An indicative value has been selected for the constant damping according to standard design. B_3 and B_4 squirrel cages have stiffness of $8 \cdot 10^7$ N/m and $1.5 \cdot 10^8$ N/m, respectively. For the linear simulations, a squirrel cage and a SFD of constant damping are employed for both bearings B_3 and B_4. The unbalance response of node 7 (first HPC stage) and node 21 (HPT stage) is presented in Figure 10.

The constant bearing damping is higher than required, therefore the results of the linear analysis underestimate the amplitudes. In particular, the values calculated are 2-2.5 times lower than the results of the nonlinear model. However, the critical speeds are sufficiently approximated by the linear analysis.

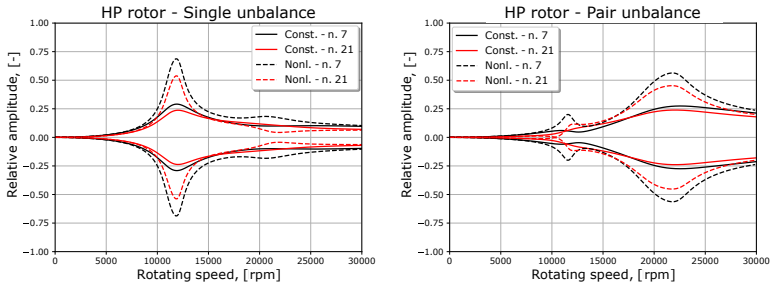

Figure 10: HP rotor unbalance response with constant and nonlinear bearings (SFD employed at B_3).

Subsequently, a nonlinear SFD is also employed for the bearing B_4. The rest of the parameters of the simulations remain the same.

Vast difference is observed between the results of the two methods. The use of two SFDs alters the quality of the unbalance response and shifts the critical speeds. The journals whirl at eccentricities close to the radial clearance ($> 90\% c_r$) and jump phenomena are observed.

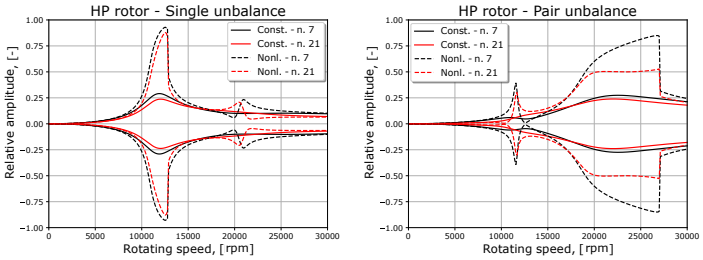

Figure 11: HP rotor unbalance response with constant and nonlinear bearings (SFD employed at B_3 and B_4).

Afterwards, a flexible squirrel cage of stiffness $3 \cdot 10^7$ N/m and a nonlinear SFD are employed for B_3, while a stiff squirrel cage of stiffness $1.5 \cdot 10^8$ N/m and constant damping are used for B_4. The weight of the HP rotor is intentionally doubled in order to provoke larger static deflection, which renders off-centered orbits and system anisotropy. The static eccentricity of the journals B_3 and B_4 is now 30.2% and 8.3% of the radial clearance, respectively, and the weight is included in the simulations. The unbalance response is approximated by the zeroth,

the first and the second-order harmonics. The unbalance response for balance grades G2.5 and G6.3 are presented in Figure 12.

One major resonance is observed at c.a. 6500 RPM for both nodes 7 and 21. The orbits are circular, but their centers are now located at $-28.4\%c_r$ and $-12.9\%c_r$, respectively. The effect of the second-order harmonic is minimal close to the resonance and its contribution is evaluated to be less than 1% of the radial clearance.

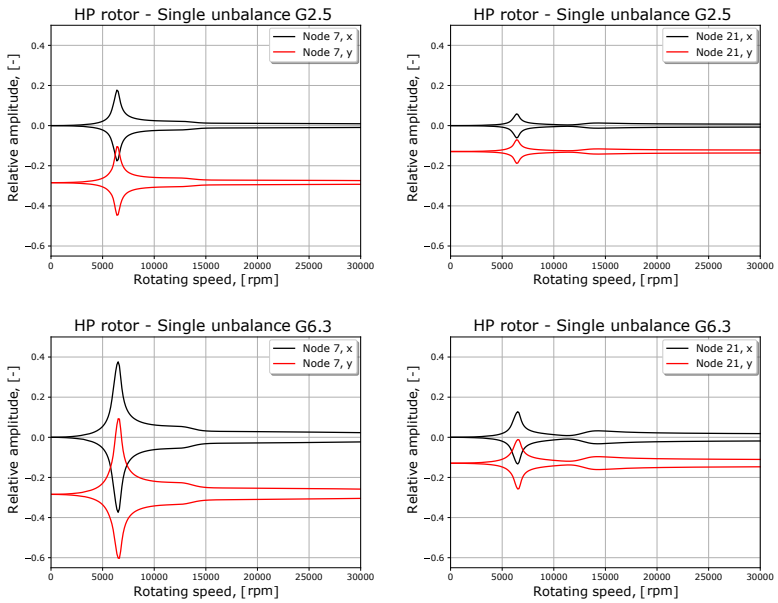

Figure 12: HP rotor single unbalance response with nonlinear bearings (SFD employed at B_3 and weight included).

The results of the multi-harmonic method are validated by comparing its results to MSC Nastran nonlinear harmonic balance for the cases examined in Figure 11. The difference between the results of the two methods is minimal and is possibly due to a small difference on the SFD geometry.

Moreover, the calculations of MSC Nastran nonlinear harmonic balance do not converge during the jump, therefore, the entire response is not displayed. On the contrary, the multi-harmonic method succeeds in passing through the jump.

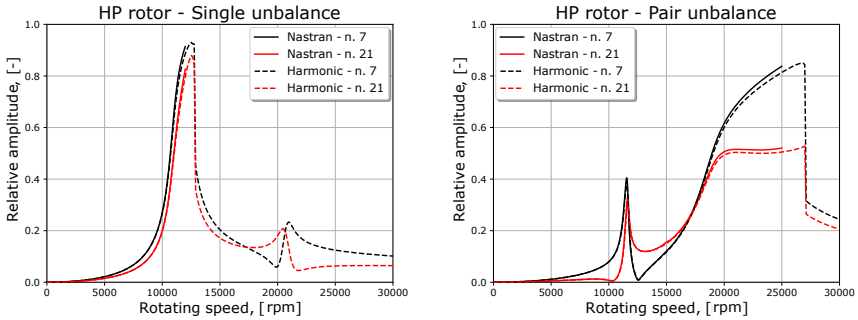

Figure 13: Comparison of the multi-harmonic method to MSC Nastran nonlinear harmonic balance.

6 Conclusion

The main problem examined in this paper is the treatment of nonlinear SFDs and bearings for simulations in the frequency domain. A new multi-harmonic method for the linearization of nonlinear bearing and SFD forces is presented. The main idea of the method is the approximation of nonlinear forces along the orbit and it is achieved using Discrete Fourier Transform. Subsequently, unbalance response is calculated by multi-harmonic analysis. The steps of the method are repeated until convergence in response amplitude is achieved, at each discrete rotating speed. Although nonlinear SFD forces are employed for the simulations of this paper, the method is general and can be used on any type and model of SFD or nonlinear bearing.

The method is tested on a Jeffcott rotor model and a realistic jet engine rotor. The results of the method are compared to those of linear harmonic analysis with constant bearing damping. It is shown that, in many cases, linear methods fail to predict engine's unbalance response, hence, it is necessary to resort to nonlinear methods, such as the multi-harmonic method. Small and large amplitudes, circular and elliptic, as well as centered and off-centered journal orbits are examined.

The method achieves to capture the transient response using only the first or the first three harmonics (along with zeroth order, which originates from the weight and the mean value of the forces). Specifically, the first-order harmonic is sufficient for circular centered orbits and only the odd-order harmonics are required for elliptic centered orbits.

Concerning off-centered orbits, there are no general rules concerning the requisite number of harmonics. Nevertheless, the first-order harmonic seems to be sufficient for off-centered circular orbits. The simulations on the Jeffcott rotor model showed that the second and the third-order harmonic majorly improve the approximation for off-centered elliptic orbits. However, higher-order harmonics do not influence significantly the response in the simulations on the HP rotor. All things considered, the first order, along with the zeroth order when weight is included, usually provides very good or, even, excellent approximation, while second and third-order harmonics are important for large orbits and small models. Extreme cases of static eccentricities and orbit radii close to the radial clearance can be an exception and even higher-order harmonics may be necessary.

All in all, the validity and the accuracy of the multi-harmonic method has been verified by conducting many simulations on a wide variety of models and conditions and comparing its results to transient response and MSC Nastran nonlinear harmonic balance.

The multi-harmonic method can be combined with linear analysis in order to avoid time-consuming calculations by making a first approximation of the unbalance response using linear simulations and, then, applying the multi-harmonic method close to the resonances. Finally, the method could be very useful during the preliminary rotor dynamic design stages of jet engines. The nonlinear method can be applied once in order to calculate forces exerted by the nonlinear bearings SFDs. After some minor changes to the model, a linear analysis can be applied using the recorded forces from the nonlinear simulation. Nevertheless, this method only works for similar rotors and bearings.

References

[1] Andrés, L. S. (2012): Damping and inertia coefficients for two open ends squeeze film dampers with a central groove: Measurements and predictions. *Journal of Engineering for Gas Turbines and Power*, **134**(10), 102506.

[2] Andrés, L. S. and Jeung, S.-H. (2015): Orbit-model force coefficients for fluid film bearings: A step beyond linearization. *Journal of Engineering for Gas Turbines and Power*, **138**(2), 022502.

[3] Andrés, L. S. and Seshagiri, S. (2013): Damping and inertia coefficients for two end sealed squeeze film dampers with a central groove: Measurements and predictions. *Journal of Engineering for Gas Turbines and Power*, **135**(11), 112503.

[4] Barrett, L. E. and Gunter, E. J. (1975): *Steady-state and transient analysis of a squeeze film damper bearing for rotor instability*. Report, University of Virginia, Charlottesville, Virginia.

[5] Ishida, Y. and Yamamoto, T. (2012): *Linear and Nonlinear Rotordynamics*. Wiley-VCH , Weinheim, Germany.

[6] Jung, S. Y. and Andrés, L. S. and Vance, J. M. (1991): Measurements of pressure distributions and force coefficients in a squeeze film damper Part I: Fully open ended configuration. *Tribology Transactions*, **34**(3), pp. 375–382.

[7] Jung, S. Y. and Andrés, L. S. and Vance, J. M. (1991): Measurements of pressure distributions and force coefficients in a squeeze film damper Part II: Partially sealed configuration. *Tribology Transactions*, **34**(3), pp. 383–388.

[8] Krodkiewski, J. M. and Sun, L. (1998): Modelling of multi-bearing rotor systems incorporating active journal bearing. *Journal of Sound and Vibration*, **210**(2), pp.215–229.

[9] Levesley, M. C. and Holmes, R., (1996): The effect of oil supply and sealing arrangements on the performance of squeeze-film dampers: An experimental study. *Proceedings of The Institution of Mechanical Engineers, Part J: Journal of Engineering Tribology*, **210**(4), pp. 221–232.

[10] Lund, J. W. (1987): Review of the concept of dynamic coefficients for fluid film journal bearings. *Journal of Tribology*, **109**(1), pp. 37–41.

[11] Nataraj, C. and Nelson, H. D. (1989): Periodic solutions in rotordynamic systems with nonlinear supports: A general approach. *Journal of Vibration and Acoustics*, **111**(2), pp. 187–193.

[12] Reinhardt, E. and Lund, J. W (1975): The influence of fluid inertia on the dynamic properties of journal bearings. *Journal of Lubrication Technology*, **97**(2), pp. 159–165.

[13] Sawicki, J. T. and Rao, T. V. V. L. N. (2001): Nonlinear prediction of rotordynamic coefficients for a hydrodynamic journal bearing. *Tribology Transactions*, **44**(3), pp. 367–374.

[14] Zeidan, F. Y. and Andrés, L. S. and Vance, J. M. (1996): *Design and Application of Squeeze Film Dampers in Rotating Machinery*. Texas A&M University, College Station, Texas.

[15] ISO 1940/1:2003(E) (2003): *Mechanical vibration - balance quality requirements for rotors in a constant (rigid) state - part 1: Specification and verification of balance tolerances*. Standard, International Organization for Standardization.

15th SIRM – European Conference on Rotordynamics,
Darmstadt, Germany, 22nd – 24th February 2023

Field balancing of flexible rotors without trial runs using the Numerical Assembly Technique

Georg Quinz [1], **Gregor Überwimmer** [1], **Michael Klanner** [1], **Katrin Ellermann** [1]

[1] Institute of Mechanics, Graz University of Technology, 8010, Graz, Austria, gquinz@tugraz.at

Abstract

The balancing of flexible rotor-bearing systems throughout multiple critical speeds is one of the most challenging tasks in rotor dynamics. The disadvantage of conventional balancing methods is that they require multiple trial runs, which are costly and time-consuming. Therefore, flexible rotor balancing methods based on the Numerical Assembly Technique (NAT) have been proposed in recent years, which substitute the measurement of influence coefficients with simulations. The advantages of NAT are that it leads to analytical solutions and is very computationally efficient.
The work aims to validate and improve the utility of NAT for the field balancing of flexible rotors. Therefore, a NAT simulation is used to balance the first two modes of a test bed without trial runs. The internal damping is included with a viscoelastic material model using fractional time derivatives. The mode shapes, eigenvalues and unbalance responses are measured and compared to values calculated with NAT, to show the accuracy of the simulation. The system is successfully balanced using influence coefficients calculated with NAT and a significant reduction of the vibration amplitude is achieved.

1 Introduction

Rotor bearing systems are balanced to avoid excessive vibration, which reduces the life span of machines. If the operational speed is in the proximity to or exceeds the first critical speed, flexible balancing techniques, like modal balancing [3] or the influence coefficient method [19], are necessary to reduce unbalance [20].
Traditional influence coefficient methods [19] require multiple trial runs, which are expensive and time-consuming. These trial runs are avoided if the influence coefficients are calculated with an accurate rotor-dynamic model [12]. In this paper, the Numerical Assembly Technique (NAT) is applied to determine influence coefficients. NAT is an efficient, quasi-analytic method to find the steady-state harmonic response and eigenvalues of rotor-bearing systems. It has been introduced in 1999 by Wu and Chou [24, 25]. The early versions of NAT are only capable of calculating the harmonic-response of one-dimensional structure, but in the last 20 years, the method has been significantly extended, especially in the field of rotor dynamics. The natural frequencies of uniform beams using NAT are determined by Chen and Wu [4, 5]. In [10] and [11], the method has been extended to include the effects of multiple lumped masses, multiple-pinned supports, and rotary inertias. Wang et al. applied these approaches to the Timoshenko beam theory and examined the effect of the slenderness ratio and the shear coefficient [23]. The effects of axial forces on Timoshenko [27] and Reddy-Bickford beams [28] has been studied by Yesilce. In 2014, NAT was extended to rotating systems and the forward and backward whirling speeds has been determined [26]. In [6], Timoshenko beams on elastic supports have been investigated and in [22] the effects of various material and geometric discontinuities have been examined using NAT. Klanner et al. extended NAT to include distributed loading [7], unbalance [8], and fractional derivative damping [9]. In recent years, Quinz et al. proposed a modal balancing technique [16] and an influence coefficient balancing technique [17] utilizing NAT. First experimental investigations concluded that the balancing procedure would benefit from the inclusion of additional damping effects like material or air damping [18].
The main aim of this work is to verify and improve the utility of an influence coefficient balancing method based on NAT. Multiple experiments are performed on a test bed, where measured and calculated values are compared and two test setups are balanced with the proposed method. The novelty of this work lies - besides the performed experiments - in the inclusion of partial time-derivative material parameters and air damping in the NAT scheme.

2 Methods

In this section, the proposed balancing method is described. It is a model-based influence coefficient method, where the influence coefficients are calculated with a simulation of the rotor-bearing system using NAT.

2.1 Numerical Assembly Technique

NAT uses a continuum model to calculate analytic solutions if the unbalance is introduced at concentrated points. For distributed unbalances it utilizes the Fourier extension method to generate semi-analytical results. Previous numeric simulations have shown that it can be used to accurately describe and balance linear rotor-bearing systems with stepped shafts and multiple disks, supported on roller bearings [16] or fluid film bearings [17] and excited by concentrated or distributed unbalances. The results of state-of-the-art FEM models converge with increasing amount of nodes to those obtained by NAT [17]. Furthermore, numerical comparisons show a reduction in computational time by a factor of ten compared to FEM [8].
The applied version of NAT improves upon the versions described in [16] and [18]. For better simulation accuracy, the Timoshenko beam theory is used instead of the Rayleigh theory, air damping is introduced and material damping is considered utilizing a fractional derivative damping model. In this paper, only the basic equations of NAT are briefly explained, a more detailed description of the applied version of NAT is found in [21].
The space fixed coordinate system *Oxyz* is defined according to Figure 1 so that *Ox* and *Oy* are perpendicular to each other and transverse to *Oz*, which passes the undeflected axis of the rotor in its bearings. In NAT, the rotor-

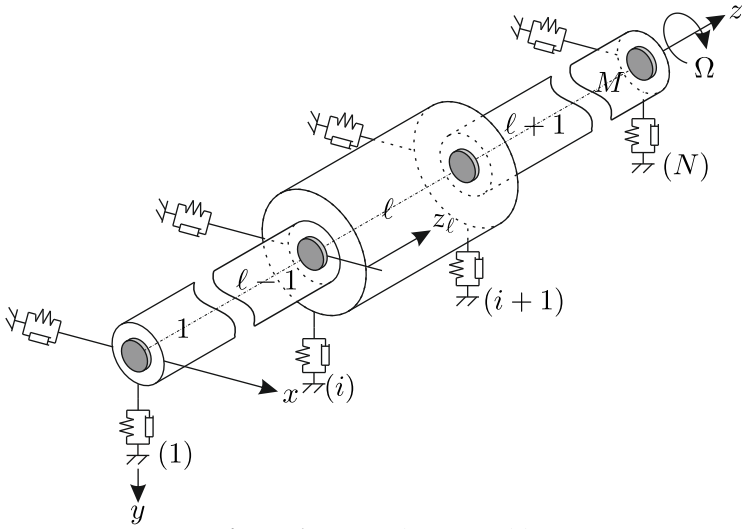

Figure 1: General rotor problem. [17]

bearing system is represented by N stations and $M = N - 1$ segments. Stations define disks, bearings, steps, and the ends of the rotor. Segments represent the cylindrical elements between the stations. For this paper, bearings are modeled as spin-speed independent spring and damper elements, although more complex representations are also possible with NAT [17]. Disks are defined with a mass $m^{(i)}$, a mass moment of inertia about the x- and y-axis $\Theta_t^{(i)}$, a mass moment of inertia about the z-axis $\Theta_p^{(i)}$, an amount of eccentricity $\epsilon^{(i)}$, and an angular position of eccentricity $\beta^{(i)}$. Segments are modeled according to the Timoshenko beam theory [2] and are described by the frequency-dependent complex Young's modulus $E_\ell^\star$, shear modulus G_ℓ, density ρ_ℓ, area of the cross-section A_ℓ, its diametric moment of area of the cross-section about the x- and y-axis I_ℓ, air damping coefficient $d_{a\ell}$ and the shear correction factor $k_{S\ell}$. Ω describes the constant spin speed of the system and ω its complex eigenvalue. In case of unbalance excitation $\Omega = \omega$. The state of the rotor is represented by a solution vector $\vec{x}$ consisting of the displacements r_x and r_y, the rotations of the cross-section φ_x and φ_y, the bending moments M_x and M_y and the shear forces Q_x and Q_y. The characteristic equations of the Timoshenko beam theory result from the equilibrium

conditions

$$\frac{\partial^2 \tilde{r}_x^+(z)}{\partial z^2} + \left(\bar{\omega}_\ell^2\, \bar{E}_{0\ell} - \bar{d}_{a\ell}\right) \tilde{r}_x^+(z) - \frac{\partial \tilde{\varphi}_y^+(z)}{\partial z} = -\frac{\bar{\Omega}_\ell^2\, \bar{E}_{0\ell}}{2} \tilde{\varepsilon}_+(z), \tag{1a}$$

$$\frac{\partial^2 \tilde{r}_y^+(z)}{\partial z^2} + \left(\bar{\omega}_\ell^2\, \bar{E}_{0\ell} - \bar{d}_{a\ell}\right) \tilde{r}_y^+(z) + \frac{\partial \tilde{\varphi}_x^+(z)}{\partial z} = \frac{\mathrm{j}\, \bar{\Omega}_\ell^2\, \bar{E}_{0\ell}}{2} \tilde{\varepsilon}_+(z), \tag{1b}$$

$$\frac{\partial^2 \tilde{\varphi}_y^+(z)}{\partial z^2} + \left(\bar{\omega}_\ell^2 - \frac{1}{\bar{E}_{0\ell}\, r_\ell^2}\right) \tilde{\varphi}_y^+(z) - \mathrm{j}\, \frac{\bar{E}_{1\ell}}{\bar{E}_{0\ell}} \frac{\partial^2 \tilde{\varphi}_{x\ell}^+(z)}{\partial z^2} + \mathrm{j}\, \bar{g}_\ell\, \tilde{\varphi}_x^+(z) + \frac{1}{\bar{E}_{0\ell}\, r_\ell^2} \frac{\partial \tilde{u}_x^+(z)}{\partial z} = 0, \tag{1c}$$

$$\frac{\partial^2 \tilde{\varphi}_x^+(z)}{\partial z^2} + \left(\bar{\omega}_\ell^2 - \frac{1}{\bar{E}_{0\ell}\, r_\ell^2}\right) \tilde{\varphi}_x^+(z) + \mathrm{j}\, \frac{\bar{E}_{1\ell}}{\bar{E}_{0\ell}} \frac{\partial^2 \tilde{\varphi}_{y\ell}^+(z)}{\partial z^2} - \mathrm{j}\, \bar{g}_\ell\, \tilde{\varphi}_y^+(z) - \frac{1}{\bar{E}_{0\ell}\, r_\ell^2} \frac{\partial \tilde{u}_y^+(z)}{\partial z} = 0, \tag{1d}$$

with

$$\bar{\omega}_\ell^2 = \frac{\omega^2\, \rho_\ell}{E_{0\ell}^\star}, \quad \bar{\Omega}_\ell^2 = \frac{\Omega^2\, \rho_\ell}{E_{0\ell}^\star}, \quad \bar{E}_{0\ell} = \frac{E_{0\ell}^\star}{G_\ell^\star\, k_{S_\ell}}, \quad \bar{E}_{1\ell} = \frac{E_{1\ell}^\star}{G_\ell^\star\, k_{S_\ell}},$$

$$\bar{d}_{a\ell} = \frac{\mathrm{j}\, \omega\, d_{a\ell}}{G_\ell^\star\, k_{S_\ell}\, A_\ell}, \quad r_\ell^2 = \frac{I_\ell}{A_\ell}, \quad \bar{g}_\ell = \frac{2\, \omega\, \rho_\ell\, \Omega}{E_{0\ell}^\star},$$

$$E_{0\ell}^\star = (a_0^E + \frac{a_1^E}{2}\left((\mathrm{j}\,(\omega-\Omega))^{\alpha_\ell^E} + (\mathrm{j}\,(\omega+\Omega))^{\alpha_\ell^E}\right)), \quad E_{1\ell}^\star = \frac{a_1^E}{2}\left(\mathrm{j}\,(\omega-\Omega)\right)^{\alpha_\ell^E} - (\mathrm{j}\,(\omega+\Omega))^{\alpha_\ell^E}.$$

Assuming a solution of the form of

$$r_{x\ell} = \tilde{r}_{x\ell}^+ \mathrm{e}^{\mathrm{i}\omega t} + \tilde{r}_{x\ell}^- \mathrm{e}^{-\mathrm{i}\omega t} \tag{2a}$$

$$r_{y\ell} = \tilde{r}_{y\ell}^+ \mathrm{e}^{\mathrm{i}\omega t} + \tilde{r}_{y\ell}^- \mathrm{e}^{-\mathrm{i}\omega t} \tag{2b}$$

$$\varphi_{x\ell} = \tilde{r}_{x\ell}^+ \mathrm{e}^{\mathrm{i}\omega t} + \tilde{\varphi}_{x\ell}^- \mathrm{e}^{-\mathrm{i}\omega t} \tag{2c}$$

$$\varphi_{y\ell} = \tilde{r}_{y\ell}^+ \mathrm{e}^{\mathrm{i}\omega t} + \tilde{\varphi}_{y\ell}^- \mathrm{e}^{-\mathrm{i}\omega t} \tag{2d}$$

leads to eight ordinary differential equations. Since the solutions have to be complex conjugated to get a real solution only four of these equations are necessary and only the equations with the $+$-index are considered

$$\frac{\partial^2 \tilde{r}_{x\ell}^+(z)}{\partial z^2} + (\overline{\omega}_\ell^2 - \overline{d}_{e\ell})\overline{r}_{x\ell}^+(z) - \frac{\partial \tilde{\varphi}_y^+(z)}{\partial z} = -\frac{\overline{\Omega}_\ell^2}{2} \epsilon(z) \mathrm{e}^{\mathrm{i}\beta(z)}, \tag{3a}$$

$$\frac{\partial^2 \tilde{r}_{y\ell}^+(z)}{\partial z^2} + (\overline{\omega}_\ell^2 - \overline{d}_{e\ell})\overline{r}_{y\ell}^+(z) + \frac{\partial \tilde{\varphi}_x^+(z)}{\partial z} = \mathrm{i}\frac{\overline{\Omega}_\ell^2}{2} \epsilon(z) \mathrm{e}^{\mathrm{i}\beta(z)}, \tag{3b}$$

$$\overline{E}_{0\ell} \frac{\partial^2 \tilde{\varphi}_{y\ell}^+(z)}{\partial z^2} + (\overline{\omega}_\ell^2 - \frac{A_\ell}{I_\ell})\overline{\varphi}_{y\ell}^+(z) - \mathrm{i}\overline{E}_{1\ell} \frac{\partial^2 \tilde{\varphi}_{x\ell}^+(z)}{\partial z^2} + \mathrm{i}2\rho\omega\Omega\tilde{\varphi}_x^+(z) + \frac{A_\ell}{I_\ell} \frac{\partial \tilde{r}_{x\ell}^+(z)}{\partial z} = 0, \tag{3c}$$

$$\overline{E}_{0\ell} \frac{\partial^2 \tilde{\varphi}_{x\ell}^+(z)}{\partial z^2} + (\overline{\omega}_\ell^2 - \frac{A_\ell}{I_\ell})\overline{\varphi}_{x\ell}^+(z) + \mathrm{i}\overline{E}_{1\ell} \frac{\partial^2 \tilde{\varphi}_{x\ell}^+(z)}{\partial z^2} - \mathrm{i}2\rho\omega\Omega\tilde{\varphi}_y^+(z) - \frac{A_\ell}{I_\ell} \frac{\partial \tilde{r}_{y\ell}^+(z)}{\partial z} = 0. \tag{3d}$$

The total solution vector of each rotor segment is the sum of the homogeneous and the particular solution $\vec{x}_\ell(z_\ell) = \vec{x}_{h\ell}(z_\ell) + \vec{x}_{p\ell}(z_\ell)$. Point unbalances or distributed unbalances are considered in the particular solution. Assembling the characteristic equations of each segment with the boundary and interface conditions results in a system of linear equations

$$\underline{\underline{A}}\vec{c} = \vec{b}, \tag{4}$$

where $\underline{\underline{A}}$ is the system matrix, $\vec{b}$ the right-hand side vector and $\vec{c}$ a vector of unknown constants. The unknown constants $\vec{c}$ determine the total solution vector $\vec{x}$, which defines the behaviour of the rotor.

2.2 Fractional derivative damping model

This paper utilizes an effective four-parameter fractional derivative damping model developed by Pritz et al. [15], a generalization of the Zener material model. The fractional Zener model has the advantage, that it accurately describes materials over a wide frequency range. In contrast to the hysteric damping model, the Zener model is also capable of representing a nearly frequency-independent, low loss factor [15]. In the time domain, the constitutive equation is

$$\sigma_{zz}(x,y,z,t) + b_{0\ell}^{E} \frac{\partial^{\alpha_\ell^E} \sigma_{zz}(x,y,z,t)}{\partial t^{\alpha_\ell^E}} = a_{0\ell}^{E} \varepsilon_{zz}(x,y,z,t) + a_{1\ell}^{E} \frac{\partial^{\alpha_\ell^E} \varepsilon_{zz}(x,y,z,t)}{\partial t^{\alpha_{0\ell}^E}}, \tag{5}$$

with $a_{0\ell}^{E}, a_{1\ell}^{E}, b_{0\ell}^{E}$ as positive real constants and the restrictions

$$a_{0\ell}^{E} < \frac{a_{1\ell}^{E}}{b_{0\ell}^{E}}, \qquad\qquad 0 < \alpha_\ell^E < 1.$$

$\frac{\partial^\bullet}{\partial t^\bullet}$ denotes a fractional derivative, which has multiple different mathematical definitions in literature. The Riemann-Liouville definition is applied in this work since it allows for a simple representation of the four-parameter model in the frequency domain. Setting $b_{0\ell}^{E} = 0$ in Equation (5) to acquire the fractional Kelvin-Voigt model results in

$$E_{\pm\ell}^{\star}(\omega) = a_{0\ell}^{E} + (\mathrm{j}\,(\omega \mp \Omega))^{\alpha_\ell^E}\, a_{1\ell}^{E}, \quad G_{\ell}^{\star}(\omega) = \frac{1}{2(1+\nu)}\, a_{0\ell}^{E} + (\mathrm{j}\,\omega)^{\alpha_\ell^E}\, a_{1\ell}^{E}, \tag{6}$$

where $E_{\pm\ell}^{\star}(\omega)$ is the complex Young's modulus, $G_{\ell}^{\star}(\omega)$ the complex shear modulus, and ν the Poisson's ratio. The parameters $a_{0\ell}^{E}$, $a_{1\ell}^{E}$ and α_ℓ^E are derived by measurements and are available for many commonly used materials [14].

2.3 Influence coefficient method

The influence coefficient method [19] enables the balancing of flexible rotor-bearing systems as long as they have a linear force-displacement behaviour. Influence coefficients $\alpha_{ik}(\Omega)$ describe the ratio of displacement to unbalance

$$\alpha_{ik}(\Omega) = \frac{x_i(\Omega)}{U_k}, \tag{7}$$

where $x_i(\Omega)$ is the displacement at position i caused by an unbalance U_k at position k. Influence coefficients are usually measured, which is very costly and time-consuming. In this paper, influence coefficients are instead calculated with NAT. The influence coefficients of all combinations of unbalance planes k and measurement planes i are called influence coefficient matrix $\underline{\underline{\alpha}}$

$$\vec{x} = \underline{\underline{\alpha}} \vec{U}, \tag{8}$$

where $\vec{x}$ are the displacements of the rotor-bearing system caused by the addition of test weights and $\vec{U}$ is the unbalance vector. By inverting the influence coefficient matrix the initial unbalance is determined from the initial unbalance response

$$\vec{U}_c = -\underline{\underline{\alpha}}^{-1} \vec{x}_0, \tag{9}$$

where $\vec{U}_c$ are the correction unbalances, and $\vec{x}_0$ are the displacements of the rotor bearings system without test weights. Mounting the correction unbalances reduces the vibration of the system. Surplus information of additional measurement planes or spin speeds can be included with the least-squares method [13].

3 Results and Discussion

In this section, the rotor-dynamic test bed, its NAT model and the performed experiments are described. First, the eigenvalues and mode shapes are measured and compared to calculations, then, the proposed balancing technique is applied to balance the first mode and later, the first two modes of a test setup.

3.1 Test bed

The rotor dynamic test bed of the Institute of Mechanic of the Graz University of Technology is shown in Figure 2. An elastic shaft with a maximal diameter of 15 mm, on which an arbitrary amount of disks can be mounted, is supported on two roller bearings. Since the supports are much stiffer than the isotropic shaft, the anisotropy of the bearing housing is negligible for the balancing process. The shaft is connected through a magnetic coupling to an electrical motor with a maximum spin speed of 400 Hz and a power of 7 kW. Four laser displacement measurement systems with an accuracy of 0.025 μm determine the unbalance response. The phase is measured with an inductive sensor that works up to 120 Hz. During operation, the test bed is secured by two safety bearings and a blast protection. All calculations are performed on an *Intel*® Core™ i7-8700 CPU with 3.2 GHz running on a Windows

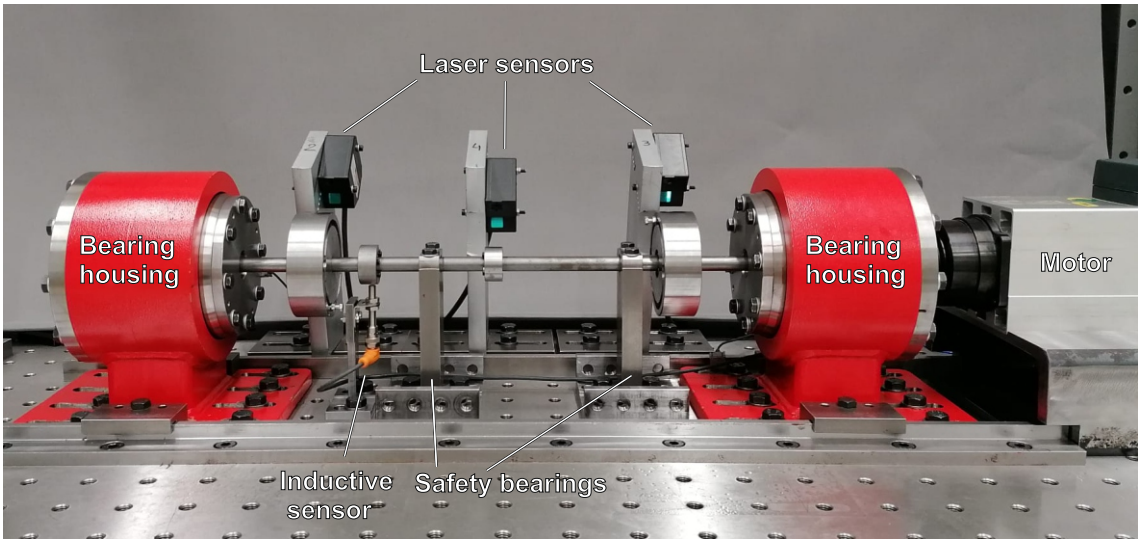

Figure 2: Rotordynamic test bed of the Institute of Mechanik of the University of Technology Graz without blast protection.

10 operating system using MATLAB™ version R2019a. For the experiments, five disks of different weights are mounted on the shaft. As is illustrated in Figure 3, weights can be mounted on two of these disks, at a radius of 42.5 mm. To maximise the effect of material damping on the rotor-bearing system, external damping is minimized, by using roller bearings and no external damping elements. Even without mounting unbalance weights, the rotor is excited by a bow of the shaft. The slow-roll bow is shown in Table 1. NAT is designed for straight rotor-bearing systems. To show that it also works reasonably well for warped shafts, the initial bow is considered in a simplified manner: The slow-roll bow is deducted at measurements before the first critical speed. At supercritical speeds, self-centering of the shaft occurs and the initial bend of the shaft is neglected.

Table 1: Bow of the pre-bent shaft.

	Left disk	Right disk
Axial position	88 mm	448 mm
Bow	0.08694 mm	0.11108 mm
Angular position	173.91°	196.53°

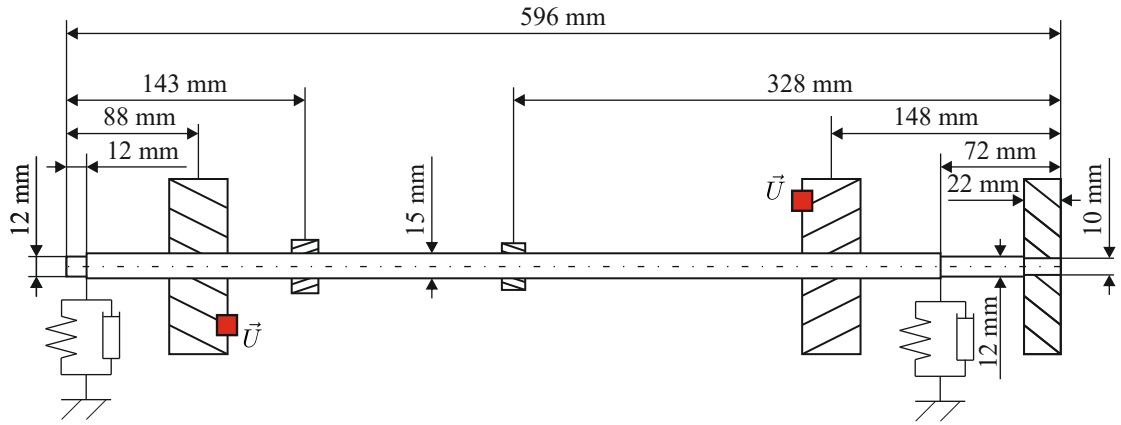

Figure 3: Setup of the test bed.

3.2 Rotor model

A mathematical model of the test bed is built with a NAT simulation. The stations of the NAT model are modelled according to Table 2, where z is the axial position, m the mass of the disks, Θ_{xy} the angular mass of the disk about the x- and y-axis, Θ_{zz} the angular mass about the z-axis, c_x the bearing stiffness in x-direction, c_y the bearing stiffness in y-direction and d the damping coefficient of the bearing. The cylindrical segments of the rotor

Table 2: Stations of the NAT model

z	m	Θ_{xy}	Θ_{zz}	c_x	c_y	d
m	kg	kg m^2	kg m^2	N/m	N/m	Ns/m
0	0	0	0	0	0	0
0.008	0	0	0	282540000	129968400	80
0.012	0	0	0	0	0	0
0.088	2.0200	0.00150	0.0028	0	0	0
0.143	0.1300	2.139×10^{-5}	3.4589×10^{-5}	0	0	0
0.268	0.0926	1.297×10^{-5}	1.9986×10^{-5}	0	0	0
0.448	2.0200	0.00150	0.0028	0	0	0
0.524	0	0	0	0	0	0
0.528	0	0	0	282540000	129968400	80
0.574	0.6471	0.0020322	0.00034134	0	0	0
0.596	0	0	0	0	0	0

are modelled with a density of 7700 $\mathrm{kg/m^3}$, a shear modulus of $8.1 \times 10^{11}\mathrm{N/m}$, a shear correction factor of 0.89, an air damping coefficient of 45 $\mathrm{Ns/m}$ and the fractional derivative damping parameters $a_0^E = 2.2 \times 10^{11}\mathrm{N/m}$, $a_1^E = 6.887 \times 10^9$, $b_0^E = 0$ and $\alpha^E = 0.3$. The unbalance of the test bed is unknown and therefore not included in the model.

3.3 Eigenfrequencies and mode shapes

As first step, the accuracy of the simulation is investigated by comparing the measured and calculated eigenvalues and mode shapes. Using a recursive search algorithm described in [16] and [17], the eigenvalues of the system are found at 59.107Hz and 145.483 Hz. As is seen in Figure 4, these values correlate with the measured excitation of the test bed at the left disk (without any additional weights), although a precise measurement of the critical speeds is not possible without balancing. The dimensionless mode shapes of the NAT calculation are also compared to measurements near the critical speeds at the axial positions $z = 0.088$ m, 0.268 m and 0.448 m in Figure 5. The NAT calculation of the test bed agrees with the measurements and can be utilized for balancing in the following experiments.

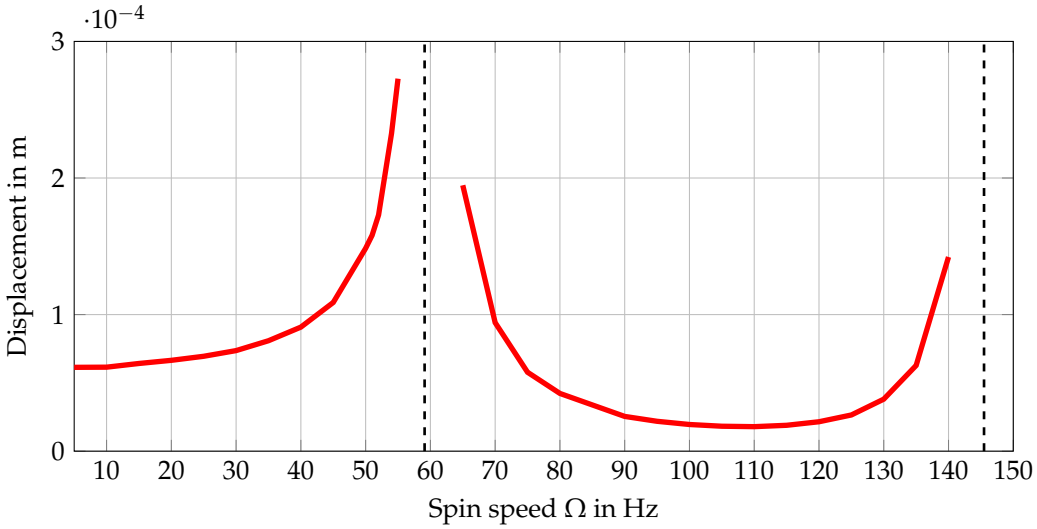

Figure 4: Unbalance response due to residual unbalance and initial bow of the rotor.

1

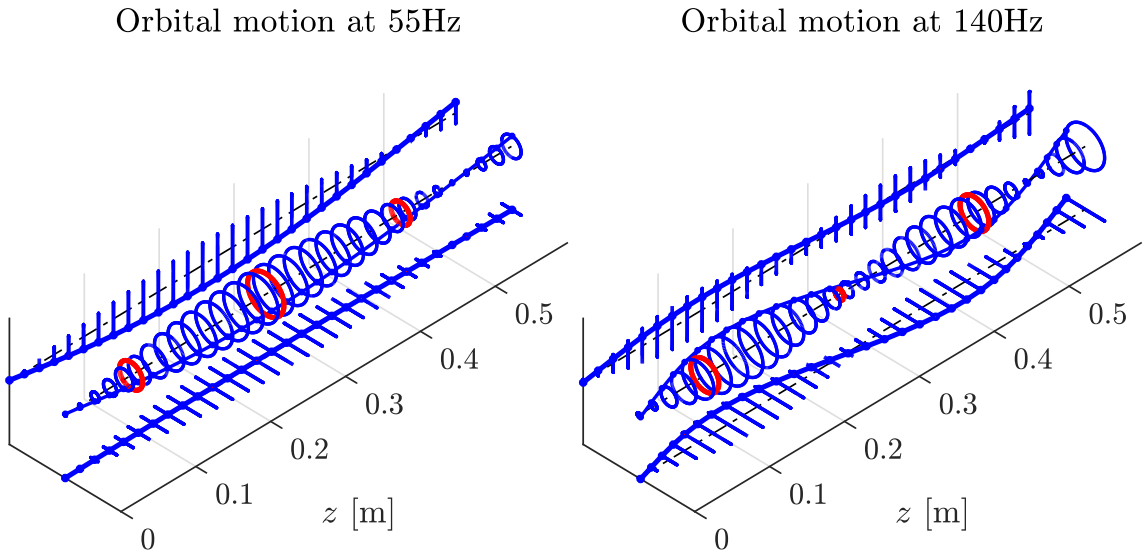

Figure 5: Comparison of mode shapes: NAT calculation in blue, measurements in red.

3.4 Balancing of 1 mode

For the first balancing test, no unbalance weights are mounted and the rotor is only excited through the eccentricity of the shaft and disks. In order to be able to easily compare the proposed balancing technique with established techniques, the system is balanced below the first eigenvalue. First, the initial vibration of the left disk is measured at 50 Hz. This is the only measurement necessary for the proposed method, which calculates the influence coefficients and the balancing weight within a total computation time of 0.019152 s. For comparison, six trial runs are performed to balance the system with a rigid balancing technique. In Table 3, the results of both approaches are compared. Both methods lead to similar results, indicating that NAT simulations are capable of substituting test runs. Mounting a balancing weight of 5.57 g at the left disk at the 356° position and at the right disk at the 328° leads to a significant reduction of vibration, as is seen in Figure 6. The amplitude of vibration due to unbalance at 50 Hz is reduced by 77.4% at the central disk.

3.5 Balancing of 2 modes

In the second balancing test, two modes of the system are balanced. To increase the excitation of the second mode, additional unbalance weights of 5.57g are mounted on a radius of 42.5mm on the left balancing disk at the

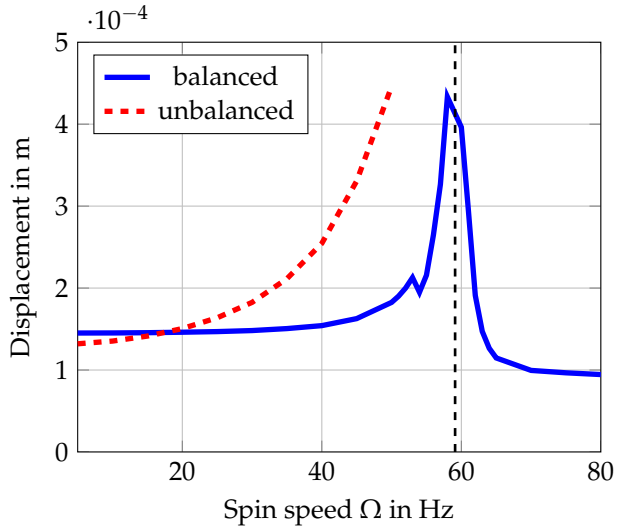

Figure 6: Balancing success of the first example at the central disk.

Table 3: Balancing weights of the first example

	NAT	Rigid balancing
Left	4.57 g	5.24 g
	355.94°	355.32°
Right	6.31 g	5.57 g
	328.04°	351.87°

0° position and at the right balancing disk at the 180° position. The unbalance response of the test bed is measured at 50 Hz and 119 Hz. The influence coefficients and balancing weights, shown in Table 4, are calculated with NAT in 0.030204 s. Mounting the calculated balancing weights on the listed positions leads to a significant reduction of

Table 4: Balancing weights of the second example.

	Left disk	Right disk
Amount	2.2229 g	10.6788 g
Position	21.205°	353.369°

vibration for the first two modes, as is shown in Figure 7.

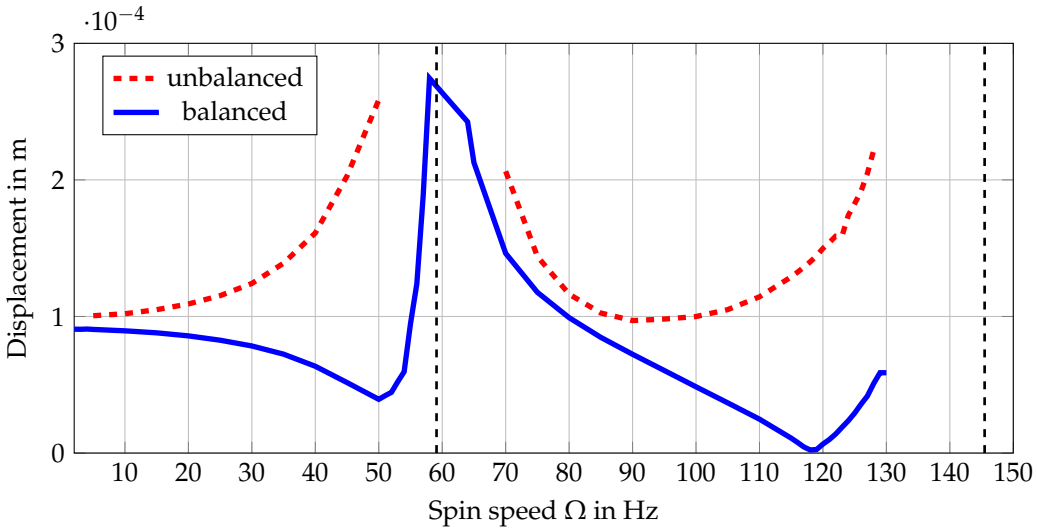

Figure 7: Balancing success of the second example at the left disk.

The reduction of vibration amplitude is catalogued in Table 5. The remaining vibration is caused to a significant part by the bow of the shaft, which is not influenced by balancing weights.

Table 5: Reduction of the vibration of the second example.

	Left disk	Right disk
50 Hz	84.78%	77.29%
128 Hz	77.04%	20.67%

3.6 Next steps

Although NAT assumes a straight rotor, a warped shaft can also be balanced reasonably well, when the initial bow is considered in a simplified manner. Nevertheless, the research indicates that the balancing success could be improved when the influence of warped shafts is introduced into the NAT scheme. Further experimental investigations should focus on systems with higher damping to examine the accuracy of the NAT simulation at critical speeds. Also, the balancing of flexible shafts supported on fluid film bearings using NAT has been performed only numerically and should be verified experimentally in future research. The influences of bearing pedestals and foundations are also worth investigating.

4 Conclusion

In this paper, the utility of a model-based balancing approach using the Numerical Assembly Technique (NAT) has been investigated on a test bed. Eigenvalues and mode shapes calculated with NAT agree with measured values. In a first balancing test, balancing weights calculated with NAT correspond closely to balancing weights found using trial runs. In a second balancing test, the first two modes of a rotor-bearing system were successfully balanced with the proposed method, leading to a reduction of vibration amplitude of up to 84.78%. The proposed method is very computationally efficient with calculation times below 0.05s to find the influence coefficients and balancing weights of both experiments. The presented experiments indicate that the proposed method can be successfully applied to balance flexible rotor-bearing systems without trial runs.

References

[1] Bagley, R. L. and Torvik, P. J. (1983): A theoretical basis for the application of fractional calculus to viscoelasticity. *Journal of Rheology,* 27(3), pp. 201-210.

[2] Bauchau, O.A. Craig, J.I. (2009): *Structural Analysis - With Applications to Aerospace Structures*. Springer Verlag, Heidelberg.

[3] Bishop, R.E.D. and Gladwell, G. M.L.,(1959): The Vibration and Balancing of an Unbalanced Flexible Rotor. *Journal Mech. Eng. Soc.,* 1, pp. 66–77.

[4] Chen, D.-W. and Wu, J.-S. (2003): The exact solutions for the natural frequencies and mode shapes of non-uniform multi-span beams carrying multiple various concentrated elements. *Structural Eng. Mech. Int. J.,* 16 (2), pp. 153-176.

[5] Chen, D.-W. (2006): The exact solutions for free vibration of uniform beams carrying multiple two-degree-of-freedom spring-mass systems. *J. Sound Vib.,* 295, pp. 342–361.

[6] Farghaly, S.H. and El-Sayed, T.A. (2016): Exact free vibration of a multi-step Timoshenko beam system with several attachments. *Mech. Syst. Signal Process.,* 72, pp. 525-546.

[7] Klanner M. and Ellermann K. (2020): Steady-state linear harmonic vibrations of multiple-stepped Euler-Bernoulli beams under arbitrarily distributed loads carrying any number of concentrated elements. *Applied and Computational Mechanics,* 14 (1), pp. 31–50

[8] Klanner M., Prem M. S. and Ellermann K. (2020): Steady-state harmonic vibrations of a linear rotor- bearing system with a discontinuous shaft and arbitrarily distributed mass unbalance. In *Proceedings of ISMA2020 International Conference on Noise and Vibration Engineering and USD2020 International Conference on Uncertainty in Structural Dynamics*. Leuven, Belgium, Sept. 7-9, pp. 1257–1272.

[9] Klanner, M. and Prem, M.S. and Ellermann, K. (2021): Steady-State Harmonic Vibrations of Viscoelastic Timoshenko Beams with Fractional Derivative Damping Models. *Appl. Mech.,* 2, pp. 789-819.

[10] Lin, H.-Y. and Tsai, Y.-C. (2006): On the natural frequencies and mode shapes of a multi-step beam carrying a number of intermediate lumped masses and rotary inertias. *Structural Eng. Mech. Int. J.,* 22, pp. 701–717.

[11] Lin, H.-Y. and Tsai, Y.-C. (2007): Free vibration analysis of a uniform multi-span beam carrying multiple spring-mass systems. *Structural Eng. Mech. Int. J.,* 302, pp. 442-456.

[12] Nordmann, R. and Knopf, E. and Abrate, B. (2018): Numerical Analysis of the Influence Coefficient Matrix for On-Site Balancing of Flexible Rotors. In *Proceedings of the 10th International Conference on Rotor Dynamics,* Rio de Janero, pp. 152-172.

[13] Nordmann, R. and Knopf, E. and Krueger, T. (2021): Balancing of Flexible Rotors by means of Calculated Influence Coefficients. In *Proceedings of the SIRM 2021 International Conference on Dynamics of Rotating Machinery,* Gdansk, Poland, February 17-19, pp. 1–13.

[14] Prem, M. S. and Klanner, M. and Ellermann, K. (1996): Identification of Fractional Damping Parameters in Structural Dynamics Using Polynomial Chaos Expansion. *Applied Mechanics,* 2(4), pp. 956-975.

[15] Pritz, T. (1996): Analysis of four-parameter fractional derivative model of real solid materials. *Journal of Sound an Vibration,* 195(1), pp. 103-115.

[16] Quinz, G., Prem, M.S., Klanner, M. and Ellermann, K. (2021): Balancing of a linear elastic rotor-bearing system with arbitrarily distributed unbalance using the Numerical Assembly Technique. *Bull. Pol. Acad. Sci. Tech. Sci.,* 69, pp. e138237.

[17] Quinz, G., Klanner, M. and Ellermann, K. (2022): Balancing of Flexible Rotors Supported on Fluid Film Bearings by Means of Influence Coefficients Calculated by the Numerical Assembly Technique. *Energies,* 15 (6), pp. 2009.

[18] Quinz, G., Klanner, M. and Ellermann, K. (2022): Balancing of rotor-bearing systems without trial runs using the Numerical Assembly Technique - An experimental investigation. In *Proceedings of ISMA2022 International Conference on Noise and Vibration Engineering and USD2022 International Conference on Uncertainty in Structural Dynamics*. Leuven, Belgium, Sept. 12-14, pp. 1542-1553

[19] Thearle, E.L. (1934): Dynamic Balancing of Rotating Machinery in the Field. *Trans. ASME,* 56, pp. 745-753.

[20] Tessarzik J. (1972): *Flexible rotor balancing by the exact point speed influence coefficient method*. Mechanical Technology Incorporated, Latham

[21] Überwimmer G., Quinz, G., Klanner, M. and Ellermann, K. (2023): Numerical investigation of rotor-bearing systems with fractional derivative material damping models. In *Proceedings of the SIRM 2023 International Conference on Dynamics of Rotating Machinery,* Darmstadt, Germany, February 22-24

[22] Vaz, J.D.C. and de Lima junior, J.J.(2016): Vibration analysis of Euler–Bernoulli beams in multiple steps and different shapes of cross section. *J. Vib. Control.,* 22, pp. 193–204.

[23] Wang, J.-R. and Liu, T.-L. and Chen, D.-W. (2007): Free vibration analysis of a Timoshenko beam carrying multiple sping mass systems with the effect of shear deformation and rotary inertia. *Structural Eng. Mech. Int. J.,* 26, pp. 1–14.

[24] Wu. J.-S. and Chou H. M. (1999): A new approach for determining the natural frequency of mode shapes of a uniform beam carrying any number of sprung masses. *Journal of Sound and Vibration,* 220 (3), pp. 451–468.

[25] Wu, J.-S. and Chen, D.-W. (2001): Free vibration analysis of a Timoshenko beam carrying multiple spring masses by using the numerical assembly technique. *Int. J. Numer. Methods Eng.,* 50, pp. 1039–1058.

[26] Wu J.-S.,Lin F.-T. and Shaw H.-J.(2014): Analytical Solution for Whirling Speeds and Mode Shapes of a Distributed-Mass Shaft With Arbitrary Rigid Disks. *Journal of Applied Mechanics,* 81 (3), pp. 034503-1–034503-10

[27] Yesilce, Y. and Demirdag, O. (2008): Effect of axial force on free vibration of Timoshenko multi-span beam carrying multiple spring-mass systems. *Int. J. Mech. Sci.,* 50, pp. 995–1003.

[28] Yesilce, Y. (2011): Free Vibrations of a Reddy-Bickford Multi-span Beam Carrying Multiple Spring-mass Systems. *Journal of Shock and Vibration,* 18, pp. 709–726.

15th SIRM – European Conference on Rotordynamics,
Darmstadt, Germany, 22nd – 24th February 2023

Investigations on Laterally Coupled Rotor-Blade-Vibrations

Schlesier K.-D [1], **Levin Rojas R.** [2], **Panning-von Scheidt L.** [3], **Ehehalt U.**[4]

[1] Institute of Dynamics and Vibration Research, Leibniz University Hannover, 30823, Garbsen, Germany, schlesier@ids.uni-hannover.de
[2] Siemens Energy, 45473 , Mülheim, Germany, roland.grein@siemens-energy.com
[3] Institute of Dynamics and Vibration Research, Leibniz University Hannover, 30823, Garbsen, Germany, panning@ids.uni-hannover.de
[4] Siemens Energy, 45473 , Mülheim, Germany, ulrich.ehehalt@siemens-energy.com

Abstract

Typically, the dynamic/mechanical analysis of turbomachinery systems is divided into rotordynamics, which focuses on the shaft-bearing system with simplified blade, disks and beam elements, and blade dynamics, which deals with isolated bladed disks. This division into two separate sections significantly simplifies the modelling and calculation effort. It is permissible as long as the natural frequencies of the two subsystems are well separated and their coupling is sufficiently weak, so that the mutual influence is negligibly small. Recent trends towards steam turbines with longer blades with lower natural frequencies and lighter rotors with higher natural frequencies increase the importance of a combined analysis of both subsystems.

In [1] vibration measurement results were presented which show increased blade amplitudes when the rotating frequency reaches half of the nodal diameter 1 resonance frequency of the blades. At the same time, a significant dip of the shaft lateral vibrations was observed at the bearings which was not predicted. This implies an interrelationship between rotor and blade vibrations.

The authors of [1] were able to reproduce these rotor unbalance induced blade vibrations with a numerical simulation of a coupled rotor-blade-model. As a next step the exact circumstances and conditions, which are responsible for the described behaviour, have to be determined. In this paper, further investigations on the aforementioned industrial rotor-blade-model are carried out to gain a better understanding on the effects of rotor-blade-coupling. The system is used as a starting point to derive the relevant parameters for the observed rotor-blade-interaction. The findings are then applied to a simplified rotor-blade-model to validate their impact on the systems behaviour. Besides steady state simulations also transient resonance passages will be investigated.

1 Introduction

Coupling between modes of a bladed disk and the shaft only occurs when the subsystems are able to exchange energy with each other. Only certain combinations of rotor and blade vibrations comply with this condition. Following coupling effects are possible for a system with identical and equispaced blades [2]:

1. Torsional shaft vibrations are coupled with a uniform circumferential vibration of the blades with nodal diameter 0 (ND 0).
2. Axial shaft vibrations are coupled with umbrella-like (ND 0) out-of-plane vibrations of the blade row.
3. Flexural lateral shaft vibrations are coupled with ND 1 in-plane vibrations of the blades.
4. Tilting vibrations of the shaft are coupled with ND 1 out-of-plane vibrations of the blades.

Modes with higher blade nodal diameters are not coupled with the shaft vibration. Fig. 1 illustrates case 3. The amplitude distributions for the first three nodal diameters are plotted for an exemplary bladed disk in individual blade coordinates and in coordinates fixed at the centre of the disk. Only the ND 1 mode has a mean amplitude different from zero in the disk coordinate system. The phase shift of $180°$ for opposing blades causes them to vibrate in the same direction, when viewed from the disk centre. This means the center of mass of the blade row changes with the blade vibration and therefore has an impact on the overall dynamics of the shaft-blade-system, the vibrations are coupled. With all higher nodal diameters the individual blade deflections sum up to balance out

each other again so the dynamics of the shaft are not influenced by higher ND vibrations of the blades. The same can be shown for case 4. Only when opposing blades vibrate with 180° phase shift the individual inertias do not compensate each other but sum up and cause tilting of the shaft.

The above exactly holds true in the case where all blades are identical. Nevertheless, taking misstuning into account, the coupling of higher nodel dameter is still negligible.

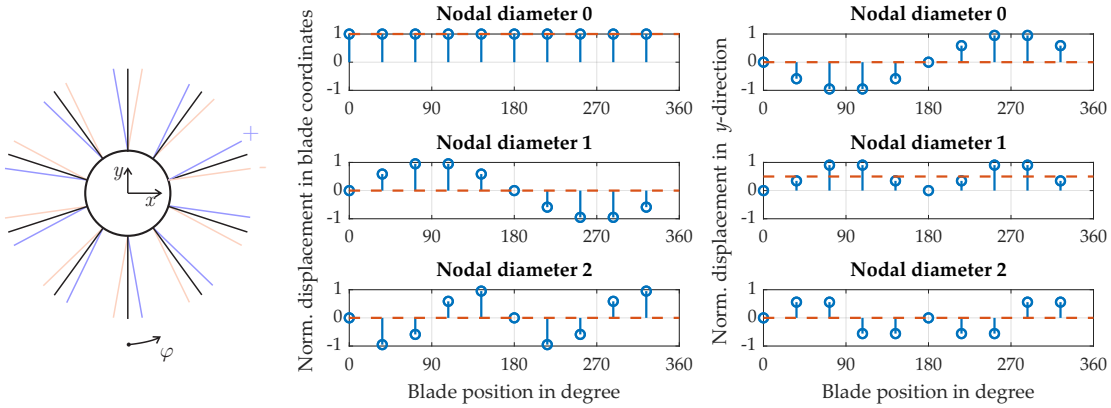

Figure 1: First three nodal diameters of a bladed disk in individual blade coordinates and in a disk fixed reference frame with the axes x and y. The blue and red lines at the blades indicate the direction of positive and negative deflection in the corresponding blade coordinate system.

Coupled torsional blade-shaft vibrations have been a topic of research for several decades [3]. By now, the phenomenon is already well understood and guidelines on how to consider it during the design stage of a new machine are available [4]. Coupled vibrations where tilting and lateral vibrations of the shaft interact with the blades ND 1 mode however, are still not fully understood and therefore will be investigated further in this paper. Interesting research on the topic can be found in [5] where blade-shaft coupling and different resonance conditions are investigated theoretically as well as experimentally, where an active magnet bearing is used as additional source of excitation. In [6] a calculation approach for simplified rotor-blade-models is presented and applied which reduces the blade row to the modes that can actually couple with the rotor vibrations.

An important parameter for the coupling between ND 1 blade modes and shaft bending is the stiffness anisotropy of the bearings and the supporting structure. An unbalanced rotor on isotropic bearings only exhibits a stationary deflection for a constant rotation frequency Ω but no vibrating excitation when viewed in a rotating frame. However, when bearings are anisotropic and the rotor orbit becomes elliptical a backward whirl component occurs in the rotating frame with double the rotation frequency, which can excite the blades [7]. Fig. 2 illustrates the displacement of the rotor for one revolution of a rotor on anisotropic bearings. It can be seen that the rotor performs two full periods around a median value during one revolution. [7] recommends to keep the first blade resonance above twice the operational speed to avoid an additional critical resonance for the blades. For modern steam turbines this is not always possible and therefore, it is important to study the related effects in order to be able to assess what significance they have in practice.

In [1] it was shown that the 2Ω excitation is not only relevant to the blade vibrations but also to the shaft vibrations. When Ω was equal to half of the first ND 1 blade eigenfrequency ($\frac{\omega_b}{2}$) the blades show a resonance

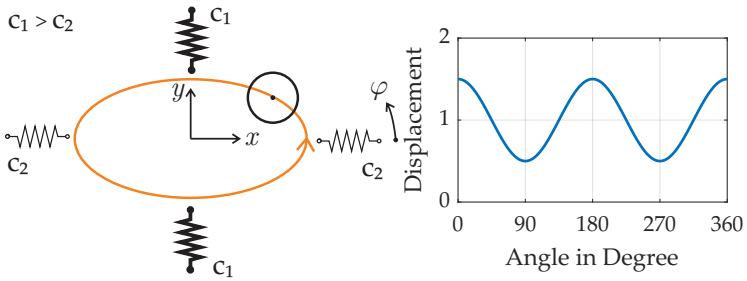

Figure 2: Displacement from the origin for one revolution of a rotor with imbalance on anisotropic bearings.

peak while the shaft exhibits a pronounced dip of vibration amplitudes which indicate a coupling phenomenon between both subsystems. For this reason, the aim of this paper is to better understand the rotor-blade coupling in this context and to determine more precisely which conditions are responsible for the behaviour described there.

Simulation Method/Theoretical Approach

The multi-frame approach used in this investigation was first presented in [8]. More details on the theoretical background can be found there. In [1] detailed information regarding the modelling of the industrial model used in this investigation can be found. Therefore, the approach is only briefly described and summarized here.

The main difficulty for the simulation of a full model with stator, rotor and bladed disk are the unavoidable time dependent terms in the system matrices which prevent the application of the conventional methods of linear rotordynamics. While the stator part with anisotropic bearings and supporting structure can be simply represented in the inertial frame, the terms related to the blades will become time dependent since the structure with individual separated blades is not rotational but only cyclic symmetric. On the other hand, in a rotating frame the blades can be described with constant terms while the anisotropic bearings and supporting components become time dependent. To minimize the computational effort resulting from this unavoidable time dependency a multi-frame approach is used. This way, the stator and supporting elements can be defined in a fixed frame while the rotating parts are defined in a rotating frame. Both frames are coupled at the bearings so the time dependency in the system matrices only occurs at the linking constraints in the form of time-dependent Lagrange multiplier constraints. However only translational displacements are considered. Therefore an error is introduced when the actual axis of rotation differs from the z-axis (axis of rotation of the undeformed rotor). For typical rotordynamic systems this error is usually small since the shaft vibration amplitudes are small compared to the dimensions of the rotor. To additionally reduce the computational effort the subsystems can be further reduced via Craig-Bampton method. The dynamic system is then solved in the time domain with an implicit Newmark scheme. To calculate a steady state response the rotational frequency is increased stepwise. At each step the amplitude is captured at the bearings and blade tips after the free vibrations have decayed. The described multi-frame approach is implemented in the Samcef/mecano solver package, which is used to perform all calculations carried out in this paper.

Industrial Model

Starting point of the investigation is the industrial model shown in [1] which shows significant coupling effects that were not predicted by conventional models with simplified, stiff disks. The behaviour was also measured during coast downs of the actual turbo machine. Therefore, this model is a valuable basis for insights into lateral rotor-blade-coupling. Since the model is a very detailed representation of the complex, real system it features many parameters which might not be relevant for the observed behaviour. For this reason the number of parameters shall be reduced to create a simplified model. First, the industrial model and the system parameters will be characterized. Then a simplified rotor model will be set up which is similar for the relevant parameters. The investigated industrial rotor is part of a turbo-generator set. Fig. 3 provides an overview of the system. Between bearing no. 5 and 6 a self synchronizing coupling is located, allowing to decouple the steam turbine part from the gas turbine/generator part. The steam turbine stator consists of three fluid-film bearings and their supporting structure, the shaft and the bladed disk which is the last stage of the steam turbine. Unbalances at three locations excite lateral shaft vibrations mainly in the regime of the second rotor bending mode of the IP/LP rotor. The bladed disk carries 58 blades. Each blade is represented in a Finite Element model by an identical mesh to avoid numerical mistuning. The strong non-linear beahviour due to untwist, stress-stiffening and spin softening etc. is considered during the super element generation for the rotation frequency of 38 Hz which is the most relevant frequency in this investigation.

Fig. 4 shows simulation results for the system. In contrast to [1] cross-coupling of the fluid-film bearings is negelected here as a first step to reduce the model complexity. Fig. 4 (a) shows the shaft orbits at a bearing location near $\frac{\omega_\mathrm{b}}{2}$. The elongated elliptical shape due to anisotropy is clearly visible. At 38 Hz the orbit gets smaller and more circle-like. The orbits are not aligned with the system coordinate axes, therefore in the following the deflection amplitude in direction of the orbit principal axes will be used for better comparability of the different systems and parameters. In Fig. 4 (b) the deflection amplitudes in direction of the orbit principal axes w and v are plotted over the rotational frequency. The deflection amplitudes are at an elevated level in a wide frequency range. The visible peak belongs to the first resonance related to the second shaft bending mode of the IP/LP rotor. Around 38 Hz the impact of the flexible, bladed disk is visible. While the amplitudes of the larger principal axis drop the amplitude for the smaller principal axis rises. The blade amplitudes show a sharp peak at $\frac{\omega_b}{2} = 38$ Hz.

The system features the following main characteristics:

- $\frac{\omega_\mathrm{b}}{2}$ lies in a region with high shaft vibration amplitudes, close to the second bending mode of the shaft.

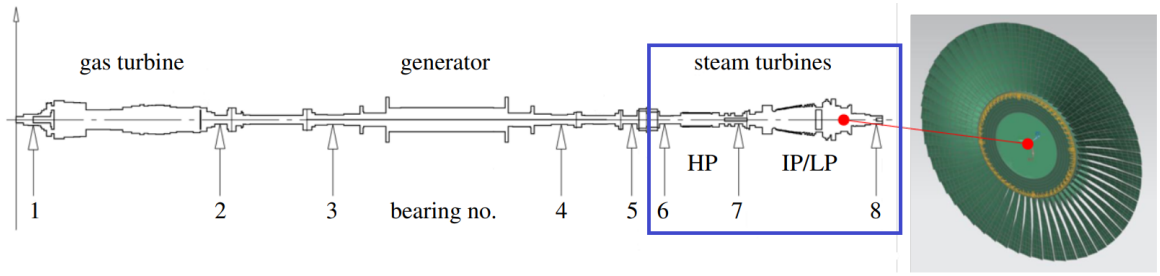

Figure 3: Outline of the industrial system. The part right of the clutch with bearings 6,7 and 8 is modeled and investigated in this paper.

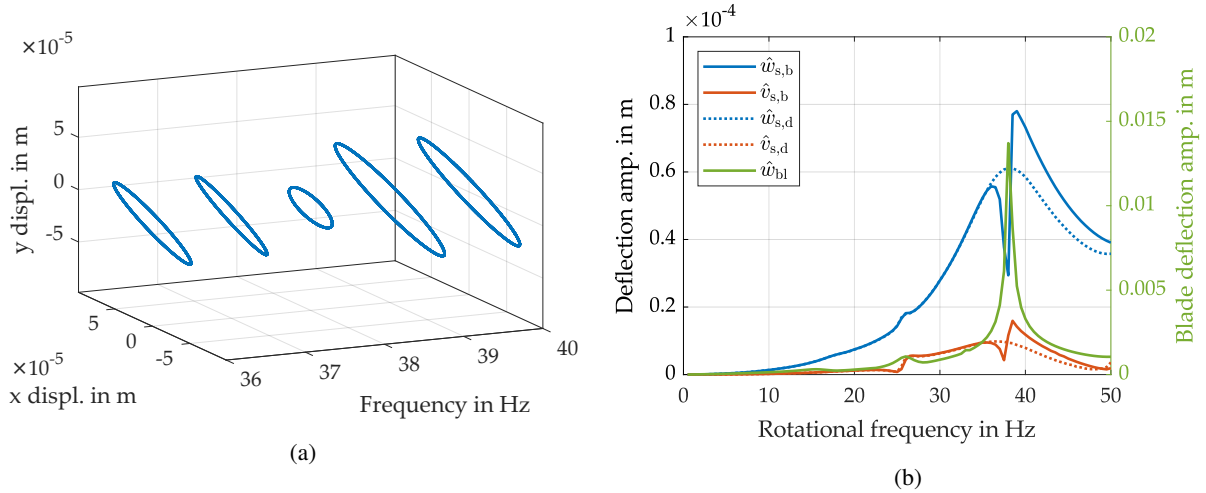

Figure 4: Simulation results for the industrial rotor. (a) Orbits of the rotor node at a bearing location. (b) Steady state deflection amplitudes w_s and v_s at a bearing location and w_b for a blade tip node. Solid lines represent the model with flexible blades, dotted lines represent a conventional model.

- High degree of anisotropy for the bearing stiffness, about 1:7 horizontal vs. vertical.
- Soft bearing stiffness compared to shaft stiffness, rotor modes are significantly split.
- Relation of disk to shaft mass is about 1:8.
- Bearings are not identical and have slightly different properties.
- Wide resonance peaks indicate high external damping from the bearings, which is typical for oil-film bearings.
- Complex, twisted blades with certain stagger angle which causes a mix of in-plane and out-of-plane vibration.
- Tilting of disk and blades due to their position on the shaft.

Transient Resonance Passages

In addition to the stepwise steady state simulations also transient resonance passages were simulated for the industrial model. In Fig. 5 the results for different sweep rates are shown. The results for the blade vibration show the common transient behaviour which can also be observed for linear single degree-of-freedom systems [9]. Faster sweep rates lead to smaller amplitudes, beating increases for higher sweep rates and results for run up and coast down are almost similar. However, the situation is different for the bearing vibrations. Significant deviations related to the resonance crossing direction can be seen. For run-ups the maximum amplitudes are generally higher than for run-downs with the same gradient and even exceed the steady state amplitude considerably. The general rule of steadily decreasing amplitudes for increased gradients is also no longer valid here. The maximum bearing vibration amplitude occurs for 2 Hz/s while faster and slower resonance passages cause smaller maximum amplitudes.

The phenomenon is similar to the TAMS effect (Transient Amplitude Amplification of Mistuned Structures), which was observed in the context of split double modes in turbine blades [10–12]. Basically, the TAMS effect describes an amplitude amplification under transient excitation compared to the maximum amplitudes possible

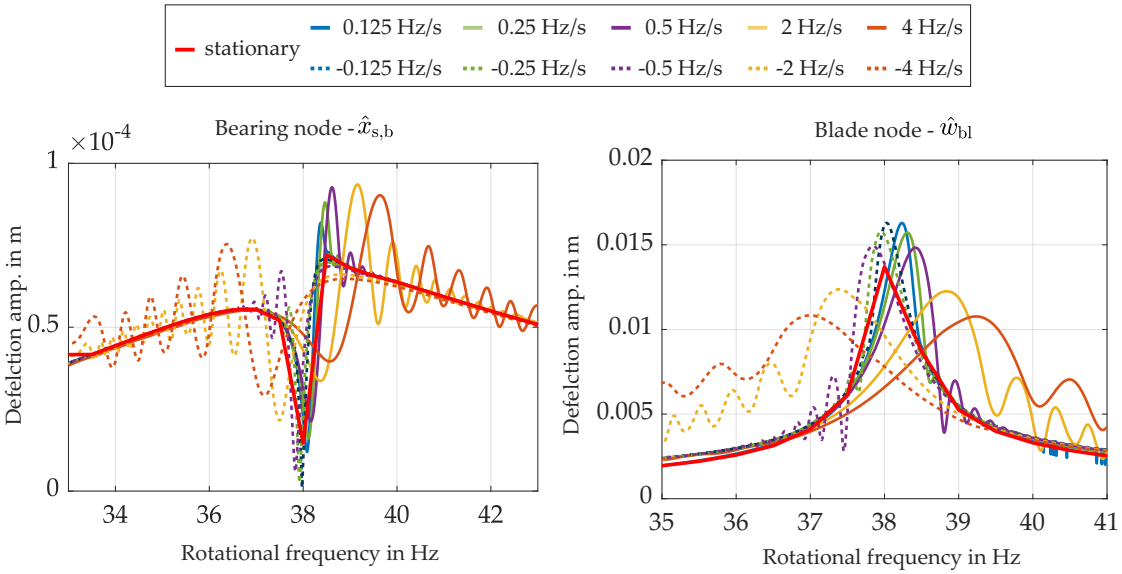

Figure 5: Calculated transient resonance passages of the industrial model with unbalance induced vibrations for different sweep rates. Results for the bearing node $\hat{x}_{s,b}$ are in inertial coordinates, results for the blade tip $\hat{w}_{bl}$ node are in rotating coordinates.

with the same mechanical system under stationary excitation. The reason for this is the excitation of two modes within a small frequency range during a resonance passage. The vibrations excited by the first resonance passed are only partially decayed when the second resonance is reached and can lead to the amplitudes subsequently exceeding the stationary maximum. However while for the TAMS effect two closely spaced modes are excited by the same engine order excitation, here two widely separated resonances are excited in short time by two different excitation mechanisms. The rotor related resonance is excited with Ω and the blade dominated resonance is excited with 2Ω due to the bearing anisotropy.

Sweep rate, frequency distance and damping have a particularly large influence on the transient superposition of the two excited resonances, as they determine the amplitude and phase position of the induced oscillation. If the maximum bearing amplitudes of a new rotor-stator system are relevant during the design phase of a new rotor it may be advisable to use transient simulations as a reference instead of the steady-state solution.

Simplified Rotor-Blade Model

Based on the parameters of the industrial system a simplified model is developed. Like a LAVAL rotor it consists of a shaft with uniform diameter supported by identical bearings at both ends. The bearings feature a significant degree of anisotropy and a relatively high stiffness proportional damping value. The rotor is designed so that the first two bending modes are in the range of 25-50 Hz and significantly split due to the anisotropic bearings. The bladed disk is attached to the shaft in the middle between both bearings to avoid tilting of the disk or any movement in axial direction to keep the system simple. The bladed disk carries 10 identical blades with a rectangular cross-section which are either oriented with a stagger angle of $0°$ or $90°$ (in-plane-blades / out-of-plane blade). An unbalance is defined at the blade disk centre node to excite lateral shaft vibrations.

The relevant parameters are summarised in the following table:

Table 1: Relevant parameters of the simplified rotor-blade model.

Rotor diameter	50 mm	Blade length	215 mm
Rotor length	1.4 m	Blade footprint	15x3 mm
Rotor weight	21.2 kg	Disk weight	2.24 kg
Bearing stiffness prop. damping	0.002	Step size	0.0001 s
Horiz. bearing stiffness	1 $\frac{\mathrm{N}}{\mu\mathrm{m}}$	Vert. bearing stiffness	7 $\frac{\mathrm{N}}{\mu\mathrm{m}}$

Simulation Results

Fig. 6 shows simulation results for the simplified rotor model with blades attached under $90°$ stagger angle. In Fig. 6(a) the bearings are isotropic. In this case there is no difference between a model with a flexible bladed disk and a model where the bladed disk is represented by a simple mass element. The blades show no sign of vibration at this configuration. In Fig. 6(b) the bearings are distinctly anisotropic. The two rotor modes due to anisotropy are clearly visible. The blades show a sharp peak in vibration amplitude at $\frac{\omega_b}{2} \approx 33\text{Hz}$. In the same range the rotor shows significant coupling effects. Similar to the industrial model, the amplitudes of both axes approach each other. The larger principal axis amplitude drops clearly while the smaller principal axis amplitude rises slightly. Apart from the clear differences in the vicinity of $\frac{\omega_b}{2}$, there are also slight differences in the range between the two rotor resonances. Fig. 7 shows the same system with anisotropic bearings but with the blades attached under $0°$ stagger angle. The length of the blades in the model is ajusted to keep $\frac{\omega_b}{2}$ at ≈ 33 Hz. However no rotor-blade-coupling effect is visible near $\frac{\omega_b}{2}$. Similar to the $90°$ arrangement, only small blade amplitudes occur in the range of the second rotor resonance at ≈ 45 Hz. The simulations show that the bearing anisotropy of the unbalanced rotor is the source of excitation for the blades through the rotor-blade-coupling. The lateral movement of the rotor mainly excites in-plane vibrations and thus mainly affects blades with $90°$ stagger angle, where the flatwise bending direction coincides with the in-plane vibration direction.

Table 2: Possible cases for the positioning of $\frac{\omega_b}{2}$ relative to the neighbouring two rotor eigenfrequencies.

Case 1	$\frac{\omega_\mathrm{b}}{2} \leq \omega_{\mathrm{r}_1} \leq \omega_{\mathrm{r}_2}$
Case 2	$\omega_{\mathrm{r}_1} \leq \frac{\omega_\mathrm{b}}{2} \leq \omega_{\mathrm{r}_2}$
Case 3	$\omega_{\mathrm{r}_1} \leq \omega_{\mathrm{r}_2} \leq \frac{\omega_\mathrm{b}}{2}$

In the following, the impact of the frequency of $\frac{\omega_b}{2}$ relative to the nearest rotor resonances is investigated. Table 2 shows the three possible cases. The first one, where $\frac{\omega_b}{2}$ is at a lower frequency than the two rotor resonances was already discussed above. To achieve the frequency shift of ω_{r_1} and ω_{r_2} a mass element is added at the blade disk centre to lower the rotor eigenfrequencies without influencing the blade resonance. Fig. 8 shows the results for case 2 and 3. The characteristics of the rotor-blade-coupling change significantly with each case. For case 1 the amplitudes of the principal orbit axis at $\Omega \approx \frac{\omega_b}{2}$ approach each other, with the amplitude of the major principal axis decreasing and the amplitude of the minor principal axis increasing. For case 3 the behavior is reversed, here the amplitudes of the principal orbit axis at $\Omega \approx \frac{\omega_b}{2}$ separate each other, with the amplitude of the major principal axis increasing and the amplitude of the minor principal axis decreasing. Case 2 seems to be a combination of the other two cases. First the maximum amplitude drops and the amplitudes approach each other followed by an amplitude amplification which even exceeds the overall maximum amplitude of the conventionally modeled system with rigid disk by a significant amount.

To verify if the observed behaviour can be generalized or if it is specific for this system the same procedure with added weights is done for the industrial model. In Fig. 9 cases 2 and 3 are shown for the industrial model. Although for the industrial model $\frac{\omega_b}{2}$ interacts with the second bending modes of the rotor instead of the first bending as in the simplified model, the behaviour is similar. Case 2 shows a amplitude reduction followed by an amplification and case 3 shows an opposing trend for the amplitudes. Therefore, the different coupling characteristics seem to be a general phenomenon that does not depend on the respective rotor mode.

From the previous comparisons it follows that certain general conditions change depending on where $\frac{\omega_b}{2}$ is located relative to the rotor resonances which changes the characteristics of the coupling on the rotor orbit. A possible explanation could be the different relation of the forward and backward whirl portion of the motion which changes significantly in the different regions. Fig. 10 shows for the conventional model two parameters with different behaviour in the regions before, after and between the two rotor resonances that could influence the characteristics of the rotor-blade-coupling. Fig. 10(a) shows the forward and backward component of the elliptical bearing orbit calculated from the orbits principal axes and the whirl direction [7]. Before the first resonance the movement is determined almost equally by the forward and the backward part with the forward part slightly predominating. Between the two rotor related resonances the backward portion exceeds the forward portion and the rotor performs a backward whirl motion. After the second resonance the backward component drops sharply and the rotor gets back to a forward whirl motion. Since the backward whirling component is the excitation mechanism for the blades it is conceivable that its value and relative height compared to the forward whirl component is relevant.

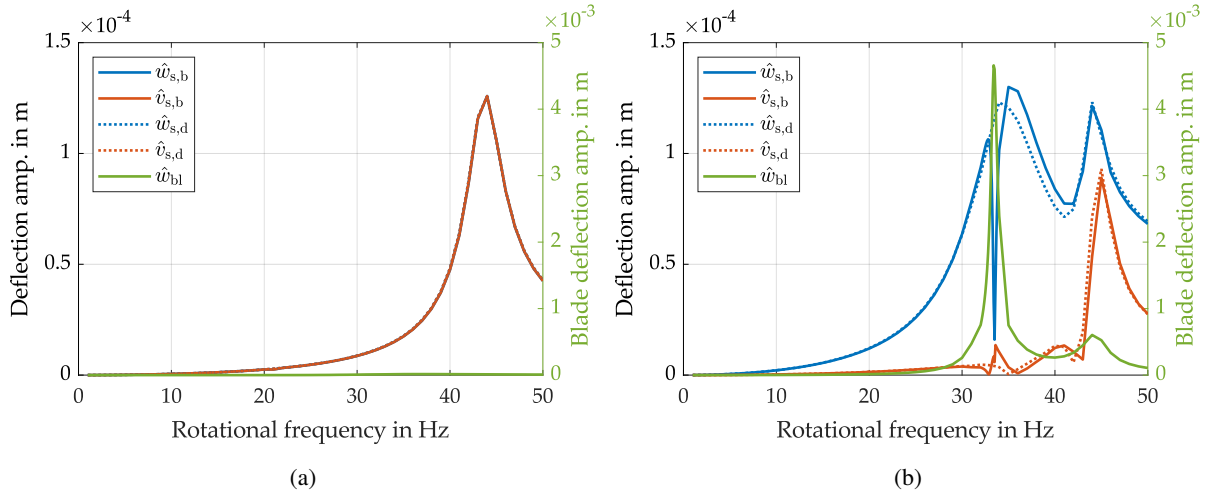

Figure 6: Steady state simulation results for the simple system with (a) stagger angle 90°, bearing stiffness in x/y: 4/4 $\frac{\mathrm{N}}{\mu\mathrm{m}}$ and (b) stagger angle 90°, bearing stiffness in x/y: 1/7 $\frac{\mathrm{N}}{\mu\mathrm{m}}$. Solid lines represent the model with flexible blades, dotted lines represent a conventional mode.

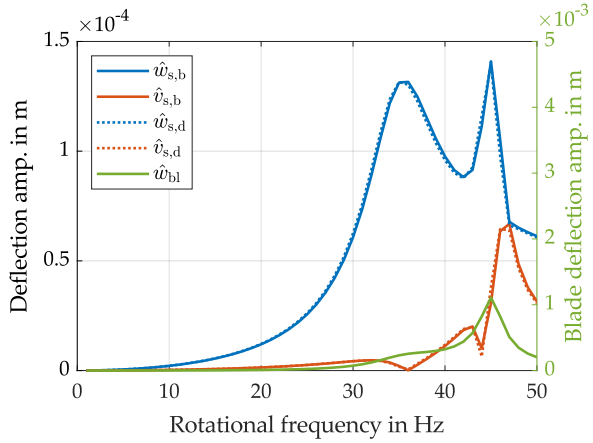

Figure 7: Steady state simulation results for stagger angle 0°, bearing stiffness 1 / 7 $\frac{\mathrm{N}}{\mu\mathrm{m}}$.

Fig. 10(b) shows the orientation of the elliptic orbits at the bearing node and of the disk centre node. The angle α between the horizontal x-axis and the larger principal axis of the orbit is plotted over the frequency. For frequencies below the first rotor resonance α is small for both orbits which indicates a nearly aligned, horizontal orientation of the orbits. With increasing frequency the deviation between both orbits becomes larger. Between the two rotor resonances the inclination angle rises sharply until the second resonance is reached. The system with flexible bladed disk shows a sharp peak at $\frac{\omega_b}{2}$ which indicates a relation between orbit orientation and coupling effects. While α reaches its maximum at the bearing node at the second rotor resonances and returns to a horizontal orientation afterwards the orbit at the disk centre reaches a nearly vertical orientation and remains at these levels even after the second rotor resonance. Here, again, significant differences can be observed in the relative orbit orientation at the different frequency ranges before, after and between the two rotor resonances. Depending on the relative orbit orientation, either one or the other of the axes of the orbits could be stretched or compressed.

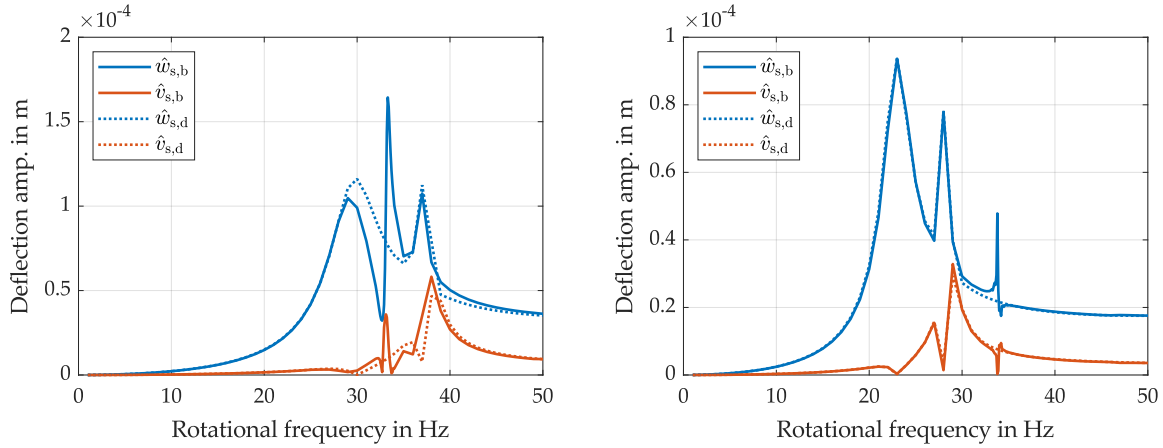

Figure 8: Deflection amplitude of the principal axes at a bearing node of the simplified rotor model. Weight is added to the rotor at the disk to shift the rotor dominated resonance relative to the blade dominated resonance which is fixed at 33.5 Hz. (a) Case 2 with 6 kg added to the rotor. (b) Case 3 with 20 kg added to the rotor.

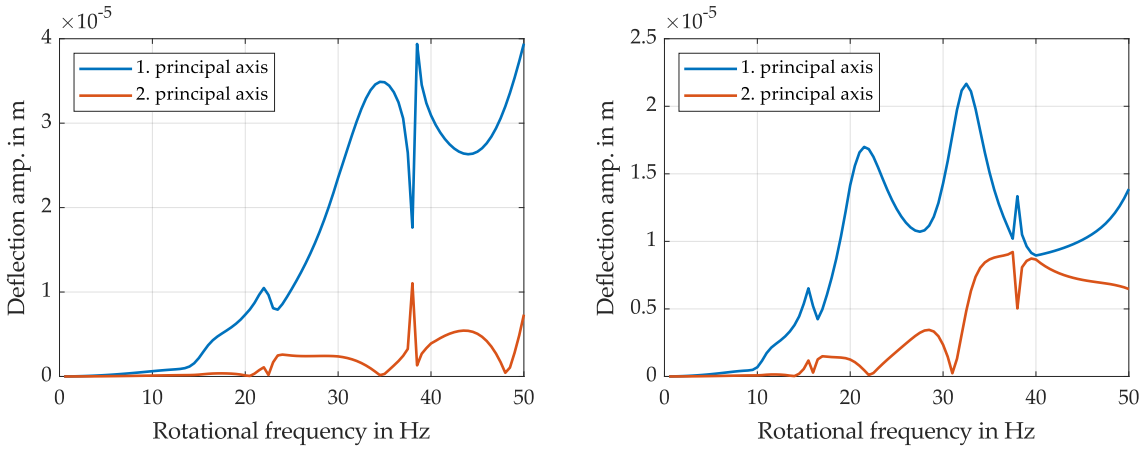

Figure 9: Deflection amplitude of the principal axes at a bearing node of the industrial rotor model.Weight is added to the rotor to shift the rotor dominated resonance relative to the blade dominated resonance which is fixed at 38 Hz. (a) Case 2 with 10 t added to the rotor. (b) Case 3 with 50 t added to the rotor.

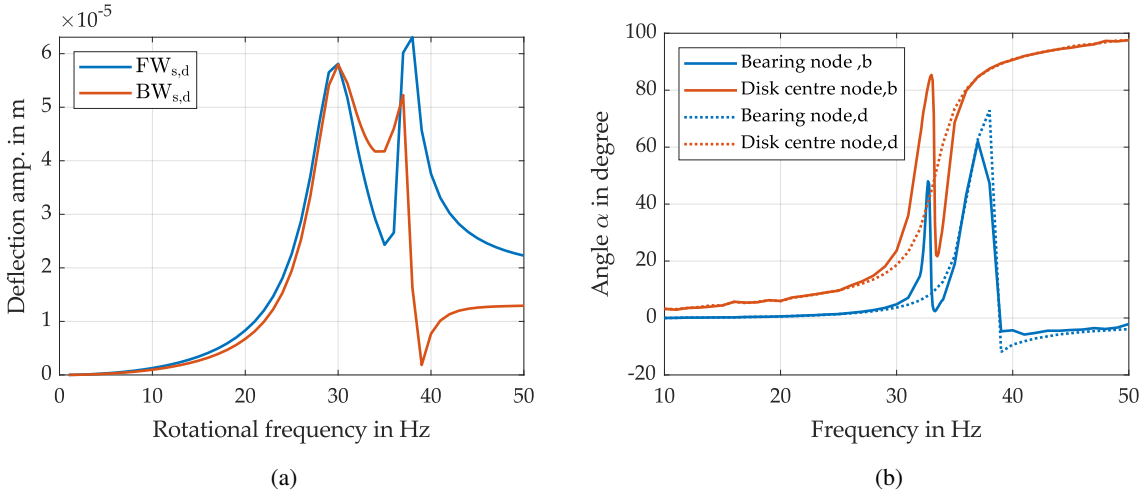

Figure 10: Different system parameters for the simplified rotor with conventional model and 6 kg added to the rotor (case 2). (a) Forward and backward component of the bearing orbit ellipsis. (b) Orientation of the bearing and disk centre orbits. α is the angle between the horizontal x-axis and the larger principal axis.

Possible Future Applications: Online Blade health Monitoring

One difficulty with industrial rotor-blade systems is that the number of sensors for vibration monitoring in operation is usually severely limited. Typically, only the bearing vibrations are monitored. For this reason, changes to the blades due to damage or wear are not directly visible to the operator, making efficient maintenance difficult. However, the rotor-blade coupling opens up possibilities to obtain information about the condition of the blades indirectly via the bearing vibrations.

In [13] the potential of on-bearing and on-casing vibration measurements is investigated to assess if they can be used to identify damaged blades. It could be shown that it is possible in limited quantities. However, anisotropy and the related excitation mechanism is not considered in the simulations. Also the combination of rotor resonance and $\frac{\omega_b}{2}$ is not considered. Near the rotor-dominated resonance the blade influence on the bearing vibrations is much more severe, as seen in the previous parts of the paper, and therefore changes in the blade vibration parameters are magnified and better visible. Fig. 11 shows exemplary simulation results where one blade of the simplified model is mistuned via additional weight at the blade tip. Two distinct dips are visible whereby the lower one, which is to be attributed to the mistuned blade, is less pronounced. The simulation shows that individual blades with deviating parameters can be identified through the bearing vibrations and that the rotor-blade coupling effects can provide an approach for indirect online blade health monitoring. The coupling of the individual blades through the disk is a limiting factor for this method. For large steam turbines with stiff disks the blades show nearly stand alone behaviour and therefore should be well suited for this approach.

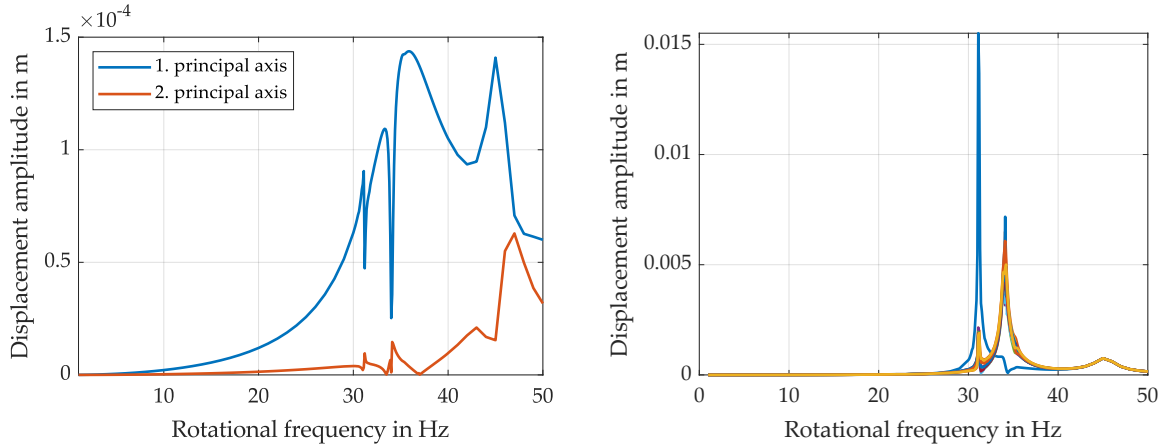

Figure 11: Steady state simulation for the simplified model with one mistuned blade (4g added at one blade tip). (a) Amplitudes at a bearing node. (b) Amplitudes for all blades.

Conclusions

In this paper, the coupling phenomenon between rotor and blade vibrations were investigated with steady-state and transient simulations of two different systems under unbalance excitation. In particular, the focus was on rotors with soft bearing stiffness, high degree of anisotropy and high external damping by the bearings, so that half of the first ND 1 blade eigenfrequency ($\frac{\omega_b}{2}$) falls into a range of high rotor amplitudes. It could be confirmed that the cause of the observed rotor-blade-interaction lies in the anisotropy of the bearings. The anisotropy causes an ND1 in-plane vibration of the blades with the frequency of 2Ω. For this vibration the blade row centre of mass deviates from the geometric centre of the disk and thereby influences the dynamics of the rotor. It was found that the characteristics of the rotor-blade-coupling significantly depends on the position of $\frac{\omega_b}{2}$ relative to the rotor related split eigenfrequencies. Three cases with different behaviour were identified. Especially when $\frac{\omega_b}{2}$ lies between two rotor natural frequencies, split by high anisotropy, the rotor-blade-coupling should be taken into account since this setup can lead to an amplitude amplification similar to or even higher than the steady-state amplitudes at the rotor related resonances. The importance of transient simulations in this context also has been demonstrated. When two resonances lie in a small frequency range or are excited simultaneously by different effects, like in this case, the vibrations induced by the first resonance might still be present when the second resonance is reached and therefore can superimpose in a way that they can even exceed the maximum steady state amplitude.

Further investigations about the impact of other parameters which are relevant for real industrial systems, like stagger angle, tilting of the bladed disk or cross-coupling at the bearings are ongoing research. Based on this, the usability for online monitoring in operation of blade damage or damping behaviour can be evaluated in the future. In addition, it is planned to validate the simulation approach through comparisons with experimental measurements.

Acknowledgments

The investigations were conducted as part of the joint research program SchauTex in the frame of AG Turbo. The work was supported by the Bundesministerium für Wirtschaft und Klimaschutz (BMWK) as per resolution of the German Bundestag under grant number 03424292D. The authors gratefully acknowledge Siemens Energy for their support and permission to publish this paper. The responsibility for the content lies solely with its authors.

References

[1] Grein, R., Ehehalt, U., Siewert, C. and Kill, N., (2021): *Rotor-Blade Interaction During Blade Resonance Drive-Through* In *Proc. ASME Turbo Expo 2021.* GT2021-59160 Vol. 9B.

[2] Matsushita, O., Tanaka, M., Kanki, H., Kobayashi, M. and Keogh, P., (2017): *Vibrations of Rotating Machinery* Springer, Tokyo.

[3] Ziebarth, H., and Termuhlen, H., (1989): *Evaluation method for the coupled system of shaft torsion and lp turbine blade deflection*. In *American Power Conference*, 1989, Vol. 51, pp. 1–7.

[4] (2009): *Mechanical Vibration - Torsional Vibration of Rotating Machinery-Part 1: Land-Based Steam and Gas Turbine Generator Sets in Excess of 50 MW, ISO 22266-1. International Organization for Standardization*.

[5] Anegawa, N., Fujiwara, H., and Matsushita, O., (2010): *Vibration Diagnosis Featuring Blade-Shaft Coupling Effect of Turbine Rotor Models.* In *ASME. J. Eng. Gas Turbines Power* 133(2).

[6] Bachschmid, N., Salvini, G., Tanzi, E., and Pesatori, E., (2015): *The influence of blade row dynamics on lateral and torsional shaft vibrations in steam turbines.* In *Proceedings of the 9th IFToMM International Conference on Rotor Dynamics*, P. Pennacchi, ed., Springer International Publishing, pp. 113 – 127.

[7] Kellenberger, W., (1984): Double-frequency forced vibration of turbine blades due to an elliptical orbit of the rotor. In *IMechE Conference on Vibrations in Rotating Machinery*, 1984, **C293/84**, IMechE.

[8] Kill, N., and D'Ambrosio, F., (2016): *Multi-frames approach in rotor dynamics.* Vibrations in Rotating Machinery *VIRM* **11**.

[9] Markert, R. and Pfützner, H. (1981): *An-und Auslaufvorgänge einfacher Schwinger*. In *Forsch Ing-Wes* Vol. 47, pp. 117–125.

[10] Bonhage, M., Adler, J.T., Kohlhoff, C., Hentschel, O., Schlesier, K.-D., Panning-von Scheidt, L. and Wallaschek, J., (2018): *Transient amplitude amplification of mistuned structures: An experimental validation*. In *Journal of Sound and Vibration* Vol. 436, pp. 236–252.

[11] Siewert, C. and Stüer, H., (2017): *Transient Forced Response Analysis of Mistuned Steam Turbine Blades During Start-up and Coast-down*. In *Proc. ASME Turbo Expo 2014.* GT2014-25654, Düsseldorf, Germany.

[12] Carassale, L., Denoël, V., Martel, C., and Panning-von Scheidt, L., (2021). *Key Features of the Transient Amplification of Mistuned Systems.* In *ASME. J. Eng. Gas Turbines Power* 143(3).

[13] Gubran, Ah. and Sinha, J., (2015): *Comparison of On-Bearing and On-Casing Vibration for Blade Health Monitoring in Rotating Machine.* In *Mechanisms and Machine Science* **23**, pp. 107–118.

15th SIRM – European Conference on Rotordynamics,
Darmstadt, Germany, 22nd – 24th February 2023

Geometrically mistuned blisks: Strain Gauge and Tip Timing vibration measurements of rotating blades with and without underplatform dampers

Katharina Brinkmann [1], **Lars Panning-von Scheidt** [1], **Heinrich Stüer** [2]

[1] Institute of Dynamics and Vibration Research, Leibniz University Hannover, 30823 Garbsen, Germany, brinkmann@ids.uni-hannover.de
[2] Siemens Energy AG, 45473 Mülheim a. d. Ruhr, Germany

Abstract

Turbine blade vibrations are often measured during operation for monitoring purposes as well as during the design development and for basic research and validation. In this paper the dynamic behaviour of an academic free-standing bladed disk is investigated at various operating points using both Strain Gauges and Blade Tip Timing measurements. The blades first bending mode was tested both without and with two different types of nonlinear underplatform friction dampers at two engine orders. Several excitation forces for the transient resonance passages were investigated, in order to evaluate the equivalence of the results from both measurement systems. In addition to the equipment effort, this comparison also includes the assessment of the recorded measurement data. For this purpose, the individual deflection-stress ratios and their development along the resonance peaks and captured forced response functions were examined. Additionally, the experimentally determined linear eigenfrequencies of all blades without the dampers were compared with the results of simulated blade alone frequencies, obtained from mesh-morphed blade Finite Element models. It is shown that both measurement systems provide comparable results for engine runs with friction nonlinearities due to the underplatform dampers, along with very good accuracy during linear testing.

Nomenclature

a	sine fitting factors
BA	blade alone
d	deflection
EO	Engine Order
H	transfer function
j	probe number
MM	mesh-morphing
N	number of probes
V	deflection-stress ratio
θ	blisk angular position
σ	stress

1 Introduction

During the operation of turbo machines, speed-synchronous or transient disturbances can generate an excitation of the turbine blades. These can result in vibration states that cause damage to the structural parts, e.g. through high cycle fatigue if the operating speed is too close to a resonance and therefore the blades experience stress above their limiting strength.

In order to prevent these fatal failures, turbine blades are being meticulously developed and are frequently monitored during operation (see [10], [12]). Measurements support the design process afterwards or during fundamental research as well as identifying a potentially critical vibration event while operating.

Depending on the application, the most commonly used measurement systems for turbine blade vibrations are Laser Doppler Vibrometers, Strain Gauges (SG) and Blade Tip Timing (TT). All of the above require distinct setups and generate different measurement variables and data, which is why the usage of more than one can both

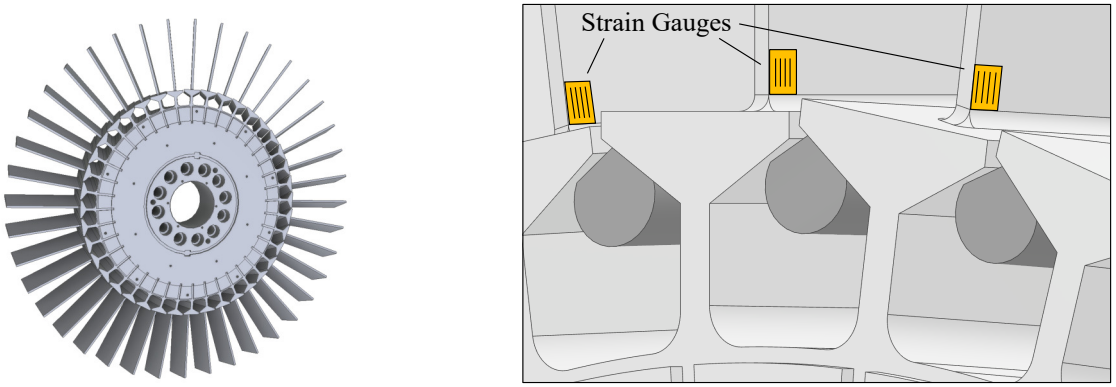

Figure 1: CAD model of the evaluated blisk with 40 free-standing blades (left) and schematic view of asymmetric underplatform friction dampers, as also used by Hoffmann et. al. [5].

support the overall quality of information about the blades dynamics and increase the understanding of each system. Several comparisons have already been made between Tip Timing and Laser Doppler Vibrometers (see [6]), as well as Strain Gauges and Tip Timing (see [4], [9]). Maywald et. al. [7] for example put the focus of their comparison on mistuning, whereas the other measurements were either applied to real turbine stages or bladed disks (and blisks) without frictional dampers.
A typical specimen of these are nonlinear underplatform dampers (UPD), which are applied to a turbine blade in order to decrease its vibration amplitude at resonance by dissipating the kinetic energy. In addition to geometric blade mistuning, each turbine blade thereby experiences different frictional contact states. Correspondingly, friction damping at large, as well as the modification to the simulations of such a blisk involving mistuning by e.g. mesh-morphing is part of current fundamental research. In this paper both effects will be evaluated through rotating measurements by means of Tip Timing and Strain Gauges.

2 Measurement setup

With the aim of simplification in academia, a turbine stage is often modelled as a blisk with a reduced complexity of the blades geometry. Within this paper the focus lies on the effect of friction damping on the blisks dynamic behaviour and the Tip Timing and Strain Gauge measurement systems, so that the shape of the free-standing blade as a simple cantilever beam is sufficient. The CAD model on the left side of Figure 1 depicts the evaluated blisk with 40 blades, that has already been designed, manufactured, equipped with Strain Gauges and measured in the course of the joint research program COOREFlex-turbo in the frame of AG Turbo (see [5]), aiming on the prediction of blisk dynamics with frictional damping.
Here two different types of underplatform dampers are used, one with a cylindrical and the other with an asymmetrical axial cross-section, the latter being shown on the right-hand side of Figure 1. In contrast to the simpler cylindrical damper this asymmetric shape causes both a larger shift in resonance frequency as well as achieving a smaller vibration amplitude for small Nodal Diameters while maintaining the same excitation force (see [8]).

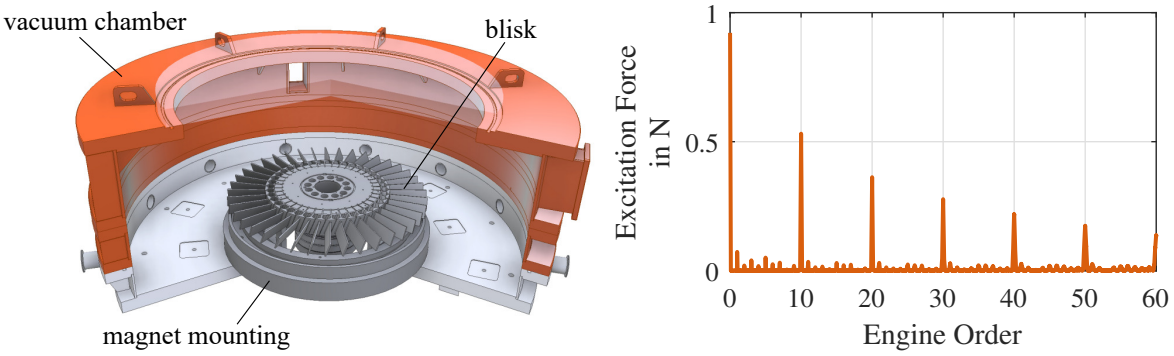

Figure 2: CAD model of the rotational test rig (left) and recorded excitation force spectrum acting on one blade, resulting from ten circumferentially even distributed magnets (right).

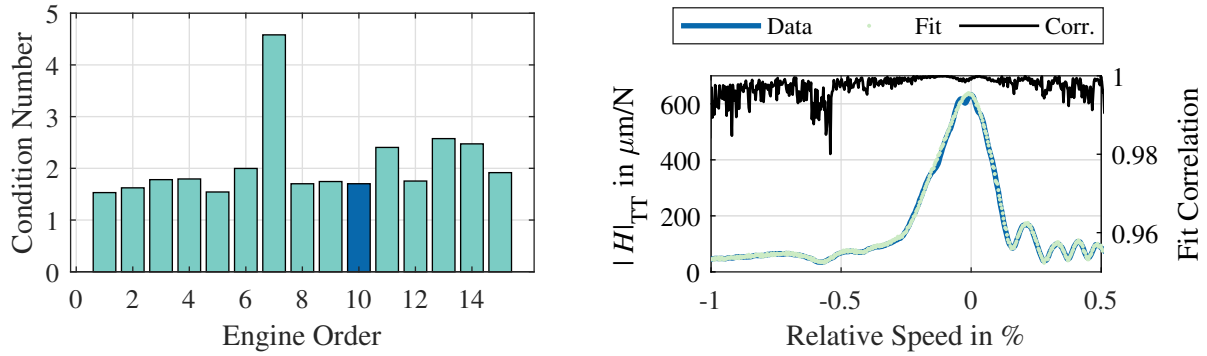

Figure 3: Condition numbers for the utilized probe positions with highlighted Engine Orders 10 (left) and the resulting correlation of a least-squares fit per speed over all probes (right) of Blade # 21.

Evenly distributed discrete permanent magnets around the circumference axially excite harmonics of their quantity in addition to a static offset. The excitation force is captured by calibrated Hall sensors (see [5]). Because of the imperfect harmonic shape of the magnetic field, this leads to the spectrum shown in Figure 2. The rotational test rig is furthermore equipped with a vacuum chamber (see Figure 2), which minimizes the possibility of an additional aerodynamic excitation and ventilation of the blisk.
The hardware and equipment for Strain Gauge measurements is already integrated in the test rig and was tested extensively in the past. From the actual Strain Gauge glued on the blade roots, the recorded measurement data is amplified and filtered via a circuit board and then transmitted to the data acquisition system via a slip ring (see [5]).
All probes of the utilized AGILIS Tip Timing system were attached to a mounting inside the test rigs vacuum chamber, that allows both a variable circumferential and axial installation of each probe individually. Additional fixtures ensure the necessary orientation and its precision.
Concerning the analysis of a synchronous vibration the positioning of the Tip Timing probes is primarily of importance. The geometrically simplest form of positioning the probes evenly distributed around the circumference has the disadvantage that harmonic oscillations may not be detected during a following least-squares fitting. According to Diamond and Heyns in [2], the ideal probe positions commonly are calculated via the condition number of the design matrix, which is a measure for the sensitivity with respect to the positioning.
Since a circumferential Nodal Diameter vibration is assumed, the design matrix can be formed by the relationship of the resulting displacements d_j with the position θ_j of the j-th probe and the unknown factors of a phase-shifted sinusoidal function a to

$$\begin{pmatrix} d_1 \\ d_2 \\ ... \\ d_j \end{pmatrix} = \begin{pmatrix} 1 & \sin(EO \cdot \theta_1) & \cos(EO \cdot \theta_1) \\ 1 & \sin(EO \cdot \theta_2) & \cos(EO \cdot \theta_2) \\ & & ... \\ 1 & \sin(EO \cdot \theta_j) & \cos(EO \cdot \theta_j) \end{pmatrix} \begin{pmatrix} a_0 \\ a_1 \\ a_2 \end{pmatrix}, \qquad (j = 1, 2, ..., N). \tag{1}$$

In order to obtain optimal angular positions, the condition number of the design matrix was minimized by means of a simple MATLAB algorithm as with Diamond and Heyns in [2]. Figure 3 depicts on the left side the condition numbers for several Engine Orders with the optimized probe positions and EO 10 (highlighted) exhibits a reasonable value according to instructions from AGILIS. This has proven sufficient accuracy for these results, as the relatively high correlation of a subsequent least-squares fit in Figure 3 demonstrates for Engine Order 10.

3 Blade allocation

Due to the Strain Gauge placement on each blade root, those individual measurement signals are naturally assigned to a specific blade number. Contrary to this, the Tip Timing software is only capable of sorting the blades relative to each other. Accordingly, in order to compare the two systems, at first it is essential to allocate both Strain Gauge and Tip Timing signals of each individual blade to one another.
Typically this can be archived either via a once per revolution sensor or, if it is not present, a manual processing like creating an artificially increased reflectance of one tip, e.g. through reflection tape. Since for this measurement

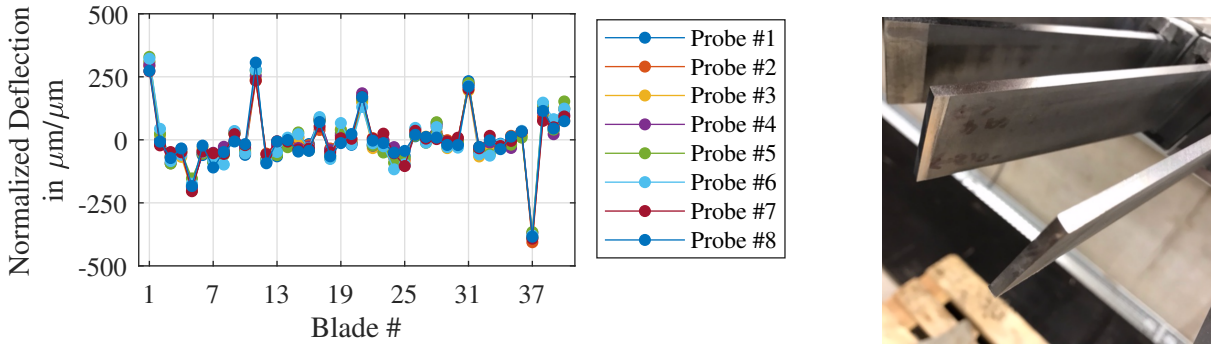

Figure 4: Normalized peaks of positive deflection every 10 blades in an exemplary stack plot (left) and a single corresponding milled blade tip (right).

each tip already has been equipped with this tape, due to its improvement of the signal-to-noise ratio, and the used Tip Timing system not being equipped with an once per revolution sensor, this allocation had to be performed manually afterwards via the collected measurement data.
First off, through manufacturing the blisk has milled tips on four blades, that are equally spread along its circumference and can easily be identified in a stack plot, where the individual blades steady state deflections are shown (see [3]). Viewing an exemplary stack plot of the blisk from outside of a resonance (see Figure 4), four evenly distributed positive outliers in the measurement data are noticeable at every 10th blade. They can be assigned to the mentioned milled blade tips, so now only four possible Strain Gauge to Tip Timing blade number assignments are left. In order to complete the allocation, both systems vibration responses were compared against each other for individual blades. Figure 5 shows the measured transfer functions from Strain Gauge and Tip Timing measurements of four neighbouring blades, where all depicted progressions are clearly distinguishable in both data sets. Consequently the assignment of the individual blade numbers could easily be achieved. Likewise the relative allocation of blades by means of the Tip Timing system from AGILIS has proven to be very robust, since the established mapping rule for this blisk is applicable to mostly all measurements.

4 Measurement results

In order to gain a comprehensive comparison of both measuring systems against each other, two Engine Order resonance crossings each were measured both linearly without the dampers and with the asymmetric or cylindrical friction damper at several excitation forces. For this purpose, the comparison is first made using the linear measurements without underplatform dampers, which are then used as a reference for the quality and the influence of

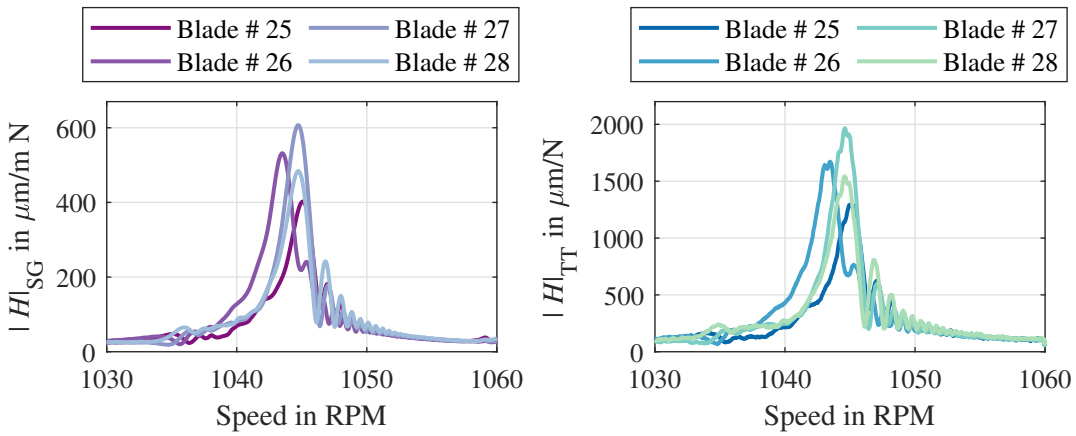

Figure 5: Individual blade transfer functions without the dampers for both Strain Gauge (left) and Tip Timing data (right) with easily distinguishable progressions.

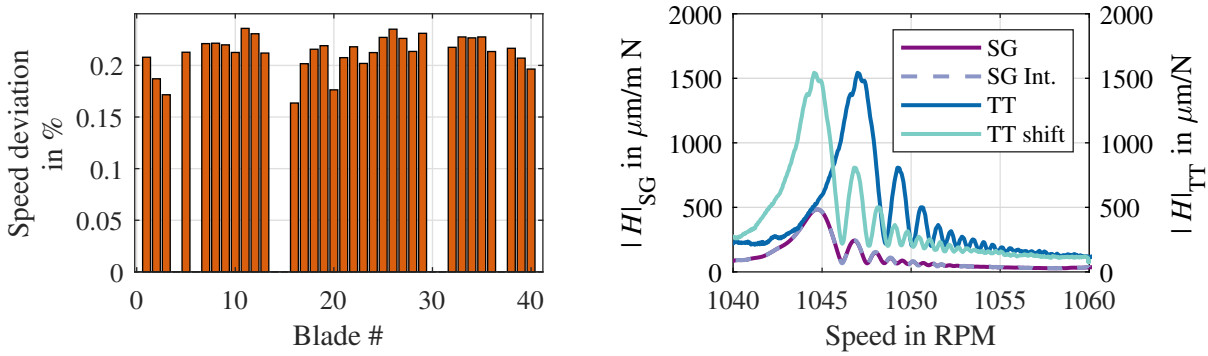

Figure 6: Speed deviation of Tip Timing measurements from the test rig acquisition (left, malfunctioning Strain Gauges left out) and shifted Tip Timing data, as well as interpolated Strain Gauge data (right) of Blade # 28.

the friction damping on the comparison of both measurement systems in the presence of mistuning. In addition to the correlation of the transfer functions $|H|_{\mathrm{SG}}$ and $|H|_{\mathrm{TT}}$, the deflection-stress ratios of individual blades are also considered, both during resonance alone and over the speed progression.
The deflection-stress ratio is defined as

$$V = \frac{d_{\mathrm{TT}}}{\sigma_{\mathrm{SG}}} \tag{2}$$

and beforehand has been determined for the first bending mode (1F) at $V = 2.9$ by comparing Laser Doppler Vibrometer and Strain Gauge measurements at standstill.

4.1 Speed calculation accuracy

An initial examination of the correlation between Tip Timing and Strain Gauge data revealed a speed deviation of about 0.2% from the measured resonances between both measurement systems, as depicted in Figure 6. Main reason for this is the limited number of data points per revolution from the Tip Timing at the relatively low operating speed and comparatively high sweep rate of $0.6\frac{\mathrm{RPM}}{\mathrm{s}}$, so that the calculation time for the Tip Timing speed may be too high. Contrary to that, the data acquisition of the test rigs speed has a higher resolution per revolution due to the installed incremental encoder.
In order to prevent polluting the results of the pursued comparison, the Tip Timing measurement data is consequently being shifted relative to its rotational speed. This is carried out by assessing the cross correlation of both data sets and moving the Tip Timing data by the resulting lags. The consequential transfer functions are shown in Figure 6, where the initial speed deviation between original Tip Timing and Strain Gauge data can easily be identified. Likewise the shifted data optically matches the Strain Gauge data, which additionally is spline interpolated for the subsequent comparison at the Tip Timing sampling points. Therefore all following comparisons are drawn between the shifted Tip Timing and the interpolated Strain Gauge data. Additionally, the data derived from seven temporarily malfunctioning Strain Gauges was left out if necessary (e.g. Figure 6).

4.2 Linear free-standing blade

First, in order to validate the measurement in general, the curves of the transfer functions and the deflection-stress ratio of the linear measurements without dampers are examined. Optically, the transfer functions for both Engine Orders have the same qualitative progression, as can be seen in Figure 7. Likewise, the beating phenomenon after the resonance peak due to the transient speed sweep can be seen in this Figure.
If one considers the progress of the deflection-stress ratio along the speed increase for individual blades, attention is drawn to the fact that it is continuously constant within the range of the resonance peak, and deviations only are present within the duration of the beat phenomenon after the resonance peak. This is probably due to the Tip Timing measurement systems internal computation method for the tip deflection from the blades time of arrival (ToA). Fundamentally though for both crossings the ratio at resonance speed on average is about $V = 3.2$. Correspondingly, the Nodal Diameter of the oscillation has no or only very little influence on the blades mode shape. Any occurring deviations presumably originate from different overall rotational speeds at both Engine Order resonance crossings.

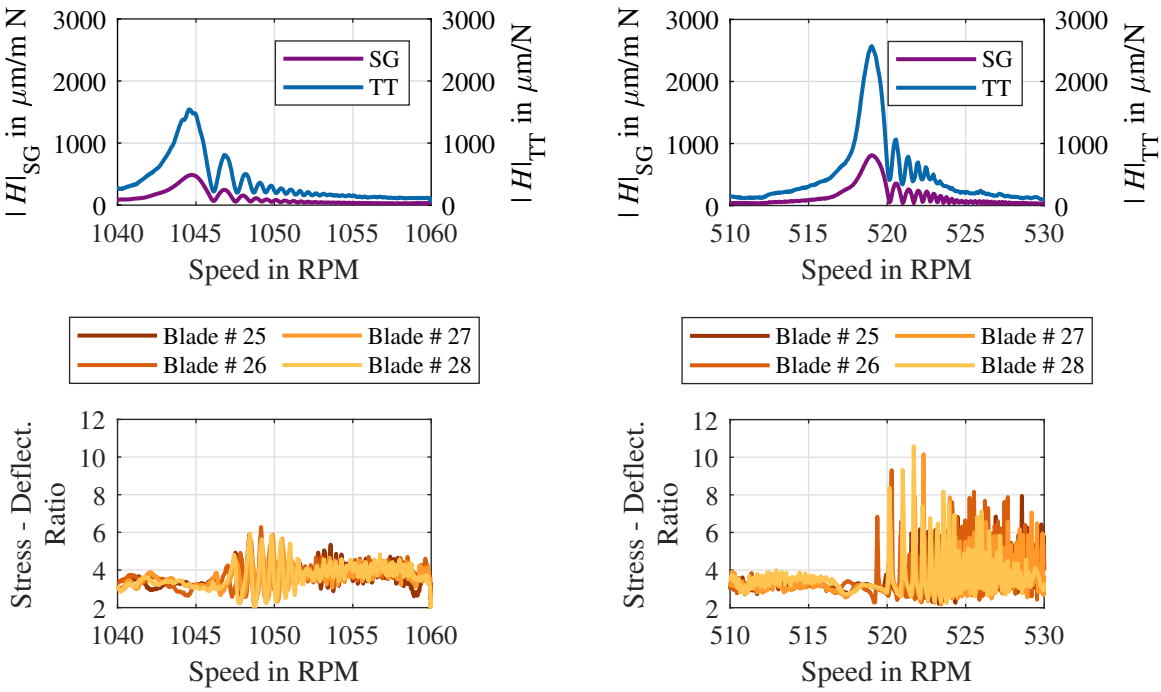

Figure 7: Transfer functions of Strain Gauge and Tip Timing data of Blade # 28 without dampers and selected blade individual deflection-stress ratios for both Engine Order 10 (left) and 20 (right) resonance crossings.

Even without the dampers, every individual blade exhibits a comparatively high spread in its transfer function due to mistuning, both in terms of amplitude and frequency of the resonance peaks shown in Figure 8. Despite all of the above, the respective deflection-stress ratio at resonance of the individual blade does not show any significant deviations (see Figure 8). Thus, as expected, the mode shapes of all turbine blades, represented by their deflection-stress ratios, are equal, regardless of the present amount of mistuning.

4.3 Nonlinear friction-damped blade

For a further assessment the measurements with the nonlinear underplatform dampers are evaluated. Here, the main focus is on the comparability of both measurement systems and the effect of the friction damping. Again, this is primarily considered via the deflection-stress ratio.
If one considers the transfer functions of individual blades in Figure 9, now with a cylindrical underplatform

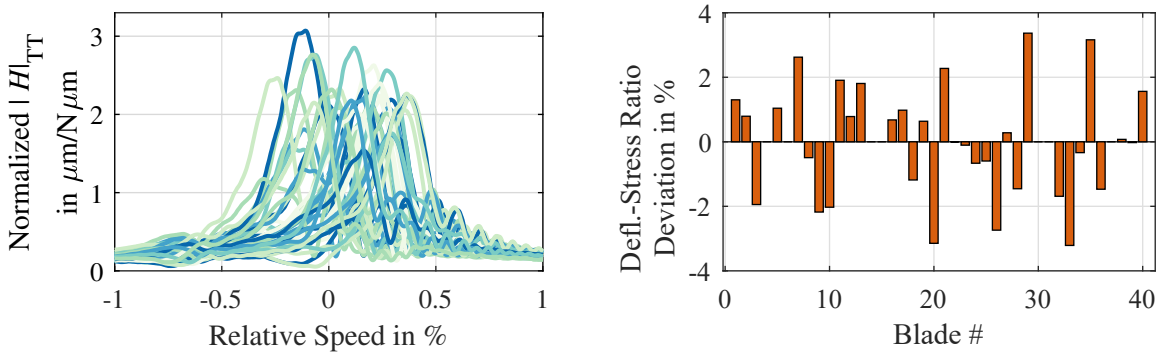

Figure 8: Blade individual response functions without the dampers during the Engine Order 10 crossing relative to the mean resonance speed (left) and the corresponding deviations from the mean deflection-stress ratios at resonance speed (right).

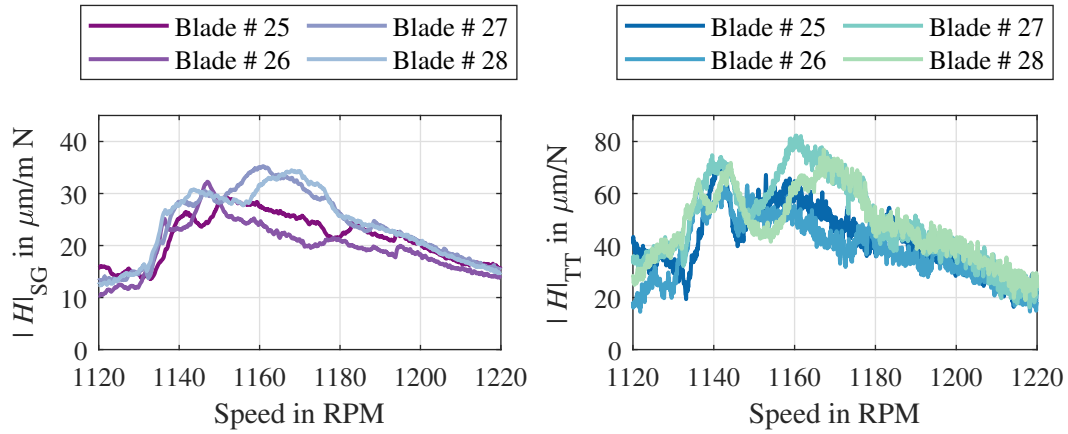

Figure 9: Individual blade response functions with a cylindrical friction damper for both Strain Gauge (left) and Tip Timing data (right) with still distinguishable shapes.

damper, a slightly reduced agreement between both measurement systems is noticeable in relation to Figure 5, but still all blades clearly can be assigned visually over their progressions along an increasing speed.
When considering the transfer functions for both underplatform dampers of an Engine Order 10 crossing in Figure 10, it is immediately noticeable that the beating phenomenon (see Figure 7) is no longer present, because of friction damping and thus a fast decay of the blades eigenfrequency response. Due to the reduced amplitude of the oscillation by means of friction damping, the signal to noise ratio is larger than without the dampers and there is no longer a distinct resonance peak, which causes the speed shift of the Tip Timing measurement data to tend to function less effectively.
As expected, both measurement results with dampers in Figure 10 exhibit a lower deflection-stress ratio in reso-

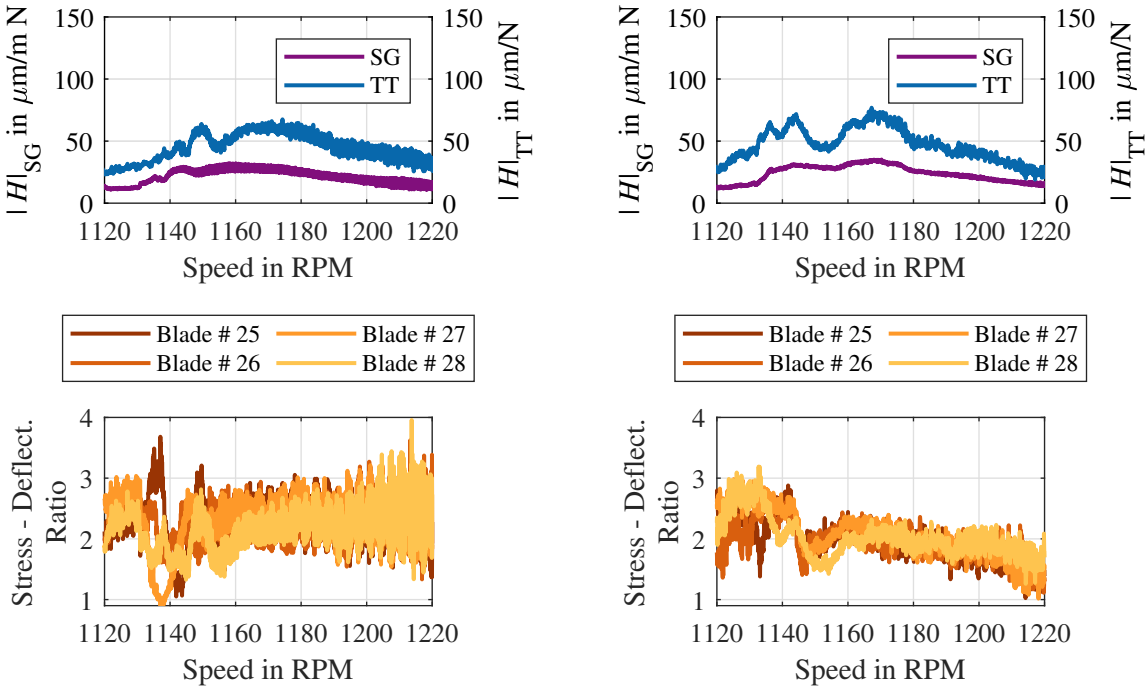

Figure 10: Transfer functions of Strain Gauge and Tip Timing data of Blade # 28 and selected blade individual deflection-stress ratios for an asymmetric (left) and a cylindrical (right) friction damper.

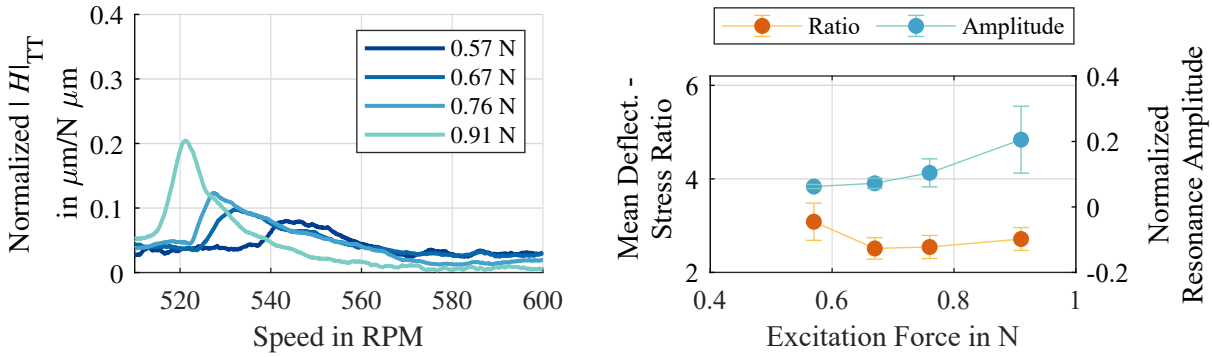

Figure 11: Normalized transfer functions of an EO 20 crossing with an asymmetric damper of Blade # 28 (left) and its normalized performance curve with mean and standard deviation values for resonance deflection-stress ratios (right).

nance than without the dampers, but differ only marginally from each other. This is due to the placement of the dampers under the blade platform, which reduces the free length of the blade. For both damper types, however the dissimilar blade stiffening due to the differently shaped contact surfaces therefore currently is negligible for this consideration.

In order to further evaluate the effect of friction damping, for both damper types the Engine Order 20 resonance crossings were measured at several magnetic force levels (see Figures 11 and 12). By increasing the excitation acting on the blade, principally the amplitude rises. This leads to at first a higher friction damping and eventually a damper, that is slipping (see [1], [8]). On the other hand, the peaks of the associated transfer functions first decrease and then, in the case of slipping, converge towards the results without dampers. This process can especially be seen in Figure 11, where at the left four transfer functions normalized by a reference amplitude are depicted. Following the increasing excitation, the progression of the transfer function converges towards the resonance speed without the dampers, as expected when slipping is present. Next to this a performance curve is shown, as presented by Cameron et. al. in [1] as the (normalized) resonance amplitude against the excitation force, and additionally the respective deflection-stress ratio. All values are depicted as the mean value along all blades with a functioning Strain Gauge for one measurement and its standard deviation.

As anticipated, a clear change can be seen in the ratios progression for both dampers in Figures 11 and 12, as the amplitude rises nonlinearly. Succinctly the ratio first declines and then rises again, with its minimum being roughly at the same excitation force as the maximally occurring damping, which is represented by the lowest peak of all transfer functions (see e.g. Figure 11). As stated by Panning et al. [8] cylindrical and asymmetric underplatform dampers exhibit dissimilar behaviour due to their different mass as well as contact surfaces, which can be observed when comparing Figures 11 and 12. Also noteworthy is the normalized resonance amplitudes rising standard deviation in the case of a slipping damper, as can be seen in Figure 11 for the highest excitation force. Some blades

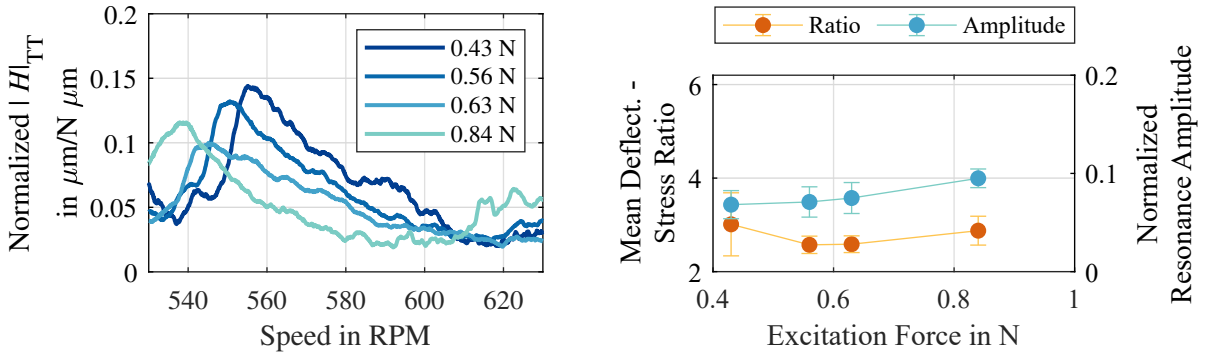

Figure 12: Normalized transfer functions of an EO 20 crossing with a cylindrical damper of Blade # 28 (left) and its normalized performance curve with mean and standard deviation values for resonance deflection-stress ratios (right).

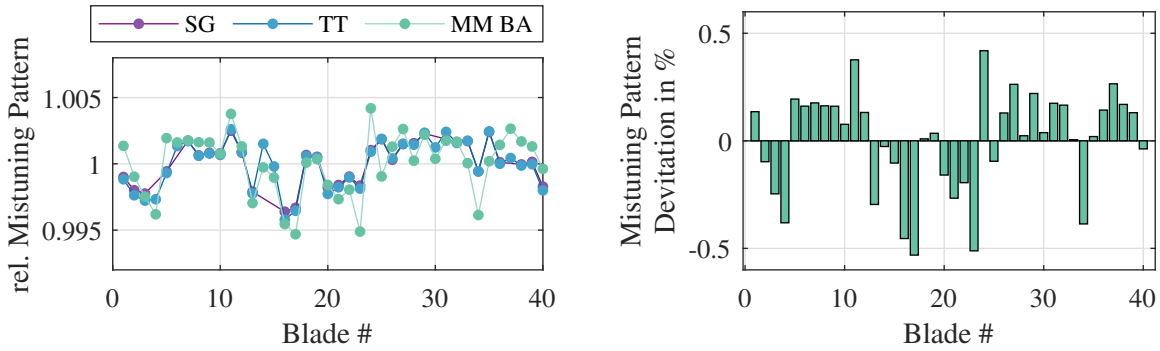

Figure 13: Blade individual 1F resonance frequency mistuning pattern measured with Strain Gauges and Tip Timing and calculated with mesh-morphing (left) and the resulting percentage deviation of mesh-morphing results against Tip Timing (right).

experience a mostly stuck damper, while others are already slipping, which derives primarily from the structural mistuning.

5 Comparative blade-alone simulations

Within the scope of another ongoing project at the Institute of Dynamics and Vibration Research (IDS) the actual geometry of the blisk has been measured at BTU Cottbus with an optical 3D measurement system and the FE model has been extended accordingly to an as-manufactured model of every blade, which will be discussed by Strehlau et. al. in [11] as well.

Structural mistuning typically is not considered in a cyclic expansion of a single simulated blisk sector. Mesh-morphing on the other hand, is a method to circumvent this by using the measured blisk geometry for the generation of a full Finite Element model (see [11]). For this paper, solely the simulated blade alone frequencies were evaluated, since only the blades could be measured sufficiently and furthermore the disk can justifiably be assumed to be rigid. The measured resonance frequencies however are determined by the maximum of the frequency response functions peak.

In this paper, only the resulting mistuning pattern in Figure 13 is considered, in order to validate it as the primary origin of the transfer function scatter (see Figure 8). For both measurement system, as well as the simulation, it represents each individual blades resonance frequency against the mean value from all blades as an percentage value.

As expected, there is a qualitatively good agreement of the patterns from Strain Gauge and Tip Timing measurements, the seven non-functioning Strain Gauges were left out for this depiction. Comparing the calculated blade alone with the Tip Timing mistuning pattern, a distinct agreement likewise is noticeable. The deviation of the calculated from the measured pattern in regard to a tuned case (value 1) is relatively low with a maximum deviation of $\pm 0.5\%$ (see Figure 13). Thus, this correlation now can validate the geometric mistuning as the fundamental reason for the scatter of the transfer functions without the dampers.

6 Conclusion

The implementation effort of a tip timing system is relatively low, but attention must be paid not only to the positioning of the probes, but also to a potentially manual blade allocation and an alignment with other measurement equipment, e.g. like the utilized speed encoder or Strain Gauges.

Despite the scattering of the transfer functions due to mistuning, the progression along the two Engine Order crossings considered without the dampers shows very good correlation between the measurement results of Strain Gauges and Tip Timing in both instances.

Similarly, the nonlinear results for both types of underplatform dampers still show a sufficiently good agreement, and the effect due to the slipping of the dampers can also be represented using both measurement systems. Considering the deflection-stress ratio, the mode shapes change as expected.

Finally the blade alone frequencies, obtained by means of mesh-morphing, display approximately the same mistuning pattern as the results without the dampers from both measurement systems and can thus indicate geometrical mistuning as the main cause for the spread of the linear transfer functions from individual blades without dampers,

as long as the blade-alone estimation is valid.
Summarising the above, it is shown that both measurement systems provide comparable results for engine runs with friction nonlinearities due to the underplatform dampers, along with very good accuracy during linear testing. Likewise, the mesh-morphed blade models are able to represent the trend of the measured mistuning pattern adequately.

Acknowledgment

For the period of these measurements, the Tip Timing system and its probes were kindly lent by the Institute of Turbomachinery and Fluid Dynamics (TFD). The investigations were conducted as part of the joint research program InnoTurbinE in the frame of AGTurbo. The work was supported by the Bundesministerium für Wirtschaft und Klimaschutz (BMWK) as per resolution of the German Federal Parliament under grant number 03EE5040A. The authors gratefully acknowledge Siemens Energy AG for their financial support and the permission to publish this paper. The responsibility for the content of the publication rests with the authors.

References

[1] Cameron, T. M.; Griffin, J. H.; Kielb, R. E.; and Hoosac, T. M. (1990): An Integrated Approach for Friction Damper Design. In *ASME. Journal of Vibration and Acoustics*, **112**(2).

[2] Diamond, D.H.; Heyns, P.S. (2018): A Novel Method for the Design of Proximity Sensor Configuration for Rotor Blade Tip Timing. In *ASME Journal of Vibration and Acoustics*, **140**(6).

[3] Fan, C.; Russhard, P.; Wang, A.; Chen, Y.; Dong, W. (2018): Analysis of blade tip timing data from fan blades with synchronous and non-synchronous vibration. In *Journal of Physics: Conference Series*, **1149**.

[4] Gillaugh, D.L.; Janczewski, T.J.; Kaszynski, A.A.; Brown, J.M.; Beck, J.A.; Nessler, C. (2020): Forced Response Variation of a Compressor Utilizing Blade Tip Timing, Strain Gages, and As-Manufactured Finite Element Models. In *Proc. of the ASME Turbo Expo 2020: Turbomachinery Technical Conference and Exposition*, Online, Sept. 21-25.

[5] Hoffmann, T.; Panning-von Scheidt, L.; Wallaschek, J. (2020): Measured and Simulated Forced Response of a Rotating Turbine Disk With Asymmetric and Cylindrical Underplatform Dampers. In *ASME. J. Eng. Gas Turbines Power*, **142**(5).

[6] Di Maio, D.; Ewins, D.J. (2012): Experimental measurements of out-of-plane vibrations of a simple blisk design using Blade Tip Timing and Scanning LDV measurement methods. In *Mechanical Systems and Signal Processing*, **28**, pp. 517-527.

[7] Maywald, T.; Beirow, B.; Heinrich, C.R.; Kühhorn, A. (2015): Vacuum Spin Test Series of a Turbine Impeller With Focus on Mistuning and Damping by Comparing Tip Timing and Strain Gauge Results. In *Proc. of the ASME Turbo Expo 2015: Turbomachinery Technical Conference and Exposition*, Montreal, June 15-19.

[8] Panning, L.; Popp, K.; Sextro, W.; Götting, F.; Kayser, A.; Wolter, I. (2004): Asymmetrical Underplatform Dampers in Gas Turbine Bladings: Theory and Application. In *Proc. of the ASME Turbo Expo 2004: Power for Land, Sea, and Air*, Vienna, June 14-17.

[9] Russhard, P. (2016): Blade tip timing (BTT) uncertainties. In *AIP Conference Proceedings*, **1740**.

[10] Rzadkowski, R.; Rokicki, E.; Piechowski, L.; Szczepanik, R. (2016): Analysis of middle bearing failure in rotor jet engine using tip-timing and tip-clearance techniques. In *Mechanical Systems and Signal Processing*, **76-77**, pp. 213-227.

[11] Strehlau, U.; Langheinrich, D.; Xiao, Y.; Panning-von Scheidt, L. (2023): Geometrically mistuned blisks: Assessment of geometric uncertainties and Finite-Element mesh morphing. In *SIRM 2023 - 15th International Conference on Dynamics of Rotating Machines*, Darmstadt, February 22-24 (abstract accepted).

[12] von Flotow, A.; Mercadal, M.; Tappert, P. (2000): Health Monitoring and Prognostics of Blades and Disks with Blade Tip Sensors. In *IEEE Aerospace Conference. Proceedings*, **6**, pp. 433-440.

15th SIRM – European Conference on Rotordynamics,
Darmstadt, Germany, 22nd – 24th February 2023

Geometrically mistuned blisks: Assessment of geometric uncertainties and Finite-Element mesh morphing

Ulrik Strehlau [1], Denny Langheinrich [1], Yue Xiao [2], Lars Panning-von Scheidt [2]

[1] Chair of Structural Mechanics and Vehicle Vibrational Technology, Brandenburg University of Technology, 03046, Cottbus, Germany, strehlau@b-tu.de
[2] Institute of Dynamics and Vibration Research, Leibniz University of Hannover, 30823, Garbsen, Germany, xiao@ids.uni-hannover.de

Abstract

Unavoidable geometric uncertainties due to the manufacturing process could significantly affect the dynamic properties of bladed disks and of blade integrated disks (blisks). These small geometric deviations from the design intention are known as mistuning. Consequently, the rotor blades are featuring different eigenfrequencies, which could possibly affect the safety and reliability of the engine. This work focuses on identifying blade geometry mistuning and investigates the effect of geometric mistuning on blade eigenfrequencies. The geometry of a blisk with 40 blades is captured by optical geometric measurement and computation models are generated from the measured point cloud. A mesh-morphing procedure is carried out to generate new FE-meshes for each individual blade. The frequency mistuning pattern of the first bending mode (1F) is calculated for morphed blade models, using Finite Element Analysis (FEA). Additionally, the deviation from the nominal geometry is represented by means of principal components analysis (PCA), in which the geometric deviation can be represented by several uncorrelated geometric mistuning modes (GMM). The computed mistuning distributions, calculated with FEA and with the PCA-GMM method are compared to experimental tip-timing results.

1 Introduction

In addition to the advantage of weight savings, the use of blade integrated disks (blisks) has the disadvantage of an adverse structural dynamic behaviour compared to compressor disks using conventionally connected blades for instance with fir tree profiles [Bei2008, Nip2011]. The reason for this specific behaviour is the lack of friction damping, which already facilitates high forced responses by itself. Moreover, the response magnifying effect of mistuning may worsen. Remarkably severe magnifications of the maximum forced response up to a factor of five have been reported by Whitehead [Whi1998] and Petrov and Ewins [Pet2003]. An overview of the phenomenon has been published by Castanier and Pierre [Cas2006]. In order to ensure a safe operation of these components, the knowledge of their structural dynamic behaviour is very important. The mistuning effect is induced by two main reasons, material inhomogeneities and geometrical deviations. The latter becomes more and more important during operation due to wear and abrasion [Kla2008].

The geometrical reasons for a blade individual behaviour are addressed in this paper. An optical 3d-geometry measurement of the academic blisk is carried out and the resulting point cloud is foundation for the two evaluation methods. Firstly, a mesh morphing procedure of a design FE-model provides a geometrically updated FE-model of the blisk, which is employed to compute the mistuning pattern of the first flap mode. Similar approaches are presented in [Sch2009, Str2011, Kas2018, May2017]. Secondly, a PCA (Principle Component Analysis) and GMM (Geometric Mistuning Modes) method is presented in order to compute the mistuning pattern of the first flap mode. Similar approaches are presented in [Sin2008, Pop2015, Car2018]. Numerical results of both approaches are compared and the correlation with tip-timing measurement data is considered.

The subject of investigation is a test blisk with 40 blades, serving as a test blisk at the Institute of Dynamics and Vibration Research, Leibniz University of Hannover. This blisk has been procured primarily for damping tests and is milled from solid and equipped with strain gauges on each blade (**Figure 1**) [Hof2020].

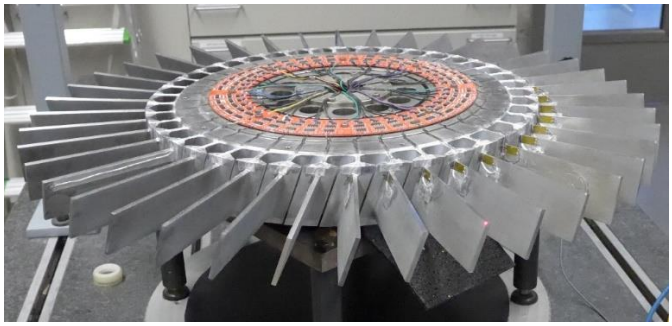

Figure 1: Test blisk of the Institute of Dynamics and Vibration Research (IDS), Leibniz University of Hannover.

2 3D-geometry measurement

Production-related deviations are the most frequent cause of mistuning of newly manufactured blisks. In order to capture these often very small differences in the blade shapes, a 3d geometry measurement is suitable. The digitisation of a real measurement object requires a careful procedure in several steps.

2.1 Preparation

In order to ensure a good handling of the measurement object during the measurement process, a mounting is designed, that supports the blisk and provides the connection to the used turntable. Optical reference points are also needed for the measurement. These are glued on a frame in order to increase the accuracy when assembling the different 3d-scans. **Figure 2** shows a CAD model of the nominal perfectly cyclic blisk and a photo of the measurement object with its mounting and reference frame.

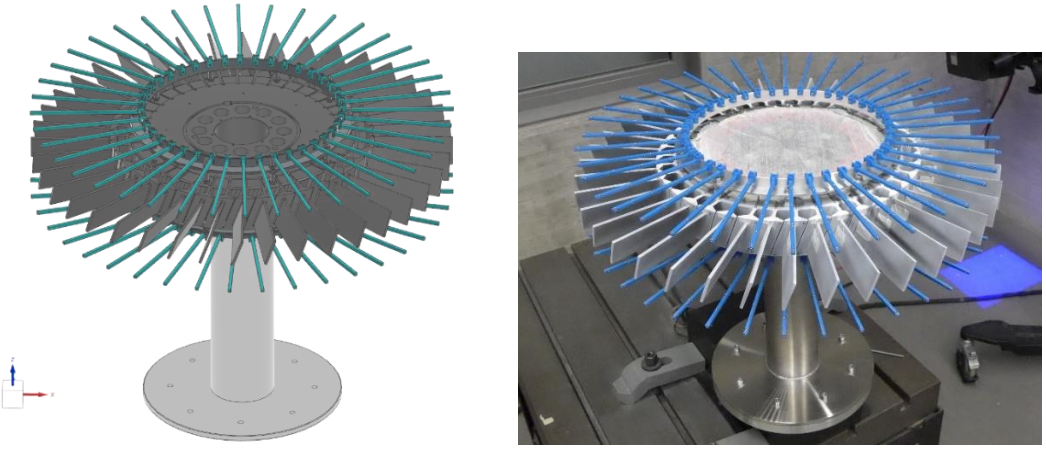

Figure 2: Blisk and mounting; CAD-model (left), photo of measurement setup (right)

2.2 Digitisation-blue light fringe projection

The digitisation takes place in two steps. First step is the photogrammetry. For this purpose, two calibrated reference bars and coded reference marks are placed in the measurement environment. By means of the reference bars the absolute position of the coded marks are known to the measurement software. In this way, the uncoded marks, that are placed on the reference frame and the blisk itself are recognisable for the digitalisation software. More than 600 photos from different perspectives around the object were taken to ensure that all of about 2,000 reference marks are recognised by the digitisation software.

The surface scan was conducted using a blue light fringe projection with 1,165 different perspectives. In this manner an almost closed surface was digitised. Some regions with a poor optical accessibility, especially at the damper pockets, could not be digitised and had to be extrapolated in these areas after the scanning process. **Figure 3** shows an example of a typical repair region with a poor optical accessibility.

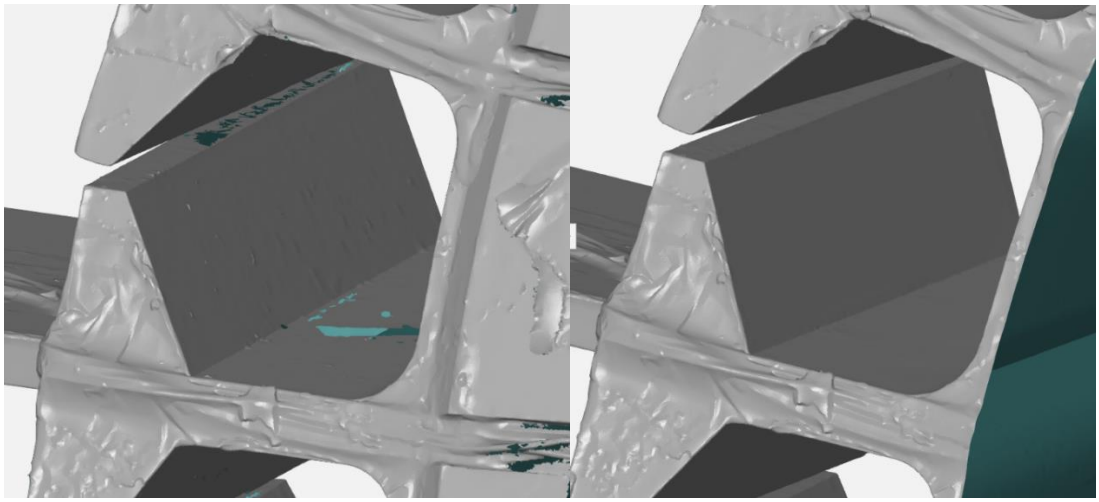

Figure 3: Measured surface in damper pocket area before (left) and extrapolation (right).

In order to get an impression of the measured and repaired surface a best fit (least square method) comparison of the measured surface and the tuned CAD geometry is carried out. Areas which do not correspond to the CAD model, especially regions with strain gauges including their cabling and its bonding are excluded from the best-fit calculation. The result is shown in **Figure 4**. Strain gauges are clearly visible and all blades show a significant twist along the longitudinal axis with respect to the nominal geometry. Also, tool marks are clearly recognisable (**Figure 5**). However, a local best-fit on a blade surface is calculated for this.

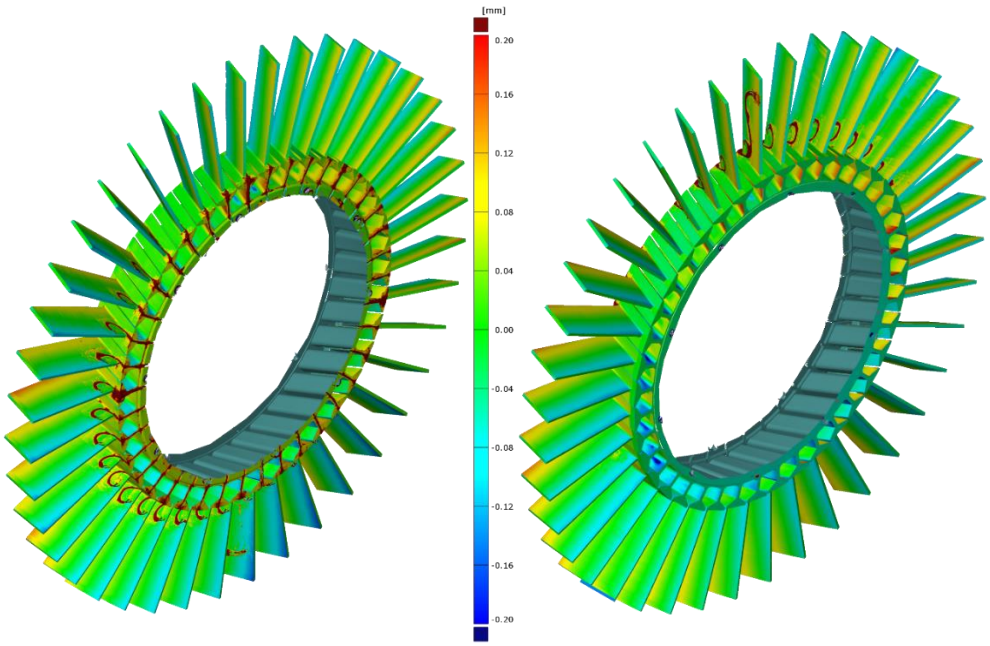

Figure 4: Real-geometry compared with CAD-geometry in a best-fit of all blades in two perspectives

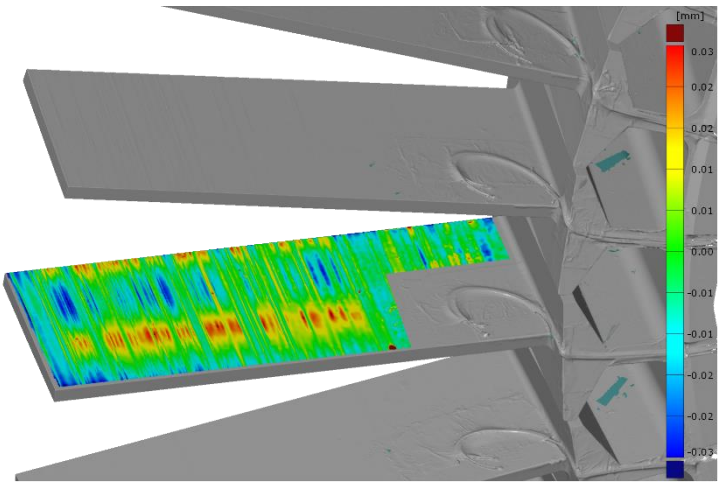

Figure 5: Real-geometry compared with CAD-geometry in a local best-fit on surface of one blade

3 Computation of models with mistuned geometry properties

In order to create a numerical model from measured blade-specific geometry properties, two different paths are chosen. Firstly, a tuned FE-model of the whole blisk is the basis for a morphing process. The characteristics of the morphed and thus mistuned FE-model are captured by computational modal analysis. Secondly, an FE sector model of the blisk is used for a PCA (Principle Component Analysis) in conjunction with a GMM (Geometric Mistuning Modes)-analysis.

3.1 Generation of the geometrically mistuned FE-model of the whole blisk

In order to get a calculation model of the measured blisk, an FE-model based on the CAD geometry of one sector is created. One sector (**Figure 6**) is meshed and its two sector boundaries feature the same node architecture. This single sector model is patterned and the 40 sectors are merged, to create a model of the whole blisk. It consists of about 4.7 million quadratic tetrahedral elements and almost 7.2 million nodes. The measured point cloud and the FE-model of the whole blisk have to be aligned.

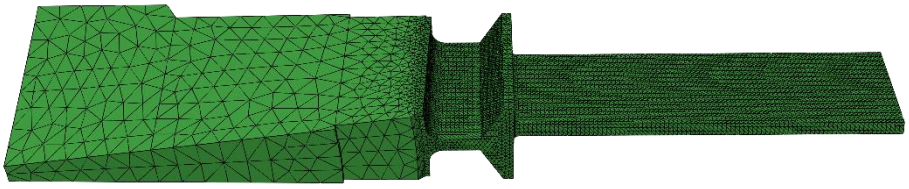

Figure 6: FE-model of one sector

Each FE-node at the surface in the blade area of the CAD-based whole blisk FE-model is moved into a plane constructed by vectors in the measured point cloud (**Figure 7**). Firstly, the ten closest neighbours (blue dots in Figure 7) of each FE-node to be morphed are searched in the measured point cloud (black dots). Then nine vectors are formed, each starting from the nearest neighbour to the nine remaining neighbours. Two of these vectors, usually one of the longest and one of the shortest vectors, are used to define the plane, in which the FE-node is moved. Both vectors have to fulfil the constraint, that the angle between them is greater than 20° and less than 160° (black arrows in Figure 7). If this constraint is violated, another combination of vectors gets checked with regard to a sufficient linear independence. The scalar product between the normal vector of the plane and the vector between FE-node and nearest neighbour in the point cloud defines the length of the shift of the FE node in the plane-normal direction (purple arrow in Figure 7). In this way each FE-node is moved by the shortest distance to the plane defined by the nearest neighbour points of the measured cloud.

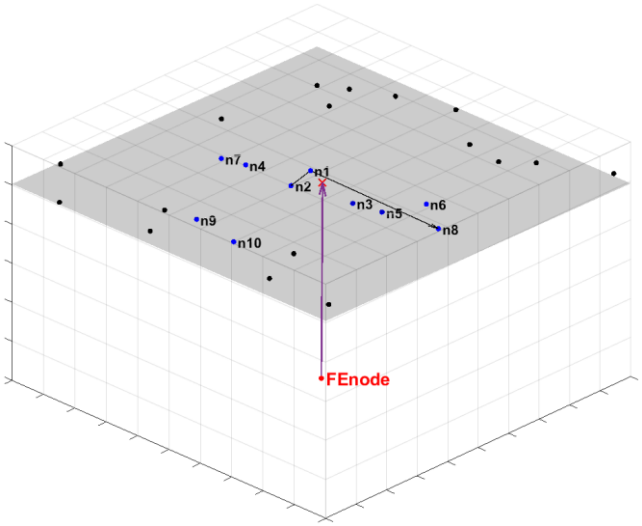

Figure 7: Artificially generated projection plane for morphing process

The FE-model of the whole blisk, generated in the descripted way, reflects the geometry with strain gauges, cables and its bondings. However, the material properties of these added parts are difficult to evaluate and even if they were known, the assignment to the individual elements in the FE-model would only be possible imprecisely. Therefore, these elements are removed from the measured point cloud. For this purpose, the areas covered with strain gauges, cables and duct tape are cut out and the resulting holes are filled using locally adapted CAD surfaces, which are sewn to the remaining point cloud. The result is shown exemplarily for one strain gauge in **Figure 8**. Although a FE-model created with this approach does not represent the real blisk vibration behaviour, it presumably shows the smallest inaccuracy, in comparison to the strain gauge influence. With the help of this FE-model, blade individual frequencies are calculated. The results are shown in section 4.

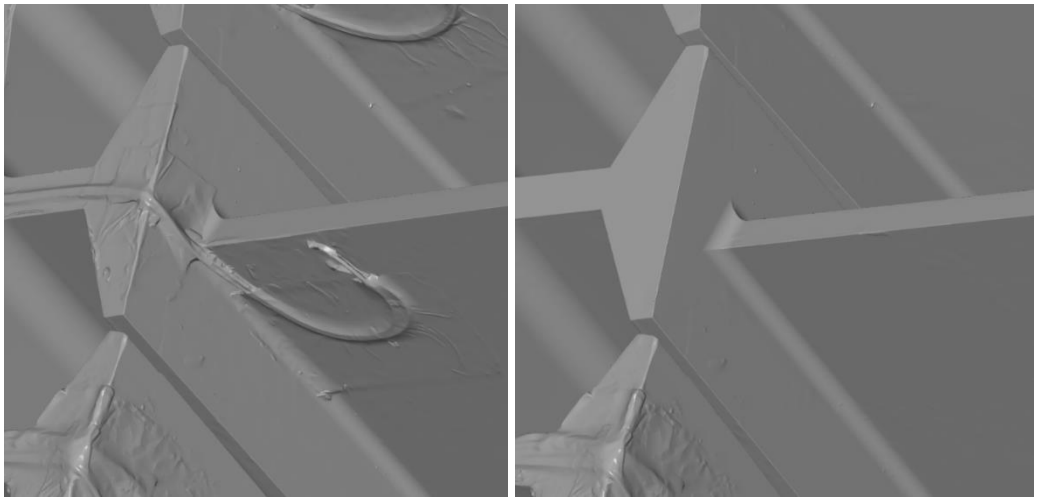

Figure 8: Measured STL-mesh original (left), with removed strain gauges (right)

3.2 PCA and geometric mistuning modes

To capture the geometrical mistuning due to manufacturing effects, PCA (Principle Component Analysis) is applied to the measured blade geometries [Sin2008]. In this step, the surface geometry S of nominal blade and surface geometries S' of real blades are compared. The geometries of real blades can be represented by the in section 3.1 morphed FE-models, because the comparison results in section 5 show that the eigenfrequencies of real blades can be represented by morphed FE-models equivalently.

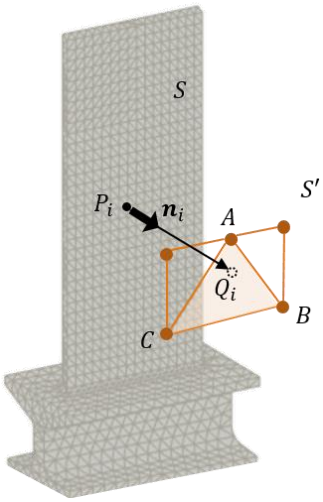

Figure 9: Projection in normal direction

In order to reduce the data dimension, the geometrical mistuning between S and S' is assumed to be dominated by the thickness variation [Car2018]. Under this assumption, a normal projection procedure is adopted (**Figure 9**). Each FE-node P_i of nominal blade surface S is projected into the real blade surface S'. The projected point is Q_i and the projection direction is the local normal direction $\boldsymbol{n}_i$ of FE-node P_i.

The normal vector $\boldsymbol{n}_i$ is calculated based on the existing unmorphed FE-mesh as shown in Figure 6. Finding the projection Q_i is carried out in following steps. Firstly, three nonaligned candidate FE-nodes A, B and C on surface S' are selected. Then the normal vector $\boldsymbol{n}_i$ can be represented by linear combination of three independent vectors, as descripted in Eq.(1).

$$[\boldsymbol{r}_{P_iA}, \quad \boldsymbol{r}_{P_iB}, \quad \boldsymbol{r}_{P_iC}]\begin{bmatrix} a \\ b \\ c \end{bmatrix} = \boldsymbol{n}_i \tag{1}$$

Here $\boldsymbol{r}_{P_iA}$, $\boldsymbol{r}_{P_iA}$ and ,$\boldsymbol{r}_{P_iC}$ represent the vectors from P_i to A, B and C in global coordinate system, respectively. If all the combination coefficients have the same sign (i.e. $a, b, c \geq 0$ or $a, b, c \leq 0$), the projected point Q_i lies within the triangle $\triangle ABC$. The selected candidate points will then be retained for calculation in the next step. Otherwise, a new set of candidate points will be generated. The coordinates of a projected point Q_i can be obtained by two other equations:

(1) Q_i is in the plane defined by A, B and C

$$[\boldsymbol{r}_{AB}, \quad \boldsymbol{r}_{AC}]\begin{bmatrix} \alpha \\ \beta \end{bmatrix} = \boldsymbol{r}_{AQ_i} \tag{2}$$

(2) Q_i is in the line defined by normal vector $\boldsymbol{n}_i$.

$$\boldsymbol{r}_{P_iQ_i} = \lambda \boldsymbol{n}_i \tag{3}$$

applying the geometrical relation $\boldsymbol{r}_{AQ_i} = \boldsymbol{r}_{AP_i} + \boldsymbol{r}_{P_iQ_i}$, the unknown variables α, β and λ can be solved by Eq.(4). The coordinates of Q_i are given by $\boldsymbol{r}_{Q_i} = \boldsymbol{r}_{P_i} + \lambda \boldsymbol{n}_i$ and the normal distance $d_i = \|\boldsymbol{r}_{P_i} - \boldsymbol{r}_{Q_i}\|$.

$$[\boldsymbol{r}_{AB}, \quad \boldsymbol{r}_{AC}, \quad -\boldsymbol{n}_i]\begin{bmatrix} \alpha \\ \beta \\ \lambda \end{bmatrix} = \boldsymbol{r}_{AP_i} \tag{4}$$

The procedure mentioned above is repeated for all FE-nodes P_i, $i = 1, \ldots, N$ in the nominal blade surface and for all morphed blade surfaces S_j', $j = 1, \ldots, 40$. Eq. (5) shows the deviation matrix $\boldsymbol{D}$, where the column $\boldsymbol{d}_j = [d_{1j}, d_{2j}, \ldots, d_{Nj}]^T$ represents the normal deviations between nominal blade surface and the j-th morphed blade surface.

$$\boldsymbol{D} = \begin{bmatrix} | & | & \cdots & | \\ \boldsymbol{d}_1 & \boldsymbol{d}_2 & \cdots & \boldsymbol{d}_{40} \\ | & | & \cdots & | \end{bmatrix} \tag{5}$$

According to PCA, each column of matrix $\boldsymbol{D}$ is subtracted from the column mean $\bar{\boldsymbol{d}}$ and the resulting matrix $\boldsymbol{X}$ is decomposed using SVD (singular value decomposition).

$$\boldsymbol{X} = \begin{bmatrix} | & | & \cdots & | \\ \boldsymbol{d}_1 - \bar{\boldsymbol{d}} & \boldsymbol{d}_2 - \bar{\boldsymbol{d}} & \cdots & \boldsymbol{d}_{40} - \bar{\boldsymbol{d}} \\ | & | & \cdots & | \end{bmatrix} = \boldsymbol{U}\boldsymbol{\Sigma}\boldsymbol{V}^T. \tag{6}$$

Here $\bar{\boldsymbol{d}}$ represents the mean geometrical deviation of all 40 morphed blades relative to the nominal one, as shown in **Figure 10** (left). Red regions and blue regions in the contour plot represent positive and negative deviations along the local normal direction, respectively. Figure 10 shows that the average blade geometry reflects a twist-dominated geometrical mismatch.

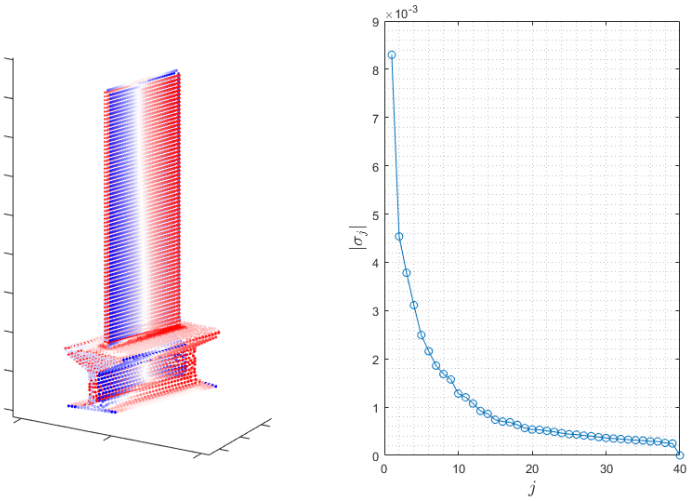

Figure 10: Average blade geometry (left) and singular values (right)

3.3 Comparison FEM-Mistuning / PCA&GMM-Mistuning

According to PCA, the matrix $\boldsymbol{U}$ in **Eq. (6)** expands the column space of deviation matrix $\boldsymbol{D}$. Thus, the columns of $\boldsymbol{U}$ can be regarded as geometric mistuning modes (GMM) included in the data set. The diagonal elements in the singular value matrix $\boldsymbol{\Sigma}$ represent the participation amplitude of each geometric mistuning mode as shown in Figure 10 (right). The first few modes have greater singular values and represent the most common geometric mismatches which almost all blades experience, such as thickness variation and twist, as shown in **Figure 11** (left). On the contrary, the mismatches represented by modes of higher order reflect more individual features which happen only to some of the blades, as shown in Figure 11 (right). They are of less importance compared to the first few modes. In order to reduce the dimension of the problem and to focus on the main mistuning features, a truncated set of 26 GMMs can be selected according to Eq. (7).

$$\sum_{j=1}^{tr} |\sigma_j| \geq 0.9 \sum_{j=1}^{40} |\sigma_j| \Rightarrow tr = 26 \tag{7}$$

$$\tilde{\boldsymbol{D}} = \begin{bmatrix} | \\ \bar{\boldsymbol{d}} \\ | \end{bmatrix} [1,1,\ldots,1] + \boldsymbol{U}_{tr}\boldsymbol{\Sigma}_{tr}\boldsymbol{V}_{tr}^T = \begin{bmatrix} | & | & \cdots & | \\ \tilde{\boldsymbol{d}}_1 & \tilde{\boldsymbol{d}}_2 & \cdots & \tilde{\boldsymbol{d}}_{40} \\ | & | & \cdots & | \end{bmatrix} \tag{8}$$

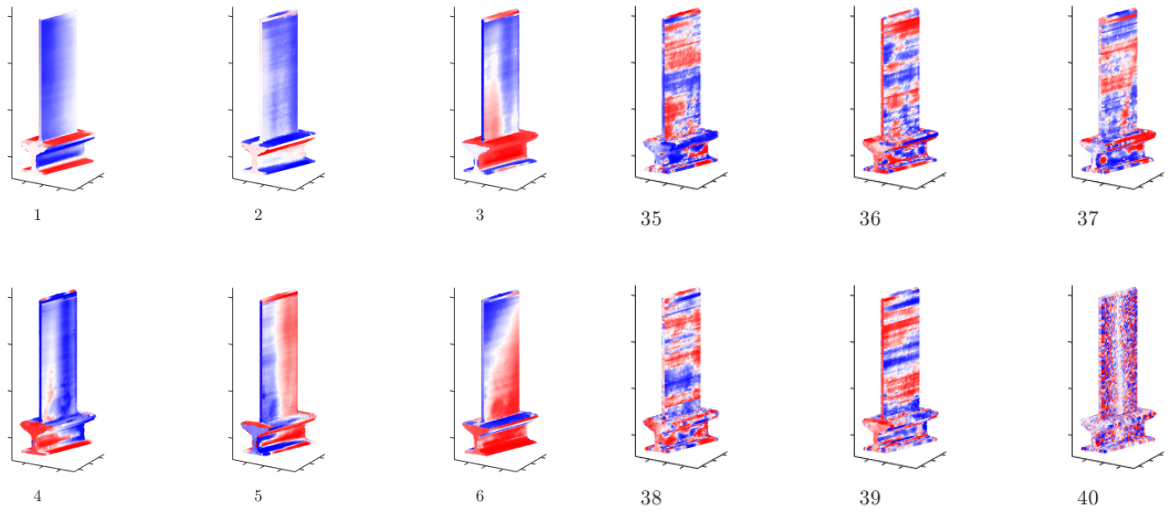

Figure 11: The first 6 geometric mistuning modes (left) and the last 6 geometric mistuning modes (right)

After truncation the deviation matrix $\boldsymbol{D}$ can be approximated by $\widetilde{\boldsymbol{D}}$ in Eq.(8) which contains a less number of modes. Applying $\widetilde{\boldsymbol{d}}_j(\,j = 1, \ldots, 40)$ as pre-defined normal deviation, it is possible to reconstruct a set of blades in which only the dominated geometric mismatches are considered. The reconstruction procedure requires a further stiffness-based mesh-morphing which is explained in [Car2018]. **Figure 12** shows the percentage error in first flap eigenfrequency using truncated GMM set. The error is small for all blades and it is thus sufficient to use the first 26 GMMs to represent the modal behaviour of geometric mistuned blades

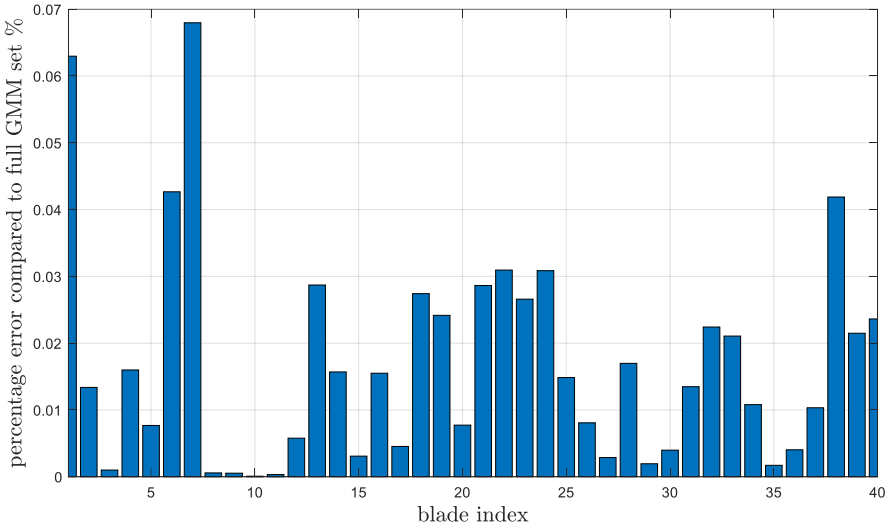

Figure 12: Percentage error of first flap eigenfrequencies using truncated GMM set

4 Comparison calculation results and tip-timing results

In this section the blade individual frequencies of the first flap mode of both calculation methods (the directly morphed FE-model and the model created with PCA-GMM-method) and the blade resonance frequencies measured in rig-tests by tip-timing are compared. Information regarding the tip-timing measurement can be found in [Bri2023].

Figure 13 shows the frequency distributions of the 40 blades in relation to their respective mean values. The deviation between both calculated results, correlate well, the differences are quite small. In contrast the tip-timing measurement results of the frequency mistuning distribution show bigger differences compared to the calculation results. Reasons for these differences are probably caused in editing the measured geometry point cloud. The removal of the strain gauges and the repair of several areas with poor optical accessibility are sources of inaccuracies and may lead to a random geometrical mismatch of the measured point cloud. The errors introduced in this way continue in the further processing of the morphed FE-meshes. Another reason for differences is the rotational speed, that is not considered in the calculations.

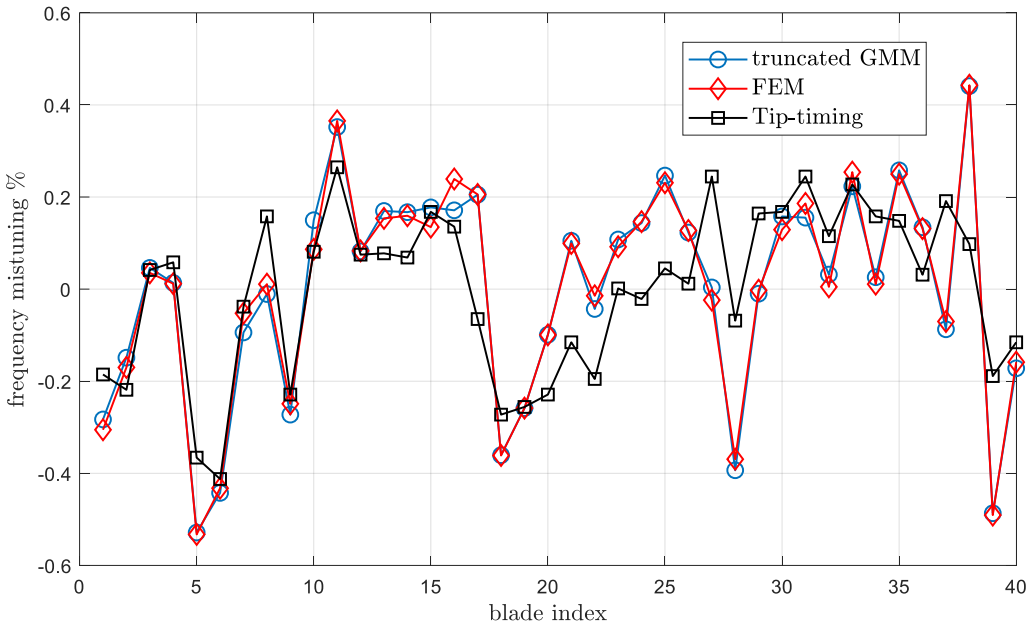

Figure 13: Frequency mistuning distribution, calculated (PCA, FEM) and measured via tip timing

5 Conclusion

Two different approaches are shown in this paper in order to create models for calculating blade individual frequencies of the first blade mode from a point cloud based on a 3d measurement. It is found that the differences between both computational models, on the one hand the directly morphed full FE-model and on the other hand the model generated by PCA (Principal Component Analysis) and GMM (Geometric Mistuning Modes) are quite small. Starting from the same measured and processed point cloud of the blisk, various morphing algorithms as well as the reduction of the computational effort of the PCA-GMM method have low impact on the calculation result of the blade individual frequencies of the first flap mode. In contrast, the differences between the calculation models and the tip-timing measurement are greater, even if the mistuning range and the rough shape of the mistuning pattern are well comparable. Especially the retouching of the strain gauges with their cables etc. as well as the manual insertion of the replacement surfaces probably leads to inaccuracies. Furthermore, the calculation results are generated with stationary systems and thus dynamic effects (stiffness) of the rotating system, with which the measurement results are generated via tip-timing, are not included und increase the uncertainty. Possible material inhomogeneities are not taken into account in the calculation model. The work should be repeated with a measurement object that requires a reduced amount of post-processing and thus eliminates the probably most important uncertainty.

Acknowledgement

The authors kindly thank the FVV eV. The research project was carried out in the framework of the industrial collective research programme (IGF no.21045 N). It was supported by the Federal Ministry for Economic Affairs and Climate Action (BMWK) through AiF (German Federation of Industrial Research Associations eV) based on a decision taken by the German Bundestag. The experimental investigations were conducted as part of the joint Research program InnoTurbinE in the frame of AG Turbo and was supported by the BMWK as per resolution of the German Federal Parliament under grant number 03EE5040A.

References

[Bei2008] Beirow, B., Kühhorn, A., Schrape, S. (2008): A Discrete Model to Consider the Influence to the Air Flow on Blade Vibrations of an Integral Blisk Compressor Rotor. ASME Paper GT2008-50613, *Proceedings of ASME Turbo Expo*, 2008, Berlin, Germany.

[Bri2023] Brinkmann, K. (2023): Geometrically mistuned blisks: Strain gauge and tip timing vibration measurements of rotating blades with and without underplatform dampers. *Proceedings of SIRM 2023* (abstract accepted), 2023 Darmstadt, Germany

[Car2018] Carassale, L., Bruzzone, S., Cavicchi, A., Brunenghi, M. (2018): Representation and Analysis of Geometric Uncertainties in Rotor Blades. ASME Paper GT2018-76385, *Proceedings of ASME Turbo Expo 2018,* Oslo, Norway.

[Cas2006] Castanier, M. P., Pierre, C. (2006), "Modelling and Analysis of Mistuned Bladed Disk Vibration: Status and Emerging Directions". *Journal of Propulsion and Power*, Vol. 22, No. 2, pp. 384-396.

[Hof2020] Hoffmann, T., Panning-von Scheidt, L., and Wallaschek, J. (2020). "Measured and Simulated Forced Response of a Rotating Turbine Disk With Asymmetric and Cylindrical Underplatform Dampers." ASME. *J. Eng. Gas Turbines Power*. May 2020; 142(5): 051002.

[Kas2018] Kaszynski, A. A., Beck, J.A., Brown, J.M. (2018), Automated Meshing Algorithm for Generating As-Manufactured Finite Element Models Directly From As-Measured For Blades and Integrally Bladed Disks. *Proceedings of ASME Turbo Expo 2018*. Paper GT 2018-76375, June 11-15, 2018, Oslo, Norway.

[Kla2008] Klauke, T., Kühhorn A., Beirow, B., Parchem, R. (2008): Blade Vibration Phenomena of HPC Bliscs Considering Manuafcturing Effects and Strain Gauge Application. *Proceedings of ASME Turbo Expo*, 2008, Berlin, Germany.

[May2017] Maywald, T., Backhaus, T., Schrape, S., Kühhorn, A. (2017). Geometric Model Update of Blisks and its Experimental Validation for a Wide Frequency Range. *Proceedings of ASME Turbo Expo 2017*, GT2017-63446, June 26-30, 2017, Charlotte, NC, USA.

[Nip2011] Nipkau, J. (2011): *Analysis of Mistuned Blisk Vibrations Using a Surrogate Lumped Mass Model with Aerodynamic Influences.* PhD Thesis, BTU-Cottbus, Shaker Verlag, ISBN: 978-3-8440-0302-4.

[Pet2003] Petrov, E. P., Ewins, D. J. (2003): Analysis of the Worst Mistuning Patterns in Bladed Disk Assemblies. *Journal of Turbomachinery*, Vol. 125, pp. 623-631.

[Pop2015] Popig, F., Hönisch, P., Kühhorn, A. (2015): Experimental and Numerical Analysis of Geometrical Induced Mistuning. *Proceedings of ASME Turbo Expo 2015*, GT2015-43272, 13-19 June 2015, Montréal, Canada.

[Sch2009] Schoenenborn, H., Grossmann, D., Satzger, W., Zisik, H. (2009): Determination of blade-alone frequencies of a blisk for mistuning analysis based on optical measurements. ASME Paper GT2009-59148, *Proceedings of ASME Turbo Expo 2009,* Orlando, Florida (USA).

[Sin2008] Sinha, A., Hall, B., Cassenti, B., Hilbert, G. (2008): Vibratory Parameters of Blades From Coordinate Measurement Machine Data. *Journal of Turbomachinery*. Vol. 130, pp. 011013-1 - 011013-8.

[Str2011] Strehlau, U. (2011): *Schaufelschwingungen realer integraler Verdichterlaufräder bei zusätzlicher Berücksichtigung höherer Moden.* PhD Thesis, BTU-Cottbus, Shaker Verlag, ISBN: 978-3-8440-0491-5.

[Whi1998] Whitehead, D. S. (1998): The Maximum Factor by Which Forced Vibration of Blades Can Increase Due to Mistuning. *Journal of Engineering for Gas Turbines and Power,* Vol 120, pp. 115-119.

SIRM 2023 – 15th International Conference on Dynamics of Rotating Machines, Darmstadt, Germany, 22nd – 24th February 2023

Numerical Evaluation of Alford Forces Acting on an Axial Expander for Supercritical CO2 Application

Edoardo Gheller [1], Steven Chatterton [1], Lorenzo Cosi [2], Gabriele Girezzi [2], Alessandro De Luca [2], Paolo Pennacchi [1]

[1] Department or Mechanical Engineering, Politecnico di Milano, 20145, Milan, Italy, {edoardo.gheller, steven.chatterton, paolo.pennacchi}@polimi.it
[2] Turbomachinery & Process Solutions, Baker Hughes, 50127, Florence, Italy, {lorenzo.cosi, gabriele.girezzi, alessandro.deluca}@bakerhughes.com

Abstract

Nowadays, supercritical carbon dioxide (S-CO2) cycles are of great interest in the scientific research especially considering the energy transition that is occurring. The S-CO2 high density and relatively low viscosity make it an interesting fluid for power generation. For large heat sources, large flowrates of fluid can be obtained. Therefore, the development of axial flow expanders can allow large power generations.

In the presence of rotor eccentricities, the aerodynamic loading of free-standing blades is not constant tangentially and will promote the lateral vibration of the rotor. The dynamic phenomenon that arises is known as Thomas-Alford force. The Thomas-Alford force determines an increase of the vibration level of the machine and a higher risk of instabilities.

In this paper, a preliminary investigation of a S-CO2 axial expander stage is performed. Different correlations proposed in the literature are adopted to estimate the magnitude of the Thomas-Alford force. A mono-dimensional code and a simplified computational fluid dynamics (CFD) model are adopted to obtain the parameters of the stage considered. In this preliminary investigation, only free-standing blades are considered.

The results obtained show a good agreement between 1D and CFD inputs required by the different correlation used. Despite this, the cross coupled stiffness calculated are widely dependent on the correlation used; then, this study can be considered as the starting point for more detailed investigations validating the correlations behavior in this environment through an unsteady CFD and/or a proper test campaign.

1 Introduction

In the energy transition and decarbonization perspective, scientific research is focusing more and more on renewable energy sources. Among the others, supercritical carbon dioxide (S-CO2) cycles are of great interest.

As reported in [1], S-CO2 cycles have a wide range of applications. They can be considered as a substitute for the water Rankine cycles in nuclear and fossil fuels power plants or they can be also applied to Waste Heat Recovery applications [9]. S-CO2 cycles can also be applied with renewable energy sources like the geothermal and the solar ones [10]. As for the fluids used in organic Rankine cycles (ORCs), S-CO2 is characterized by large density and low viscosity. The big advantage of S-CO2 is that is not flammable, not toxic, and has a much lower impact on the environment than most of the gases used for ORCs.

Typically, the power generation for Waste Heat Recovery cycles is performed by radial expanders. However, if large heat sources are available, there may be the possibility to process larger flowrates of working fluid to generate more power. For this reason, there is a great interest in developing axial expanders. However, due to the large flowrates and physical properties of the S-CO2, the blades will need to sustain large aerodynamic loading. If free-standing blades are considered, a small eccentricity of the shaft with respect to the casing would determine a non-homogenous tangential distribution of clearance. As a result, the blades will be non-homogeneously loaded. Eventually, the inhomogeneity of the load causes unsteady forces orthogonal to the defection which promotes the vibration of the shaft and increases the risk of instabilities. This phenomenon is known as Alford force in the literature. Actually, it was first investigated by Thomas [19] in 1958 for axial turbines and then by Alford [2] in

1965 for axial compressors (indeed, for turbomachinery in general). Most of the papers of Thomas were written in German, and were not popular in the United States, so the phenomenon started to be named in the English literature as “Alford force”.

As reported in [18], the model proposed by Thomas for turbines is generally accepted. In the case of an eccentricity as that shown in Figure 1, the effect of the horizontal force F_x can be modeled by means of as a cross coupled stiffness K_{xy}:

$$K_{xy} = \frac{F_x}{+Y} = \frac{T\beta}{D_p h} \tag{1}$$

where $+Y$ is the shaft deflection, T is the stage torque, D_p is the mean diameter and h is the blade height. Parameter β was introduced by Alford as the change in the thermodynamic efficiency but now is considered as an empirical factor to match computational predictions with experimental data. For turbines, generally $1 < \beta < 5$, [18].

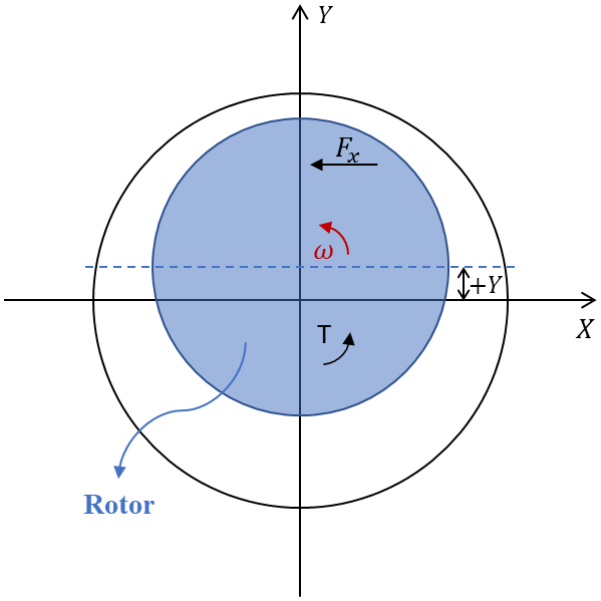

Figure 1: Schematic representation of whirling rotor.

Different models regarding axial compressors are present in the literature.

Ehrich et al. proposed the parallel compressor model, [6], where the shaft whirling is neglected and a static eccentricity is considered instead. The circumferential evolution of the clearance is considered half at minimum clearance and half at maximum clearance.

Spakovszky et al. in [17] considered the non-stationary motion of the shaft for which a complex fluid model is adopted to extract the flow quantities necessary for the evaluation of the Alford force.

Song and Cho in [14] presented a model to evaluate the rotodynamic forces in a compressor generated by non-uniform tip clearance. The model is based on the analysis presented by Song and Martinez-Sanchez in [15,16] developed for axial turbines and on the experimental campaign presented in [11] and is based on the “actuator disk” approach. The modeling of the flow in the clearance region is also necessary.

More recently, Pan et al. in [12,13] investigated with Computational Fluid Dynamics (CFD) the dynamic forces acting on an off-centered un-shrouded axial steam turbine. The authors also investigated the shape of the tip of the blade and the clearance on the dynamic forcing. In [3], the authors proposed a CFD study on the first stage of a high-pressure steam turbine focused on the effect of the shroud and labyrinth seals.

In [8], Ehrich et al. compared the results obtained with the previously mentioned models with experimental results obtained with a testbench recreating the operation of an axial compressor.

A similar phenomenon happens also in the case of shrouded blades. As reported by Alford [2], the shaft orbiting causes a tangential non-homogeneous distribution of pressure inside the seal that eventually worsen the orbiting phenomenon. Similar conclusions are reported by Ehrich et al. in [7]. More recently, CFD was applied to study the effect of dry gas seal of radial expanders for S-CO2 applications, [20,22,23]. In [21], the authors investigated the effect of the length, depth, and number of teeth on the performance of a labyrinth seal for S-CO2 applications. In [4,5], the authors presented a detailed study on the effect of shroud seals on the fluid flow of an axial S-CO2 turbine stage.

Regarding the blade aerodynamic forcing, most of the research present in the literature focused on axial compressors since they are more sensible to instabilities than turbines. However, the physical properties of S-CO2 are very different from those of the gases usually processed in axial expanders. The aerodynamic loading exerted by the S-CO2 on the blades can be significantly higher than the one exerted by steam. Therefore, it is worth to address this topic in the design of the axial turbine for S-CO2 cycles.

In this paper, a stage of an axial expander for S-CO2 is considered. The stage parameters are extracted with two approaches. At first, a simplified mono-dimensional model based on the mean line approach is applied; then, a CFD model of the blade channel is used along with the simulation of the leakage flow at the tip of the blade. In Section 2, the models used for the evaluation of the stage parameters are introduced together with the correlations adopted to evaluate the Alford force. The results obtained are reported and discussed in Sections 3 and 4 respectively. The prediction of the Alford forces is partially affected by the model selected for the evaluation of the stage parameters (1D and CFD are almost aligned) and, above all, by the correlation used. Finally, the conclusion are drawn in Section 5.

The results reported in this paper highlight the necessity to further investigate the phenomenon at least for a validation of the correlation that is more accurate for S-CO2 application. However, also more sophisticated models to extract the stage parameters will be helpful in improving the estimation of the Alford force. Another approach, in the short term and beyond a test case with the required geometric and thermodynamics conditions, could be to address this subject as a sensitivity analysis on a full rotor behavior to evaluate if the instability risk is avoided even with the most – conservative correlation that provide the worst cross – coupled stiffness.

2 Materials and Methods

2.1 Stage parameters

The investigation is focused on a stage of an axial turbine for S-CO2 applications. A simplified meridional view of the flow path is shown in Figure 2.

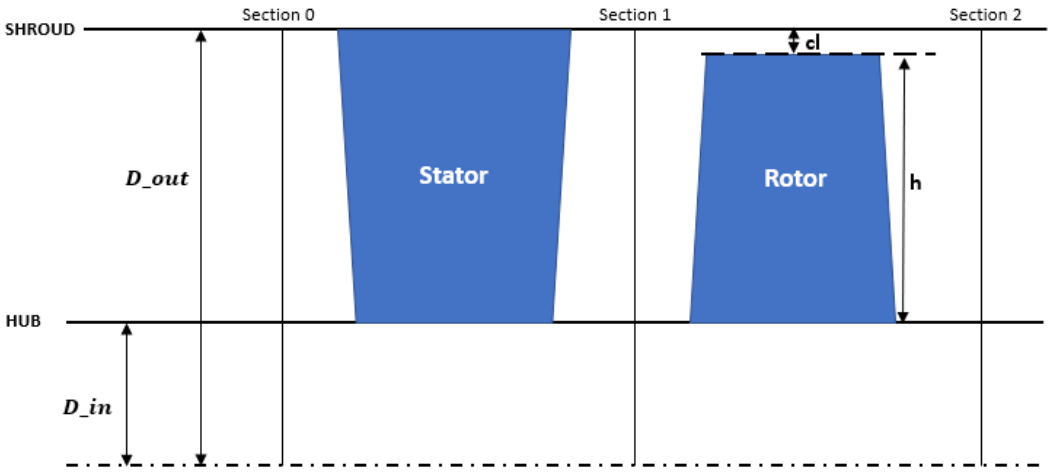

Figure 2: Stage 2D schematization.

The outer and inner diameters are respectively D_{out} and D_{in}, h is the rotor blade height and cl is the radial tip clearance between the rotor blade and the shroud casing. The mean diameter D_p is calculated as:

$$D_p = D_{in,2} + \frac{h}{2} \tag{2}$$

The rotor blade is unshrouded. The analysis is carried out at five different levels of clearance. The percent increments with respect to the nominal clearance (cl_1) are listed in Table 1.

Table 1: Dimensionless levels of rotor blade clearance considered for analysis.

cl_1	cl_2	cl_3	cl_4	cl_5
1	*1.24*	*1.42*	*1.61*	*1.79*

2.2 1D model

At first, the analysis is carried out at mean-line level. A 1D code works on a single geometric streamline, the mean-line, where it solves the velocity triangles of a turbine stage by means of loss and deviation correlations. The losses of the row are estimated together with the turn efficiency considering different loss mechanisms. Clearly, blade geometry is reduced to a short set of parameters complemented by default rules.

The total-to-total pressure ratio is considered fixed for the 5 levels of tip clearance reported in Table 1. The tip clearance is assumed uniform tangentially. The 1D model returns the estimated performance of the stage at the design point (cl_1) and at the four off-design conditions ($cl_2 - cl_5$). The outputs include the torque generated by the rotor blading which serves as input for all the models presented in the first paragraph. The information made available by the 1D code provides a measure of the efficiency penalty and of the power/torque reduction as a function of the tip clearance.

Therefore, the underlying assumption for the subsequent rotor dynamic analysis is that the outputs of those five runs are to be merged to model a unique non-uniform tangential distribution of torque. Considering the highly unsteady nature and tangential non-uniformity of the investigated phenomenon, this is of course a significant simplification to be validated by more complex modelling strategies.

Two more assumptions need to be introduced. The fluid is treated as a semi-perfect gas. The approximation on the evaluation of the thermodynamic properties with respect to a rigorous real fluid modelling is negligible considering the narrow thermodynamic space covered by the expansion of a single stage and the wide margin from the phase transition guaranteed by the highly supercritical conditions imposed by the cycle. The second assumption is on the secondary flows. Given the purpose of this assessment, neither wheel space nor shroud cavities are included in the calculation domain to avoid unnecessary complexity for the 3D CFD analysis and not to taint the evidences related to the investigated phenomenon.

2.3 CFD model

The same approach and assumptions of the 1D model are adopted for the 3D CFD analysis carried. The commercial code ANSYS CFX is selected for the analysis. For each tip clearance level, a RANS (Reynolds-averaged Navier Stokes) simulation is run.

The single-block grids (OH type) are realized in Numeca AutoGrid™ environment and are then imported in ANSYS CFX. The mesh, with more than 1.5 million elements for both stator and rotor, is built to comply with all the standard quality metrics. The clearance region above the blade tip is meshed with a number of cells in the radial direction proportional to the opening itself (increasing from cl_1 to cl_5) as the blade is of the unshrouded type. Boundary conditions and fluid modelling are the same of the 1D model setup. The selected turbulence model, common to all the cases, is the SST K-Omega, typical option for gas turbine CFD simulations. This model combines the advantages of the K-Epsilon for the free-stream region with those of the K-Omega for the resolution of the boundary layer. Therefore, it offers a good prediction of flow separation and the ability to account for the transport of the principal shear stress in adverse pressure gradient boundary layers. The turbulence model selection is not expected to significantly affect the analysis results provided that the turbulence properties are correctly initialized. A medium level of turbulence intensity is applied as a boundary condition for all the investigated cases. Furthermore, the presence of the meshed clearance (symmetric or asymmetric) region above the blade tip is not driving the turbulence model selection as SST K-Omega is expected to return accurate results in any near-wall regions, blade tip included.

In summary, the analysis setup fully adheres to the standard template adopted for CFD analysis on gas turbines.

3D CFD enables the detailed assessment of the flow field of the tip clearance. The information extracted from the simulation post processing is anyway the overall torque of the stage, as required by all the correlations evaluating Alford forces.

2.4 Correlations

The dimensionless stage torques obtained for the different clearances of the rotor blade, and used to feed the correlations, are presented in Figure 3. Dimensionless torques is obtained by normalizing the dimensional torque by the value obtained for cl_1 .

The Alford correlation has been shown in Equation (1). The cross-coupled stiffness coefficient K_{xy} is evaluated for different values of the parameter β .

In [6] the parallel compressor model is introduced. The static eccentricity Y is considered and the whirling motion is neglected. The tangential distribution of clearance is simplified as shown in Figure 4. Half the rotor has the minimum radial clearance (cl_1). The other half has the maximum radial clearance (cl_5).

In [6], Ehrich proposed to evaluate β as:

$$\beta = \frac{2(T_5 - T_1)}{(T_5 + T_1)\left[\left(\frac{cl}{h}\right)_5 - \left(\frac{cl}{h}\right)_1\right]} \tag{3}$$

where T_5 and T_1 are the stage torques for cl_5 and cl_1 respectively.

Once β is calculated, Equation (1) is applied to evaluate the Alford force.

In [17], the effect of the whirling motion is taken into consideration. However, neither the 1D model nor the CFD model can be applied to obtain the unsteady flow quantities. Therefore, a simplified approach is considered. The tangential evaluation of the aerodynamic forces is evaluated only considering an eccentric rotor. For the analysis, $100\ \mu m$ and $200\ \mu m$ peak-to-peak eccentricities are considered for the minimum and the maximum clearance values in Table 1. The tangential distribution of the torque T_θ caused by the static eccentricity is obtained with an interpolation.

Then, the tangential distribution of the force f_θ is:

$$f_\theta = \frac{T_\theta}{D_p} \tag{4}$$

The tangential evolution of f_θ for the 1D model and the CFD model are shown in Figure 5.

If synchronous *1X* vibrations are considered, the force F_x is defined as:

$$\begin{bmatrix} F_x \\ F_y \end{bmatrix} = \begin{bmatrix} 1 & 0 \\ 0 & 1 \end{bmatrix} \begin{bmatrix} \int_0^{2\pi} f_\theta \sin(\vartheta)\, d\vartheta \\ -\int_0^{2\pi} f_\theta \cos(\vartheta)\, d\vartheta \end{bmatrix} \tag{5}$$

where ϑ is the tangential coordinate.

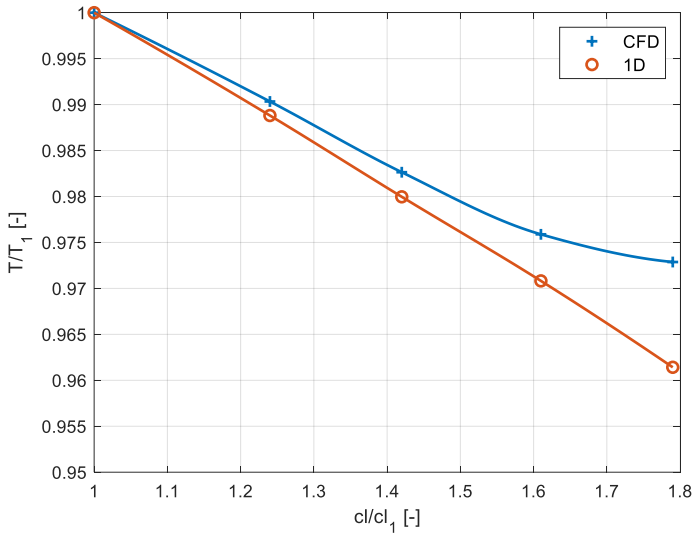

Figure 3: Torque at different levels of rotor blade clearance - 1D vs CFD.

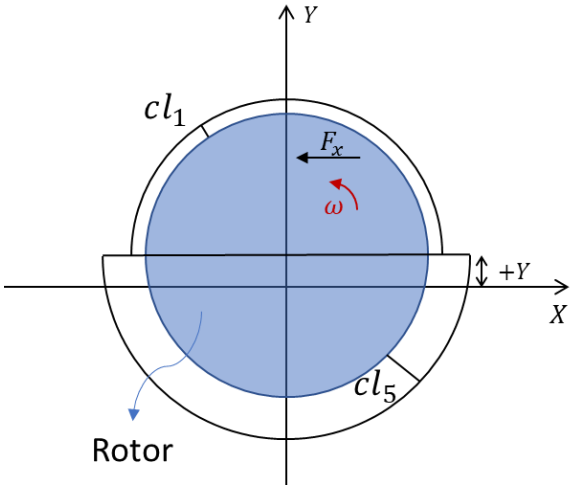

Figure 4: Schematic representation of parallel compressor model, [6].

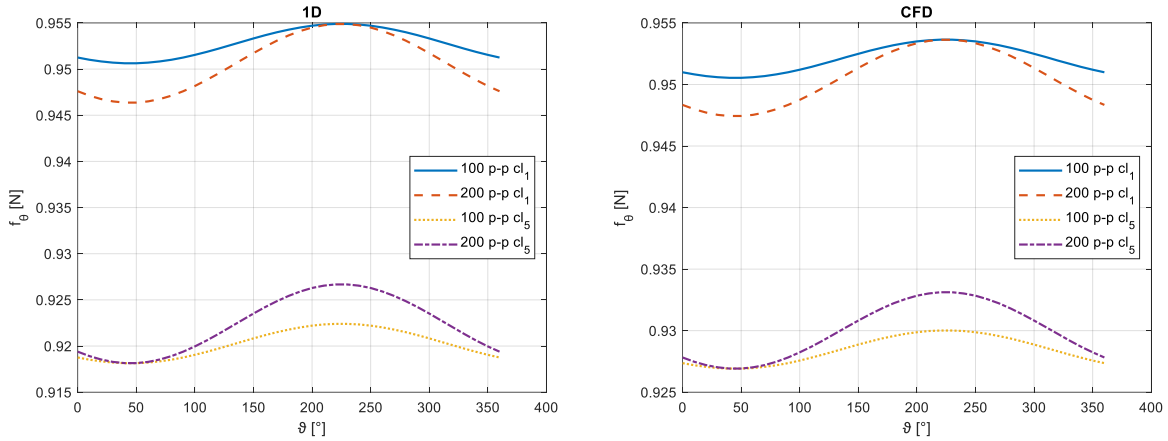

Figure 5: Tangential evolution of f_θ for *100* and *200 p-p* eccentricity for cl_1 and cl_5. (Left) 1D model, (Right) CFD model

3 Results

The results obtained with the different correlations are presented in this section. The evolution of the absolute value of K_{xy} with the radial clearance for the 1D and CFD models is shown in Figure 6. Those results are obtained by applying the Alford correlation, Equation (1), to the data shown in Figure 3 and in Table 1.

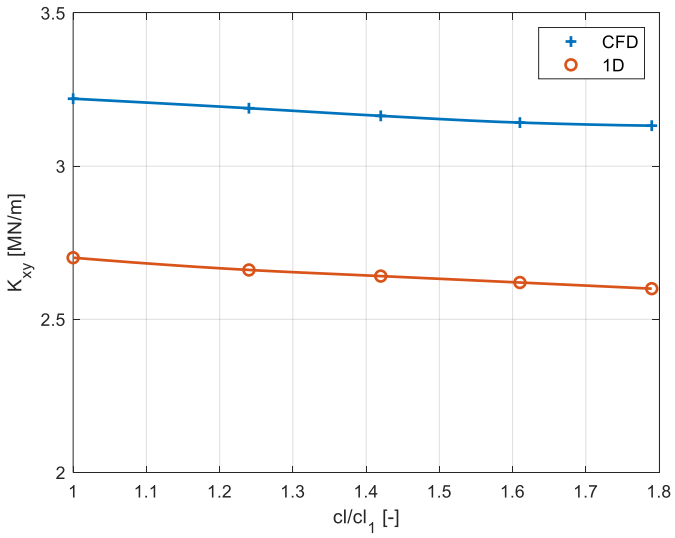

Figure 6: Evolution of K_{xy} with tip clearance considering Alford correlation for 1D and CFD model.

If β is calculated according to in Equation (3), the resulting values obtained for K_{xy} by applying Equation (1) are listed in Table 2. Both the 1D and CFD models are considered. Results reported by Figure 6 and Table 2 highlight that the cross-coupled stiffness is approximately constant over the evaluated clearance domain while it shows a large variability based on the correlation used for the Alford force estimation. Therefore, from now on, the results are presented as average values covering the whole tip clearance span.

Table 2: Results for Ehrich correlation for 1D and CFD model.

Model	$\boldsymbol{\beta}$	$\boldsymbol{K_{xy}\,[MN/m]}$
1D	*-2.15*	*-5.78*
CFD	*-1.50*	*-4.77*

Equation (5) is applied to obtain F_x in the case of Spakovszky correlation. Then Equation (1) is applied to calculate K_{xy}. In this case, the static eccentricity considered is $+Y = 50\mu m$ for the $100\mu m$ peak-to-peak case and $+Y = 100\mu m$ for the $200\mu m$ peak-to-peak. The results obtained for the 1D model and the CFD model are listed in Table 3. Since these results are not affected by the clearance and the static eccentricity, only the results for cl_1 and $+Y = 50\mu m$ are reported; it is strictly connected to the definition reported in Equation (5) where a double force value variation due to a double amplitude is divided by a double eccentricity.

Table 3: Results for Spakovszky correlation for 1D and CFD model.

Model	**Clearance level**	$\boldsymbol{+Y\,[\mu m]}$	$\boldsymbol{K_{xy}\,[MN/m]}$
1D	*1*	*50*	*-0.44*
CFD	*1*	*50*	*-0.38*

4 Discussion

Considering the results of application of the Alford correlation, reported in Figure 6, lower cross-coupled stiffness and then aerodynamic forces are obtained if the 1D model is considered instead of the CFD one. With this difference on the inputs required for the correlation, the difference between the 1D and CFD results is around -15%. In addition, directly connected to the slope of trending lines of Figure 3, the impact on torque of radial clearance variation of the rotor blade is larger for 1D than CFD model, respectively 4% for the 1D model and 3% for the CFD model.

According to the frame of reference indicated in Figure 1, a negative value of the cross-coupled stiffness K_{xy} indicates the promotion of forward whirl, typical for turbines, [18]. The torque positive direction selected in this paper is the opposite than the one indicated by Alford, [2]. Therefore, the values of K_{xy} shown in Figure 6 are negative ad forward whirl is predicted with the Alford correlation. When the Ehrich correlation is applied to both the 1D and CFD model negative values for β are obtained, see Table 2. Therefore, negative values are obtained for K_{xy} predicting a forward whirl phenomenon. Since the Ehrich correlation is more connected to the torque variation with clearance, it is quite straightforward that the larger cross-coupled stiffness is obtained for 1D model that is characterized by a higher trending line slope, see Figure 3. Moreover, the simplified 1D model overestimates of $+21\%$ the value of K_{xy} with respect to the CFD prediction.

The results obtained with the Spakovszky correlation are listed in Table 3. Also in this case a forward whirl is predicted. The discussion provided on the results obtained with the Ehrich correlation is applicable also in this case. However, the results obtained with the Spakovszky correlation are one order of magnitude lower than the results obtained with the Ehrich correlation. As a matter of fact, both the 1D and CFD results are much lower, in absolute value, than the ones obtained with the Alford and Ehrich correlations. The hypotheses of stationary condition and the interpolation of the torque tangential evolution are too strict, and the results obtained could lose significance. On the other hand, it could be that this last correlation, more connected to the aerodynamic behaviour of the analysed stage, provides results closer to the real phenomenon. However, a more detailed investigation is required to reduce the uncertainty for this application.

As summary, the results reported in this paper are an initial evaluation of the Alford effect for a S-CO2 application. Different behaviours are obtained considering the different correlations. Different results are obtained with the application of the 1D and CFD models. However, the major effect on the value of the cross-coupled stiffness K_{xy} is related to the choice of the correlation. From a quantitative point of view, the Ehrich correlation provides values higher than the ones obtained with the Alford correlation of 110% for the 1D model and 48% for the CFD model. Similarly, the Spakovszky correlation provides, in general, values an order of magnitude lower if compared both with the Ehrich and Alford correlations. As highlighted by the results shown in this paper, both the 1D and CFD model give comparable results. Therefore, the simplified 1D approach can be used for the investigation at this stage of the analysis since the flow path modelling is not as impacting as the choice of the correlation. A more detailed investigation of the effect of the Alford force on this S-CO2 application is required.

5 Conclusions

In this paper, the Alford effect in an axial turbine stage for S-CO2 application is investigated. The Alford effect is introduced using the different empirical correlations already published in the literature.

The parameters characterizing the stage are obtained with a 1D mean line model and a CFD model. The Alford, Ehrich, and Spakovszky correlations are selected, considering the data available for the 1D and CFD models considered and their results on the estimation of K_{xy} are shown. All three models agree in the prediction of forward whirl excitation, a typical phenomenon for axial turbines. Nonetheless, a deeper investigation is required to fully comprehend the phenomenon of the Alford force.

Focusing on the numerical models adapted, the uncertainty introduced in the analysis by using the 1D or the CFD model is an order of magnitude lower than the uncertainty in the final value of the cross-coupled stiffness obtained with the different correlations. Therefore, reliable results can be obtained applying the 1D model, reducing the complexity and computational cost required by analysis based on CFD. It is understood that the fairly good agreement between 1D and CFD results can be leveraged as far as overall performance parameters and/or section averaged quantities are to be provided to Alford effect correlations. Therefore, 1D data provide consistent feedback when dealing with the conceptual and the preliminary design phases of new products. The use of CFD data is recommended for detailed analyses to be executed once the flow path design is mature, thus enabling the designer to evaluate local flow conditions and to estimate the impact related to the introduction of complex 3D geometrical features.

In general, the correlations considered agree that the cross-coupled stiffness estimated for the considered stage is of the order of $10^6\ N/m$. This value is generally common for a whole turbine and not for a single stage as in this case; this result is an additional confirmation of the huge impact of the S-CO2 density and of the need to properly address this phenomenon on the development of an axial turbine for S-CO2 power generation.

Future works are necessary to better understand the phenomenon of the Alford force on the S-CO2 applications at least for a validation of the correlation that is more accurate for them. To get a proper validation, the only worthwhile way is a specific test bench even simplified but capable to reproduce the phenomenon. However, also more sophisticated models to extract the stage parameters will be helpful in improving the estimation of the Alford force. In the short term, without developing an experimental test rig that reproduces the geometrical and thermodynamic conditions, a sensitivity analysis can be performed on the whole rotor structure. The instability

risk should be assessed considering the different values of the cross-coupled stiffness obtained with the different correlations to establish how harmful the Alford force can be for this application.

References

[1] Ahn, Y., Bae, S.J., Kim, M., Cho, S.K., Baik, S., Lee, J.I., et al. (2015) Review of supercritical CO2 power cycle technology and current status of research and development. *Nuclear Engineering and Technology*. 47 (6), 647–661.

[2] Alford, J. (1965) Protecting Turbomachinery From Self-Excited Rotor Whirl. *Journal of Engineering for Gas Turbines and Power*. 333–342.

[3] Cao, L.H., Wang, J.X., Li, P., Hu, P.F., and Li, Y. (2017) Numerical Analysis on Steam Exciting Force Caused by Rotor Eccentricity. *Shock and Vibration*.

[4] Du, Q. and Zhang, D. (2020) Numerical Investigation on Flow Characteristics and Aerodynamic Performance of a 1.5-Stage SCO2 Axial-Inflow Turbine with Labyrinth Seals. *Applied Sciences (Switzerland)*. 10 (1).

[5] Du, Q., Zhang, L., Zhang, D., and Xie, Y. (2020) Numerical investigation on flow characteristics and aerodynamic performance of shroud seal in a supercritical CO2 axial-flow turbine. *Applied Thermal Engineering*. 169.

[6] Ehrich, F. (1993) Rotor whirl forces induced by the tip clearance effect in axial flow compressors. *Journal of Vibration and Acoustics, Transactions of the ASME*. 115 (4), 509–515.

[7] Ehrich, F. (1968) Aeroelastic instability in labyrinth seals. *Journal of Engineering for Gas Turbines and Power*. 90 (4), 369–374.

[8] Ehrich, F.F., Spakovszky, Z.S., Martinez-Sanchez, M., Song, S.J., Wisler, D.C., Storace, A.F., et al. (2000) Unsteady Flow and Whirl-Inducing Forces in Axial-Flow Compressors: Part II—Analysis. *Journal of Turbomachinery*. 123 (3), 446–452.

[9] Kim, Y.M., Sohn, J.L., and Yoon, E.S. (2017) Supercritical CO2 Rankine cycles for waste heat recovery from gas turbine. *Energy*. 118 893–905.

[10] Li, M.J., Zhu, H.H., Guo, J.Q., Wang, K., and Tao, W.Q. (2017) The development technology and applications of supercritical CO2 power cycle in nuclear energy, solar energy and other energy industries. *Applied Thermal Engineering*. 126 255–275.

[11] Martinez-Sanchez, M., Jaroux, B., Song, S.J., and Yoo, S. (1995) Measurement of turbine blade-tip rotordynamic excitation forces. *Journal of Turbomachinery*. 117 (3), 384–392.

[12] Pan, Y., Yuan, Q., Huang, G., Gu, J., Li, P., and Zhu, G. (2020) Numerical investigations on the blade tip clearance excitation forces in an unshrouded turbine. *Applied Sciences (Switzerland)*. 10 (4).

[13] Pan, Y., Yuan, Q., Huang, G., Zhu, G., and Li, P. (2020) Numerical analysis of the aerodynamic performance and excitation forces in a transonic turbine cascade with flat-tip and squealer-tip blades. *Proceedings of the Institution of Mechanical Engineers, Part C: Journal of Mechanical Engineering Science*. 234 (22), 4377–4389.

[14] Song, S.J. and Cho, S.H. (2000) Nonuniform flow in a compressor due to asymmetric tip clearance. *Journal of Turbomachinery*. 122 (4), 751–760.

[15] Song, S.J. and Martinez-Sanchez, M. (1996) Rotordynamic forces due to turbine tip leakage - Part I: Blade scale effects. in: ASME 1996 International Gas Turbine and Aeroengine Congress and Exhibition, GT 1996.

[16] Song, S.J. and Martinez-Sanchez, M. (1996) Rotordynamic forces due to turbine tip leakage - Part II: Radius scale effects and experimental verification. in: ASME 1996 International Gas Turbine and Aeroengine Congress and Exhibition, GT 1996.

[17] Spakovszky, Z.S. (2000) Analysis of aerodynamically induced whirling forces in axial flow compressors. in: Proceedings of the ASME Turbo Expo, .

[18] Storace, A.F., Wisler, D.C., Shin, H.-W., Beacher, B.F., Ehrich, F.F., Spakovszky, Z.S., et al. (2000) Unsteady Flow and Whirl-Inducing Forces in Axial-Flow Compressors: Part I—Experiment. *Journal of Turbomachinery*. 123 (3), 433–445.

[19] Thomas H.J. (1958) Instabile Einenschwingungen von Turbinenläufern angefacht durch die Spaltströmungen Stopfbuschen und Beschauflungen. *Bull. de l'A.I.M*. 71 (11/12), 1039–1063.

[20] Yang, J., Zhao, F., Zhang, M., Liu, Y., and Wang, X. (2021) Numerical analysis of labyrinth seal performance for the impeller backface cavity of a supercritical CO2 radial inflow turbine. *CMES - Computer Modeling in Engineering and Sciences*. 126 (3), 935–953.

[21] Yuan, H., Pidaparti, S., Wolf, M., Edlebeck, J., and Anderson, M. (2015) Numerical modeling of supercritical carbon dioxide flow in see-through labyrinth seals. *Nuclear Engineering and Design*. 293 436–446.

[22] Zhu, D. and Bai, S. (2021) Ultra-high-speed TEHL characteristics of T-groove face seal under supercritical CO2 condition. *Industrial Lubrication and Tribology*. 73 (3), 523–530.
[23] Zhu, D. and Bai, S. (2021) Thermoelastohydrodynamic characteristics of supercritical CO2 spiral groove face seals. *Industrial Lubrication and Tribology*. 73 (1), 153–162.

15th SIRM – European Conference on Rotordynamics,
Darmstadt, Germany, 22nd – 24th February 2023

Generalised Sommerfeld's lubricants theory supported by MD simulation of slip length

Seyedmajid Mehrnia [1], Maximilian Kuhr [2], Peter F. Pelz [3]

[1] Chair of Fluid Systems, Technische Universität Darmstadt, 64287, Darmstadt, Germany, Seyedmajid.mehrnia@fst.tu-darmstadt.de
[2] Chair of Fluid Systems, Technische Universität Darmstadt, 64287, Darmstadt, Germany, Maximilian.Kuhr@fst.tu-darmstadt.de
[3] Chair of Fluid Systems, Technische Universität Darmstadt, 64287, Darmstadt, Germany, Peter.Pelz@fst.tu-darmstadt.de

Abstract

The presence of wall slip has a significant impact on the Stribeck curve for the infinite journal bearing. In this paper, molecular dynamics (MD) simulation is employed to calculate the slip length of Newtonian fluid confined between two iron smooth surfaces. MD simulations are accomplished by LAMMPS open-source software. The lubrication oil served in this research is polyalphaolefin base oil consisting of 1-Decane molecules. Results revealed that with decreasing temperature, the shear stress values, as well as dynamic viscosity, increase as an Arrhenius law. Besides, results indicate that slip length is increasing with decreasing gap height as an asymptotic expansion.

Keywords: Slip length, journal bearing, molecular dynamics, shear rate

1 Introduction

Lubricants are widely used to reduce unwanted friction between the sliding surfaces of rotating machines. The goal is to reduce wear, prolong the lifecycle of the components and therefore reduce cost and environmental impact while keeping the usage of lubricant fluids at a minimum. When working with fluid dynamics, one important boundary condition that is used to calculate the flow properties of Newtonian fluids is the no-slip boundary condition. It states that the tangential velocity component of the fluid in contact with a stationary wall is also zero. While ignoring slip velocity in the macroscopic scale, this is not applicable in the microfluidic scale [1]. A large slip length indicates lower friction of the fluid and lower drag of solids moving in or in contact with the liquid. Therefore, creating tribological systems with surfaces that increase the slip length may be desired.

Numerous experiments [1] and simulations [2, 3, 4] showed that the usual magnitude of the slip length is in the order of tens of nanometers. The magnitude of slip length has an important influence on the flow properties in the micro and nanoscale. The experimental studies of slip length are complex because it is tough to resolve the fluid velocity profile in the region near the liquid-solid interface at these length scales. Alternatively, molecular dynamics (MD) simulation have been widely employed to investigate the slip properties of liquid flowing past a solid wall since it can resolve the velocity profile from the atomistic level [2, 3, 4]. Moreover, there are no assumptions about the slip velocity at the interface are required. So far, numerous studies have been performed with the goal of linking the slip length to the physical parameters of liquid and surface parings, though, no explicit dependence of slip on solid-liquid interactions or surface geometry has been accomplished yet.

Hydrodynamic bearings, i.e. slider or journal bearings, are the most widely used bearings and are often decisive for the availability and function of machines, e.g. turbo-machinery. However, they are also decisive for the energetic quality of these machines and thus for the sustainability of their functional performance. Sommerfeld discussed the paradox between Coulomb friction and Newtonian, i.e. viscous friction, for journal bearings. In Coulomb friction, the tangential frictional drag force component is proportional to the normal force component and independent of the relative velocity of the two friction partners. In contrast, in Newtonian friction, the frictional force is independent of the normal force but proportional to the relative velocity [1].

The dimensionless Stribeck curve introduced by Sommerfeld (see figure 1) for the no-slip condition, i.e. λ=0, confirmed that there is also an asymptotic friction characteristic of the Coulomb type for small relative velocities, i.e. large Sommerfeld numbers, in the area of hydrodynamic lubrication. In this limiting case, the friction force becomes independent of the relative velocity, as in the case of Coulomb friction. In the limiting case of large relative velocity, i.e. small Sommerfeld number, the results of Sommerfeld present the results of viscous Newtonian friction. Here, it could be generalised that the results for wall slip, indicate the relevance of wall slip for a typical journal bearing. In this paper, it is used the MD simulation method to calculate the slip length values, which is explained in the next section.

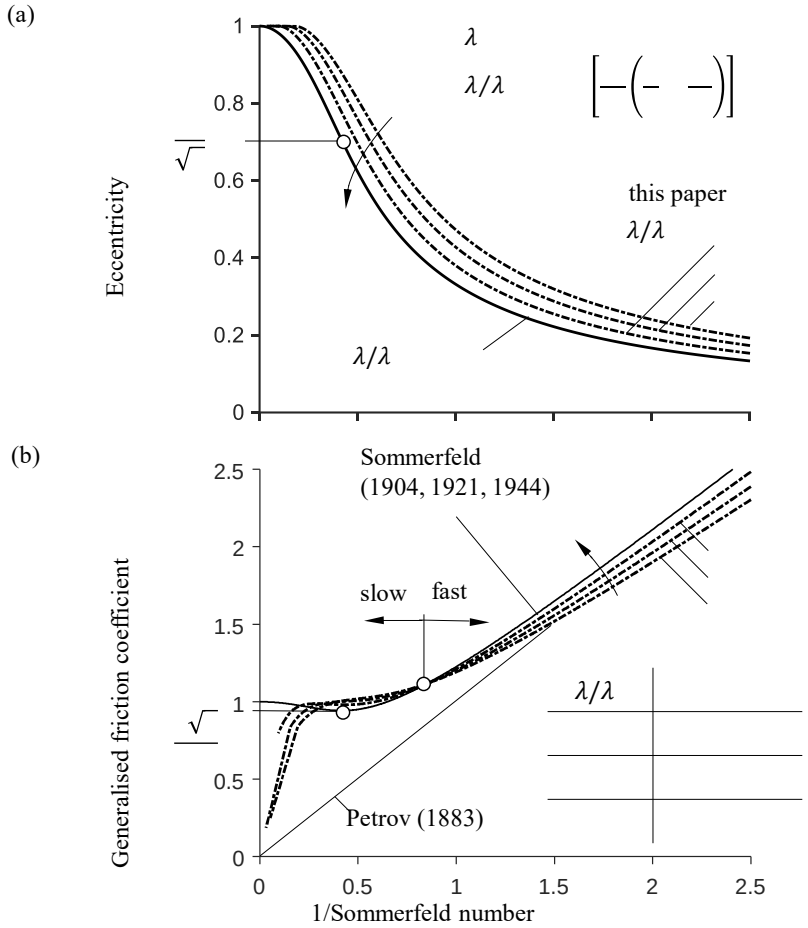

Figure 1: (a) The dimensionless force-displacement curve and (b) the dimensionless Stribeck curve without dry friction introduced by Sommerfeld for an infinite journal bearing with wall slip [1].

2 Simulation

MD simulations have long been used successfully to provide a representative behavior of atomic motion. MD simulations are based on the integration of the coupled differential equations of Newton's law of motion. The trajectories of the atoms can then be tracked by numerically solving the equations with a time-stepping algorithm in conjunction with initial positions and boundary conditions. However, MD simulations are prone to cumulative errors when used with inadequate solving algorithms [5]. The most commonly employed numerical integration method for MD simulations is the algorithm proposed by Verlet [5]. To use the Verlet algorithm with initial values for place and velocity of the atom i, a Taylor series is constructed with the timestep Δt.

Choosing an appropriate timestep Δt determines both the accuracy and the efficiency of the computation. The timestep Δt must be smaller compared to characteristic time periods of the system, to keep the cumulative error small in comparison to the solution. In terms of error propagation, the advantage of the Verlet algorithm lies in an associated global error of $O(h^2)$ compared to $O(h)$ of Euler's method for differential equations. The Verlet algorithm is also used by the LAMMPS software [5] to integrate Newton's equations of motion. The force acting upon the atom depends on an energy function. Thus, it is of utmost importance to choose a sufficient potential

function, which accurately describes the dynamics of a molecular system. If adequate integration algorithms, potential functions and parameter selections are chosen, the only major limitations of standard MD simulations are time and size scales. Time scales usually remain in the tens of nanoseconds. Which also depends on the number of atoms and molecules in the simulation. A higher number of particles as well as lower shear rates, increase the equilibration time and thus affects the overall simulation time and computational effort. Both of these can be partially compensated by the ever-advancing performance of parallel supercomputing. For this purpose, this study also makes use of the Lichtenberg supercomputer to allow for a more complex system with a larger time and size scale.

To reduce the computational effort, neighbor list as proposed by Verlet [5] is usually implemented in MD-Simulation algorithms. The neighbor list can be updated depending on the velocity of the system. Higher present velocities create a higher chance of new atoms approaching the vicinity of the central atom. The following interaction can then only be considered if a new neighbor list for that timestep is built. The potential energy function usually consists of bonded and unbonded interaction potentials [5]:

$$U_{bonded} + U_{unbonded} \tag{1}$$

A general potential function which includes both intra- and intermolecular forces is given by Eq. (2)

$$\begin{aligned}(\vec{r}) \quad & \sum_{bonds} \frac{k_{i,l}}{} \left(l_i - l_{i,0}\right) \\ & + \sum_{angles} \frac{k_{i,\theta}}{} \left(\theta_i - \theta_{i,0}\right) \\ & + \sum_{torsions} \frac{V_n}{} + \cos(n\omega - \gamma \\ & + \sum_{i=1}^{N} \sum_{j=i+}^{N} \varepsilon_{ij} \left[\left(\frac{\sigma_{ij}}{r_{ij}}\right) \quad \left(\frac{\sigma_{ij}}{r_{ij}}\right)^6\right] \\ & + \sum_{i=1}^{N} \sum_{j=i+}^{N} \frac{q_i q_j}{4\pi\epsilon_0 \epsilon r_{ij}}\end{aligned} \tag{2}$$

The first four terms describe the bonded interactions, and the last two represent the unbonded interactions. The first term describes a harmonic potential which increases in energy when the bond length l_i deviated further from the equilibrium value $l_{i,0}$. The second term also is a harmonic potential which is summed over all the angle deviations $\theta_i - \theta_{i,0}$ from the reference angle $\theta_{i,0}$ of bonded atoms. The third term includes a torsion potential where γ refers to a phase factor that determines the minimum value of the torsional angle. The fourth term deploys a second torsion angle energy, which takes the geometry of the molecule into account. The last two terms are used to describe unbonded interactions. Here, the energy is calculated between all pairs of atoms i and j. As depicted in the formula above, these forces are usually modeled by using a Lennard-Jones (LJ) potential for van der Waals interactions and a Coloumbic potential for electrostatic interactions between the atoms. For modeling the walls, simple spring potentials can be employed or a more sophisticated force field for metals can be chosen. For this research, the EAM potential is used to model the iron walls. The Embedded-Atom Method (EAM) is a popular choice for modeling the force field of metals and alloys.

To decrease computational cost and expand the time and size scales of an MD simulation Coarse-Grain-Models like Unite Atom (UA) are often employed. Coarse-grain models can reduce the amount of complexity in a molecular system by grouping atoms into summarized structures. Well-designed Coarse-Grain-Models can retain the accuracy of the all-atom counterpart by smoothening the energy landscape to a reasonable resolution. Coarse-grain-Models can typically be used with similar force field formulas, e.g., harmonic bonds, LJ-potentials etc., as all-atom models, which makes them easy to utilize.

Polyalphaolefins (PAO) are synthetic lubricants consisting of oligomerized alpha olefins, which are alkenes with a carbon double bond starting at the α-carbon atom position. The result is a mixture of olefin dimers, trimers and tetramers (see Figure 2) [2, 3].

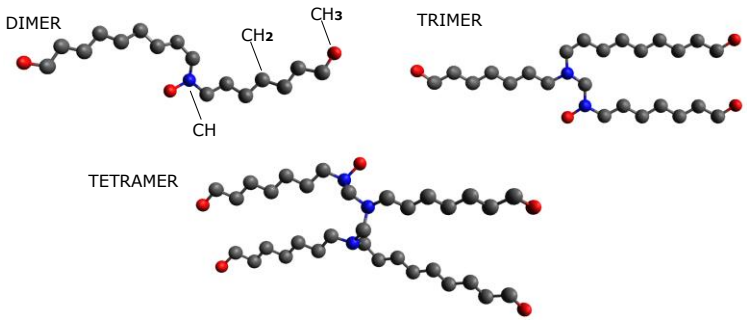

Figure 2: PAO molecule Structure, a mixture of the 1-Decane dimer, trimer, and tetramer.

Compared to mineral oil-based lubricants, synthetic PAO lubricants offer superior thermal and oxidative stability and are highly shear stable, with the additional benefits of being non-corrosive and non-toxic to mammals. Their shear stability stems from the alkyl groups preventing the molecules from easily aligning themselves in an orderly way, thus reducing contact surface and intramolecular interaction between the molecules. This also leads to the beforementioned thermal stability, keeping a high viscosity even at low temperatures. With all these characteristics, PAO oils reduce friction, wear, and energy consumption, while also lasting 5-10 times longer than their mineral oil counterparts. PAOs are widely used in the industrial and automotive sectors as well as high-performance applications.

Past studies have shown that United Atom Coarse-Grain models can accurately depict the behavior of hydrocarbons at various pressures [4]. One of them is the NERD Force Field for linear and branched alkanes, which can be extended to suit alpha olefins [2]. For the coarse-graining, CH_3, CH_2 and CH groups are modeled as single interaction sites. The NERD Force Field employs an LJ potential for non-bonded interaction sites, excluding intramolecular interactions within 3 bonds of the same molecule. A standard Lennard-Jones 12-6 potential is used for this non-bonded interaction.

The simulation box consists of a 3-dimensional rectangular shape with periodic boundary conditions in the x- and y direction. Lubricant molecules were designed by Avogadro software [6], and then assembled and optimized by the Packmol software [7]. A non-periodic boundary is imposed in the z-direction. Figure 3 shows the MD simulation box generated by Packmol software. To prevent molecules from interacting with each other over the periodic boundary, sufficient box dimensions must be met. A common approach for alkanes up to CH_x-groups demands a system size of minimum the backbone length of the molecule plus two times the cutoff distance of the Lennard-Jones-potential. With an estimated length of a 1-decane molecule of 1.32 nm and an LJ-cutoff distance of 1 nm, the chosen box size of 5 to 30 nm satisfies these criteria. The two parallel walls are comprised of a body-centric cubic (bcc) lattice of iron atoms with a lattice constant of 2.87 Å. The walls span the entire simulation box in the x- and y-direction. The height of the stationary smooth wall is 2 nm. The fluid is confined between the stationary and the moving wall, inducing a shear-driven Couette flow.

To obtain the slip length, the velocity profile is linearly extrapolated from bulk liquid data at the central region. This means that the bins adjacent to the walls are not considered in the linear fit. The obtained linear formula is then used to calculate the slip length by calculating the length λ at which the velocity would reach zero.

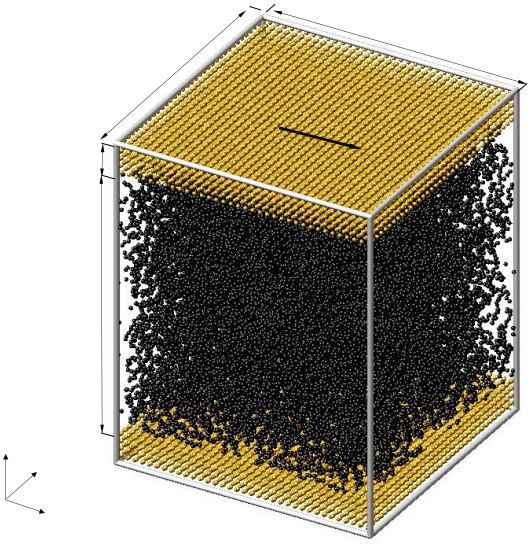

Figure 3: MD simulation box generated by Packmol software. The PAO molecules are confined between iron atom surfaces.

3 Results

To verify the simulation, the density and viscosity values of oil were calculated. The mass density distribution across the gap in Figure 4 shows the molecular layering of the PAO oil molecules. Regions close to the surfaces are the adsorption layer with high sudden mutation and oscillations in the mass density profiles. It can be seen that the 1-Decane dimer has the lowest values of density. It is also found that the atomic boundary layers had slightly higher density peaks for the tetramer than the atomic boundary layers of the trimer. It is interesting to note the splitting of the peak near the surfaces in the density profile. That can be demonstrated by the less area of repulsion of the UA groups where they can approach the surfaces further closely, possibly binding more firmly to the iron wall. The measured density values of the PAO 2, 4 & 6 were 0.80, 0.825, and 0.835 g/mL, respectively. The calculated densities of three molecule structures agree with the measured mass densities.

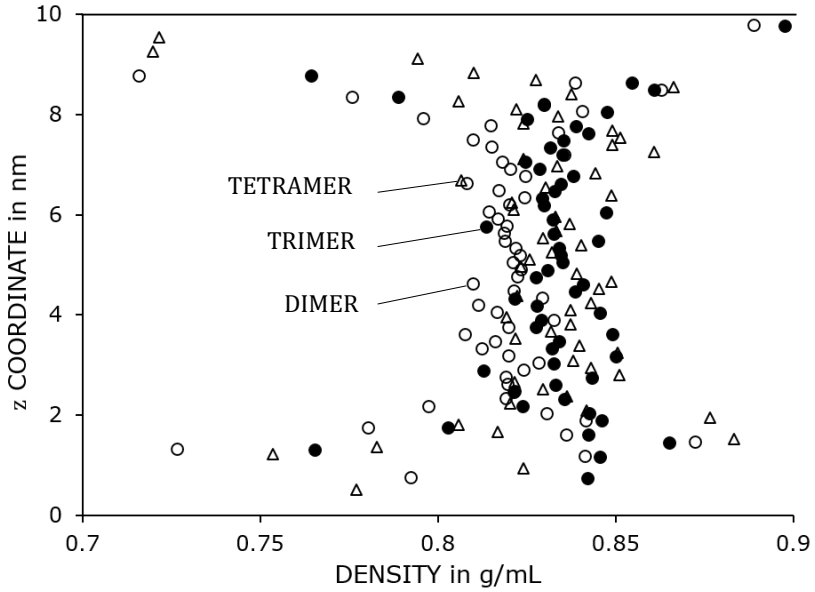

Figure 4: Calculated averaged density of three different structures of 1-Decane**.**

Viscosity is a fluid property that shows how resistant that liquid is to flow. Higher viscous fluids carry much longer to flow from their container than a relatively lower viscosity fluid. To quantify viscosity, it simulated bulk fluid consisting of a number of very thin layers. In order for the liquid to flow, a force will be required to slip these

layers relative to one another. The force required is assumed to be directly proportional to the area of the layers in contact with one another and the different velocities between the layers. Also, the force is inversely proportional to the distance between the layers.
The dynamic viscosity of the liquid μ was estimated as the ratio of the shear stress σ_{xz} and the shear rate $\dot{\gamma}$, $\sigma_{xz}/\dot{\gamma}$. To calculate the shear stress, a general formulation of stress tensor for many-body interaction potentials under periodic boundary conditions was utilised [7]. Figure 5 has shown apparent dynamic viscosity as a function of different apparent shear rates of PAO 6 oil at different temperatures. Viscosity alters with temperature, typically becoming smaller as the temperature is elevated. This trend happens due to the raised kinetic motion at higher temperatures enables the breaking of intermolecular bonds between adjacent molecule layers. A significant amount of research has been carried out in an attempt to comprehend the exact nature of the temperature variation of viscosity. One relatively straightforward model considers that the viscosity follows an 'Arrhenius-law' equation [1] of the form

$$\sim \exp\left(-\frac{E}{\mathcal{R}T}\right) \tag{3}$$

where μ is the viscosity, $\mathcal{R}$ is 8.3145 J/mol K, and T is the temperature. The activation energy can either be estimated straight produced at two specific temperatures and a rate constant at two temperatures [1]. The calculated activation energy is about 26 kJ/mol

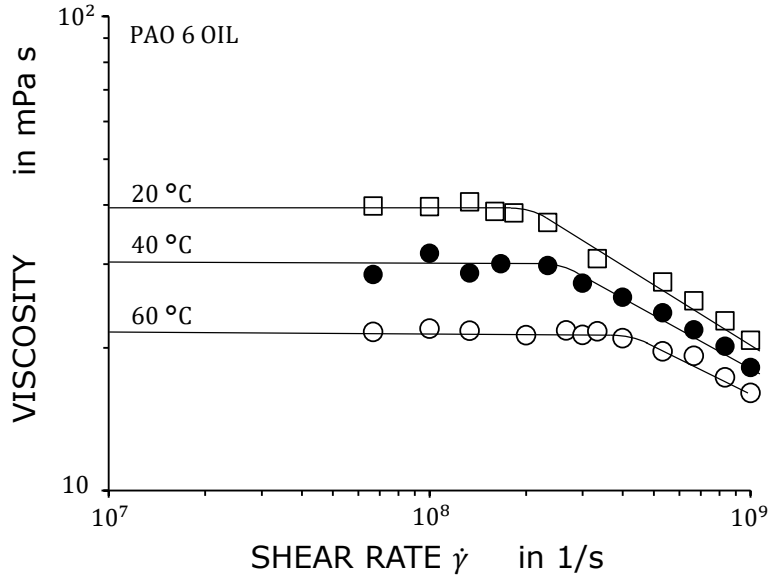

Figure 5: Apparent dynamic viscosity as a function of different apparent shear rates for PAO 6 oil. As the temperature increased, the viscosity values decreased as an Arrhenius behavior.

Figure 6 shows the calculated values of λ versus gap heights and asymptotic expansion Eq. (4) as solid lines. It was assumed the initial wall distance $a = 5$ nm for three different molecules. For $h \to 0$ the slip length becomes infinite. For $h \to \infty$, it is expected a constant value of the slip length $\lambda \to \lambda_\infty$. Hence, an asymptotic expansion reads

$$\lambda = \lambda_\infty \left(1 + \frac{a}{h}\right) \tag{4}$$

Through this expansion, infinite slip λ_∞ is determined for three different molecules of PAO oil. The general trend of the diagrams shows a steep decrease in wall slip up to 10 nm oil film thickness. It may state that the liquid behavior adjacent to the wall is too complex to be explained by a slip length related to the shear stress.

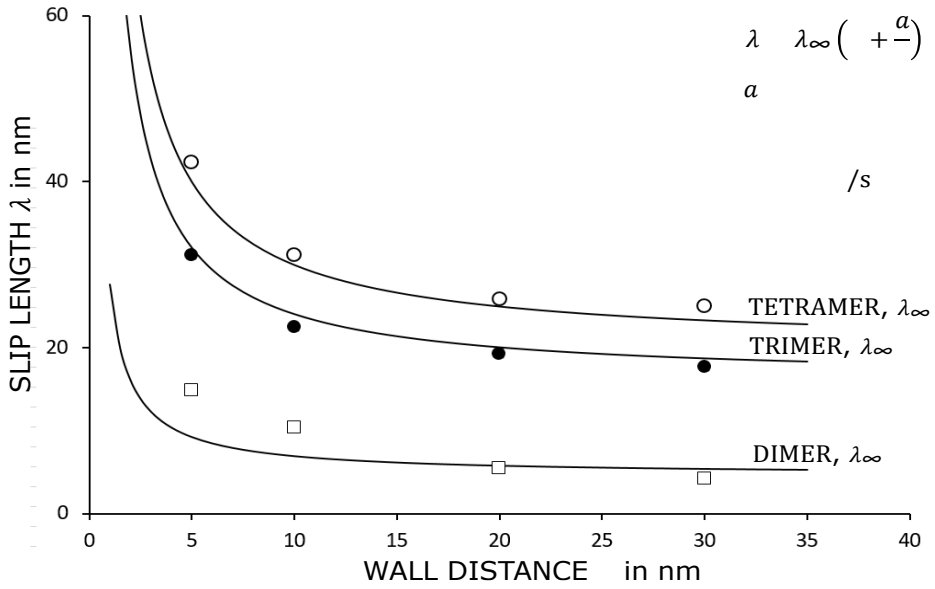

Figure 6: Slip length λ as a function of wall distance h for PAO oil molecules. As the apparent shear rate is below the critical shear rate, the slip length values should be independent of the shear rate.

4 Conclusion

This paper employed an investigation of the shear flow of PAO oils within two smooth iron surfaces to calculate slip length with application in a journal bearing. The united-atom method helped capture molecular trends in the tribological modeling of large and complex models due to its comparably low computational cost. In order to be convinced that the performance seen in MD simulations is representative of an actual dynamical system, a proper Force Field that is qualified for the density and viscosity prediction of branched alkane was selected. For more reliability of the simulation results, verification of the method was accomplished for the metal-alkane interface. The slip length values were calculated by averaging Couette velocity profiles that the velocity profiles were linear up.

The results showed that the slip length is highly dependent on the molecular shape. We concluded that by raising the number of branches, slip increases in agreement with the previous MD modeling [4]. The viscosity calculation showed that the critical shear rate increases with increasing temperature. This result indicates that PAO lubricant can show various lubrication performances based on temperature. Also, the shear stress calculation showed that the viscosity decreases with increasing temperature.

Acknowledgement

We kindly acknowledge the financial support by the German Research Foundation (DFG) within the Collaborative Research Centre 1194 "Interaction of Transport and Wetting Processes" - Project-ID 265191195, sub-project C06. The computing time was granted by Lichtenberg HPC computer resources at TU Darmstadt. We appreciate the Hessian Competence Center for High-Performance Computing – funded by the Hessen State Ministry of Higher Education, Research, and the Arts – for helpful advice.

References

[1] Pelz P. F., Corneli T., Mehrnia S., Kuhr M. (2022): Temperature-dependent wall slip of Newtonian lubricants. *Journal of Fluid Mechanics*, 948, A8.

[2] Mehrnia S., Pelz P. F. (2021): Slip length of branched hydrocarbon oils confined between iron surfaces. *Journal of Molecular Liquids*, 336, 116589.

[3] Mehrnia S., Pelz P. F. (2022): Tribological design by Molecular Dynamics simulation – The influence of molecular structure on wall slip and bulk shear. *Chemical Engineering & Technology*, 202200448.

[4] Jabbarzadeh A., Atkinson J. D., Tanner R. I. (1999): Wall slip in the molecular dynamics simulation of thin films of hexadecane. *Journal of Chemical Physics*, 110, 2612-2620.

[5] Plimpton S. (1995): Fast parallel algorithms for short-range molecular dynamics. *Journal of Computational Physics,* 117, 1–19.

[6] Hanwell M. D, Curtis D. E, Lonie D. C, Vandermeersch T., Zurek E., Hutchison G. R (2012): Avogadro: An advanced semantic chemical editor, visualization, and analysis platform. *Journal of Cheminformatics,* 4-17.

[7] Thompson A. P., Plimpton S. J., Mattson W. (2009): General formulation of pressure and stress tensor for arbitrary many-body interaction potentials under periodic boundary conditions. *J. Chem. Phys.* 131 154107.

15th SIRM – European Conference on Rotordynamics,
Darmstadt, Germany, 22nd – 24th February 2023

Study on localized defect model and identification in elastohydrodynamic lubricated ball bearings using support vector machine.

Laís Carrer [1], Luís Otavio Garavaso [2], Gregory Bregion Daniel[3], Tiago Henrique Machado[4], Katia L. Cavalca[5]

Dept. of Integrated Systems, School of Mechanical Engineering, UNICAMP St. Mendeleyev, 200, 13083-860, Campinas, SP, Brazil,
[1] laiscarrer@hotmail.com; [2] otaviogaravaso@gmail.com; [3] gbd@unicamp.br; [4] thmach@unicamp.br;
[5] katia@unicamp.br

Abstract

The increasing demand for numerical models that accurately represent real-life applications, supporting the development of techniques for fault diagnoses and analysis, has driven researchers to elaborate and refine models for reliable condition monitoring of rotating machines. In this context, this work trains the support vector machine (SVM) algorithm with pre-processed acceleration data to investigate different ball bearings defects according to their type and location. The system consists of four ball bearings, pedestals, a gearbox, and a flywheel, including random errors and position fluctuations in the simulations. Noise is added to the vibration signal to approximate the response to experimental data from the literature. The contact model between each sphere and raceways considers elastohydrodynamic (EHD) lubrication, assuming a reduced model in the reactions bearing forces. The complete 34 degrees of freedom system of equations are solved by outputting vibration signals for different conditions of faulty and healthy bearings. The defects are modeled according to their location, i.e., inner-race, outer-race, or single rolling element, with sinusoidal ball trajectory into the spall. The application of Fast Kurtogram (FK) is proposed as a pre-processing tool for the optimal frequency range selection to improve the identification process.

1 Introduction

The mathematical formulation presented in [1] is a classic approach to the study of bearing dynamics. Its application includes fault modeling [2]–[4] and it is also used in the present work for comparison in some cases. A similarity between most models for angular contact ball bearings is the absence of damping effects of the lubricant film thickness, present at the contact interfaces. Generally, this effect is considered as Hertz dry contact, or the lubrication model neglects the participation of the rolling elements relative motion.

The elastohydrodynamic theory most accurately represents the lubricated contact. Nevertheless, it leads to high computational costs, resulting in few studies combining this theory with the contact stiffening and damping of the lubricant film, preferring classical models. Studies in [6] and [7] on the nonlinear effects of EHD were further adapted to take into account variations in fluid properties due to temperature and pressure. In the work of [8], a reduced order model for the lubricated contact in deep groove bearings was proposed, using an implicit nonlinear formulation to adjust the solution for the transient EHD contact point [9]. In this work, the first step is the numerical solution for the EHD lubricated contact obtained by the Multi-Level Multi-Integration (MLMI) algorithm [10] and

[11]. A reduced model can be applied by optimization of equivalent stiffness parameters and linear damping parameters to adjust the contact forces curves in the bearing elements and, subsequently, in the complete bearing equivalent coefficients, [12], [13] and [14]. In [15] and [16], the authors modeled a complete rotor-bearing system based on the work of [17] for experimental comparison purposes. The rotor model includes the shaft and disk finite element model using the well-known Timoshenko's beam theory for the shaft. In this approach, inertia, elasticity, and shear effects are taken into account, which was widely employed based on [18] and [19] respectively.

An extended analysis in [20] compared numerical model and test rig measurements for gear bearing systems using a 34 DOF model, from a lumped mass parameter model. The model included localized faults on the outer and inner race, as well as in sphere elements, using Hertzian contact model. The approach considers the stiffness coefficient varying in time, but it neglects the damping effect. Given continuity of this work [21], the authors numerically included the model of extended faults (rough surface) in both inner and outer races.

In [22] the authors investigated the fault size estimation. The identification considered two fault interactions with the rolling elements, the entry point, with low frequency response - when a rolling element enters a localized defect, and the successive exit point. An empirical model-based signal processing method was proposed to effectively identify the entry point and the differentiation for the exit of the fault.

A comprehensive work on the state of the art regarding fault diagnosis for rolling element bearing can be found in [23]. This paper reviews key concepts in the analysis of bearing faults and it gives a brief introduction to rolling elements inherent cycle stationarity, also pointing to the analysis of the envelope signals as a more efficient source of information in the diagnosis than raw signals analysis, presenting enhancement methods for extracting and filtering information of bearing signals.

The work of [24] shows the spectral kurtoses (SK) as a powerful technique to indicate the presence and location of a series of transients in the frequency domain, hence, the effect signature caused by localized faults. In the same year, [25] applied this method to vibratory monitoring of the rotating machine, but mainly as an auxiliary tool to detect filters able to extract the mechanical signature of the fault, being one of the most important advantages of this approach, as opposed to other classical techniques, finding the optimal frequency band to be processed. Later, [26] presented the concept of Fast Kurtogram (FK), i.e., the fast computation of the kurtogram, mostly feasible in industry and user-friendly, as it displays the optimum choice for frequency/frequency resolution. Consequently, the FK is selected in the present work to process the envelope spectrum analysis.

Several researchers have applied supervised methods of machine learning to bearings fault identification, [27] performed SVM having as features the eigenvectors extracted response using principal component analysis. [28] proposed an automatization process using one class v-SVM to identify abnormal signals using the frequency spectrum as input prior to an envelope analysis. [29] aimed to find an optimum number of features for SVM and PSVM classifiers for statistical and histogram features of time domain signal classification of roller bearing faults. [30] detected and identified wind turbine bearing faults using fault-specific features by envelope analysis as input for training models, achieving an automatic identification. The one-class support vector machine method was able to detect the fault earlier but it still demanded additional techniques to identify the fault location.

The present work uses the SVM for identifying and classifying the bearings condition using simulated noisy vibration signals, recognizing specific patterns that may indicate the occurrence of faults. Due to the noise and its eventual impact on the time response, data processing can be necessary to reduce its influence, preserving as much information as possible. Hence, the Fast Kurtogram (FK) is proposed to identify the optimal frequency range and frequency resolution capable of improving the identification process.

2 Methodology

2.1 Bearing model

Initially, the static load and rotation speeds on the bearing elements must be determined to be the inputs for the EHD contact simulations. The outputs must be the angular speeds, contact forces and displacements between the rolling elements and the raceways surfaces, so the EHD non-linear parameters for the restitutive force and the linear damping coefficients can be defined.

At this point, a reduced-order model represents the nonlinear restoring contact force for the bearing characterization, in both contacts between spheres and internal/external raceways. The multilevel numerical integration algorithm solves the EHD to successive adjusting of the parameters of equivalent nonlinear stiffness

K, displacement exponent d and the residual force ΔF. The Levenberg-Marquardt optimization algorithm is applied to the static equilibrium data for this purpose. The parameters of the reduced-order model must be able to reproduce the force versus displacement curve, as shown in Equation (1) [14].

$$F = K\delta^d + \Delta F \tag{1}$$

The model for the rotor bearing system is based on the work of [21]. The spall on the bearings is modeled according to Figure 1(b) as a function of $h(\theta_f)$,

$$h(\theta_f) = C_d \left(1 - \left|\cos\left(\pi \frac{\theta_f}{\theta}\right)\right|\right) \tag{2}$$

Figure 1(a) shows three possible cases for the configuration between the spall and the sphere-raceway dimension, being C_s the spall depth and C_m the possible depth base on the width and sphere-raceway radius of curvature. Case I shows $C_s > C_m$, case II considers $C_s = C_m$ and case III$C_s < C_m$. It is always considered Cd the minimum of C_s and C_m.

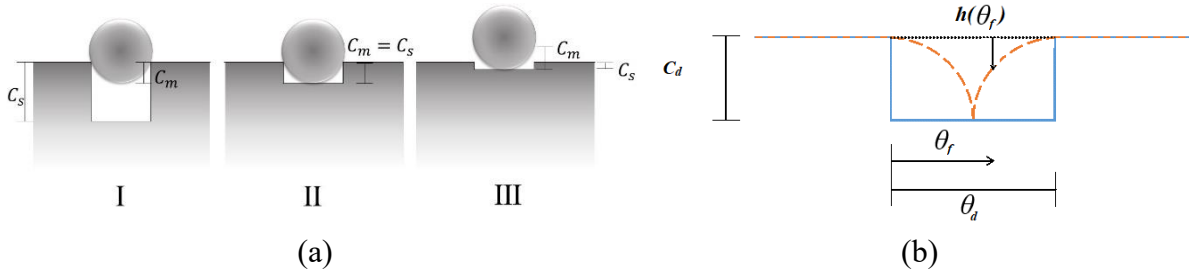

Figure 1 (a) Extension of the fault based on the sphere size (b) Improved ball trajectory**.**

The system in [20,21] contains a gear-pinon pair and four ball bearings. The contact model in the bearings was here updated to EHD lubrication, as a reaction for each bearing node equilibrium in F_y, F_z, $F_{\dot{y}}$ and $F_{\dot{z}}$,

$$F_y = \sum_{j=1}^{Z} \left[\left(K\left(z_m \cdot cos(\psi_j) + y_m \cdot sin(\psi_j)\right)^d + \Delta F - h(\theta_f)\right) \cdot cos(\psi_j)\right] \tag{3}$$

$$F_z = \sum_{j=1}^{Z} \left[\left(K\left(z_m \cdot cos(\psi_j) + y_m \cdot sin(\psi_j)\right)^d + \Delta F - h(\theta_f)\right) \cdot sin(\psi_j)\right] \tag{4}$$

Considering the local damping in each contact as D, the reaction forces due to dissipative effects are:

$$F_{\dot{y}} = \sum_{j=1}^{Z} \left[\left(D\left(\dot{z}_m \cdot cos(\psi_j) + \dot{y}_m \cdot sin(\psi_j)\right) + \omega_c\left(z_m \cdot sin(\psi_j) + y_m \cdot cos(\psi_j)\right)\right) \cdot cos(\psi_j)\right] \tag{5}$$

$$F_{\dot{z}} = \sum_{j=1}^{Z} \left[\left(D\left(\dot{z}_m \cdot cos(\psi_j) + \dot{y}_m \cdot sin(\psi_j)\right) + \omega_c\left(z_m \cdot sin(\psi_j) + y_m \cdot cos(\psi_j)\right)\right) \cdot sin(\psi_j)\right] \tag{6}$$

2.2 Support vector machine identification

Support vector machine is a well-known method for supervised machine learning. Developed by [31], it consists of solving a non-linear optimization problem of the convex objective function,

$$\begin{cases} \min\limits_{w,b} \Phi = \dfrac{1}{2} w^T w + C \sum\limits_{i=1}^{N} \xi_i \\ subject\ to: (w^T x_i + b) d_i > 1 - \xi_i \\ \xi_i \geq 0 \end{cases} \tag{7}$$

where ξ is the slack variable for outliers' control, C is a constant, x_i is the i-th support vector, b is the bias, $d_i \in \{-1,1\}$ and w is the weight vector.

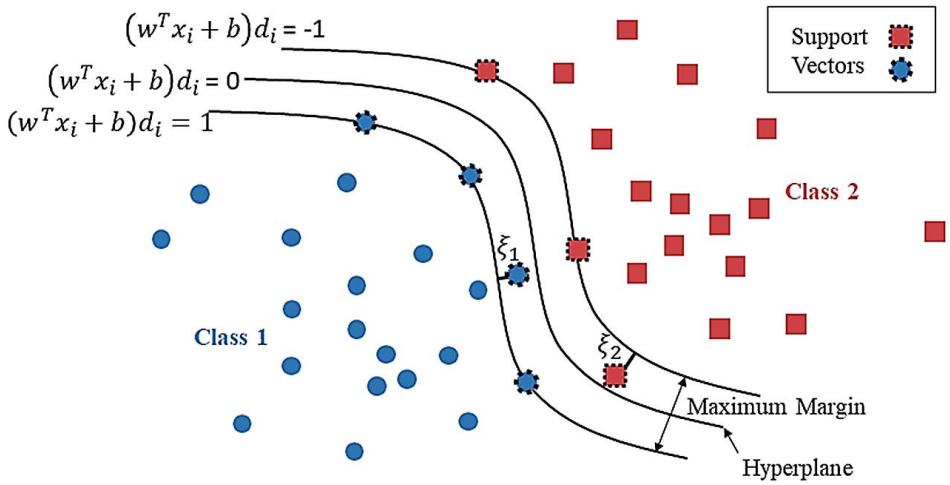

Figure 2 Representation of two classes separated by a hyperplane solved by SVM

Figure 2 illustrates how the method separates the data into specific classes by maximizing the margin distance between the adjacent vectors in each class, denominating then support vectors. In the optimization process they consist of non-trivial solutions and, most of the time, incur a penalty when a sample is misclassified or within the margin boundary. The data fully outside the limits, namely, everything but the support vectors, can fluctuate under the condition of not surpassing the decision boundaries, in a way the result is independent of this remaining data [32].

When the hyperplane that divides different classes is not assumed linear, it is required to map the patterns, Φ, and take it to a feature space (FS) of higher unknown order, where the data can be linearly approached. For the optimization, it is only needed the scalar product of the mapping Φ in the FS and the result when returning to the input space is a Kernel, K , function that satisfies Mercer's Theorem [33]. This work uses the radial basis function (RBS):

$$K(u,v) = \exp(-\gamma \|u - v\|^2) \tag{8}$$

where γ is a constant that defines how broad the Gaussian-like curve is.

The automation process accomplishes a variation of cases in the same rotation speed and load condition. The variation of this data consists in randomizing the extension and depth of the three types of faults, changing these parameters inside acceptable limits. In sequence, an approximate 25 dB white noise addition to the resulting signal emulates an ambient acquisition noise. These signals are then divided into segments. The different segments are the samples and each point of the acceleration signal in time is an attribute. Those samples are separated into test and training samples to proceed with the SVM analyses and to obtain the Confusion matrix.

To enhance the signal analysis, fast computation of the kurtogram, as proposed in [26] is carried out. This process consists in finding the optimal pair, carrier frequency, and frequency band that maximizes the kurtosis of the signal. The kurtosis, the fourth statistic central moment, is a common tool to identify impact-like signals, as in the case of bearings with an initial spall.

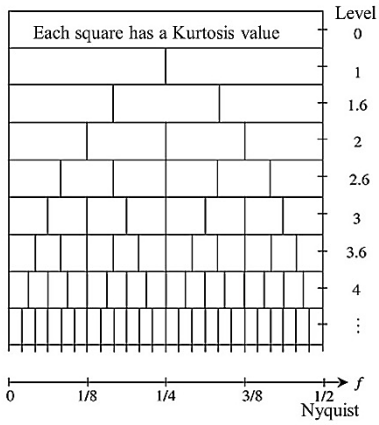

Figure 3 Fast kurtogram map of the (frequency/frequency resolution) plane

Figure 3 shows the construction of the fast kurtogram, based on [26], structured as a filter bank, computing the kurtosis values for each level that represents a bandpass frequency per central frequency, in which an FIR filter is performed. Each kurtosis value has the corresponding dyad, frequency, and frequency resolution, designated to perform the envelope analysis, or in this work case, each pair frequency and frequency resolution are computed for all the training samples.

3 Results and Discussion

The data used in this work is a simulation of the system presented in the work of [34]. The system was subject to a 50-Nm load and 10Hz rotational frequency. Vibration signals were sampled at 48 kHz, the bearings have an 0º contact angle, 7.12 mm sphere diameter, and a pitch diameter of 38.5 mm. The outer race spall has 0.8 mm wide and has an assumed depth of 19.1 µm, while the inner race has a depth of 27.6 µm. The ball defect is 0.5 mm wide with an assumed depth of 10.7 µm when touches the inner race, and 7.4 µm depth for the outer race.

Figure 4 presents the time vibration signal for inner race defect bearing and Figure 5 shows the corresponding power spectrum density (PSD) against the health bearing signal response. Pink noise was added with a resulting SNR of 20 dB approximately, to compare and validate the response with [21].

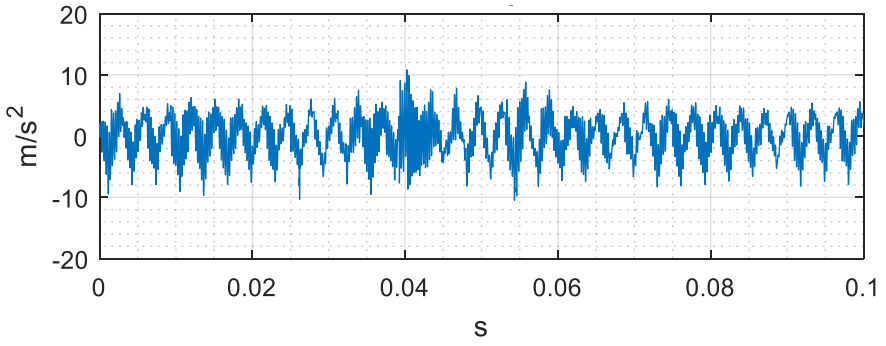

Figure 4 Acceleration time signal of the ball bearing with inner race defect.

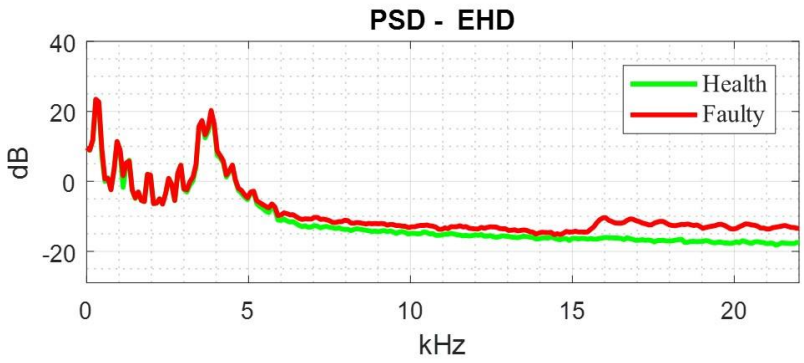

Figure 5 PSD of a health bearing (green) and bearing with inner race defect (red).

To determine the size of the input feature, it is necessary to guarantee that every sample contains at least one fault signature in the time domain, there is, the fault effectively passing through the bearing load zone. The required number of points is the sampling frequency (FS) divided by the minimum of all the frequencies that can modulate the signal fault. In the current case, the sphere defect is responsible for modulating the signal not only by the sphere spin velocity but also depending on the cage angular velocity of 4.07 Hz. So, considering an unfiltered signal, for the fault signal to be seen at least once, is necessary 0.25 seconds, resulting in 11.794 points needed, given a FS of 48000 Hz. For convenience, the number of points is practically doubled to 24 thousand points.

The samples from simulated signals represent four cases: health bearings, outer race fault, inner race fault, and sphere fault. Variations from the assumed parameters of width and depth, as the proportion to the initial spall shown in table 1, must be combined to create the data set, separating slices of the acceleration signal in time to replicate different instances of the same case and creating more samples.

Table 1. Cases of fault parameters combination

Cases	The proportion of the initial spall depth and width	Number of samples
I	0.13 – 0.6 – 1.3 – 6.0	1920
II	0.13 – 0.6 – 1.3	1080
III	0.13 – 0.36 – 0.6	1080
IV	0.6 –1.3 – 3.65	1080

White noise is added to the vibration signal and kept the same for all samples with different amplitudes. It represents an acquisition noise for realistic system representation. The achieved SNR varied from sample to sample, resulting in an average of 25 dB.

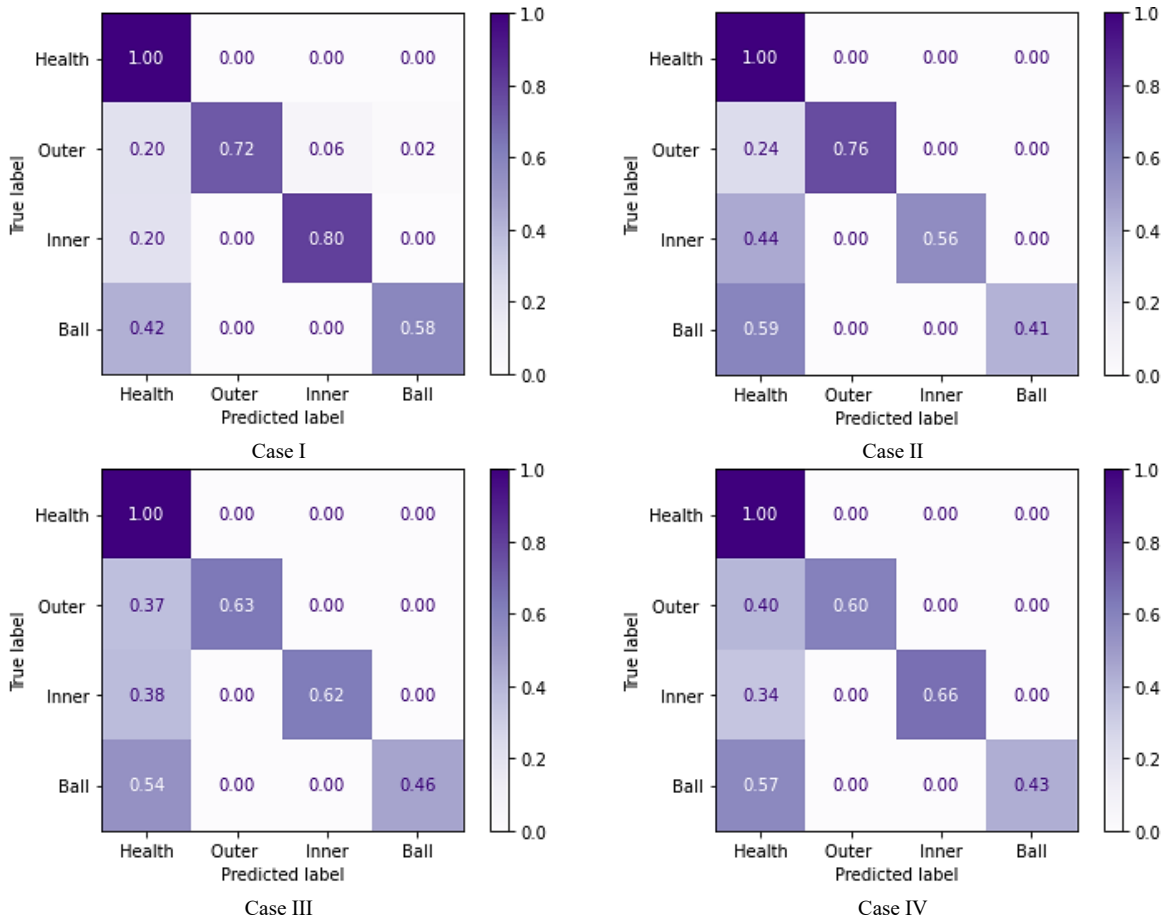

Figure 6. Confusion matrix for the four cases selected.

The confusion matrices resulting from the SVM analysis for each case are presented in Figure 6. The SVM algorithm gives a considerable number of false negatives, indicating health bearing between 20 and 60% defective samples, especially in case of spheres fault.

After performing the fast kurtogram for all training set and organizing which pair frequency/band is the most recurrent in each label, it is necessary to compute the bandwidth that occurs the most for each carrier frequency. The next step is the definition of the carrier frequency of highest occurrence for each of the four condition classes: health, outer race, inner race, and sphere defect. Table 2 shows these results for case I.

Table 2 Carrier frequency and bandwidth modes for labels for case I**.**

Labels	Carrier frequency [Hz]	Bandwidth [Hz]
Ball	7500	3000
Health	6000	12000
Inner	21000	6000
Outer	20000	6000

The four possible ways of filtering all the input data according to each condition led to the necessity of considering all of the faulty cases. Rearranging the features in a way of keeping the same number of samples, but increasing the number of features in every sample, all the input data are filtered and concatenated, according to the three fault cases, presented in figure 7.

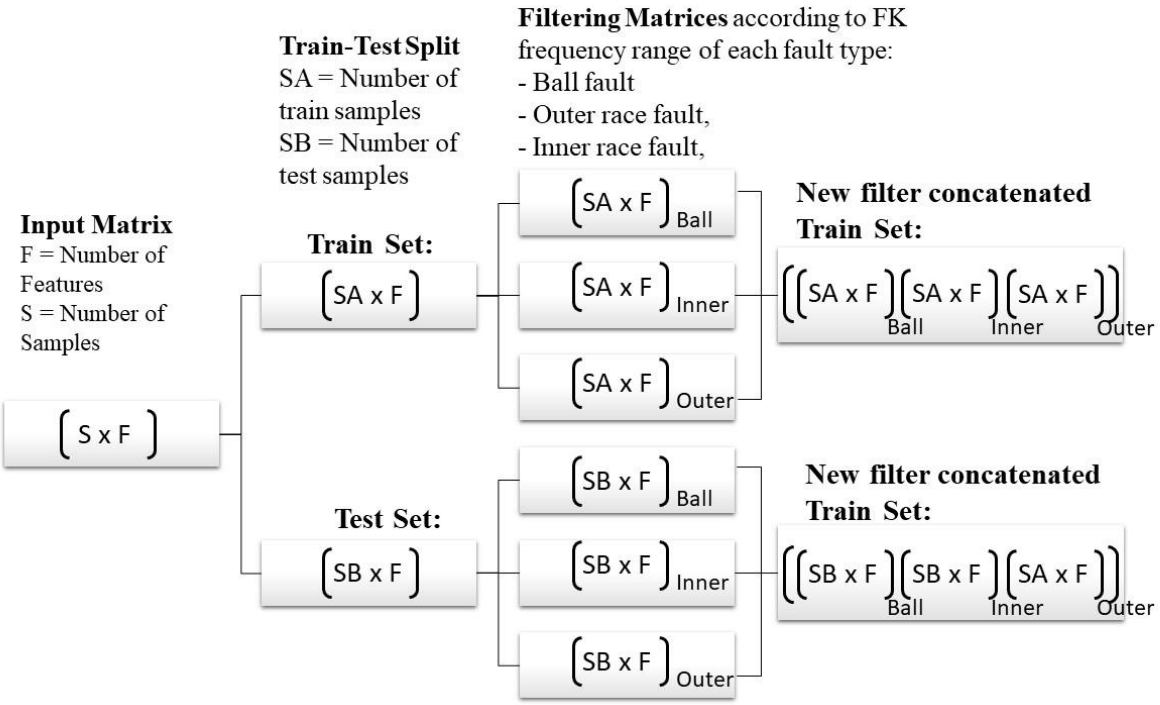

Figure 8 Schematic representation of filtering and concatenating matrices for SVM.

The resulting confusion matrices are presented in Figure 8.

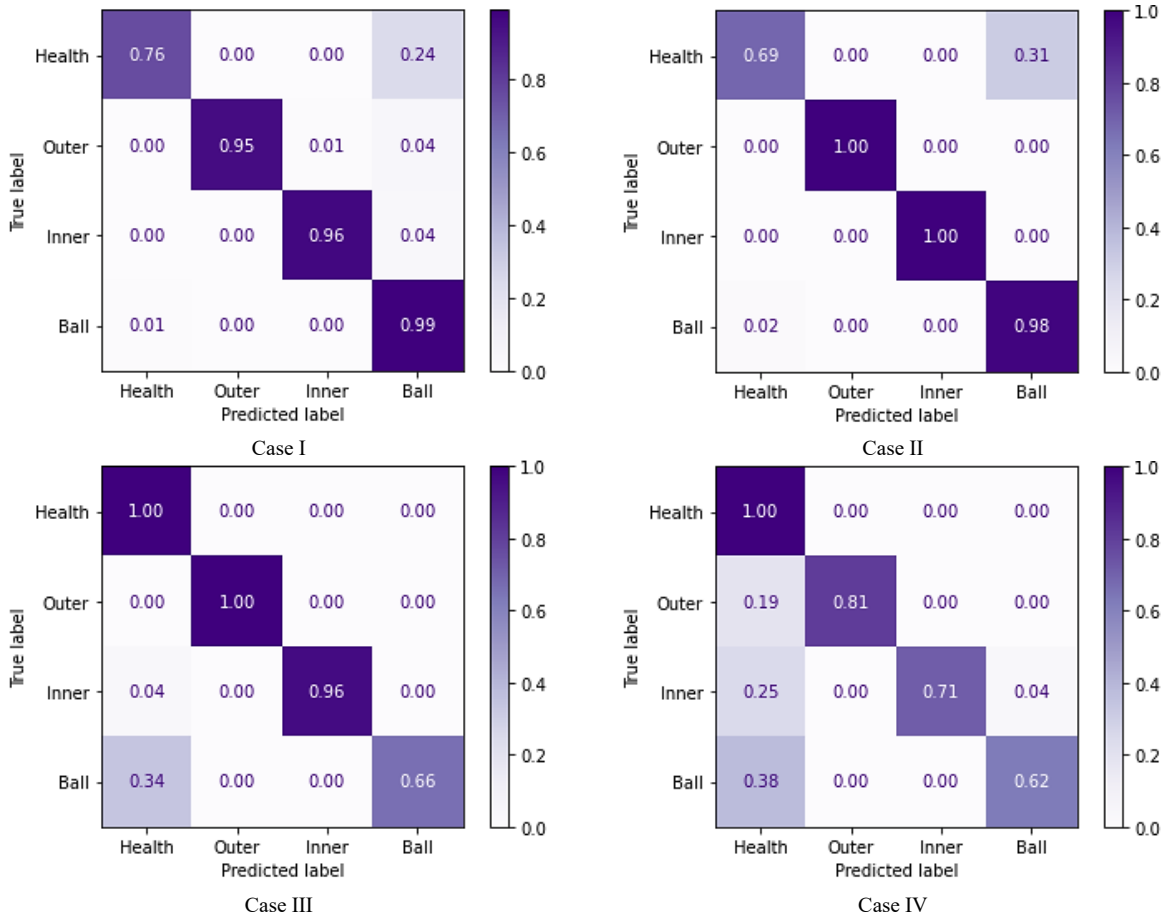

Figure 8 Confusion matrix after FK selection and filtering

Table 3 reports the accuracy improvement using FK as a preprocessing for input features augmentation.

Table 3 Accuracies for each case study

	Case I	Case II	Case III	Case IV
Accuracy	77.50%	69.62%	69.62%	69.25%
Accuracy/FK	91.66%	91.11%	91.85%	79.63%
Relative Improvement	18.27%	30.87%	31.93%	14.99%

It is noticeable the SVM process accuracy rises by a higher number of samples since a better accuracy could be achieved for case I. However, after the process of filtering and concatenating the input data according to the FK, cases II and III significantly improved, practically reaching the case I accuracy, after the same process.

7 Conclusion

The present work uses the support vector machine for classifying the operation of ball bearings subject to elastohydrodynamic lubrication when exposed to four distinct working conditions: healthy, with an inner or an outer race fault, or with a ball defect.

The data is generated by modeling the bearing contact as a reduced elastohydrodynamic lubrication model. Next, pink noise is added to the generated signals to compare and validate the methodology with the literature, showing that the reduced model theory can represent the complexity of the interaction behavior of forces and displacements without increasing the computational costs.

In conclusion, the support vector machine algorithm is promising for identifying and classifying mechanical faults in ball bearings. In addition, the fast kurtogram, by selecting the frequency range of the signals with the most information about the defects, has proven to be a powerful feature engineering tool, improving the SVM's accuracy by more than 10% for all cases.

Future studies should investigate whether the fast kurtogram feature engineering method can improve the performance of other machine learning algorithms, such as artificial neural networks or gradient boosting machines. Furthermore, for complete validation of the proposed methodology, the support vector machine, and the fast kurtogram should be evaluated on experimental data.

Acknowledgment

The authors thank the financial support of Petrobras-CENPES and CNPq.

References

[1] T. A. Harris, *Rolling Bearing Analysis*. New York: John Wiley & Sons, 1991.

[2] L. Niu, H. Cao, Z. He, and Y. Li, "Dynamic modeling and vibration response simulation for high speed rolling ball bearings with localized surface defects in raceways," *J. Manuf. Sci. Eng. Trans. ASME*, 2014, doi: 10.1115/1.4027334.

[3] J. Liu and Y. Shao, "An improved analytical model for a lubricated roller bearing including a localized defect with different edge shapes," *JVC/Journal Vib. Control*, vol. 24, no. 17, pp. 3894–3907, 2018, doi: 10.1177/1077546317716315.

[4] J. Liu, Z. Shi, and Y. Shao, "An analytical model to predict vibrations of a cylindrical roller bearing with a localized surface defect," *Nonlinear Dyn.*, vol. 89, no. 3, pp. 2085–2102, 2017, doi: 10.1007/s11071-017-3571-5.

[5] J. Liu and Y. Shao, "Vibration modelling of nonuniform surface waviness in a lubricated roller bearing," *JVC/Journal Vib. Control*, vol. 23, no. 7, pp. 1115–1132, 2017, doi: 10.1177/1077546315589675.

[6] D. Dowson, "A generalized Reynolds equation for fluid-film lubrication," *Int. J. Mech. Sci.*, vol. 4, no. 2, pp. 159–170, 1962.

[7] D. Dowson and G. R. Higginson, *Elasto-Hydrodynamic Lubrication*, SI. Oxford: Pergamon Press, 1977.

[8] Y. H. Wijnant, J. A. Wensing, and G. C. Nijen, "THE INFLUENCE OF LUBRICATION ON THE DYNAMIC BEHAVIOUR OF BALL BEARINGS," *J. Sound Vib.*, vol. 222, no. 4, pp. 579–596, May 1999, doi: 10.1006/jsvi.1998.2068.

[9] Y. H. Wijnant, *Contact Dynamics in the field of Elastohydrodynamic Lubrication*. 1998.

[10] C. H. Venner and A. A. Lubrecht, *Multilevel Methods in Lubrication*, Vol 37. Tribology Series. Elsevier, 2000.

[11] C. H. Venner, G. Popovici, P. M. Lugt, and M. Organisciak, "Film Thickness Modulations in Starved Elastohydrodynamically Lubricated Contacts Induced by Time-Varying Lubricant Supply," *J. Tribol.*, vol. 130, no. 4, Oct. 2008, doi: 10.1115/1.2958069.

[12] F. Nonato and K. L. Cavalca, “On the non-linear dynamic behavior of elastohydrodynamic lubricated point contact,” *J. Sound Vib.*, 2010, doi: 10.1016/j.jsv.2010.05.014.
[13] F. Nonato and K. L. Cavalca, “An approach for including the stiffness and damping of elastohydrodynamic point contacts in deep groove ball bearing equilibrium models,” *J. Sound Vib.*, 2014, doi: 10.1016/j.jsv.2014.08.011.
[14] L. Bizarre, F. Nonato, and K. L. Cavalca, “Formulation of five degrees of freedom ball bearing model accounting for the nonlinear stiffness and damping of elastohydrodynamic point contacts,” *Mech. Mach. Theory*, 2018, doi: 10.1016/j.mechmachtheory.2018.03.001.
[15] L. Carrer, L. Bizzarre, and K. Cavalca, “Analysis of a Rotor Supported by Angular Contact Ball Bearings Under EHD Lubrication,” in *Proceedings of the 10th International Conference on Rotor Dynamics – IFToMM. IFToMM 2018*, Mechanisms., W. H. Cavalca K., Ed. Springer, 2019, pp. 398–412.
[16] L. Carrer, L. Bizarre, and K. L. Cavalca, “Rotor-angular contact ball bearing system study using EHD lubrication and comparison with experimental tests,” in *Proceedings of IMEchE VIRM 12*, Bath: IMechE, London, 2020, pp. 182–191.
[17] R. Aini, “Vibration monitoring and modelling of shaft/bearing assemblies under concentrated elastohydrodynamic condition,” Kingston Polytechnic, 1990.
[18] H. D. Nelson, “A Finite Rotating Shaft Element Using Timoshenko Beam Theory,” *J. Mech. Des.*, vol. 102, no. 4, pp. 793–803, Oct. 1980, doi: 10.1115/1.3254824.
[19] H. D. Nelson and J. M. McVaugh, “The Dynamics of Rotor-Bearing Systems Using Finite Elements,” *J. Eng. Ind.*, vol. 98, no. 2, pp. 593–600, May 1976, doi: 10.1115/1.3438942.
[20] N. Sawalhi and R. B. Randall, “Simulating gear and bearing interactions in the presence of faults. Part II: Simulation of the vibrations produced by extended bearing faults,” *Mech. Syst. Signal Process.*, vol. 22, no. 8, pp. 1952–1966, 2008, doi: 10.1016/j.ymssp.2007.12.002.
[21] N. Sawalhi and R. B. Randall, “Simulating gear and bearing interactions in the presence of faults. Part I. The combined gear bearing dynamic model and the simulation of localised bearing faults,” *Mech. Syst. Signal Process.*, vol. 22, no. 8, pp. 1924–1951, 2008, doi: 10.1016/j.ymssp.2007.12.001.
[22] A. Chen and T. R. Kurfess, “Signal processing techniques for rolling element bearing spall size estimation,” *Mech. Syst. Signal Process.*, vol. 117, pp. 16–32, 2019, doi: 10.1016/j.ymssp.2018.03.006.
[23] R. B. Randall and J. Antoni, “Rolling element bearing diagnostics-A tutorial,” *Mech. Syst. Signal Process.*, vol. 25, no. 2, pp. 485–520, 2011, doi: 10.1016/j.ymssp.2010.07.017.
[24] J. Antoni, “The spectral kurtosis: A useful tool for characterising non-stationary signals,” *Mech. Syst. Signal Process.*, vol. 20, no. 2, pp. 282–307, 2006, doi: 10.1016/j.ymssp.2004.09.001.
[25] J. Antoni and R. B. Randall, “The spectral kurtosis: Application to the vibratory surveillance and diagnostics of rotating machines,” *Mech. Syst. Signal Process.*, vol. 20, no. 2, pp. 308–331, 2006, doi: 10.1016/j.ymssp.2004.09.002.
[26] J. Antoni, “Fast computation of the kurtogram for the detection of transient faults,” *Mech. Syst. Signal Process.*, vol. 21, no. 1, pp. 108–124, 2007, doi: 10.1016/j.ymssp.2005.12.002.
[27] L. Shuang and L. Meng, “Bearing fault diagnosis based on TEO and SVM,” *Proc. 2007 IEEE Int.*, no. 1, 2007.
[28] D. Fernández-Francos, D. Marténez-Rego, O. Fontenla-Romero, and A. Alonso-Betanzos, “Automatic bearing fault diagnosis based on one-class m-SVM,” *Comput. Ind. Eng.*, vol. 64, no. 1, pp. 357–365, 2013, doi: 10.1016/j.cie.2012.10.013.
[29] V. Sugumaran and K. I. Ramachandran, “Effect of number of features on classification of roller bearing faults using SVM and PSVM,” *Expert Syst. Appl.*, vol. 38, no. 4, pp. 4088–4096, 2011, doi: 10.1016/j.eswa.2010.09.072.
[30] J. Saari, D. Strömbergsson, J. Lundberg, and A. Thomson, “Detection and identification of windmill bearing faults using a one-class support vector machine (SVM),” *Meas. J. Int. Meas. Confed.*, vol. 137, pp. 287–301, 2019, doi: 10.1016/j.measurement.2019.01.020.
[31] V. N. Vapnik, *The Nature of Statistical Learning Theory*. New York: Springer, 1995.
[32] Christopher M. Bishop, *Pattern Recognition and Machine Learning*. 2006.
[33] C. Cortes and V. Vapnik, “Support-vector networks,” *Mach. Learn.*, vol. 20, no. 3, pp. 273–297, Sep. 1995, doi: 10.1007/BF00994018.
[34] N. Sawalhi, “Diagnostics, Prognostics and Fault Simulation,” no. April, 2007, [Online]. Available: https://www.unsworks.unsw.edu.au/permalink/f/a5fmj0/unsworks_1509.

15th SIRM – European Conference on Rotordynamics,
Darmstadt, Germany, 22nd – 24th February 2023

Database approach for force calculation of journal bearings with oil feed holes: An application to turbocharger bearings

Gantasala S.[1], **Koutsovasilis P.** [2] **and Baum C.** [3]

Dynamics Simulation & Methods, BorgWarner Systems Eng. GmbH, 67292, Kirchheimbolanden, Germany
[1] sgantasala@borgwarner.com, [2] pkoutsovasilis@borgwarner.com, [3] cbaum@borgwarner.com

Abstract

The dynamic pressure generated within journal bearings can be predicted using the Reynolds equation and it is generally coupled to rotor equations of motion for predicting their dynamic behavior. Such simulations for high-speed rotating machinery require high computational efforts. Many different methods exist in the literature to efficiently solve the Reynolds equation for a plain journal bearing (without any features like oil feed holes or grooves). The database approach is one of these methods where the Reynolds equation is non-dimensionalized and transformed into a partial differential equation that only depends on two independent parameters. These parameters are functions of bearing dimensions, lubricating oil viscosity, rotor state variables, and rotational speed. A database of bearing forces can be created by considering different sets of values for these two parameters within their finite range. Such a database can be used to predict bearing forces using multivariate interpolation. The authors extended this approach to consider oil feed holes in the journal bearings by introducing two additional parameters. The Reynolds equation expressed in terms of these four parameters is solved using the MATLAB PDE toolbox to generate the database. The vibration response of a turbocharger rotor supported on a semi-floating journal bearing consisting of oil feed holes is investigated using the proposed database approach. The oil feed holes modeling improved the predictability of sub-synchronous vibrations when compared with experimental results. In the end, the impact of a different number of oil feed holes on the turbocharger rotordynamics response is also presented.

1 Introduction

Turbocharger rotors are either supported by the journal and thrust bearings or ball bearings [1]. They play a vital role in maintaining the overall functioning of the system [2]. Turbochargers are complex machines that operate at high rotational speeds and experience higher temperatures, flow-induced disturbances from turbine and compressor, engine excitations, etc [2, 3, 4]. They also induce vibrations and forces that are transferred to the connecting parts radiating unavoidable noise in the vehicles [5]. The majority of the turbochargers use either semi- or full-floating journal bearings as shown in Figure 1. These bearings have two oil films, inner and outer oil films [6]. Turbocharger rotors are flexible and they generally operate above their first bending critical speed. These resonances are dampened by the journal bearings allowing an overall smoother operation of the rotor. Yet, the journal bearings experience instabilities due to the self-excited vibrations known as oil whirl/oil whip [2, 6]. These instabilities in the two oil films occur at different rotational speeds and the instability in one oil film is usually dampened by the other oil film to reach a limit cycle. Due to that such systems operate safely even at higher rotational speeds. Oil supply conditions to journal bearings like pressure and temperature are specific to the engine and vary according to its running conditions. Turbochargers should have acceptable vibration behavior at all operating and boundary conditions like different oil supply conditions, bearing clearances, and assembly imbalances, with heat transfer from turbine, housings, and viscous shear in the oil films, etc. This generally is confirmed through testing on a hot gas stand or on engines. Due to that design cycles are time-consuming and incur higher costs. Advanced simulations capturing complex elasto-hydro-aero-thermo-dynamic behavior of the turbocharger system can address these concerns and bring down the design cycle times.

The journal bearings are supplied with lubricating oil through feed holes or grooves in the circumferential or axial direction. The dynamic pressure generated inside journal bearings can be predicted by solving the Reynolds equation, a linear second-order partial differential equation (PDE) derived with certain assumptions [7]. Simplified models using short or long-bearing theories can be applied for circular bearing geometries when their length-to-

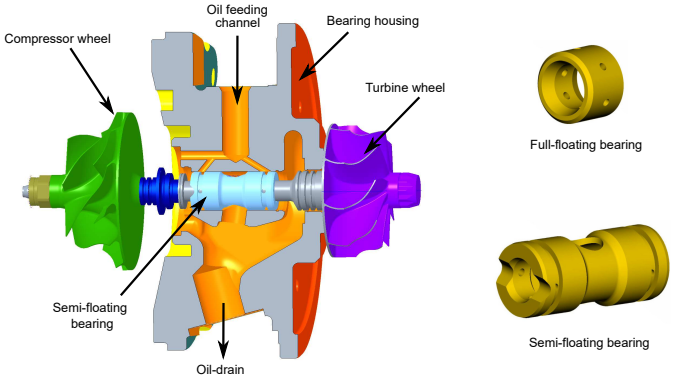

Figure 1: Typical automobile turbocharger system components

diameter (L/D) ratio values are within a certain range [7]. For other L/D ratio values, non-circular bearing surfaces, and bearing geometries with specific features like oil holes, and grooves, the Reynolds equation needs to be solved by numerical methods. Several approaches like the finite element method (FEM), finite difference method (FDM), spectral methods, finite volume method (FVM), etc. can be applied to solve the Reynolds equation [8]. Alternatively, a database is created for the bearing forces at certain non-dimensional parameters derived from the Reynolds equation of a plain journal bearing and used in the rotor dynamic simulations in [9, 10]. In two other works [11, 12], a database approach is proposed using the principle of the superposition of the partial solutions of the Reynolds equation. The partial solutions are obtained by solving the Reynolds equation after exclusively considering viscous shear flow, squeeze effects, and pressure supply boundary conditions at oil grooves or holes. But the accuracy of their approach in fluid pressure and bearing force calculations is unknown. In the current work, the authors propose an extension to the database approach to be applicable for bearings with oil feed holes. The Reynolds equation is transformed and expressed in terms of four independent parameters without making any further assumptions. These parameters are functions of bearing dimensions, rotational speed, rotor state variables, and oil properties and also they take values within a finite range only. The Reynolds equation is solved using MATLAB PDE toolbox [13] for various combinations of the values for these four parameters to build a database and it is described in detail in the next section.

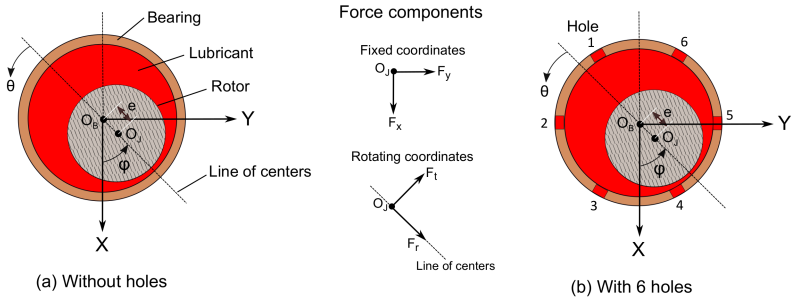

Figure 2: Eccentric rotor (a) bearing without holes and (b) bearing with holes

The rotor operates at an eccentric position from the bearing center during operation (refer to Figure 2) forming converging and diverging clearance regions about the line of center axis. The oil film pressure becomes negative in the Reynolds equation solution in the semicircle region where clearance increases from minimum to maximum value in the direction of rotation of the shaft. Liquids under normal operating conditions do not withstand negative pressures which lead to oil film rupture and cavitation. Gumbel boundary condition [7] is used in this study due to its simplicity where negative pressures are disregarded by equating them to zero. This boundary condition is suitable for run-up simulations but it does not fulfil fluid continuity, and also does not satisfy the conservation of mass throughout the fluid and cavitation regions within the bearing. It is possible to consider complex cavitation boundary conditions like Jacobson, Floberg, and Olsson, Elrod cavitation models [14, 15] that satisfy these conditions while generating the required database. The authors want to consider it in future studies. The knowledge about the influence of oil feed holes on rotor vibrations is limited and especially their influence on turbocharger rotor vibrations is not investigated in detail in the literature to the best knowledge of authors. In the current work, the

run-up vibration response of a turbocharger rotor supported on a semi-floating journal bearing is simulated using the proposed database approach without and with oil feed holes modelled. The simulation results are compared with the test results on an engine test bed. The current paper is organized in the order of sections discussing the database approach and rotor modelling, results, and conclusions.

2 Numerical modelling

2.1 Database approach for plain bearings

The Reynolds equation governing dynamic pressure generated within journal bearings in its non-dimensional form is given as follows,

$$\frac{\partial}{\partial\theta}\left(H^3\frac{\partial\bar{p}}{\partial\theta}\right)+\left(\frac{D}{L}\right)^2\frac{\partial}{\partial\bar{z}}\left(H^3\frac{\partial\bar{p}}{\partial\bar{z}}\right)=12\left\{\dot{\varepsilon}cos(\theta)+\varepsilon\left(\frac{\dot{\varphi}}{\Omega}-\frac{1}{2}\right)sin(\theta)\right\}, \tag{1}$$

where the non-dimensional variables can be expressed as $\bar{p}=\frac{p}{\mu\Omega}\left(\frac{c}{R}\right)^2$, $H=\frac{h}{c}=1+\varepsilon cos(\theta)$, $\bar{z}=\frac{z}{L/2}$, $\varepsilon=\frac{e}{c}$, $\dot{\varepsilon}=\frac{\dot{e}}{c\Omega}$, p is the dynamic pressure, h is the oil film thickness around the bearing circumference, μ is the oil viscosity, Ω is the angular velocity of the shaft, c is the bearing radial clearance, R and L are the bearing radius and length respectively, and $D=2R$, θ and z are the bearing's angular and axial coordinates, e is the eccentric distance between shaft and bearing centers, φ is the attitude angle, $\frac{\partial}{\partial\theta}$, $\frac{\partial}{\partial\bar{z}}$ and $\frac{\partial}{\partial t}$ refers to the spatial and temporal derivatives of a variable. Either end of the bearing is exposed to ambient pressure boundary conditions.

The non-dimensional pressure in the Equation 1 depends on the following three variables whose values are unbounded for a specific bearing geometry and rotational speed:

$$\begin{aligned}&\varepsilon\in[0,1],\\&\dot{\varepsilon}\in\Re,\\&\dot{\varphi}\in\Re.\end{aligned} \tag{2}$$

The Equation 1 is divided by $\sqrt{\dot{\varepsilon}^2+\left\{\varepsilon\left(\frac{\dot{\varphi}}{\Omega}-\frac{1}{2}\right)\right\}^2}$ and a new variable for pressure is defined as $\hat{p}=\frac{\bar{p}}{\sqrt{\dot{\varepsilon}^2+\left\{\varepsilon\left(\frac{\dot{\varphi}}{\Omega}-\frac{1}{2}\right)\right\}^2}}$. Then Equation 1 will change to the form as given below,

$$\frac{\partial}{\partial\theta}\left(H^3\frac{\partial\hat{p}}{\partial\theta}\right)+\left(\frac{D}{L}\right)^2\frac{\partial}{\partial\bar{z}}\left(H^3\frac{\partial\hat{p}}{\partial\bar{z}}\right)=12\left\{\frac{\dot{\varepsilon}}{\sqrt{\dot{\varepsilon}^2+\left\{\varepsilon\left(\frac{\dot{\varphi}}{\Omega}-\frac{1}{2}\right)\right\}^2}}cos(\theta)+\frac{\varepsilon\left(\frac{\dot{\varphi}}{\Omega}-\frac{1}{2}\right)}{\sqrt{\dot{\varepsilon}^2+\left\{\varepsilon\left(\frac{\dot{\varphi}}{\Omega}-\frac{1}{2}\right)\right\}^2}}sin(\theta)\right\}. \tag{3}$$

After introducing a new variable $\alpha=tan^{-1}\left(\frac{\varepsilon\left(\frac{\dot{\varphi}}{\Omega}-\frac{1}{2}\right)}{\dot{\varepsilon}}\right)$ in the Equation 3, it will change to the following equation,

$$\frac{\partial}{\partial\theta}\left(H^3\frac{\partial\hat{p}}{\partial\theta}\right)+\left(\frac{D}{L}\right)^2\frac{\partial}{\partial\bar{z}}\left(H^3\frac{\partial\hat{p}}{\partial\bar{z}}\right)=12\left\{cos(\alpha)cos(\theta)+sin(\alpha)sin(\theta)\right\}. \tag{4}$$

The transformed Reynolds equation will now only depend on two variables which are functions of rotor state variables, bearing clearance and rotational speed. The values of these two variables are also confined to a finite range as follows,

$$\begin{aligned}&\varepsilon\in[0,1],\\&\alpha\in[0,2\pi].\end{aligned} \tag{5}$$

A finite number of values m for ε and n for α are defined within their finite range and using different combinations of these two parameters, the Reynolds equation is solved for the dynamic pressure $\hat{p}$ for mxn times. After applying the Gumbel boundary condition, the pressure is integrated to calculate the bearing forces in rotating coordinates using the following equation,

$$F_r = \left\{ \int_0^{2\pi} \int_0^1 \hat{p} cos(\theta) d\theta d\bar{z} \right\} \mu\Omega \left(\frac{R}{c}\right)^2 RL \sqrt{\dot{\varepsilon}^2 + \left\{ \varepsilon \left(\frac{\dot{\varphi}}{\Omega} - \frac{1}{2} \right) \right\}^2},$$
$$F_t = \left\{ \int_0^{2\pi} \int_0^1 \hat{p} sin(\theta) d\theta d\bar{z} \right\} \mu\Omega \left(\frac{R}{c}\right)^2 RL \sqrt{\dot{\varepsilon}^2 + \left\{ \varepsilon \left(\frac{\dot{\varphi}}{\Omega} - \frac{1}{2} \right) \right\}^2}. \tag{6}$$

Then the database of bearing forces for F_r and F_t with a matrix size of m by n is generated as shown below,

$$F_r = \begin{bmatrix} f_{11} & \cdots & f_{n1} \\ \vdots & \ddots & \vdots \\ f_{m1} & \cdots & f_{mn} \end{bmatrix}_{mxn}, F_t = \begin{bmatrix} f_{11} & \cdots & f_{n1} \\ \vdots & \ddots & \vdots \\ f_{m1} & \cdots & f_{mn} \end{bmatrix}_{mxn}. \tag{7}$$

It is used as a lookup table while solving equations of motion of the rotor system for calculating bearing forces using multivariate interpolation.

2.2 Database approach for bearing with oil feed holes

The journal-bearing geometry with oil feed holes after unwrapping is shown in Figure 3 along with applicable boundary conditions. The Dirichlet boundary condition at the oil feed holes region does not permit following the same approach as explained in the last section to create the database. Instead, the database can be generated for the feed holes case from the dimensional form of the Reynolds equation given in Equation 8,

$$\frac{\partial}{\partial\theta}\left\{\frac{H^3}{R^2}\frac{\partial p}{\partial\theta}\right\} + \frac{\partial}{\partial z}\left\{H^3\frac{\partial p}{\partial z}\right\} = 12\left\{\frac{\dot{e}\mu}{c^3}cos(\theta) + \frac{e\mu}{c^3}\left(\dot{\varphi} - \frac{\Omega}{2}\right)sin(\theta)\right\}. \tag{8}$$

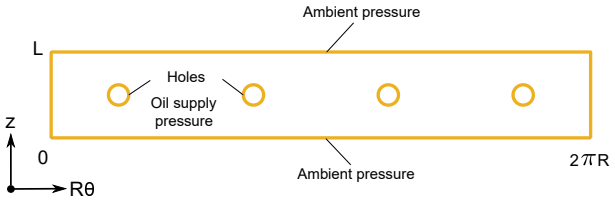

Figure 3: Unwrapped geometry of a bearing with oil feed holes

Three new variables $\xi = \frac{\dot{e}\mu}{c^3}$, $\eta = \frac{e\mu}{c^3}\left(\dot{\varphi} - \frac{\Omega}{2}\right)$ and $u = \frac{1}{\sqrt{1+\xi^2+\eta^2}}$ are introduced into the Equation 8 and after a rearrangement of the terms on the right side of the equation, it changes to the following form,

$$\frac{\partial}{\partial\theta}\left\{\frac{H^3}{R^2}\frac{\partial p}{\partial\theta}\right\} + \frac{\partial}{\partial z}\left\{H^3\frac{\partial p}{\partial z}\right\} = 12\frac{\sqrt{1-u^2}}{u}\left\{\frac{\xi}{\sqrt{\xi^2+\eta^2}}cos(\theta) + \frac{\eta}{\sqrt{\xi^2+\eta^2}}sin(\theta)\right\}. \tag{9}$$

Additional variable $\beta = tan^{-1}\left(\frac{\eta}{\xi}\right)$ is introduced to further simplify the equation to the form,

$$\frac{\partial}{\partial\theta}\left\{\frac{H^3}{R^2}\frac{\partial p}{\partial\theta}\right\} + \frac{\partial}{\partial z}\left\{H^3\frac{\partial p}{\partial z}\right\} = 12\frac{\sqrt{1-u^2}}{u}\left\{cos(\beta)cos(\theta) + sin(\beta)sin(\theta)\right\}. \tag{10}$$

The database approach is implemented for the Reynolds equation expressed in the rotating coordinates where the bearing geometry mesh starts at the line of centers axis. But it is not valid anymore for the oil feed holes due to the fixed locations of these holes on the bearing circumference. The mesh instead needs to start at a fixed location such as the vertical axis. Based on the orientation of the line of centers axis with feed holes and vertical axis, the pressure profile will be different due to the pressure supply boundary condition at the feed holes region. This introduces an additional variable, the attitude angle in the Reynolds equation as given below,

$$\frac{\partial}{\partial\theta}\left\{\frac{\bar{H}^3}{R^2}\frac{\partial p}{\partial\theta}\right\}+\frac{\partial}{\partial z}\left\{\bar{H}^3\frac{\partial p}{\partial z}\right\}=12\frac{\sqrt{1-u^2}}{u}\left\{cos(\beta)cos(\theta)+sin(\beta)sin(\theta)\right\}, \tag{11}$$

where, $\bar{H}=1+\varepsilon cos(\theta+\varphi)$.

The above equation depends on the following four variables for a bearing geometry with specific values for its length, width, hole diameter, number of holes (n_{holes}), and oil supply pressure,

$$\begin{aligned}&\varepsilon\in[0,1],\\&\beta\in[0,2\pi],\\&u\in(0,1],\\&\varphi\in\left[0,\frac{2\pi}{n_{holes}}\right].\end{aligned} \tag{12}$$

As the oil feed holes are uniformly distributed around the bearing circumference, using their symmetric arrangement, the range of values for attitude angle φ to consider in the database generation will reduce from $[0,2\pi]$ to $\left[0,\frac{2\pi}{n_{holes}}\right]$. A finite number of values p for ε, q for β, r for u and s for φ are considered within their finite range and using different combinations of their values, the Reynolds equation is solved for the dynamic pressure for pxqxrxs times. After applying the Gumbel boundary condition, the pressure is integrated to calculate the bearing forces in rotating coordinates using the following equation,

$$\begin{aligned}F_r&=\int_0^{2\pi}\int_0^L pcos(\theta)Rd\theta dz,\\F_t&=\int_0^{2\pi}\int_0^L psin(\theta)Rd\theta dz.\end{aligned} \tag{13}$$

The size of the database and computational time required for solving the Reynolds equation for pxqxrxs times increases if a finer resolution is used for the values of these four variables. The data calculated can be represented in the form of a four-dimensional database as shown in Figure 4. It is used for calculating bearing forces while solving the equations of motion using multivariate interpolation which only takes low computational effort.

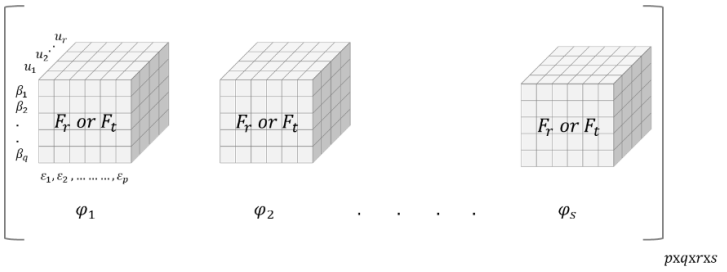

Figure 4: Database for forces of a bearing with oil feed holes

3 Results & Discussion

3.1 Case study: Turbocharger vibration behavior

A turbocharger rotor as shown in Figure 1 is considered in this section as a case study. This turbocharger rotor is supported on a semi-floating journal bearing. It consists of a circumferential groove on the outer oil film as shown in Figure 1 which constantly supplies oil to the inner oil film through feed holes at the supply pressure. The outer oil film is modelled as a squeeze film damper and it interacts with the inner oil film through bearing vibrations. The major dimensions of the system along with some important boundary and operation conditions are given in Table 1. The rotor is modelled using Timoshenko beam finite elements and the authors used MATLAB-based rotor

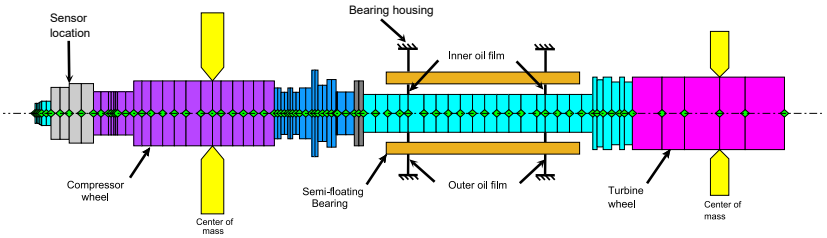

Figure 5: Finite element model of the turbocharger rotor supported on a semi-floating journal bearing

Table 1: Turbocharger rotor and journal bearing details

Variable	Value	Units
Rotor Mass	0.159	kg
Rotor length	0.124	m
Rotational speed (Ω)	up to 210000	rpm
Bearing:		
Inner film (L_i/D_i) ratio	0.54	
Inner film radial clearance (c_i)	12	µm
Outer film (L_o/D_o) ratio	0.56	
Outer film radial clearance (c_o)	40	µm
Number of oil holes (n_H)	4	
Oil hole radius (r_H)	0.7	mm
Oil type	SAE 0W20	
Oil supply pressure (P_{sup})	4	bar
Oil supply pressure (T_{sup})	100	$^\circ C$

software developed by Friswell et al. [16]. The beam element considers 4 degrees of freedom (DOF) per node which are transverse and rotational movements along the horizontal and vertical axis. The finite element method (FEM) model of this turbocharger along with the bearing is shown in Figure 5. The compressor and turbine inertia properties are lumped at their center of mass location. The rotor FEM model is connected to the bearing which in turn is connected to the bearing housing through oil films.

The pressure and temperature of oil entering the turbocharger system mainly depend on the engine speed, load, and operating temperatures. Higher oil pressure and lower temperature are possible when starting a cold engine, whereas higher temperature and low oil pressure are possible under hot engine idling conditions. The oil supply conditions impact turbocharger's rotordynamic behavior and subsequently its sub-synchronous vibration behavior can be different. Turbochargers are usually tested at all these extreme oil supply conditions on engines before undertaking their mass production. The test data of a turbocharger tested on an engine at specific oil supply conditions is used to validate simulation results in this paper. Simulations are performed for oil supply at $4\,bar$ at $100^\circ\,C$ without and with considering oil supply holes in the bearing modelling. These simulation results are compared to measurements in Figure 6 where vibrations measured at the shaft nut (refer to sensor location in Figure 5) location are processed to create the waterfall plots. Major loads in turbochargers are generated by the unbalances in the system and it is low in the current case as this turbocharger is balanced after assembling and used in the tests. The turbocharger is supplied oil continuously at $4\,bar$ at $100^\circ\,C$ and its speed changes with time. The oil film temperatures, oil viscosity and bearing clearances change with rotational speed due to the heat transfer from the turbine and housings, oil film shear in the inner oil films. All these parameters are used as input to the rotordynamics simulations which are either measured in the tests or obtained from advanced multi-physics simulations. The current paper discusses neither the methods used for determining them nor reports the values of these parameters explicitly as they are the proprietary information of the organization and also out of the scope of this paper. Otherwise, consistently same inputs are used in the simulations without and with oil feed holes which warrants the difference in the results of these cases solely due to the oil feed holes modelling in the bearing. The rotordynamics simulation results are usually non-dimensionalized and compared.

Two types of sub-synchronous vibrations are common in the case of semi-floating bearings due to the oil whirl in inner oil film [6]. The rotor becomes unstable at low rotational speeds due to oil whirl and reaches a stable limit cycle (first bifurcation) and the sub-synchronous vibrations (Sub1) excite conical vibration mode. The rotor further bifurcates at high rotational speeds where the first sub-synchronous vibrations become unstable and the second limit cycle arises. This second sub-synchronous vibration (Sub2) excites the cylindrical mode of the rotor. The

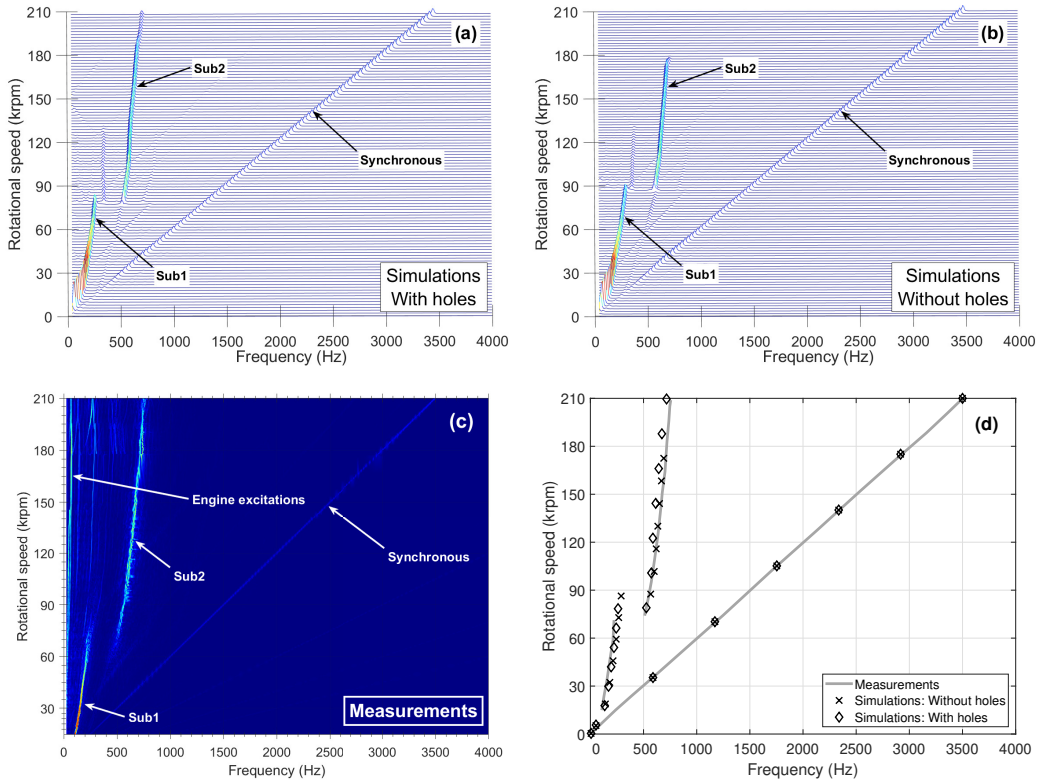

Figure 6: (a)-(c) Waterfall plots of the run-up vibration response at sensor location (d) comparison of rotor synchronous and sub-synchronous vibration components at $4\,bar$, $100^{\circ}\,C$ oil supply

vibration amplitudes of the rotor at these limit cycles will be moderate and generally do not interfere with their safe operation [6]. The combination of operating conditions like low unbalance, moderate oil viscosity ($100^{\circ}\,C$ oil supply), and higher oil pressure ($4\,bar$) induced dominant (compared to synchronous vibrations) sub-synchronous vibrations like Sub1 and Sub2 in the test results in Figure 6. The Sub2 vibrations are under-predicted by the plain bearing model and they exist until 172000 rpm only in contrast to the oil feed holes model which predicts Sub2 until maximum speed similar to the test results. The rotational speeds at which the Sub1 and Sub2 vibrations exist in the waterfall plots depend on the oil supply conditions and the resultant temperatures in the oil films. In addition to these sub-synchronous vibrations, synchronous vibrations due to the residual unbalance in the system and additional vibrations at speeds corresponding to engine orders are also visible in the measurement results. Only the frequency representation of vibrations is used for comparison with test measurements in the current work. It is possible to compare the vibration amplitudes vs. rotational speed by filtering engine vibrations from test measurements but they are excluded here for brevity.

Other performance variables like the bearing load capacity, forces transmitted to housing, and power losses are difficult to measure in the tests on an engine. But they can be calculated using rotordynamics simulations. However, their accuracy depends on the maturity of the simulation models and the preciseness of inputs used. The journal eccentricities, bearing forces, and power loss calculated for the compressor and turbine side journal bearings using the bearing models without and with oil feed holes are compared in Figure 7. They are normalized with maximum values obtained in the simulations. The bearing inner oil film forces with oil feed holes modelled increases by an average of around 24% in the mid-high turbo speed range. Other variables shown in that figure are increasing in the same speed range as follows. The inner oil film eccentricity increases by an average of around 24%. This indicates a drop in the load capacity of the bearing when oil feed holes are modelled. Dynamic forces generated due to the fluid pressure in the outer oil film are transferred to the bearing housing which is generally radiated as the noise at the corresponding vibration frequencies. These forces are predicted to be higher by an average of around 32% with oil feed holes modelling. The power loss due to lubrication shear in the inner oil film is also calculated to be higher with the oil feed holes modelling. This is mainly due to the increase in eccentricity and also due to the increase in area around the bearing surface that generates positive dynamic pressure when the oil supply pressure boundary condition is considered at feed holes. As a result, power loss increased by an average of around 32%

at 4 bar, 100° C oil supply. The power loss calculation will not be accurate with the Gumbel boundary condition [14, 15]. It needs to be verified if the relative difference may still be true when the cavitation boundary condition is implemented into the database generation. All these comparisons show the improvement in results with more detailed bearing models used in the simulations. The difference in the results without and with oil feed holes is not significant for the balanced rotor used in the tests. This may change for other unbalance situations in the hardware as rotor unbalance changes over time during the operation.

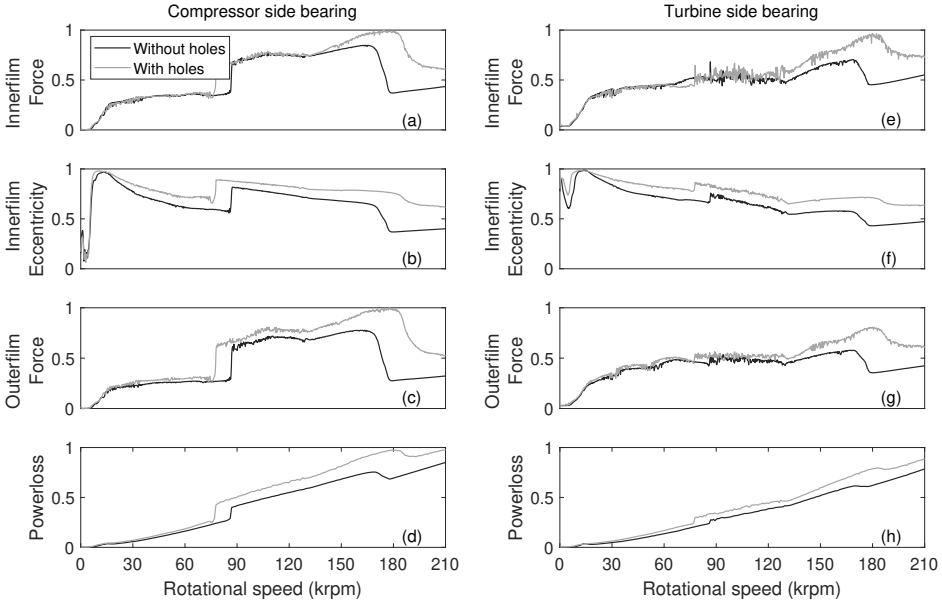

Figure 7: Comparison of innerfilm forces, eccentricity, outerfilm forces, powerloss (a)-(d) compressor side bearing (e)-(h) turbine side bearing between without and with oil feed holes at 4 bar, 100° C oil supply

The accuracy of the database approach depends on the number of values considered for the four independent variables (refer to Equation 12) in the Reynolds equation. In the current work, the following values are used for generating the database, $p = 60, q = 60, r = 60$ and $s = 11$. It took around 14 hours on an ordinary workstation to generate the database. The run-up simulations using the database approach took nearly 30 hours and it varies with the convergence of MATLAB ODE solver for different operating and boundary conditions. It might take several days if the Reynolds equation needs to be solved along with the equations of motion solution. Simulations with the database approach take at least $3-4$ times higher time than with the short bearing theory. The bearing forces calculated using the state variables from the run-up response of the turbocharger rotor and following the database approach are compared in Figure 8 with the direct solution of the Reynolds equation solved using the MATLAB PDE toolbox. The average error in bearing forces calculation with the database approach is close to 6% for the compressor side bearing and 8% for the turbine side bearing. The extension proposed to the database approach is limited to semi-floating bearings, as an additional Dirichlet boundary condition for centrifugal pressure at oil feed holes has to be considered for full-floating bearings due to their rotational speed.

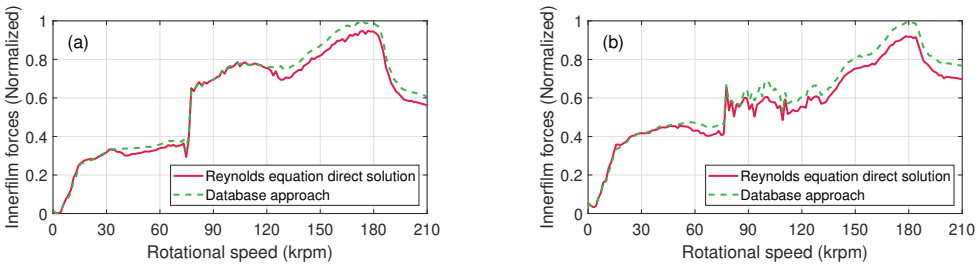

Figure 8: Comparison of inner film force calculation of bearing with oil feed holes: direction solution vs. database approach (a) compressor side bearing (b) turbine side bearingg

3.2 Influence of the number of holes on turbocharger rotordynamic behavior

The feed holes are essential to supply sufficient oil into the bearings to avoid starvation and control temperature rise due to the fluid shear in the oil films. The semi-floating bearing used in the turbocharger case study consists of 4 feed holes. It is unknown if the number of feed holes in that design is optimum or not. Further investigations with 2 and 6 holes in the bearing are carried out here to assess the influence of a number of feed holes on turbocharger rotordynamic behavior. Oil flow to the bearing will be lower with 2 holes and high with 6 holes in the bearing. As a result, inner oil film temperatures decrease with an increasing number of oil holes. It is assumed that sufficient oil is supplied to the inner film of the bearing independent of the number of oil holes for the sake of comparing rotordynamics behavior entirely. The waterfall plots of the vibrations simulated at the sensor location with 2, 4, and 6 holes are compared in Figure 9. The results show relatively lower sub-synchronous vibrations when the oil feed holes in the bearing are minimum. The Sub2 vibrations are confined up to 185 krpm when there are only 2 holes considered in the bearing (refer to Table 2). The Sub1 vibrations are extended until 121 krpm in the case of 6 oil feed holes. The bearing outer film forces are also compared in Figure 10. They are respectively normalized with the maximum value calculated in the case of 4 holes which is considered as a reference. The outer film forces are low in the case of 2 oil feed holes and high in the case of 6 oil feed holes in the bearing. Lower sub-synchronous vibrations and low-bearing outer film forces are respectively positive indicators for better load capacity and lower noise emissions from the system. Thus the consideration of 2 oil feed holes in the bearing is optimum if enough oil flow into the inner film of the bearing can be ensured. It can be either checked with computational fluid dynamics simulations or tested on a gas stand or engine test cell. The case study discussed in this work brings forward additional features like the number of feed holes and their diameter into the bearing design studies to optimize their performance.

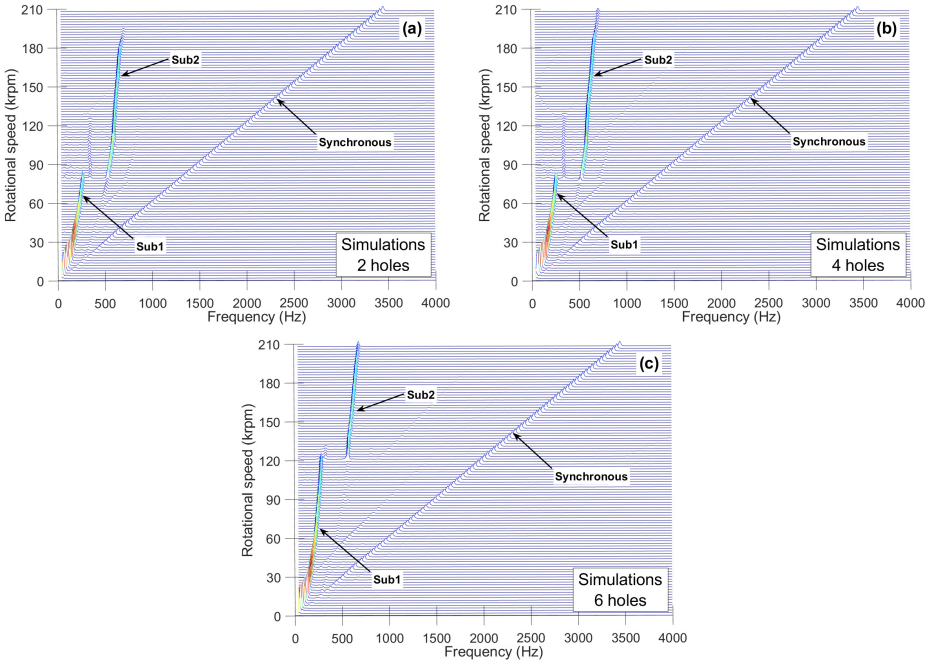

Figure 9: Influence of the number of feed holes on the run-up vibration response (simulations) at sensor location for 4 bar, 100° C oil supply

4 Summary & Conclusions

A database approach for the calculation of forces of journal bearings considering oil feed holes is successfully demonstrated in this work and it is useful for efficiently solving the equations of motion of high-speed machinery. The vibration behavior of an automobile engine turbocharger rotor supported on a semi-floating journal bearing is also investigated in this study. Simulation results without and with oil feed holes in the bearing model are compared to measured results at 4 bar, 100° C oil supply. The bearing model with oil feed holes better predicted Sub2 similar to the test results. The impact of oil feed holes modelling is not immense on the shaft motion behavior for the balanced rotor case used in this study. But it improved the prediction of other bearing performance variables such as load capacity and transmitted forces. It is hardly possible to measure them in the tests on an engine. So, accurate prediction using better models allows us to choose an optimum design and can substitute tests required for the qualification of bearing systems for new turbocharger applications. The bearing with the least number of feed holes

possible is found to be a good design choice for the turbocharger rotor investigated in this study. The influence of feed holes can be predominant at other operating or boundary conditions and nonetheless, their modelling offers an additional dimension to the bearing design studies to improve their performance.

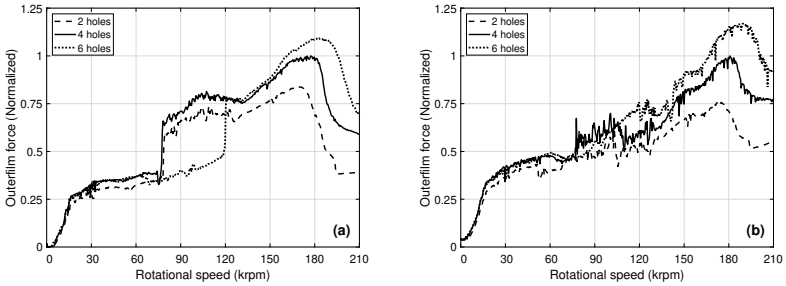

Figure 10: Comparison of bearing outer film forces with 2, 4, and 6 holes (a) compressor side bearing, (b) turbine side bearing

Table 2: Variation in the extent of sub-synchronous frequencies with number of oil feed holes

Sub-synchronous vibrations		Rotational speed		
		2 holes	4 holes	6 holes
Sub1	Start	0	0	0
	End	77 krpm	77 krpm	121 krpm
Sub2	Start	77 krpm	77 krpm	121 krpm
	End	185 krpm	210 krpm	210 krpm

References

[1] D. Zeppei, S. Koch, A. Rohi, Ball bearing technology for passenger car turbochargers, MTZ worldwide 77 (11) (2016) 26–31.

[2] H. Nguyen-Schäfer, Rotordynamics of automotive turbochargers, Springer, 2015.

[3] L. San Andres, A. Maruyama, K. Gjika, S. Xia, Turbocharger nonlinear response with engine-induced excitations: predictions and test data, Journal of engineering for gas turbines and power 132 (3) (2010) 032502.

[4] L. San Andrés, V. Barbarie, A. Bhattacharya, K. Gjika, On the effect of thermal energy transport to the performance of (semi) floating ring bearing systems for automotive turbochargers, Journal of engineering for gas turbines and power 134 (10) (2012) 102507.

[5] X. Robin, N. Driot, Investigation of turbocharger structure borne noise using multi-disciplinary strategy, Aachen Acoustic Colloquium, 2013.

[6] B. Schweizer, Total instability of turbocharger rotors—physical explanation of the dynamic failure of rotors with full-floating ring bearings, Journal of sound and vibration 328 (1-2) (2009) 156–190.

[7] Y. Hori, Hydrodynamic lubrication, Springer Science & Business Media, 2006.

[8] F. Thiery, S. Gantasala, J.-O. Aidanpää, Numerical evaluation of multilobe bearings using the spectral method, Advances in Mechanical Engineering 9 (7) (2017) 1687814017707135.

[9] Z. Chen, Y. Jiao, S. Xia, W. Huang, Z. Zhang, An efficient calculation method of nonlinear fluid film forces in journal bearing, Tribology transactions 45 (3) (2002) 324–329.

[10] A. Chasalevris, J.-C. Louis, Evaluation of transient response of turbochargers and turbines using database method for the nonlinear forces of journal bearings, Lubricants 7 (9) (2019) 78.

[11] P. Novotny, J. Dlugoš, A. Prokop, K. Řehák, P. Raffai, Effective computational model for a solution of turbocharger rotor dynamics, Journal of Vibroengineering 19 (2) (2017) 724–736.

[12] C. Zhang, R. Men, H. He, W. Chen, Effects of circumferential and axial grooves on the nonlinear oscillations of the full floating ring bearing supported turbocharger rotor, Proceedings of the Institution of Mechanical Engineers, Part J: Journal of Engineering Tribology 233 (5) (2019) 741–757.

[13] I. The MathWorks, Partial Differential Equation Toolbox, Natick, Massachusetts, United State (2019). URL `https://de.mathworks.com/help/pde/`

[14] S. Alakhramsing, R. Van Ostayen, R. Eling, Thermo-hydrodynamic analysis of a plain journal bearing on the basis of a new mass conserving cavitation algorithm, Lubricants 3 (2) (2015) 256–280.

[15] I. Chatzisavvas, Efficient thermohydrodynamic radial and thrust bearing modeling for transient rotor simulations, Ph.D. thesis, Technische Universität Darmstadt (2018).

[16] M. I. Friswell, J. E. Penny, S. D. Garvey, A. W. Lees, Dynamics of rotating machines, Cambridge university press, 2010.

15th SIRM – European Conference on Rotordynamics,
Darmstadt, Germany, 22nd – 24th February 2023

Influence of the Lomakin effect on the performance of journal bearings and annular seals for steady-state and dynamic operation conditions

Robin M. Robrecht [1], **Peter F. Pelz** [2]

[1] Chair of Fluid Systems, Technische Universität Darmstadt, 64287 Darmstadt, Germany,
robin.robrecht@tu-darmstadt.de
[2] Chair of Fluid Systems, Technische Universität Darmstadt, 64287 Darmstadt, Germany,
peter.pelz@tu-darmstadt.de

Abstract

The Lomakin effect influences the rotordynamic characteristics not only of seals but also of journal bearings with axial flow. Recent findings have shown that the corresponding pressure loss coefficient is circumferentially distributed. If this distribution is supplied to hydrodynamic lubrication film models it can improve the predictions of load bearing capacity and attitude angle in steady-state cases. Thus, in the present paper a dynamic case was studied to investigate the influence of the circumferentially distributed loss coefficient on rotordynamic coefficients.

Three-dimensional CFD flow simulations in a rotating reference frame have been conducted to determine the loss coefficient distribution and to compute a set of linear rotordynamic coefficients. Additionally, two sets of computations have been conducted with the lubrication film model CAPM. For one computation a standard pressure loss formulation was used while the the other computation was supplied with the loss coefficient distribution determined by CFD. The results show generally a good agreement between the CFD and both CAPM results. Unfortunately, the model results determined with use of the loss coefficient distribution show no improvement compared to the standard formulation. However, a physically consistent and accurate treatment of the boundary conditions allows better analyses and improvements of other model aspects.

1 Introduction

Journal bearings and annular seals have considerable impact on the rotordynamics of hydraulic turbomachinery like centrifugal pumps. The pressure difference over a seal results in a significant axial flow additional to the circumferential Couette flow due to the shaft rotation. The same can be said for media-lubricated journal bearings which use the process medium as lubricant. In both cases the axial flow results in an entrance pressure loss which has significant influence on the load bearing capacity resp. stiffness of a bearing or seal. This is called the Lomakin effect [1, 2].

The Lomakin effect has to be accounted for by hydrodynamic lubrication film models which are needed for prediction of load or dynamic forces on the rotor. The corresponding pressure loss is usually modeled by means of Bernoulli's equation with a pressure loss coefficient as inlet boundary condition. Recently, it was found that the loss coefficient is not a constant but a circumferential distribution around the annulus [11]. If provided to lubrication film models, it can improve predictions of load bearing capacity, attitude angle and leakage flow for steady-state operation conditions.

In general, the established lubrication models can be divided into three types: Reynolds' equation, one-dimensional bulk flow models and two-dimensional bulk flow models. All three types have certain shortcomings which can result in unacceptable prediction uncertainty. Thus, the Clearance-Averaged Pressure Model (CAPM) has been developed [5, 7, 8, 10]. The CAPM is a general superordinate model for plain annuli and can reliably predict forces on the rotor including the Lomakin effect at laminar and turbulent flow.

In the present paper, the loss coefficient distribution is analyzed by means of quasi steady-state three-dimensional CFD simulations in a rotating reference frame for a dynamic case at turbulent flow. The entrance pressure loss distribution is determined and supplied to the CAPM as boundary condition. The influence on model prediction accuracy for rotordynamic coefficients of stiffness, damping and inertia is quantified and compared to the CFD results and results of the CAPM with standard boundary conditions.

Nomenclature

$\Delta\tilde{p}$	axial pressure difference across the bearing	$L \coloneqq \tilde{L}/\tilde{R}$	nondimensional bearing length
$\tilde{\bar{C}}_z$	average axial velocity equal to total axial volume flow divided by gap area	$Re \coloneqq \tilde{\Omega}\tilde{R}\tilde{\bar{h}}/\tilde{\nu}$	Reynolds number
		β	attitude angle
$\tilde{\bar{h}}$	mean gap height or fluid film thickness	$\vec{F} \coloneqq \frac{2\,\vec{\tilde{F}}}{\tilde{\varrho}\tilde{\Omega}^2\tilde{R}^4 L}$	nondimensional force vector
		$c_\varphi \coloneqq \tilde{c}_\varphi/(\tilde{\Omega}\tilde{R})$	nondimensional circumferential velocity component
$\tilde{\nu}$	fluid kinematic viscosity	$c_z \coloneqq \tilde{c}_z/\tilde{\bar{C}}_z$	nondimensional axial velocity component
$\tilde{\Omega}$	journal rotational speed		
$\tilde{\varrho}$	fluid density	F	nondimensional bearing load
$\tilde{L}$	bearing length	$h \coloneqq \tilde{h}/\tilde{\bar{h}}$	nondimensional gap height
$\tilde{R}$	journal radius	$p \coloneqq \frac{2\,\tilde{p}}{\tilde{\varrho}\tilde{\Omega}^2\tilde{R}^2}$	nondimensional pressure
$\tilde{r}, \varphi, \tilde{z}$	cylindrical coordinates	$r \coloneqq \tilde{r}/\tilde{R}$	nondimensional radial coordinate
$\tilde{s} \coloneqq \tilde{R} + \tilde{\bar{h}} - \tilde{r}$	channel coordinate	$s \coloneqq \tilde{s}/\tilde{h}$	nondimensional channel coordinate
$\tilde{x}, \tilde{y}, \tilde{z}$	Cartesian coordinates		
γ	tilt angle for journal misalignment	$z \coloneqq \tilde{z}/\tilde{L}$	nondimensional axial coordinate
$\omega \coloneqq \tilde{\omega}/\tilde{\Omega}$	orbit frequency ratio	$M;\, m$	nondimensional inertia coefficients
$\phi \coloneqq \tilde{\bar{C}}_z/(\tilde{\Omega}\tilde{R})$	flow number	$C;\, c$	nondimensional damping coefficients
$\psi \coloneqq \tilde{\bar{h}}/\tilde{R}$	relative gap height		
$\varepsilon \coloneqq \tilde{\varepsilon}/\tilde{\bar{h}}$	relative eccentricity	$K;\, k$	nondimensional stiffness coefficients
ζ	pressure loss coefficient		

2 Clearance-Averaged Pressure Model

The Clearance-Averaged Pressure Model (CAPM) is a general lubrication film model and solver for incompressible flow in full circular bearings or annular seals. It was first derived and implemented by Lang [7] and since then was improved, verified and validated by Robrecht et al. [10], Robrecht and Pelz [11], Kuhr, Lang and Pelz [5], Kuhr, Nordmann and Pelz [6].

The model geometry of a generic annular gap of a bearing or seal is depicted in figure 1. Throughout the paper, variables with tilde denote dimensional quantities and the corresponding variables without tilde the dimensionless quantities. The rotor has the radius $\tilde{R}$, rotational speed $\tilde{\Omega}$ and can be dislocated with the eccentricity $\tilde{\varepsilon}$ and misaligned with the tilt angle γ. It performs an orbital motion with rotational frequency $\tilde{\omega}$ around the stator centerline. The stator has the length $\tilde{L}$ and radius $\tilde{R} + \tilde{\bar{h}}$ where $\tilde{\bar{h}}$ is the mean gap height. The gap with variable gap height $\tilde{h}$ is filled with fluid of kinematic viscosity $\tilde{\nu}$ and density $\tilde{\varrho}$. The total volume flow though the annular gap due to an axial pressure difference $\Delta\tilde{p}$ is characterized by the mean axial velocity $\tilde{\bar{C}}_z$. The fluid enters the gap with a circumferential velocity which can vary due to "preswirl". The only fundamental assumption of the CAPM is $\tilde{\bar{h}} \ll \tilde{R}$ (or $\psi \ll 1$) which is easily fulfilled for journal bearings and annular seals. This assumption leads to a negligible pressure gradient over the gap height where the name CAPM stems from.

The CAPM is based on a cylindrical coordinate system $(\tilde{r}, \varphi, \tilde{z})$ in a rotating reference frame with the same rotational speed $\tilde{\omega}$ as the orbit motion. Thus, the absolute velocity $\vec{\tilde{c}}$ is given with

$$\vec{\tilde{c}} \approx \vec{\tilde{w}} + \tilde{\omega}\tilde{R}\,\vec{e}_\varphi \,. \tag{1}$$

The rotating coordinate system eliminates the time dependency caused by the orbital rotor motion. Furthermore we assume incompressible flow as well as constant material properties of the Newtonian fluid and exclude cavitation and wear effects from our considerations. Additionally, we define the channel coordinate $\tilde{s} \coloneqq \tilde{R} + \tilde{\bar{h}} - \tilde{r}$ so that $\vec{e}_s = -\vec{e}_r$. From here on we will only use nondimensional variables (without tilde) whose definitions can be found in the nomenclature.

The considered control volume for the model extends over the complete gap height and infinitesimal segments in axial and circumferential direction. Due to $\psi \ll 1$, the pressure gradient $\partial p/\partial s \approx 0$ is negligible, cf. [12, 13].

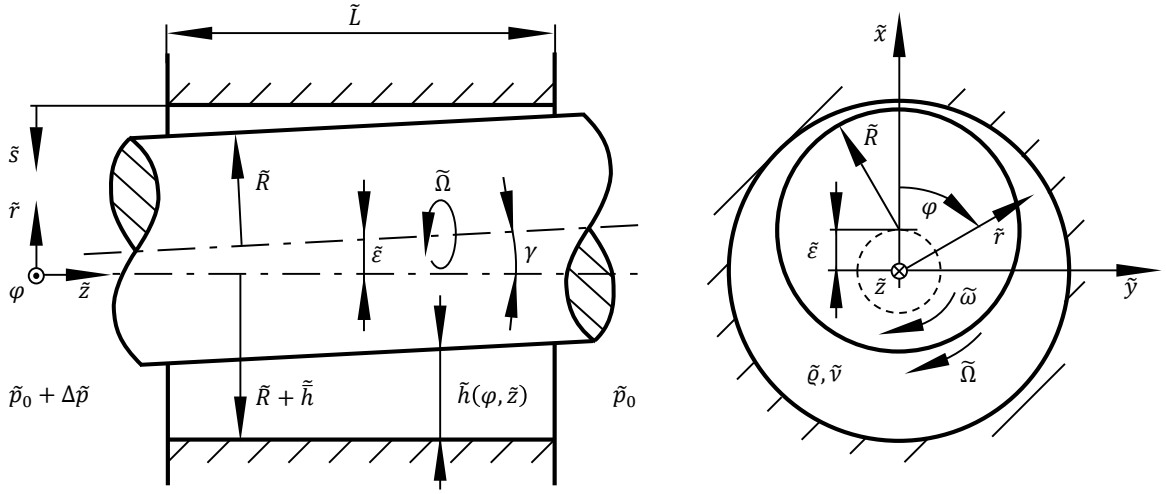

Figure 1: Model of an annular gap for the CAPM.

The function of gap height is defined as

$$h(\varphi, z) = 1 - (\varepsilon + \varepsilon_\gamma) \cos\varphi \tag{2}$$

with the additional eccentricity ε_γ caused by misalignment with tilt angle γ. Throughout this study, we assume $\gamma = \varepsilon_\gamma = 0$. On this basis, the governing equations of the CAPM are given by Lang [7]. The nondimensional continuity equation, the circumferential and axial momentum equations for steady-state flow in this control volume read

$$\frac{\partial}{\partial\varphi}\left(h\int_0^1 w_\varphi \,\mathrm{d}s\right) + \frac{\phi}{L}\frac{\partial}{\partial z}\left(h\int_0^1 c_z \,\mathrm{d}s\right) = 0\,, \tag{3}$$

$$\frac{\partial}{\partial\varphi}\left(h\int_0^1 w_\varphi^2 \,\mathrm{d}s\right) + \frac{\phi}{L}\frac{\partial}{\partial z}\left(h\int_0^1 w_\varphi\, c_z \,\mathrm{d}s\right) = -\frac{h}{2}\frac{\partial p}{\partial\varphi} + \frac{1}{2\,\psi}\,\tau_{s\varphi}|_0^1 \text{ and} \tag{4}$$

$$\phi\frac{\partial}{\partial\varphi}\left(h\int_0^1 w_\varphi\, c_z \,\mathrm{d}s\right) + \frac{\phi^2}{L}\frac{\partial}{\partial z}\left(h\int_0^1 c_z^2 \,\mathrm{d}s\right) = -\frac{h}{2L}\frac{\partial p}{\partial z} + \frac{1}{2\,\psi}\,\tau_{sz}|_0^1\,. \tag{5}$$

The terms of the remaining fluid shear stresses and the Coriolis force can be neglected as result of an analysis of order of magnitude [7].

To close the equation system (3) to (5), ansatz functions for the velocity profiles $w_\varphi(s, \varphi, z)$ and $c_z(s, \varphi, z)$ have to be defined so that the integrals over s can be evaluated. The ansatz functions are of the form $c(s, \varphi, z) = \mathrm{fn}(s,\, c^*)$ where $c^*(\varphi, z)$ is a characteristic flux variable like gap mean velocity, center-line velocity or specific volume flow.

For laminar flow, the profiles can be given as

$$w_\varphi(s, \varphi, z) = \left(-6\frac{\dot{V}_\varphi}{h} - 6\,\omega + 3\right)s^2 + \left(6\frac{\dot{V}_\varphi}{h} + 6\,\omega - 2\right)s - \omega \text{ and} \tag{6}$$

$$c_z(s, \varphi, z) = \frac{6}{\phi}\frac{\dot{V}_z}{h}\left(-s^2 + s\right)\,. \tag{7}$$

with the specific volume flows $\dot{V}_\varphi(\varphi, z)$ and $\dot{V}_z(\varphi, z)$ as characteristic flux variables [11]. For turbulent flow at

moderate Reynolds numbers the profiles can be stated with power law ansatz functions

$$w_\varphi(s,\varphi,z) = \begin{cases} (W_\varphi + \omega)\,(2s)^{1/n_\varphi} - \omega\,, & 0 \le s \le 0.5 \\ (W_\varphi + \omega - 1)\,(2-2s)^{1/n_\varphi} - \omega + 1\,, & 0.5 < s \le 1 \end{cases} \tag{8}$$

$$c_z(s,\varphi,z) = \begin{cases} C_z\,(2s)^{1/n_z}\,, & 0 \le s \le 0.5 \\ C_z\,(2-2s)^{1/n_z}\,, & 0.5 < s \le 1 \end{cases} \tag{9}$$

with the center line velocities $W_\varphi(\varphi,z)$ and $C_z(\varphi,z)$ as characteristic flux variables and the empirical exponents n_φ and n_z [7]. For typical bulk flow models at high Reynolds numbers, the ansatz function is simply constant 1 and the gap mean velocities $\bar{w}_\varphi(\varphi,z)$ and $\bar{c}_z(\varphi,z)$ are the characteristic flux variables:

$$w_\varphi(\varphi,z) = \bar{w}_\varphi \text{ and} \tag{10}$$

$$c_z(\varphi,z) = \bar{c}_z\,. \tag{11}$$

Furthermore, the wall shear stress terms $\tau_{s\varphi}|_0^1(\varphi,z)$ and $\tau_{sz}|_0^1(\varphi,z)$ in eqs. (4) and (5) have to be given as function of the same characteristic variables. For turbulent flow the well known model by Hirs [3] is used which is common for bulk flow models, too. For laminar flow the gradients of the velocity profiles can be used to calculate the analytical expressions.

The independent variables φ and z then are discretized in a finite differencing scheme and the system of coupled nonlinear partial differential equations is solved by means of a SIMPLEC algorithm [14]. The results are the pressure field $p(\varphi,z)$ and the two fields of the characteristic variables over φ and z. The solution will also give the flow number with prescribed pressure difference or vice versa.

It is possible to compute the three components of each of the resulting force and torque vector on the rotor. For this we make use of an additional Cartesian coordinate system $(\tilde{x},\tilde{y},\tilde{z})$ which rotates with $\tilde{\omega}$ as well, see figure 1. Thus, the $\tilde{x}$-coordinate always is directed in the direction of eccentricity. The force components of most interest are the lateral ones which are given with

$$F_x = \int_0^1 \int_0^{2\pi} -p\,\cos\varphi\cos\gamma\,\mathrm{d}\varphi\,\mathrm{d}z \text{ and} \tag{12}$$

$$F_y = \int_0^1 \int_0^{2\pi} -p\,\sin\varphi\cos\gamma\,\mathrm{d}\varphi\,\mathrm{d}z\,. \tag{13}$$

Furthermore, we define a resulting force (bearing load) as magnitude of the planar force vector with

$$F = \sqrt{F_x^2 + F_y^2}\,. \tag{14}$$

similar to a Sommerfeld number. The bearing attitude angle can be calculated with

$$\beta = \arctan\left|F_y\,/F_x\right|\,. \tag{15}$$

Finally, the linear rotordynamic coefficients in an inertial frame of reference $(\tilde{x}',\tilde{y}',\tilde{z}')$ in the form of

$$-\begin{bmatrix} F_x' \\ F_y' \end{bmatrix} = \begin{bmatrix} M & m \\ -m & M \end{bmatrix} \begin{bmatrix} \ddot{x}' \\ \ddot{y}' \end{bmatrix} + \begin{bmatrix} C & c \\ -c & C \end{bmatrix} \begin{bmatrix} \dot{x}' \\ \dot{y}' \end{bmatrix} + \begin{bmatrix} K & k \\ -k & K \end{bmatrix} \begin{bmatrix} x' \\ y' \end{bmatrix} \tag{16}$$

are readily obtained in the rotating frame at different orbit frequencies ω at a constant (small) eccentricity ε for small rotor motion about the concentric position [2, 7]. Transformation of equation (16) into the rotating reference frame with the orbit motion yields the corresponding equations

$$F_x/\varepsilon = \;\; M\,\omega^2 - c\;\omega - K \text{ and} \tag{17}$$

$$F_y/\varepsilon = -m\,\omega^2 - C\,\omega + k \tag{18}$$

which are used for parameter identification. The nondimensional definitions of the rotordynamic coefficients are

$$\{M;\, m\} \coloneqq 2\frac{\psi}{L}\frac{\{\tilde{M};\, \tilde{m}\}}{\tilde{\varrho}\tilde{R}^3}\,, \tag{19}$$

$$\{C;\, c\} \coloneqq 2\frac{\psi}{L}\frac{\{\tilde{C};\, \tilde{c}\}}{\tilde{\varrho}\tilde{R}^3\tilde{\Omega}} \text{ and} \tag{20}$$

$$\{K;\, k\} \coloneqq 2\frac{\psi}{L}\frac{\{\tilde{K};\, \tilde{k}\}}{\tilde{\varrho}\tilde{R}^3\tilde{\Omega}^2}\,. \tag{21}$$

3 Lomakin effect and boundary conditions

When an axial flow component is present, the entrance of an annulus represents a sudden contraction of the flow cross section which leads to a flow separation at the entrance edge due to fluid inertia. The resulting separation bubble is a further reduction of the flow cross section after which it expands again. This results in a pressure loss of Carnot type. Due to the higher velocity in the wider part of the eccentric gap there will be a greater pressure loss. This is shown exemplary in the left of figure 2. The right diagram shows the circumferential pressure distribution at the gap entrance. The resulting pressure field in the fluid film will exert a centering force on the rotor and will increase the bearing stiffness. This effect was first described by Lomakin [9] and is well known in the application of annular seals [1, 2]. Nonetheless, the effect also occurs in journal bearings when an axial flow component is present, even at laminar flow conditions [11].

The Lomakin effect can be modeled by means of Bernoulli's equation from the inlet plenum to the gap entrance with a pressure loss term. Usually, the pressure loss coefficient is assumed to be a constant but it was shown that it is circumferentially distributed [11]. Furthermore, typically the orbit motion is neglected due to the assumption of very small amplitudes. Here, we want to derive a physically consistent formulation considering the rotating reference frame due to the orbit motion.

Assuming steady-state flow in the rotating reference frame and a plenum with approximately constant total pressure before the entrance of the annular gap, Bernoulli's equation along a streamline from the plenum to a point directly at the gap inlet is given by

$$\left(\bar{C}_{\varphi,\,\mathrm{plenum}} - \omega\right)^2 + \Delta p = p(\varphi) + \left[1 + \zeta(\varphi)\right]\left[\bar{w}_\varphi^2(\varphi) + \phi^2\,\bar{c}_z^2(\varphi)\right] \tag{22}$$

with the pressure difference over the annular gap $\Delta p \approx \mathrm{const.}$, the volume averaged plenum circumferential velocity $\bar{C}_{\varphi,\,\mathrm{plenum}} \approx \mathrm{const.}$, the gap height averaged velocity components $\bar{w}_\varphi$ and $\bar{c}_z$ at the gap entrance, cf. [11].

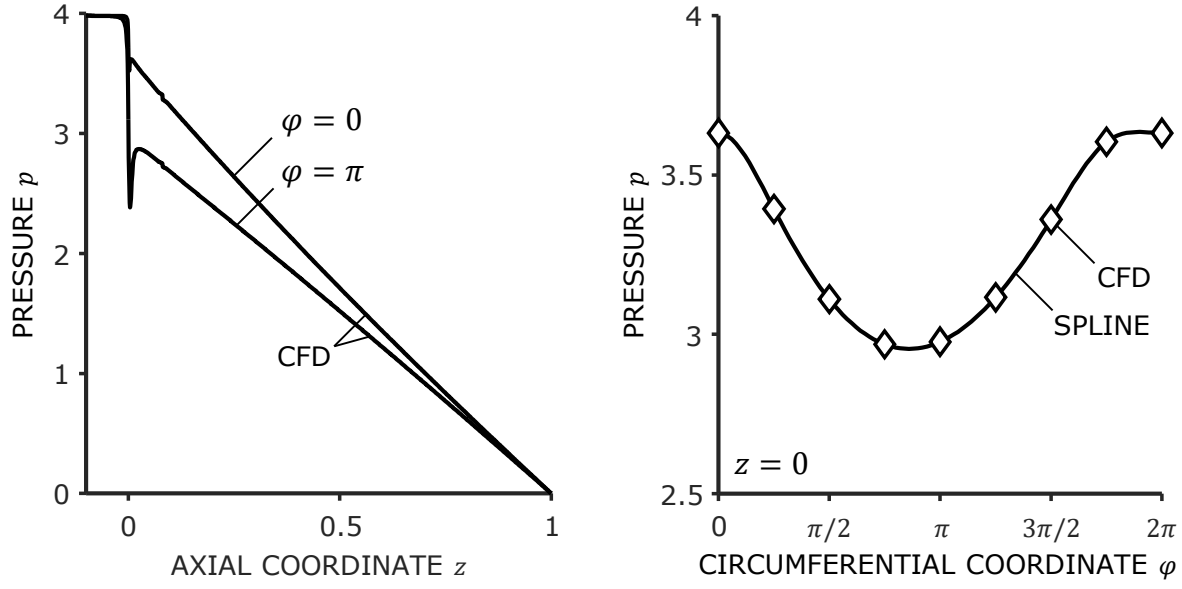

Figure 2: Axial and circumferential pressure distribution due to the Lomakin effect (study case $\omega = 0$).

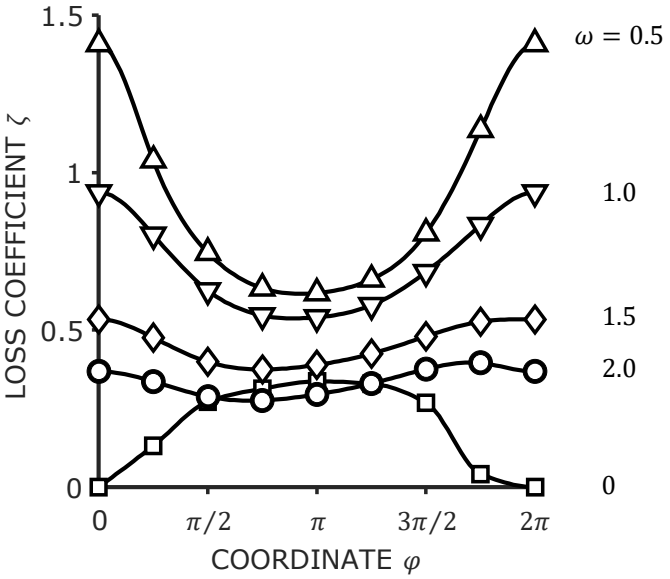

Figure 3: Circumferential distribution of the entrance pressure loss coefficient for the five different orbit rotational frequencies determined by CFD.

The empirical pressure loss coefficient is defined as

$$\zeta := \frac{2\,\Delta\tilde{p}_{\mathrm{loss}}}{\tilde{\varrho}\,|\vec{\tilde{w}}|^2}\,. \tag{23}$$

The plenum circumferential velocity is usually small (cf. table 2) and can be neglected for actual plenum type inlets. For other inlet geometries it could vary which is usually called "preswirl". This might also affect $\bar{w}_\varphi(\varphi)$ at the gap entrance which is typically unknown. Furthermore, the loss coefficient can be a function of the circumferential coordinate and in general can be dependent on all model parameters, cf. [10, 11]:

$$\zeta = \zeta\left(\varphi, \varepsilon, \gamma, \omega, Re, \phi, \psi, L\right)\,. \tag{24}$$

With a known distribution of $\zeta(\varphi)$ for a given parameter set the average value is calculated with

$$\bar{\zeta} := \frac{1}{2\pi}\int_0^{2\pi} \zeta(\varphi)\,\mathrm{d}\varphi\,. \tag{25}$$

Bernoulli's equation (22) is needed as boundary condition for integro-differential models like the CAPM to consider the Lomakin effect. The numerical solution of the governing equations (3) to (5) of the CAPM requires boundary conditions for all three dependent variables c^*_φ, c^*_z and p. Equation (22) at the inlet ($z = 0$) is a nonlinear boundary condition coupling the pressure and the velocity. While the axial velocity component is governed by the prescribed pressure difference resp. the flow number, an additional condition for the circumferential velocity at the gap entrance is needed. In the gap the boundary layers will be fully developed after a short length and the gap averaged circumferential velocity will adjust to an average value of $\bar{c}_\varphi \approx 0.5$ which is a good general guiding value. However, the exact value can be influenced by "preswirl" which means the circumferential velocity in the plenum before the gap.

The boundaries at $\varphi = 0$ and $\varphi = 2\,\pi$ are treated with a periodicity condition. At the outlet ($z = 1$) the boundary conditions are more simple. It is reasonable to assume the outlet to be of a plenum type, too. Thus, the pressure at the gap outlet without loss of generality is $p = p_0 = 0$.

4 Results

To investigate the influence of the Lomakin effect and the circumferential distribution of the entrance pressure loss coefficient, a numerical study by means of three-dimensional CFD simulations has been conducted. The

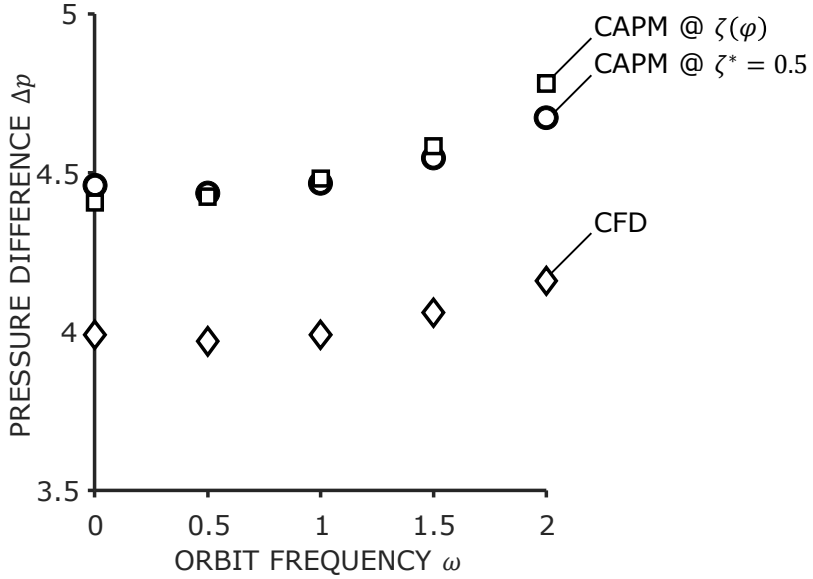

Figure 4: Pressure differences over orbit frequency.

numerical setup is very similar to the one described by Robrecht and Pelz [11] where an detailed description is given and a grid study has been performed. The main difference is that the simulations in the present paper are quasi steady-state in a rotating reference frame. This allows to consider a circular orbit motion of the rotor about the stator center axis similar to the method of the CAPM described in section 2.

The nondimensional parameters of the study are listed in table 1. It is a case of a media-lubricated journal bearing which is represented by a moderate Reynolds number and significant flow number. The geometry and operation conditions have been chosen so that the results of the present study can be validated with published experimental data for rotordynamic coefficients published by Kuhr [4]. The value for the eccentricity ε has been chosen to be at the upper limit of the range of linearity of the rotordynamic coefficients. This has been done to show the maximum influence of the circumferential distribution of the entrance loss coefficient. The values of the orbit rotational frequency ω are typical arbitrary values used for parameter identification [2].

The results of the CFD simulations have been used to evaluate the circumferential distribution of the entrance pressure loss according to equation (22) with the method described by Robrecht and Pelz [11]. The method is to determine the mean values over the gap height of the pressure, circumferential and axial velocity component at the gap entrance. Due to the disturbance of the separation bubble (compare figure 2) the pressure needs to be extrapolated from the gap to the entrance region. This is done at eight discrete positions around the circumference. The discrete distribution is made continuous be means of a periodic interpolation spline.

The results are shown in figure 3. It can be seen that the loss coefficient is a pronounced function of the circumferential coordinate. The steady-state case $\omega = 0$ shows the typical form with the maximum around the widest part of the gap. At the narrowest part the coefficient is zero, which shows there is no flow separation. The case $\omega = 0.5$ shows the maximum values and a reversed form. This is caused by generally very small values of $\bar{w}_\varphi$ at $\omega = 0.5$ and the minimum of $\bar{c}_z$ at $\varphi = 0$. The curves at the other orbit frequencies are successively lower and more flat. The corresponding mean values $\bar{\zeta}$ are listed in table 2.

Moreover, the circumferential velocity in the plenum due to "preswirl" can be characterized by a volume averaged value

$$\bar{C}_{\varphi,\,\mathrm{plenum}} \coloneqq \frac{1}{V_{\mathrm{plenum}}} \iiint_{V_{\mathrm{plenum}}} c_\varphi \,\mathrm{d}V \,. \tag{26}$$

Table 1: Parameters of the CFD study.

Re	ϕ	L	ψ	ε	γ	ω
4000	0.7	1.3	0.0042	0.4	0	0; 0.5; 1; 1.5; 2

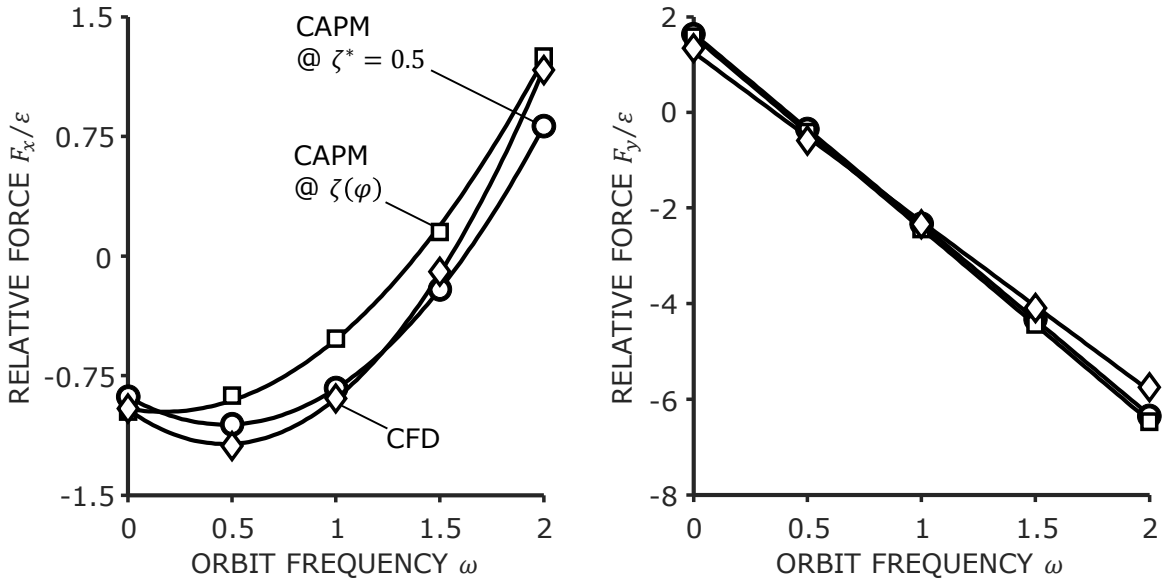

Figure 5: Relative forces over orbit frequency and polynomial fitting curves for parameter identification.

The value is somewhat arbitrary since it depends on the specific integration domain. Nonetheless, it can give an indication of the value of the gap entrance.

The CFD results show that the circumferential velocity at the gap entrance $\bar{c}_\varphi$ is only a weak function of the circumferential coordinate and in good approximation can be considered constant. The average value defined by

$$\bar{C}_{\varphi,\,0} \coloneqq \frac{1}{2\pi}\int_0^{2\pi} \bar{c}_\varphi(z=0)\,\mathrm{d}\varphi\,. \tag{27}$$

is used as velocity boundary condition at the gap inlet for the CAPM. The average values of the mean plenum circumferential velocity, the mean circumferential velocity at the gap entrance, the mean loss coefficient and the pressure difference of the five CFD simulations are listed in table 2.

For comparison, computations by means of the CAPM have been carried out. The first set of computations uses Bernoulli's equation (22) with the parameters of table 2 and the splines for $\zeta(\varphi)$ of figure 3. The other set uses the typical form of Bernoulli's equation (cf. [10]) without consideration of the rotating reference frame and a typical constant value of $\zeta^* = 0.5$.

Figure 4 shows the resulting pressure difference Δp across the bearing. The three sets of markers show the results of the CFD and the two CAPM computations as described above. The simulations show a very slight increase of pressure difference with increasing orbit frequency ω. Both CAPM computations give almost the same results which qualitatively agree very well with the simulation. Quantitatively, the CAPM predictions show an roughly constant offset of 0.5 over the whole orbit frequency range compared to the simulation results.

Figure 5 show the lateral forces F_x and F_y relative to the eccentricity ε over the orbit frequency ω. The markers represent the computation results and the curves represent the polynomial fitting curves according to equation (18) which are used for parameter identification. In x-direction the results of all three models are different and the CAPM results with $\zeta(\varphi)$ are generally too high. In y-direction the two sets of CAPM computations are almost the same and differ slightly from the simulation results.

Table 2: Results of the five CFD cases.

ω	$\bar{C}_{\varphi,\,\mathrm{plenum}}$	$\bar{C}_{\varphi,\,0}$	$\bar{\zeta}$	Δp
0	0.18	0.34	0.21	3.99
0.5	0.13	0.29	0.88	3.97
1.0	0.13	0.28	0.69	3.99
1.5	0.13	0.27	0.45	4.06
2.0	0.14	0.29	0.33	4.16

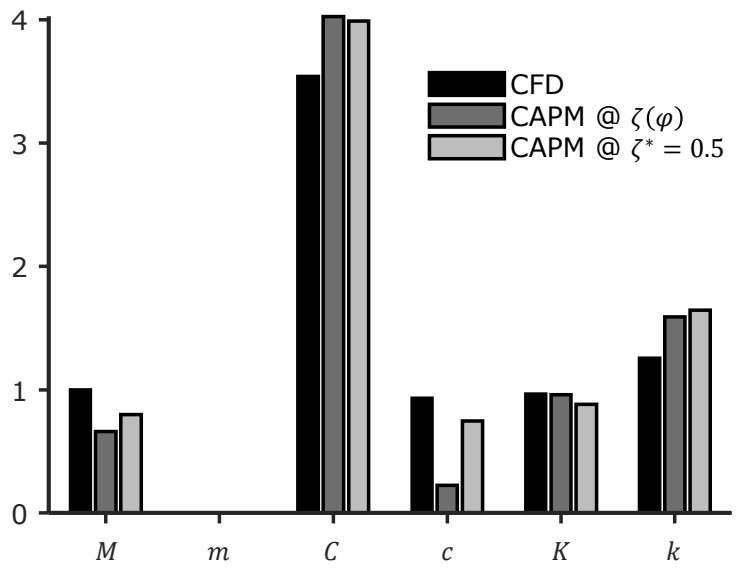

Figure 6: Rotordynamic coefficients of the three models.

The identified rotordynamic coefficients of the three models are shown in figure 6. In general, there is a good agreement between CFD and CAPM. The predictions for the direct inertia M are a little too low compared to the simulations (66 %, 80 %). The cross-coupled inertia is zero as usual. The model predictions for the direct damping C is a little to high (114 %, 113 %). The cross-coupled damping c is significantly too low for the CAPM results with $\zeta(\varphi)$ (24 %) and a little too low for the CAPM with constant ζ^* (80 %). The agreement for direct stiffness K is very good (100 %, 92 %). Finally, the predictions for the cross-coupled stiffness k are a little too high (127 %, 131 %). All values for the rotordynamic coefficients approximately agree with experimental values determined by Kuhr [4].

5 Conclusion

In the present study the Lomakin effect was revisited due to recent findings for laminar flow [11]. It was found that the corresponding entrance pressure loss coefficient is a circumferential distribution and can improve the prediction accuracy of lubrication film models for steady-state cases in journal bearings and annular seals. In the present study, a dynamic case at turbulent flow was investigated by means of CFD simulations and compared to the lubrication film model CAPM. The influence of the loss coefficient on the prediction accuracy of the CAPM for rotordynamic coefficients was analyzed.

The results confirm that the entrance pressure loss coefficient is a pronounced circumferential distribution for turbulent flow, too. The curves differ qualitatively and quantitatively for varying orbit frequencies. The curves were then supplied to the CAPM as inlet boundary condition. The results of the CFD, the CAPM with circumferentially distributed loss coefficient and the CAPM with the typical constant loss coefficient have been used to compute three sets of rotordynamic coefficients and have been compared.

The results show generally a good agreement between the CFD simulation and the CAPM. The circumferential distribution can only provide a marginal improvement to the prediction of direct and cross-coupled stiffness. However, the prediction of direct inertia is slightly worse and cross-coupled damping is significantly worse. Nonetheless, the physically consistent and accurate description of the boundary conditions allows to distinguish different physical effects in the context of the whole model and can help to improve other corresponding aspects, e.g. the shear stress model for dynamic cases.

References

[1] Brennen, C. E. [1994]. *Hydrodynamics of pumps*, Oxford science publications, Concepts ETI, Norwich, Vt.

[2] Childs, D. W. [1993]. *Turbomachinery rotordynamics: Phenomena, modeling, and analysis*, Wiley, New York.

[3] Hirs, G. G. [1973]. A bulk-flow theory for turbulence in lubricant films, *Journal of Lubrication Technology* **95**(2): 137.

[4] Kuhr, M. M. G. [2022]. *Dynamische Eigenschaften axial durchströmter Ringspalte*, Shaker Verlag, Darmstadt.
[5] Kuhr, M. M. G., Lang, S. R. and Pelz, P. F. [2022]. Static force characteristic of annular gaps – experimental and simulation results, *Journal of Tribology* **144**(11).
[6] Kuhr, M. M. G., Nordmann, R. and Pelz, P. F. [2022]. Dynamic force and moment characteristics of annular gaps - simulation results and evaluation of the relevance of the tilt and moment coefficients, *Journal of Tribology* pp. 1–42.
[7] Lang, S. [2018]. *Effiziente Berechnung von Gleitlagern und Dichtspalten in Turbomaschinen: Dissertation, Technische Universität Darmstadt, 2017*, Shaker Verlag, Aachen.
[8] Lang, S. and Pelz, P. F. [2016]. Unified prediction of hydrodynamic forces in plain annular seals and journal bearings by means of an analytically derived design tool, *Pump Users International Forum 2016*, Pumps + Systems Association within VDMA e.V, Frankfurt am Main.
[9] Lomakin, A. A. [1958]. Calculation of the critical speed and the conditions to ensure dynamic stability of the rotors in high pressure hydraulic machines, taking account of the forces in the seals (in russian), *Energomashinostroenie* **14**(4).
[10] Robrecht, R. M., Kuhr, M. G. M. and Pelz, P. F. [2019]. Capm vs. bulk flow - reliable and efficient prediction of forces and leakage for annular gaps in pumps, *Pump Users International Forum 2019*.
[11] Robrecht, R. M. and Pelz, P. F. [2022]. The lomakin effect at laminar flow in journal bearings – modeling and simulation, *Tribology International* **175**: 107792.
[12] Spurk, J. and Aksel, N. [2008]. *Fluid Mechanics*, 2nd ed. 2008 edn, Springer Berlin Heidelberg and Springer International Publishing AG, Berlin, Heidelberg and Cham.
[13] Szeri, A. Z. [2005]. *Fluid film lubrication: Theory and design*, Cambridge Univ. Press, Cambridge.
[14] van Doormaal, J. P. and Raithby, G. D. [1984]. Enhancements of the simple method for predicting incompressible fluid flows, *Numerical Heat Transfer* **7**(2): 147–163.

15th SIRM – European Conference on Rotordynamics,
Darmstadt, Germany, 22nd – 24th February 2023

Reynolds equation's dimension reduction using Galerkin method for journal bearings

Gantasala S.[1], **Baum C.** [2] **and Koutsovasilis P.**[3]

Dynamics Simulation & Methods, BorgWarner Systems Eng. GmbH, 67292 Kirchheimbolanden, Germany
[1] sgantasala@borgwarner.com, [2] cbaum@borgwarner.com, [3] pkoutsovasilis@borgwarner.com

Abstract

Dynamic simulations of rotor systems supported on journal bearings require a solution for the Reynolds equation at every time step. Such simulations for high-speed rotors can be time-consuming. A novel method is demonstrated in this paper where the pressure variation along the bearing length is represented by a basis function satisfying the boundary conditions at the bearing ends. The basis function can be a polynomial or an exponential function whose coefficients are functions of the bearing length (L) to diameter (D) ratio. The same basis function is used as a test function to reduce the dimension of the Reynolds equation to 1D using the Galerkin method. The reduced differential equation is solved using the pseudospectral method (PSM). The computational effort required for solving the reduced equation is on par with short/long bearing theories. Bearing forces and peak dynamic pressure generated within the bearings as predicted by this equation are compared with the solution of the two-dimensional Reynolds equation solved using the MATLAB PDE toolbox. In the end, the dynamic response of a turbocharger rotor supported on finite length full-floating journal bearings is simulated using this reduced equation and also compared with the results obtained using short bearing theory and 2D Reynolds equation solution for bearings. The approach demonstrated in this work can also be extended for pressure calculations in gas and thrust bearings.

1 Introduction

Journal bearings are commonly used in rotating machinery due to their longer life, low cost, and superior damping properties compared to any other types of bearings. Such bearings are susceptible to certain instabilities like oil whirl/whip, which often settle to a stable limit cycle. It is possible to limit the overall impact of these instabilities on rotor vibrations by choosing an appropriate bearing design. Mathematical modelling of the bearings and their coupling to the rotor model will allow predicting the rotor's vibration behavior. Such simulations need to be accurate and fast enough to carry out large bearing design studies considering bearing dimensions as design variables. The pressure generation inside journal bearings can be predicted by solving the Reynolds equation, a linear second order partial differential equation (PDE) derived with certain assumptions [1]. Several approaches like finite element method (FEM), finite difference method (FDM), spectral methods, finite volume method (FVM), etc. can be applied to solve the Reynolds equation [2]. Simplified models like long and short bearing approximations to the Reynolds equation are applicable to bearings if their length to diameter ratios are $L/D > 2$ and $L/D \leq 0.5$ respectively which will reduce the PDE to one dimension (1D) either in axial or circumferential coordinate. Hence, the less computational effort is required to solve the resultant 1D equation. But, bearing forces are inaccurate at higher eccentricities with these simple models. However, these approximations are not applicable for other L/D ratios. A correction factor was proposed to forces [3] or pressure [4] obtained from short bearing theory to extend its validity for bearing dimensions with L/D ratios up to 1.25. Many studies can be found in the literature where solutions are proposed for the two-dimensional Reynolds equation using various methods. Few of them are based on the approximate analytical methods [7, 6, 5], database method [8, 9, 11] and scaled boundary finite element method [10]. Recently, Baum et al. [12] applied Galerkin's method to reduce the dimension of the compressible Reynolds equation for efficiently calculating airfoil journal bearing forces. They have proposed an approach to determine an optimal base function for pressure variation along the bearing length from the 2D Reynolds equation solution. Later, they used it as a test function in Galerkin's method to eliminate the length coordinate resulting in a reduced equation in only the circumferential coordinate. Their approach is not described in detail and also the accuracy of the reduced equation is not discussed. The authors adopted their idea to derive a reduced equation for

journal bearing in the current work and proposed an approach to extend its validity for a wide range of L/D ratios. The accuracy of the reduced equation at various eccentricities and L/D ratios is compared with the solution of the Reynolds equation using MATLAB PDE toolbox [13]. In the end, the run-up vibration response of a turbocharger rotor supported on two full-floating bearings with $L/D = 1$ for their inner oil films is simulated using the Reynolds equation (both reduced and not reduced) and short bearing theory.

2 Mathematical modelling

The hydrodynamic pressure generated within journal bearings (refer to Figure 1) can be calculated using the Reynolds equation. For more details on its derivation and underlying assumptions refer to [1] and the equation is

$$\left(\frac{1}{R}\right)^2 \frac{\partial}{\partial\theta}\left(h^3\frac{\partial P}{\partial\theta}\right) + \frac{\partial}{\partial z}\left(h^3\frac{\partial P}{\partial z}\right) = 12\mu\left(\frac{\Omega}{2}\frac{\partial h}{\partial\theta} + \frac{\partial h}{\partial t}\right), \tag{1}$$

where P is the dynamic pressure generated in the bearing, h is the oil film thickness around the bearing circumference, μ is the oil viscosity, Ω is the angular velocity of the shaft, θ and z are the bearing circumferential and axial coordinates, $\frac{\partial}{\partial\theta}$, $\frac{\partial}{\partial z}$ and $\frac{\partial}{\partial t}$ refers to the spatial and temporal derivatives of a variable, and

$$\begin{aligned} h &= c + e\cos(\theta), \\ \frac{\partial h}{\partial\theta} &= -e\sin(\theta), \\ \frac{\partial h}{\partial t} &= \dot{e}\cos(\theta) + e\dot{\phi}\sin(\theta), \end{aligned} \tag{2}$$

where c is the bearing radial clearance, e is the eccentric position of the shaft center from the bearing center along the line of centers as shown in Figure 1, φ is the attitude angle, $\dot{e}$ and $\dot{\varphi}$ are the velocities of eccentricity and attitude angle.

The Reynolds equation given in Equation 1 can be transformed into the non-dimensional form as given below,

$$\frac{\partial}{\partial\theta}\left(H^3\frac{\partial\bar{P}}{\partial\theta}\right) + \frac{1}{4}\left(\frac{D}{L}\right)^2\frac{\partial}{\partial\bar{z}}\left(H^3\frac{\partial\bar{P}}{\partial\bar{z}}\right) = 12\left\{\dot{\varepsilon}\cos(\theta) + \varepsilon\left(\frac{\dot{\varphi}}{\Omega} - 0.5\right)\sin(\theta)\right\}, \tag{3}$$

where D is the bearing diameter, $\bar{P} = \frac{P}{\mu\Omega}\left(\frac{c}{R}\right)^2$ is the non-dimensional pressure, $H = 1 + \varepsilon\cos(\theta)$ is the non-dimensional film thickness with $\varepsilon = \frac{e}{c}$ and $\bar{z} = \frac{z}{L}$, $\dot{\varepsilon} = \frac{\dot{e}}{c\Omega}$.

2.1 Short bearing theory

Pressure variation along the bearing circumference is negligible in comparison to that along its length for $L/D \leq 0.5$. Thus the Reynolds equation given in Equation 3 is reduced to one dimension and can be integrated easily to get an analytical expression for the pressure. Typical boundary conditions for a journal bearing at the bearing ends are equal to atmospheric pressure as it is exposed to ambient conditions. The expression for fluid film pressure with short bearing approximation and after applying the boundary conditions is given in Equation 4,

$$\bar{P} = -\frac{24}{H^3}\left(\frac{L}{D}\right)^2\left\{\dot{\varepsilon}\cos(\theta) + \varepsilon\left(\frac{\dot{\phi}}{\Omega} - 0.5\right)\sin(\theta)\right\}\bar{z}(1-\bar{z}). \tag{4}$$

2.2 Galerkin method

The dynamic pressure generated within the journal bearing can be represented as a product of two independent functions as given in Equation 5,

$$\bar{P}(\theta,\bar{z},t) \approx \hat{\bar{P}}(\theta,\bar{z},t) = \bar{P}_\theta(\theta,t)\,\bar{P}_z(\bar{z}). \tag{5}$$

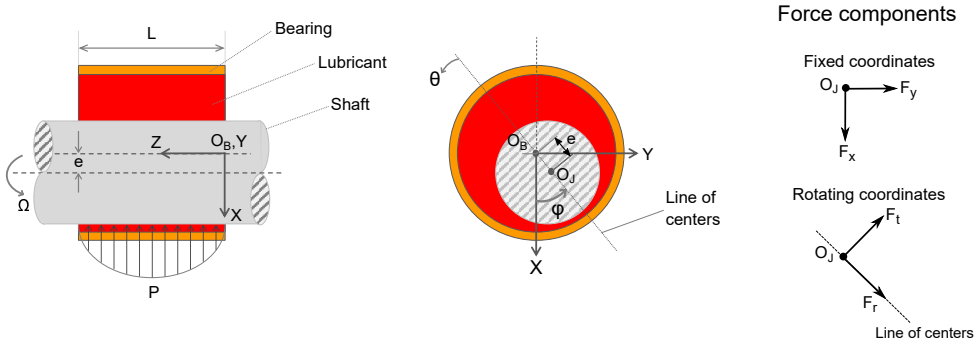

Figure 1: Details of a journal bearing

After comparing Equations 4 & 5, we can assume a polynomial function like $\bar{P}_z\left(\bar{z}\right) = 4\bar{z}(1-\bar{z})$ for pressure variation along the bearing length coordinate. Initially, the Reynolds equation reduction procedure is demonstrated using this polynomial function which is valid for bearings whose $L/D \leq 0.5$, and later the extension of this methodology is presented for other L/D ratios. The pressure function assumed in Equation 5 should satisfy the boundary conditions of the bearing and also when substituted in the Reynolds equation make the residual (refer to Equation 6) small, i.e.

$$\epsilon\left(\theta, \bar{z}, t\right) = \frac{\partial}{\partial\theta}\left(H^3\frac{\partial\hat{\bar{P}}}{\partial\theta}\right) + \frac{1}{4}\left(\frac{D}{L}\right)^2\frac{\partial}{\partial\bar{z}}\left(H^3\frac{\partial\hat{\bar{P}}}{\partial\bar{z}}\right) - f\left(\theta, \varepsilon_x, \varepsilon_y, \dot{\varepsilon}_x, \dot{\varepsilon}_y\right), \tag{6}$$

where right hand side of the Equation 3 is represented as $f\left(\theta, \varepsilon_x, \varepsilon_y, \dot{\varepsilon}_x, \dot{\varepsilon}_y\right)$.

The $\bar{P}_z\left(\bar{z}\right)$ function is also used as a weighing function and following the weighted residual method, the inner product of the residual with this function is made zero (performed for half bearing length) as given in Equation 7,

$$\int_0^{0.5} \epsilon\left(\theta, \bar{z}, t\right)\bar{P}_z\left(\bar{z}\right)d\bar{z} = 0. \tag{7}$$

The final equation after integration will be independent of the length coordinate $\bar{z}$ as given in Equation 8,

$$\frac{4}{5}\frac{\partial}{\partial\theta}\left(H^3\frac{\partial\bar{P}_\theta}{\partial\theta}\right) - 2\left(\frac{D}{L}\right)^2 H^3\bar{P}_\theta = f\left(\theta, \varepsilon_x, \varepsilon_y, \dot{\varepsilon}_x, \dot{\varepsilon}_y\right). \tag{8}$$

The $\bar{P}_\theta$ is an unknown function in the final equation that can be solved using numerical methods like finite element, finite difference, or spectral methods [2]. Beyond the $L/D \leq 0.5$, the pressure variation along the bearing length deviates from the function $\bar{P}_z\left(\bar{z}\right) = 4\bar{z}(1-\bar{z})$. The pressure variation along the bearing length at an eccentricity value of $\varepsilon = 0.8$ for various L/D ratios within the range of $0.25 - 10$ for a journal bearing is shown in Figure 2. It is difficult to find one function like $\bar{P}_z\left(\bar{z}\right) = 4\bar{z}(1-\bar{z})$ to represent pressure variation along the bearing length that is applicable for all L/D ratios and also for all eccentricities. Therefore, it is proposed in the current work to divide the bearing dimensions into the following two ranges: $0.25 \leq L/D \leq 3$ and $3 \leq L/D \leq 10$. After analyzing the pressure profiles in Figure 2, the fluid pressure at lower L/D ratios can be represented using higher order polynomials but at higher ratios, the exponential function fits better. Accordingly, a fourth-order polynomial satisfying bearing's boundary condition is chosen for $0.25 \leq L/D \leq 3$ as given in the Equation 9,

$$\bar{P}_z\left(\bar{z}\right) = a_4\bar{z}^4 + a_3\bar{z}^3 + a_2\bar{z}^2 + a_1\bar{z}. \tag{9}$$

This range can be extended or reduced with the consideration of higher or lower order polynomials respectively. The polynomial coefficients a_1, a_2, a_3, a_4 are determined from curve fitting to the respective pressure profiles in Figure 2. The values of these coefficients vary with L/D ratios as shown in Figure 3. After substituting the polynomial function given in Equation 9 into the Equations 5-7 we get a reduced differential equation as given in the Equation 10,

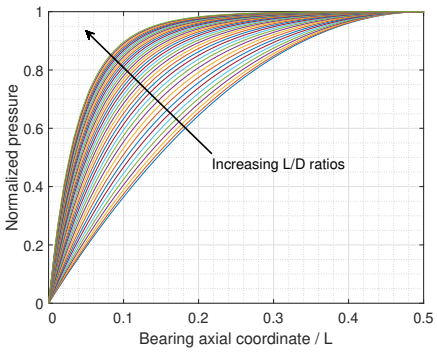

Figure 2: Normalized pressure variation along half bearing length at various L/D ratios between $0.25 - 10$

$$A_1 \frac{\partial}{\partial \theta}\left(H^3 \frac{\partial \bar{P}_\theta}{\partial \theta}\right) + A_2 \left(\frac{D}{L}\right)^2 H^3 \bar{P}_\theta = A_3 f\left(\theta, \varepsilon_x, \varepsilon_y, \dot{\varepsilon}_x, \dot{\varepsilon}_y\right), \tag{10}$$

where the variables A_1, A_2, A_3 are functions of polynomial coefficients given as follows,

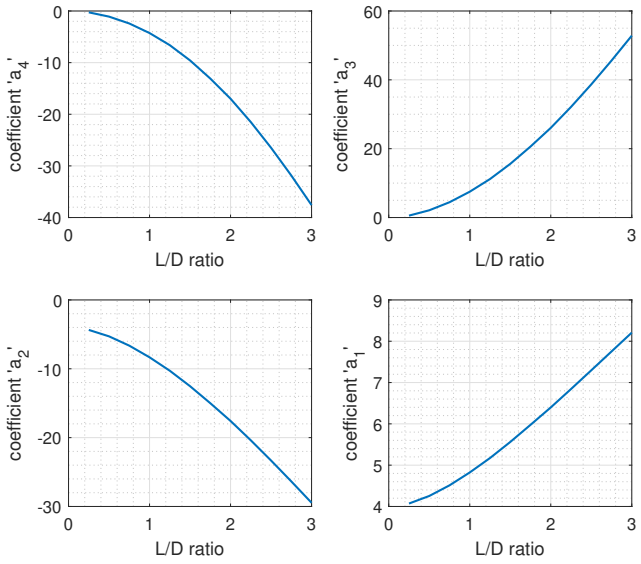

Figure 3: Polynomial coefficients values at various L/D ratios between $0.25 - 3$

$$A_1 = \frac{70a_4^2 + 315a_3a_4 + 720a_2a_4 + 1680a_1a_4 + 360a_3^2 + 1680a_2a_3 + 4032a_1a_3 + 2016a_2^2 + 10080a_1a_2 + 13440a_1^2}{322560},$$

$$A_2 = \frac{90a_4^2 + 315a_3a_4 + 588a_2a_4 + 1260a_1a_4 + 252a_3^2 + 840a_2a_3 + 1680a_1a_3 + 560a_2^2 + 1680a_1a_2}{26880},$$

$$A_3 = \frac{6a_4 + 15a_3 + 40a_2 + 120a_1}{960}.$$

The reduced equation given in Equation 10 is applicable for bearing dimensions within $0.25 \leq L/D \leq 3$ range. In the same way, for bearing dimensions in the range of $3 \leq L/D \leq 10$, an exponential function satisfying boundary conditions as given in the Equation 11 is chosen,

$$\bar{P}_z\left(\bar{z}\right) = a\left(e^{b\bar{z}} - e^{c\bar{z}}\right). \tag{11}$$

The variables a, b, c are determined from the curve fitting to the respective pressure profiles shown in Figure 2. The values of these coefficients vary with L/D ratios as shown in the below Figure 4. This exponential pressure function is substituted in the Equations 5-7 to get a reduced differential equation as given in Equation 12,

$$B_1 \frac{\partial}{\partial\theta}\left(H^3 \frac{\partial \bar{P}_\theta}{\partial\theta}\right) + B_2 \left(\frac{D}{L}\right)^2 H^3 \bar{P}_\theta = B_3 f\left(\theta, \varepsilon_x, \varepsilon_y, \dot{\varepsilon}_x, \dot{\varepsilon}_y\right), \tag{12}$$

where the variables B_1, B_2, B_3 are functions of exponential function variables given as follows,

$$B_1 = -a^2\left(\frac{2e^{(b+c)/2}}{b+c} - \frac{2}{b+c} + \frac{1}{2b} + \frac{1}{2c} - \frac{e^b}{2b} - \frac{e^c}{2c}\right),$$

$$B_2 = \frac{a^2\left(b^2 - 2b^2e^{(b+c)/2} - 2c^2e^{(b+c)/2} - 2bc + c^2 + b^2e^b + c^2e^c + bce^b + bce^c\right)}{8\left(b+c\right)},$$

$$B_3 = \frac{a\left(b - c - be^{c/2} + ce^{b/2}\right)}{bc}.$$

The reduced equation given in Equation 12 is applicable for bearings with dimensions in the range of $3 \leq L/D \leq 10$.

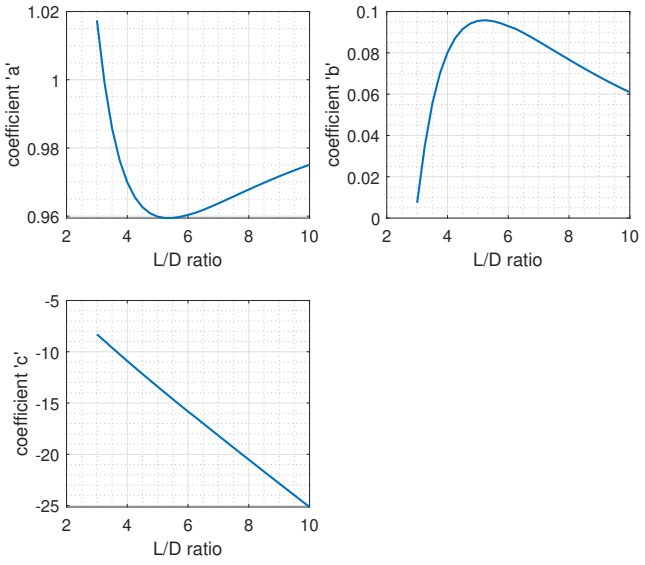

Figure 4: Exponential function variables values at various L/D ratios between $3 - 10$

The basic criteria for choosing the basis function are that they better represent the pressure variation along the bearing length, need to be integrable, and also satisfy the pressure boundary conditions at the bearing ends. The

reduced 1D differential equation (Equations 10 & 12) with $\bar{P}_\theta$ as a dependant variable is solved in the current study using pseudospectral method (PSM). The details of this method are not described here and refer to [14] for further details. The 2D pressure profile around a bearing surface can be calculated using the 1D pressure profile $\bar{P}_\theta$ along with the respective $\bar{P}_z$ function. The Gumbel boundary condition [1] is applied in this study where the negative pressures in $\bar{P}_\theta$ are disregarded by equating them to zero. This is a simple boundary condition to implement but it does not fulfill fluid continuity, and also does not satisfy conservation of mass throughout the fluid and cavitation domains. It is also possible to consider complex approaches that satisfy these conditions like Jacobson, Floberg and Olsson, Elrod cavitation models [15] and can be coupled to this Galerkin reduction method. After applying the boundary condition, bearing forces are calculated in the fixed coordinates (F_x, F_y in Figure 1) as given in Equation 13,

$$\begin{aligned} F_x &= 2\int_0^{2\pi}\int_0^{0.5} \bar{P}_\theta \bar{P}_z cos(\theta+\varphi)\mu L\Omega \frac{R^3}{c^2} d\theta d\bar{z}, \\ F_y &= 2\int_0^{2\pi}\int_0^{0.5} \bar{P}_\theta \bar{P}_z sin(\theta+\varphi)\mu L\Omega \frac{R^3}{c^2} d\theta d\bar{z}. \end{aligned} \tag{13}$$

To evaluate the accuracy of the reduced equations, bearing forces from full and reduced equations are compared in the next section. The 2D Reynolds equation is solved using the MATLAB PDE toolbox [13]. The bearing forces at different eccentricities are compared using the Sommerfeld number (S) as given in the Equation 14,

$$S = \frac{\mu\Omega LD}{2\pi W}\left(\frac{R}{c}\right)^2, \tag{14}$$

where $W = \sqrt{F_x^2 + F_y^2}$.

The proposed Galerkin reduction method can be extended for thrust bearings, gas bearings, and airfoil bearings. The computational time will be reduced by many times as it eliminates one dimension in the Reynolds equation offering the possibility to use more complex and intensive cavitation algorithms. However, the accuracy of the proposed approach needs to be verified when more complex and accurate cavitation models are used. This method also has a limitation that it cannot be applicable for bearing geometries with features like oil feed holes, partial circumferential grooves, and pressure dams.

3 Results and Discussion

A typical pressure profile in the circumferential ($\bar{P}_\theta$) and axial ($\bar{P}_z$) directions calculated for an arbitrary bearing geometry and operating conditions are shown in Figure 5 along with its 2D profile calculated using the Equation 5. As detailed in the previous section, one of the two 1D differential equations given in Equations 10 and 12 is chosen based on the bearing L/D ratio and solved for estimating $\bar{P}_\theta$ instead of solving the 2D Reynolds equation. After that bearing forces can be calculated using Equation 13 and the accuracy of the results with the Galerkin method are compared in the next section.

3.1 Bearing forces comparison

The reduced and full Reynolds equation at steady state conditions (velocity terms in the right-hand side of the Equation 3 are ignored) are solved at different eccentricities in the range of $0.1 - 0.9$ and different L/D ratios to calculate the bearing forces. These forces are expressed in the form of Sommerfeld number and compared for a few cases in Figure 6 (a)-(e). The relative error between the solutions of these two equations is also compared in Figure 6 (f). The results of the reduced equation match very well with the results of the full Reynolds equation solution. The maximum relative error at various L/D ratios between $0.25 - 10$ are plotted in Figure 7. The error is lowest at $L/D = 0.25$ when the fourth order polynomial function is used in the Galerkin reduction and it increases with increasing L/D ratios until 3. The same error is highest at $L/D = 3$ and it further decreases with increasing L/D ratio until 10 when an exponential function is used in the Galerkin reduction. The error can be further reduced by using higher order polynomials or any other mathematical functions but they may make the reduction procedure and also the coefficients of the reduced equation further complex.

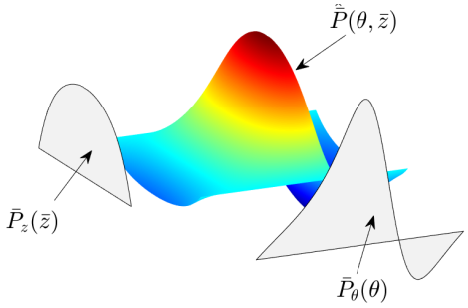

Figure 5: Dynamic pressure profile around the bearing surface (unwrapped) and its decomposition along the circumferential and length directions

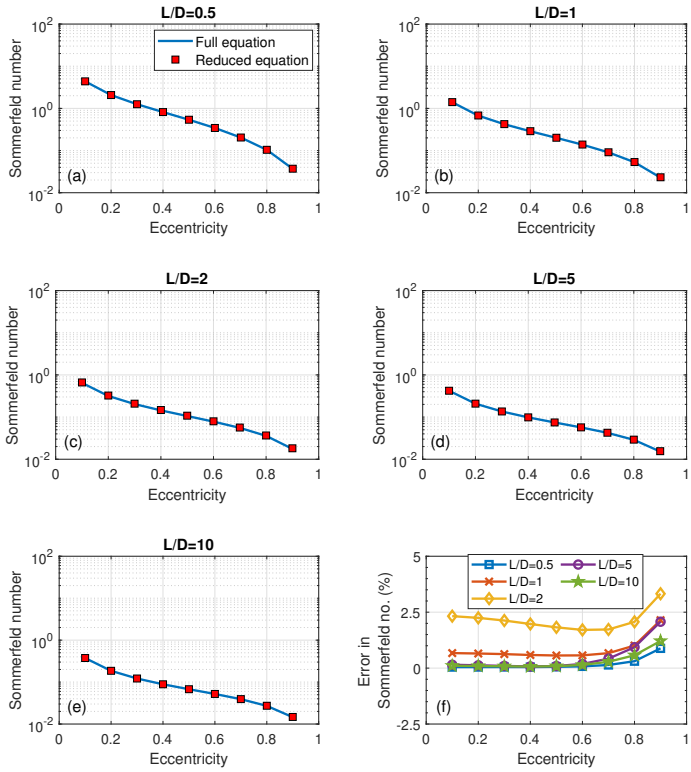

Figure 6: Comparison of Sommerfeld number calculated with full and reduced Reynolds equation

3.2 Turbocharger rotor simulations

The run-up vibration response of a turbocharger rotor supported on two identical full-floating bearings with a circumferential groove on the outer surface as shown in the Figure 8 is simulated. The details of the rotor and bearings are given in Table 1. The rotor is modelled using finite beam elements and the authors used the mode superposition method in this work to derive the reduced model considering the first six flexible bending vibration modes of the rotor. The operating speed of turbochargers will generally be below their second bending vibration mode frequency, so the number of vibration modes considered in the reduction is sufficient to capture the system's dynamic behavior accurately. The reduced model equations of motion are solved using the $ode15s$ solver within MATLAB with zero initial conditions for both displacements and velocities of the modal coordinates. The rotor is accelerated from 0 to maximum speed 300000 rpm linearly in 10 $seconds$. The circumferential groove splits the outer surface into two shorter-width oil films which are modelled using the short bearing theory. These two oil films are exposed to oil supply pressure boundary conditions at one end and atmospheric pressure boundary conditions at the other end. The oil flows from the circumferential groove to oil feed holes and then enters the inner oil film, but these feed holes are not modelled in this work. The inner oil film is modelled as a plain bearing and

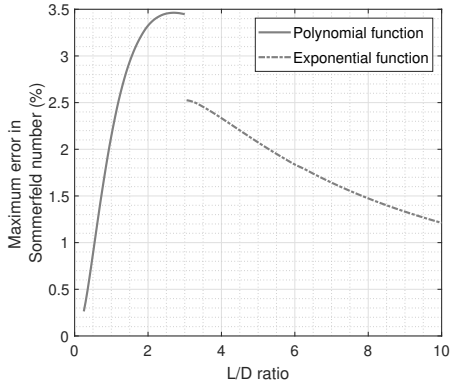

Figure 7: Comparison of Sommerfeld number calculated with full and reduced Reynolds equation

exposed to atmospheric pressure at either end of the bearing length. The inner oil film forces are calculated using the short bearing theory, 2D, and reduced Reynolds equation. The authors used the Spectral method or the global Galerkin method described in [17] for solving 2D Reynolds equation in the run-up simulations. It is an efficient and semi-analytical approach for solving fluid pressure in plain bearings.

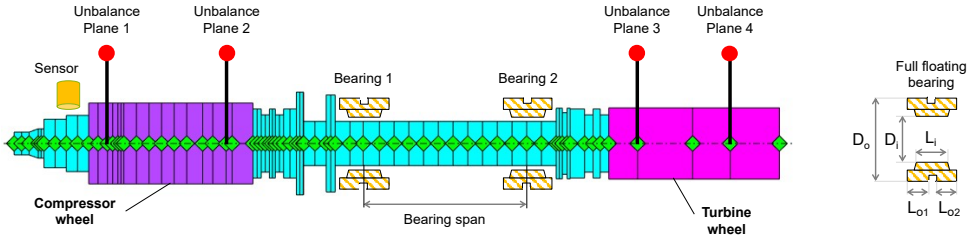

Figure 8: FEM model of the turbocharger rotor supported on full-floating bearings

Table 1: Turbocharger rotor and journal bearing details

Variable	Value	Units
Rotor Mass	0.065	kg
Rotor length	0.1	m
Rotational speed (Ω)	upto 300000	rpm
Bearing span	0.021	m
Total unbalance	0.14	$g-mm$
Bearing:		
Inner oil film ($\frac{L_i}{D_i}$) ratio	1.0	
Outer oil film ($\frac{L_{o1}+L_{o2}}{D_o}$) ratio	0.7	
Bearing radial clearances ($\frac{c_i}{c_o}$)	0.36	
Oil type	SAE 0W20	
Oil supply pressure	1	bar
Oil supply temperature	150	$^{\circ}C$

The vibration response simulated at the sensor location using these methods is compared in Figure 9 (a) and their waterfall plots are shown in Figure 9 (b)-(d). Three types of sub-synchronous vibrations Sub1, Sub2, and Sub3 are common in the case of full-floating bearings due to the oil whirl in the inner and outer oil films [16]. The rotor becomes unstable at low rotational speeds due to the oil whirl in the inner oil film and reaches a stable limit

cycle (first bifurcation) and the sub-synchronous vibrations (Sub1) excite conical vibration mode. The rotor further bifurcates at high rotational speeds where the first sub-synchronous vibrations become unstable and a further limit cycle arises. Based on the rotor and bearing parameters, and operating and boundary conditions, several possibilities exist for these limit cycles. Either sequential or simultaneous limit cycles due to the unstable oil whirl in the inner oil film (Sub2) and outer oil film (Sub3) exciting the rotor cylindrical mode and conical mode respectively are possible [16]. In the current case, Sub1 vibrations exist from the $0 - 50000\ rpm$ range and Sub2 vibrations exist for a short speed range. But these instabilities due to the inner oil film whirl are not severe when compared to the Sub3 vibrations due to the oil whirl in the outer oil film. Such dominant Sub3 vibrations are typical with full-floating bearings when supplied oil at low pressure and high-temperature conditions. The nature of these sub-synchronous vibrations will change if oil at a higher pressure and low-temperature conditions is supplied to the bearings.

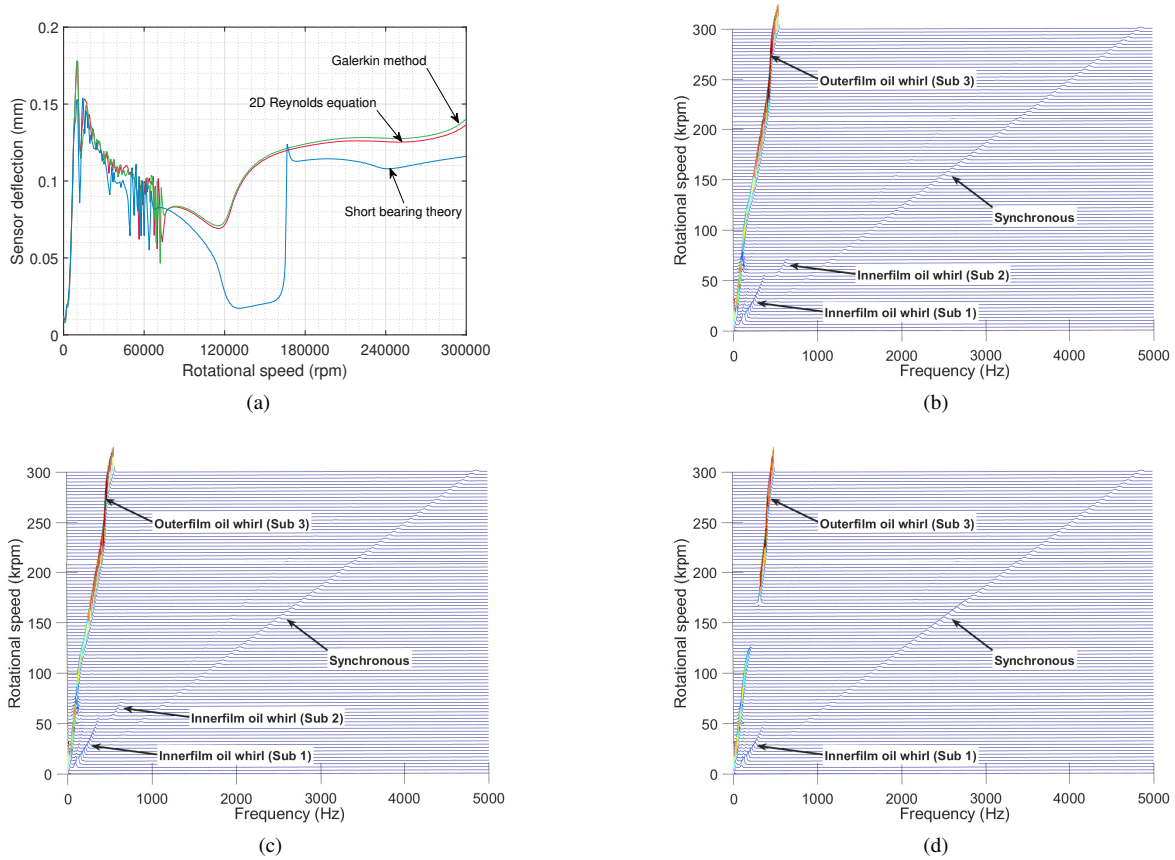

Figure 9: (a) Comparison of sensor deflections, waterfall plots of the run-up vibration response at sensor location simulated using (b) 2D Reynolds equation, (c) Galerkin method, and (d) short bearing theory

The inner oil film L/D ratio is equal to 1 which neither belongs to the short nor the long bearing theory applicable geometries. Usually, the 2D Reynolds equation needs to be solved to accurately predict bearing dynamic pressure and forces. But due to the high computational effort requirement, the short bearing theory is often used for run-up simulations which introduce an error in the results which can be observed in the sensor deflections shown in Figure 9 (a). The computational time taken for simulating the run-up in $10\ s$ using all three methods for calculating bearing forces on the same computer are compared in Table 2. The results presented in this section confirm that the same accuracy level as the 2D Reynolds equation is achieved with the reduction method without severely increasing the computational effort when compared to the case of using the short bearing theory.

4 Conclusions

A method to reduce the dimension of the Reynolds equation to 1D that can be used to accurately predict the dynamic pressure generated within the plain bearings is demonstrated in this work. This method is applicable for bearings with dimensions whose L/D ratio is within the range of $0.25 - 10$. The error in bearing forces predicted by the reduced and 2D Reynolds equation is less than 3.5%. The computational effort required is comparable to the case that uses short bearing theory. Due to this, it is now possible to simulate the run-up vibration response of

Table 2: Computational time comparison

Method	Time	Units
2D Reynolds equation	26	$hours$
Galerkin reduction	11	$hours$
Short bearing theory	7	$hours$

high-speed rotors supported on the finite-length journal bearings in less time. Simulations of the turbocharger rotor supported on two finite-length full-floating bearings highlight the differences between the results with the short and finite bearing models. The bearing forces, rotor deflections, and sub-synchronous vibrations are under-predicted when pressure variation along the bearing circumference is ignored in the short bearing theory. Simulation results with the Galerkin reduced equation match very well with those predicted by the 2D Reynolds equation model for bearings. The proposed method achieves the accuracy of the 2D Reynolds equation model with relatively low computational effort.

References

[1] Hori, Y. Hydrodynamic lubrication. (Springer Science & Business Media,2006)

[2] Thiery, F., Gantasala, S. & Aidanpää, J. Numerical evaluation of multilobe bearings using the spectral method. *Advances In Mechanical Engineering*. **9**, 1687814017707135 (2017)

[3] Barrett, L., Allaire, P. & Gunter, E. A finite length bearing correction factor for short bearing theory. (1980)

[4] Ritchie, G. Nonlinear dynamic characteristics of finite journal bearings. (1983)

[5] Sfyris, D. & Chasalevris, A. An exact analytical solution of the Reynolds equation for the finite journal bearing lubrication. *Tribology International*. **55** pp. 46-58 (2012)

[6] Bastani, Y. & Queiroz, M. A new analytic approximation for the hydrodynamic forces in finite-length journal bearings. (2010)

[7] Wang, Y., Liu, Z., Kang, W. & Yan, J. Approximate analytical model for fluid film force of finite length plain journal bearing. *Proceedings Of The Institution Of Mechanical Engineers, Part C: Journal Of Mechanical Engineering Science*. **226**, 1345-1355 (2012)

[8] Chen, Z., Jiao, Y., Xia, S., Huang, W. & Zhang, Z. An efficient calculation method of nonlinear fluid film forces in journal bearing. *Tribology Transactions*. **45**, 324-329 (2002)

[9] Chasalevris, A. & Louis, J. Evaluation of transient response of turbochargers and turbines using database method for the nonlinear forces of journal bearings. *Lubricants*. **7**, 78 (2019)

[10] Pfeil, S., Gravenkamp, H., Duvigneau, F. & Woschke, E. An efficient semi-analytical solution of the Reynolds equation. *PAMM*. **20**, e202000067 (2021)

[11] Novotny, P., Dlugoš, J., Prokop, A., Řehák, K. & Raffai, P. Effective computational model for a solution of turbocharger rotor dynamics. *Journal Of Vibroengineering*. **19**, 724-736 (2017)

[12] Baum, C., Hetzler, H., Schröders, S., Leister, T. & Seemann, W. A computationally efficient nonlinear foil air bearing model for fully coupled, transient rotor dynamic investigations. *Tribology International*. **153** pp. 106434 (2021)

[13] The MathWorks, I. Partial Differential Equation Toolbox. (2019), https://de.mathworks.com/help/pde/

[14] Gantasala, S., Praveen Krishna, I. & Sekhar, A. Dynamic analysis of rotors supported on journal bearings by solving Reynolds equation using pseudospectral method. *Proceedings Of The 9th IFToMM International Conference On Rotor Dynamics*. pp. 1009-1019 (2015)

[15] Alakhramsing, S., Van Ostayen, R. & Eling, R. Thermo-hydrodynamic analysis of a plain journal bearing on the basis of a new mass conserving cavitation algorithm. *Lubricants*. **3**, 256-280 (2015)

[16] Schweizer, B. Total instability of turbocharger rotors—physical explanation of the dynamic failure of rotors with full-floating ring bearings. *Journal Of Sound And Vibration*. **328**, 156-190 (2009)

[17] Chatzisavvas, I. Efficient thermohydrodynamic radial and thrust bearing modeling for transient rotor simulations. (Technische Universität,2018)

15th SIRM – European Conference on Rotordynamics,
Darmstadt, Germany, 22nd – 24th February 2023

Influence of Fluid-Film-Cavitation on the Dynamics, Stability and Oscillation Behavior of High-Speed Rotor Systems

Huaxin Dong [1], Bernhard Schweizer [1]

[1] Institute of Applied Dynamics, Technical University of Darmstadt, Otto-Berndt-Straße 2, 64287, Darmstadt, Germany, dong@ad.tu-darmstadt.de

Abstract

Fluid film cavitation may strongly affect the vibration and stability behavior of rotors supported in hydrodynamic journal bearings. Different cavitation effects are distinguished in literature. Considering hydrodynamic bearings, cavitation is mainly caused by surrounding air, which is sucked into the bearing gap and also by outgassing of dissolved gases. Diverse physical and numerical approaches have been suggested in order to incorporate fluid film cavitation in the Reynolds equation. Here, a mass-conserving two-phase cavitation method is applied, where a nonlinear relationship is used to describe the dependency between density and pressure of the oil/gas-mixture. Different two-phase modelling approaches are presented and compared. Run-up simulations with a rotor/bearing co-simulation model are carried out to investigate the dynamics and especially the bifurcation behavior of rotor/bearing systems including a two-phase cavitation approach. The numerical model for the rotor/bearing system consists of a multibody subsystem for the rotor and several finite element subsystems for the fluid films. Diverse high-speed rotor/bearing systems are analyzed, namely systems with single oil film bearings and systems with full-floating ring bearings. The influence of the cavitation parameters on the nonlinear vibration behavior of the rotor/bearing system is investigated. The different cavitation approaches are also compared with respect to numerical efficiency.

1 Bearing model

1.1 Mass-conserving cavitation models

Different methods exist to physically and mathematically describe fluid film cavitation in hydrodynamic bearings [3]. Here, a two-phase cavitation approach is used. Therefore, a mixture approach is applied to represent the mixture of lubricant and gas in the bearing gap. With the nonlinear lubricant fraction function ϑ according to $\vartheta(p) = \rho(p)/\rho_0 = \eta(p)/\eta_0$, $\vartheta'(p) = \partial\vartheta(p)/\partial(p)$, an averaged value for density ρ and viscosity η is calculated as a function of the local pressure p. Note that p_0 denotes the ambient pressure and $\rho_0 = \rho(p_0)$ as well as $\eta_0 = \eta(p_0)$ (ρ_0 and η_0 denote the properties of the liquid lubricant; the gas portion can be neglected). The function ϑ separates the full-film zone ($p \geq p_0$) from the cavitation zone ($p < p_0$). In the full-film zone ($\vartheta \approx 1$, $\vartheta' \ll 1$), the oil almost behaves like an incompressible fluid. In the cavitation zone ($0 < \vartheta < 1$), ϑ decribes the mixture between oil and gas (air or dissolved lubricant).

Here, four different functions $\vartheta(p)$ (or $\vartheta(x)$, $x = p/p_0$) are used and compared, see Figure 1.

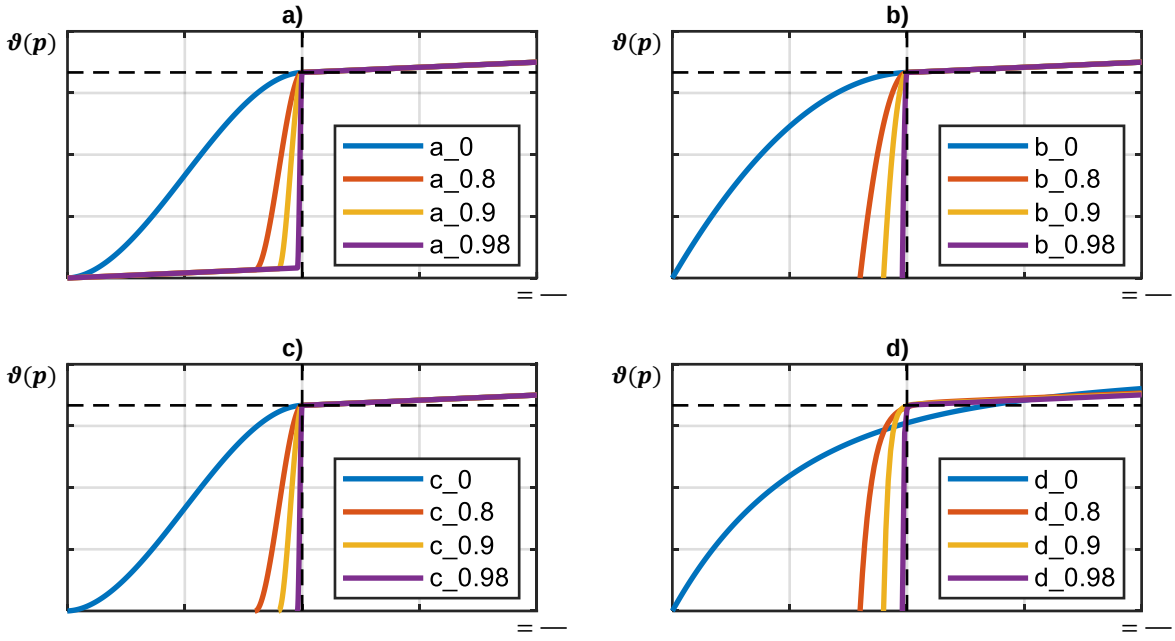

Figure 1: Ansatz functions a), b), c) and d) for the lubricant fraction function.

a) Regularized step function:

In the first approach, a regularized step function is used, which is mathematically described by a third order polynomial for the transition zone ($x_0 < x < 1$, e.g. $x_0 = 0.9$) and linear functions with a small gradient for the high pressure zone ($x \geq 1$) and the low pressure zone ($x \leq x_0$) so that ϑ' is continuous, see Figure 1(a). Using the regularized step function, numerical problems may occur. Due to the high gradient $\vartheta' \gg 1$ in the transition zone, a large convection term is produced in the compressible Reynolds equation. In the high pressure zone and also in the low pressure zone, the small gradient $\vartheta' \ll 1$ yields a very small coefficient for the $\partial p/\partial t$- term in the time-dependent Reynolds equation. Both, very small and very large values of ϑ' entail stiff differential equations so that appropriate numerical approaches and stabilization techniques have to be applied (see [11], section 4.2.1.3). Abbreviations: $a\_0 \rightarrow x_0 = 0$; $a\_0.8 \rightarrow x_0 = 0.8$; $a\_0.9 \rightarrow x_0 = 0.9$; $a\_0.98 \rightarrow x_0 = 0.98$.

b) Polynomial of degree 2:

Within the second ansatz, the polynomial $\vartheta(x) = ax^2 + bx + c$ with $a = (\vartheta_0' - \vartheta_0' x_0 - 1)/(x_0^2 - 2x_0 + 1)$, $b = \vartheta_0' - 2a$ and $c = 1 - a - b$ ($x_0 = const.$, $\vartheta_0' = const. \ll 1$) is used in the region $x \leq 1$. In the high pressure zone $x > 1$, the linear function $\vartheta_0'(x-1) + 1$ is used to provide a small gradient $\vartheta' = \vartheta_0'$. Abbreviations: $b\_0 \rightarrow x_0 = 0$; $a\_0.8 \rightarrow x_0 = 0.8$; $b\_0.9 \rightarrow x_0 = 0.9$; $b\_0.98 \rightarrow x_0 = 0.98$, see Figure 1(b).

c) Polynomial of degree 3:

Here, the polynomial $\vartheta(x) = ax^3 + bx^2 + cx + d$ with $a = (2 - 2\vartheta_0' + 2\vartheta_0' x_0)/(x_0^3 - 3x_0^2 + 3x_0 - 1)$, $b = -a(3x_0^2 - 3)/(2x_0 - 2)$, $c = \vartheta_0' - 3a - 2b$ and $d = 1 - a - b - c$ ($x_0 = const.$, $\vartheta_0' = const. \ll 1$) is used in the region $x \leq 1$. In the high pressure zone $x > 1$, again the linear function $\vartheta_0'(x-1) + 1$ is used to provide a small gradient $\vartheta' = \vartheta_0'$. It should be mentioned that the ansatz a) with $x_0 = 0$ equals the polynomial ansatz of degree 3 (i.e. $a\_0 = c\_0$). Abbreviations: $c\_0 \rightarrow x_0 = 0$; $c\_0.8 \rightarrow x_0 = 0.8$; $c\_0.9 \rightarrow x_0 = 0.9$; $c\_0.98 \rightarrow x_0 = 0.98$, see Figure 1(c).

d) Exponential function:

The lubricant function can also be implemented by an exponential function according to $\vartheta(x) = 1 - e^{-k(x-x_0)} + \vartheta_0'(x - x_0)$ with $k = const.$, $x_0 = const.$ and $\vartheta_0' = const. \ll 1$. The function $\vartheta_0'(x - x_0)$ is added in order to provide a small gradient $\vartheta'(x) \approx \vartheta_0'$ in the high pressure zone. The following parameters have been chosen in this work: d_0 $\rightarrow k = 2, x_0 = 0$; d_0.8 $\rightarrow k = 20, x_0 = 0.8$; d_0.9 $\rightarrow k = 50, x_0 = 0.9$; d_0.98 $\rightarrow k = 200, x_0 = 0.98$, see Figure 1(d).

Using a two-phase cavitation model, the compressible time-dependent Reynolds equation

$$-2H\vartheta'\frac{\partial p}{\partial t}+\frac{\partial}{\partial\phi}\left[\left(\frac{C}{R}\right)^2\frac{H^3}{6\eta_0}\frac{\partial p}{\partial\phi}\right]+\left(\frac{R}{B}\right)^2\frac{\partial}{\partial\overline{z}}\left[\left(\frac{C}{R}\right)^2\frac{H^3}{6\eta_0}\frac{\partial p}{\partial\overline{z}}\right]-\omega H\vartheta'\frac{\partial p}{\partial\phi}=\vartheta\left[\omega\frac{\partial H}{\partial\phi}+2\frac{\partial H}{\partial t}\right] \tag{1}$$

has to be used to calculate the pressure field $p(\phi,\overline{z})$. ϕ represents the circumferential coordinate, $\overline{z}$ is the dimensionless axial coordinate of the bearing. $H=1+D_x\sin\phi-D_y\cos\phi$ denotes the gap function, where D_x and D_y represent the components of the dimensionless displacement of the journal center. $\varepsilon=\sqrt{D_x^2+D_y^2}/C$ defines the dimensionless eccentricity. The bearing has the radius R, the axial width B and the nominal radial clearance C. ω denotes the angular velocity of the rotor.

Here, single oil film bearings with a circumferential oil groove are considered, see Figure 2(a). The boundary conditions are illustrated in Figure 2(b). At the two boundaries of the circumferential oil groove, the Dirichlet boundary condition $p=p_{in}$ is applied, where p_{in} denotes the oil inlet pressure. At the axial boundaries, special Neumann boundary conditions are used [11], namely

$$\left(\frac{R}{B}\right)^2\left(\frac{C}{R}\right)^2\left[\frac{H^3}{6\eta_0}\frac{\partial p}{\partial\overline{z}}\right]_{\phi,\,\overline{z}=0}=g(p),\quad\left(\frac{R}{B}\right)^2\left(\frac{C}{R}\right)^2\left[\frac{H^3}{6\eta_0}\frac{\partial p}{\partial\overline{z}}\right]_{\phi,\,\overline{z}=1}=-g(p) \tag{2}$$

with the pressure dependent penalty function $g(p)=ae^{b\frac{p-p_0}{p_0}}$, where $a\ll1$ and $b\gg1$. Hence, in the high pressure region ($p\geq p_0$) one gets $\partial p/\partial\overline{z}\gg1$, so that the pressure is almost the ambient pressure p_0. In the cavitation region ($p<p_0$) one gets $\partial p/\partial\overline{z}\ll1$, so that the axial flow is almost zero.

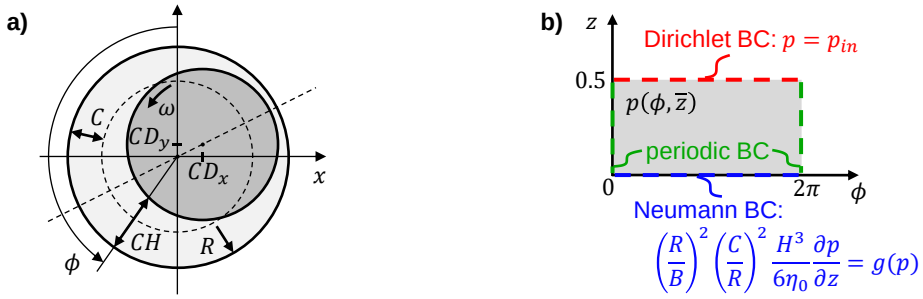

Figure 2: a) Bearing geometry with a circumferential oil groove; b) Developed gap geometry with boundary conditions.

1.2 Non-mass-conserving cavitation models

To discuss the influence of fluid film cavitation on the rotordynamic behavior, we also consider non-mass conserving cavitation approaches. On the one hand, we use the well-known half-Sommerfeld boundary conditions (Gümbel approach), where the incompressible Reynolds equation is used and the pressure below the ambient pressure is ignored. On the other hand, a penalty approach is applied. Therefore, the following Reynolds equation is considered

$$\frac{\partial}{\partial\phi}\left[\left(\frac{C}{R}\right)^2\frac{H^3}{6\eta}\frac{\partial p}{\partial\phi}\right]+\left(\frac{R}{B}\right)^2\frac{\partial}{\partial\overline{z}}\left[\left(\frac{C}{R}\right)^2\frac{H^3}{6\eta}\frac{\partial p}{\partial\overline{z}}\right]=\omega\frac{\partial H}{\partial\phi}+2\frac{\partial H}{\partial t}-\mathrm{Pen}(p) \tag{3}$$

with the penalty term $\mathrm{Pen}(p)=ae^{-b\frac{p-p_0}{p_0}}$ ($a\ll1$, $b\gg1$). This term may be interpreted as an artificial source term: fluid is provided into the cavitation zone so that p is always larger than p_0. Note that the penalty approach produces smooth pressure functions at the cavitation boundaries, while the half-Sommerfeld boundary conditions entire a non-smooth pressure profile.

In Section 3.2 and Section 3.3, full-floating ring bearings with a circumferential oil groove in the outer fluid film gap are considered, see Figure 3(c) and 3(d).

2 Rotor/bearing co-simulation model

The rotor/bearing system is decomposed into several subsystems: one subsystem for the rotor (multibody system [12], MBS) and further subsystems for each fluid film (finite element systems). The MBS is coupled with the FE-subsystems by a co-simulation method [8][16][17]. Here, an explicit sequential coupling approach (Gauss-Seidel type) is used, where the MBS-subsystem is used as the master subsystem. A force/displacement decomposition technique is applied, i.e. output variables of the MBS subsystem are kinematical variables, whereas the output variables of the FE-subsystems are resultant forces/torques of the different fluid-films. The co-simulation is executed in the following way. Firstly, subsystem 1 (rotor, master) integrates from the macro-time

point T_n to T_{n+1} with the macro-time step H. For the numerical integration of the equations of motion of the MBS, the bearing forces/torques are required. Therefore, extrapolated bearing forces/torques are used. Secondly, the FE-subsystems (slaves) are integrated from T_n to T_{n+1}. For the numerical integration of the FE-subsystem, kinematical quantities of subsystem 1 are required. Therefore, interpolated coupling variables are used.

Within the master-slave approach, a variable macro-time grid is used, which is defined by the step-size of the master-subsystem. Here, the MBS is solved with a BDF solver (absolute and relative error = $1E-6$, $H_{max} = 1E-6$ s) [4]. The FE-subsystems are also solved with a BDF integrator (absolute error = $1E-6$, relative error = $1E-5$, $H_{max} = 1E-6$ s). The coupling variables are extrapolated and interpolated with quadratic polynomials.

3 Simulation results with different rotor models

Transient run-up simulations have been performed with different rotor/bearing models, see Figure 3, to study the influence of the cavitation model on the rotordynamic vibration and stability behaviour [10][18]. Additional information on the rotor models can be found in [13][14][15].

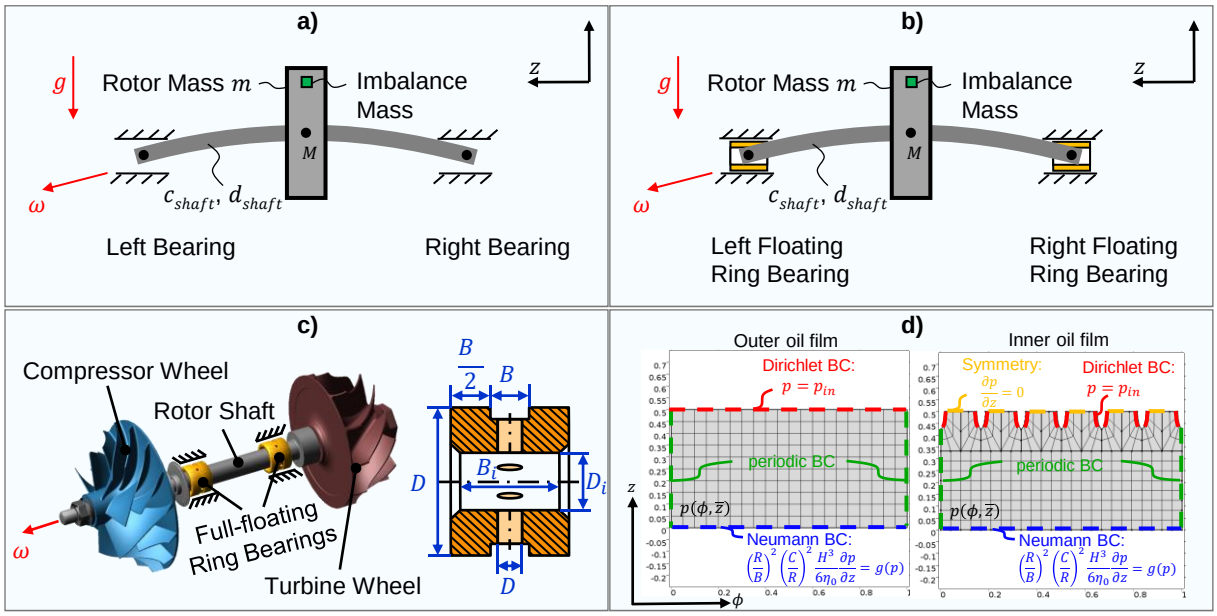

Figure 3: Rotor models: (a) Jeffcott rotor in single oil film bearings; (b) Jeffcott rotor in full-floating ring bearings; (c) Turbocharger in full-floating ring bearings; (d) Developed gap geometry with boundary conditions and mesh.

The first rotor system is a Jeffcott rotor symmetrically supported in two single oil film bearings with a circumferential oil groove, see Figure 3(a). Two cases are considered: (i) small external damping and (ii) large external damping. Note that the external damping force is applied in the center M of the rotor mass according to $\underline{F}_{d_e} = -d_e\left[\dot{r}_x^M, \dot{r}_y^M\right]^T$. The parameters for case (i) are given in Table 1. The same parameters have been used for case (ii) with two exceptions: d_e = 500 Ns/m and c = 2000 N/mm.

Table 1: Parameters of the Jeffcott rotor with single oil film bearings for case (i)

Name	Symbol	Value	Unit
Rotor mass	m	6	kg
Unbalance	U	3	gmm
Shaft stiffness	c	5000	N/mm
External damping	d_e	1	Ns/m
Internal shaft damping	d_i	0.1	Ns/m
Bearing width	B	20	mm
Bearing diameter	D	25	mm
Nominal radial bearing clearance (warm)	C	35	µm
Oil viscosity (warm)	η	12	mPas
Ambient pressure	p_0	1	bar
Inlet pressure	p_{in}	1	bar

The second rotor system is identical with the first rotor, however, full-floating ring bearings with a circumferential oil groove in the outer fluid film gap are used, see Figure 3(b). The parameters of the rotor system are given in Table 2.

Table 2: Parameters of the Jeffcott rotor with full-floating ring bearings

Name	Symbol	Value	Unit
Rotor mass	m	6.2	kg
Unbalance	U	3	gmm
Shaft stiffness	c	20000	N/mm
External damping	d_e	1	Ns/m
Internal shaft damping	d_i	0.1	Ns/m
Floating ring mass	m_F	70	g
Diameter of connecting channels	D	3	mm
Circumferential oil groove	B	3.5	mm
Inner bearing width	B_i	20	mm
Inner bearing diameter	D_i	25	mm
Inner nominal radial bearing clearance (warm)	C_i	35	µm
Inner oil viscosity (warm)	η_i	12	mPas
Outer bearing width	B	2·8.5	mm
Outer bearing diameter	D	34	mm
Outer nominal radial bearing clearance (warm)	C	40	µm
Outer oil viscosity (warm)	η	22	mPas
Oil density	ρ_{oil}	830	kg/m^3
Ambient pressure	p_0	1	bar
Inlet pressure	p_{in}	2	bar

The third rotor system is a turbocharger rotor supported in full-floating ring bearings with the subsequent model parameters given in Table 3.

Table 3: Parameters of the turbocharger rotor with full-floating ring bearings

Name	Symbol	Value	Unit
Rotor mass	m	6.2	kg
Compressor unbalance	U	1	gmm
Turbine unbalance	U_T	2	gmm
Floating ring mass	m_F	68.82	g
Diameter of connecting channels	D	3	mm
Circumferential oil groove	B	3.5	mm
Inner bearing width	B_i	20	mm
Inner bearing diameter	D_i	25	mm
Inner nominal radial bearing clearance on the compressor side (warm)	C_i	35.19	µm
Inner nominal radial bearing clearance on the turbine side (warm)	C_i^T	35.61	µm
Inner oil viscosity on the compressor side (warm)	η_i^C	13.29	mPas
Inner oil viscosity on the turbine side (warm)	η_i^T	10.47	mPas
Outer bearing width	B	2·8.5	mm
Outer bearing diameter	D	34	mm
Outer nominal radial bearing clearance on the compressor side (warm)	C	47.99	µm
Outer nominal radial bearing clearance on the turbine side (warm)	C_o^T	46.03	µm
Outer oil viscosity on the compressor side (warm)	η	23.26	mPas
Outer oil viscosity on the turbine side (warm)	η_o^T	19.98	mPas
Oil density	ρ_{oil}	830	kg/m^3
Ambient pressure	p_0	1	bar
Inlet pressure	p_{in}	2	bar

3.1 Jeffcot rotor with single oil film bearings

To study the influence of the different cavitation models on the vibration and bifurcation behaviour, run-up simulations are carried out. The rotor speed is increased linearly from 0 to 900 Hz in 3 s. Figure 4(a) and 4(b) depict the rotor vibration in y-direction for the four two-phase cavitation models with $x_0 = 0.9$ as well as for the two non-mass-conserving cavitation approaches for the two cases (i) low and (ii) high external damping. In Figure 4(c) and 4(d), corresponding frequency spectra are shown, namely the FFT of the run-up simulation with the

Penalty approach for case (i) and the FFT of the curve d_0.9 for case (ii). As can be seen in Figure 4(c), the rotor gets unstable (oil whirl/whip) at $t \approx 750$ ms and remains unstable since the external damping is very small. For the case of high external damping, see Figure 4(d), the rotor becomes unstable (oil whirl/whip) at $t \approx 700$ ms. The unstable region can, however, be driven through and the rotor gets stable again at $t \approx 1110$ ms.

Figure 4(e)-(h) show the dimensionless bearing eccentricities for the different cavitation models with $x_0 = 0$, $x_0 = 0.8$, $x_0 = 0.9$ and $x_0 = 0.98$ for the case of low external damping. Significant differences can be observed between the mass-conserving cavitation models with $x_0 = 0$, $x_0 = 0.8$ and $x_0 = 0.9$ and the non-mass-conserving cavitation approaches (the two- phase approaches become unstable earlier); comparatively small differences are detected for $x_0 = 0.98$. The difference between the two non-mass conserving approaches is rather small.

In Figure 4(i)-(l), corresponding plots are shown for the case of higher external damping. Substantial differences can be detected between the run-up simulations with the mass-conserving and the non-mass-conserving cavitation approaches. While the two non-mass-conserving cavitation approaches only exhibit a small region of instability with very small whirl/whip-amplitudes, significantly larger whirl/whip-amplitudes are obtained with the mass-conserving models. The onset of the whirl/whip oscillation is earlier with the two-phase models. However, the instability is also passed through so that the system is stabilized again at higher rotor speeds.

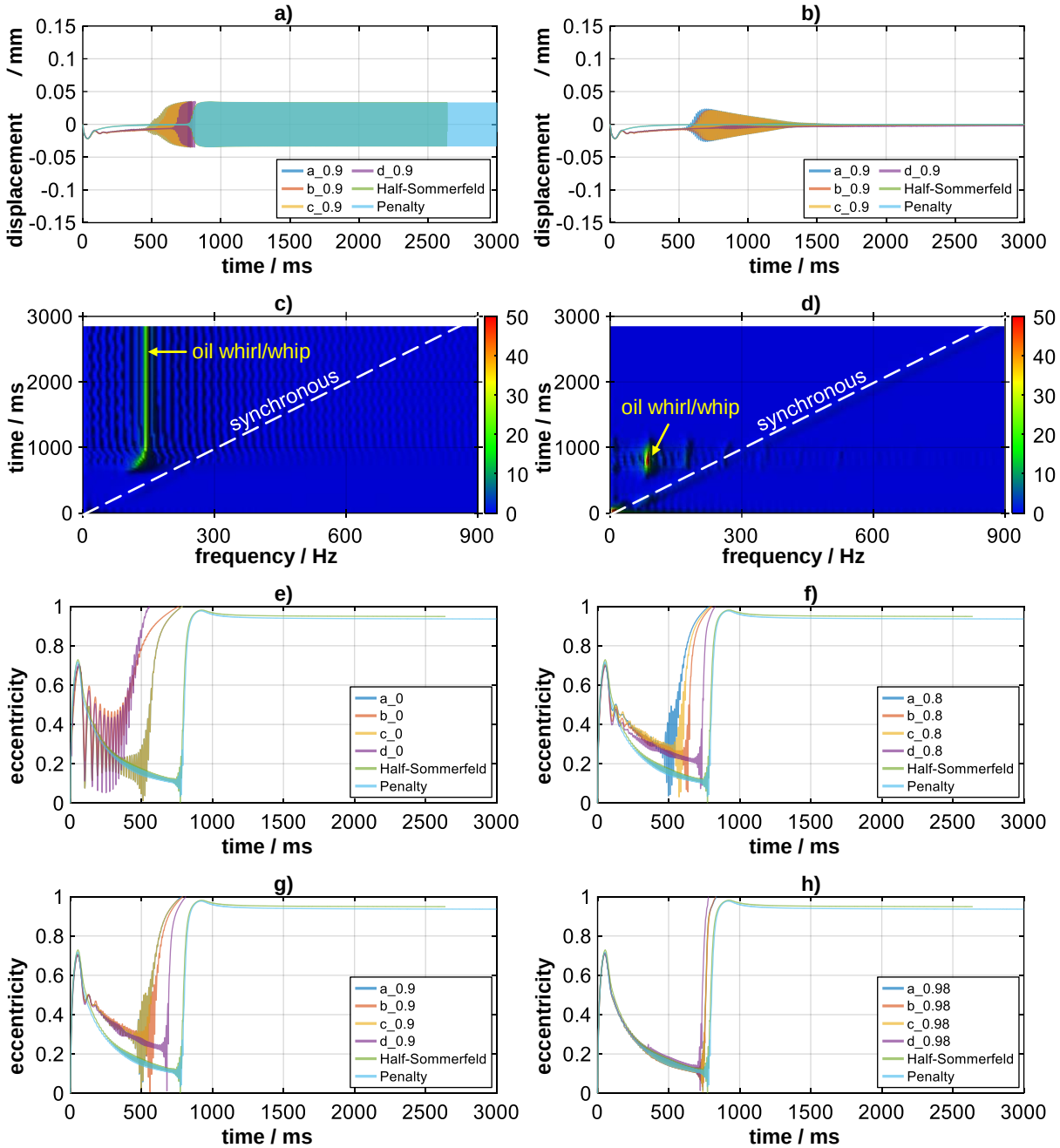

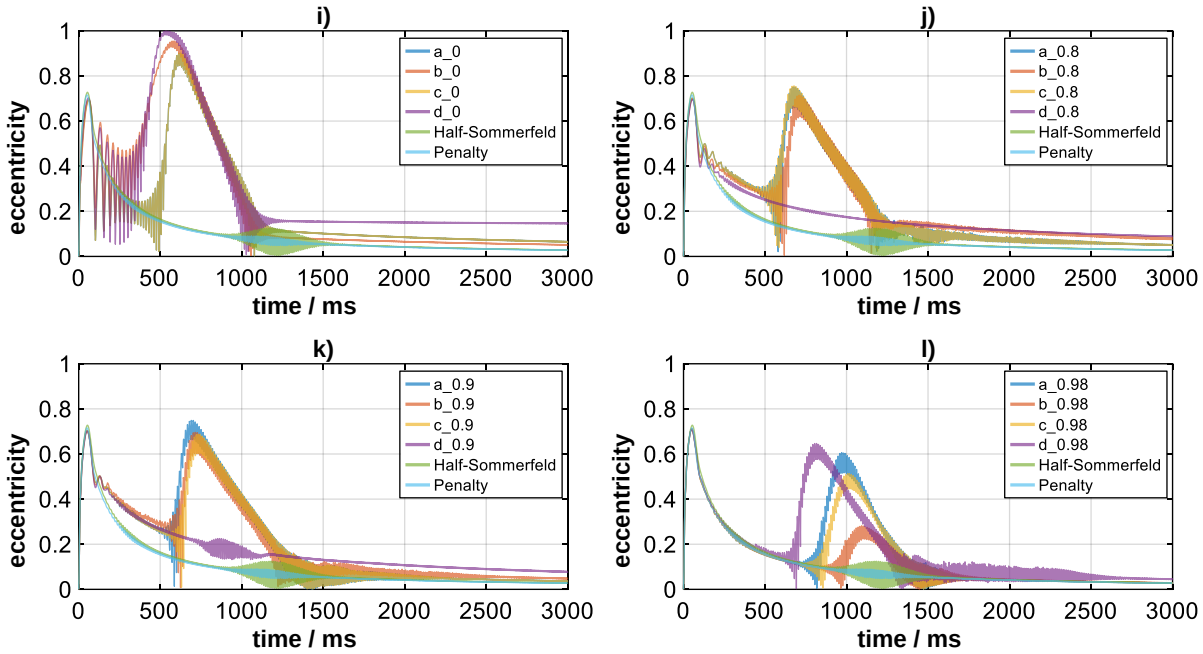

Figure 4: Run-up simulation of the Jeffcott rotor in single oil film bearings with different cavitation models and cavitation parameters: (a) and (b) Displacement r_y^M of rotor mass in y-direction for $d_e = 1$ Ns/m and $d_e = 500$ Ns/m ($x_0 = 0.9$); (c) and (d) FFT of r_y^M for $d_e = 1$ Ns/m (penalty ansatz) and $d_e = 500$ Ns/m (d_0.9). Dimensionless bearing eccentricities ε: (e) $d_e = 1$ Ns/m and $x_0 = 0$; (f) $d_e = 1$ Ns/m and $x_0 = 0.8$; (g) $d_e = 1$ Ns/m and $x_0 = 0.9$; (h) $d_e = 1$ Ns/m and $x_0 = 0.98$; (i) $d_e = 500$ Ns/m and $x_0 = 0$; (j) $d_e = 500$ Ns/m and $x_0 = 0.8$; (k) $d_e = 500$ Ns/m and $x_0 = 0.9$; (l) $d_e = 500$ Ns/m and $x_0 = 0.98$.

3.2 Jeffcot rotor with full-floating ring bearings

Now, the Jeffcott rotor supported in full-floating ring bearings is investigated with the help of run-up simulations [15]. Results are collected in Figure 5. Figure 5(a) illustrates the rotor vibration in y-direction for the four two-phase cavitation models with $x_0 = 0.9$ and for the two non-mass-conserving cavitation approaches. A frequency spectrum for the Penalty approach is shown in Figure 5(b): the rotor gets unstable at $t \approx 620$ ms, where the whirl/whip of the inner fluid films are generating self-excited rotor vibrations. After the whirl/whip of the inner fluid films is driven through at $t \approx 2200$ ms, the outer fluid films get unstable and produce a corresponding oil whirl/whip oscillation. The influence of the cavitation parameter x_0 on the bifurcation behaviour is discussed in the Figure 5(c)-(h). Marked differences can be observed between the mass-conserving and the non-mass-conserving approaches. The deviations between the different mass-conserving models are, however, comparatively small.

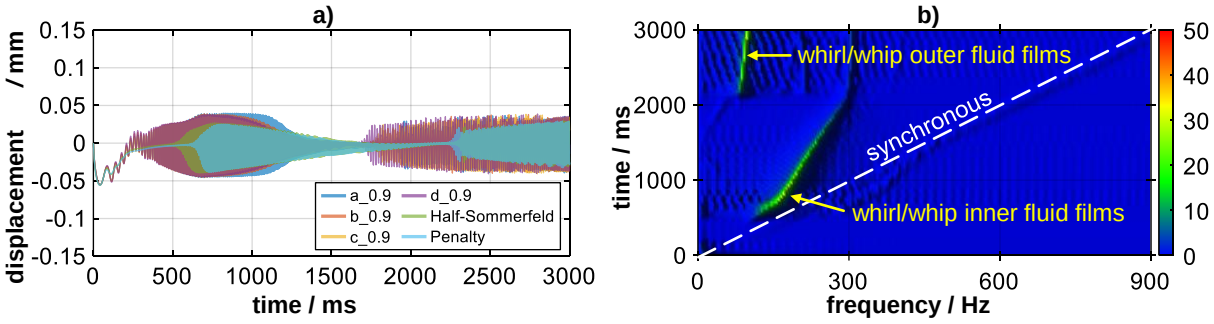

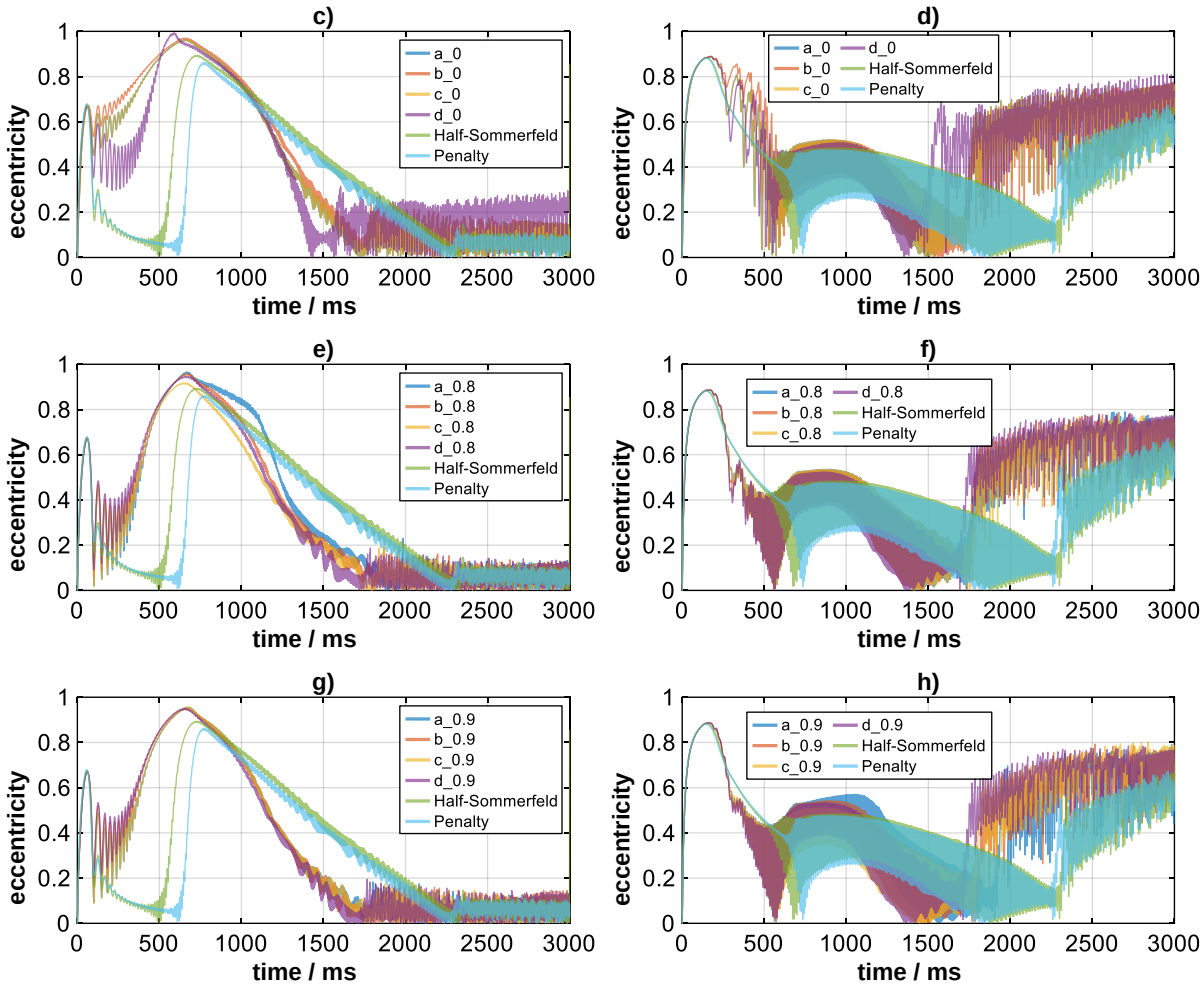

Figure 5: Run-up simulation of Jeffcott rotor in full-floating ring bearings with different cavitation models and cavitation parameters: (a) and (b) Displacement r_y^M of rotor mass in y-direction with $x_0 = 0.9$ and FFT with penalty ansatz. Dimensionless inner and outer bearing eccentricities ε_i and ε_o: (c) and (d) $x_0 = 0$; (e) and (f) $x_0 = 0.8$; (g) and (h) $x_0 = 0.9$.

The simulation times for the different cavitation models are collected in Table 4. As can be seen, very significant differences may be observed between the different cavitation approaches.

Table 4: Simulation time of Jeffcott rotor in full-floating ring bearings

Cavitation model	time	Cavitation model	time
a_0	84.2 hours	c_0	100.1 hours
a_0.8	186.3 hours	c_0.8	177.6 hours
a_0.9	239.9 hours	c_0.9	224.6 hours
b_0	84.2 hours	d_0	60.9 hours
b_0.8	143.5 hours	d_0.8	66.7 hours
b_0.9	187.7 hours	d_0.9	57.5 hours

3.3 Turbocharger model

Finally, a turbocharger rotor is considered (see [14] for further details), which is supported in two full-floating ring bearings, see Figure 3(c). Run-up simulations – the rotor speed is increased linearly from 0 to 1200 Hz in 4 s – have been carried out to examine the influence of the cavitation model on the dynamics of the system. Figure 6(a) depicts the vertical displacement of the compressor wheel for five different mass-conserving models and for the non-mass-conserving Penalty approach. The bearing eccentricities of the inner and outer fluid films of the compressor- and turbine-sided bearing are shown in Figure 6(b)-(e). Run-up spectra for the cavitation model d_0.9 and for the Penalty approach are depicted in Figure 6(f)-(g). Three subsynchronous oscillations are observed with all cavitation models. For a detailed physical description of the bifurcations and subsynchronous vibrations, we would like to refer to literature (see, e.g., [1][2][5][6][7][13][14]).

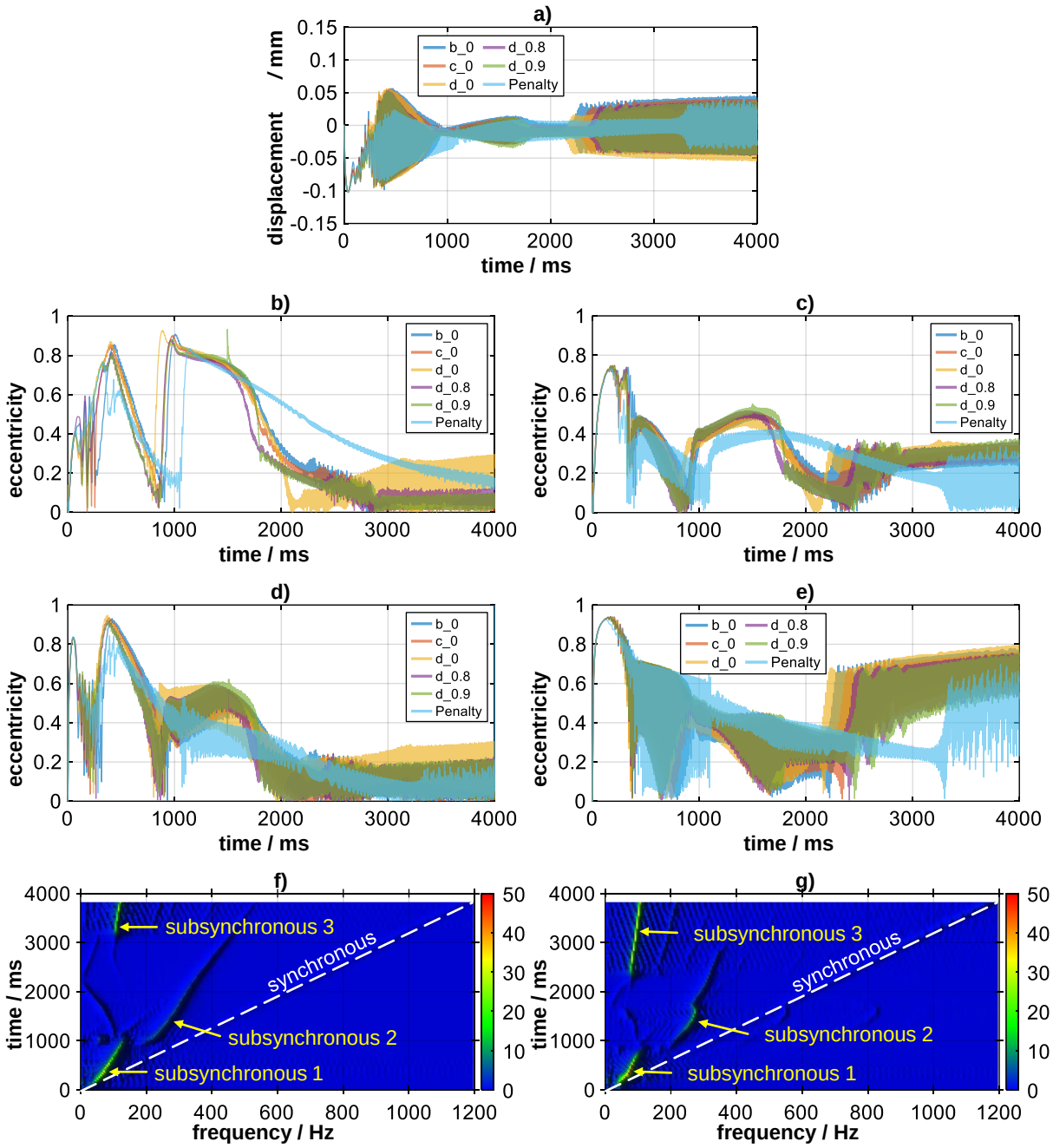

Figure 6: Run-up simulation of turbocharger with different cavitation models and cavitation parameters: a) Displacement r_y^C of the compressor center in y-direction; b) and c) inner and outer bearing eccentricities compressor-sided; d) and e) inner and outer bearing eccentricities turbine-sided; f) und g) FFT of r_y^C with penalty ansatz and ansatz d_0.9.

As in Section 3.2, the differences between the diverse mass-conserving models are rather small. However, large differences with respect to the simulation time are observed, see Table 5.

Table 5: Simulation time of turbocharger

Cavitation model	time
b_0	14.7 days
c_0	22.3 days
d_0	5.5 days
d_0.8	7.2 days
d_0.9	12.2 days

5 Conclusion

The influence of different mass-conserving and non-mass-conserving cavitation models on the vibration and bifurcation behavior of rotor systems has been investigated. Therefore, a Jeffcott rotor supported in single and full-floating ring bearings has been considered. Furthermore, a commercial turbocharger rotor supported in full-floating ring bearings has been analyzed. Rather large differences have been observed between the simulation results obtained with the mass-conserving and the non-mass-conserving cavitation algorithms. Noticeable deviations between the various mass-conserving have also been detected for the Jeffcott rotor model with single oil film bearings. For the Jeffcott rotor with full-floating ring bearings and also for the turbocharger rotor, the deviations between the mass-conserving models have been rather small. Comparing the simulation times required with the different mass-conserving algorithms, comparatively large differences have been detected. To improve and optimize the simulation time, the proper choice of an adequate cavitation approach is an important issue.

References

[1] A. Boyaci, Numerical Continuation Applied to Nonlinear Rotor Dynamics, *Procedia IUTAM* 19 (2016) 255-265.

[2] A. Boyaci, D. Lu, B. Schweizer, Stability and bifurcation phenomena of Laval/Jeffcott rotors in semi-floating ring bearings, *Nonlinear Dynamics* (2015), 1535-1561.

[3] M.J. Braun and W.M. Hannon, Cavitation formation and modelling for fluid film bearings: a review. In IMechE Journal of Engineering Tribology 224.9 (2010), pp. 839-863.

[4] K.E. Brenan, S.L. Campbell and L.R Petzold, Numerical solution of initial-value problems in differential-algebraic equations, Volume 14, Siam (1996).

[5] A. Chasalevris, Finite length floating ring bearings: Operational characteristics using analytical methods, Tribology International 94 (2016) 571–590.

[6] A. Chasalevris, Stability and Hopf bifurcations in rotor-bearing-foundation systems of turbines and generators, *Tribology International* 145 (2020) 106154.

[7] R. Eling, M. te Wierik, R. van Ostayen, D. Rixen, Rotordynamic and Friction Loss Measurements on a High Speed Laval Rotor Supported by Floating Ring Bearings, *Lubricants* 5 (1) (2017) 7.

[8] T. Meyer, J. Kraft, B. Schweizer, Co-Simulation: Error Estimation and Macro-Step Size Control, *Journal of Computational and Nonlinear Dynamics* 16 (4) (2021).

[9] A. Muszynska, *Rotordynamics*, CRC press, 2005.

[10] C. J. Myers, Bifurcation Theory Applied to Oil Whirl in Plain Cylindrical Journal Bearings, *ASME Journal of Applied Mechanics* 51 (1984) 244-250.

[11] G. Nowald, Numerical Investigation of Rotors in Floating Ring Bearings using Co-Simulation. Dissertation, Technical University of Darmstadt (2018).

[12] A. Shabana, *Dynamics of Multibody Systems*, Cambridge University Press, 2005.

[13] B. Schweizer, M. Sievert, Nonlinear Oscillations of Automotive Turbocharger Turbines, *Journal of Sound and Vibration* 321 (2009) 955-975.

[14] B. Schweizer, Dynamics and stability of turbocharger rotor, *Archive of Applied Mechanics* 80 (2010) 1017-1043.

[15] B. Schweizer, Oil Whirl, Oil Whip and Whirl/Whip Synchronization Occurring in Rotor Systems with Full-Floating Ring Bearings, *Journal of Nonlinear Dynamics* 57 (2009).

[16] B. Schweizer, D. Lu, Semi-Implicit Co-Simulation Approach for Solver Coupling, *Archive of Applied Mechanics* 84 (12) (2014) 1839-1769.

[17] B. Schweizer, P. Li, D. Lu, Explicit and Implicit Co-Simulation Methods: Stability and Convergence Analysis for Different Solver Coupling Approaches, *Journal of Computational and Nonlinear Dynamics*, 10 (5) (2015).

[18] J.K. Wang, M.M. Khonsari, Bifurcation Analysis of a Flexible Rotor Supported by Two Fluid-Film Journal Bearings, *Journal of Tribology - Transactions of the ASME* 128 (3) (2006) 594-603.

15th SIRM – European Conference on Rotordynamics,
Darmstadt, Germany, 22nd – 24th February 2023

Simulation of the Mixed Lubrication Regime of Foil-Air Bearings

Arved Hess [1], **Jens Weber** [2]

[1] MA, HTWG Konstanz, 78462, Konstanz, Germany, arhess@htwg-konstanz.de
[2] MA, HTWG Konstanz, 78462, Konstanz, Germany, jens.weber@htwg-konstanz.de

Abstract

Foil-air bearings (FABs) are predominantly used for high-speed, oil-free applications. Offering many advantages such as friction loss at high speeds, stability and price, they lack, however, load capacity as well as start-up and coast-down friction wear resistance.

The friction losses of FABs have been studied experimentally by many authors, e.g. [11]. In order to predict the friction and, consequently, the lifespan of a FAB, the start-up and coast-down regimes are modelled in such a way that allows for accurate, efficient simulation and later optimisation of lift-off speed and wear characteristics.

The proposed simulation method applies the Kirchhoff-Love plate theory to the top foil mapping [20]. This system of differential equations is coupled with the underlying compliant foil to simulate the displacement due to the pressure buildup. Consequently, this coupled system allows for simulation from almost zero rounds per minute (rpm) to full speed. The underlying simulation model uses the finite difference method for spatial discretisation and a temporal explicit Runge-Kutta method.

Difficulties to overcome are the smooth combination of various friction regimes across the sliding surfaces as well as the synchronous coupling of Reynolds, deformation and kinematic equations with highly non-linear terms. Introducing an exponential pressure component based on Greenwood and Tripp's theory avoids impingement between the rotor and foil.

Nomenclature

d	thickness of foil $[\mathrm{m}]$
$D = 2R$	rotor diameter / radius $[\mathrm{m}]$
e_0	average of standard deviation of surface roughness $[\mathrm{m}]$
e	rotor displacement $[\mathrm{m}]$
E	Young's modulus $[\mathrm{N\,m^{-2}}]$
f	force $[\mathrm{N}]$
$F_{5/2}$	Gaussian distribution function $[-]$
h	gap height $[\mathrm{m}]$
$H = \frac{h}{e_0}$	non-dim. gap height $[-]$
k_{sf}	local compliant foil stiffness per unit area $[\mathrm{N\,m^{-3}}]$
$K_{\mathrm{sf}} = \frac{k_{\mathrm{sf}} e_0}{p_0}$	non-dim. local compliant foil stiffness $[-]$
$k_{\mathrm{tf}} = \frac{E d^3}{12(1-\nu)}$	top foil stiffness prefactor $[\mathrm{N\,m}]$
$K_{\mathrm{tf}} = k_{\mathrm{tf}} \frac{e_0}{p_0 R^4}$	non-dim. top foil stiffness prefactor $[-]$
L	bearing length $[\mathrm{m}]$
m	mass of the rotor $[\mathrm{kg}]$
$_{\mathrm{m,n}}$	matrix subscripts
$M_{\mathrm{tf}} = \frac{e_0 \rho_{\mathrm{tf}} d_{\mathrm{tf}}}{4 p_0}$	non-dim. mass of top foil $[-]$
p	pressure $[\mathrm{N\,m^{-2}}]$
$P = \frac{p}{p_0}$	non-dim. pressure $[-]$
$p_0 = \min(p_{\mathrm{amb}})$	reference pressure $[\mathrm{N\,m^{-2}}]$
s	state vector
s'	non-linear function on right hand of state equation $[-]$
t	time $[\mathrm{s}]$
w	deformation of foil $[\mathrm{m}]$
x, y	x and y position $[\mathrm{m}]$
$\epsilon = \frac{e}{\sigma}$	non-dim. rotor displacement $[-]$
$\zeta = \frac{z}{R}$	non-dim. longitudinal position $[-]$
η, β, σ	roughness parameters $[\mathrm{m,m,m}]$
η_{hys}	hysteretic damping loss factor $[-]$
μ	air viscosity $[\mathrm{N\,s\,m^{-2}}]$
ν	Poisson's ratio $[-]$
θ	angular coordinate $[\mathrm{rad}]$
$\Lambda = \frac{6\mu\Omega}{p_0}\left(\frac{R}{\sigma}\right)^2$	bearing number $[-]$
ρ	material density $[\mathrm{kg\,m^{-3}}]$
τ	non-dim. time $[-]$
$\Psi = P_{\mathrm{ff}} H$	non-dim. dependent vector of state variable $[-]$
ω	circular frequency, whirl speed $[\mathrm{rad\,s^{-1}}]$
Ω	rotation speed $[\mathrm{rad\,s^{-1}}]$

1 Introduction

Compared to other types of aerodynamic bearings, foil-air bearings (FABs) offer superior damping qualities and allow for thermal and rotational expansion of the rotor because of their compliant structure. However, the top foil separates from the rotor only after pressure buildup due to rotation. Thus, with each start and stop cycle, boundary and mixed friction are presently leading to unwanted friction losses and wear. Essentially this is the same effect reported by Stribeck [19]. Additionally, preloading the bearings can lead to increased stability at high speeds [10]. Hence, preloading leads to an unwanted conflict of goals, as the load is one of the main contributing factors to friction and wear.

The friction and wear of preloaded FABs have been experimentally quantified by Mahner et al. or San Andrés and Abraham Chirathadam [11, 16], among other authors. Therefore, the first local minimum torque measurement during start-up or coast-down is defined as the lift-off speed. Other methods of identifying the lift-off speed have been suggested, e.g. by Baginski and Żywica [1].

Modelling of the coupled system is mostly done by solving the pressure buildup with the Reynolds equation and deformation of the foil structure using various linear and non-linear structure models, e.g. [2]. The rotor motion is generally solved by defining a force equilibrium by integrating of the pressure acting on the rotor and summing up all external forces.

There has been plenty of analysis of oil-bearing start-up friction experimentally and computationally, e.g. [13, 14, 18]. The asperity contact pressure for oil bearings is often modelled by applying Greenwood and Tripp's widely used theory. There seems to be good agreement between simulation and measurement for oil-bearings which is the basis for exerting these known theories to FABs.

2 Numerical Approach

The investigated rotor-bearing model is based on three-lobe bearing design optimised for low-lift-off speeds and sufficient stability at high speeds. The numerical representation is simple to focus on modelling the boundary friction and transition to full aerodynamic lift. The following limiting conditions are introduced:

- The rotor does not tilt in the bearing; there are only two degrees of freedom for movement
- The temperature is constant
- The viscosity is constant
- The pressure at the axial ends of the bearing is kept constant
- All simplifications introduced by the compressible Reynolds equation [4]

Figure 1 depicts the basic design of the physical model.

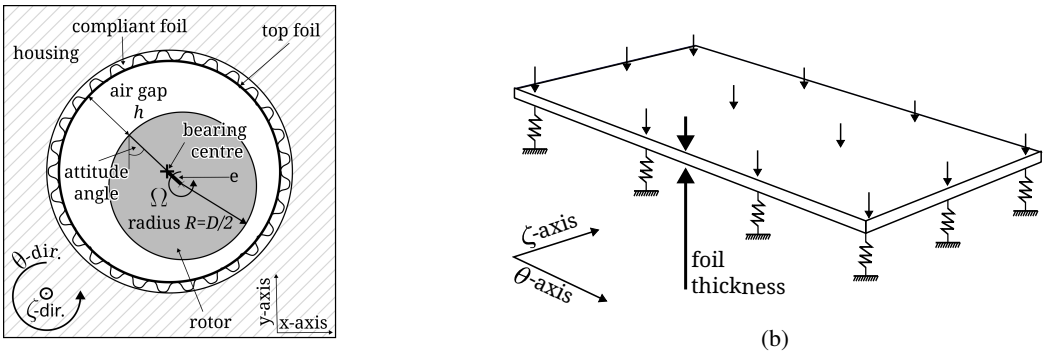

(a) (b)

Figure 1: Rotor bearing system (a) and top foil supported by springs with pressure acting on the top side (b).

The following substitution is used for non-dimensionalising the time derivatives (1).

$$\mathrm{d}t = \frac{2}{\Omega(t)}\mathrm{d}\tau \quad \longrightarrow \quad \frac{\partial \cdot}{\partial t} = \frac{\Omega(t)}{2}\frac{\partial \cdot}{\partial \tau} \quad \longrightarrow \quad \dot{(\cdot)} = \frac{\Omega}{2}(\cdot)' \tag{1}$$

A fully coupled system of equations is set up to simulate the start-up or coast-down behaviour of a FAB. The state variables for one node are listed in equation (2).

$$\boldsymbol{s} = \left[\, \Psi \;\; H \;\; H' \;\; \boldsymbol{\epsilon} \;\; \boldsymbol{\epsilon}' \,\right]^{\intercal}, \qquad \boldsymbol{s}' = \left(\left[\, \Psi \;\; H \;\; H' \;\; \boldsymbol{\epsilon} \;\; \boldsymbol{\epsilon}' \,\right]^{\intercal}\right)' \tag{2}$$

The vector comprises all dependent variables in their discretised form, with Ψ being the product of non-dimensional fluid film pressure (P_{ff}) and H, which is the non-dimensional gap height between the rotor and the top foil. The last two elements of vector $\boldsymbol{s}$ are the non-dimensional eccentricity $\boldsymbol{\epsilon}$ of the rotor from the bearing centre and its corresponding derivative with respect to non-dimensional time. The state vector can be integrated for each time step with its interconnected system of non-linear equations, which will be further explained in subsection 2.4. As all Ψ values are equal to H for ζ-edge nodes, they are removed from the system vector and system of equations. m is the number of node points in the θ-direction and n in the ζ-direction. $\boldsymbol{\epsilon}$ contains two entries, namely the x- and the y-coordinates of the rotor centre. All variables combined lead to a system with $m(n-2)+2\times mn+2\times 2$ variables and equations.

This approach has been widely used, e.g. by [3, 17]. The system of equations comprises the following equations:

- **Reynolds equation** for fluid flow (see subsection 2.1)
- **Foil deformation equation** based on force equilibrium on top foil (see subsection 2.2)
- **Equations of motion** of the rotor (see subsection 2.3)

The following sections will describe the modelling of these physical regimes.

2.1 Reynolds Equation

The fluid flow is modelled using the isothermal and compressible Reynolds equation in the form of cylindrical coordinates in equation (3).

$$\underbrace{\frac{1}{R^2}\frac{\partial}{\partial\theta}\left(\frac{p_{\text{ff}}h^3}{\mu}\frac{\partial p_{\text{ff}}}{\partial\theta}\right)+\frac{\partial}{\partial z}\left(\frac{p_{\text{ff}}h^3}{\mu}\frac{\partial p_{\text{ff}}}{\partial z}\right)}_{\text{Poiseuille flow}} = \underbrace{6\Omega\frac{\partial p_{\text{ff}}h}{\partial\theta}}_{\text{Couette flow}} + \underbrace{12\frac{\partial p_{\text{ff}}h}{\partial t}}_{\text{Unsteady flow}} \tag{3}$$

In this formula, various assumptions are made, e.g., the flow velocity perpendicular to the circumferential direction pointing to the centre of rotation being zero. These simplifications are widely used, and their accuracy is for instance discussed by Pinkus and Sternlicht [15].

2.2 Foil Deformation

The foil deformation is modelled time-dependent with damping as well as with mass inertia. The mass inertia term does not contribute significantly to the response of the bearing at low speeds (see equation (4)). A pressure equilibrium on the top foil defines the equation.

$$\underbrace{k_{\text{tf}}\nabla^2\nabla^2 w}_{\substack{\text{force from}\\ \text{top foil deformation}}} + \underbrace{k_{\text{sf}}w}_{\substack{\text{force from}\\ \text{compliant foil}\\ \text{deformation}}} + \underbrace{k_{\text{sf}}\frac{\eta_{\text{hys}}}{\omega}\dot{w}}_{\substack{\text{damping force from}\\ \text{compliant foil}}} + \underbrace{\rho_{\text{tf}}d_{\text{tf}}\ddot{w}}_{\substack{\text{mass inertia force}\\ \text{from}\\ \text{top foil}}} = \underbrace{p-p_{\text{amb}}}_{\substack{\text{pressure acting on}\\ \text{top foil}}} \tag{4}$$

The variable k_{tf} is the geometry-dependent stiffness of the top foil and k_{sf} the stiffness of the supporting compliant foil based on the simple elastic foundation model (SEFM) from [21]. ω represents the whirl frequency of the rotor. Subsequently, it is assumed that $\omega=\Omega$, which is a simplification also used by Bonello and Pham [3]. Lastly, ρ_{tf} and d_{tf} are the density and thickness of the top foil.

Due to the bearing number Λ approaching zero at slow rotor speeds, there is practically no pressure buildup from the Reynolds equation (3) [15]. Consequently, another force must be acting on the foil to separate it from the rotor. This force is estimated using Greenwood and Tripp's model of contact pressure due to rough surfaces

touching each other. The basic approach for solving two surfaces in boundary lubrication has been described by Sander et al. for oil-lubricated journal bearings. However, for setting up a fully-coupled model for FABs, the pressure buildup from Reynold's equation and Greenwood and Tripp's model must be combined. First, the contact pressure p_{GT} for boundary friction as described in subsubsection 2.2.1. Second, the fluid film pressure p_{ff} which is defined through the Reynolds equation (3).

$$p = p_{\text{GT}} + p_{\text{ff}} \tag{5}$$

In this approach, the underlying compliant foil is not coupled in θ- or ζ-direction, which, depending on the geometry of the compliant foil, can be inaccurate. However, it has been shown that a SEFM model seems to be in good agreement with measurements in many cases [12].

The Kirchhoff-Love plate model couples deflections in θ- and ζ-direction and distributes point contacts across the top foil. A linear Kirchhoff-Love plate equation is used for simplicity, ignoring the non-linearity effects of large deformations. The assumption of small deflections for the plate theory seems inadequate as this assumption is only valid up to deflections smaller than 20% of the plate thickness, which is usually exceeded by preloading the bearing or with high unbalance and, thus, large rotor movements [20]. However, the goal is to prove that a full 2D simulation is feasible even with zero net aerodynamic force acting on the top foil free edges for runs from zero rpm to full separation of the top foil from the rotor. Moreover, the stiffening effect of the curvature of the top foil is modelled by an artificial stiffening in the ζ-direction by treating the top foil material as orthotropic with different Young's moduli in θ- and ζ-direction. This approach has been used by San Andrés and Kim [17] before. The boundary conditions of the Kirchhoff-Love plate are modelled using Kirchhoff's supplementary forces.

Compared to other approaches, when simulating very low speeds, the pressure buildup from the Reynolds equation is practically zero. This behaviour of the Reynolds equation is discussed in subsubsection 2.2.2.

2.2.1 Contact Pressure

The contact pressure is modelled using an asperity pressure approach considering the rotor-foil combination's surface roughness. This approach has been suggested by Greenwood and Tripp [6] and has since found widespread usage in the simulation of elastohydrodynamic lubrication phenomena. The pressure in this model is solely dependent on the distance h and is used as an independent variable in equation (6)

$$p_{\text{GT}} = \frac{8\sqrt{2}}{15}\pi\left(\eta\beta\sigma\right)^2\sqrt{\frac{\sigma}{\beta}}E_{\text{eff}}F_{5/2}(H) \tag{6}$$

The non-dimensional surface height H is defined as $H = h/e_0 = h/\sigma$. Furthermore, η, β and σ are experimental roughness parameters, and E_{eff} is the effective combined elastic modulus between foil and rotor e. g. defined in [9].

The Gaussian distribution function $F_{5/2}$ is approximated algebraically by various authors to speed up numerical simulations [8, 5]. The approximation used in this approach is based on [8].

$$F_{5/2}(H) = 0.616634\, e^{0.00121735H^4 - 0.02342695H^3 - 0.2696729H^2 - 1.7433954H} \tag{7}$$

It has to be noted that the contact pressure model is only defined for $0 < H \leq 4$. The discontinuity leads to a non-smooth transition between the two pressure sources, which leads to small time steps and inaccuracies in the transition region in this modelling approach.

2.2.2 Considerations of Low Speeds and Small Gaps

Pinkus and Sternlicht [15] elaborated on the inaccuracy of the compressible Reynolds equation for tiny bearing numbers (Λ) as well as small gaps. The inaccuracies arise due to the continuum theory of flow not modelling the flow conditions correctly at these conditions. The flow in these regions is more accurately described as molecular flow. One method for simulating these conditions is to use "slip flow" models. These models discard the "no-slip" conditions on boundary surfaces and can be used to advance the continuum flow model into regions of the molecular flow. However, it is also stated that the incompressible Reynolds equation is a good approximation for low bearing numbers. The incompressible Reynolds equation is linear when uncoupling p from h and can be solved very efficiently.

2.3 Rotor Motion

The rotor motion is modelled in two dimensions. As for initial simulations, a symmetrical bearing is assumed with load solely acting on its centre plane. It is derived by force equilibrium on the centre of gravity (CG) of the rotor (8).

$$m\ddot{\boldsymbol{e}} = \boldsymbol{f}_{\text{foil}} + \boldsymbol{f}_{\text{ext}} = \boldsymbol{f}_{\text{rot}} \tag{8}$$

With $\boldsymbol{f}_{\text{rot}}$ being the resultant force vector acting on the CG of the rotor and $\ddot{\boldsymbol{e}}$ the acceleration vector of the CG of the rotor. Moreover, $\boldsymbol{f}_{\text{foil}}$ is the force acting on the rotor surface due to the pressure p, and $\boldsymbol{f}_{\text{ext}}$ is the resultant vector of all external forces acting on the rotor.

Rotational inertia forces do not act on the rotor as the reference system is in the CG. All forces acting on the rotor are depicted in figure 2a.

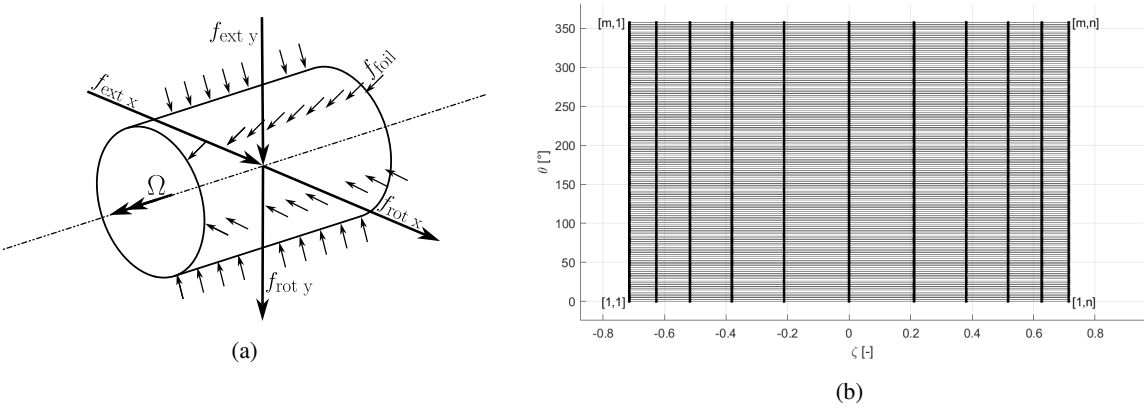

(a) (b)

Figure 2: Forces acting on the rotor (a) and non-uniform grid for simulation (b).

The pressure force from the foil (f_{foil}) is the integral of the sum of the contact pressure (p_{GT}) and the fluid film pressure (p_{ff}) (9)

$$\boldsymbol{f}_{\text{foil}} = \begin{bmatrix} f_{\text{foil x}} \\ f_{\text{foil y}} \end{bmatrix} = R^2 \int_{-L/2R}^{+L/2R} \int_{0}^{2\pi} (p_{\text{GT}} + p_{\text{ff}}) \begin{bmatrix} \cos(\theta) \\ \sin(\theta) \end{bmatrix} \mathrm{d}\theta \mathrm{d}\zeta \tag{9}$$

2.4 System of Equations

A system of non-linear differential equations is formulated for solving the transition from very low rpm to lift-off speeds. This system of equations consists of the Reynolds equation in non-dimensional form (10), the equation for foil deformation (11) and the forces acting on the rotor (12). The non-dimensional values are $\Psi = P_{\text{ff}}H$ and $H = h/e_0 = h/\sigma$. Additionally, K_{tf} and K_{sf} are non-dimensional stiffnesses, and M_{tf} is the non-dimensional top foil mass. The non-dimensional rotor displacement $\boldsymbol{\epsilon}$ is defined as $\boldsymbol{e}/\sigma$. Furthermore, the non-dimensional pressure $P = p/p_0$ is used, which again is the sum of contact and fluid film pressure.

$$\frac{\partial}{\partial\theta}\left(\Psi H^2 \frac{\partial(\Psi/H)}{\partial\theta}\right) + \frac{\partial}{\partial\zeta}\left(\Psi H^2 \frac{\partial(\Psi/H)}{\partial\zeta}\right) = \Lambda\frac{\partial\Psi}{\partial\theta} + \Lambda\frac{\partial\Psi}{\partial\tau} \tag{10}$$

$$K_{\text{tf}}\nabla^2\nabla^2 W + K_{\text{sf}}W + K_{\text{sf}}\frac{\eta_{\text{hys}}}{2}W' + M_{\text{tf}}W'' = P - P_{\text{amb}} \tag{11}$$

$$\frac{m\sigma\Omega^2}{4}\boldsymbol{\epsilon}'' = \boldsymbol{f}_{\text{rot}} \tag{12}$$

The equations below show the relationship between the non-dimensional deformation W and height H.

$$W = H - H_0 + \epsilon_x \cos(\theta) + \epsilon_y \sin(\theta), \qquad W' = H' + \epsilon'_x \cos(\theta) + \epsilon'_y \sin(\theta), \qquad W'' = H'' + ... \tag{13}$$

H_0 is the initial height profile of the undeformed foil. Negative H_0 occurs at preloaded areas.

2.5 Discretisation

All spatial dimensions are discretised using higher-order finite difference formulations on non-uniform grids. The order for the spatial discretisation is the 4th order in the circumferential (θ) direction and the 6th order in the longitudinal direction (ζ). The difference in order is due to numerical instabilities at regions with large second derivatives. For the same reason, a non-uniform mesh refines regions of high pressure gradients. Figure 2b shows the full mesh for the case detailed in the appendix. Previous simulation results show moderately high state vector derivatives in the ζ-direction despite being near the edges. The derivates in θ-direction are comparatively high, necessitating higher mesh density along this axis. Consequently, the cell's aspect ratio is high, and the individual cells are elongated.

The spatial discretisation is based on the finite difference model with higher order accuracy in both directions. The temporal discretisation uses an implicit Runge-Kutta formula.

2.6 Computation Procedure for Simulation

Figure 3 depicts a flow chart for the simulation steps with the essential substeps.

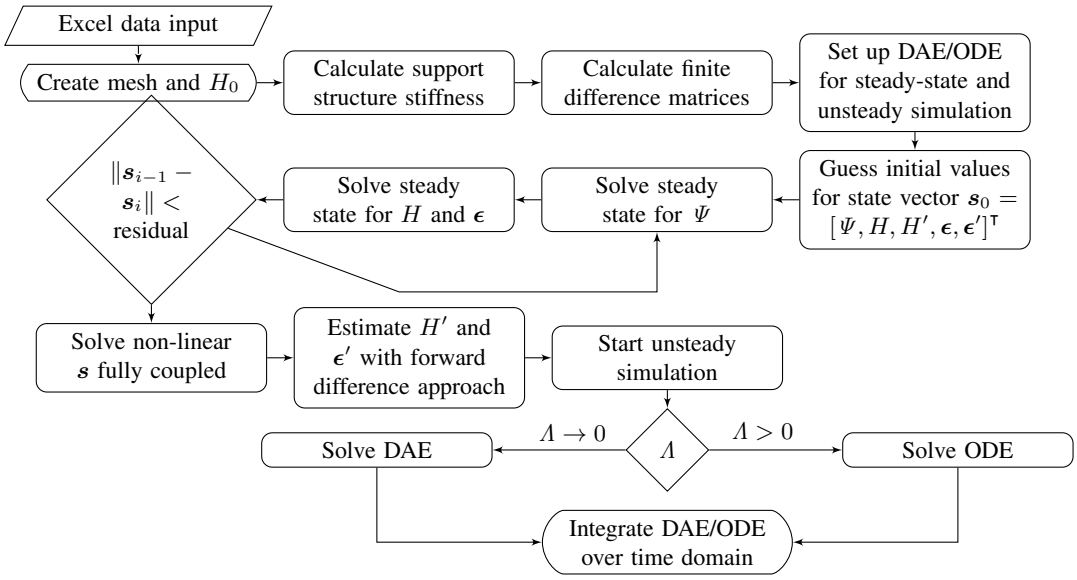

Figure 3: Flow chart for a start and stop cycle simulation.

Before the unsteady simulation of the fully coupled system can be performed, it is crucial to have correct initial conditions for the state vector $\boldsymbol{s}$. Otherwise, the unsteady simulation will fail. To find proper initial conditions for the non-linear equations, the system is first solved uncoupled for steady-state conditions. An initial state vector for a fully coupled system is found by updating the state variables iteratively. The approximated state vector is input for a fully coupled steady-state simulation. This approach is used as the high gradients of the second derivatives of the Reynolds equation, and the higher-order terms of the Greenwood-Tripp model lead to numerical oscillations that prohibit finding a solution for the fully coupled system. To guess fitting initial conditions for the unsteady simulation, the state variables Ψ' and ϵ' are estimated using finite differences in non-dimensional time. Numerical instabilities tend to increase with decreasing Λ. This instability is due to the ordinary differential equation (ODE) becoming increasingly stiff, and thus, the duration of the time steps must be reduced. A solution to this is to switch the ODE system to a differential-algebraic system of equations (DAE) for the Reynolds equation terms.

3 Results and Discussion

Figure 4 depicts a resulting orbit plot from 1 to 10000rpm with 261.8 turns. As expected, the orbit centres follow an up and right pointing so-called "Gumbel Curve" approaching the bearing centre. Moreover, the amplitude of the orbit is growing due to the increasing influence of the unbalance force.

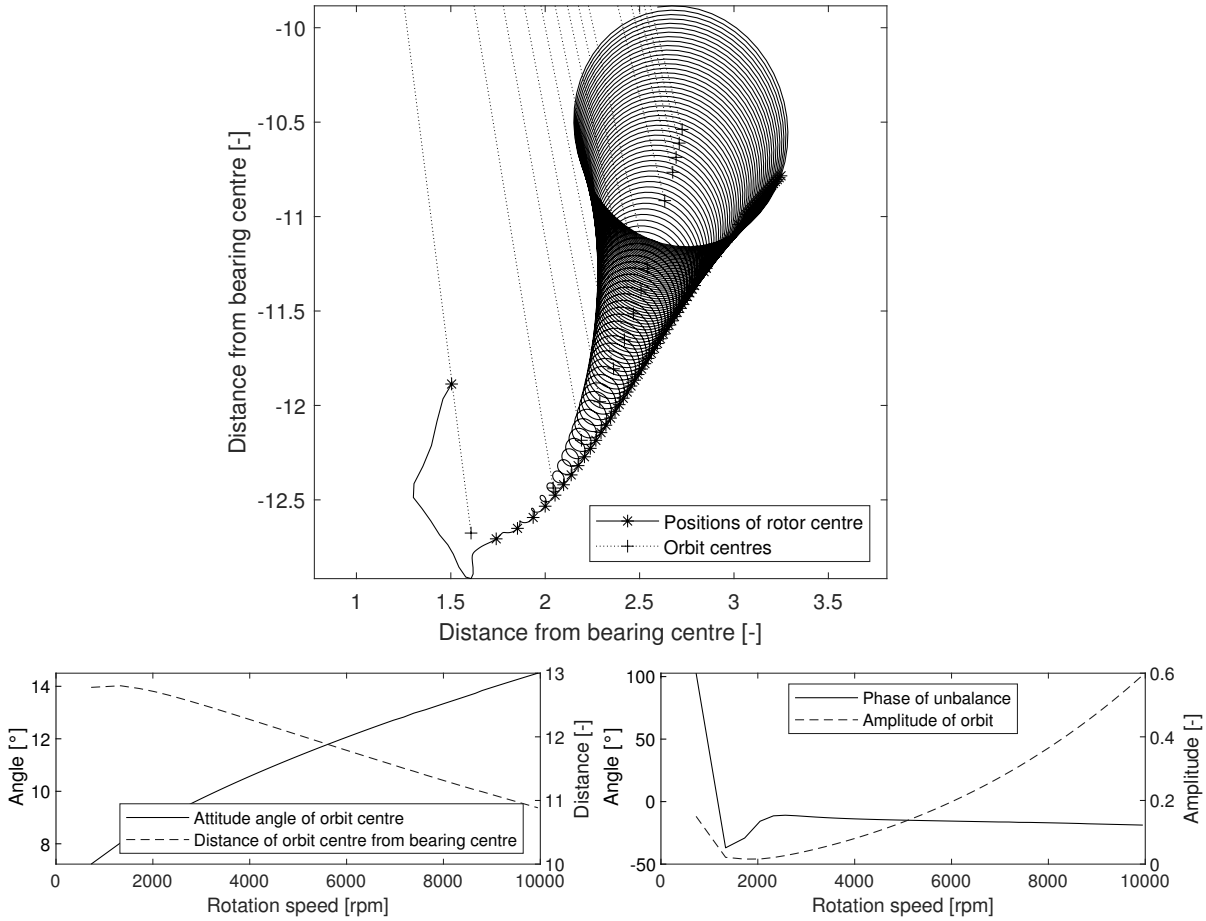

Figure 4: Orbit plot (top) with attitude angle plot (bottom left) and phase/amplitude plot (bottom right) during start-up.

The pressure buildup from very low speeds results mainly from contact pressure due to the very low bearing numbers. The pressure from the fluid film approaches zero at zero rpm (see figure 5a). It can be seen that the sum of contact pressure and fluid film pressure follows a slightly rising slope. Interestingly in the region where the contact pressure approaches zero, a discontinuity exists in the curve of maximum pressures. This could be explained by the limitation of the employed Greenwood and Tripp model. Contrary to many other experimental drag torque measurements, the transition between mixed and aerodynamic lubrication occurs at low speeds. This could be due to the relatively soft compliant foil and low preload, but it requires further analysis.

Interestingly, even at very low rpm, the characteristic aerodynamic pressure wedges are formed with shallow effective pressure buildup, as seen in figure 6. Further worth noting are the sharp down-pointing peaks of pressure near the ζ-edges of the bearing in the transition region. Whether they are purely numerical or physical is yet to investigate. However, these peaks seem to coincide with the peaks of contact pressure (see figure 7) at 500 and 1000rpm. These peaks appear to agree with typical wear locations on foils going through multiple start-stop cycles. It seems intuitive that the contact pressure is highest where the aerodynamic pressure is the lowest, e.g. zero fluid flow pressure buildup on the ζ-edges.

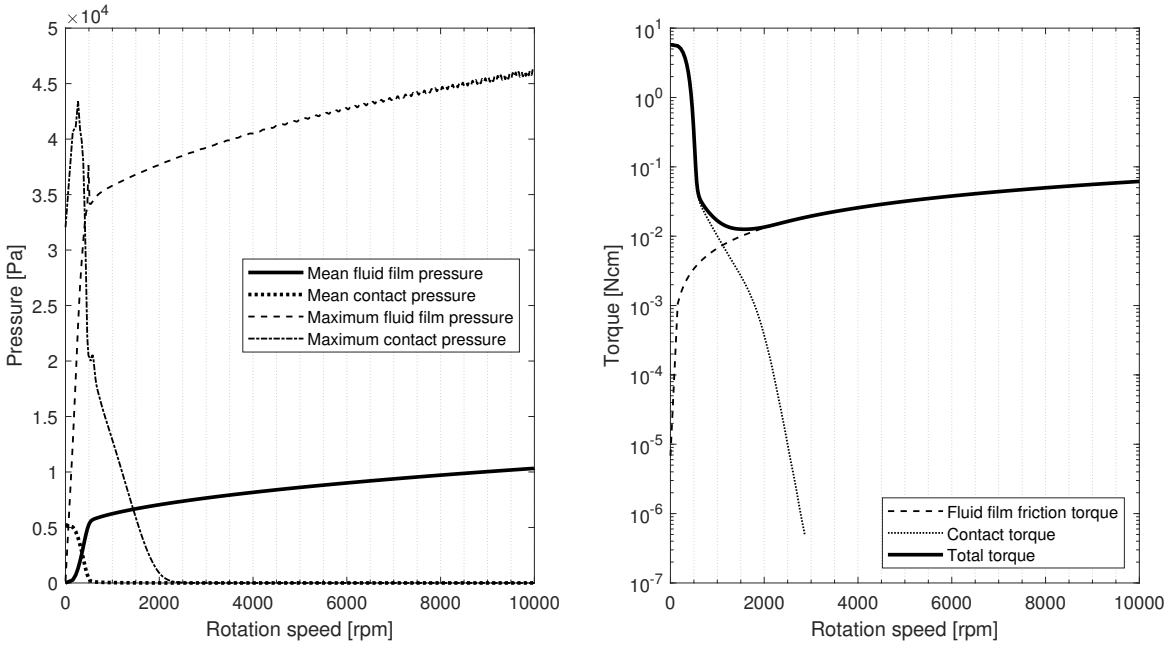

(a) (b)

Figure 5: Pressure (a) and torque during start-up (b).

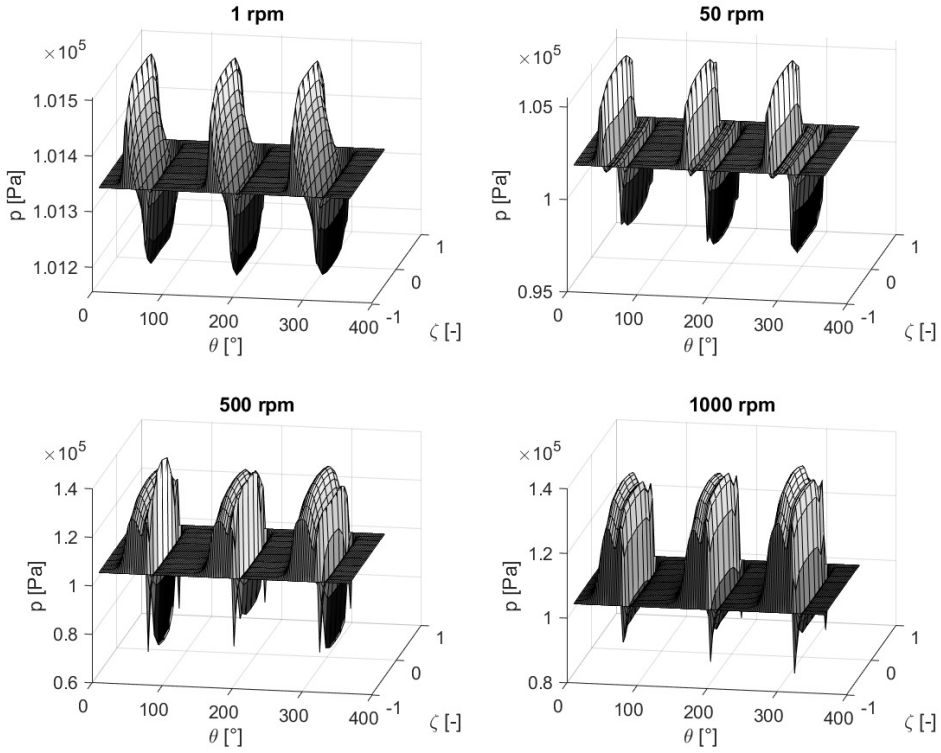

Figure 6: Aerodynamic pressure at different speeds.

The most engaging result is the representation of the torque generated by the bearing (see figure 5b). It is evaluated by the integral of contact pressure over the surface with an arbitrary friction coefficient of 0.2 for contact

pressure and by using Petroff's Law as an approximation for viscous torque generated by the fluid flow [7]. The logarithmic scale shows the transition between contact and fluid film torque and the typical "Stribeck-Gumbel" curve of a foil bearing.

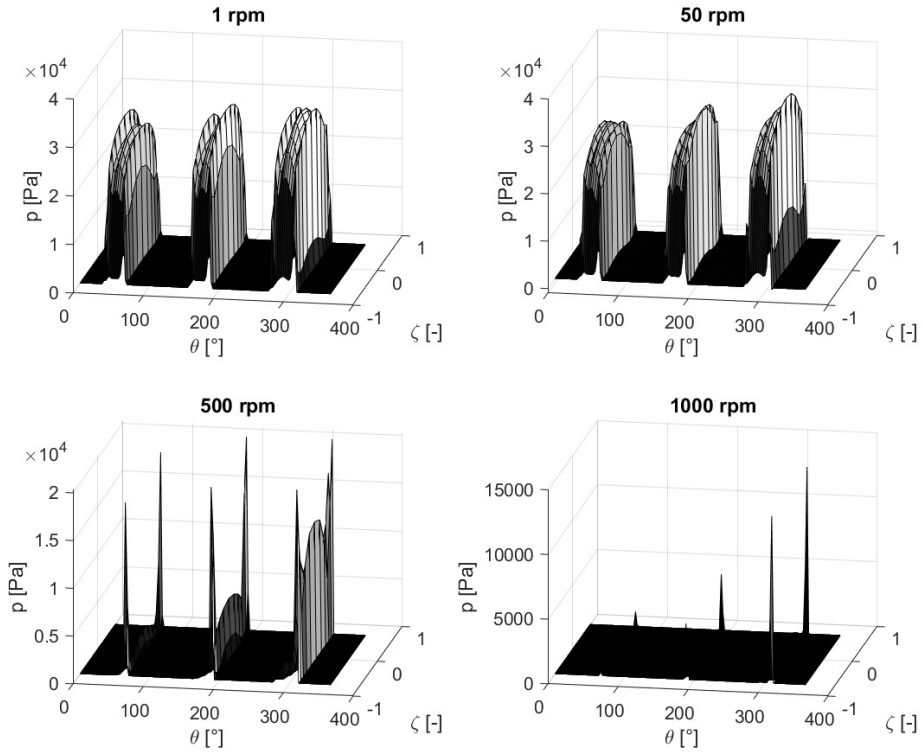

Figure 7: Contact pressure at different speeds.

4 Summary and Outlook

The presented approach combines two often ignored physical properties of FABs, which are the variation of height in two dimensions and the introduction of contact pressure due to insufficient pressure buildup at low speeds. It has been shown that it is feasible to simulate the transition between mixed lubrication and aerodynamic lubrication, even for preloaded foil bearings. Due to the simulation of the foil deformation in two dimensions, the contact pressure in the mixed lubrication regime can be determined without the limitation of constant air gaps in the ζ-direction.

It has been demonstrated that the typical "Stribeck-Gumbel" curve can be qualitatively predicted by the presented simulation approach.

The edges are typical locations of wear for FABs after several start-stop cycles. In order to increase the lifespan of the bearing, the wear has to be reduced. The presented simulation technique coherently predicts the locations of high mechanical impact and the corresponding force in the expected regions. After validating the results, an optimisation attempt of the compliant foil structure or bearing housing contour can be made in future studies to decrease mechanical wear during start-up or coast-down.

The time-steps for very low speeds are expected to be very small as the stiffness of the state equation increases with a decreasing bearing number.

The current approach uses a relatively simple finite difference model which could be replaced by a numerically more stable and accurate discretisation, e.g. finite elements. Moreover, the entirely linear model for the foil deformation is a shortcoming of this approach.

In future steps, the model will be validated using experimental data and refined to become a helpful tool for predicting the wear and lifespan of FABs.

Appendix

The following table 2 lists the simulation regime

Table 2: Start cycle conditions for simulation

Start [rpm]	Stop [rpm]	Duration [s]	Ramp	Rounds [-]	Unbalance [gmm]
1	10000	1.0	linear	261.8	0.1

The design parameters are summarised in table 3.

Table 3: Geometry of the simulated FAB

Diameter (D) [mm]	Length (L) [mm]	Preload [µm]	Foil thickness (d) [mm]	Pads [-]	Compliant foil stiffness (k_{sf}) [N/m³]
35.0	25.0	10	0.1	3	1.7×10^9

References

[1] Pawel Baginski and Grzegorz Żywica (2018): "Determination of the Lift-Off Speed in Foil Bearings Using Various Measurement Methods". In: *Mechanics and Mechanical Engineering* 22, pp. 415–424.

[2] Christoph Baum et al. (2021): "A computationally efficient nonlinear foil air bearing model for fully coupled, transient rotor dynamic investigations". In: *Tribology International* 153, p. 106434. ISSN: 0301-679X.

[3] Philip Bonello and Hai Minh Pham (2014): "The efficient computation of the nonlinear dynamic response of a foil–air bearing rotor system". In: *Journal of Sound and Vibration* 333.15, pp. 3459–3478.

[4] D. Dowson (1962): "A generalized Reynolds equation for fluid-film lubrication". In: *International Journal of Mechanical Sciences* 4.2, pp. 159–170. ISSN: 0020-7403.

[5] JA Greenwood (2008): "Discussion: Approximation of the integral of the asperity height distribution for the Greenwood-Tripp asperity contact model". In: *Proceedings of the Institution of Mechanical Engineers* 222.J7, p. 995.

[6] James A Greenwood and JH Tripp (1970): "The contact of two nominally flat rough surfaces". In: *Proceedings of the institution of mechanical engineers* 185.1, pp. 625–633.

[7] V.K. Jadon and S. Verma (2010): *Analysis and Design of Machine Elements*. I.K. International Publishing House Pvt. Limited. ISBN: 9789380026473.

[8] Radosław Jedynak (2019): "Exact and approximate solutions of the infinite integrals of the asperity height distribution for the Greenwood-Williamson and the Greenwood-Tripp asperity contact models". In: *Tribology International* 130, pp. 206–215.

[9] K. L. Johnson (1985): *Contact Mechanics*. Cambridge University Press.

[10] Tae Ho Kim and Luis San Andres (2009): "Effects of a mechanical preload on the dynamic force response of gas foil bearings: measurements and model predictions". In: *Tribology transactions* 52.4, pp. 569–580.

[11] Marcel Mahner et al. (2019): "An experimental investigation on the influence of an assembly preload on the hysteresis, the drag torque, the lift-off speed and the thermal behavior of three-pad air foil journal bearings". In: *Tribology International* 137, pp. 113–126. ISSN: 0301-679X.

[12] Sebastian von Osmanski, Jon S Larsen, and Ilmar F Santos (2017): "On the incorporation of friction into a simultaneously coupled time domain model of a rigid rotor supported by air foil bearings". In: *Technische Mechanik-European Journal of Engineering Mechanics* 37.2-5, pp. 291–302.

[13] Nadir Patir and HS Cheng (1978): "An average flow model for determining effects of three-dimensional roughness on partial hydrodynamic lubrication". In.

[14] Nadir Patir and HS Cheng (1979): "Application of average flow model to lubrication between rough sliding surfaces". In.

[15] O. Pinkus and B. Sternlicht (1961): *Theory of Hydrodynamic Lubrication*. McGraw-Hill.

[16] Luis San Andrés and Thomas Abraham Chirathadam (2012): "A metal mesh foil bearing and a bump-type foil bearing: Comparison of performance for two similar size gas bearings". In: *Journal of engineering for gas turbines and power* 134.10.

[17] Luis San Andrés and Tae Ho Kim (2006): "Computational analysis of gas foil bearings integrating 1D and 2D finite element models for top foil". In: *Annual Progress Report to Turbomachinery Research Consortium, TRC-B&C-1-06, Texas A&M University*.

[18] David E Sander et al. (2016): "Simulation of journal bearing friction in severe mixed lubrication–Validation and effect of surface smoothing due to running-in". In: *Tribology international* 96, pp. 173–183.

[19] Richard Stribeck (1902): "Die wesentlichen Eigenschaften der Gleit- und Rollenlager". In: *Zeitschrift des Verein Deutscher Ingenieure—Vereins Deutscher Ingenieure*.

[20] R. Szilard (2004): *Theories and Applications of Plate Analysis: Classical, Numerical and Engineering Methods*. Wiley. ISBN: 9780471429890.

[21] J.A. Walowit and J.N. Anno (1975): *Modern Developments in Lubrication Mechanics*. Applied Science Publishers. ISBN: 9780853345923.

15th SIRM – European Conference on Rotordynamics,
Darmstadt, Germany, 22nd – 24th February 2023

Simulation of foil bearing supported rotor systems

Steffen Nitzschke [1], **Elmar Woschke** [1], **Christian Daniel** [1]

[1] Institute of mechanics, Otto–von–Guericke University Magdeburg, 39106, Magdeburg, Germany,
{steffen.nitzschke}{elmar.woschke}{christian.daniel}@ovgu.de

Abstract

The paper deals with the numerical implementation of a bump type foil bearing in a rotor dynamic simulation in order to calculate Campbell diagram and perform run-up time integration. The realised workflow utilizes an online numerical solution of the Reynolds partial differential equation applied to ideal gas law based on finite volume method in combination with different models for the foil deformation.

A common approach is to use a 1d discretisation in circumferential direction assuming steady state conditions frequently based on analytical formulation of bump foil stiffness or finite element model of foil. This can be easily enhanced to a 2d ansatz in order to take misalignment or tilting motion of shaft into account. To describe the damping of the foil structure in an appropriate way, the time dependent foil deformation behaviour needs to be considered, which requires inclusion of inertia properties as well as a friction model. For the sake of simplicity, the friction model is handled by a Rayleigh damping approach, while a finite element based 2d-foil model is introduced. The described formulation leads to further state space equations, which are solved either by an implicit Runge-Kutta- or a Newmark-algorithm embedded in the time integration of rotor equation of motions, where the latter are treated always by the implicit Runge-Kutta solver.

1 Introduction

An essential point in the design of rotor dynamic systems is the bearing arrangement. Compared to more conventional bearing concepts such as plain and roller bearings, gas or foil bearings have significantly lower power losses, which is primarily due to the low viscosity and the associated shear stresses of the fluid used (air). Further advantages are the omission of lubricant feeding system, large temperature range, which allow for conditions of use beyond the limits of oil based bearings.

As a consequence of the low viscosity small clearance is mandatory to ensure a reasonable load carrying capacity. In order to compensate temperature growth as well as centrifugal growth of shaft, the bearing shell is designed to allow elastic deformation, which is usually realised by a system of metal foils, e.g. top foil and underlying bump foil. Moreover, the relative motion between the foils provides additional damping.

During the design process rotor dynamic simulations need to be carried out in order to predict amplitudes due to unbalance as well as subsynchronous vibrations, where the latter indicates the stability limit of the system.

2 Literature review

Typically, the task in the design of rotating systems is to predict the vibration amplitudes. For this purpose, Campbell diagrams are created in which the dependence of the natural frequencies on the rotor speed is compared with corresponding excitation frequencies from unbalance or other mechanisms in order to identify possible resonance regions. In a first approximation, linear isotropic bearing properties are assumed for this purpose, which applies well to rolling bearings. When journal bearings are used, the properties are load- and speed-dependent and can be taken from tables. Such models can also be used to obtain information on damping and the stability limit.

From a scientific point of view, the branching behavior of the solution is also of interest in order to determine the existence and number of equilibrium positions above the stability limit. The associated bifurcation analyses are based on eigenvalue considerations [7, 9, 24], often assuming geometric limit cases in order to derive analytical solutions of the Reynolds PDE[1] (short bearing theory, wide bearing theory and comparable finite length solutions).

[1] PDE – Partial Differential Equation

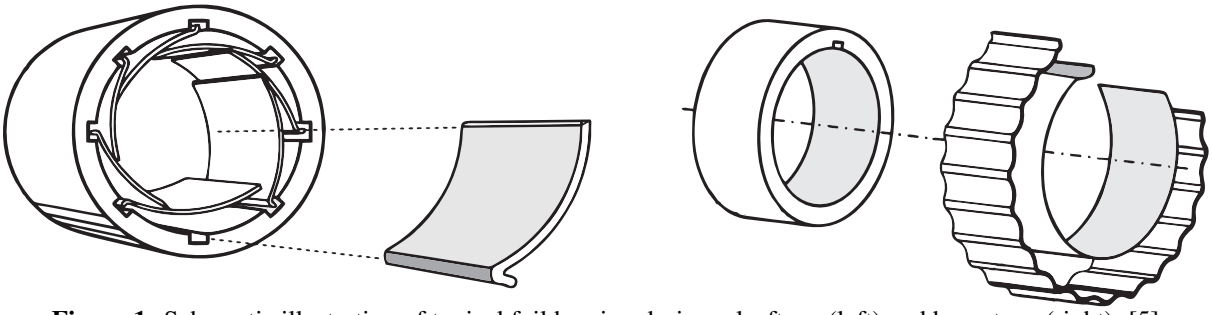

Figure 1: Schematic illustration of typical foil bearing designs: leaftype (left) and bumptype (right). [5]

In contrast, for the prediction of the actual vibration behavior under arbitrary external loads, general bearing design and without restriction of the rotor motion behavior, a numerical time integration of the equations of motion including online solution with respect to hydro- and thermodynamics has to be performed, which reflects the state of the art in the field of liquid lubricated journal bearings [1, 4, 8, 14, 25].To reduce the effort for the online solution of the Reynolds PDE, recent developments rely on semi-analytical finite element approaches[2][26, 27].

However, the focus in air bearings investigations is still often set on stationary considerations. Air bearings, specifically the foil bearings addressed here, are characterized not only by the alternative fluid but also by a compliant bearing shell structure to improve load carrying capacity and reduce frictional losses.

The typical designs of foil bearings are shown in Figure (1), while bearings with bump structure often being the subject of investigation. The modeling of the bearings varies primarily in the representation of the foil structure. Starting with simple spring models with locally constant spring stiffness (SEFM[3]) [5, 11, 13, 29, 30] increasingly complex approaches have been pursued. Of particular note is the LEFSM[4], where the bump structure is mapped based on point masses interacting via three-joint kinematics as well as springs and frictional contacts [19, 20, 31, 33].

Alternatively, the foil structure can be modeled using finite shell elements that also represent the geometric contour [17, 18, 21]. The described approaches have in common that the foil deformation is averaged over the width direction, which reduces the computational effort, but neglects effects like skewing/tilting and hence contact at the bearings edges.

Furthermore, the temperature effects in film-supported rotor systems are occasionally addressed. Gad and Kaneko [10] use an analytical model assuming pure Couette flow in the fluid.

In contrast, Michel [23] applies the finite volume method to the energy transport problem to determine spatially resolved temperatures in wave, film and foils. Similarly, Mahner [22] also analyzes steady states, consistently using FE approaches to discretize the energy equation. The discretization of the rotor and foils is two-dimensional in each case, while the gap is meshed in three dimensions.

As a third point, dynamic issues are also addressed. For reasons of efficiency, simple foil models (analogous to SEFM) are used, neglecting thermodynamics [16, 34].

With such a model subsynchronous oscillations can be simulated. However, comparisons with measured data sometimes reveal large discrepancies [32] , which is due, among other things, to the neglect or incomplete coupling of the above-mentioned influences.

3 Model

As pointed out in the abstract, this paper aims for enhancement of foil model in order to reproduce tilting due to shaft bending motions, while other tasks like advanced friction contact model or thermodynamic analysis of the bearing are left open for later investigation.

---

[2] SBFEM - Scaled Boundary Finite Element Method
[3] SEFM - Simple Elastic Foundation Model
[4] LEFSM - Lumped-Element Foil Structure Model

3.1 Reynolds PDE for air bearings

As a basis for the investigation of the dynamic behavior of air-bearing systems, the nonlinear stiffness and damping characteristics resulting from the R-PDE

$$\frac{\partial}{\partial x}\left(\frac{\varrho(p)\,h^3}{12\eta}\,\frac{\partial p}{\partial x}\right)+\frac{\partial}{\partial y}\left(\frac{\varrho(p)\,h^3}{12\eta}\,\frac{\partial p}{\partial y}\right)=u_{\mathrm{m}}\frac{\partial(\varrho(p)\,h)}{\partial x}+\frac{\partial(\varrho(p)\,h)}{\partial t} \tag{1}$$

have to be mapped. In Equation (1), a pressure-density relation must be incorporated, e.g. the ideal gas law $\varrho = p/(R\cdot T)$, which is true to a good approximation for air as a fluid in the gap. The resulting nonlinear character of the equation necessitates iterative solution strategies, which for efficiency reasons is ideally implemented using the Newton-Raphson method. Hence, Equation (1) is discretised on the bearing surface domain with a set of $n_x \times n_y$ nodes using FVM[5] by applying

$$\int_0^{2\pi r}\int_{-b/2}^{b/2}\ldots dxdy=\sum_i\left(\iint_{\Omega_i}\ldots dxdy\right)\quad\text{for}\quad i=1\ldots n_x\times n_y \tag{2}$$

to Equation (1), which then yields a corresponding set of equations

$$\underline{f}(\underline{p})=\underline{r}-\underline{\underline{A}}(\underline{p})\cdot\underline{p}=0\quad. \tag{3}$$

A Taylor series expansion then yields the Newton-Raphson iteration scheme

$$\underline{p}^{(i+1)}=\underline{p}^{(i)}-\underline{\underline{J}}(\underline{p}^{(i)})^{-1}\,\underline{f}(\underline{p}^{(i)}) \tag{4}$$

with the Jacobian

$$\underline{\underline{J}}(\underline{p}^{(i)})=\left.\frac{\partial\underline{f}}{\partial\underline{p}}\right|_{\underline{p}^{(i)}}-\left(\underline{\underline{A}}(\underline{p}^{(i)})+\left.\frac{\partial\underline{\underline{A}}}{\partial\underline{p}}\right|_{\underline{p}^{(i)}}\underline{p}^{(i)}\right)\quad. \tag{5}$$

However, for foil bearings their deformation u_{el} has to be considered as part of the air gap

$$h(x,y)=c\,(1-\epsilon\,\cos\gamma)+u_{\mathrm{el}}\quad. \tag{6}$$

Furthermore, the transient term in Equation (1) serves as link to the motion of rotor and foil structure on the one hand and attenuates the pressure development on the other hand

$$\frac{\partial(p\,h)}{\partial t}=\vartheta\,\frac{\partial h}{\partial t}+h_r\,\frac{\partial p}{\partial t}=\vartheta\,\dot{h}+h\,\frac{\partial p}{\partial t}\quad. \tag{7}$$

While $\dot{h}$ is directly linked to the translational velocity of the rotor as well as the foil, the transient development of the density or pressure respectively needs to be discretised w.r.t. time, e.g. by a backward difference

$$h\,\frac{\partial p}{\partial t}=\left.h\right|_t\,\frac{p_t-p_{t-\Delta t}}{\Delta t} \tag{8}$$

[5] FVM – Finite Volume Method

for each finite volume i. The FVM process requires the integration of Equation (8), which on the 2d grid with mesh size $\Delta x \times \Delta y$ results in

$$\iint_{\Omega_i} h \, \frac{\partial p}{\partial t} \, dxdy = h\Big|_t \, \frac{\Delta x \Delta y}{\Delta t} \, p_t - h\Big|_t \, \frac{\Delta x \Delta y}{\Delta t} \, p_{t-\Delta t} \quad . \tag{9}$$

While the last term enters in the right hand side $\underline{r}$ of Equation (3), the first one applies to the diagonal of $\underline{\underline{A}}$. Since Δt is a rather small value, Equation (9) serves as a kind of penalty formulation between the current and the past pressure, which avoids timeless changes. Furthermore, this relation ensures the positive definiteness of $\underline{\underline{A}}$, which allows a unique solution, even if no explicit fluid supply is present, which is usually the case in foil bearings.

3.2 Equations of motion

Depending on its speed, the shaft can either be modeled with rigid or elastic properties, which is in both cases mapped by the general equation of motion

$$\underline{\underline{M}}_{\text{MBS}}(\underline{q}) \, \underline{a} + \underline{h}_{\omega}(\underline{w}, \underline{q}, \underline{\dot{q}}) + \underline{h}_{el}(\underline{q}, \underline{\dot{q}}) = \underline{h}_a(\underline{q}) \quad \text{with} \quad \underline{a} = \begin{bmatrix} \underline{\ddot{r}}_A \\ \underline{\dot{w}} \\ \underline{\ddot{q}} \end{bmatrix} \tag{10}$$

resulting from a multibody simulation approach. Therein, $\underline{r}$ and $\underline{x} = [\alpha \ \beta \ \gamma]^T$ denote translational and rotational degrees of freedom for rigid body motions, where the orientation $\underline{x}$ is kinematically linked to the rotational speed $\underline{\omega}$. Furthermore, $\underline{q}$ are modal coordinates, which map superimposed elastic deformations according to the typical BFRF[6] approach. Stiffness and damping of the elastic structure enter via $\underline{h}_{el}$, while $\underline{h}_{\omega}$ represent centrifugal, gyroscopic and Coriolis forces. In contrast, outer forces as well as the nonlinear bearing forces (resulting from the pressure distribution p by integration w.r.t. bearing surface) enter via the right hand side vector $\underline{h}_a$.

In general, Equation (10) can also be used to handle the foil deformation, but since the foil does not move w.r.t. the inertial system

$$\underline{\underline{M}} \, \underline{\ddot{u}}_{\text{el}} + \underline{\underline{D}} \, \underline{\dot{u}}_{\text{el}} + \underline{\underline{K}} \, \underline{u}_{\text{el}} = \underline{f}_{\text{el}} \tag{11}$$

may also be used, e.g. for the sake of simplicity or due to efficiency reasons. Details on different methods to determine the mass, damping and stiffness matrices are given in Section 4.2. Since the pressure in the bearing acts on the foil as well as on the shaft, the bearing forces enter also in Equation (11) in the vector $\underline{f}_{\text{el}}$.

3.3 Time integration

Typically, the mechanical degrees of freedom are arranged in the state-space form

$$\underline{z}_{\text{MBS}} = [\underline{r}_a \ \underline{x} \ \underline{q} \ \underline{\dot{r}}_a \ \underline{\omega} \ \underline{\dot{q}}] \quad . \tag{12}$$

Accordingly, the corresponding deriviations w.r.t. time can be gathered by solving Equation (10) for the accelerations

$$\underline{\dot{z}}_{\text{MBS}} = [\underline{\dot{r}}_a \ \underline{\dot{x}} \ \underline{\dot{q}} \ \underline{\ddot{r}}_a \ \underline{\dot{\omega}} \ \underline{\ddot{q}}] \equiv \underline{f}(t, \underline{z}_{\text{MBS}}) \quad . \tag{13}$$

Starting with some initial values $\underline{z}_{\text{MBS}}(t = 0)$ a time integration scheme for ODEs[7]

$$\underline{z}_{\text{MBS},t+\Delta t} = \int_{\hat{t}=t}^{\hat{t}=t+\Delta t} \underline{f}(t, \underline{z}_{\text{MBS},t}) \, d\hat{t} \tag{14}$$

---

[6] BFRF – Body Fixed Reference Frame
[6] ODE – Ordinary Differential Equation

can be applied for their successive solution. Here, a semi-implicit one-step algorithm of second order based on [12] has proven as suitable. Therein, automatic choice of time step is implemented using an embedded algorithm of third order.

While this method is well suited for non-linear stiff systems with comparatively small number of unknowns, for larger systems of the type of Equation (11) a Newmark method

$$\underline{\underline{K}}^* \underline{u}_{\mathrm{el},t+\Delta t} = \underline{f}^* \qquad \text{with} \tag{15}$$

$$\underline{\underline{K}}^* = \underline{\underline{K}} + \frac{1}{\beta \Delta t^2}\,\underline{\underline{M}} + \frac{\gamma}{\beta \Delta t}\,\underline{\underline{D}} \tag{16}$$

$$\underline{f}^* = \underline{f}_{\mathrm{el},t} + \left[\frac{1}{\beta \Delta t^2}\,\underline{u}_{\mathrm{el},t} + \frac{\gamma}{\beta \Delta t}\,\dot{\underline{u}}_{\mathrm{el},t} + \left(\frac{1}{2\beta} - 1\right)\,\ddot{\underline{u}}_{\mathrm{el},t}\right]\,\underline{\underline{M}} \tag{17}$$

$$+ \left[\frac{\gamma}{\beta \Delta t}\,\underline{u}_{\mathrm{el},t} + \left(\frac{\gamma}{\beta} - 1\right)\,\dot{\underline{u}}_{\mathrm{el},t} + \left(\frac{\gamma}{2\beta} - 1\right)\Delta t\,\ddot{\underline{u}}_{\mathrm{el},t}\right]\,\underline{\underline{D}} \tag{18}$$

is often the better choice. The parameters are set as $\gamma = 0.6$ and $\beta = \frac{1}{4}(\gamma + 0.5)^2$ in order to add numerical damping for high-frequency modes and to ensure unconditional stability [28]. Again an error estimator [35] is used to control the step size following the recommendations in [28]. However, in order to use Newmark together with the ODE solver, a common time step is chosen based on the minimal time step $\Delta t = \min(\Delta t_{\mathrm{MBS}}, \Delta t_{\mathrm{Newmark}})$. Finally, this time step is also used for the treatment of the transient term Equation (9) in the Reynolds PDE, where a decoupled backward Euler method is applied as suggested in [15].

4 Results

The described model needs to be validated against measurements or simulation results present in the literature. One of the earliest papers with comparatively good description of the used equipment and the measured data was written by Ruscitto in 1978 [29], which has over the years turned out as a kind of bench mark [2, 3, 6]. On an overhung shaft supported in ball bearings, the test bearing is placed at the free end. The test bearing housing, on which the load is applied, is able to move translatory but rotations are constrained. The bearing parameters as well as operating conditions are given in Table (1). The data was used to set up a finite element model of top and bump foil using four-node shell element[8]. The resulting model as well as the used constraints are shown in Figure (2). The model can be used to determine the system matrices, which occur in Equation (10). Alternatively, the radial stiffness of the foil structure is determined by applying unit loads in radial direction on each node. In order to avoid in this case intersection of bump and top foil, both are connected node to node in radial direction where the top foil touches the bump foil. Averaging the displacements and inverting then yields a radial stiffness $c_{FE,average} = 10 \times 10^{10}\,\mathrm{N/m^3}$, which is larger than the analytical formula by Heshmat $c_{analytical} = 0.47 \times 10^{10}\,\mathrm{N/m^3}$ [11], whereby top foil stiffness neglected .

4.1 Steady state validation

According to the experimental test procedure in [29], the simulation was set up as single mass oscillator with the foil bearing supporting the bearing housing, while the shaft was only able to rotate. Here, the 1d-ODE foil model was chosen to model the foil, cf. Section 4.2. The load was applied by a smooth transition from zero to full value in order to avoid shock. Once the initial disturbances have been vanished, the minimal gap was determined.

[8] In Ansys: SHELL181 – four-node element with six degrees of freedom at each node.

Table 1: Parameters and operating conditions according to [29]

width	38.1	mm	shaft speed	30000/45000/60000	1/min
diameter	38.1	mm	load	5 . . . 200	N
clearance	57.0	μm			
no. of bumps	26	[−]	ambient pressure	101325	Pa
bump width	3.556	mm	viscosity	$1.85 \cdot 10^{-5}$	$\mathrm{N\,s/m^2}$
bump height	0.508	mm			
bump distance	4.572	mm			
foil thickness	0.106	mm			

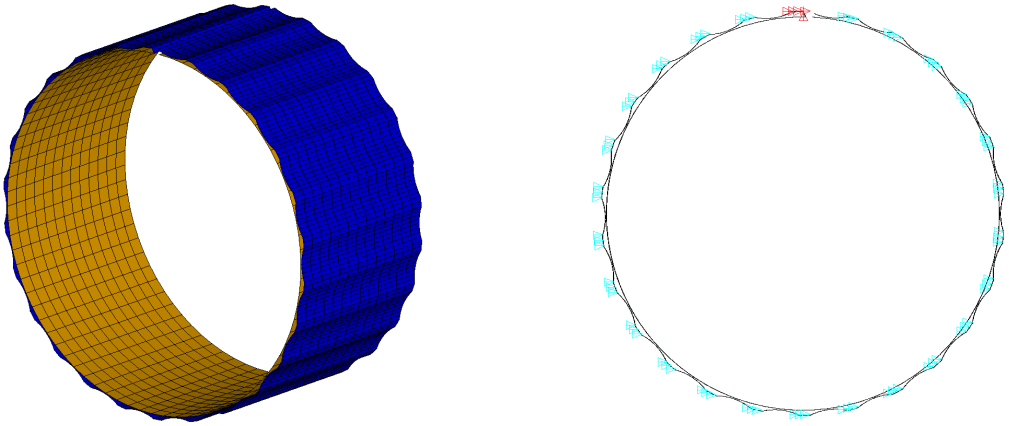

Figure 2: FE model of foil structure according to [29] with shell elements: top-foil (yellow ocher) and bump-foil(blue) in 3D view (right) and 2d view with boundary conditions (left). Cyan symbols mark the constrained radial displacements of bump foil, while red symbols mark the clamping of both foils at the bearing's top.

The comparison of measurement and simulation shows overall a good accordance for all loads as well as for all rotational speeds, cf. Figure (3). Two graphs are available for each measured rotational speed, where one relates to the minimal gap in the bearing center line, while the second graph illustrates the minimal gap on a slice parallel to the center line, but axially shifted by a quarter of the bearing width. The latter is expected to match the axial average of the foil displacement, which is a good measure for the results of the 1d-ODE foil model, since this is based on the axial averaged pressure. It can be seen, that the simulation results are always slightly above the measurement mean graphs for all rotational speeds. However, due to the typical pressure distribution one would expect the center values to be larger than the mean values, which is only true for $45.000\,1/\mathrm{min}$ and $60.000\,1/\mathrm{min}$. Ruscitto mentions tilting/cocking as possible reason for the differing behaviour at $30.000\,1/\mathrm{min}$; other authors [2] argue, that the stated bearing clearance in the reference is too large and should be diminished in order to get the

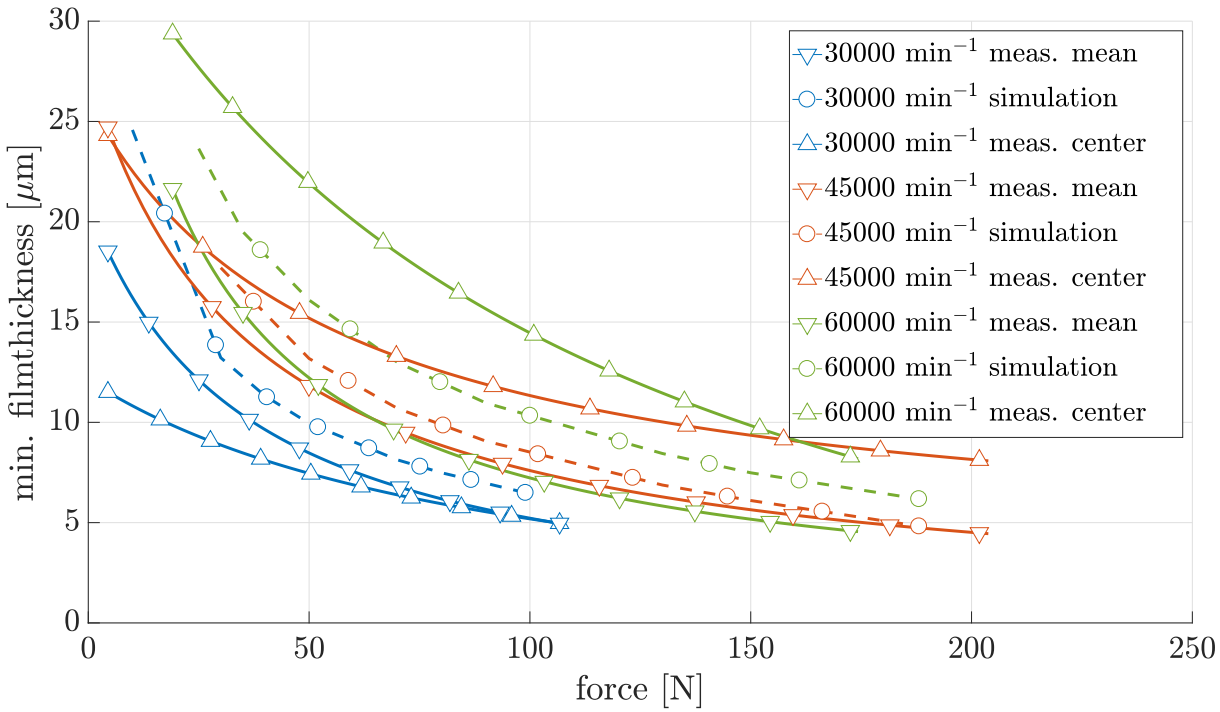

Figure 3: Minimal film thickness vs. applied force at different speeds: Measurement data was available at bearing centerline (center) and on the half between the center and the edge, which is expected to coincide with the axial mean value (mean) [29]. Since simulation was performed with axial averaged foil deflection, the results correlates with the mean measurements.

curve in better coincidence.

4.2 Different foil models

For the sake of simplicity and better comparability, different foundation models for the foil structure are created

1: 1d-ODE: constant foil displacement in axial direction with simple elastic foundation,
2: 1d-Newmark: constant foil displacement in axial direction with simple elastic foundation,
3: 2d-ODE: 2d foil deflection is allowed with finite element-based elastic foundation,
4: 2d-Newmark: 2d foil deflection is allowed with finite element-based elastic foundation.

The first one is as mentioned earlier widely used in literature since it provides a good compromise between accurateness and computational cost. However, its main drawback is the missing ability to map misalignment or tilting between shaft and foil structure/housing. This is tolerable during bearing design but in analyses of the whole rotor-bearing system in order to check the occurrence of subsynchrounous vibrations, the model lacks of damping. Hence, model 3 and 4 are introduced, which account for possible tilting. They use a finite element based elastic foundation according to Figure (2) instead of simple elastic foundation. This ensures an axial coupling between nodes, especially at the bearing edges: Due to pressure boundary at the bearing edge the resulting load is always zero there. Hence, in models without cross coupling between the nodes, the deformation at the bearing edge is per se zero, which doesn't map the reality and moreover leads to massive rigid body contact there. In the 1d models 1 and 2 this is avoided by axial averaging. However, therewith the model 3 and 4 are able to handle tilting shaft motions. Moreover, the models differ by the method used for integrating Equation (10) w.r.t. time. While model 1 and 3 use the force-states approach common in multibody system simulation in conjunction with the ODE integrator Equation (14), the models of type 2 and 4 use the Newmark method described in Equation (15).

Both time integration methods are to be compared here, since handling a foil structure with $2 \times n_x \times n_y$ force states in an ODE method causes comparatively large state vectors. The used ODE method involves a Jacobian, which must be computed repeatedly by numerical differentiation. This leads to a large number of additional calls of the equations of motion as well as the Reynolds-PDE and hence to high computational effort. In contrast, the Newmark method is well suited for larger number of unknowns as they occur in FE-systems.

Hence, at first the 1d models with simple elastic foundation, but different time integration methods are compared, cf. Figure (4). The figure shows a good accordance of both methods, which proves the general applicability of the Newmark method in this context. Besides, the Newmark method is even with low numbers of unknowns as they appear in the models slightly faster than the pure ODE approach (reduction $\Delta t_{rel} \approx 1\%$).

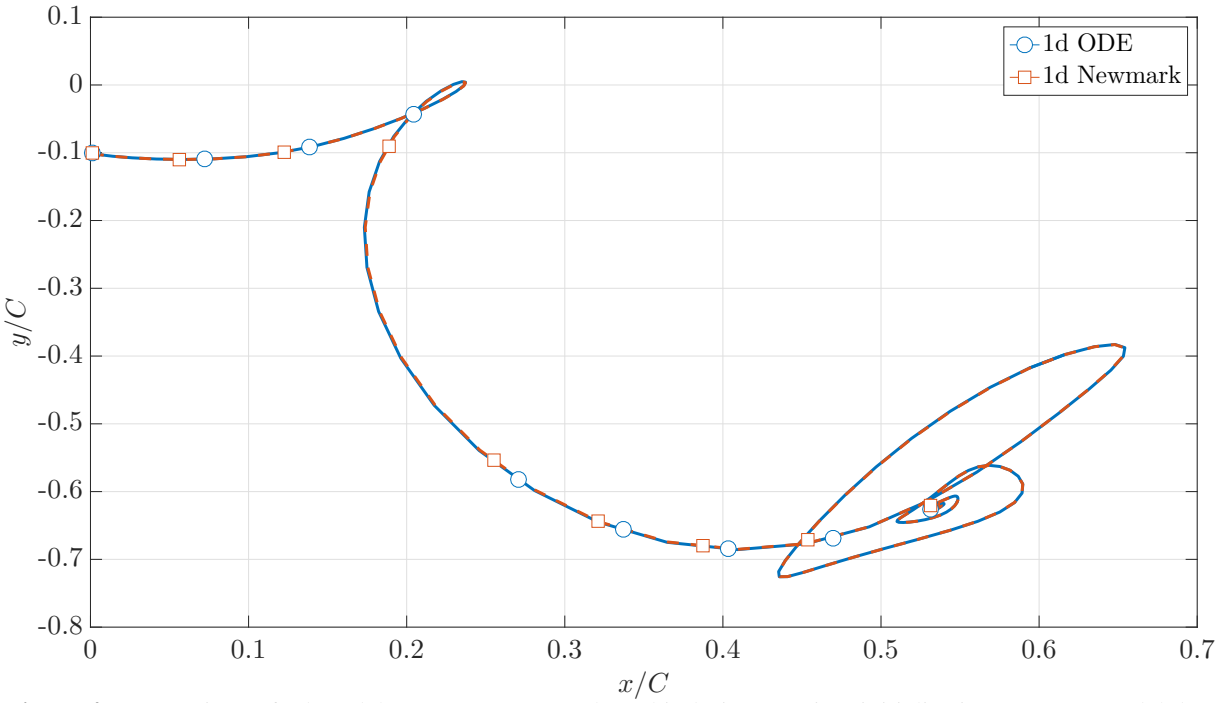

Figure 4: Comparison of 1d models ODE vs. Newmark: Orbit during transient initialisation process. Model data corresponds to Table (1).

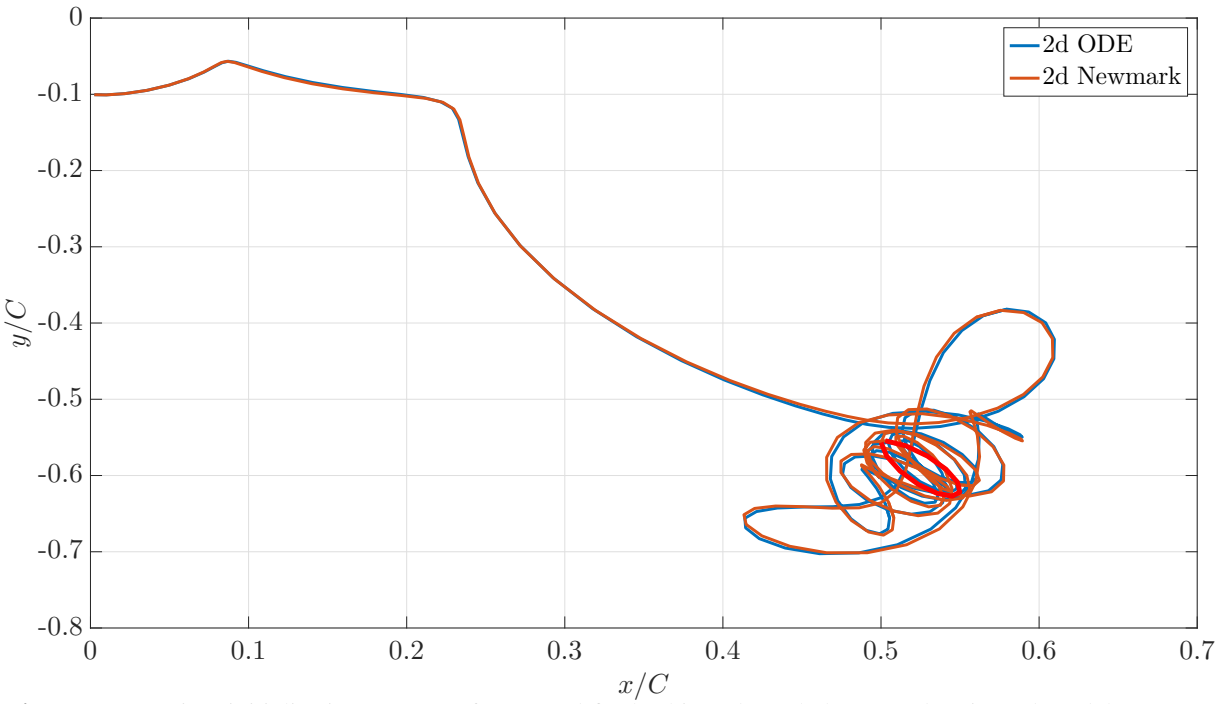

Figure 5: Transient initialisation process of rotor and final orbit under unbalance (red) using 2d models ODE vs Newmark.

The results obtained with model type 3 and 4 including finite element foil structure are shown in Figure (5). Again the transient initialisation process under steady load of $40\,\mathrm{N}$ at $45.000\,1/\mathrm{min}$ and an additional unbalance is plotted. The results of both methods coincide very well at the beginning while later on some minor differences occur.

The corresponding pressure distribution as well as the top foil deformation are plotted in Figure (6). In the foil deflection, the underlying bump structure and the clamping of both foils at the bearing's top are readily identifiable. However, the pressure distribution is – at least under this load scenario – still smooth; the bump structure is not recognizable here. Finally, a look on the computational effort shows, that Newmark 2d method is with significantly faster than the ODE method (reduction $\Delta t_{rel} \approx 80\%$). This is due to the large amount of force states ($2 \times n_x \times n_y = 2 \times 79 \times 14 = 2212$) in the ODE method, which causes high effort for obtaining the Jacobian needed in

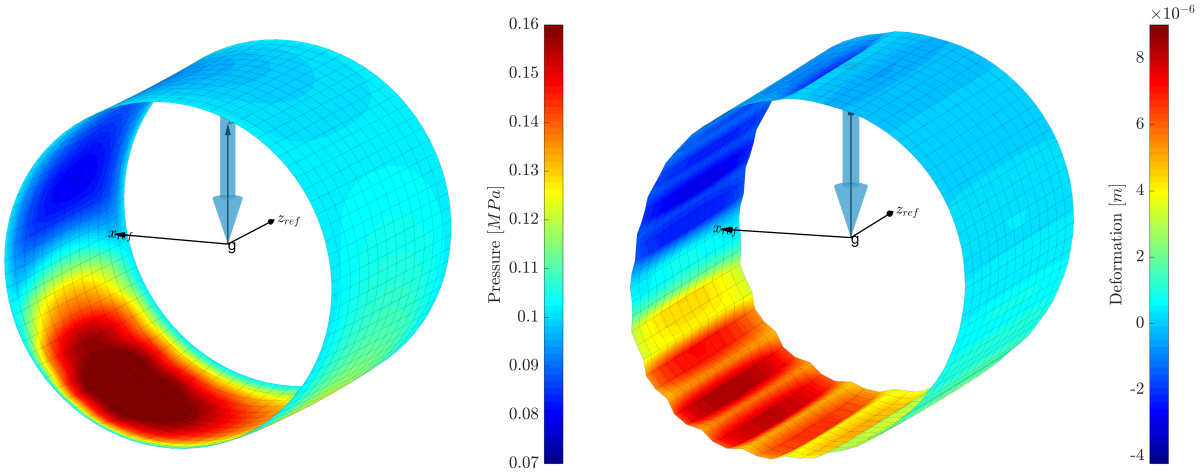

Figure 6: 3d representation of pressure (left) and top foil deformation (right) according to model type 3. Bump structure as well as clamping of foil on top of bearing are readily identifiable. The blue arrow represents direction of load. Instant of time corresponds to maximal deflection of final orbit in Figure (5).

Equation (14).

5 Outlook

The paper at hand aims for the simulation of rotor-bearing systems with foil bearings. Since in the complete model tilting may occur due to shaft bending motion, the bearing model should be able to handle this. Hence, the usual simple elastic foundation model was enhanced based on a FE model of bump and top foil structure.

Of course, the foil model is still rather simple, since damping was only considered by Rayleigh approach. Thus, the next step will be to consider both foils as separated bodies in the sense of multibody systems in order to introduce contact forces at their intersection using a penalty-like contact formulation in normal direction as common in FE applications. If necessary, a nonlinear penalty stiffness characteristic, e.g. based on the roughness contact according to Greenwood-Williamson/Tripp, may be better suited in the context of time integration, since this enables a continuous transition during the contact closing process and thus tends to provide larger time step sizes. In addition to the described normal contact, the tangential contact needs to be modeled using a rheological friction model (e.g. Coulomb models or Jenkins elements), which makes it possible to take into account the relevant damping properties of the film structure in the rotor dynamics.

With regard to the numerical aspects, the FE foil model can be transformed into the modal space in order to reduce the number of unknowns by selecting only relevant mode shapes. Additionally, due to the decoupling of foil degree of freedoms this allows for replacing the solution of the linear system of equations in the Newmark method Equation (15) by simple division, which will decrease the necessary computational effort.

Nomenclature

d	diameter	ψ	relative clearance $\left(=\frac{2\,c}{d}\right)$
b	width	β	bulk modulus of oil
h	film width	ω	rotational speed
p	pressure	η	dynamical viscosity of oil
t	time	Ω	computational domain
u_m	effective surface velocity $\left(=\frac{\omega_\mathrm{shaft}-\omega_\mathrm{shell}}{2}\,\frac{d}{2}\right)$	ε	relative eccentricity $\left(=\frac{2\,e}{d}\right)$
x	circumferential coordinate	ρ	density
y	axial coordinate	ν	Poisson's ratio
c	absolute clearance	E	Young's modulus
$\underline{\underline{K}}$	stiffness matrix	$\underline{\underline{J}}$	Jacobian
$\underline{\underline{M}}$	mass matrix	$\underline{\underline{r}}$	right hand side vector
$\underline{\underline{D}}$	damping matrix	$\underline{\underline{f}}$	force vector

References

[1] Alakhramsing, S., van Ostayen, R. and Eling, R. (2015). Thermo-hydrodynamic analysis of a plain journal bearing on the basis of a new mass conserving cavitation algorithm, *lubricants* **3**(2): pp. 256–280.

[2] Andrés, L. S. and Kim, T. H. (2009). Analysis of gas foil bearings integrating FE top foil models, **42**(1): pp. 111–120.

[3] Andrés, L. S. and Kim, T. H. (2010). Thermohydrodynamic analysis of bump type gas foil bearings: A model anchored to test data, **132**(4).

[4] Baldauf, M. (2019). *Thermal-Hydraulic Coupling of Floating Ring Bearings in Transient Run-up Simulations of Automtove Turbochargers*, PhD thesis, Universität Kassel.

[5] Baum, C. (2017). *Zur Dynamik einfacher Rotoren in aerodynamischen Radialgleitlagern mit Pufferfolie*, PhD thesis, Karlsruher Institut für Technologie.

[6] Bonello, P. and Pham, H. (2014). The efficient computation of the nonlinear dynamic response of a foil–air bearing rotor system, **333**(15): pp. 3459–3478.

[7] Boyaci, A. (2011). *Zum Stabilitäts- und Bifurkationsverhalten hochtouriger Rotoren in Gleitlagern*, Dissertation, Karlsruher Institut für Technologie.

[8] Chatzisavvas, I. (2018). *Efficient THD Radial and Thrust Bearing Modeling for Transient Rotor Simulations*, PhD thesis, TU Darmstadt.

[9] Chouchane, M. and Amamou, A. (2011). Bifurcation of limit cycles in fluid film bearings, *International Journal of Non-Linear Mechanics* **46**(9): pp. 1258–1264.
[10] Gad, A. M. and Kaneko, S. (2015). Fluid flow and thermal features of gas foil thrust bearings at moderate operating temperatures, *Proceedings of the 9th IFToMM International Conference on Rotor Dynamics*, Springer International Publishing, pp. 1223–1233.
[11] Heshmat, H., Walowit, J. A. and Pinkus, O. (1983). Analysis of gas-lubricated foil journal bearings, *Journal of Lubrication Technology* **105**(4): pp. 647–655.
[12] Hosea, M. and Shampine, L. (1996). Analysis and implementation of tr-bdf2, *Applied Numerical Mathematics* **20**(1): pp. 21–37.
[13] Iordanoff, I. (1999). Analysis of an aerodynamic compliant foil thrust bearing: Method for a rapid design, *Journal of Tribology* **121**(4): pp. 816–822.
[14] Irmscher, C., Nitzschke, S. and Woschke, E. (2019). Transient thermo-hydrodynamic analysis of a laval rotor supported by journal bearings with respect to calculation times, *SIRM – 13th International Conference Dynamics of Rotating Machinery*, Copenhagen, Denmark. Paper-ID 25.
[15] Kumar, A. and Booker, J. F. (1991). A finite element cavitation algorithm, *Journal of Tribology* **113**(2): pp. 279–284.
[16] Larsen, J. S., Nielsen, B. B. and Santos, I. F. (2015). On the numerical simulation of nonlinear transient behavior of compliant air foil bearings, *SIRM – 11th International Conference on Vibrations in Rotating Machines*, Magdeburg, Germany. Paper-ID 39.
[17] Larsen, J. S., Varela, A. C. and Santos, I. F. (2014). Numerical and experimental investigation of bump foil mechanical behaviour, *Tribology International* **74**: pp. 46–56.
[18] Lee, D.-H., Kim, Y.-C. and Kim, K.-W. (n.d.). The dynamic performance analysis of foil journal bearings considering coulomb friction: Rotating unbalance response, **52**(2): pp. 146–156.
[19] Leister, T., Seemann, W. and Bou-Saïd, B. (2019). Bifurcation analysis of rotors on refrigerant-lubricated gas foil bearings, *SIRM — 13th International Conference on Dynamics of Rotating Machines*, Copenhagen, Denmark. Paper-ID 58.
[20] Lez, S. L., Arghir, M. and Frene, J. (2007). A new bump-type foil bearing structure analytical model, *Journal of Engineering for Gas Turbines and Power* **129**(4): pp. 1047–1057.
[21] Mahner, M. (2021). *Numerical Analyzes andExperimental Investigations ofAir Foil Journal Bearings*, PhD thesis, Technische Universität Darmstadt.
[22] Mahner, M., Lehn, A. and Schweizer, B. (2016). Thermogas- and thermohydrodynamic simulation of thrust and slider bearings: Convergence and efficiency of different reduction approaches, *Tribology International* **93**: pp. 539–554.
[23] Michel, H. (2020). *Entwicklung eines numerischen Modells zur Beschreibung von Gasfolienlagern unter Berücksichtigung der Temperatur*, PhD thesis, TU Berlin.
[24] Miraskari, M., Hemmati, F. and Gadala, M. S. (2017). Nonlinear dynamics of flexible rotors supported on journal bearings—part i: Analytical bearing model, *Journal of Tribology* **140**(2).
[25] Nitzschke, S., Woschke, E., Schmicker, D. and Strackeljan, J. (2016). Regularised cavitation algorithm for use in transient rotordynamic analysis, *International Journal of Mechanical Sciences* **113**: pp. 175–183.
[26] Pfeil, S., Gravenkamp, H., Duvigneau, F. and Woschke, E. (2021a). High-order sbfem solution of the reynolds equation, *PAMM* **21**(1): pp. e202100028.
[27] Pfeil, S., Gravenkamp, H., Duvigneau, F. and Woschke, E. (2021b). Scaled boundary finite element method for hydrodynamic bearings in rotordynamic simulations, *International Journal of Mechanical Sciences* **199**: pp. 106427.
[28] Rapolder, M. (2000). *Parallele Finite-Element-Simulation der Bauwerk-Boden-Interaktion mit adaptiven Zeitintegrationsverfahren*, PhD thesis, Technische Universität München.
[29] Ruscitto, D., McCormick, J. and Gray, S. (1978). Hydrodynamic air lubricated compliant surface bearing for an automotive gas turbine engine. i. journal bearing performance, *Technical report*, Mechanical Technology, Inc., Latham, NY (USA).
[30] Schlums, H. and Sadri, H. (2015). Folienlager als Lösung für eine ölfreie Rotorlagerung FVV1157 (Heft 1075), *Abschlussbericht*, Forschungsvereinigung Verbrennungskraftmaschinen.
[31] Schlums, H., Sadri, H., Schmiedeke, H. and Prechavut, N. (2019). Folienlager II – Betriebssichere aerodynamische Folienlager für die Lagerungschnell laufender Rotoren FVV1267 (Heft 1198), *Abschlussbericht*, Forschungsvereinigung Verbrennungskraftmaschinen.
[32] Temis, J., Temis, M., Egorov, A. and Gavrilov, V. (2015). Numerical and experimental investigation of rotor-simulator in foil gasdynamic bearings for compact gas turbine, *Proceedings of the 9th IFToMM International Conference on Rotor Dynamics*, Springer International Publishing, pp. 1247–1258.

[33] von Osmanski, S., Larsen, J. S. and Santos, I. F. (2017). A fully coupled air foil bearing model considering friction – theory and experiment, *Journal of Sound and Vibration* **vol. 400**: pp. pp.660–679.

[34] von Osmanski, S., Larsen, J. S. and Santos, I. F. (2019). Modelling of compliant-type gas bearings: A numerical recipe, *SIRM -– 13th International Conference on Dynamics of Rotating Machines*, Copenhagen, Denmark. Paper-ID 44.

[35] Zienkiewicz, O. C. and Xie, Y. M. (1991). A simple error estimator and adaptive time stepping procedure for dynamic analysis, **20**(9): pp. 871–887.

15th SIRM – European Conference on Rotordynamics,
Darmstadt, Germany, 22nd – 24th February 2023

Analysis of the influence of axial forces on the permanent magnet bearing of a turbopump and methods to reduce the magnetic bearing error

Pascal Wielsch [1], Gerd Manthei [1]

[1] Mechanical Engineering and Power Engineering, Technische Hochschule Mittelhessen, University of applied Sciences, 35390, Gießen, Germany, pascal.wielsch@me.thm.de (P.W.), gerd.manthei@me.thm.de (G.M.)

Abstract

The rotors of turbomolecular pumps (TMPs) are subject to continuous further development in various aspects to meet the increasing requirements. Vibration and noise emissions are becoming more relevant. Applications such as electron microscopes or ion mobility spectrometers require a low vibration level of the TMP used.

The rotor of a TMP always has a certain residual unbalance, which results in radial forces that are transmitted to the housing via the bearing and lead to vibrations and noise. In practice the installation of a rotor with a high balance quality does not always result in low vibration and noise emissions from the TMP.

The bearing system of the TMP rotor consists of a combination of ball bearing and passive permanent magnet bearing (PMB). The PMB of such TMP with hybrid-bearing is focus of this study. Due to intrinsic imperfections in the magnetic rings, there is an additional radial force that can affect the running characteristics of rotor and pump, called magnetic bearing error.

During TMP operation, the heating of the rotor leads to an axial displacement between the rotor and stator magnetic rings and thus to a change of the radial rotor forces. With the aid of an experimental investigation, this behavior was reproduced and the effect, that the magnetic bearing error exhibits a strong dependence on the axial displacement between the stator and rotor, was observed for the first time. The experimental results showed that this dependence of the magnetic bearing error strongly influences the first resonance of the rotor in terms of amplitude and resonance frequency.

By means of a simulation, a deeper understanding of the magnetization properties and their influence on the generation of additional forces on the rotor was derived. An optimization approach was developed to select and optimize the arrangement of magnetic rings within the PMB based on their individual magnetization properties. This reduces the dependence of the magnetic bearing error on axial forces.

The derived measures contribute to the overall objective of reduced vibrational and noise emissions of a TMP and an improved transfer of the balance quality of the rotor to the pump.

1 Introduction

In the last few years, increasing demands on the turbomolecular pumps with hybrid-bearing system have characterized its secondary properties in particular. In addition to primary properties relating to pump performance, such as ultimate pressure or pumping speed, secondary properties are becoming increasingly relevant. In addition to service life, compactness or cleanliness in terms of a particle-free vacuum and the outgassing behavior of the components, this also includes the vibrational and noise emissions of the TMP, the NVH (Noise Vibration Harshness) emissions. In order to meet the increasing requirements, continuous further development of TMP is necessary, resulting in non-trivial rotor and housing geometries [17].

The focus of a dissertation in which this publication is included is particularly on the rotordynamic design of the TMP rotors, the optimization of the balancing technology and the balancing quality transfer. Thus, the subject matter fits into the field of optimization of NVH emissions. The present work is limited to a TMP with a bearing system composed of a permanent magnet bearing and an oil lubricated ball bearing, hereinafter referred to as hybrid bearing. A primary question of the research project is to investigate the causes of TMPs with noticeable vibration and noise even with a well-balanced rotor. Increased vibration and noise emissions affect numerous applications in which these vacuum pumps are employed, such as electron microscopes or ion mobility spectrometers [14]. Therefore, it is relevant that the underlying causes are investigated in order to be able to realize an optimization of NVH emissions. Thus, a contribution to meet the continuously increasing requirements for TMP can be made.

In addition to other possible causes of TMPs with noticeable vibration and noise, such as residual unbalance of a rotor before installation in the housing, assembly errors or damage in the ball bearing [3], the focus of the present investigation is on the coupling between rotor and housing of the pump via the PMB. On the one hand, the general coupling of the rotor via the bearing is relevant, since unbalance-induced forces are transmitted to the housing and, consequently, to the application. However, it is known from the work of Katter [8] that certain magnetic properties in the PMB have an influence on the generation of additional, undesirable forces on the rotor. Furthermore, the rotor heats up more during operation than the pump housing. The linear expansion results in an axial displacement between the stator and the rotor within the PMB and thus generates additional axial forces. In addition, when the rotor is mounted in the TMP, the stator part of the PMB is replaced (balancing machine system vs. pump), so that the magnetic properties are different. These facts fall into the field of balance quality transfer and could be another cause of TMPs with noticeable vibration and noise even with low residual unbalance.

These findings have laid the foundation for why this paper focuses on the investigation of the PMB of a hybrid-bearing TMP. The term hybrid bearing, i.e. the combination of PMB and ball bearing, should not be confused with a hybrid magnetic bearing as described in [18]. The influence of additional forces in the PMB on the rotor dynamics and running behavior due to certain magnetic properties as well as axial displacements between the stator and rotor will be discussed more detailed. In the context of the present work, an alternative simulation approach is presented. The simulative results are verified by an experiment. Here it is observed for the first time that the so-called magnetic bearing error shows a strong dependence on axial forces. Finally, an optimization approach for reducing the axial force-dependent magnetic bearing error is presented. This can be targeted in practice to contribute to the overall goal of optimizing NVH emissions in hybrid bearing TMPs.

2 Fundamentals on hybrid-bearing turbomolecular pumps with permanent magnetic bearing

Magnetic bearings in general have numerous advantages over other types of bearings, such as conventional roller or plain bearings. They operate without mechanical contact and thus allow very high rotor speeds without frictional wear [11]. This results in maintenance free operation, lower noise generation and significantly lower transmission of vibrations to adjacent components [15]. By eliminating the need for lubricants, magnetic bearings can be used in environments where the highest level of cleanliness is required. This makes them particularly suitable for use in TMPs to create an (ultra) high vacuum. Other applications of magnetic bearings include high-speed turbines, compressors, centrifuges, flywheels or high-precision machine tools [11]. Magnetic bearings can be divided into active, passive and electrodynamic systems. Lang [9] shows in his work that passive systems with permanent magnets can achieve comparable bearing pressures as active magnetic bearings, especially considering the required volume. Kabelitz and Fremerey [7] refer to the use in TMPs and list further advantages of a passive PMB: low cost due to the absence of electronic components (e.g. coils & control technology), compact design, auto-centering of the rotor (e.g. in case of power failures or external shocks) or operability in case of power failures. For the aforementioned reasons, passive permanent magnetic bearings have gained acceptance in TMP in recent years, which is why this paper is limited to this type of bearing.

The essential structure of a modern TMP with hybrid bearing is described in the patent application by Conrad and Mädler [4]. The structure of a typical PMB used there is shown schematically in **Figure 1a** and describes the object of investigation of the present work as an example. The PMB consists of several axially magnetized permanent magnet rings which are divided into a stator and a rotor magnet stack. The stator rings are arranged concentrically to the rotor rings on the inside. The radial bearing gap is located between the two magnet stacks. Due to the high rotor speed and centrifugal forces, there is a possibility of destruction of the magnet rings, so that the rotor magnet stack requires an external radial support on the outside [5].

The PMB under investigation is a radial bearing of repulsive design, where the magnetic rings are stacked axially and have opposite polarization (identical magnetic poles are axially opposite to each other). The pair of rings consisting of stator and rotor at the same axial height has the same magnetization direction, resulting in radial repulsion and thus radial centering due to the rotational symmetry of the rings. Axially magnetized permanent magnet rings are used for reasons of availability and easier manufacturability [19]. It is necessary to use a hard-magnetic material, such as neodymium-iron-boron or samarium-cobalt. These materials have a very high coercivity and therefore cannot be demagnetized by adjacent magnetic rings of the same material. They are therefore particularly suitable for a repulsive configuration [19]. Other possible configurations of radial or thrust bearings according to attractive or repulsive configuration are listed in the dissertation of Betschon [2].

In the previous chapter, the hybrid bearing arrangement of the TMP has already been briefly mentioned. The reason for the use of a ball bearing is described below. The Earnshaw's Theorem states that it is not possible to statically stabilize a body using only a passive bearing with permanent magnets. A PMB has a negative axial stiffness equal to twice the radial stiffness. For this reason, an additional bearing is needed, e.g. an additional rolling bearing, to control the axial degree of freedom [9]. The ball bearing is used for radial and axial support of the rotor (see **Figure 1**b).

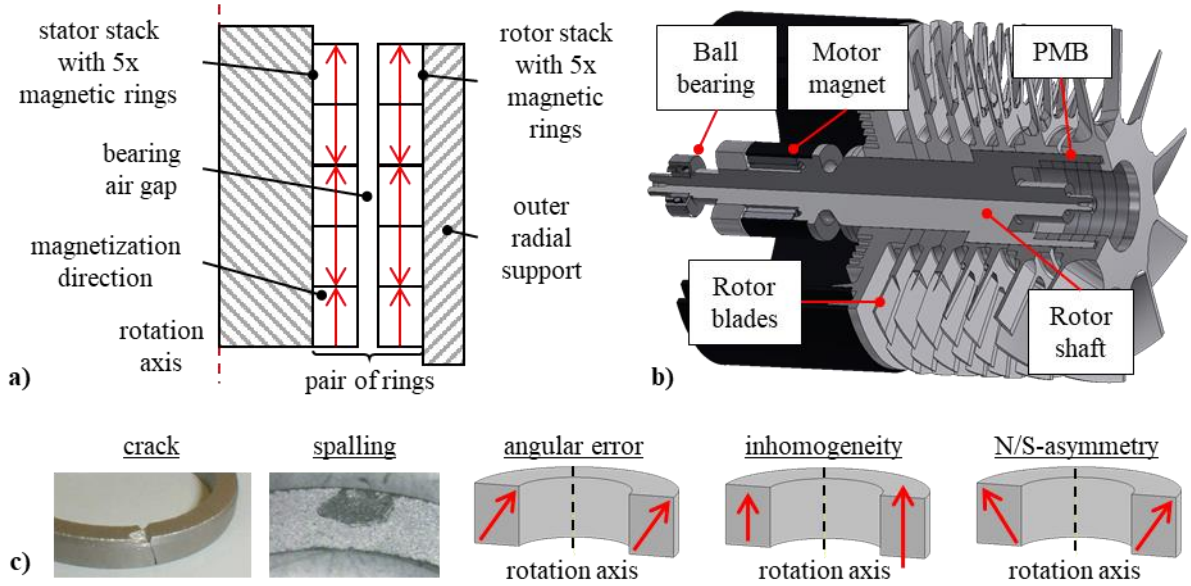

Figure 1: a) Cross-section through the exemplary structure of the PMB of a TMP with 5 ring pairs (not to scale). b) 3D model of a TMP rotor (three-quarter section view) c) Images of mechanical defects such as cracks and spalling as well as relevant characteristics of permanent magnetic rings for quality control: angular errors, inhomogeneities and N/S asymmetries are typical error patterns resulting from intrinsic magnetization properties.

In the past, there have been various publications with the objective of increasing the stiffness of the PMB while using as little material as possible. An increase in radial stiffness can be achieved by a suitable ratio between air gap width and axial height of the magnetic rings or ring width and height [4]. The stacking of several rings as well as the use of a rotating magnetization direction also lead to an increase of the stiffnesses as described in [21]. The structure of the PMB of modern TMPs shown in **Figure 1a** has been proven successful in recent years and is used as a basis for this work. This distinguishes it from other publications, since the focus is not on increasing the radial stiffness by optimizing the PMB geometry, but on the intrinsic magnetization properties of the individual rings. It is known from the manufacturing processes used (isostatic or tool pressed) for permanent magnet rings that magnetic deviations can occur. For this reason, the individual magnetization properties of the single rings are checked to carry out quality controls, thus increasing the quality of the PMB. Reese [13] describes a possible setup as well as the procedure for checking the quality characteristics of a permanent magnet ring. This includes, for example, checking for fractures, cracks and spalling in the material, as well as angular errors, inhomogeneities and north/south asymmetries (see **Figure 1c**).

3 Methods for evaluation, validation and optimization of the magnetic bearing error of TMPs

This methods chapter starts with the theory and describes the use of a simulation to determine the resulting forces on the rotor based on the individual intrinsic magnetization properties, taking axial displacements into account. Subsequently, an experimental setup is described, which provides a new insight into an axial force-dependent magnetic bearing error and thus validates the simulations. At the end of this chapter, the development and validation of an approach to optimize of the axial force-dependent magnetic bearing error is presented.

3.1 Theoretical investigation of the PMB of a TMP as well as the magnetic properties based on a simulation

Numerous investigations and theoretical calculation approaches for PMB already exist. A paper by Yonnet [20] describes a method for estimating stiffness and force of simple PMB configurations, consisting of a single stator and rotor ring, that is limited to a 2-dimensional problem. The work of Jiang et al. [6] extends the calculation to a 3-dimensional problem and employs the magnetic vector potential. Here axial and radial displacements can be considered in the PMB. Other authors have performed other calculation methods of PMB (see [9], [10] and [12]). Lang's dissertation generally presents a comprehensive review on PMB and is based on a similar calculation approach as described in this chapter.

In contrast to the publications mentioned above, this work investigates the influence of the individual magnetization properties of each ring as well as their composition within the PMB, which is basically a 3-dimensional problem. Furthermore, the resulting forces on the rotor of the TMP are of interest. The theoretical approach of this work is implemented into the MATLAB environment and designed to investigate the objective. The resulting simulation allows the calculation of the resulting forces in the PMB of a hybrid-bearing TMP, taking into account the magnetization properties of the individual rings as well as axial displacements between stator and rotor.

The structure of the MATLAB simulation is described below. First, the geometry of the PMB is designed according to a repulsive setup with axially magnetized rings. The number of ring pairs, dimensions of the rings as well as the size of the radial bearing gap can be freely designed here. In addition, it is possible to shift the individual rings radially and axially, whereby the focus is on the axial shift of the entire rotor magnet stack. The static magnetic field is then calculated based on the individual ideally magnetized stator and rotor rings. This is done for all defined field points in the near field region, i.e. in a radius of a few centimeters around the magnetic rings. In the next step, the individual intrinsic magnetization properties of the single rings are considered. These are divided into individual ring segments, whereby the magnitude as well as the angle of the magnetization can be varied, deviating from an ideal axial magnetization. The resulting additional magnetic field is calculated and the vector addition of the magnetic field of the previously assumed ideal magnetic rings is performed for all defined field points.

The basis for the calculation is the surface current model. Tangential surface currents occur at the shell surfaces of a magnet with axial magnetization (see **Figure 2a**) since no adjacent elementary currents occur there. Due to the repulsive structure, opposing surface currents are present at the bearing gap. Because of the force effect between the ring magnets, radial repulsion occurs in all directions and a radial bearing is formed [5]. Urankar describes an analytical method for calculating the vector potential as well as the magnetic field of a thin circular conical cylindrical segment, which is the basis of this work. The shell segment carries a surface current and can have an arbitrary tangential circumferential and axial length. During the calculation, Jacobian elliptic functions and complete and incomplete elliptic integrals of the first, second and third kind are used. The equations derived from Urankar are fully adopted in the underlying MATLAB simulation and can be found in [16, p. 915]. Therefore, they are not described in detail in this publication. For the case of the ideally magnetized ring, only surface currents occur on the tangentially extending surfaces, so the formulas simplify to the case of the derived complete, nonconical cylinder. However, for rings that are not ideally axially magnetized, surface currents also occur at the top and bottom faces. In addition, the intrinsic magnetization properties vary along the circumference of the ring, so that the generally derived Urankar equations must be used for ring segments of any size.

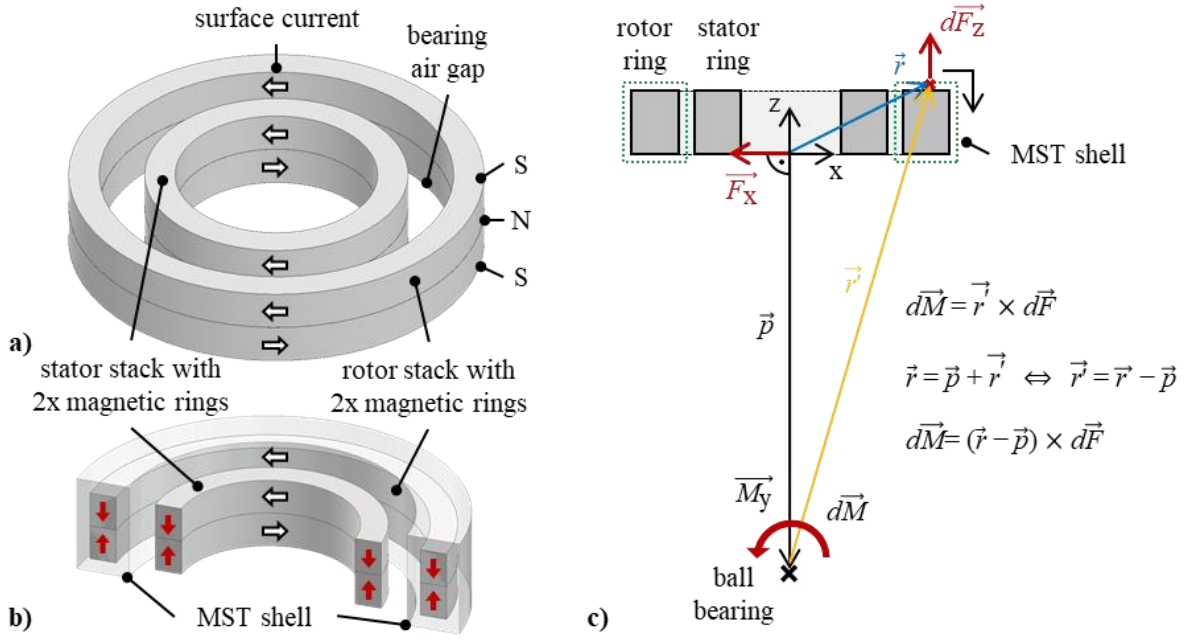

Figure 2: a) Axially magnetized rings exhibit tangential surface currents. For clarity, only an exemplary 2-ring pair PMB is shown here and the bearing air gap is significantly larger. b) Cross-section of the exemplary PMB showing the MST shell which only encloses the rotor magnet stack for the calculation of forces. c) Schematic representation of the simulation model of a hybrid-bearing TMP rotor

After the distribution of the magnetic field over the defined field points is calculated, the resulting forces can now be determined with the help of the Maxwell stress tensor (MST). This method is used, among others, in the work of Bekinal [1]. The MST describes the relationship between electromagnetic forces and mechanical forces, moments and impulses. Each individual field point can be assigned a mechanical stress state via the MST. The forces can then be determined by integrating the stresses along a closed surface. Only one magnet (stack) may be included in this process [9]. The rotor magnet stack in the form of a closed MST shell is chosen here as the integration path (see **Figure 2b**).

At this point, the present publication further differs from other published methods and provides a novel approach by considering a rotor with PMB and ball bearing (see **Figure 2c**). The forces just calculated in the individual field points along the closed MST shell (dotted green line), hereafter referred to as intrinsic forces $d\vec{F}$, generate individual torques $d\vec{\vec{M}}$ in the ball bearing via the rotor $\vec{p}$, respectively the virtual lever arm $\vec{r}$. These individual iteratively determined torques $d\vec{M}$ are now added vectorially. Due to the support of the rotor in the ball bearing, the torque there leads to resulting radial forces. Only those torque components are of interest which lead to a radial deflection of the rotor in the PMB. The assumption is made that the displacements in the PMB are very small compared to the length of the rotor, so that a perpendicularity between the rotor $\vec{p}$, the resulting force $\overrightarrow{F_x}$ and the torque $\overrightarrow{M_y}$ in the ball bearing applies. On the other hand, the vector sum of the intrinsic axial forces is used as the resulting axial force, since the rotor is free to move axially in the PMB. Based on this model assumption, the torque in the ball bearing generated by the intrinsic forces in the magnetic bearing is mapped in the horizontal plane of the PMB. For example, intrinsic axial forces $d\vec{\vec{F}}_z$ generate a torque $\overrightarrow{M_y}$ via the rotor as a lever arm, which results in a radial force $\overrightarrow{F_x}$.

Of particular interest for the objective of this work is the magnetic bearing error (MBE), i.e. the total radial deflection of the rotor (peak-to-peak) within the magnetic bearing from the axis of symmetry between the two bearing points. This is determined from the resulting radial force F_r as well as the radial stiffness k_r. The radial stiffness k_r in turn can be derived from the axial force F_{ax} and stiffness k_{ax} during axial displacement dz, as shown in (1).

$$k_{ax}(z) = \frac{dF_{ax}}{dz}, \qquad k_r(z) = -0{,}5 \cdot k_{ax}(z), \qquad \text{MBE} = \frac{F_r}{|k_r(z)|} \cdot 2 \tag{1}$$

The underlying Urankar equations of this MATLAB simulation only calculate static resulting forces, therefore another novel assumption is made. The operation of the TMP leads to a rotation of the rotor rings and their magnetic induced forces. This leads to a harmonic rotating radial force and the magnetic bearing error. The simulation results can thus be transferred to practice, so that an application-related theoretical analysis of the PMB of a TMP is possible. The influence of axial displacements (due to heating of the rotor during operation) as well as the individual magnetization properties (due to the manufacturing processes of permanent magnet rings) on the resulting radial force in the described system can thus be investigated in detail.

3.2 Experimental investigation of the magnetic bearing error of a TMP

For the experimental investigation of the magnetic bearing error of a TMP, a special test setup is used (see **Figure 3**), which is similar to the setup of a balancing machine system for TMP rotors. This experimental setup is chosen because the bearing arrangement is very similar to the bearing arrangement inside the TMP itself. In addition, the setup offers the possibility that the radial deflection in the bearing points can be measured using eddy current sensors. This inductive measurement principle measures the total radial deflection of the rotor from the symmetry axis with an accuracy of a few µm. The stator of the magnetic bearing can be moved axially. This allows adjustment of the relative displacement between the stator and the rotor, which occurs when the rotor is heated inside the pump and thus expands in length. The axial force correlating with the axial displacement is measured by a sensor located in the mounting support for the bearing.

To check the magnetic bearing error, the rotor is mounted in the experimental setup, accelerated to a low speed and the radial deflection in the PMB is measured. A low speed in the range of a few revolutions per second is already sufficient here to be able to measure the radial deflection of the magnetic bearing error. This process is repeated at different relative axial displacements, whereby these are precisely set via the measured axial force. A total of 21 rotors are measured in this way, with the magnetic bearing error exceeding the limit for a majority of the rotors. These rotors are selected intentionally because the magnetic bearing error of the so-called rejected rotors in particular, is to be reduced. 17 of these rotors are also accelerated to the corresponding maximum speed in order to check the influence of the axial displacement on the run-up behavior of the rotor and at higher speeds.

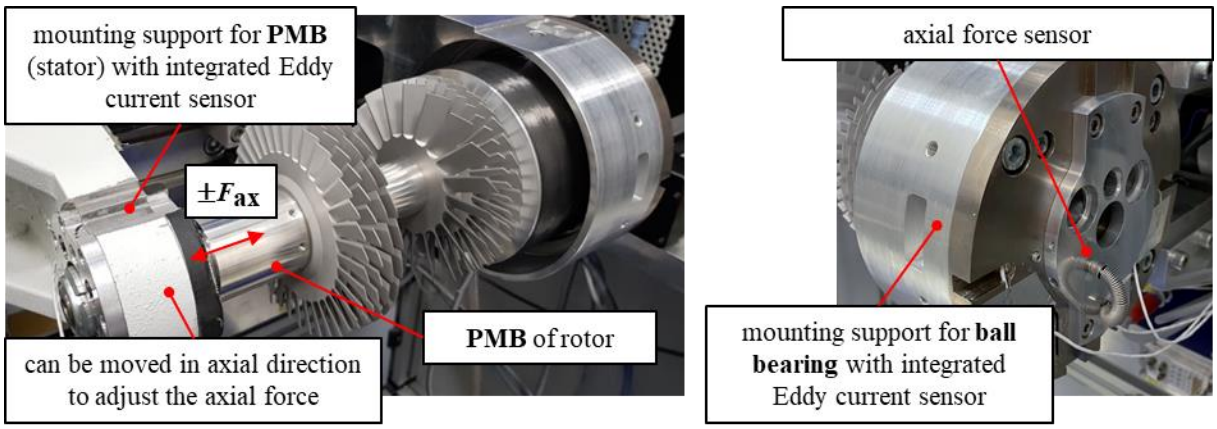

Figure 3: Experimental setup for the investigation of the magnetic bearing error: the stator part of the PMB can be moved axially to adjust the axial force. The radial displacement within the PMB is measured at different axial forces.

The magnetic bearing error is a vector, because the measured radial displacement has a magnitude (total displacement “peak-to-peak" in µm) as well as a direction. This phase direction is referenced by a Hall sensor, which measures the polarity of the motor. Within the scope of the investigation, both magnitude and phase of the magnetic bearing error vector are evaluated.

3.3 Optimization approach for the PMB to reduce the axial force-dependent magnetic bearing error

The interim findings to date lay the foundation for the development of an optimization approach. This offers the possibility of reducing the axial force-dependent magnetic bearing error of the PMB by using a combinatorial approach as well as the MATLAB simulation described above. Here, additional MATLAB program modules are necessary. First, a program part is used to reconstruct the magnetization properties from the raw magnetic data of real rings. The code is adapted so that the magnetic properties can be transferred to the corresponding ring segments and read into the MATLAB simulation as starting parameters in a suitable manner. On the other hand, coefficient matrices are developed and used to describe the influence of the intrinsic magnetization properties of a single ring segment on the generation of forces in the entire rotor. These coefficient matrices are developed with the help of numerous simulations by calculating the resulting forces due to different amplitudes of the individual magnetic properties as a function of the axial displacement. Trend lines describing the influence can be derived from the results. The parameters of the trend lines are mapped in the coefficient matrices and are valid for a defined PMB geometry (including the axial displacement) independent of the magnetization properties.

A method to compensate for magnetic deviations from the state of ideal magnetization is known from a method by Katter [8]. However, this refers solely to the error pattern of the north/south-asymmetry. The procedure of the present optimization approach is described below. At the beginning, a certain number of magnetic rings is selected and measured in the quality control device. Subsequently, the reconstruction of the magnetization properties takes place. This results in magnetic ring models in the simulation whose properties of the individual ring segments correspond to the magnetization of the real rings. Now the PMB configurations are built up from all possible combinations (permutations without repetitions) of the magnetic ring models used. In this step, the rings of each PMB configuration are rotated and aligned with each other according to the deviation of their primary magnetic preferred direction from the cylinder symmetry axis. This is already done inside the magnetic bearing to reduce the initial magnetic bearing error [8]. The calculation of the magnetic bearing error curve shape is performed using the coefficient matrices. Here, systems of equations are solved for all ring segments so that the individual force components are known, based on the individual magnetization characteristics. These are added vectorially for each PMB configuration so that the resulting radial force curves are obtained as a function of axial displacement (based on defined grid points) for all combinations. Subsequently, a rating criterion is determined for all individual force curves. This represents the sum of all displacement vectors between the individual grid points and thus describes the vector change of the magnetic bearing error, taking magnitude and phase into account. Finally, the best PMB combinations with the smallest possible vector change are selected in an iterative step, whereby the combinations of already used rings are sorted out. Magnetic ring combinations whose rating criterion is above a specified threshold are also sorted out. This results in PMB combinations of real magnetic rings with the lowest possible axial force-dependent magnetic bearing error.

The verification of the optimization approach is carried out simulatively and experimentally in cooperation with a company. For the first case, 100 real magnetic rings are measured in order to reconstruct the magnetization properties. After applying the optimization approach, 16 (out of 20 theoretically possible) optimized PMBs (5-

ring-pair) are obtained here, since some ring combinations are not used due to a threshold being exceeded. Subsequently, the axial force-dependent course of resulting radial force or magnetic bearing error is calculated for all combinations using the method from chapter 3.1. Here, the reconstructed magnetization properties are also considered. For comparison, the results of non-optimized PMB, but with the same reconstructed magnetic rings, are used. However, the combinations are chosen such that the magnetic rings are stacked according to their extracted order, resulting in 16 random combinations of PMB.

In the experimental verification, a total of 110 TMPs are built with optimized PMBs. The optimization approach is used to determine the magnetic ring combinations and assemble them in real rotors. Some optimized rotors are checked in the experimental test setup and the measured values are compared with those of non-optimized or the already measured (rejected) rotors. The overall target considers not only the rotor but also the entire TMP. Therefore, an additional evaluation of all optimized rotors is performed as part of the standardized functional testing at the manufacturer. In this process, relevant parameters are evaluated during the balancing process of the rotors as well as the final functional test of the complete pump. These parameters are then compared with data from identical TMPs with non-optimized PMBs from the same production period.

4 Results

4.1 Theoretical and experimental investigation of the PMB with focus on magnetic properties and the magnetic bearing error of a TMP

By using MATLAB simulations, the influences of the intrinsic magnetization properties as a function of the axial displacement can be theoretically investigated. Typical magnetic error patterns, which have already been briefly described in **Figure 1b**, have different effects on the rotor and can be better taken into account in the future. The findings of the theoretical investigation confirm and extend some statements on individual magnetic error patterns from the publication of Katter [8]. **Figure 4** summarizes their effects on the generation of additional radial and axial forces as a function of axial displacement. The inhomogeneity represents a deviation in magnitude of the magnetization from the average magnetic field of the entire ring. It leads to an offset of the radial force curve. The angular error represents a deviation of the magnetic preferred direction from the symmetry axis of the magnetic ring and describes the opening angle of the parabolic curve shape. The north/south-asymmetry is a rotational symmetric tilting of the magnetization and leads exclusively to additional axial forces.

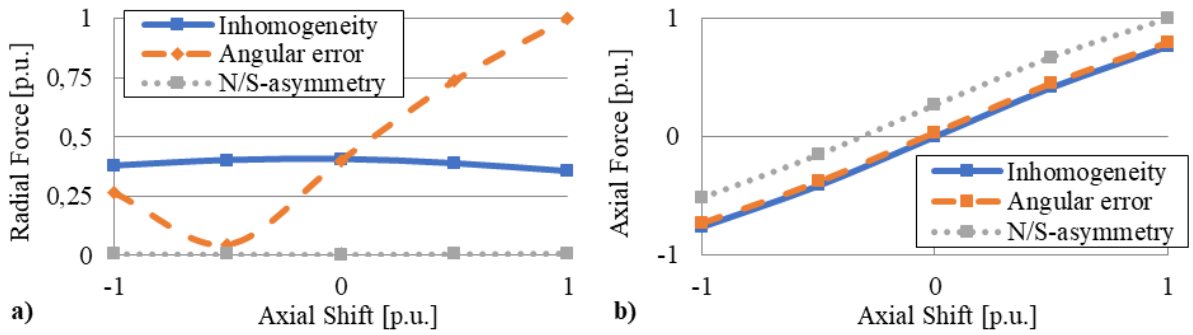

Figure 4: a) Inhomogeneity and angular error both result in additional radial forces with different dependence on axial displacement, but no axial forces. b) The slope of the axial force curve results from the axial displacement itself. The N/S-asymmetry generates additional axial forces only (parallel displacement of the force curve).

During the experimental investigation, an interesting phenomenon was observed for the first time. The measured total radial deflection of the rotor within the PMB at a low, predefined rotor speed (magnetic bearing error) is very strongly dependent on axial displacements between stator and rotor. **Figure 5a** shows typical curves, which were observed in all 21 rotors in varying extents. The magnitude of the magnetic bearing error generally shows a parabolic curve shape and is in the range of a few µm. The phase of the magnetic bearing error vector also varies differently by up to 180° (not shown). Through the practical know-how of the cooperating company, it is clear that a very strong influence on the residual unbalance of a few 100 mg can thus be expected.

The run-up measurements carried out up to the maximum operating speed show that both the amplitude of the first rigid-body mode of the rotor and its resonance frequency also change very strongly (see **Figure 5b**). The decrease in radial stiffness due to axial displacement cannot be the sole reason for this strong change. This observation will not be pursued further in this investigation, so that the cause remains still unclear.

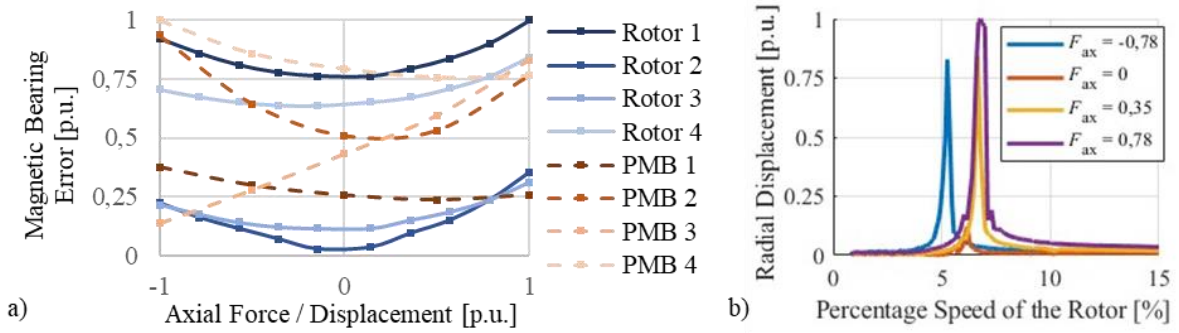

Figure 5: a) The results of four rotors (experimental) respectively four PMB (simulative) show a strong dependence of the magnetic bearing error at different axial forces and thus under variation of the axial displacement. b) The first rigid-body mode of a single rotor (amplitude & frequency) also changes significantly during run-up at different axial forces.

The phenomenon observed in the experimental investigations can also be verified with theoretical simulations. From the axial force-dependent curve of the resulting radial force, the curve shape of the magnetic bearing error itself can be estimated, taking into account the changing radial stiffness. Both curves are qualitatively very similar, so that experiment and simulation validate each other (see **Figure 5a**). For the comparison, axial force (experiment; blue lines) and axial displacement (simulation; orange dashed lines) are to be equated. From the findings of the theoretical investigation, however, it is clear that primarily the angular error or the individual magnetization angle appears to be the cause for the strong dependence on the axial force. At this point it should be mentioned that the angular error as well as the North/South-asymmetry in the simulation consists from a suitable configuration of the magnetization angle of the individual ring segments.

Furthermore, the theoretical investigation of PMB with real, reconstructed magnetic rings has shown that the order of identical magnetic ring models can have a relevant influence on the radial force curve. This means that not only the intrinsic magnetization properties themselves, but their individual arrangement within the PMB has to be considered. Based on this insight, an optimization approach for the design of PMBs was developed, whose objective is to reduce the amount of magnetic bearing error as well as its dependence on axial displacement by a suitable combination of rings based on their intrinsic magnetization properties.

4.2 Simulative and experimental results prove that the optimization approach reduces the axial force-dependent magnetic bearing error

Regardless of the calculation of a very large number of possible magnetic ring combinations, reasonable computation times are achieved for the optimization approach, since MATLAB is specifically designed for matrix calculation. Determining the optimal combinations from 24 rings (~ 5 million possible combinations) takes only about two minutes. The simulative verification of the optimization approach shows a significant improvement of the axial force dependent magnetic bearing error (see **Figure 6a & b**). The curve of 16 optimized PMB is significantly flatter than the one of 16 non-optimized PMB. The rating criterion for estimating the vectorial change (magnitude and phase) of the magnetic bearing error is also significantly lower.

The first part of the experimental verification also shows much flatter curves for the rotors with 39 optimized PMB and a reduction of the magnetic bearing error itself (see **Figure 6c & d**). This is represented by the mean value at an axial force of about 0.36 p.u. There are no rotors above the threshold (red horizontal line) although a completely new method for combining magnetic rings was employed. As expected, the curves of 13 rejected rotors (dashed curves) are partially above the limit. However, even the 22 non-optimized rotors show measurement values close to or above the threshold. In addition, the amplitude of the magnetic bearing error is generally higher.

In the second part of the experimental verification, a comparison is made between all optimized (110x) and non-optimized specimens (~ 4,500x) in the same period. The relevant parameters are determined with the aid of a database query. In the course of the standardized functional test, some rotors or TMP can have multiple test runs. The causes here can be very numerous, e.g. incorrect mounting of the ball bearing or leaks, and are not always attributable to the PMB. For this reason, some of the data collected must be checked and cleansed manually, which is not practicable in the case of the comparative data due to the large data set of approx. 4,500 entries. For the evaluation, however, a basis of comparison as identical as possible is created by comparing only final or complete runs. For example, the amplitude of the first rigid-body mode is measured several times during the pump test. Test runs that ended prematurely are not considered. The relative changes of the optimized PMB are shown in **Table 1** and tend to show an improvement of the evaluated parameters in different amounts. For example, in the balancing process, the magnetic bearing error is significantly reduced, the residual unbalance of the rotor as well as the housing vibrations of the pump are also slightly reduced.

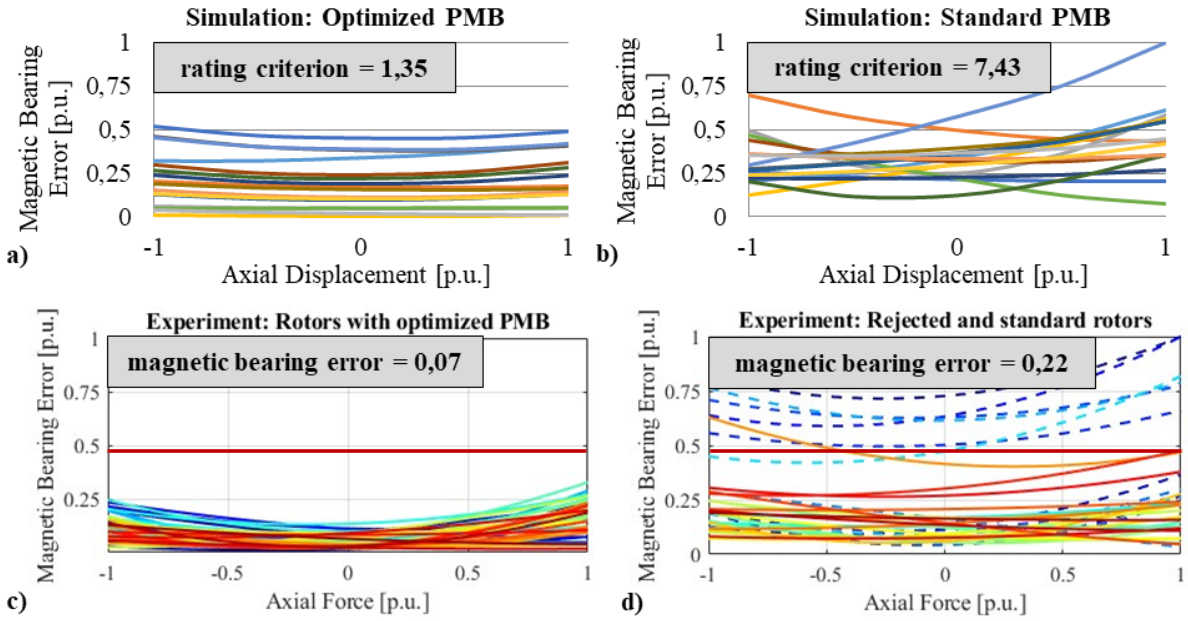

Figure 6: All four graphs show the magnetic bearing error as a function of axial displacement (simulation) or axial force (experiment): the upper row shows the results of the simulative verification with PMB (a & b). The bottom row shows the experimental measurement of real rotors (c & d).

However, no particularly large influence is to be expected here, since both parameters relate to the maximum rotor speed and the magnetic bearing error only prevails at low speeds. The amplitude of the first rigid-body mode, on the other hand, is reduced clearly, which is to be expected due to the optimization of the magnetic bearing error itself. In particular, when evaluating the functional test of the entire TMP, it should be noted that numerous other causes can have an influence on the results.

Table 1: The optimization approach achieves a slight to significant improvement in the context of rotor balancing (magnetic bearing error, residual unbalance) and TMP functional testing (vibration at final speed, amplitude of first rigid-body mode) compared to parameters from a database of over 4,500 non-optimized rotors.

	Magnetic bearing error	Residual unbalance	Vibration amplitude at final speed	Amplitude of 1st rigid-body mode
Reduction of optimized PMB	-29%	-5%	-3%	-15%

In general, both the simulative and the experimental verification of the optimization approach show that the objective of reducing the magnetic bearing error itself as well as the dependence on axial displacements is met. To be mentioned is that the magnetic rings used are taken from a device for automated quality control and measured again on a separate device to obtain the required raw data. In this process, non-negligible measurement inaccuracies which have an influence on the optimization approach were observed, although the same measurement methodology was employed. The optimization approach is based on the reconstructed raw magnetic data and is less efficient if the data do not correspond to the real magnetization. In a next step, it is therefore necessary to examine whether the measurement inaccuracies can be further reduced and thus the benefit of the optimization approach can be increased in practice.

5 Conclusion

In this publication, the PMB of a hybrid-bearing TMP was investigated in detail to determine the influence of additional resulting forces on the rotor dynamics and running behavior due to the magnetic properties as well as axial displacements between stator and rotor. A simulation model was developed that can be used to investigate the effects of intrinsic magnetization properties on the generation of undesirable forces on the rotor. This has provided a more focused understanding of typical magnetic error patterns in a hybrid bearing TMP. Experimental investigations have shown for the first time that the magnetic bearing error has a strong axial dependence and thus influences the balancing quality transfer. This phenomenon was theoretically confirmed in the simulations and the causes were identified, which lie in an unsuitable combination of permanent magnet rings based on their magnetic properties, especially the angular error. With these findings, an optimization approach was developed. It allows the targeted design of PMBs and demonstrates the reduction of the magnetic bearing error as well as its dependence on axial displacements. In addition, it is now possible to optimize the PMB geometry of a hybrid bearing TMP.

The obtained knowledge as well as the possibility to reduce the magnetic bearing error contribute to the overall objective and support the optimization of balancing quality transfer and NVH emissions. Based on the observations, a possible cause for hybrid-bearing TMPs with noticeable vibration and noise even with low residual unbalance was found. The proven reduction in the amplitude of the first rigid-body mode has a positive effect on rotor run-up and thus numerous applications, such as ion mobility spectrometers. Furthermore, the tendency of a reduction of the housing vibrations at rated rotor speed is noticeable. Since the magnetic bearing error cannot be separated in the balancing process, another possible influence is expected here.

In a subsequent study as part of the associated dissertation, the correct consideration of the axial force-dependent magnetic bearing error in the balancing of the rotors will be investigated. Furthermore, additional ideas for the advancement of the optimization approach itself have been arisen during the investigation. These can be considered in addition to the verification of the measurement inaccuracies observed in the quality control of the permanent magnet rings. The cause originally suspected in the introduction, namely that a change of the magnetic bearing stator has a significant influence on the balancing quality transfer, was also not considered further for the time being, but continues to represent a possible research question.

References

[1] Bekinal, S. I., Anil, T. R., and Jana, S. (2012): Analysis of Axially Magnetized Permanent Magnet Bearing Characteristics. *Progress In Electromagnetics Research B,* 44, pp. 327–343.

[2] Betschon, F. (2000): *Design Principles of Integrated Magnetic Bearings*. Dissertation, Swiss Federal Institute of Technology Zürich, Zürich.

[3] Casaro, F. (1989): Vibrations in turbomolecular pumps: Spectra and source location. *Journal of Vacuum Science & Technology A* 7, 3, pp. 2377–2380.

[4] Conrad, A., Mädler, M. (2015): *Vakuumpumpe und Permanentmagnetlager,* EP 3 135 932 A1.

[5] Fremerey, J. K. (2000): *Permanentmagnetische Lager*. Abteilung Magnetlager- und Antriebstechnik, Jülich.

[6] Jiang, W., Allaire, P. E., Baloh, M. J., and Wood, H. G. (2002): Forces and moments in axially polarized radial permanent magnet bearings. *8th International Symposium on Magnetic Bearing* August 26-28, pp. 521–526.

[7] Kabelitz, H.-P., Fremerey, J. K. (1988): Turbomolecular vacuum pumps with a new magnetic bearing concept. *Vacuum* 38, 8-10, pp. 673–676.

[8] Katter, M. (2004): *Radiales Magnetlager, Verfahren zur Bearbeitung eines Ringmagneten sowie deren Verwendung,* EP 1 477 695 B1.

[9] Lang, M. (2003): *Berechnung und Optimierung von passiven permanentmagnetischen Lagern für rotierende Maschinen*. Dissertation, Technische Universität Berlin, Berlin.

[10] Marth, E., Jungmayr, G., and Amrhein, W. (2014): A 2-D-Based Analytical Method for Calculating Permanent Magnetic Ring Bearings With Arbitrary Magnetization and Its Application to Optimal Bearing Design. *IEEE Trans. Magn.* 50, 5, pp. 1–8.

[11] Polajzer, B. (2010): *Magnetic Bearings : Theory and Applications*. INTECH d.o.o., Zagreb, Croatia.

[12] Ravaud, R., Lemarquand, G., and Lemarquand, V. (2009): Force and Stiffness of Passive Magnetic Bearings Using Permanent Magnets. Part 1: Axial Magnetization. *IEEE Trans. Magn.* 45, 7, pp. 2996–3002.

[13] Reese, C. (1996): *Anordnung und Verfahren zur Klassifizierung von Dauermagneten,* DE 196 07 841 C2.

[14] Schäfer, V., Wielsch, P. (2021): How To Reduce Vibroacoustic Emissions For Your Turbopumps? In *3rd Wiley Analytical Science Virtual Conference 2021*, Wiley.

[15] Sobottka, G., Hübner, K.-D. (1981): Dauermagnetische Radiallager und Axiallager: Entwicklungsstand und Tendenz. *MM MaschinenMarkt* 87. Jahrgang, Heft 5 + 10, pp. 2–5.

[16] Urankar, L. K. (1982): Vector potential and magnetic field of current-carrying finite arc segment in analytical form, Part II: Thin sheet approximation. *IEEE Trans. Magn.* 18, 3, pp. 911–917.

[17] Wirth, A. (2016): *Applicative Challenges for today's Turbo Molecular Pumps*. Invited Paper VT-TuM1, Nashville, TN.

[18] Yanliang, X., Yueqin, D., Xiuhe, W., and Yu, K. (2006): Analysis of hybrid magnetic bearing with a permanent magnet in the rotor by FEM. *IEEE Trans. Magn.* 42, 4, pp. 1363–1366.

[19] Yonnet, J.-P. (1978): Passive magnetic bearings with permanent magnets. *IEEE Trans. Magn.* 14, 5, pp. 803–805.

[20] Yonnet, J.-P. (1981): Permanent magnet bearings and couplings. *IEEE Trans. Magn.* 17, 1, pp. 1169–1173.

[21] Yonnet, J.-P., Lemarquand, G., Hemmerlin, S., and Olivier-Rulliere, E. (1991): Stacked structures of passive magnetic bearings. *Journal of Applied Physics* 70, 10, pp. 6633–6635.

15th SIRM – European Conference on Rotordynamics,
Darmstadt, Germany, 22nd – 24th February 2023

An Alternative Active Hybrid Fluid-Magnetic Bearing System for Rotor Dynamic Control

Diogo Stuani Alves [1], Nicola Bailey [2], Patrick Keogh [3]

[1] Department of Mechanical Engineering, University of Bath, BA2 7AY, Bath, UK, dsa41@bath.ac.uk
[2] Department of Mechanical Engineering, University of Bath, BA2 7AY, Bath, UK, nyb21@bath.ac.uk
[3] Department of Mechanical Engineering, University of Bath, BA2 7AY, Bath, UK, enspsk@bath.ac.uk

Abstract

Several industrial sectors, including aerospace, energy, and automotive, are dependent on rotating machines, such as turbines, motors, turbo generators, pumps, or compressors. Thus, there is a continually growing need to improve performance, whilst reducing costs and pollutant agents associated with system operation. To achieve these goals, strategies to control the rotor dynamic behaviour are critical. One approach to control the dynamics of a rotating system is through changing the bearing characteristics, directly altering the stiffness and/or damping of the system as a whole. A traditional bearing can become an active bearing through combining it with any element that enables control, thus making it an active hybrid bearing. In the case of a traditional conical bearing, its dynamic characteristics could easily be manipulated through compensation of the shaft axial position, which could be achieved via a thrust magnetic bearing. Therefore, this paper proposes to create an alternative hybrid bearing which consists of a radial conical fluid bearing and a thrust magnetic bearing to improve performance. The assessment of the concept is evaluated through the analysis of the rotor in the frequency domain, with results showing that the rotor vibration can be reduced by up to 70%.

1 Introduction

Excessive vibration in rotating machines has been a topic of concern for many years. Additionally, the presence of this machinery in every industrial sector has pushed engineers to improve system performance and reduce the costs and pollutant agents associated with its operation. In this regard, strategies to control the rotor dynamic behaviour are crucial. Therefore, these tendencies have driven research and development of controllable bearings, which are commonly known as active bearings. An active bearing is one which is capable of change its characteristics over time. Active magnetic bearings are the most common type and have been successfully used in rotating machines for fault tolerant and vibration control [1, 19, 21]. However, high cost and low damping capabilities are drawbacks for their use in every machine. Moreover, any traditional bearing (for example, ball or fluid film) can become controllable through combining it with an element that enables such control [17], creating an active hybrid bearing.

Jensen and Santos [11] developed an active tilting pad journal bearing to control the vibrations of a rotor and its foundation. Pressurised oil was supplied to the chambers behind the pads to make them move. A similar approach was proposed by Pai and Parkins [18]. Combining a ball bearing, springs, and piezoelectric actuators, Heindel et al. [9] developed a hybrid active bearing to suppress the bearing forces and the rotor resonances. Zapomel et al. [24] developed a new mathematical model of a magneto-rheologic fluid film damper to control the lateral displacement of a rotor. Another interesting design of a hybrid bearing was proposed by Chasalevris and Dohnal [3]. In this case, they allowed the bottom part of a hydrodynamic bearing to move vertically, which was supported by a beam spring and a chamber containing oil to provide spring and damping capabilities to the part. The bearing was passively controlled by the forces generated by the fluid film between the journal and bearing inner surface. Finally, El-Shafei [5] assembled a radial magnetic bearing on top of a radial journal bearing to create a new concept of an active hybrid bearing.

Despite the advantages of hybrid bearings, they are not regularly used in industrial rotating machinery due to their design complexity. Instead, fluid film bearings are commonly used because of their high load carrying

capacity and damping properties. In addition, by modifying the fluid film thickness or clearance, it is possible to control the dynamic behaviour of the bearing, which is not a simple task when a traditional geometric format is used. Nevertheless, if a conical bearing is utilised, then its dynamic characteristics could be easily manipulated through compensation of the shaft axial position.

Conical bearings are usually applied to high-speed rotating machines and were first developed to combine thrust and radial bearings in one single element. One of the first conical bearing studies was produced by Rowe [20], where this component was analysed in a grinding spindle, whereas Ettles and Svoboda [6] investigated the application of a double inclined conical journal bearing to centrifugal pumps. Hannon and Braun [7] based their work on [4] to develop a generalised mathematical formulation for the Reynolds and Energy equations for a conical bearing. A study by Hong et al. [10] presented the dynamic characteristics (stiffness and damping coefficients together with stability) of pocket conical bearings. A numerical analysis considering magneto-rheologic fluid and surface roughness was developed by Sharma and Kumar [23].

It is evident that the literature is scarce on papers that explore the relationship between the fluid film thickness and axial position of the shaft to control the bearing characteristics and consequently the rotor behaviour. One of study discuss the use of different types of control strategies to improve the friction loss in conical journal bearings. In this case Kazakov et al. [12] used hydrostatic pressure to force the shaft moving in the axial direction, and therefore change the bearing average clearance. Therefore, this work proposes a proof of concept of an alternative hybrid bearing for use in small to mid-range machinery. It consists of radial conical fluid bearing and a thrust magnetic bearing, such that the magnetic bearing can sustain the thrust force generated by the pressure field, and by applying a stronger or weaker reaction force actuate the shaft axial position. This arrangement is expected to improve the load carrying capacity and/or reduce the vibration levels, with analysis of the rotor completed in the frequency domain.

2 System modelling

2.1 Conical hydrodynamic bearings

The basis of the classical hydrodynamic lubrication theory is given by the Reynolds equation, which is derived from the Navier-Stokes and continuity equations under simplifying assumptions. For conical bearings (see Figure 1), the problem is conveniently formulated if the Reynolds equation is written in spherical coordinates, with one of the angles being constant and equal to the inclination angle γ, as presented by:

$$\frac{1}{rsin(\gamma)}\frac{\partial}{\partial r}\left[rsin(\gamma)h^3\frac{\partial p}{\partial r}\right]+\frac{1}{r^2sin^2(\gamma)}\frac{\partial}{\partial \theta}\left[h^3\frac{\partial p}{\partial \theta}\right]=6\mu\omega\frac{\partial h}{\partial \theta}+12\mu\frac{\partial h}{\partial t}, \tag{1}$$

where, r and θ are the radial and circumferential coordinates. The pressure is denoted by p, the lubricant viscosity by μ, the rotating speed of the journal by ω, time by t, and the fluid film thickness by h, which depends on the nominal clearance h_0 and the position of the centre of the journal in x, y, and z directions, as shown by:

$$h=h_0-\left[e_ycos(\theta)+e_zsin(\theta)\right]cos(\gamma)+e_xsin(\gamma). \tag{2}$$

The solution of Equation (1) gives the pressure distribution generated by the fluid film. Nevertheless, the Reynolds equation does not have a complete analytical solution, and therefore, the Finite Volume Method can be used to numerically solve it. Once the pressure is known, one can obtain the bearing reaction forces by integrating it over the inner surface of the bearing, giving:

$$\begin{aligned} f_x &= \int_{R_1}^{R_2}\int_{\theta_1}^{\theta_2} psin(\gamma)rsin(\gamma)drd\theta\,, \\ f_y &= -\int_{R_1}^{R_2}\int_{\theta_1}^{\theta_2} pcos(\theta)cos(\gamma)rsin(\gamma)drd\theta, \\ f_z &= -\int_{R_1}^{R_2}\int_{\theta_1}^{\theta_2} psin(\theta)cos(\gamma)rsin(\gamma)drd\theta. \end{aligned} \tag{3}$$

Since the hydrodynamic forces present a low degree of nonlinearity, they are usually linearised through a first order Taylor series expansion around journal's equilibrium position as:

$$\begin{aligned} f_x &= f_{x0} + k_{xx}\Delta x + k_{xy}\Delta y + k_{xz}\Delta z + c_{xx}\Delta\dot{x} + c_{xy}\Delta\dot{y} + c_{xz}\Delta\dot{z}, \\ f_y &= f_{y0} + k_{yx}\Delta x + k_{yy}\Delta y + k_{yz}\Delta z + c_{yx}\Delta\dot{x} + c_{yy}\Delta\dot{y} + c_{yz}\Delta\dot{z}, \\ f_z &= f_{z0} + k_{zx}\Delta x + k_{zy}\Delta y + k_{zz}\Delta z + c_{zx}\Delta\dot{x} + c_{zy}\Delta\dot{y} + c_{zz}\Delta\dot{z}. \end{aligned} \tag{4}$$

in which the derivatives of the forces with respect to the journal position and velocity are the stiffness and damping coefficients used to represent the bearing dynamics in the rotating system [15] of the form:

$$k_{mn} = \left.\frac{\partial f_m}{\partial n}\right|_{x_0,y_0,z_0} \qquad c_{mn} = \left.\frac{\partial f_m}{\partial \dot{n}}\right|_{x_0,y_0,z_0} \qquad (m,n = x,y,z). \tag{5}$$

a)

b)

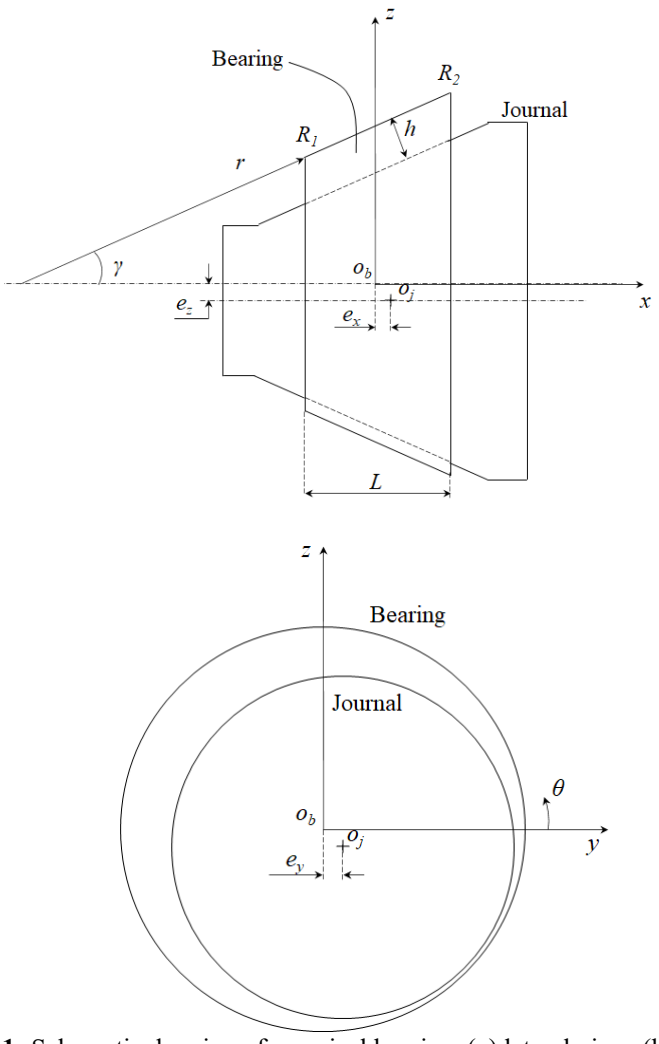

Figure 1: Schematic drawing of a conical bearing. (a) lateral view, (b) frontal view.

Assuming the bearing is infinitely short, it is possible to neglect the effects of the circumferential pressure gradient in Equation (1), and, therefore, an analytical solution becomes viable. Despite this simplification, the pressure calculated with the analytical solution is in reasonable agreement with the complete solution for bearings having a length-diameter ratio up to 0.5 [8]. The main advantage of the analytical solution is its nearly instantaneous computational time.

Therefore, applying the hypothesis of an infinitely short bearing to the Reynolds equation and rearranging, produces:

$$\frac{d}{dr}\left[r\frac{dp}{dr}\right] = \left(6\mu\omega\frac{\partial h}{\partial\theta} + 12\mu\frac{\partial h}{\partial t}\right)\frac{r}{h^3}. \tag{6}$$

Expanding the left-hand side of Equation (6), and rearranging:

$$\frac{d^2p}{dr^2} + \frac{1}{r}\frac{dp}{dr} = \left(6\mu\omega\frac{\partial h}{\partial\theta} + 12\mu\frac{\partial h}{\partial t}\right)\frac{1}{h^3}, \tag{7}$$

which is a nonhomogeneous second order differential equation with variable coefficients. The solution of Equation (7) can be obtained using the substitution $u = dp/dr$ and integration factor $\mu(r) = e^{ln(r)} = r$. For the boundary conditions, it is known that the relative pressure value at $r = R_1$ and $r = R_2$ is zero. Thus, the analytical equation for the pressure as a function of r and θ is:

$$\begin{aligned} p(\theta, r) &= A\frac{r^2}{4} + C_1 ln(r) + C_2, \\ A &= \left(6\omega\frac{\partial h}{\partial\theta} + 12\frac{\partial h}{\partial t}\right)\frac{\mu}{h^3}, \\ C_1 &= -A\frac{(R_1^2 - R_2^2)}{4[ln(R_1) - ln(R_2)]}, \\ C_2 &= -\frac{A}{4}\left\{R_1^2 - \frac{(R_1^2 - R_2^2)}{[ln(R_1) - ln(R_2)]}ln(R_1)\right\}. \end{aligned} \tag{8}$$

2.2 Rotating system

The Finite Element Method is a classical method to model the dynamics of flexible bodies and will be implemented in this work. With it, a continuous body can be represented by the superposition of several simpler elements that can be considered continuous themselves. The kinetic and potential energies can then be calculated with the work of the nonconservative forces for all elements. Thus, applying the Lagrange formulation produces the equation of motion for the rotating shaft system [13]:

$$\mathbf{M}\ddot{\mathbf{q}} + (\mathbf{C} + \omega\mathbf{G})\dot{\mathbf{q}} + \mathbf{K}\mathbf{q} = \mathbf{f} \tag{9}$$

with **M**, **C** = α**M** + β**K**, **G** and **K** denoting the mass, damping, gyroscopic and stiffness matrices, respectively. The vector containing the degrees of freedom is **q**, **f** is the vector containing the external forces, and α and β are the proportionality coefficients for internal damping.

The present work also includes axial vibration with the classical lateral vibrations, causing each node to have five degrees of freedom, where shaft torsion is neglected. To model the shaft lateral vibration, the Timoshenko beam element model is used [16], while the axial vibration was modelled using the axial bar element [2]. Moreover, the disk is modelled as a rigid disk element with gyroscopic effects.

It is possible to solve Equation (9) in the frequency domain by assuming a harmonic solution of the type $\mathbf{q} = \mathbf{Q}e^{j\omega t}$. Therefore, the transfer function for the rotating system is:

$$\mathbf{Q} = (-\omega^2\mathbf{M} + j\omega(\mathbf{C} - \omega\mathbf{G}) + \mathbf{K})^{-1}\mathbf{f} \tag{10}$$

2.3 Magnetic bearing

The purpose of the thrust magnetic bearing in this system is to sustain the thrust forces applied by the conical bearings and, by applying a greater or lower reaction force be able to control the axial position of the whole rotor. Figure 2 provides a schematic of a magnetic thrust bearing. It has an opposing pair configuration, and the resultant axial force will be the sum of the forces generated by the coils individually. Thus, the magnetic force developed by a pair of coils is [22]:

$$f_{mb} = \frac{\mu_0 A_c N_c^2 (i_1 + i_c)^2}{\left[\frac{l_i}{\mu_r} + 2(l_0 - x)\right]} - \frac{\mu_0 A_c N_c^2 (i_2 - i_c)^2}{\left[\frac{l_i}{\mu_r} + 2(l_0 + x)\right]} \tag{11}$$

where l_i is the path length through the coil core, l_0 is the nominal air gap, μ_r is the relative permeability of the magnetic core, μ_0 is the relative permeability of air, A is the area of the face of the pole, N_c is the number of coil

windings, i_1 and i_2 are the bias current for each coil of the pair, and i_c is the control current. Linearising Equation (11) around $x = i_c = 0$, one has:

$$f_{mb} = k_i i_c + k_s x \tag{12}$$

with k_i and k_s denoting the current gain and negative stiffness, respectively.

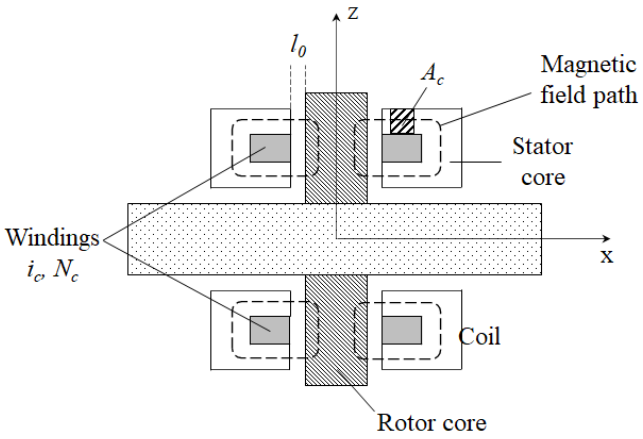

Figure 2: Schematic drawing of a thrust magnetic bearing.

It is possible to obtain the control current using PID feedback control. Since the dynamics of the system is solved in the frequency domain, the effects of the integral gain can be neglected, and PD feedback control can be used with proportional gain k_p and derivative gain k_d. Therefore, the force exerted by the magnetic bearing is:

$$f_{mb} = -(k_i k_p - k_s)x - k_i k_d \dot{x} \tag{13}$$

As presented, x and $\dot{x}$ represent the vibration of the rotor around the axial central position. However, it is extremely important the right demand is sent to the controller such the shaft is placed in the correct axial position, which in turn will modify the conical bearing film thickness and the rotor vibration response. Figure 3 presents the block diagram for the system control.

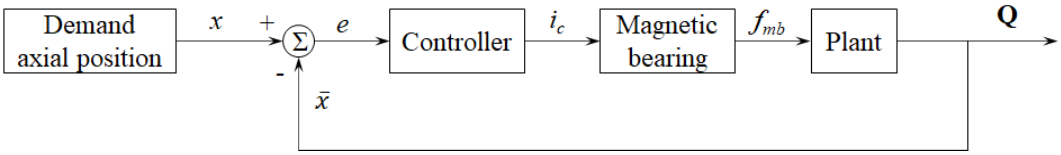

Figure 3: Control block diagram.

The first block is responsible for producing the demand for the controller, i.e., the axial position in which the rotor core should be located at a specific rotating speed. The desirable position is the one that minimises the vibration of the rotating system. Thus, considering the axial position of the rotor as a variable, it is possible to solve a minimisation problem to reduce the rotor vibration. As the problem is unidimensional, a very simple but robust procedure, the dichotomic search, can be used [14]. In addition, the objective function considers the Euclidean norm of the rotor vibration at the disks and bearing positions. Since the calculation of the conical bearing coefficients are the most computationally expensive part of the processes, this task is accomplished taking into account the analytical solution. Then, the feedback control is used to maintain the rotor core in the desired position and reduce its axial and lateral vibrations.

3 Results and discussion

The simulations were accomplished using the rotor set up provided in Figure 4. This rotor is composed of 21 Timoshenko beams elements and three rigid disk elements at nodes 8, 13 (both with diameter equal to 95 mm and length equal to 47 mm) and 21 (diameter equal to 60 mm and length equal to 25 mm), the last one acting as the rotor core for the thrust magnetic bearing. The shaft, which is 550 mm long and has a diameter of 12 mm, is supported by two identical conical bearings placed at nodes 3 and 18. Table 1 shows the bearing relevant data, and the structural damping is taken to be proportional only to the stiffness matrix **K**, in which $\beta = 1.5 \times 10^{-5}$ s. The

shaft and disks are made of steel with elastic modulus $E = 200$ GPa and density $\rho = 7850$ kg/m^3. The parameters needed for the operation of the magnetic bearing and control are shown in Table 2. Moreover, two unbalance masses (m = 1.7 g) were introduced at nodes 7 and 8 - which represent the right and left faces of disks 1 and 2, respectively - at 37 mm far from the disk centre and 180º out of phase.

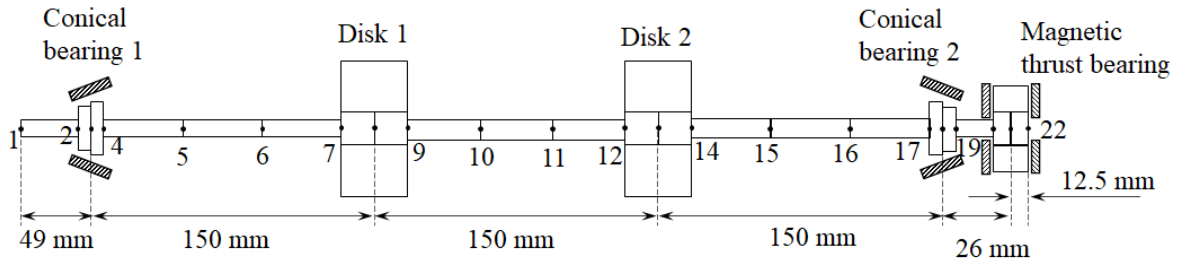

Figure 4: Finite element model of the shaft.

Table 1: Conical fluid-film bearing parameters

Bearing smaller diameter ($R_1 sin(\gamma)$)	31 mm
Inclination angle (γ)	20º
Bearing length (L)	18 mm
Bearing nominal clearance (h_0)	90 µm
Lubricant viscosity (µ)	65 mPa.s

Table 2: Magnetic bearing control parameters

Negative stiffness (k_s)	1.94×10^6 N/m
Current gain (k_i)	530 N/A
Proportional gain (k_p)	3×10^6 A/m
Derivative gain (k_d)	5×10^3 As/m

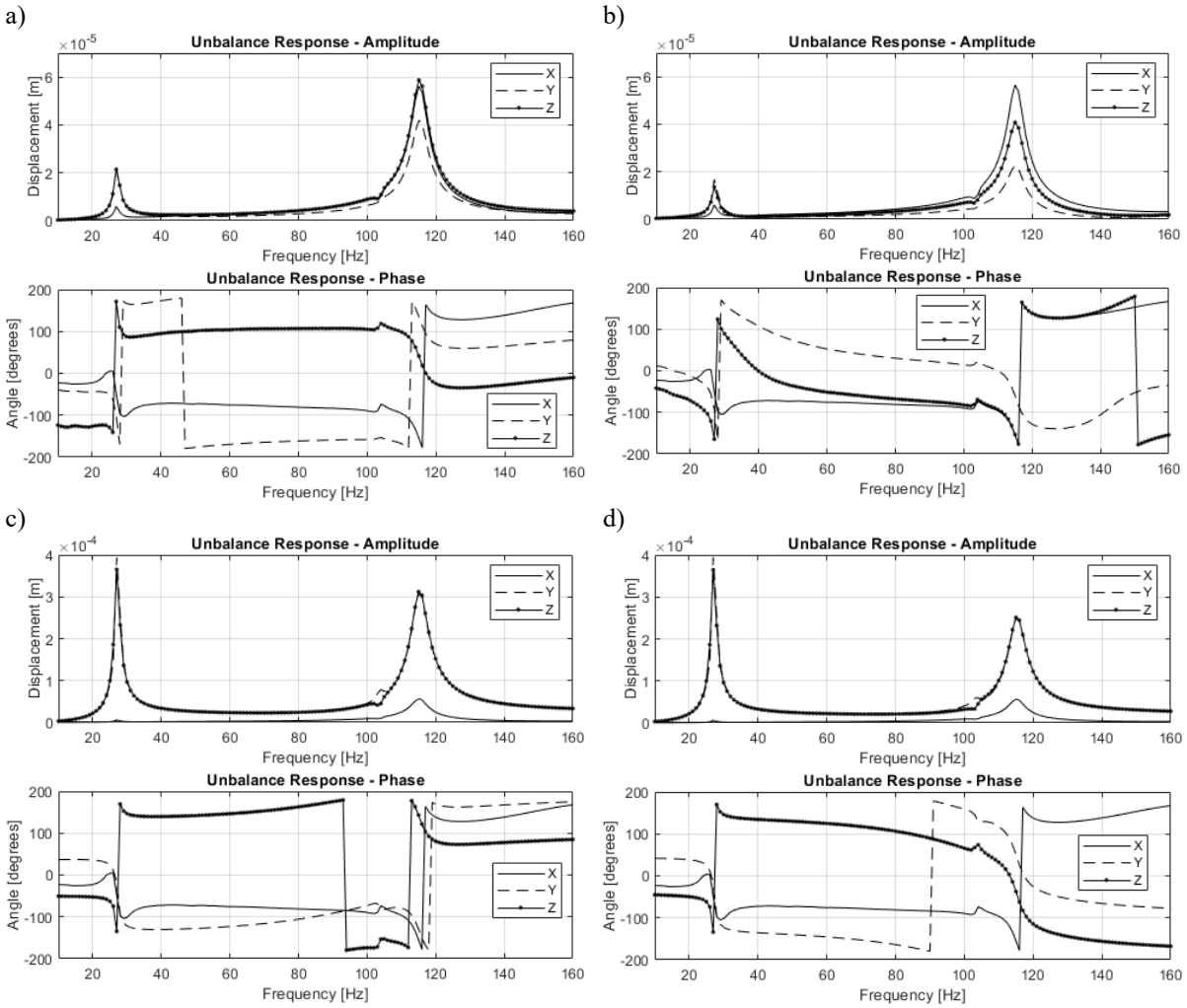

Figure 5: Unbalance response of the rotor without control. (a) bearing 1, (b) bearing 2, (c) disk 1, (d) disk 2.

Figure 5 presents the unbalance response of the rotor at disks and bearings positions when no control is applied to the system. The system presents two critical speeds, one at 27 Hz and one at 115 Hz. Since bearing 2 is between

a disk and the rotor core, the static load applied to this bearing is greater and it will have a higher eccentricity than bearing 1. Therefore, for the same nominal clearance, bearing 2 will be stiffer than bearing 1, which is shown by its lower vibration levels. It is also possible to observe that the vibration levels due to the second critical speed are greater in the left-hand side of the system. The system was simulated with both bearings having their conicity in the same direction when the control was enabled. However, when no control is available, the hydrodynamic bearings must have their conicity opposing to each other to balance the axial forces, as presented in Figure 1.

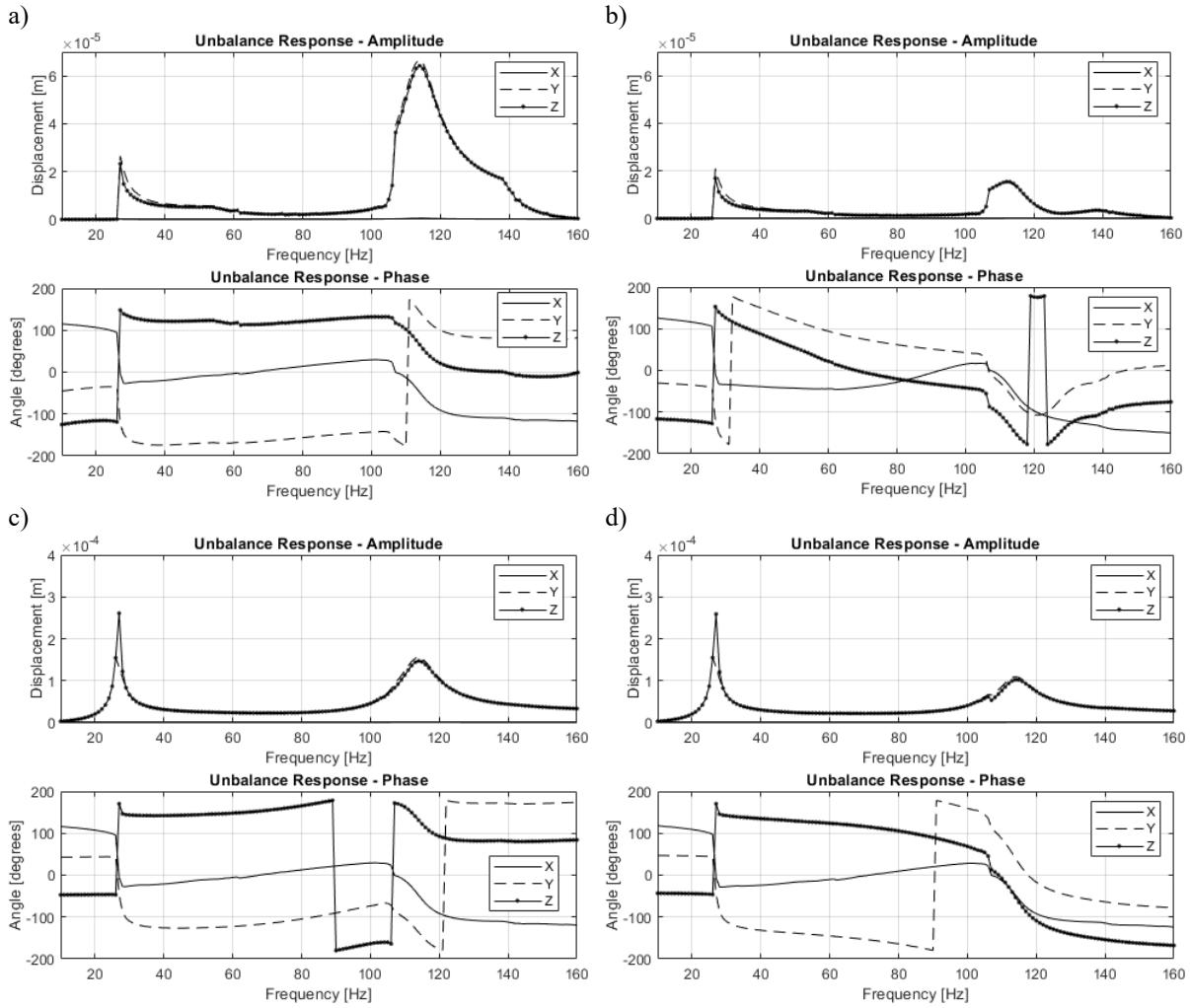

Figure 6: Unbalance response of the rotor with position and vibration control. (a) bearing 1, (b) bearing 2, (c) disk 1, (d) disk 2.

The unbalance response of the controlled rotor is shown in Figure 6. In this situation, the optimisation process finds the axial position that reduces the rotor vibration. This is possible due to the dependence of the fluid film thickness on the axial position, which will affect the pressure field and, consequently, the stiffness and damping characteristics of the bearings and rotating system – a negative position tends to reduce the nominal clearance and increase the load carrying capacity of the bearing. The demand position and the force that must be exerted by the magnetic bearing can be seen in Figure 7. Therefore, the disk unbalance response indicates an average reduction of 34% in the first critical speed vibration levels and 53% in the second critical speed vibration level. However, there is an increase in the vibration at the bearings due to the disk displacements being much greater than the journal displacements and dictating the value of the objective function. Thus, the axial position found is the one which improves the vibration at these positions, causing an increase in the nominal clearance and making the bearings less stiff (Figure 7). This combination results in the observed behaviour.

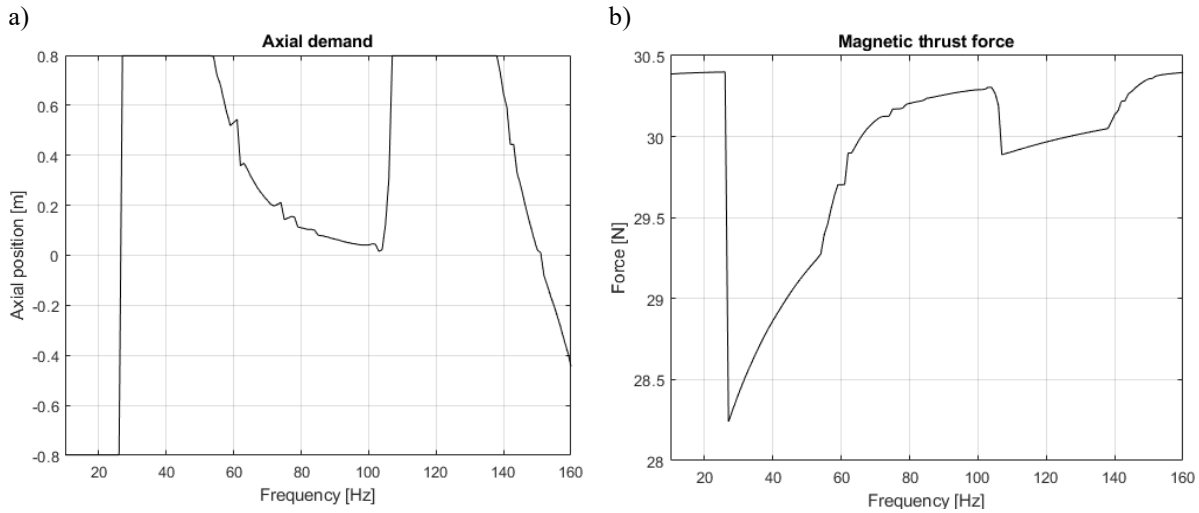

Figure 7: Magnetic bearing behaviour. (a) axial position demand, (b) force that must be exerted by the magnetic bearing to achieve the demand.

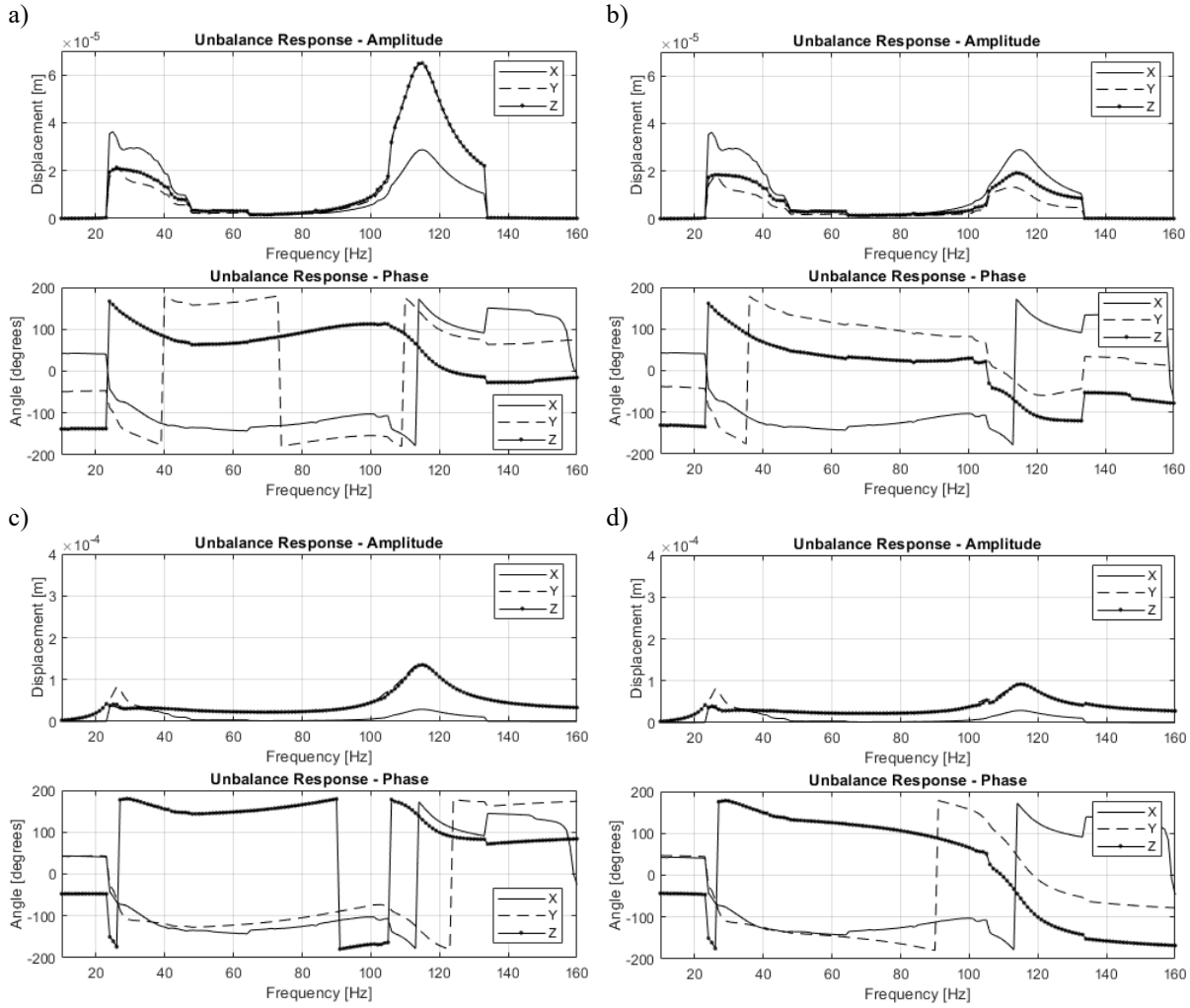

Figure 8: Unbalance response of the rotor with position control only. (a) bearing 1, (b) bearing 2, (c) disk 1, (d) disk 2.

In the previous simulation the feedback signal considered both the axial demand and vibration of the rotor core. Due to the conical bearings coupling the axial and lateral dynamics, the reduction of the axial vibration increases the vibration in the *y*-*z* plane, which makes the control sub-optimum. However, one can achieve greater reductions of the lateral vibrations if only the average vibration of the rotor core (i.e. its static axial position) is provided as feedback, as shown in Figure 8. In this situation, an average reduction of 79% and 60% is expected in the first and

second critical speeds at the disk positions. However, as the vibrations at the bearings increase, the axial vibration is greatest when the rotor crosses the first natural frequency.

4 Conclusions

The concept of a hybrid bearing that combines a conical hydrodynamic bearing and a thrust magnetic bearing is presented in this work. A system composed of a shaft, two disks, two conical bearings, and a magnetic thrust bearing, was analysed by means of its unbalance response.

The controller demand was calculated by a unidimensional minimisation of the vibration at specific points of the rotor, namely the bearing and disk positions. Due to the vibration of the disks being greater than those of the bearings, they were considered the most influential parameters of the objective function. Therefore, by analysing the results, it is possible to conclude that the concept is promising, as it was able to reduce the most significant vibrations included in the objective function.

Moreover, two different feedback strategies were evaluated, one with axial position and vibration signals and the other with just the axial position signals. Because the axial and lateral vibrations are coupled, the axial vibration reduction caused an increase of the lateral vibrations, which reduced the effectiveness of this control strategy. When no axial vibration control was set, the strategy could reduce the lateral vibrations by an average of 70%, however, the axial vibrations became prominent vibration at the bearings.

The fact that the concept uses information of the disks and bearing displacements for the demand calculation might cause some issues for its use in existing real machines. Therefore, possible solutions for this problem would be the use of the axial vibration measured at the magnetic bearing position to adapt the position of the shaft. In addition, it is well known that proximity sensors, and/or accelerometers are embedded at the journal bearing position. Then, it would be possible to use these data, and knowledge about the modal shapes of the rotor, to estimate the vibration at the disk positions, and use it for the optimisation procedure. Another possibility would be the use of the proposed bearing with rigid rotors instead of flexible ones. All these situations would be evaluated in future works regarding this project.

To conclude, the bearing concept presented in this paper is a viable alternative for the development of future active hybrid bearings and it can successfully control rotor vibrations, which will improve the performance of rotating system and delay maintenance operations, reducing costs.

Acknowledgement

The authors thank the Engineering and Physical Sciences Research Council – EPSRC grant [EP/P006930/1] for the financial support.

References

[1] Abulrub, A.H.G., Sahinkaya, M.N., Burrows, C.R., Keogh, P.S. (2006): Adaptive control of active magnetic bearings to prevent rotor-bearing contact. In: *Proceedings of the ASME 2006 International Mechanical Engineering Congress and Exposition*. *Dynamic Systems and Control, Parts A and B*. Chicago, USA, Nov. 5-10, pp. 1523-1529.

[2] Bathe, K. (1982): *Finite Element Procedures in Engineering Analysis*. Prentice-Hall, New Jersey.

[3] Chasalevris, A., Dohnal, F. (2015): A journal bearing with variable geometry for the suppression of vibrations in rotating shafts: Simulation, design, construction and experiment. *Mechanical Systems and Signal Processing*, 52-53, pp. 506-528, http://dx.doi.org/10.1016/j.ymssp.2014.07.002.

[4] Dowson, D. (1962): A generalized Reynolds equation for fluid-film lubrication, *International Journal of Mechanical Science*, 4, pp.159-170.

[5] El-Shafei, A. (2018): SEMAJIB: A versatile high performance smart bearing, In *Cavalca K., Weber H. (eds) Proceedings of the 10th International Conference on Rotor Dynamics – IFToMM,* IFToMM 2018, Mechanisms and Machine Science, 62, Springer, Charm, pp. 372-385.

[6] Ettles, C., Svoboda, O. (1975): The application of double conical journal bearings in high speed centrifugal pumps — Part 1. *Proceedings of the Institution of Mechanical Engineers*. 189(1), pp. 221-230, doi:10.1243/PIME_PROC_1975_189_030_02

[7] Hannon, W.M., Braun, M.J. (2007): Numerical solution of a fully thermally coupled generalized universal Reynolds equation (GURE) and its application. Part 1: Conical bearings. *Tribology Transactions*, 50, pp. 540-557, DOI: 10.1080/10402000701631742.

[8] Hashimoto, H., Wada, S., Ito, J. (1987): An application of short bearing theory to dynamic characteristic problems of turbulent journal bearings, *Journal of Tribology*, 109, pp. 307-314.

[9] Heindel, S., Becker, F., Rinderknecht S. (2017): Unbalance and resonance elimination with active bearings on a Jeffcott rotor. *Mechanical Systems and Signal Processing*, 85, pp. 339-353, http://dx.doi.org/10.1016/j.ymssp.2016.08.016.

[10] Hong, G., Xinmin, L., Shaoqi, C. (2009): Theoretical and experimental study on dynamic coefficients and stability for a hydrostatic/hydrodynamic conical bearing. *Journal of Tribology*, 131, 041701, DOI: 10.1115/1.3176991.

[11] Jensen, K.M., Santos, I.F. (2022): Design of actively-controlled oil lubrication to reduce rotor-bearing-foundation coupled vibrations - theory & experiment. *Proceedings of the Institution of Mechanical Engineers, Part J: Journal of Engineering Tribology*. 236(8), pp. 1493-1510. doi:10.1177/13506501221100615.

[12] Kazakov, Y.N., Kornaev, A.V., Shutin, D.V., Li, S., Savin, L.A. (2022): Active fluid-film bearing with deep Q-network agent-based control system. *Journal of Tribology*, 144, 081803, DOI: 10.1115/1.4053776.

[13] Lalanne, M., Ferraris, G. (1998): *Rotordynamics prediction in engineering*. Wiley, Chicester.

[14] Luenberger, D. G., Ye, Y. (2008): *Linear and nonlinear programming*. Springer Science + Business Media LLC, New York.

[15] Lund, J.W. (1987): Review of the concept of dynamic coefficients for fluid film journal bearings. *ASME Journal of Tribology*, 109(1), pp. 37-41.

[16] Nelson, H. D. (1980): A finite rotating shaft element using Timoshenko beam theory. *ASME Journal of Mechanical Design*, 102(4), pp. 793-803.

[17] Ortega, A.B., Navarro, G.S., Ocampo, J.C., Salazar, M.O., Valdés, G.V. (2012): Automatic balancing of rotor-bearing systems. *Advances on analysis and control of vibrations - Theory and applications*, Mauricio Zapateiro de la Hoz and Francesc Pozo, DOI: 10.5772/48621.

[18] Pai, R., Parkins, D.W. (2018): Performance characteristics of an innovative journal bearing with adjustable bearing elements. *Journal of Tribology*, 140, DOI: 10.1115/1.4039134.

[19] Park, J., Palazzolo, A., and Beach, R. (2008): MIMO Active vibration control of magnetically suspended flywheels for satellite IPAC service. *ASME. J. Dyn. Sys., Meas., Control*, 130(4): 041005. https://doi.org/10.1115/1.2936846.

[20] Rowe, W.B. (1967): Experience with four types of grinding machine spindles, In *Proceedings of the 8th International MTDR Conference*, Manchester, United Kingdom, pp. 453-477.

[21] Schweitzer, G. (2011): Applications and research topics for active magnetic bearings. In *Gupta, K. (eds) IUTAM Symposium on Emerging Trends in Rotor Dynamics*. IUTAM Bookseries, vol. 1011, Springer, Dordrecht. https://doi.org/10.1007/978-94-007-0020-8_23.

[22] Schweitzer, G., Maslen, E.H. (2009), *Magnetic bearings: theory, design and application to rotating machinery.* Springer-Verlag, Berlin.

[23] Sharma, S.C., Kumar, A. (2021): On the behaviour of roughened conical hybrid journal bearing system operating with MR lubricant. *Tribology International*, 156, 106824, https://doi.org/10.1016/j.triboint.2020.106824.

[24] Zapomel, J., Ferfecki, P., Kozanek, J. (2017): Modelling of magnetorheological squeeze film dampers for vibration suppression of rigid rotors. *International Journal of Mechanical Sciences*, 127, pp. 191-197, https://doi.org/10.1016/j.ijmecsci.2016.11.009.

15th SIRM – European Conference on Rotordynamics,
Darmstadt, Germany, 22nd – 24th February 2023

Effect of motor control on torsional vibration response in variable speed drive systems

Urho Hakonen [1], **Sampo Laine** [2], **Sampo Haikonen** [3], **Raine Viitala** [4]

[1,2,3,4] Department of Mechanical Engineering, Aalto University, 02150, Espoo, Finland, urho.hakonen@aalto.fi

Abstract

This paper investigates the torsional response of an electric powertrain considering the effect of the control methods of the electric motor drive, consisting of a variable frequency drive and an electric motor. The vibratory torque occurring in the mechanics of an electric powertrain driven with classical induction motor control methods (open-loop V/Hz and closed-loop V/Hz) were compared. The simulated powertrain was accelerated to a chosen operating speed and a sinusoidal torque excitation was applied. The shaft vibratory torque was calculated over a range of motor operating speeds. The analysis was conducted on simulation results produced using an electric motor drive simulator and a torsional vibration analysis software. The simulation results indicate that the control has a major effect on the torsional response of the powertrain, especially in the case of an improperly configured control system. The combination of the software used is an open-source toolchain for simulating the effects of motor control on the torsional vibration response of powertrain mechanics.

1 Introduction

Electric motor driven powertrains can be controlled with a variable frequency drive (VFD). VFDs are an increasingly common option for powertrains where varying the operating speed and torque of the electric motor is required. The electric drive may excite the torsional modes of the connected mechanical drivetrain [3, 10]. Excitations originate from torque harmonics produced by the electric motor or the VFD. Another possible source of instability is the closed-loop control of the electric drive. VFD controlled powertrains have allegedly caused several incidents with torsional problems [5].

Often the model of the electrical subsystem is not available for modelling torsional dynamics, or there is a lack of suitable tools to combine the electrical and mechanical subdomains. Furthermore, treating the electrical and mechanical subsystems separately may complicate the analysis of the combined system or yield incorrect results. For these reasons, it is hard to fully anticipate the behaviour of a VFD-driven powertrain at its design phase.

In this paper, the torsional response of an electric powertrain is investigated, considering the effect of open-loop V/Hz and closed-loop V/Hz control methods of the electric drive. A powertrain model is constructed using open-source tools programmed in Python. The mechanical drivetrain model is created using the torsional vibration analysis software openTorsion [1] and connected to an induction motor model created with the electric drive simulation tool motulator [2]. Motulator is used to simulate the powertrain in time domain. The simulated powertrain is accelerated to a chosen operating speed and excited with sinusoidal torque variation. Vibratory torque response in the drivetrain shafts is calculated from the steady-state part of the simulated response. The results are then compared for the effect of motor control method on torsional response of the powertrain.

2 Methods

The electric powertrain model consists of a model of the mechanics, a model of an electric motor drive system and motor control algorithms (Figure 1). The electric motor drive system includes a model of an induction motor and a model of a power converter. The electric motor drive model and the control algorithms similar to the ones in this paper are thoroughly documented in [2].

2.1 Electric motor drive system

The electric drive model can be used to calculate accurate torque produced by the motor, as the motor is affected by the vibration of the flexible drivetrain. Additionally, the electric motor adds electromagnetic stiffness and

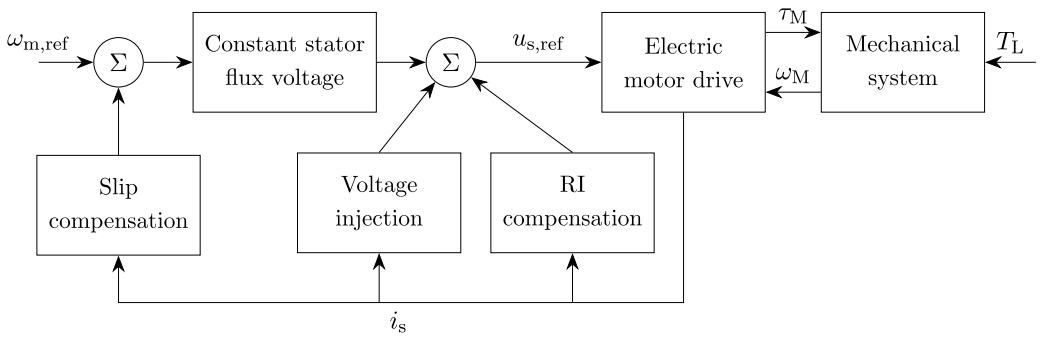

Figure 1: A block diagram of the electric powertrain with V/Hz control, where $\omega_{\mathrm{m,ref}}$ is the rotational speed reference, $u_{\mathrm{s,ref}}$ is the stator voltage reference and i_s is the stator current. The mechanical drivetrain is loaded with the electromagnetic torque τ_{M} produced by the motor and the external excitation torque T_{L}. The mechanical rotational speed ω_{M} of the drivetrain affects the state of the electric motor. In open-loop control, the voltage reference for the electric motor drive is calculated using the stator frequency reference and the constant stator flux reference. Slip compensation, RI compensation and voltage injection are added in closed-loop control. [9]

damping to the powertrain system [6]. Methods for estimating the effect of electromagnetic stiffness and damping to torsional vibration are discussed in [8].

The well known inverse-Γ-equivalent circuit model (Figure 2) presented by Slemon [11] is used to model the induction motor. The model is implemented in stator coordinates and complex space vectors are used. The voltage equations are

$$\begin{aligned} \frac{d\boldsymbol{\psi}_{\mathrm{s}}}{dt} &= \boldsymbol{u}_{\mathrm{s}} - R_{\mathrm{s}}\boldsymbol{i}_{\mathrm{s}} \\ \frac{d\boldsymbol{\psi}_{\mathrm{R}}}{dt} &= -R_{\mathrm{R}}\boldsymbol{i}_{\mathrm{R}} + \mathrm{j}p\omega_{\mathrm{M}}\boldsymbol{\psi}_{\mathrm{R}} \end{aligned} \tag{1}$$

where $\boldsymbol{u}_{\mathrm{s}}$ is the stator voltage, $\boldsymbol{i}_{\mathrm{s}}$ and $\boldsymbol{i}_{\mathrm{R}}$ are the stator and rotor currents, R_{s} and R_{R} are the stator and rotor resistances respectively, p is the number of pole pairs and ω_{M} is the rotor mechanical rotational speed. The stator and rotor flux linkages are

$$\begin{aligned} \boldsymbol{\psi}_{\mathrm{s}} &= L_\sigma \boldsymbol{i}_{\mathrm{s}} + \boldsymbol{\psi}_{\mathrm{R}} \\ \boldsymbol{\psi}_{\mathrm{R}} &= L_{\mathrm{M}}(\boldsymbol{i}_{\mathrm{s}} + \boldsymbol{i}_{\mathrm{R}}) \end{aligned} \tag{2}$$

where L_σ is the leakage inductance and L_{M} is the magnetizing inductance. The electromagnetic torque of the motor is

$$\tau_{\mathrm{M}} = \frac{3p}{2}\mathrm{Im}\{\boldsymbol{i}_{\mathrm{s}}(\boldsymbol{\psi}_{\mathrm{s}})^*\}. \tag{3}$$

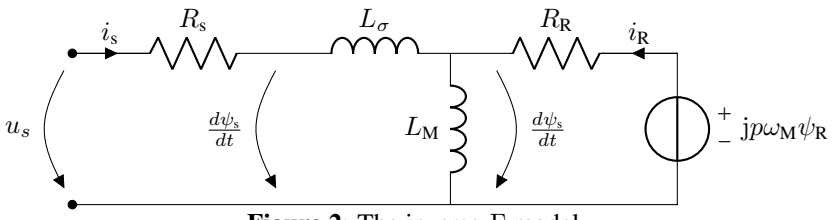

Figure 2: The inverse-Γ model.

The power converter included in the motor drive system is an equivalent model of a lossless inverter. The inverter model is used to calculate AC-voltage from a constant DC-voltage source.

The motor control methods used are open-loop V/Hz and closed-loop V/Hz control. In V/Hz control, the motor speed is adjusted based on a reference speed command by altering the supply frequency and voltage fed to the motor. A discrete-time implementation of V/Hz control similar to the control presented in [9] is used in the powertrain simulation. This implementation uses measured stator current as feedback. In closed-loop V/Hz control, gain parameters affecting stator voltage and stator frequency are included in the control for stabilizing the electrical dynamics of the drive. Setting the gain parameters to zero results in an open-loop configuration.

2.2 Mechanical model and torsional response analysis

A shaft-line finite element model [7] of the powertrain mechanics is created. In the shaft-line finite element method (FEM) the mechanics are modelled as one-dimensional lumped masses with inertia connected by massless shafts with torsional stiffness (Figure 3). The modelled mechanics consist of three lumped masses and two shafts, thus a system with three degrees of freedom is used to present the equations.

The shaft-line finite element method is used to form the equations of motion

$$\mathbf{M}\ddot{\boldsymbol{\theta}}(t) + \mathbf{C}\dot{\boldsymbol{\theta}}(t) + \mathbf{K}\boldsymbol{\theta}(t) = \mathbf{T}(t) \tag{4}$$

where **M** is the mass matrix, **C** is the damping matrix and **K** is the stiffness matrix. The vector $\boldsymbol{\theta}$ contains the rotational angles at the ends of each element and the vector **T** contains the motor torque and the external load torque. The mass matrix **M**, the stiffness matrix **K** and the vector **T**(t) are

$$\mathbf{M} = \begin{bmatrix} I_1 & 0 & 0 \\ 0 & I_2 & 0 \\ 0 & 0 & I_3 \end{bmatrix} \quad \mathbf{K} = \begin{bmatrix} k_1 & -k_1 & 0 \\ -k_1 & k_1 + k_2 & -k_2 \\ 0 & -k_2 & k_2 \end{bmatrix} \quad \mathbf{T}(t) = \begin{bmatrix} \tau_{\mathrm{M}}(t) \\ 0 \\ T_{\mathrm{L}}(t) \end{bmatrix} \tag{5}$$

where τ_{M} is the electromagnetic torque of the motor and T_{L} is the external load torque. The damping matrix **C** is formed by using estimated modal damping as presented in [4]:

$$\begin{aligned} \hat{\mathbf{M}} &= \boldsymbol{\Phi}^{\mathrm{T}}\mathbf{M}\boldsymbol{\Phi} \\ \hat{\mathbf{C}} &= \mathrm{diag}(2\xi_i\omega_i) \cdot \hat{\mathbf{M}} \\ \mathbf{C} &= \boldsymbol{\Phi}^{-\mathrm{T}}\hat{\mathbf{C}}\boldsymbol{\Phi}^{-1} \end{aligned} \tag{6}$$

where ξ_i is the modal damping coefficient of mode i and ω_i is the i^{th} torsional natural frequency. The natural frequencies and the matrix containing the mode shape vectors $\boldsymbol{\Phi} = \begin{bmatrix} \varphi_1 & \varphi_2 & \ldots & \varphi_i \end{bmatrix}$ of the mechanical model are solved from the undamped eigenvalue problem $\left(\mathbf{K} - \omega_i^2\mathbf{M}\right)\varphi_i = \mathbf{0}$.

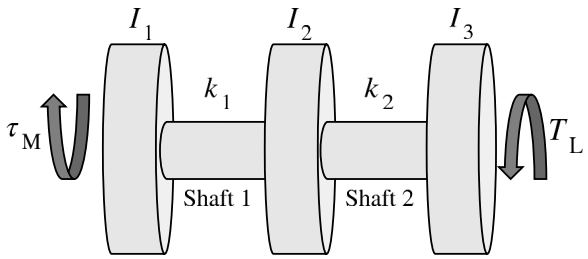

Figure 3: A shaft-line model of a drivetrain. Disk inertia is denoted with I and shaft rotational stiffness with k.

Transient analysis is required to calculate the response of the drivetrain shafts as the electric powertrain is simulated in time domain. The equations of motion (Equation 4) of a linear time-invariant system can be represented in a state-space form

$$\dot{\boldsymbol{x}}(t) = \mathbf{A}\boldsymbol{x}(t) + \mathbf{B}\mathbf{u}(t). \tag{7}$$

The state matrix **A** and the input matrix **B** are

$$\mathbf{A} = \begin{bmatrix} \mathbf{0} & \mathbf{I} \\ -\mathbf{M}^{-1}\mathbf{K} & -\mathbf{M}^{-1}\mathbf{C} \end{bmatrix} \qquad \mathbf{B} = \begin{bmatrix} \mathbf{0} \\ -\mathbf{M}^{-1} \end{bmatrix} \tag{8}$$

where **I** is a 3x3 identity matrix in this three degrees of freedom case selected for analysis. The state vector $\mathbf{x}(t)$ and the input vector $\mathbf{u}(t)$ are

$$\mathbf{x}(t) = \begin{bmatrix} \boldsymbol{\theta}(t) \\ \dot{\boldsymbol{\theta}}(t) \end{bmatrix} \qquad \mathbf{u}(t) = \begin{bmatrix} \mathbf{0} \\ \mathbf{T}(t) \end{bmatrix} \tag{9}$$

where $\boldsymbol{\theta}(t)$ are the rotations, $\dot{\boldsymbol{\theta}}(t)$ are the rotational speeds at the drivetrain nodes and $\mathbf{T}(t)$ is the torque vector.

The shaft torque T_j^s of drivetrain element j can be solved using the torsional stiffness of the shaft and the rotation of the element ends as follows:

$$T_j^s = k_j(\theta_{i+1} - \theta_i). \tag{10}$$

where θ_i is the rotation of node i and k_j is the torsional stiffness of shaft j. The total response is received by calculating the shaft torque at each time step. In a case where the electromagnetic effects are not considered, the harmonic response can be calculated for each excitation frequency with methods presented in [4].

2.3 Simulation

The electric powertrain simulation model was created using the torsional vibration analysis tool openTorsion and the motor drive simulator motulator. OpenTorsion was used to construct a state-space model of the drivetrain as described in section 2.2. The mechanics were tuned so that the first natural frequency of the drivetrain is $f_1 = 20.12$ Hz so that it is in the operating range of the simulated motor making the effect of the motor on the torsional response more apparent. The specifications of the drivetrain are presented in Table 1. A modal damping coefficient of 2 % is recommended for torsional analysis according to [4].

Table 1: Specifications of the simulated electric powertrain.

Drivetrain parameter	**Symbol**	**Value**	**Unit**
First shaft stiffness	k_1	15	kNm/rad
Second shaft stiffness	k_2	10	kNm/rad
First disk moment of inertia	I_1	0.8	kgm^2
Second disk moment of inertia	I_2	0.5	kgm^2
Third disk moment of inertia	I_3	0.7	kgm^2
First natural frequency	f_1	20.12	Hz
Modal damping coefficient	ξ_i	0.02	-
Motor parameter	**Symbol**	**Value**	**Unit**
Nominal speed	ω_{M}	1477	rpm
Frequency	f	50	Hz
Current	i	81	A
Voltage	u	400	V
Power	P	45	kW
Torque	T_{M}	291	Nm
Poles	p	4	-
Rotor resistance	R_{R}	57	mΩ
Stator resistance	R_{s}	29	mΩ
Leakage inductance	L_σ	2.2	mH
Magnetizing inductance	L_{M}	24.5	mH

A 45-kW four-pole induction motor was modelled using the inverse-Γ model with rated motor operating values and estimated motor parameters. The specifications of the 45-kW induction motor are presented in Table 1.

Motulator in :tric motor. The state-space mod(

The electric state is given by voltage equation solved from the state-space mod(:e.

The simulati(rating speed and to ensure the tor ɔ the non-driven end of the power

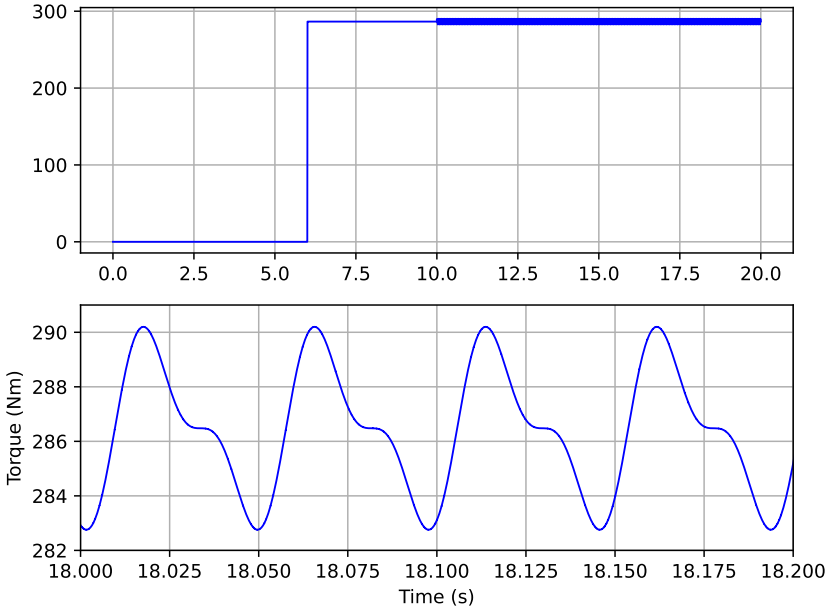

Figure 4: The applied torsional excitation was a sum of two sinudoids with amplitudes of 2% and 1% of the motor nominal torque and frequencies of 1x and 2x drivetrain rotational speed respectively. The DC-component of the excitation data equals the motor nominal torque.

3 Results

The simulation results were the torsional response of the drivetrain shafts in time domain (Figure 5). To make the analysis of the torsional response more convenient, the steady-state part of the response was converted to frequency domain with discrete Fourier transform. The simulation was repeated for operating speeds between 900 and 1500 rpm. The operating speed was increased in steps of 10 rpm for speeds 900-1200 rpm and 1300-1500 rpm between individual simulations. For speeds 1200-1300 rpm the operating speed was increased in steps of 1 rpm as in this range the response amplitude is the highest due to the first natural frequency of the drivetrain and for this reason it was of the largest interest.

The total torsional response of the shafts of the simulated powertrain driven with an induction motor with V/Hz control are presented in Figure 6. The amplitude represents the vibratory torque power at the corresponding rotational speed, received by integrating the frequency domain response. The response was calculated for both open-loop and closed-loop V/Hz control. Additionally, for baseline, the response of a model where the electric motor is modelled as a single lumped mass without electromagnetic effects and motor control was solved in frequency domain using steady-state forced response analysis methods presented in [4].

The effect of the electromagnetic stiffness and damping can clearly be seen in the simulation results. The peak amplitude of the response of the system without the control and the motor model is at the first natural frequency of the drivetrain. The first natural frequency of the powertrain increases when the electric motor model is added. This is due to the added electromagnetic stiffness of the electric motor drive. The amplitude of the response under open-loop V/Hz control is higher than the response of the model with only the mechanical drivetrain, indicating that the open-loop control reduces damping. The drivetrain parameters were chosen so that reduced damping can be observed. The damping effect of closed-loop V/Hz control was also observed, as the response amplitude with open-loop control was larger than with closed-loop control.

4 Conclusion

The vibratory torque occurring in the mechanics of an electric powertrain driven with open-loop V/Hz and closed-loop V/Hz control methods were compared. The simulated powertrain was accelerated to a chosen operating speed and a sinusoidal torque excitation was applied. The shaft vibratory torque was calculated over a range of motor

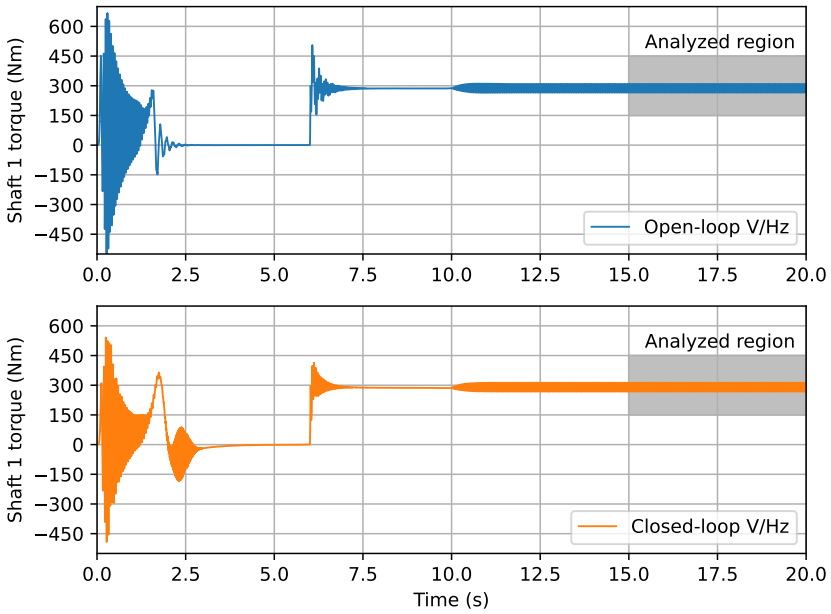

Figure 5: The time domain response of shaft 1 in open-loop and closed-loop V/Hz control at the operating speed of 1250 rpm. The transient part at 0 to 2.5 seconds is due to motor startup. The transient part at 6 seconds is caused by the constant load. The sinusoidal excitation was applied at 10 seconds. The highlighted steady-state part was used to calculate the response in frequency domain.

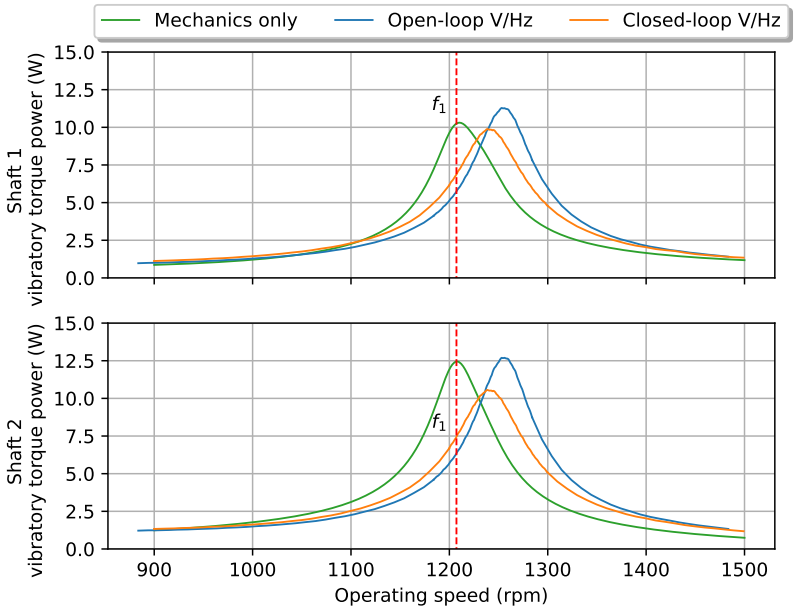

Figure 6: Torsional response of the drivetrain shafts in open-loop and closed-loop V/Hz control and without the electric drive model.

operating speeds. The analysis was conducted on simulation results produced using a motor drive simulator and a torsional vibration analysis software. The results demonstrate the importance of the inclusion of an electric motor drive model in torsional vibration analysis, especially if the natural frequency of the mechanics is in or near the operating speed range of the motor.

The combination of the software used is an open-source toolchain for simulating the effects of motor control on the torsional vibration response of powertrain mechanics. Inclusion of the effects of electric drives on the torsional

vibration response of a drivetrain helps prevent and troubleshoot unexpected vibration problems in powertrains already in the design phase. Future work includes torsional analysis of a simulated electric powertrain driven with additional control algorithms and comparison of simulation results to experimental measurements.

References

[1] Aalto ARotor, (2022), OpenTorsion: Open-Source Backend for Torsional Vibration Analysis, Github repository, `https://github.com/Aalto-Arotor/openTorsion`

[2] Aalto Electric Drives, (2022), Motulator: Motor Drive Simulator in Python, Github repository, `https://github.com/Aalto-Electric-Drives/motulator`

[3] Bruha, M. and Peroutka, Z. (2015): Torsional vibration in large variable speed drive systems: Origin and mitigation methods. *17th European Conference on Power Electronics and Applications*, pp. 1–10, doi: 10.1109/EPE.2015.7309169.

[4] Chen, W.-J. and Gunter, E.-J. (2005): *Introduction to Dynamics of Rotor-Bearing Systems*. Trafford Publishing, Victoria, BC.

[5] Corbo, M.-A. (2021): VFDs - The torsional analyst's best friend or worst enemy? *Gas Machinery Research Council 2021 Gas Machinery Conference*, Louisville, Kentucky.

[6] Feese, T. and Kokot, A. (2016): Electromagnetic Effects on the Torsional Natural Frequencies of an Induction Motor Driven Reciprocating Compressor With a Soft Coupling *45th Turbomachinery & 32nd Pump Symposia*, Houston, Texas.

[7] Friswell, M.-I. (2010): *Dynamics of Rotating Machines*. Cambridge University Press, Cambridge.

[8] Hauptmann, E.-G., Eckert, W.-F. and Howes, B.-C. (2013): The Influence on Torsional Vibration Analysis of Electromagnetic Effects Across an Induction Motor Air Gap *Gas Machinery Conference*, Albuquerque.

[9] Hinkkanen, M., Tiitinen, L., Mölsä, E. and Harnefors, L. (2022): On the Stability of Volts-per-Hertz Control for Induction Motors. *IEEE Journal of Emerging and Selected Topics in Power Electronics*. 10(2), pp. 1609–1618, doi: 10.1109/JESTPE.2021.3060583.

[10] Mishra S., Palazzolo, A.-B., Han, X., Li, Y. and Kulhanek, C. (2020): Torsional Vibrations in Open Loop Volts Hertz Variable Frequency Drive Induction Motor Driven Mechanical Systems. *IEEE Texas Power and Energy Conference*, pp. 1–6, doi: 10.1109/TPEC48276.2020.9042586.

[11] Slemon, G.-R. (1989): Modelling of Induction Machines for Electric Drives. *IEEE Transactions on Industry Applications*, 25(6), pp. 1126–1131.

15th SIRM – European Conference on Rotordynamics,
Darmstadt, Germany, 22nd – 24th February 2023

Fault diagnosis on rotating systems with big data analytics

Lucas Papacharalabos [1], Pantelis Nikolakopoulos [2]

[1] Mechanical Engineering and Aeronautics Department, University of Patras, 26500, Patras, Greece, lpapacharalabos@gmail.com

[2] Mechanical Engineering and Aeronautics Department, University of Patras, 26500, Patras, Greece, pnikolakop@upatras.gr

Abstract

Rotating systems exist in a wide range of applications. In these systems, an uncontrolled oscillation can lead to resonances, which may result in devastating consequences for the systems. In this work real experimental data were used, from an experiment that had been conducted by NSF I/UCR Center for Intelligent Maintenance Systems. These data are analyzed in many studies, and a fault detection algorithm for a rolling bearing is developed, with the Support of Vector Machine (SVM) method. The performance and the validity of the method was checked by testing the algorithm with a laboratory test-to-failure experiment and data obtained from a fault-seeded bearing test ring.

1 Introduction

The study of rotating systems on a scientific level date back to the middle of the 19th century. These systems are found in most technological constructions, therefore the study of their behavior in various situations is considered necessary for the efficiency of each machine. The dynamic analysis of the rotating systems is an issue that piqued the interest of many scientists, during the development and the continuing rise of the use of the machines. A worth noted job has been presented by Fernández-Francos et.al [1], in which initially a one-class m-SVM is used to distinguish between normal and faulty conditions and then the problem is being localized with band-pass filters and Hilbert Transform. The oscillations and imbalances in a rotating system became more and more apparent while the machines were operated at higher speeds. Therefore, methods of modeling and scientific study of these systems had to be developed [2,3,7].

Nowadays the applications of rotating systems take place in a lot of areas of human life, such as transportation (internal combustion engines, turbojets, etc.),the production of electricity (gas turbines, wind turbines, generators) but also household appliances (vacuum cleaners, washing machine, etc.).

A very important part of rotating systems is their mounting. The axles are mounted with roller or sliding bearings. In this work are studied the roller bearings. As mechanical elements, roller bearings require a certain analysis to define their characteristics, such as durability and corrosion [7]. Their behavior can be considered linear in a simplified model, but for a more accurate approach to reality it is worthwhile to include non-linearities in their analysis. One such study is that of Dong-Soo Lee and Dong-Hoon Choi, [2] who study the behavior of roller bearings as multistage shaft support elements for cases of linear and nonlinear bearing stiffness.

Qiu et.al [5] processed real data for rolling element bearing prognostics using Wavelet transformation.

A machine may lose its functionality due to mechanical faults. Damages arise as a result of friction, environmental conditions, and fatigue of materials after a period in operation. So, it is worth researching the analysis and identification of those characteristics on a machine or a component, which indicate a possible failure and therefore damage to the system. This item is studied in the work of Guanqiu Qi, el al[4] who develop an algorithm for failure diagnosis and prediction, of a reciprocating compressor located on an offshore oil rig using the SVM method. More specifically, this work analyzes big data, which were being collected for five years. These data were first preprocessed and then classified by Gaussian distribution into significant and non-significant to diagnose defects. Another remarkable study is that of Hyung-Chul Jung and Susan Krumdieck [6], in which a Radial Inflow Turbine Rotor-Bearing System is being analyzed on the platform of ANSYS APDL, and a modal and mass unbalance response analyses were carried out with six cases having different shaft

diameters and bearing arrangements. Using SVM combined with multidimensional parameters of EMD Yerui Fanet al [9] developed an algorithm for bearing fault diagnosis. This proposed model is evaluated through experiments and comparative studies. A very interesting approach of fault diagnosis with SVM is made by Chih-Jer Lin et.al [10] in which the separating hyperplane and the parameters C and γ of the SVM classifier are found using the PSO and artificial fish-swarm algorithm (AFSA). In this work the linear Kernel function is used to create the Hyperplane. Another work that is worth to mention that of Mohammed Hakim et.al [11]. In this work fault diagnosis is succeeded using different methods of deep learning (Convolutional neural networks, Auto-encoder and stacked auto-encoder, Generative adversarial network, Recurrent neural network, Deep belief networks) and at the end it is made a comparison between the machine learning and deep learning on the case of fault diagnosis. A well-documented approach to rolling bearings fault diagnosis is this of Bo Penget.al [12]. In this survey paper are summarized the fault diagnosis methods of the rolling bearings based on vibration signals from the perspectives of faults detection and fault type recognition.

In the current work experimental data were used, from an experiment that had been conducted by NSF I/UCR Center for Intelligent Maintenance Systems. These data were analyzed in many studies so to achieve a fault detection algorithm with the SVM method. Also, the performance of the method is checked by testing the algorithm with real data from a laboratory test-to-failure experiment and data obtained from a fault-seeded bearing test. The manipulation of the big data in combination with SVM method in order to get diagnosis in a rolling bearing, using open-source data, is the main contribution of this work.

2 Theory

2.1 Support Vectors Machines (SVMs)

Vapnik [8] proposed Support Vectors Machine (SVM) for the first time, and since then it is a very popular approach to deal with the problem of classification. The base of SVM is the principle of Structural Risk Minimization (SRM) in the statistical learning theory, and it has outstanding generalization performance. SRM is used to maximize the margin between different classes. That is the reason why SVM is a useful statistical learning theory that can be used to deal with engineering problems. The main idea of SVM is to use a linear separating hyperplane for the division of the training samples into two classes.

With linear classification function SVM separates the training data into two classes with a linear separating hyperplane. Figure 1 depicts the data of two classes, where the squares belong to the negative class and the circles are of the positive class. SVM method creates a linear boundary in the middle of the two classes. The distance of the two imaginary lines represents the maximum margin. The points that are crossed by the imaginary lines are called support vectors.

Support vectors are the most important points because they define all the information used to design the classifier.

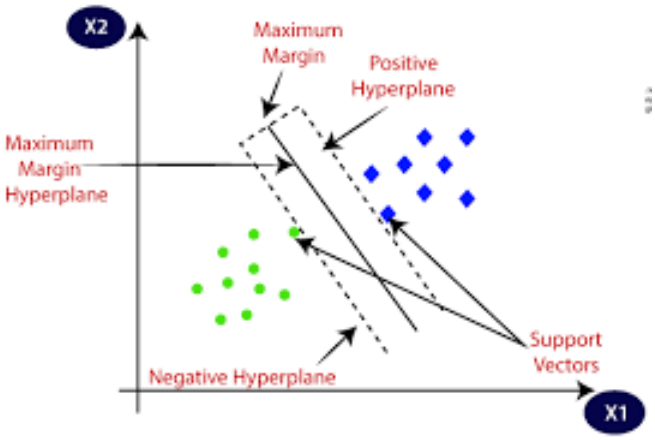

Figure 1: Two classes classification using SVM.

So, the datapoints:

$$(x_1, y_1), \ldots, (x_l, y_l), x \in R^n, y \in \{+1, -1\} \quad (1)$$

can be divided by a hyperplane equation:

$$(w \cdot x) + b = 0 \ (2), \qquad (w \cdot x_i) + b \geq 1 \ \text{ if } y_i = 1 \ (3), \qquad (w \cdot x_i) + b \leq 1 \ \text{ if } y_i = -1 \ (4)$$

The optimal hyperplane is the one that can make sure that the distance between the different classes of samples is maximum. The separating hyperplane is explained using the equations (3) and (4).Then we try to find the optimal hyperplane by obtaining the minimum of the function below (6):

$$\Phi(w) = \frac{1}{2} \parallel w \parallel^2 = \frac{1}{2}(w \cdot w) \ (5)$$

Lagrange function is constructed in (6).

$$L(w, b, \alpha) = \frac{1}{2} w^T \cdot w - \sum_{i=1}^{n} \alpha_i [y_i (w^T \cdot x_i - b) - 1] \quad (6)$$

α_i is Lagrange multiplier, which should satisfy the constraint $\alpha_i \geq 0, i = 1, \ldots, l$. When condition (5) reaches its extremum, the corresponding points should satisfy Equations (7) and (8).

$$\frac{\partial L}{\partial b} = 0 \Rightarrow \sum_{i=1}^{n} \alpha_i y_i = 0 \ (7), \qquad \frac{\partial L}{\partial w} = 0 \Rightarrow w = \sum_{i=1}^{n} \alpha_i y_i x_i \ (8)$$

Substitute Equations (7) and (8) into Lagrange function and eliminate w and b.

$$w(\alpha) = \sum_{i=1}^{l} \alpha_i - \frac{1}{2} \sum_{i,j}^{l} \alpha_i \alpha_j y_i y_j (x_i, x_j) \quad (9)$$

Equation (9) should under the constraint $\alpha_i \geq 0, i = 1, \ldots, l$ and $\sum_{i=1}^{l} \alpha_i y_i = 0$. Those $x_i \cdot s$ with $\alpha_i > 0$ are termed support vectors (SVs). The label of a testing data x_i can then be obtained by

$$f(x) = \text{sign}\left(\sum_{x_i \in X_{svM}} \alpha_i y_i (x \cdot x_i) + b \right) (10), \qquad Where \quad w = \sum_{x_i \in X_{SVM}} \alpha_i y_i x_i$$

Non-linear classification is always caused by nonlinearities or noise. In the case of the training samples cannot be separated linearly, so Cortes introduced the nonnegative variables ξ_i and penalty function $F(\xi) = \sum \xi_i$ to promote the optimal hyperplane to general situation. the nonnegative Cortes variables ξ_i and penalty function $F(\xi) = \sum \xi_i$, are used, so to promote the optimal hyperplane to general situation. A slack variable is introduced to condition (5).

$$y_i (w^T \cdot \varphi(x_i) + b) \geq 1 - \xi_i \ (11), \qquad \min \frac{1}{2} \parallel w \parallel^2 + C \sum \xi_{i\,i=1}^{l} \quad (12)$$

The general classification hyperplane is minimum value of Equation (12) under the constrain (11).With the condition $y_i (w \cdot x_i + b) \geq 1 - \xi_i$ is defined the value of the penalty term(c). The formula used on both occasions (Linear, Non-linear) is the same, but the constraint α_i is different, because it is depended on the $0 \leq \alpha_i \leq C$. Therefore, using an appropriate inner product Kernel function $K(x_i, y_i)$ in the optimal classification plane can achieve linear classification after a nonlinear transformation, and the computational complexity is not increased. The objective function is represented below.

$$W(\alpha) = \sum_{i=1}^{l} \alpha_i - \frac{1}{2} \sum_{i,j=1}^{l} \alpha_i \alpha_j y_i y_j k(x_i, x_j) \quad (13)$$

The kernel is always used in input space because it can map the input samples into feature space and apply dot product in that space. There are many kinds of kernel, such as Polynomial Kernel Function, Linear Kernel Function, Sigmoid Kernel Function and Radian Basis Function (RBF), which are commonly used and showed in Table 1. For the current investigation the RBF method is used because a stochastic signal is analyzed.

Table 1: Examples of Kernel functions

Kernel functions	Formula
Linear	$k(x_i, y_i) = x_i \cdot x_j$
Polynomial	$k(x_i, y_i) = \left(\gamma x_i \cdot x_j + r\right)^d, \gamma > 0$
Radian basis function	$k(x_i, y_i) = \exp\left(-\gamma \lVert x_i - x_j \rVert^2\right), \gamma > 0$
Sigmoid	$k(x_i, y_i) = \tanh\left(\gamma x_i \cdot x_j + r\right)$

3 Data Analysis

3.1 Data Model

In this work, it is studied the oscillation signal from rolling bearings, which work until failure. In figure 2, the experimental setup is depicted:

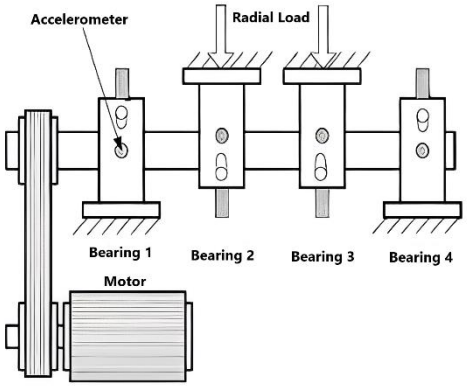

Figure 2: Experimental set up. [5]

Purpose of this study is the analysis of the signal, so an algorithm to be developed that will detect the existence of a fault in the components of the signal. The signal used consists of experimental data which are obtained from an experiment that was conducted by the NSF I / UCR Center for Intelligent Maintenance Systems (IMS –www.imscenter.net) with the support of Rexnord Corp. in Milwaukee, WI.

3.2 Experimental set up

Four bearings were installed on a shaft, as presented in figure 2. The rotation speed was kept constant at 2000 RPM by an AC motor coupled to the shaft via rub belts. A radial load of 6000 lbs is applied onto the shaft and bearing by a spring mechanism. All bearings are force lubricated.

Rexnord ZA-2115 double row bearings were installed on the shaft as shown in Figure 2. PCB 353B33 High Sensitivity Quartz ICP accelerometers were installed on the bearing housing (two accelerometers for each bearing [x- and y-axes] for data set 1, one accelerometer for each bearing for data sets 2 and 3). Sensor placement is also shown in Figure 2. All failures occurred after exceeding the designed lifetime of the bearing which is more than 100 million revolutions. The fault occurred on the outer ring of the Bearing 1 [5].

The time response of the signal is shown in figure 3.

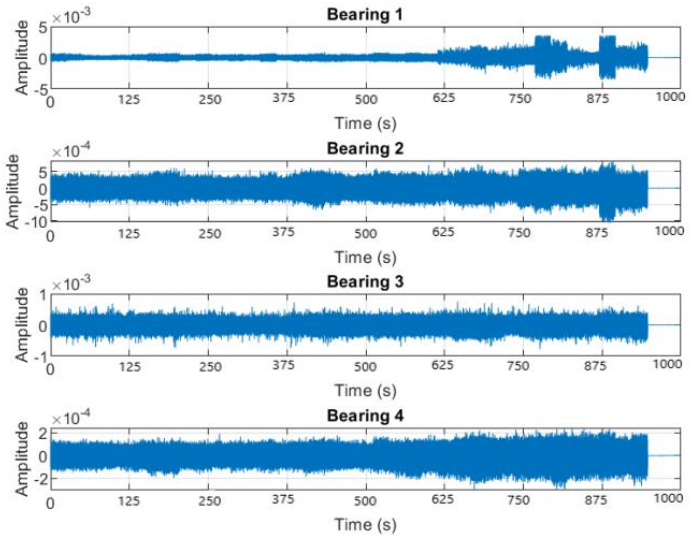

Figure 3: Time response for each bearing.

3.3 Fault diagnosis

Firstly, the signal is divided into eight datasets according to the date of the recording. The model is trained using a number of datasets. Then predictions were made with the rest of the data, so to check how the algorithm works with new signal but also to understand how the amount of data that were used to train the model, affects its effectiveness.

A system of permutations is being used to train the model. So, a set of 68 models is created. These models constitute every possible combination of training and validation, with the SVM method, of the available data. So, for the models 1-16 the algorithm was trained with 6 datasets (3 datasets of healthy operation and 3 datasets with incorrect operation) and validated with the rest 2, for the models 17-52 the algorithm was trained with 4 datasets (2 datasets of healthy operation and 2 datasets with incorrect operation) and validated with the rest 4 and for the models 53-68 the algorithm was trained with 2 datasets (1 dataset of healthy operation and 1 dataset with incorrect operation) and validated with the rest 6.

This was done so that we could be sure that our model has been properly trained and that it can make a correct diagnosis with new data as an input. Figure 4 shows with a flowchart how this fault diagnosis work.

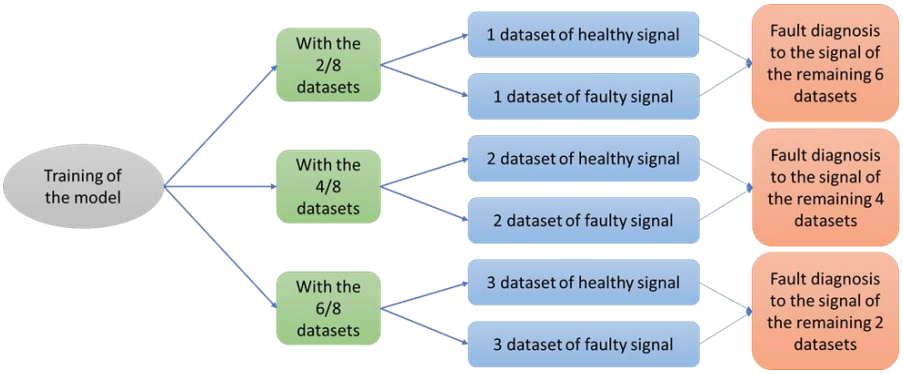

Figure 4: Model Training flow chart.

For the SVM model was used classification. The algorithm recognizes two classes, one for the healthy operation, with value -1 and one for the faulty operation with value +1. The system studied consists of a nonlinear and stochastic signal that has been produced by a physical experiment. So, in these cases the kernel function used is the Radial Basis Function (RBF).

The development of the fault diagnosis algorithm has been made with MATLAB.

4. Results

The results we obtained following this procedure are quite encouraging and exceed 79% in success rate.

In the Figures 5 and 6 is depicted the Fourier and Hilbert transform of the signal on the first and the last day of the experiment respectively. On the top of the pictures is also depicted the normalized signal. It is easily visible that on the first day the amplitude has lower values than on the eighth day. Another difference between the two figures 5 and 6 is on the power spectrum density of the Fourier transform. Finally, the content of energy changes from the first to the last day and that is depicted from on the Hilbert transform. From these diagrams, related to Hilbert transform, comes the result that the oscillation is more intense the last day of the experiment, which is a result of the damaged function of the bearings.

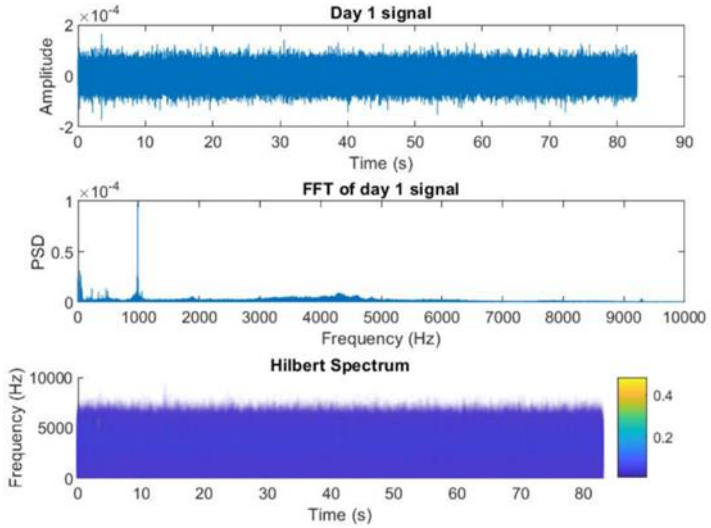

Figure 5: First day dataset.

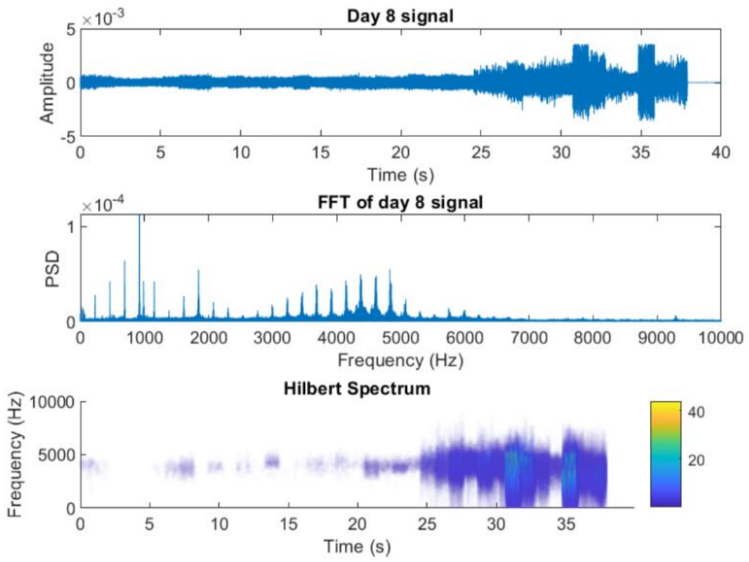

Figure 6: Last day dataset.

In figure 7 are presented the results of the algorithm for the three different cases. The success rate of the models that are trained with 6/8 datasets (100%) is a result of the success rate of 16 models. Respectively the success rate of the models that are trained with 4/8 datasets (79.17%) is a result of the success rate of 35 models and the success rate of the models that are trained with 2/8 datasets (95.83%) is a result of the success rate of 15

models. In conclusion the success rate of the models that have been trained with 4/8 datasets is the most reliable because it comes up from a greater number of test than the success rate on the other cases.

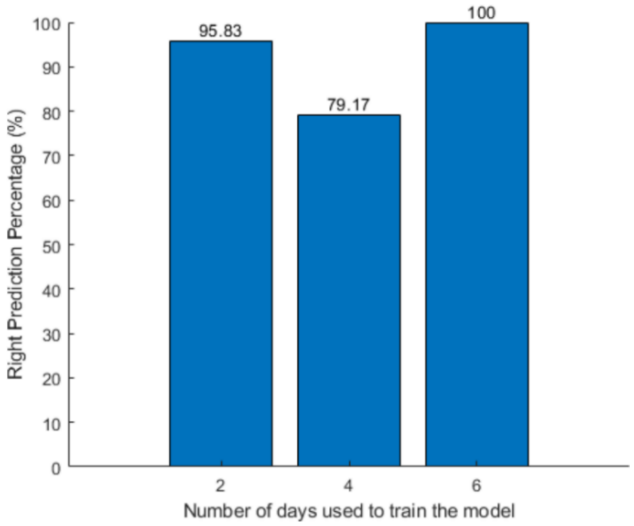

Figure 7: Success rate of the models that have been trained with 2 out of the 8 datasets, with 4 out of the 8 datasets and with 6 out of the 8 datasets respectively.

The Fourier and Hilbert transforms were applied to the entire signal, but we present in this paper only the first and the last day to save space.

To be clear, it is not so important to set a general success rate as it is to study each case individually. As already mentioned, a system of permutations is applied so to gain as much results as possible from the available data. So, a set of 68 models is created. These models constitute every possible combination of training and validation, with the SVM method, of the data we have. In this work 20.152.320 sensor measurements data used per model .

To make the content of the figure 8 clearer, it is worth mentioning that in every model, the value -1 (negative) means the non-detection of damage to the signal, while the value +1 (positive) means the detection of damage to it. In Figure 8 four different colors appear, where each is assigned to one state (blue → true negative, orange → true positive, yellow → false negative, purple → false positive). The states true positive and true negative, state the correct detection of damage or not, respectively. On the other hand, the false positive and false negative situations indicate the incorrect detection of damage or not, respectively.

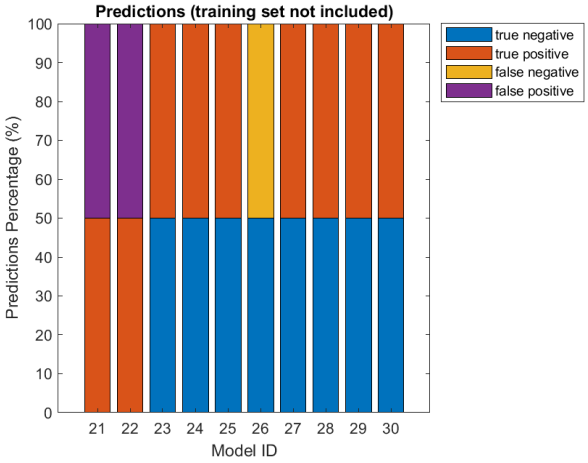

Figure 8: Example of the results for the models 21-30.

To be more specific for the models 1-16 the algorithm was trained with 6 datasets and validated with the rest 2, for the models 17-52 the algorithm was trained with 4 datasets and validated with the rest 4 and for the models 53-68 the algorithm was trained with 2 datasets and validated with the rest 6, as it shown in figure 4.

5. Conclusions

In this work real experimental data free from the literature were used, from Cincinnati University, by NSF I/UCR Center for Intelligent Maintenance Systems. The used data analyzed in many studies, in order to develop a fault detection algorithm using the support vector machine method. The performance of the method was also checked by relevant laboratory data. The below main conclusion may be addressed:

Figure 7 depicts the overall results for the three cases of training-validation tests that we conducted.

It is noticeable that the models that used 6/8 datasets for their training show a success rate that reaches 100%. Of course, this case is quite ideal as in most of the cases, there is not available such an amount of recording material, that can be used for training.

The remarkable part of this study is that the other two cases had also a high success rate. Specifically, the models that had been trained with the 4/8 dataset noted a 79.17% success rate and the models that had been trained with 2/8 datasets marked 95.83% success rate.

The result that is obtained from these results is that the SVM method is adequate to train a model that makes successful predictions of upcoming failure even with a small amount of data as a sample.

Acknowledgement

The authors acknowledge the NSF I / UCR Center for Intelligent Maintenance Systems for the open used data.

References

[1] Diego Fernández-Francos, David Martínez-Rego, Oscar Fontenla-Romero, Amparo Alonso-Betanzos (2013): Automatic bearing fault diagnosis based on one-class ν-SVM, *Computers & Industrial Engineering*,47(1), pp. 357-365.

[2] Dong-Soo Lee, D.-H. C. (1997): A Dynamic Analysis of a Flexible Rotor in Ball Bearings with Nonlinear Stiffness Characteristics, International Journal of Rotating Machinery, *International Journal of Rotating Machinery*, 3(2), pp. 73-80.

[3] Genta, G. (2005): Dynamics of Rotating Systems, New York.

[4] Guanqiu Qi, Zhiqin Zhu, Ke Erqinhu, Yinong Chen, Yi Chai, Jian Sun (2017): Fault-diagnosis for reciprocating compressors using big data and machine learning, *Simulation Modelling Practice and Theory*, 80, pp. 104-127.

[5] Hai Qiu, Jay Lee, Jing Lin, Gang Yu (2005): Wavelet filter-based weak signature detection method and its application on rolling element bearing prognostics, *Journal of Sound and Vibration*, 289(4-5), pp. 1066-1090.

[6] Jung, H.-C. & Krumdieck, S. (2014): Rotordynamic Modelling and Analysis of a Radial Inflow Turbine Rotor-Bearing System, *International Journal of Precision Engineering and Manufacturing*, 15(11), pp. 2285-2290.

[7] Kotzalas, M., Harris, T. (2006): Advanced Concepts of Bearing Technology, New York

[8] Vladimir Vapnik (2000): The Nature of Statistical Learning Theory, 2nd Edition, Springer,USA.

[9] Yerui Fan, Chao Zhang, Yu Xue, Jianguo Wang, Fengshou Gu (2020): A Bearing Fault Diagnosis Using a Support Vector Machine Optimized by the Self-Regulating Particle Swarm, *Shock and Vibration*, 2020, Article ID 9096852, 11 pages.

[10] Chih-Jer Lin, Wen-Lin Chu, Cheng-Chi Wang, Chih-Keng Chen, I-Ting Chen (2019): Diagnosis of ball-bearing faults using support vector machine based on the artificial fish-swarm algorithm, *Journal of Low Frequency Noise, Vibration and Active Control*, 39(4), pp. 954-967.

[11] Mohammed Hakim, Abdoulhdi A. Borhana Omran, Ali Najah Ahmed, Muhannad Al-Waily, Abdallah Abdellatif (2022): A systematic review of rolling bearing fault diagnoses based on deep learning and transfer learning: Taxonomy, overview, application, open challenges, weaknesses and recommendations, *Ain Shams Engineering Journal*, in press.

[12] Bo Peng, Ying Bi, Bing Xue, Mengjie Zhang, Shuting Wan (2022): A Survey on Fault Diagnosis of Rolling Bearings, *Algorithms*, 15(10), pp. 347

15th SIRM – European Conference on Rotordynamics,
Darmstadt, Germany, 22nd – 24th February 2023

Evaluation of the extended Kalman filter in the identification of roller bearing total parameters

Danilo Alvaro da Silva [1], Gregory Bregion Daniel [2], Katia Lucchesi Cavalca [3], Natalia Akemi Hoshikawa Tsuha [4]

[1] Department of Integrated Systems, School of Mechanical Engineering, University of Campinas, 13083-970, Campinas, Brazil, d190801@dac.unicamp.br
[2] Department of Integrated Systems, School of Mechanical Engineering, University of Campinas, 13083-970, Campinas, Brazil, gbdaniel@fem.unicamp.br
[3] Department of Integrated Systems, School of Mechanical Engineering, University of Campinas, 13083-970, Campinas, Brazil, katia@fem.unicamp.br
[4] Department of Integrated Systems, School of Mechanical Engineering, University of Campinas, 13083-970, Campinas, Brazil, natalia.akemi@fem.unicamp.br

Abstract

Identification of lubricated bearings parameters represents an activity of great interest in real applications, either to allow the adjustment of numerical models, to verify and correct operating conditions, or even to use these parameters for monitoring the equipment. Over the years, several methods for identifying dynamic coefficients of lubricated bearings have been used by the scientific community. Among these methods, filtering techniques have shown to be promising in different applications, since they present a relatively low computational cost and consider prediction-correction strategies. Thus, this work aims to evaluate the use of the extended Kalman filter (EKF) technique in the estimation of the roller bearing total parameters. Numerical tests performed in this work showed that EKF can successfully estimate roller bearing parameters, although low damping values can be insensitive to the dynamic response of the contact and, consequently, cause deviations in the final estimation. The results obtained in this work have shown satisfactory parameter estimation considering different signal-to-noise ratios for the measured signal.

1 Introduction

Lubricated journal bearings are machine elements which provide radial supporting to the rotor and relative motion in rotor-bearing systems. Since these support elements strongly influence the dynamic characteristics of the entire rotor-bearing system, much effort has been made to improve the theoretical predictions and experimental characterization of the dynamic properties of bearings. Over the years, different methods for parameter identification have been proposed. The use of filtering techniques such as the Kalman filter can be somewhat adequate in several applications, taking into account its relatively low computational cost and implementing complexity.

Within this scenario, some works have explored filtering techniques to identify rotor and bearing parameters, as can be seen in the literature. An EKF is developed in [1] to estimate the equivalent dynamic coefficients for hydrodynamic bearings in rotor-dynamic applications from noisy measurements of the shaft displacement in response to imbalance and impact excitation. In previous studies [2], the authors proposed a new unbalance loads identification method using augmented Kalman filter algorithms, which proved good performance in online and real-time unbalance parameter identification. A novel method for identifying oil starvation in hydrodynamic journal bearing using EKF is proposed in [3], the method is suitable to identify oil starvation in real-time from noisy vibration signal. Another work recently published [4] uses EKF for predicting failures in feedback control systems and particularly in actuators. Despite the previously mentioned works, the use of EKF to identify roller bearings parameters has not yet been properly explored in the literature. It is important to mention that the identification of the parameters of the total lubricated contact force model in roller bearings represents a complex

task, mainly due to the significant differences between the orders of the parameters of stiffness, damping and surface separation constant.

Therefore, based on the total lubricated contact force model of the roller bearing, this work aims to evaluate the use of the extended Kalman filter technique for estimation of the roller bearing total parameters, in order to asses the accuracy in the parameter estimation and identify the main advantages and limitations in this application.

2 Roller bearing model

The roller bearing force model is based on the dynamic relation between the rolling elements and the inner and outer rings. On nonconforming contacts of rollers and raceways, the resulting lubrication is elastohydrodynamic one (EHL) which considers the elastic deformation on the contact area and concurrently the oil film dynamics. Once the EHL system of equation is numerically solved, the responses of the contact dynamics are used to calculate the parameters of the EHL force reduced model of the roller bearing [5]. In this chapter the theoretical bases of the EHD lubrication related to roller bearings is presented.

2.1 Elastohydrodynamic lubrication

The elastohydrodynamic lubrication system of equations is given by the Reynolds equation, the oil film thickness equation, and the equation of contact motion. The Reynolds equation describes the lubricant fluid dynamics on the bearing:

$$\frac{\partial}{\partial x}\left(\frac{\rho h^3}{\eta}\frac{\partial p}{\partial x}\right)+\frac{\partial}{\partial y}\left(\frac{\rho h^3}{\eta}\frac{\partial p}{\partial y}\right)=6u_s\frac{\partial(\rho h)}{\partial x}+12\frac{\partial(\rho h)}{\partial t} \tag{1}$$

where p is the lubricant pressure, h is the oil film thickness, η is the fluid viscosity, ρ is the oil density, u_s is the sum of the velocities of both contact surfaces, t is the time reference and x-y are the circumferential and axial coordinates of the contact domain, in which x-axis is aligned with the direction of rotation of the bodies in contact and the y-axis is tangential to the velocity u_s. As a boundary condition for Reynolds equation, the Gümbel cavitation model is assumed and the pressure is positive or null in the entire domain.

Due to the reduced contact area between the rolling element and rings, the pressure tends to be considerably elevated causing instantaneous elastic deformation on the contact roller-raceway. Consequently, the oil film thickness equation needs to consider the integration of pressure through the entire area of the contact domain Ω:

$$h(x,y,t)=-\delta(t)+\frac{x^2}{2R}+\frac{2}{\pi E'}\iint_\Omega\frac{p(x',y',t)}{\sqrt{(y-y')^2+(x-x')^2}}dx'dy' \tag{2}$$

where h is the lubricant oil film thickness, δ is the mutual approach between the contact bodies, R is the equivalent radius of curvature in the contact and E' is the reduced modulus of elasticity.

The equilibrium of the EHL model is given by the pressure distribution on the contact bodies and the applied external load f, resulting in the following equation of motion of the contact:

$$m_e\ddot{\delta}(t)+\iint_\Omega p(x,y,t)\,dx\,dy=f(t) \tag{3}$$

where the equivalent roller mass is m_e and the acceleration between contact bodies is $\ddot{\delta}$.

In addition to the fundamental equations of elastohydrodynamic lubrication – Reynolds equation, film thickness equation, and contact motion equation – oil properties are functions of pressure due to the high-pressure conditions resulting from this type of lubrication [5]. The viscosity-pressure relationship $\eta(p)$ and the density-pressure relationship $\rho(p)$ are respectively given by Equations (4) and (5):

$$\eta(p)=\eta_0\exp\left\{\frac{\alpha\,p_0}{z}\left[-1+\left(1+\frac{p}{p_0}\right)^z\right]\right\} \tag{4}$$

$$\rho(p)=\rho_0\left(\frac{5.9\cdot10^8+1.34\cdot p}{5.9\cdot10^8+p}\right) \tag{5}$$

where η_0 is the viscosity and ρ_0 is the density at atmospheric pressure p_0, α is the pressure-viscosity coefficient and parameter z is the viscosity-pressure ratio.

The system of elastohydrodynamic equations is numerically solved by finite difference method and then solved using a classic numerical approach for EHL problems of multilevel techniques Multigrid and MLMI (Multilevel Multi-Integration) [6] in combination with Newmark-Beta integration scheme for time domain solution [5]. Afterwards, coefficients maps can be stored to bearing characterization under different operation condition.

2.2 Contact force model

To model the roller bearing dynamic behaviour, the EHL contact between roller and ring is represented by a single degree of freedom as seen in Figure 1. On elastohydrodynamic lubricated contacts, the contact force f is separated in restitutive f_k and dissipative f_c terms:

$$f = f_k + f_c \tag{6}$$

The EHL restitutive force f_k of the total roller bearing contacts can be written as [7], [8]:

$$f_k = k_t \cdot \delta_t + \Delta F_t \tag{7}$$

where parameter k_t is the equivalent EHL stiffness of total roller bearings contacts, the parameter ΔF_t is a surface separation EHL constant, and the variable δ_t is the total mutual approach between the rolling element and inner raceway displacement δ_i and rolling element and outer raceway mutual approach δ_o:

$$\delta_\mathrm{t} = \delta_\mathrm{i} + \delta_\mathrm{o} \tag{8}$$

Mutual approach δ_i and δ_o are numerically calculated at the static equilibrium position by the system of elastohydrodynamic equations of section 2.1 under a range of external forces for each raceway. The mutual approach must be positive or at least null to guarantee that the contact is on an elastohydrodynamic lubrication regime.

Later, the Levenberg-Marquardt method is applied to curve-fit force and displacement and calculate stiffness k_t and parameter ΔF_t. Equation (7) has an outstanding characteristic of being an explicit EHL force-displacement relation with independent parameters of stiffness and surface separation constant ΔF_t.

The dissipative term of the contact force is a characteristic of lubricated surfaces. In the proposed model [5], the dissipative EHL contact force f_c is composed of a linear viscous damping c_t and velocity $\dot{\delta}_t$:

$$f_c = c_t \cdot \dot{\delta}_t \tag{9}$$

The equivalent damping of total contacts of the roller bearing c_t is calculated considering that inner ring damping c_i and outer ring damping c_o are in series, as seen in Figure 1:

$$\frac{1}{c_t} = \frac{1}{c_i} + \frac{1}{c_o} \tag{20}$$

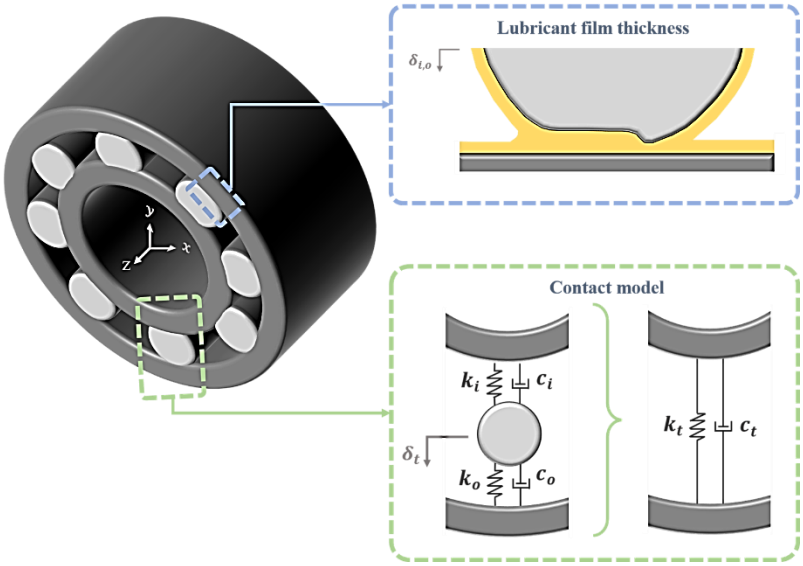

Figure 1: Roller bearing model under elastohydrodynamic lubrication.

In the free vibration of EHL contact equation of motion, given by Equation (3), with the initial condition of perturbation in the equilibrium position of mutual approach $\delta(t)$, there is only restitutive energy. When the problem reaches the steady-state condition ($t \to \infty$), energy is dissipated during contact vibration. The EHL viscous damping can be calculated by applying the principle of energy conservation [5]:

$$c_{i,o} = \frac{\frac{1}{2}k_{i,o}\left[\delta_{i,o}(\infty) - \delta_{i,o}(0)\right]^2}{\int_0^{t\to\infty}\left(\dot{\delta}_{i,o}(t) - \dot{\delta}_{i,o}(0)\right)^2 dt} \tag{31}$$

where index i and o refer to the inner raceway and outer raceway respectively. Therefore, the total lubricated contact force of the roller bearing is:

$$f = k_t\delta_t + \Delta F_t + c_t\dot{\delta}_t \tag{12}$$

3 The extended Kalman filter for parameter estimation

The Extended Kalman filter operates by using the predict-update (prediction-correction) phases. The predict phase gives a prior estimate of the state and its covariance at time step n based on process equation. The update phase uses new observation at time step $n+1$ to correct the deviation of the prior estimate. When using the discrete-time extended Kalman filter for estimating the unknown parameters of a system, these parameters must be treated as a random constant variable. So, if θ_i is constant then it is modeled as

$$\theta_i[n+1] = \theta_i[n] + \zeta_i[n] \tag{13}$$

Where $\{\zeta_i[n]\}$ is a zero-mean Gaussian white noise term that allows the Kalman filter to change its estimate of $\theta_i[n]$. To estimate the unknown parameters, an augmented state space model is introduced by making $\theta_i[n]$ also as a state variable. Thus, the augmented state space model can be written as

$$\begin{bmatrix}\boldsymbol{x}[n+1]\\ \boldsymbol{\theta}[n+1]\end{bmatrix} = \begin{bmatrix}f_n^{or}(n,\boldsymbol{x}[n],\boldsymbol{\theta}[n],u[n])\\ \boldsymbol{\theta}[n]\end{bmatrix} + \begin{bmatrix}\boldsymbol{\xi}[n]\\ \boldsymbol{\zeta}[n]\end{bmatrix} \tag{14}$$

$$\boldsymbol{r}[n+1] = \boldsymbol{f}_n(n,\boldsymbol{r}[n],u[n]) + \boldsymbol{w}[n] \tag{15}$$

$$\boldsymbol{y}[n] = \boldsymbol{h}_n(n,\boldsymbol{r}[n]) + \boldsymbol{v}[n] \tag{16}$$

Where $\boldsymbol{r}[n+1]$ is the augmented state vector, whose distribution is assumed to be a Gaussian random variable, $\boldsymbol{y}[n]$ the noisy measurement vector, $u[n]$ the known input at time n, $\boldsymbol{w}[n]$ the process noise and $\boldsymbol{v}[n]$ the measurement one. These $\boldsymbol{w}$ and $\boldsymbol{v}$ are assumed to be uncorrelated zero-mean Gaussian white noises with time-invariant covariance matrices Q and R. In general, $\boldsymbol{x}[n]\epsilon\boldsymbol{R}^m$, $\boldsymbol{\theta}[n]\epsilon\boldsymbol{R}^p$, $\boldsymbol{\xi}[n]\epsilon\boldsymbol{R}^w$, $\boldsymbol{\zeta}[n]\epsilon\boldsymbol{R}^s$, $\boldsymbol{v}[n]\epsilon\boldsymbol{R}^q$, $q \le m$, and $p, w, s \ge 1$.

$\boldsymbol{f}_n^{or}$, $\boldsymbol{f}_n$ and $\boldsymbol{h}_n$ are vector-valued functions. $\boldsymbol{f}_n^{or}$ is the original process equation of the system. Following the state augmentation, $\boldsymbol{f}_n$ and $\boldsymbol{h}_n$ are then treated as the nonlinear process and the nonlinear observation equations at time n, respectively. In practice, at least $\boldsymbol{f}_n$ or $\boldsymbol{h}_n$ must be a nonlinear function in order to apply the extended Kalman filter. The filtering equations are derived from a linearization procedure of the Equations (15) and (16) to yield the first- or second-order EKF [9], [10]. The second-order "correction" term can be used to reduce the linearization error of the EKF for highly nonlinear systems. Considering the identification of roller bearings coefficients, the first-order filter is considered in this work. Thus, the Taylor series expansion of the Equation (15), rejecting the high-order remaining terms, is

$$\boldsymbol{r}[n+1] = \boldsymbol{f}_n(n,,\hat{\boldsymbol{r}}[n|n],u[n]) + f_r[n](\boldsymbol{r}[n] - \hat{\boldsymbol{r}}[n|n]) \tag{17}$$

Where $f_r[n] = \frac{\partial \boldsymbol{f_n}}{\partial r}\Big|_{\hat{\boldsymbol{r}}}$ is the Jacobian of the vector $\boldsymbol{f}_n$, evaluated at the latest estimate, $\hat{\boldsymbol{r}}[n|n]$. The predicted state to time $n+1$ from time n obtained by taking the expectation of Equation (17) conditioned on given data is

$$\hat{\boldsymbol{r}}[n+1|n] = \boldsymbol{f}_n(n,\hat{\boldsymbol{r}}[n|n],u[n]) \tag{18}$$

The state prediction error is obtained by subtracting Equation (18) from Equation (17). Consequently, the state prediction covariance can be stated as

$$P[n+1|n] = f_r[n]P[n|n]f_r[n]^T + Q[n] \tag{19}$$

Similarly, the predicted measurement is written as

$$\hat{\boldsymbol{y}}[n+1|n] = \boldsymbol{h}_n(n+1,\hat{\boldsymbol{r}}[n+1|n]) \tag{20}$$

The measurement prediction covariance or innovation covariance is

$$S[n+1|n] = h_r[n+1]P[n+1|n]h_r[n+1]^T \tag{21}$$

Where $h_r[n+1] = \frac{\partial \boldsymbol{h_n}}{\partial r}\Big|_{\hat{\boldsymbol{r}}}$ is the Jacobian of the vector $\boldsymbol{h}_n$. Lastly, the expression of the filter gain, the update equation for the state and covariance are sequentially

$$G[n+1] = P[n+1|n]h_r[n+1]^T\{S[n+1|n]\}^{-1} \tag{22}$$

$$\hat{\boldsymbol{r}}[n+1|n+1] = \hat{\boldsymbol{r}}[n+1|n] + G[n+1](\boldsymbol{z}[n+1] - \hat{\boldsymbol{y}}[n+1|n]) \tag{23}$$

$$P[n+1|n+1] = (I - G[n+1]h_r[n+1])P[n+1|n] \tag{24}$$

$\boldsymbol{z}[n+1]$ is the noisy observation which is the input to the filter. Then $\hat{\boldsymbol{r}}[n+1|n]$ and $P[n+1|n]$ are the state estimate and its covariance before the observation $\boldsymbol{z}[n+1]$ is processed, and $\hat{\boldsymbol{r}}[n+1|n+1]$ and $P[n+1|n+1]$ are the state estimate and its covariance after the measurement is processed. The discrete-time EKF can be summarized using the following algorithm

- Initialization at $n = 0$:
  $\hat{\boldsymbol{r}}_0 = \mathbb{E}[\boldsymbol{r}_0]$
  $P_0 = \mathbb{E}[(\boldsymbol{r} - \hat{\boldsymbol{r}}_0)(\boldsymbol{r} - \hat{\boldsymbol{r}}_0)^T]$
- For $n = 1,2,\dots,T$
  (I) Compute the following partial derivative matrices:
  $$f_r[n] = \frac{\partial f_n}{\partial r}\Big|_{\hat{\boldsymbol{r}}}$$
  (II) Perform the state prediction $\hat{\boldsymbol{r}}[n+1|n]$ and estimation-error covariance $P[n+1|n]$
  (III) Compute the following partial derivative matrices:
  $$h_r[n+1] = \frac{\partial \boldsymbol{h}_n}{\partial r}\Big|_{\hat{\boldsymbol{r}}}$$
  (IV) Compute the filter gain $G[n+1]$, then the update of the state estimate, $\hat{\boldsymbol{r}}[n+1|n+1]$, and estimation-error covariance, $P[n+1|n+1]$
  (V) Let $n := n + 1$ and iterate to item I.

4 Roller bearing parameter estimation

Considering the Equation (12) for the total lubricated contact force of the roller bearing, the aim is to estimate the unknown and constant parameters k_t, ΔF_t and c_t. Therefore, these parameters must be modelled as random state variables and its values are estimated via extended Kalman estimator, accordingly the previous section. The case-study used in this work is based on [5], in which a static load (W) and a sinusoidal excitation are added to the model described by Equation (12), yielding the following equations

$$f = \mathrm{W} + F\sin(\omega_e t) \tag{25}$$

$$k_t\delta_t + \Delta F_t + c_t\dot{\delta}_t = \mathrm{W} + F\sin(\omega_e t) \tag{26}$$

$$\dot{\delta}_t = -\frac{k_t}{c_t}\delta_t - \frac{1}{c_t}\Delta F_t + \frac{1}{c_t}\mathrm{W} + \frac{1}{c_t}F\sin(\omega_e t) \tag{27}$$

So, given $[x\ \theta_1\ \theta_2\ \theta_3]^T = [\delta_t\ c_t\ \Delta F_t\ k_t]^T$, if we replace $\dot{x}$ by $(x[n+1] - x[n])T_s^{-1}$, where $T_s > 0$ denotes the sampling time, the model becomes the following discrete-time nonlinear state-space description:

$$\begin{bmatrix} x[n+1] \\ \theta_1[n+1] \\ \theta_2[n+1] \\ \theta_3[n+1] \end{bmatrix} = \begin{bmatrix} x[n] + T_s\left(-\frac{\theta_3[n]}{\theta_1[n]}x[n] - \frac{\theta_2[n]}{\theta_1[n]} + \frac{\mathrm{W}}{\theta_1[n]} + \frac{F}{\theta_1[n]}\sin(\omega_e n T_s)\right) \\ \theta_1[n] \\ \theta_2[n] \\ \theta_3[n] \end{bmatrix} + \begin{bmatrix} \xi[n] \\ \zeta_1[n] \\ \zeta_2[n] \\ \zeta_3[n] \end{bmatrix} \tag{28}$$

$$y[n] = x[n] + v[n] \tag{29}$$

Being

$$f_r[n] = \begin{bmatrix} 1 - \frac{\hat{\theta}_3[n]}{\hat{\theta}_1[n]}T_s & -\frac{T_s(-\hat{\theta}_3[n]\hat{x}[n] - \hat{\theta}_2[n] + \mathrm{W} + F\sin(\omega_e n T_s))}{\hat{\theta}_1^2[n]} & -\frac{1}{\hat{\theta}_1[n]}T_s & -\frac{\hat{x}[n]}{\hat{\theta}_1[n]}T_s \\ 0 & 1 & 0 & 0 \\ 0 & 0 & 1 & 0 \\ 0 & 0 & 0 & 1 \end{bmatrix} \tag{30}$$

$$h_r[n+1] = [1 \quad 0 \quad 0 \quad 0] \tag{31}$$

5 Results

In this section the roller bearing parameters c_t, ΔF_t, and k_t are estimated at rotation speeds of 10, 20 and 30 Hz. To generate the displacement signals, the roller bearing parameters introduced in Equation (27) were obtained for NJ 202 bearing data given in Table 1 [5], the lubricant data refer to ISO VG 32 oil at 27 ºC. Table 2 shows the calculated bearing parameters [5] referred to as theoretical ones (parameters of reference) from this point forward.

Table 1: Data of roller bearing NJ 202

Number of rolling elements	10
Rolling element diameter [mm]	5.5
Effective length of roller [mm]	4.6
Bearing pitch diameter [mm]	24.8

Table 2: Theoretical parameters for numerical displacement responses

Rotation speed [Hz]	c_t [$Nm^{-1}s$]	ΔF_t [N]	k_t [Nm^{-1}]
10	6.42	24.71	$7.39x10^7$
20	5.19	39.08	$7.69x10^7$
30	5.06	51.30	$7.76x10^7$

As the total mutual approach δ_t is the only observation available, the noise variance related to it is set as $1x10^{-18}$ m^2, while the measurement noise variance is $1.5x10^{-15}$ m^2. The noisy measurement signal (observation) then obtained amounts to the signal-to-noise ratio of 30 dB. The static load is 90 N, and the excitation force amplitude is assumed to be 94.5 N (5% of W). These settings are maintained for the three rotation speeds mentioned above. Figure 2 shows the displacement observation simulated at 10 Hz, with 1000 data points, and $\delta_t(0) = 0$. It is noteworthy that only the steady-state signals are used here.

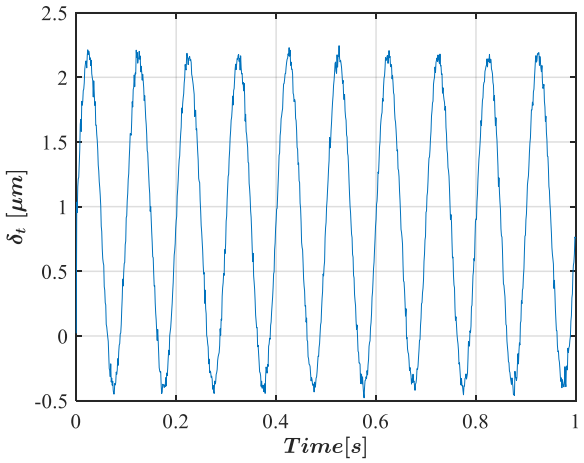

Figure 2: Displacement observation at rotation speed of 10 Hz.

The filter input parameters summarized in Table 3 are used for performing the first-order EKF. The initial state estimate of δ_t is assumed to be the first value of the truncated displacement sequence when neglecting the transient part. Following similar consideration made in [11], the error covariance matrix P_0 was set under the assumption that the initial bearing parameters estimates were 100% in error.

Table 3: Input parameters of the filter

$\hat{\mathbf{r}}_0$ [10Hz]	$[8.83x10^{-7}\quad 8\quad 50\quad 1x10^8]^T$	P_0	$diag([1\quad 1x10^2\quad 1x10^3\quad 1x10^{16}])$
$\hat{\mathbf{r}}_0$ [20Hz]	$[6.62x10^{-7}\quad 7\quad 50\quad 1x10^8]^T$	P_0	$diag([1\quad 1x10^2\quad 1x10^3\quad 1x10^{16}])$
$\hat{\mathbf{r}}_0$ [30Hz]	$[4.98x10^{-7}\quad 7\quad 80\quad 1x10^8]^T$	P_0	$diag([1\quad 1x10^2\quad 1x10^3\quad 1x10^{16}])$
R	$1.5x10^{-15}$	Q	$diag([1x10^{-18}\quad 1x10^{-5}\quad 1x10^{-5}\quad 1x10^4])$

Figures 3-5 show the estimation results of the bearing parameters at 10 Hz using the first-order EKF algorithm. The average value after stabilization is taken as the estimated value, in the whole-time interval of 0.2 to 0.5 s. So, Table 4 exhibits the estimated results for the three rotating speeds considered.

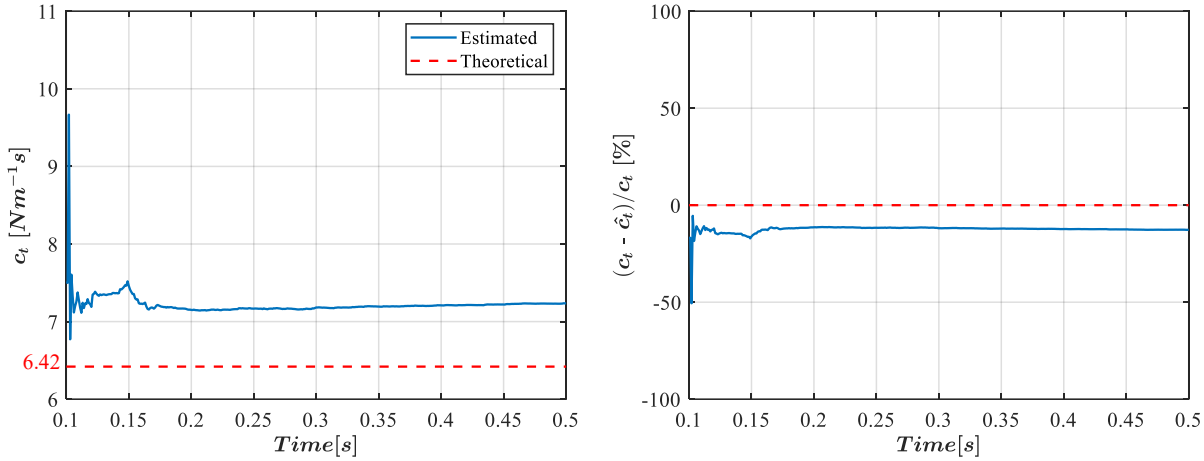

Figure 3: Estimated-Theoretical comparison. (Left) Total damping parameter estimation, (right) Relative estimation error of the total damping parameter

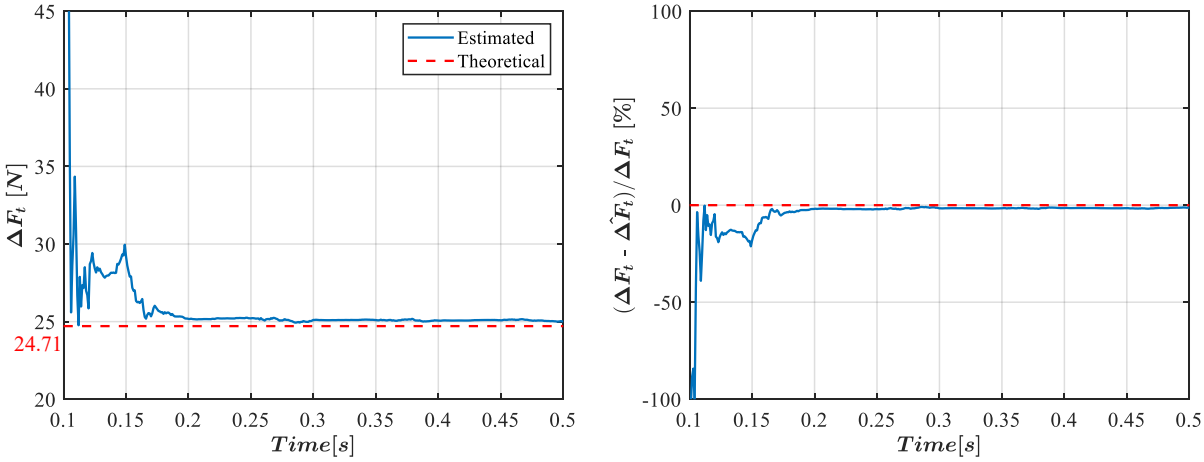

Figure 4: Estimated-Theoretical comparison. (Left) Estimation of the total surface separation parameter, (right) Relative estimation error of the total surface separation parameter

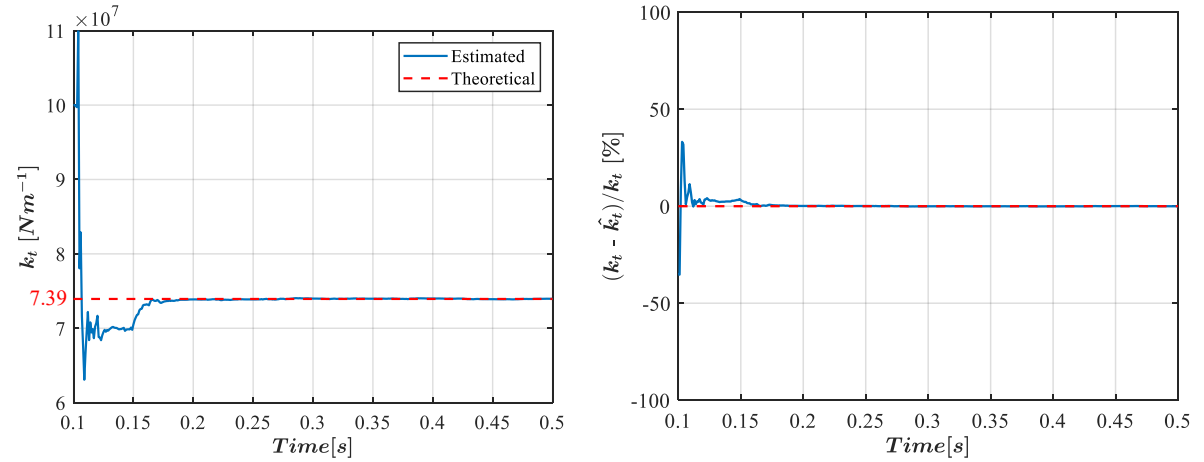

Figure 5: Estimated-Theoretical comparison. (Left) Estimation of the total stiffness parameter, (right) Relative estimation error of the total stiffness parameter

Table 4: Estimated results for the roller bearing parameters – SNR of 30 dB

[Hz]	Parameters	Theoretical	Estimated	Rel. Error [%]
10	c_t	6.42	7.20	12.15
	ΔF_t	24.71	25.04	1.34
	k_t	$7.39x10^7$	$7.40x10^7$	0.02
20	c_t	5.19	6.61	21.48
	ΔF_t	39.08	39.61	1.36
	k_t	$7.69x10^7$	$7.69x10^7$	0.02
30	c_t	5.06	6.78	33.99
	ΔF_t	51.30	51.70	0.78
	k_t	$7.76x10^7$	$7.76x10^7$	0.01

It can be seen that there is little difference between the theoretical references and the estimated parameters given in Table 4 except for the damping coefficient. Numerical simulations were carried out with different combinations of the filter input parameters, even so the filter showed insensitive to improve the estimates of the total damping parameter. One of the plausible reasons for this is the low influence of this parameter in the system response. To verify such assumption, the estimated parameters were inserted in Equation (27) for reconstructing the displacement and velocity signals. Figure 6 shows the theoretical displacement signal together with the reconstructed one.

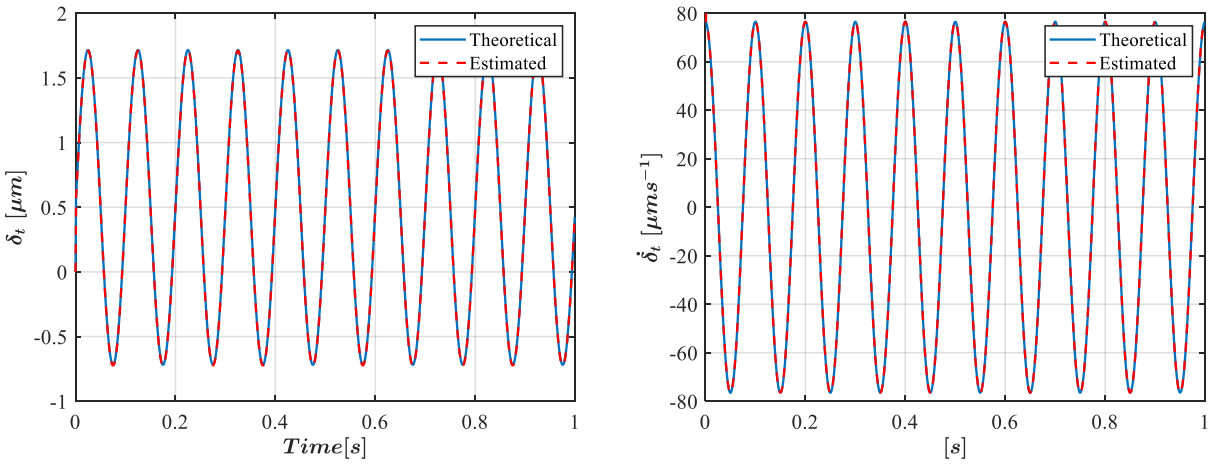

Figure 6: Estimated-Theoretical comparison. (Left) Theoretical displacement signal and reconstructed one, (right) theoretical velocity signal and reconstructed one.

As noted in Figure (6), the responses are rather close to each other, which suggests that the influence of the total damping parameter in this application is largely suppressed due to its short order regarding the order of the total stiffness and surface separation parameters. Based on the tests performed, it can be attested that the filter performance was more significantly affected by the initial state estimate and its error covariance matrix.

Regarding the measurement noise, the filter still showed satisfactory performance for a value of $1.5x10^{-14}$ m^2, which corresponds to a signal-to-noise ratio of about 20 dB, the results are given in Table 5.

Table 5: Estimated results for the roller bearing parameters – SNR of 20 dB

[Hz]	Parameters	Theoretical	Estimated	Rel. Error [%]
10	c_t	6.42	7.58	21.50
	ΔF_t	24.71	26.30	6.43
	k_t	$7.39x10^7$	$7.29x10^7$	1.30
20	c_t	5.19	6.41	23.51
	ΔF_t	39.08	40.68	4.09
	k_t	$7.69x10^7$	$7.59x10^7$	1.22
30	c_t	5.06	6.43	27.08
	ΔF_t	51.30	52.85	3.02
	k_t	$7.76x10^7$	$7.67x10^7$	1.23

6 Conclusion

This paper presents the EKF method to estimate the total roller bearing parameters from simulated noisy measurements. The EKF satisfactory estimated the total stiffness and surface separation parameters, but it needs to be improved in identifying the total damping parameter. However, due to the low damping present in this kind of bearings, the model representativeness may eventually not be compromised. Besides, even the endeavor to calculate damping deserves respect, this case study practically points out that any other possible damping in the system should prevail. The filter performance was more significantly influenced by the initial values of the bearing parameters and its error covariance matrix. As seen in the literature, if the initial error and the noises are not too large, then the EKF performs well. In general, EKF has successfully estimated the roller bearing parameters presenting satisfactory results for a signal-to-noise ratio of up to about 20 dB. Future studies intend to improve the proposed method in order to estimate the parameters of roller bearings in operation on a dedicated test bench for testing lubricated bearings. In addition, other filtering techniques will be explored to improve accuracy in identifying roller bearing parameters.

Acknowledgement

The authors would like to thank Petrobras-CENPES and CNPq Grants #307941/2019-1 and #314583/2021-1 for supporting the research.

References

[1] Miller, B. A., & Howard, S. A. (2009): Identifying bearing rotor-dynamic coefficients using an extended Kalman filter. Tribology Transactions, 52(5), 671-679.

[2] Zou, D., Zhao, H., Liu, G., Ta, N., and Rao, Z. (2019): Application of augmented Kalman filter to identify unbalance load of rotor-bearing system: Theory and experiment. Journal of Sound and Vibration, 463, 114972.

[3] Oliveira, M. V. M., Fioravanti, A. R., and Daniel, G. B. (2022): Identification of oil starvation in hydrodynamic journal bearing using rotor vibration and Extended Kalman Filter. Tribology International, 169, 107469.

[4] Moulahi, M. H., & Ben Hmida, F. (2022). Using extended Kalman filter for failure detection and prognostic of degradation process in feedback control system. Proceedings of the Institution of Mechanical Engineers, Part I: Journal of Systems and Control Engineering, 236(1), 182-199.

[5] Tsuha, N. A. H., Cavalca, K. L. (2020): Stiffness and damping of elastohydrodynamic line contact applied to cylindrical roller bearing dynamic model. Journal of Sound and Vibration, 481, 115444.

[6] Venner, C. H., Lubrecht, A. A. (2000): Multilevel Methods in Lubrication. Elsevier, Tribology Series, Netherlands.

[7] Tsuha, N. A. H., Cavalca, K. L. (2020): Finite line contact stiffness under elastohydrodynamic lubrication considering linear and nonlinear force models. Tribology International, 146, 106219.

[8] Tsuha, N. A. H., Nonato, F., Cavalca, K. L. (2017): Formulation of a reduced order model for the stiffness on elastohydrodynamic line contacts applied to cam-follower mechanism. Mechanism and Machine Theory, 113, pp. 22-39.

[9] Bar-Shalom, Y., Li, X.R. and Kirubarajan, T. (2004): Estimation with applications to tracking and navigation: theory algorithms and software. John Wiley & Sons.

[10] Simon, D. (2006). *Optimal state estimation: Kalman, H infinity, and nonlinear approaches*. John Wiley & Sons.

[11] Miller, B. A., & Howard, S. A. (2009). Identifying bearing rotor-dynamic coefficients using an extended Kalman filter. Tribology Transactions, 52(5), 671-679.

15th SIRM – European Conference on Rotordynamics,
Darmstadt, Germany, 22nd – 24th February 2023

Generalised Few-shot Learning for Rotor System Diagnosis

Aleksanteri Hämäläinen [1], **Aku Karhinen** [1], **Jesse Miettinen** [1] **Raine Viitala** [1]

[1] Department or Mechanical Engineering, Aalto University, 02150, Espoo, Finland, aleksanteri.hamalainen@aalto.fi

Abstract

Current methods of rotor system condition monitoring require a substantial amount of manual work for large fleets of machines. Data-driven automated fault diagnosis models based on deep learning (DL) have the potential to drastically reduce the amount of time spent on manual analysis. However, there is often a lack of data from the entire range of possible operating conditions of a system. The poor generalisation of most DL-based models to operating conditions not present in the training data decreases their usefulness in industry applications. This paper investigates the generalisation ability of a few-shot learning method using only a single example to learn each new class. A prototypical network with a modified Deep Convolutional Neural Networks with Wide First-layer Kernels (WDCNN) architecture was used as the few-shot model. The generalisation of the model was studied from sensor to sensor and across operating speeds. The results indicate that the model is robust to changes in sensor orientation and relatively robust against changes in sensor location. Additionally, the model showed promising results when tested on operating speeds many times higher or lower than it was trained on. The results show that few-shot learning methods have the potential to work in industry applications where limited training data is available. This research also gives an excellent baseline for future research on the generalisation of few-shot learning methods on rotor system fault diagnosis over large changes in operating conditions.

1 Introduction

Condition-based maintenance (CBM) has been recognised as the best maintenance strategy for machines that should operate for lengthy periods of time uninterrupted [15]. An effective CBM strategy relies on accurate and frequent assessments of the machine condition. With such assessments, the maintenance plans can be optimised for each machine individually. In order to produce frequent machine condition assessments, online monitoring is often required. Unfortunately, online monitoring can be laborious for experts, if the frequency of the required condition assessments is high. Fortunately, numerous automatic condition monitoring algorithms have been developed [7, 12, 14, 15]. The automatic condition monitoring algorithms can be categorised into fault detection, fault diagnosis and fault prognosis algorithms [15]. A large proportion of the latest research has focused on fault diagnosis based on vibration [12]. Vibration data is often used because it includes patterns that characterise normal and faulty motion of the rotating system components [15]. Furthermore, numerous powerful signal processing tools for vibration data exist [15, 18, 27].

A great majority of the recent automatic fault diagnosis models for vibration data employ machine learning (ML) [7, 12, 14]. These ML based diagnosis models either employ manually designed features and traditional ML models, or deep learning (DL) models, which learn features autonomously [12]. Deep learning models have been shown to learn to recognise vibration patterns from time series data directly [6, 17, 26]. Furthermore, some studies have implied that deep learning models achieve better diagnosis results than traditional machine learning based models with manually selected features [9, 13, 26]. Learning features autonomously may also save excessive manual effort required for the design of the features.

Despite the recently achieved remarkable accuracies with DL-based fault diagnosis models, most of these proposed models generalise poorly to real machines in real operating conditions. This is because commonly used supervised learning hinders generalisation [2]. Results with DL models trained with supervised learning perform unsatisfactorily if the training data is not identically distributed with the test data [3]. Therefore, it is crucial that supervised model optimisation is performed with data that includes all realistic operating conditions and faults. This criterion is very difficult to fulfill, and most publications proposing novel deep learning models neglect it. Thus, the applicability of the majority of the DL-based fault diagnosis models for real world machines

is questionable. Moreover, many publications demonstrate experiments on fault data acquired from a simple test rig that was operated under relatively non-varied operating conditions [25].

In this work prototypical networks are used, which are optimised with a variant of supervised learning. This variant is known as few-shot learning, which essentially trains the diagnosis model to learn how to learn. The results show that this form of meta-learning is an effective solution for most generalisation problems related to supervised learning and lack of data.

This work advances the current experimental paradigm employed in DL-based fault diagnosis research in two dimensions. First, the fault diagnosis models are evaluated on data acquired on a relatively complex rotating system. Second, the data distributions between the training data and the test data differ significantly: Experiments are performed where the operating speeds in the test data are different from the operating speeds in the training data. Furthermore, the experiments in this work also investigate fault diagnosis model performances on test data acquired with different sensors from the training data.

2 Related work

Fault diagnosis model optimisation based on supervised learning requires numerous training samples of each health condition. However, acquiring such a dataset with all relevant fault conditions present in varied operating conditions can be difficult. A number of studies have recently proposed various meta-learning approaches that seem promising for sparse data problems. These meta-learning approaches can be categorised as few-shot, one-shot and zero-shot settings. In few-shot settings the aim is to optimise the model to learn a new class from very few examples. The one-shot setting is similar, but the model is required to learn new classes from a single example. In zero-shot setting the models learn to recognise an example from a new class based only on meta descriptions.

There have been several relatively successful attempts to develop meta-learning models based on deep learning architectures. Siamese networks consist of two CNN-based feature extractors and a common distance metric head for similarity assessment of pair-wise inputs [11]. The pair-wise similarity assessment network works in a comparable way, but is augmented with memory [10]. However, Siamese networks may require training separately for all k-shot tasks. Some potentially more flexible models are, for example, matching networks [21], prototypical networks [19], and relation networks [20].

Recent fault diagnosis studies based on meta-learning have shown that these techniques are promising for learning from sparse fault data [2]. For example, Siamese nets based on WDCNN architecture performed highly accurately on the common bearing fault benchmark dataset by Case Western Reserve University (CWRU) [24]. Another study proposed to employ WDCNN trained with supervised learning as a feature extractor for the embedding layer adapted from matching networks [22]. In addition, the prototypical network approach was experimented on with a convolutional neural network that processed vibration data in the time and the frequency domains [23]. However, the majority of the studies have lacked data with largely varied rotating speeds. Moreover, there are few studies reporting results of few-shot techniques on data where the test fault data is acquired from a different location than the train fault data.

3 Methods

Few-shot models classify new samples based on support examples. The support examples are typically provided as a set $S = (\mathbf{x}_1, \mathbf{y}_i)...(\mathbf{x}_M, \mathbf{y}_M)$, where $\mathbf{x}_i$ is an example, such as a vibration sample, and $\mathbf{y}_i$ is the corresponding class label. The few-shot setting can be described based on the number of different classes in S and the number of examples from each class. That is, the support set consisting of N classes and K examples per class establishes an N-way K-shot setting. N and K are not required to match between training and actual use, but best results have been observed when the number of support examples K is matched in training and testing, and the number of classes N is equal or higher when training [19]. In general, having a larger number of classes N or less support examples K per episode makes the classification problem harder.

Prototypical networks employ an embedding model with learnable parameters to project support and query examples to a $\mathbb{R}^D$ dimensional space. Prototypes for each class are computed as the mean of the K embedded support examples belonging to that class. New samples from the query set are classified based on the distances of their embedding to the class prototypes. Figure 1 visualises the classification procedure of a query sample $\hat{\mathbf{x}}$ based on L2 distance to three prototypes $\mathbf{P}_i$, each computed from three support examples.

The rest of this section presents in more detail the architecture for the embedding network, the dataset employed for experiments, and the specifics of training the model. Subsection 3.1 details the feature maps and layers of the embedding model. Subsection 3.2 discusses the artificial gear faults, the data acquisition process and the down-scaled azimuth thruster test rig. Subsection 3.3 describes the formation of few-shot episodes and other training

algorithm related details.

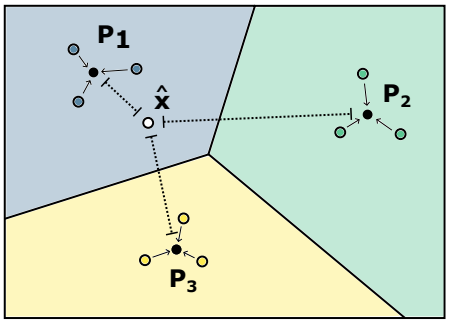

Figure 1: Visualised computation and classification using prototypes. Each prototype P_n is the mean of the surrounding samples translated into the embedding space. Each colored area describes the area where a sample would be classified to the class 1, 2, or 3. $\hat{x}$ corresponds to a sample that can be classified by comparing the distance to each prototype.

3.1 Embedding Model

The embedding model employed in this study is adapted from a previously proposed model known as Deep Convolutional Neural Networks with Wide First-layer Kernels (WDCNN) [26]. WDCNN is an effective model for vibration data -based condition monitoring . The WDCNN has five convolutional layers, each of which consists of a 1D convolution, batch normalization, a ReLU activation and a max pool in the respective order. The first 1D convolution has a kernel size of 64, and the following 1D convolutions have a kernel size of 3. The wide first-layer kernels are effective at processing temporal patterns. The shorter kernels of the rest of the layers can compute informative higher lever features from the first-layer features. The max pool layers are used to reduce the resolution of the features between layers [16]. The specifics of the convolutional layers can be seen in Table 1. The convolutional layers are followed by two fully connected (FC) layers used to form the class labels.

Table 1: The adapted WDCNN architecture

Layer	Channels In	Channels Out	Kernel	Stride	Padding
`Conv1D`	1	16	64x1	16	24
`MaxPool1D`	16	16	2x1	2	0
`Conv1D`	16	32	3x1	1	1
`MaxPool1D`	32	32	2x1	2	0
`Conv1D`	32	64	3x1	1	1
`MaxPool1D`	64	64	2x1	2	0
`Conv1D`	64	64	3x1	1	1
`MaxPool1D`	64	64	2x1	2	0
`Conv1D`	64	64	3x1	1	1
`MaxPool1D`	64	64	2x1	2	0
`FC`	640	512	N/A	N/A	N/A

The adapted WDCNN in this work includes a few light architectural modifications to the original model. First, the adapted model only includes one fully-connected layer, which computes the final embedding for the given input. In addition, as the input size of 6000 used in this study is larger than the 2048 used in the original WDCNN, the input width of the fully connected layer has been increased to match the output of the last convolutional layer. Because the magnitudes of the input values differ significantly across operating speeds, the model includes a normalisation function, which normalizes the embedding vectors to unit length. Additionally, multiplying the unit length embedding vector with 100 was found to considerably increase model convergence stability and speed. A depiction of the model can be seen in Figure 2.

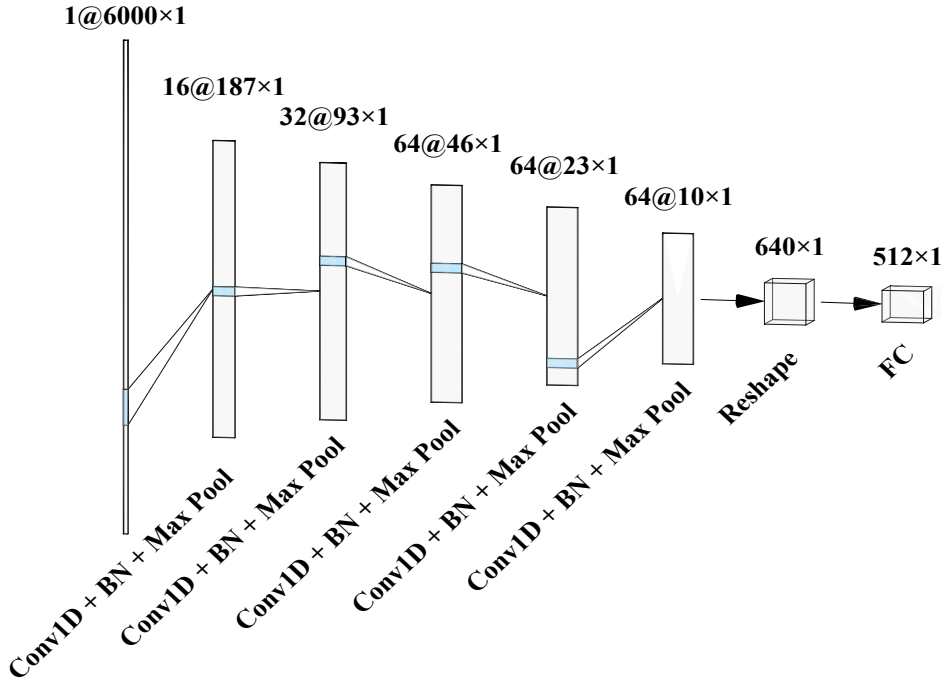

Figure 2: Feature maps of the adapted WDCNN for embedding vibration data

3.2 Dataset

The data was acquired with a small-scale azimuth thruster test bench designed to share the lowest natural frequencies with a real thruster [4]. This test rig includes two servomotors at both ends of the drivetrain. The first servomotor serves as the driving motor, and the second simulates the propeller loads of the thruster. The test-rig also includes two gearboxes (gearbox 1 and 2) with gear ratios of 1:3 and 1:4, respectively. The test bench was modified by replacing gearbox 2 with a bevel gear with an open structure, which enabled the introduction of versatile deliberate gear faults.

Four accelerometers were used to measure vibration data simultaneously. The accelerometers are named here S1, S2, S3, and S4. S1, S2, and S3 were mounted on the second gearbox at 90 degree angles to each other. S4 was mounted on a bearing support between the drive motor and gearbox 1. All of the accelerometers had a sampling rate of 3 kHz. Figure 3 shows the test rig at the configuration employed for data acquisition for this study.

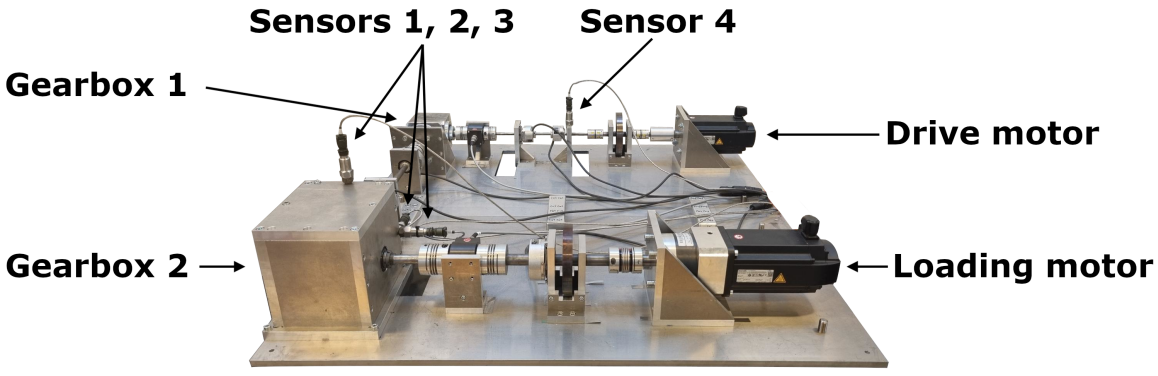

Figure 3: A small scale azimuth thruster with the relevant parts indicated. The large gear box contains the bevel gear where artificial gear faults were produced.

The dataset includes measurements of 10 different health states. The first state is the healthy state with no changes to the powertrain, and the remaining 9 are fault states. The fault states were created by attaching thin

metal sheets, referred to as shims from here on, to the teeth of the pinion gear of gearbox 2 shown in Figure 3. One, two or three shim sheets were added at a time, with thicknesses of 0.01 mm, 0.03 mm, or 0.05 mm. All sheets added at a time were the same thickness. The attached shims change the vibration pattern of the test bench, as seen in Figure 5. Each of the health states were measured at 6 different drive motor speeds: 250, 500, 750, 1000, 1250, and 1500 RPM. For the rest of this paper, a class refers to a combination of a health state, an operating speed expressed in RPM and the sensor used to measure it. The combination of fault states, drive motor speeds and sensors add up to $10 \cdot 6 \cdot 4 = 240$ possible separate classes. A breakdown of the dataset can be seen in Figure 4.

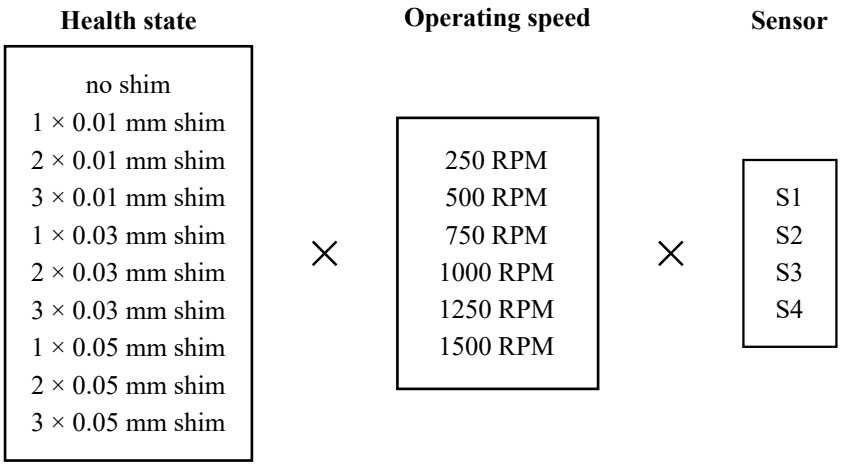

Figure 4: Breakdown of all the different variables that form a class in the dataset.

Each combination of fault state and RPM was recorded for 150 seconds. The recordings were divided into 2 the second windows used as examples in this study. The 2 second example corresponds to 6000 sensor samples at the 3 kHz sampling frequency. These time series examples were employed in training and testing. The 2 s window size was chosen to include one or more pinion gear revolutions per example even at lower drive motor speeds. At the lowest drive motor speed (250 RPM) the pinion gear with the shim sheets rotates at a rate of $1.389\ 1/\mathrm{s}$. Figure 5 shows two examples at 1000 RPM: the first with no shims attached and the second with one 0.05 mm shim sheet attached.

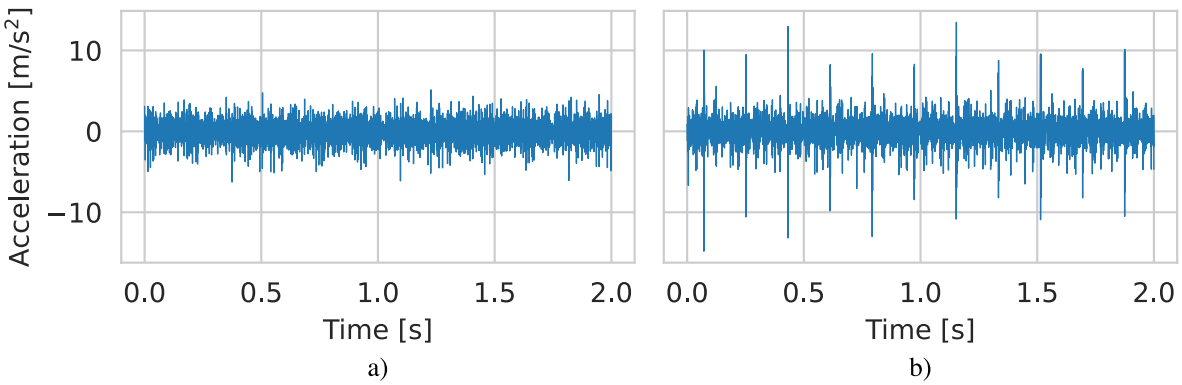

Figure 5: Examples of the 2 second windows used in training and testing the model at 1000 RPM: (a) no shims (b) 1 x 0.05 mm shim

3.3 Training

The classes in the dataset were divided into test and training sets depending on the test case. To increase the amount of examples available for training, example overlap was used. Support and query example pools were not kept separate, but no overlap was allowed between support and query examples.

Training was done with successive N-way K-shot episodes as described by Snell et al. [19]. All training was done with one-shot classification problems, i.e. K=1. Ten classes per episode, i.e. N=10, were used in training for both 5-way and 10-way tests. The L2 distance was used as the distance metric between query embeddings and prototypes. Loss for each training episode was calculated using cross entropy loss.

For training, the standard stochastic gradient descent (SGD) optimizer with a learning rate of 0.0076, momentum of 0.95, and a weight decay of 0.0012 was used. Additionally, a step learning rate scheduler was used with a step size of 10 and a gamma of 0.99. The embedding vector length used was 512. Values for the hyperparameters were found with a combination of manual testing and the hyperparameter optimization framework Optuna [1].

4 Results

This section presents the results for two case studies: sensor to sensor and RPM to RPM experiments. In the sensor to sensor experiment, a separate model is trained with each sensor and then tested against each of the rest. In the RPM to RPM experiment, models are trained with either a set of low or high operating speeds and then tested on the other. Test runs were repeated 10 times to mitigate the stochastic nature of neural network training. The accuracy of each separate test run was computed using a number of random episodes depending on the experiment type and the results shown are the averages of these test runs. It is important to note that the full test set includes more than N classes, but only the classification accuracy of the N classes in an episode, 5 for 5-way and 10 for 10-way, is considered. Different combinations of these N classes were used to give a more robust estimate of the models performance.

4.1 Case study I: Sensor to Sensor experiments

This case study evaluates how well the model generalizes to vibration samples from sensors it has not been trained on. A model was trained on each of the four sensors separately, and then tested against all of the remaining sensors. Figure 6 shows classification accuracies for these experiments. The average accuracy in the 5-way case is 96.23 %, and 92.07 % in the 10-way case. We can also see that in both cases models trained with sensors S1, S2, and S3 generalize very well when tested on any of the other two sensors. This shows that the method is robust to changes in sensor orientation. When the model is trained or tested on S4, the results are slightly worse, but the model is still able to generalise even with the change in sensor location.

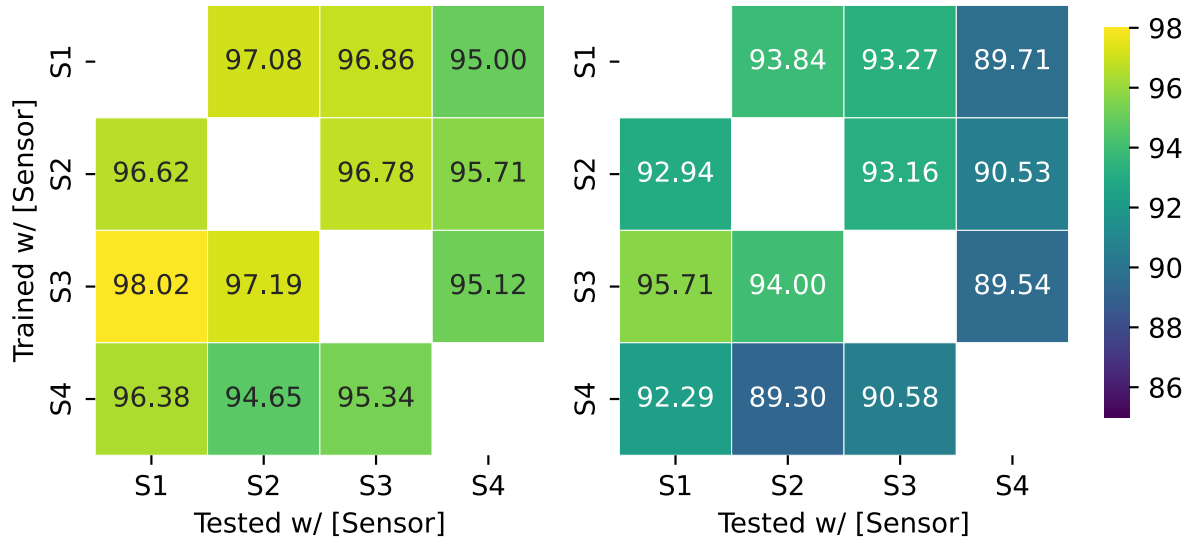

a) N=5 b) N=10

Figure 6: 5-way (a) and 10-way (b) results of the sensor to sensor experiments. Each accuracy is an average over 10 test runs.

4.2 Case study II: RPM to RPM experiments

This case study evaluates how well the model generalizes to unseen drive motor speeds. Models were trained on low operating speeds and tested against high operating speeds (low-to-high) and vice versa (high-to-low). The low operating speeds include 250, 500, and 750 RPM, and the high operating speeds include 1000, 1250, and 1500 RPM. All 10 health states were used. Furthermore, this case study was divided into two sub-experiments. In the first, training and testing were done separately for all sensors. In the second, the model was trained on all sensors and then tested separately against each sensor.

Figure 7 shows the classification accuracies of the single sensor training sub-experiment. From the figure we can see that relatively good accuracies were achieved when generalizing to operating speeds closer to the ones used to train the model with. However, especially in the low-to-high case, accuracies are promising even on the operating speed furthest from the ones used for training.

Unlike in the sensor to sensor generalisation experiment, clear differences can be seen between the sensors. The best performing sensor is S2, which maintains a nearly 90 % accuracy in all of the cases when tested on the two RPMs nearer to the training values. On the other hand, S3 is over 20 pp worse than S2 in some comparisons. Sensor alignment thus seems to have a major impact on generalization between operating speeds, as sensors S2 and S3 are located very close to each other.

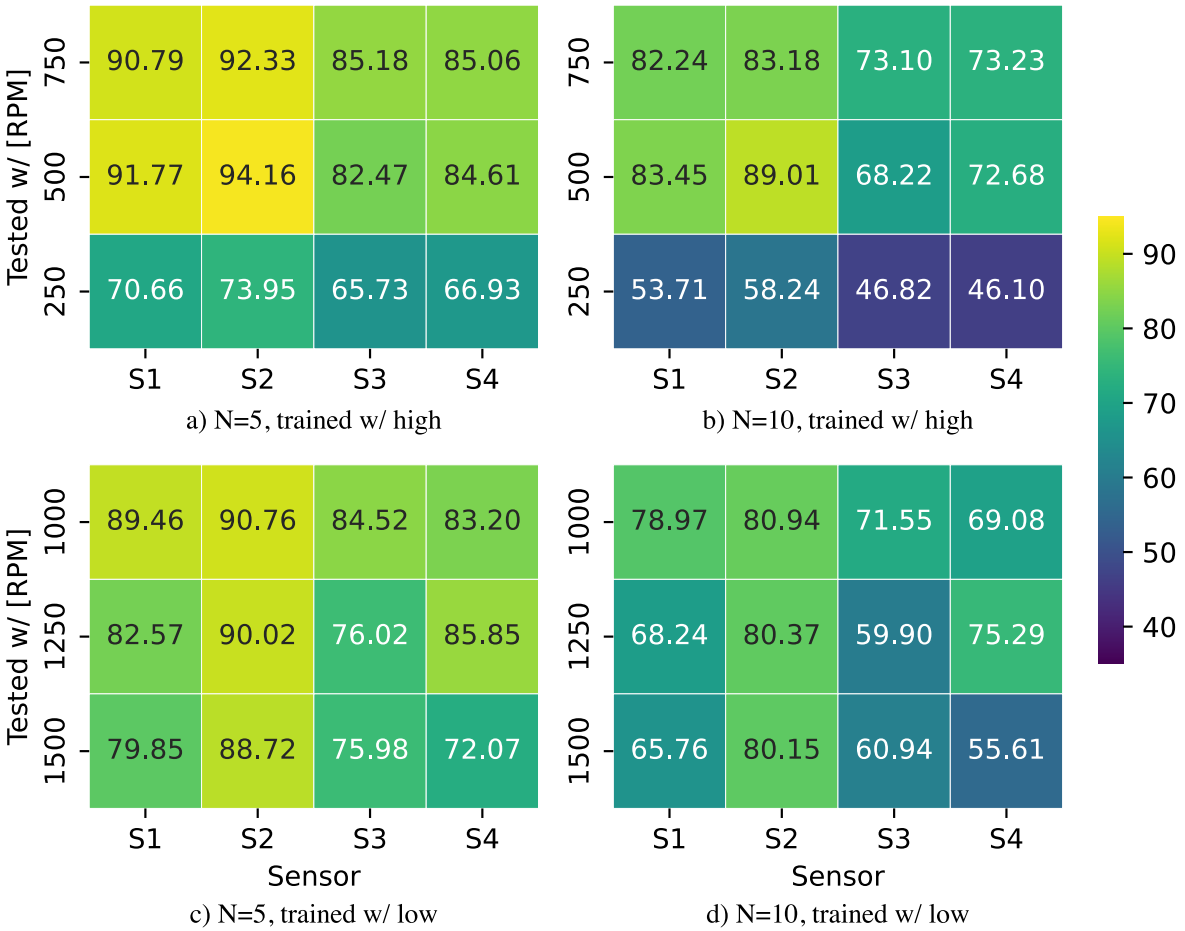

Figure 7: 5-way (left) and 10-way (right) classification accuracies of the RPM to RPM experiments when each model was trained with a single sensor. The upper half show results when trained on high operating speeds and tested on low operating speeds, and the bottom half shows the opposite case. Each accuracy is an average over 10 test runs.

Figure 8 shows the results for the multi sensor training sub-experiment. Similarly to the single sensor training sub-experiment, overall results are better when testing against operating speeds closer to those used for training.

However, in contrast to the single sensor case, there is slightly less differences between the accuracies achieved with each sensor.

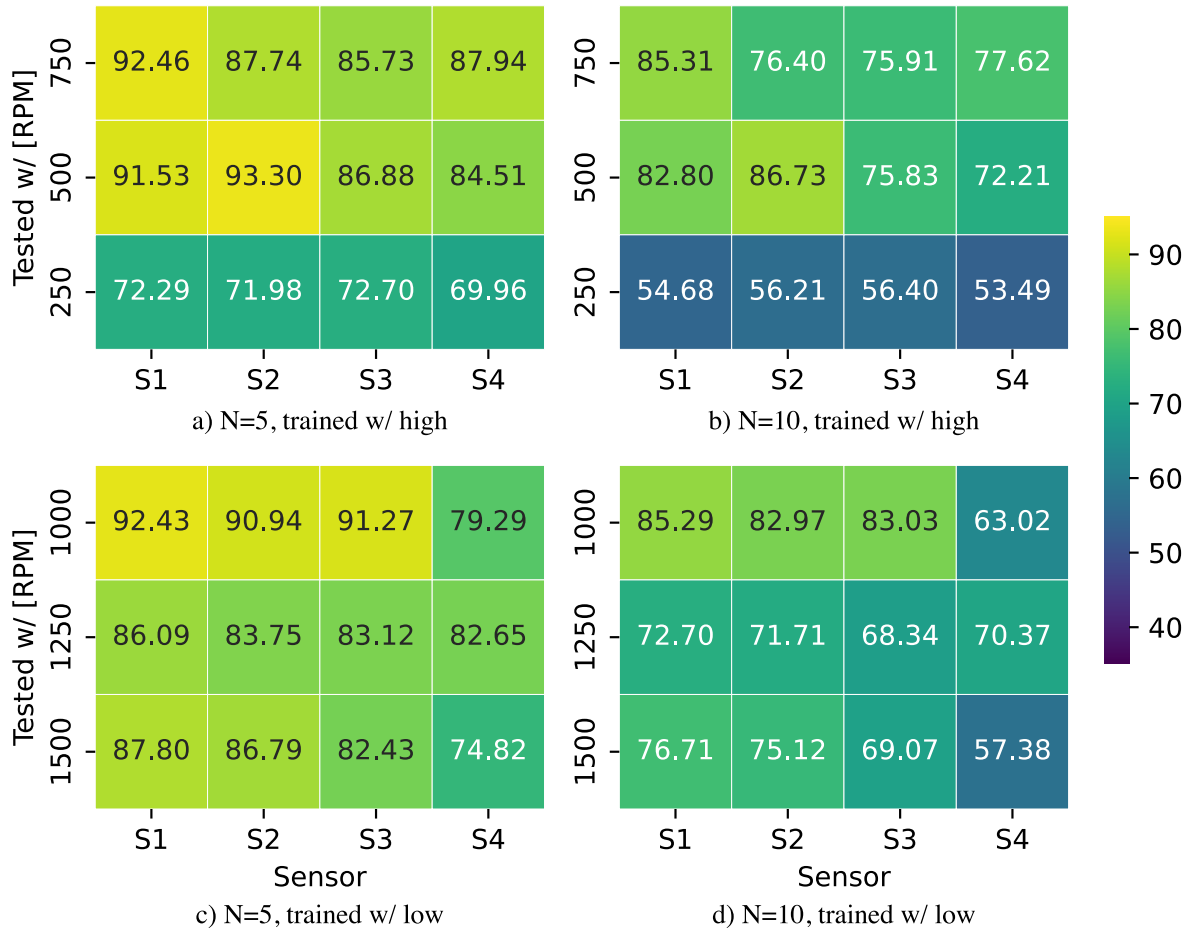

Figure 8: 5-way (left) and 10-way (right) classification accuracies of the RPM to RPM experiments when each model was trained with all sensors and tested on a single sensor. The upper half shows results when trained on high operating speeds and tested on low operating speeds, and the bottom half shows the opposite case. Each accuracy is an average over 10 test runs.

Table 2: Comparison between training each model with a single sensor (single-type) and training each model with all the sensors (multi-type)

Trained w/	N-way	Type	Min [%]	Mean [%]	Max [%]
High	5	Single	65.73	81.97	94.16
		Multi	69.96	**83.09**	93.30
	10	Single	46.10	69.16	89.01
		Multi	53.49	**71.13**	86.73
Low	5	Single	72.07	83.25	90.76
		Multi	74.82	**85.12**	92.43
	10	Single	55.61	70.57	80.94
		Multi	57.38	**72.98**	85.29

The minimum, mean, and maximum accuracies of the different test cases for single and multi sensor training

are summarized in Table 2. On average, training on multiple sensors results in 1.84 % better results than training on a single sensor. Additionally, in no case was the mean accuracy worse or the minimum accuracy lower when trained on multiple sensors than when trained on a single sensors. However, in some cases better maximum accuracies were achieved when the model was trained with only the sensor used for testing. This would indicate that training on multiple sensors can be beneficial even when results from the exact sensor used for training are available, depending on the aim of the model.

5 Discussion

The results for both sensor to sensor and RPM to RPM generalization are promising for future applications. Case study I (Section 4.1) shows that the few-shot learning model generalizes well to sensors it has not been trained on. That is, the model diagnosis accuracy was satisfactory on previously unseen vibration patterns acquired with sensors in new orientations and in new locations. This implies that few-shot learning models could generalize to fleets of rotor systems, without a need to train a separate model for each separate system.

Case study II (Section 4.2) shows that the method generalizes to a relatively broad range of operating speeds. This removes the need to manually create examples of rotor faults at a large number of possible operating speeds, significantly reducing the need for manual work. Few-shot learning also seems to be a promising model in situations where an artificial dataset is hard to create and real world data is only sparsely available from multiple operating conditions.

Few studies demonstrating such detailed results on few-shot rotor fault diagnosis generalization between sensors and operating speeds have been done before. The differences in vibration signals from different operating speeds are especially large in this study, as the different RPMs used were from such a large range. The changes in the operating speed change both the amplitude of the vibration signal, and the number of rotations captured in each sample.

An interesting topic for future research would be studying the change in generalisation when using examples converted into the frequency domain. Studies have shown good results in machine health state classification when using frequency domain input [5, 8, 23]. Another path for research would be studying results when both testing sensor and operating speed are different than the ones used in training. Lastly, showing the ability to classify multiple faults occurring simultaneously is important for industry use.

6 Conclusions

In this paper a few-shot learning method shown to generalise well with a low number of examples in classification problems was applied to vibration data. Generalisation across operating speeds and from sensor to sensor were tested. The trained models were found to generalize well to similar sensors and to operating speeds relatively far from those used in training. Overall these results are significant in showing that few-shot learning could be a viable method for use in condition monitoring applications. Especially so when it is not possible to separately train a model for each possible machine and operating condition. Improving the generalisation abilities of ML based rotor system fault diagnosis models would increase their usefulness in industry applications.

Acknowledgment

This work was supported by Academy of Finland as part of the High-Speed Elecromechanical Energy Conversion Systems (HiECS) research project.

References

[1] Akiba, T., Sano, S., Yanase, T., Ohta, T. and Koyama, M. [2019]. Optuna: A next-generation hyperparameter optimization framework, *Proceedings of the 25rd ACM SIGKDD International Conference on Knowledge Discovery and Data Mining*.

[2] Feng, Y., Chen, J., Xie, J., Zhang, T., Lv, H. and Pan, T. [2022]. Meta-learning as a promising approach for few-shot cross-domain fault diagnosis: Algorithms, applications, and prospects, *Knowledge-Based Systems* **235**: 107646.
URL: *https://www.sciencedirect.com/science/article/pii/S0950705121009084*

[3] Goodfellow, I., Bengio, Y. and Courville, A. [2016]. *Deep Learning*, MIT Press. `http://www.deeplearningbook.org`.

[4] Haikonen, S., Koene, I., Keski-Rahkonen, J. and Viitala, R. [2022]. Small-scale test bench of maritime thruster for digital twin research, *2022 IEEE International Instrumentation and Measurement Technology Conference (I2MTC)*, pp. 1–6.

[5] He, Y., Zang, C., Zeng, P., Wang, M., Dong, Q. and Liu, Y. [2021]. Rolling bearing fault diagnosis based on meta-learning with few-shot samples, *2021 3rd International Conference on Industrial Artificial Intelligence (IAI)*, pp. 1–6.

[6] Hendriks, J., Dumond, P. and Knox, D. [2022]. Towards better benchmarking using the cwru bearing fault dataset, *Mechanical Systems and Signal Processing* **169**: 108732.

[7] Hoang, D.-T. and Kang, H.-J. [2019]. A survey on deep learning based bearing fault diagnosis, *Neurocomputing* **335**: 327–335.

[8] Hu, Y., Liu, R., Li, X., Chen, D. and Hu, Q. [2022]. Task-sequencing meta learning for intelligent few-shot fault diagnosis with limited data, *IEEE Transactions on Industrial Informatics* **18**: 3894–3904.

[9] Jing, L., Zhao, M., Li, P. and Xu, X. [2017]. A convolutional neural network based feature learning and fault diagnosis method for the condition monitoring of gearbox, *Measurement* **111**: 1–10.

[10] Kaiser, L., Nachum, O., Roy, A. and Bengio, S. [2017]. Learning to remember rare events, *International Conference on Learning Representations*.

[11] Koch, G., Zemel, R., Salakhutdinov, R. et al. [2015]. Siamese neural networks for one-shot image recognition, *ICML deep learning workshop*, Vol. 2, Lille, p. 0.

[12] Lei, Y., Yang, B., Jiang, X., Jia, F., Li, N. and Nandi, A. K. [2020]. Applications of machine learning to machine fault diagnosis: A review and roadmap, *Mechanical Systems and Signal Processing* **138**: 106587.

[13] Li, C., Sanchez, R. V., Zurita, G., Cerrada, M., Cabrera, D. and Vásquez, R. E. [2015]. Multimodal deep support vector classification with homologous features and its application to gearbox fault diagnosis, *Neurocomputing* **168**: 119–127.

[14] Liu, R., Yang, B., Zio, E. and Chen, X. [2018]. Artificial intelligence for fault diagnosis of rotating machinery: A review, *Mechanical Systems and Signal Processing* **108**: 33–47.

[15] Randall, R. B. [2021]. *Vibration-based condition monitoring: industrial, automotive and aerospace applications*, John Wiley & Sons.

[16] Scherer, D., Müller, A. and Behnke, S. [2010]. Evaluation of pooling operations in convolutional architectures for object recognition, *International conference on artificial neural networks*, Springer, pp. 92–101.

[17] Shenfield, A. and Howarth, M. [2020]. A novel deep learning model for the detection and identification of rolling element-bearing faults, *Sensors* **20**(18).

[18] Smith, W. A. and Randall, R. B. [2015]. Rolling element bearing diagnostics using the case western reserve university data: A benchmark study, *Mechanical Systems and Signal Processing* **64-65**: 100–131.

[19] Snell, J., Swersky, K. and Zemel, R. [2017]. Prototypical networks for few-shot learning, *Advances in neural information processing systems* **30**.

[20] Sung, F., Yang, Y., Zhang, L., Xiang, T., Torr, P. H. and Hospedales, T. M. [2018]. Learning to compare: Relation network for few-shot learning, *Proceedings of the IEEE Conference on Computer Vision and Pattern Recognition (CVPR)*.

[21] Vinyals, O., Blundell, C., Lillicrap, T., Wierstra, D. et al. [2016]. Matching networks for one shot learning, *Advances in neural information processing systems* **29**.

[22] Wang, D., Zhang, M., Xu, Y., Lu, W., Yang, J. and Zhang, T. [2021]. Metric-based meta-learning model for few-shot fault diagnosis under multiple limited data conditions, *Mechanical Systems and Signal Processing* **155**: 107510.

[23] Wang, Y., Chen, L., Liu, Y. and Gao, L. [2021]. Wavelet-prototypical network based on fusion of time and frequency domain for fault diagnosis, *Sensors* **21**(4).

[24] Zhang, A., Li, S., Cui, Y., Yang, W., Dong, R. and Hu, J. [2019]. Limited data rolling bearing fault diagnosis with few-shot learning, *IEEE Access* **7**: 110895–110904.

[25] Zhang, S., Zhang, S., Wang, B. and Habetler, T. G. [2020]. Deep learning algorithms for bearing fault diagnostics—a comprehensive review, *IEEE Access* **8**: 29857–29881.

[26] Zhang, W., Peng, G., Li, C., Chen, Y. and Zhang, Z. [2017]. A new deep learning model for fault diagnosis with good anti-noise and domain adaptation ability on raw vibration signals, *Sensors* **17**(2).

[27] Zhao, R., Yan, R., Chen, Z., Mao, K., Wang, P. and Gao, R. X. [2019]. Deep learning and its applications to machine health monitoring, *Mechanical Systems and Signal Processing* **115**: 213–237.

15th SIRM – European Conference on Rotordynamics,
Darmstadt, Germany, 22nd – 24th February 2023

Nonlinear vibration analysis of a high speed turbocharger rotor in ball bearings - simulation and measurement

Christoph Baum [1], **Jürgen Brezina** [2], **Sudhakar Gantasala** [3], **Panagiotis Koutsovasilis** [4]

Dynamics Simulation & Methods, BorgWarner Systems Engineering GmbH, 67292 Kirchheimbolanden, Germany, {[1] cbaum, [3] sgantasala, [4] pkoutsovasilis}@borgwarner.com

Abstract

Most turbocharger rotors in vehicles are operated within oil-lubricated fluid film bearings. However, for high performance and reduced friction losses a ball bearing system is superior. But there are several technical challenges that need to be mastered in order to design, build and produce a reliable product for series applications. Examples are high temperatures and temperature ranges due to the exhaust gases and different surrounding conditions in combination with tight clearances and furthermore the fast rotational speeds at which these machines are typically operated. In particular for the latter mentioned, vibrations, inherent to rotating devices, are gaining on importance. They frequently come along with either high dynamical loads, which could lead to a failure of the bearing or overall system, generate noise or both.

Besides hardware testing simulation is utilized to cope with the systems behaviour and investigate the source as well as the vibration characteristics. To do this, a flexible rotor model of the turbocharger is coupled to a nonlinear ball bearing model considering the specific geometry and number of balls, for example. Here, and in contrast to many other rotating machines operated in two separate bearings, a single bearing cartridge design is utilized. Run-up simulations within time-domain are performed and compared with measurements with good agreement.

1 Introduction

Developing a new vehicle engine requires the definition for targets, which depend on the specific type of vehicle, target customers, pricing, etc.. But now-days, independent of these criteria there is additional requirement gaining on importance: sustainability. This copes for example with the used materials, production methods, overall energy consumptions and emissions. In order to reduce the required energy and emissions of the vehicle during operation, a turbocharger for combustion engines improves the engine's efficiency and enables downsizing. Thus,

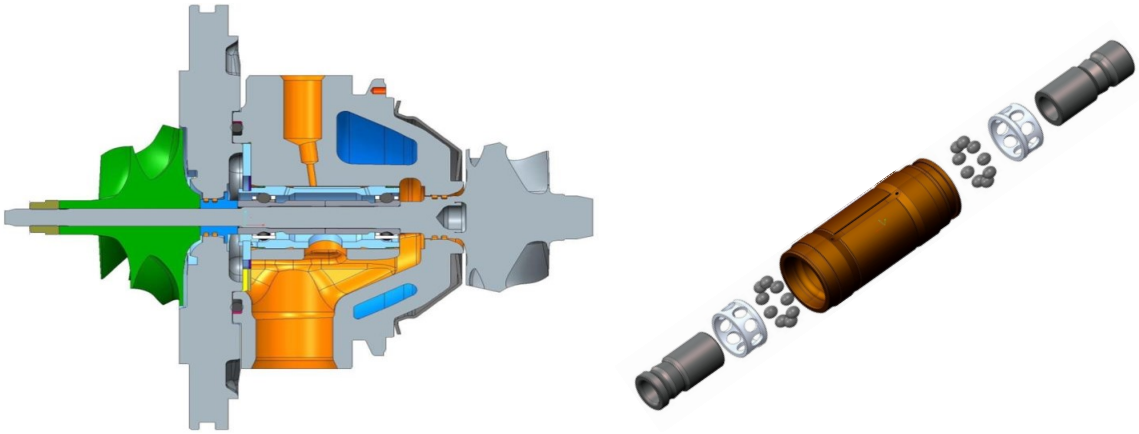

(a) Cross section of a turbocharger in ball bearings. (b) BorgWarner's ball bearing cartridge design.

Figure 1: Design of turbocharger and cartridge

Symbol	Bezeichnung	Wert
	compressor wheel diameter	$41\,\mathrm{mm}$
	turbine wheel diameter	$35\,\mathrm{mm}$
$n_{\max}$	maximum rotational speed (hardware)	260 krpm
m	rotor mass	$\approx 110\,\mathrm{g}$
n_W	number of balls per row	9
R_{bh}	cartridge radius (outside)	$8.5\,\mathrm{mm}$

Table 1: Quantities of the turbocharger rotor and bearing system.

the same power can be provided with a smaller engine displacement, resulting in a lower fuel consumption and reduction of CO_2- Emissions.

Aiming for a maximization of the engine's performance, the efficiency of the turbocharger should be maximized, too. Typically, a customization of the turbocharger according to the engine requirements starts with definition and selection of the aero components within a matching process. Consequently, the compressor and turbine wheel and the volutes are defined and designed. Furthermore, when the overall performance of the turbocharger is quantified, friction losses from the bearing system are taken into account. When targeting an optimizing of the performance, these losses have to be minimized. Most turbochargers are operated in oil lubricated radial and axial bearings. there, during operation a load carrying fluid film is build, separating rotating and non-rotating parts. Shear stresses within the fluid result in friction torque acting on the rotor, and thus, generates power loss. The friction torque depends on the viscosity of the fluid. Reducing the viscosity will reduce the friction losses, but could lead to severe vibration issues and might end up in a failure of the rotor-bearing system. Another approach to minimize bearing friction is to introduce a rolling element bearing system, [17].

Figure 1 shows an example of a turbocharger with a ball bearing system. Within the cross-section, as depicted in Figure 1a, the turbine wheel is located on the right, the compressor wheel on the left and the bearing housing in between, including the ball bearing cartridge in its centre. The bearing system is pre-assembled as a cartridge, see Figure 1b. It consists of two sets of spherical rolling elements, their cages, two inner and a single outer ring. Table 1 lists some properties of the system.

Since turbocharger applications with ball bearings are less common than with oil lubricated bearings the available literature is also less extensive. Some fundamentals about bearing modelling are published in the book of HARRIS and KOTZALAS [8], the dissertation of WENSING [16] or the publication [6] of LIEW et al. for example. TANIMOTO et al. present in [15] the superior behaviour of silicon nitride ceramic balls over steel balls in automotive turbo charger bearings. The system discussed here uses this material, too. DANIEL et al. investigate in [4] the dynamics of turbochargers operated in ball bearings. But, in contrast to the presented system it utilizes two single deep grove ball bearings. ASHTEKAR and SADEGHI investigate within [1] the dynamics of a turbo charger test rig and a coupled dynamic model for commercial vehicles applications with larger wheels and lower rotational speeds. In [2], CONLEY and SADEGHI measured the turbo charger motion and derive an overall simulation model including a ball bearing cartridge system. Similar to here, sub-synchronous vibrations at low speeds are observed.

2 Performance Measurement

The friction generated within the bearing system is experimentally determined on a special test rig at BorgWarner's Tech Center, see Figure 2a. Figure 2b shows as an example the measured and post-processed data of the smallest available bearing cartridge design of BorgWarner (framesize BB01) and of an equivalent oil-lubricated bearing system tested with the same rotor. The test was conducted with a 0W20 oil for identical supply conditions, i.e. $90\,^{\circ}\mathrm{C}$, $2\,\mathrm{bar}$. The diagram shows the power losses over the rotor speed for each core group, normalized by the maximum power loss of the ball bearing system. It can be seen, that the journal bearing system generates a bit more than twice as much friction losses as the equivalent ball bearing system independent of the rotational speed. Thus, a turbocharger operated in ball bearings has a higher (thermodynamic) efficiency and furthermore operates superior in transient operation. For example, if the driver wants the vehicle to accelerate quickly, the turbocharger requires, due to the lower friction in the bearing system, a shorter time to reach its max. speed. Consequently, the supplied air of the turbocharger within a constant time frame is higher and the acceleration of the vehicle improves.

But, due to the very high rotational speeds of these systems dynamical loads and vibrations topics or rotor dynamics in general have to mastered. In order to analyse, simulate and design the rotating components and the bearing system a simulation model is derived, validated and utilized.

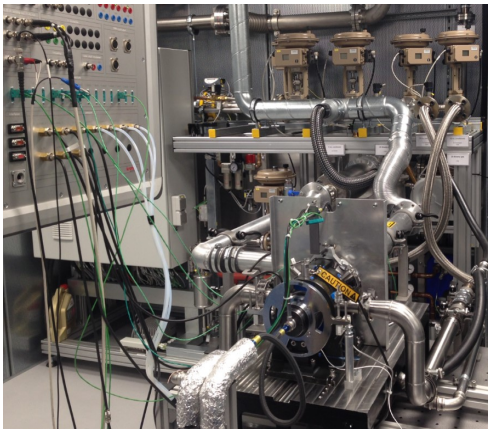

(a) BorgWarner's turbo friction test rig in Kirchheimbolanden.

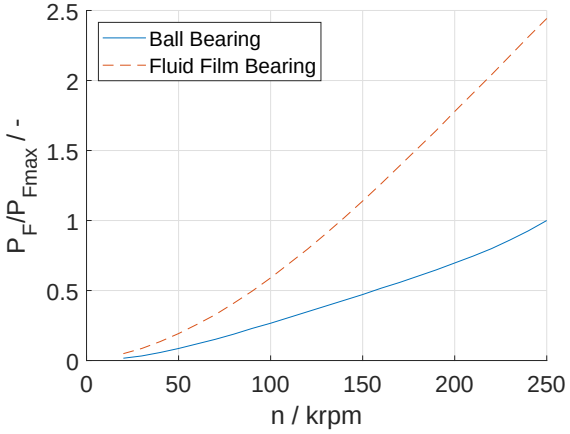

(b) Comparison of bearing friction power losses over rotor speed.

Figure 2: Friction test rig and measured friction.

3 Physical Model

The overall simulation model combines three sub-models of the rotor, the ball bearing cartridge and a fluid film model representing the squeeze film dampers acting between cartridge and bearing housing. All sub-models are fully coupled within the numerical simulation and solved in parallel. Each sub-model is briefly introduced in the following subsections.

3.1 Bearing Model

3.1.1 Macro geometry, positions and velocities

Within the bearing cartridge, see Figure 1b, two sets of spherical rolling elements, two inner and a single outer ring are modelled. Similar to conventional deep groove ball bearings, each set is built of n_W number of balls with the same diameter d_W, see Figure 3b. Furthermore, both inner and outer rings are geometrically defined by their radii of curvatures r_J and r_A, see Figure 3a, and the inner- and outer-ring raceway contact diameter d_i and d_o, see Figure 3b. The bearings are designed with clearance. The diametral clearance

$$G_r = d_o - d_i - 2d_W \tag{1}$$

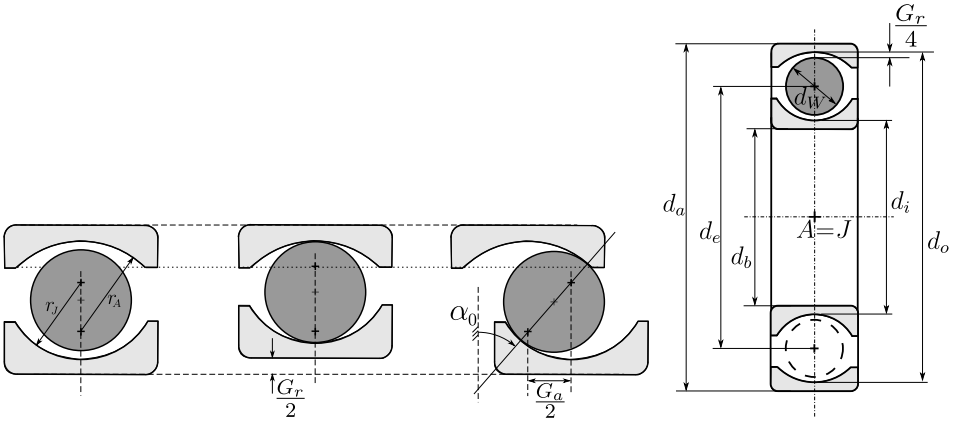

(a) (b)

Figure 3: Geometry paramaters of the ball bearing model.

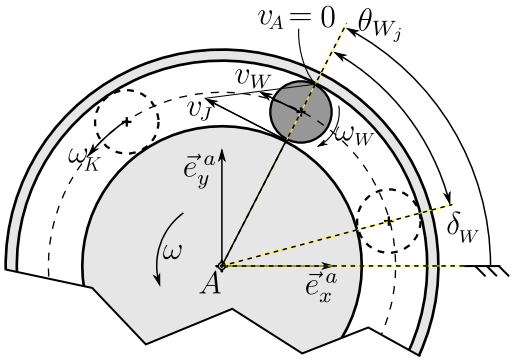

Figure 4: Angles and velocities of moving parts within the bearing.

quantifies the distance the inner ring can translated within the cross-sectional plane in total, when the position of the outer ring is fixed. Similar, the axial clearance G_a measures the overall distance the inner ring can translate axially. In the later mentioned case a line defined by both contact points between balls and raceways defines the free contact angle α_0, see Figure 3a. In general, during operation, the displacement of the inner ring will neither be purely radial nor purely axial. And, as a result, only a reduced number of balls are in contact with both rings at a certain time t. To identify the active balls, which are in contact with both rings, the positions of all balls with respect to a space fixed reference frame have to be determined.

Under the assumption of pure rolling the relative velocity of both contact points on a ball and a ring are equal zero (no slip). The speed of the inner ring raceway can be deduced through the angular velocity of the rotor and its diameter $v_J = \omega \frac{d_i}{2}$, see Figure 4. The velocity of the outer ring, since not rotating, is zero, $v_A = 0$. Thus, through linear interpolation, the translational velocity of a ball's centre can be determined as

$$v_W = \frac{1}{2}(v_J - v_A) = \omega \frac{d_i}{4}, \tag{2}$$

and consequently the angular velocity of the cage as

$$\omega_K \approx \frac{2v_W}{d_W + d_i} = \frac{d_i}{2(d_W + d_i)}\omega. \tag{3}$$

The corresponding position of the considered ball can then be deduced by integration with respect to time

$$\theta_{W_j}(t) = \int \omega_K \, \mathrm{d}t, \tag{4}$$

while the initial position of one ball $\theta_{W_j}(t = 0)$ is, without loosing generality, assumed to be zero. Since the bearing has a cage guiding the rolling elements, but which is not physically modelled, the position of all other balls can be deduced using the angle $\delta_W = \frac{2\pi}{n_W}$ between two neighbouring balls, see Figure 4. No equation of motion for each ball is considered within the model, their position is deduced from the kinematics of the surrounding and moving structures.

3.1.2 Contact Model

Due to the clearance, only a few balls are in contact with both rings when the shaft is rotating. Solely, only the active balls are transferring the loads from the rotor to the outer ring. For ideal geometries a point contact between both bodies exist, which will result in high local contact pressures and stresses, causing a local deformation within the contact zone. *Hertzian* contact theory [9], [10] is applied to describe the contact mechanics, see [11], [12], [5], [8] e.g.. A lubricating fluid within the contact zone is neglected, which leads to the problem of dry contacts.

Figure 5a shows two generic bodies with a single contact point. Both bodies (Index 1 and 2) are approximated - at least within the contact zone - by ellipsoids. The variables $r_{ix}, r_{iz}, i = 1, 2$ denote the principal radii of curvature within two perpendicular directions. Both, convex and concave contact geometries are covered within

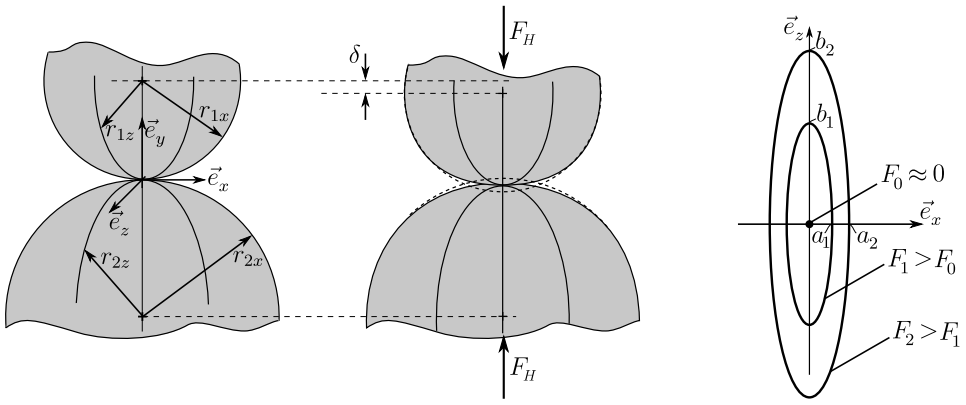

(a) Generalized contact bodies. (b) Contact ellipse.

Figure 5: Parameters and Geometry of the contact problem.

this approach. For the investigated deep groove and angular contact bearings a single convex contact appears, while all others are concave. For the latter mentioned case the radius, where the centre point is positioned outside the body, is considered negative.

Due to an acting load F_H, both bodies will deform within the contact area and the ideal point contact will transform into a contact zone, see Figure 5a. Within the framework of the *Hertzian* contact theory, it is assumed, that both bodies are linear elastic, homogeneous and isotropic and deformations are fully elastic. Furthermore, the dimensions of the contact area are assumed to be much smaller than the dimension of both bodies characterized by their radii of curvature. The governing equations are derived on the basis of the elastic-half space theory. In addition, loads are assumed to act only normal to the surface, while shear stresses within the contact zone are neglected. HERTZ postulates, a pressure (or normal stress) distribution of elliptical shape

$$\sigma = \sigma_{max} \left[1 - \left(\frac{x}{a}\right)^2 - \left(\frac{z}{b}\right)^2 \right]^{1/2}, \tag{5}$$

where a and b are both semi axes, see Figure 5b. Their ratio is defined as the non-dimensional parameter

$$\kappa = \frac{b}{a}. \tag{6}$$

The maximum pressure within the contact zone is given by

$$\sigma_{max} = \frac{3F_H}{2\pi ab}, \tag{7}$$

whereas F_H is the applied force.

The contact ellipse and consequently both semi-axes a and b are a function of the applied load F_H and the actual geometry (radii $r_{i,j}, i = 1, 2; j = x, z$). Several relationships between the contact geometry (radii) and the ratio of the semi-axes κ are proposed, see [12], [11], [16], [8] for example. Here, the approach

$$D_c = \frac{(\kappa^2 + 1)\mathcal{E} - 2\mathcal{F}}{(\kappa^2 - 1)\mathcal{E}} \tag{8}$$

given in [8] is used. The variable

$$D_c = \frac{(\frac{1}{r_{1x}} - \frac{1}{r_{1z}}) + (\frac{1}{r_{2x}} - \frac{1}{r_{2z}})}{\frac{1}{r_{1x}} + \frac{1}{r_{2x}} + \frac{1}{r_{1z}} + \frac{1}{r_{2z}}}, \tag{9}$$

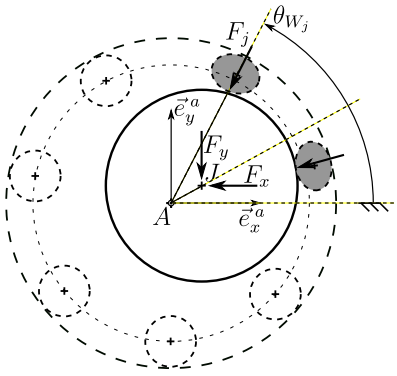

(a)

Figure 6: Sketch of contact forces between balls and inner raceway and deduced force acting on the rotor.

can be determined from the radii of curvature. Within (8),

$$\mathcal{F} = \int_0^{\pi/2} \left[1 - \left(1 - \frac{1}{\kappa^2}\right) \sin^2 \phi\right]^{-1/2} \, \mathrm{d}\phi \tag{10}$$

is an elliptical integral of first kind,

$$\mathcal{E} = \int_0^{\pi/2} \left[1 - \left(1 - \frac{1}{\kappa^2}\right) \sin^2 \phi\right]^{1/2} \, \mathrm{d}\phi \tag{11}$$

an elliptical integral of second kind. Once $\mathcal{F}, \mathcal{E}$ and κ are iteratively determined, the force displacement relationship of both bodies in contact

$$F_H = \begin{cases} k_H \delta^{3/2} & \text{if } \delta \geq 0 \\ 0 & \text{if } \delta < 0 \end{cases} \tag{12}$$

can be evaluated, using the equivalent Hertzian contact stiffness

$$k_H = \left(\frac{2\pi^2 \mathcal{E} R \kappa^2 E'^2}{9\mathcal{F}^3}\right)^{1/2}, \tag{13}$$

with the reduced Youngs-Modulus $E' = 2(\frac{1-\nu_1^2}{E_1} + \frac{1-\nu_2^2}{E_2})^{-1}$, and R' the mean reduced radius of both bodies.

Knowing the contact force of a single ball, the resulting force acting on the rotor can be determined by summing up the forces of all balls, which are active, respective in contact, see Figure 6a:

$$\vec{F} = F_x \vec{e}_x^{\,a} + F_y \vec{e}_y^{\,a} + F_z \vec{e}_z^{\,a} = \sum_{j=1}^{n_W} \vec{F}_j. \tag{14}$$

Similarly, the resulting force acting on the outer ring can be determined.

3.2 Squeeze Film Damper Model

The squeeze film damper acting between the outer ring of the cartridge and the bearing housing is modelled on the basis of the conventional assumptions of fluid film theory: the fluid is considered as a continuum, the flow is laminar, the gap height h in radial direction is much smaller than the dimensions in circumferential and axial direction and the curvature of the fluid domain is neglected, see [14], [7] for example. Applying these assumption

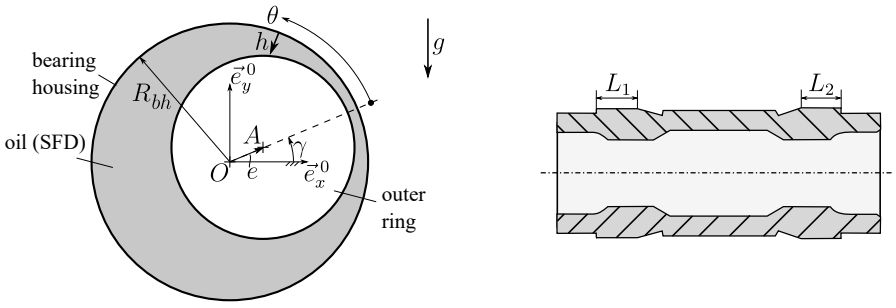

(a) Geometry and coordinates of squeeze film damper model.

(b) Axial dimensions of squeeze film dampers on outer ring.

Figure 7: Sketch of squeeze film damper model and geometry.

to the *Navier-Stokes-Equations* and combing the relationships with the continuity equation leads to the *Reynolds-Equation*

$$\frac{1}{R_{bh}^2}\frac{\partial}{\partial\theta}\left[h^3\frac{\partial p}{\partial\theta}\right]+h^3\frac{\partial^2 p}{\partial z^2}=12\mu\frac{\partial h}{\partial t}, \tag{15}$$

which determines after solving the fluid pressure within the gap. Equation (15) was initially derived by REYNOLDS in 1886, [13]. Note, that the right hand-side is simplified with respect to the standard form, since the outer ring is not rotating ($\omega_A = 0$). The parameters within (15) are the viscosity of the fluid μ, the inner radius of the bearing housing R_{bh} and the length of the squeeze film damper L. The cartridge has two squeeze films dampers. Their length is denoted with an index 1 or 2 within Figure 7b to distinguish between both sides. The independent variables are θ, z and the time t. Within (15), the dependent variable is the unknown fluid pressure p. Furthermore, the film height h is a function of the eccentricity $e = e(t)$ of the outer ring centre A, the clearance h_0 and circumferential position θ:

$$h = h_0 - e\cos\theta, \tag{16}$$

whereas tilting or misalignment of the cartridge with respect to the housing is neglected. To solve (15), pressure boundary condition on both axial ends $p(z=\frac{L}{2}) = p(z=-\frac{L}{2}) = 0$ of the squeeze film dampers are assumed. Here, the pressure gradient in circumferential direction is considered to be small compared to the pressure gradient in axial direction, since $2L < R_{bh}$. Thus, the first term in (15) is neglected and short-bearing theory is applied, see [14] e.g., resulting in the pressure

$$p(\theta,z) = -\frac{6\mu}{h^3}\frac{\partial h}{\partial t}\left[\left(\frac{L}{2}\right)^2 - z^2\right]. \tag{17}$$

Negative pressures, when occurring, are neglected by applying the GUEMBEL condition $p_G = \max(p,0)$. The resulting force acting on the outer ring and in opposite direction on the bearing housing is deduced by integration of the pressure field after projecting in the respective direction through

$$\vec{F}_{SFD} = \underbrace{-\left[R_{bh}\int_{-\pi}^{\pi}\int_{-\frac{L}{2}}^{\frac{L}{2}} p_G\cos\theta \;\; \mathrm{d}z\,\mathrm{d}\varphi\right]}_{F_x}\vec{e}_x^{\,0} \underbrace{-\left[R_{bh}\int_{-\pi}^{\pi}\int_{-\frac{L}{2}}^{\frac{L}{2}} p_G\sin\theta \;\; \mathrm{d}z\,\mathrm{d}\varphi\right]}_{F_y}\vec{e}_y^{\,0}. \tag{18}$$

3.3 Rotor Model

The turbocharger shaft is modelled as a flexible body using finite elements, see Figure 8. A 3D CAD model is the starting point and a modal analysis is conducted. In order to minimize the computational costs in time transient simulations, a model order reduction by means of CRAIG-BAMPTON is applied, [3]. Master-nodes at the bearing and wheel locations are defined. In the last step the turbine and compressor wheel are linked to the flexible shaft as rigid bodies.

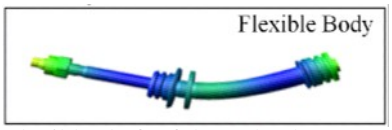

Figure 8: Flexible shaft of the turbocharger rotor model.

3.4 Simulation vs. Measurement

The commercial software package MSC Adams is used to simulate the transient behaviour of the fully coupled system, consisting of the rotor, which combines shaft and wheels, both ball bearings combined to a single cartridge and the two squeeze film dampers. Simulations are performed within the time domain. A typical simulation scenario is a run-up test case, whereas the rotor speed increases linear with time. The vibrations of the system are usually assessed by analysing the oscillations of the shaft nut. This part fixes the compressor wheel to the shaft, see Figure 1a on the left end in gold. Typically, the identified vibrations are transformed in the frequency domain. Figure 9a shows such a simulation result. Here, first order vibrations - identifiable as the diagonal - are visible over the whole speed range, with maximum amplitudes at approx. 180 krpm. Additionally, sub-synchronous vibrations with distinct amplitudes are occurring almost over the whole speed range, too. They appear the most dominant also around 180 krpm.

Furthermore, measured oscillations of the corresponding shaft-nut deflections within the frequency domain are shown in Figure 9b for comparison. Distinct first order vibrations can be observed there, as well . Additionally, sub-synchronous vibration amplitudes are also present, independent of the operating speed of the rotor. Within the hardware test, the highest amplitudes of the sub-synchronous vibrations appear at slightly lower shaft speeds as within the simulations. Their related frequency in test and model are in good agreement. Within the lower rotor speed range the sub-synchronous vibrations are similar to measurement, while their multiple order vibration is more dominant within the measurement. At high speeds, some deviations for the sub-synchronous vibrations are visible.

4 Summary

Ball bearing systems in turbocharger applications are quite rare. Never the less, they have some benefits compared to hydrodynamic bearing systems. A major one is their lower friction loss, which will at the end improve the transient response of the vehicle and the efficiency of the charging system and thus the engine. One the other hand some challenges have to be met, when utilizing ball bearings in turbochargers. One copes with the high rotational speeds and the vibrations generated through the rotating device. To examine the transient behaviour, a simulation

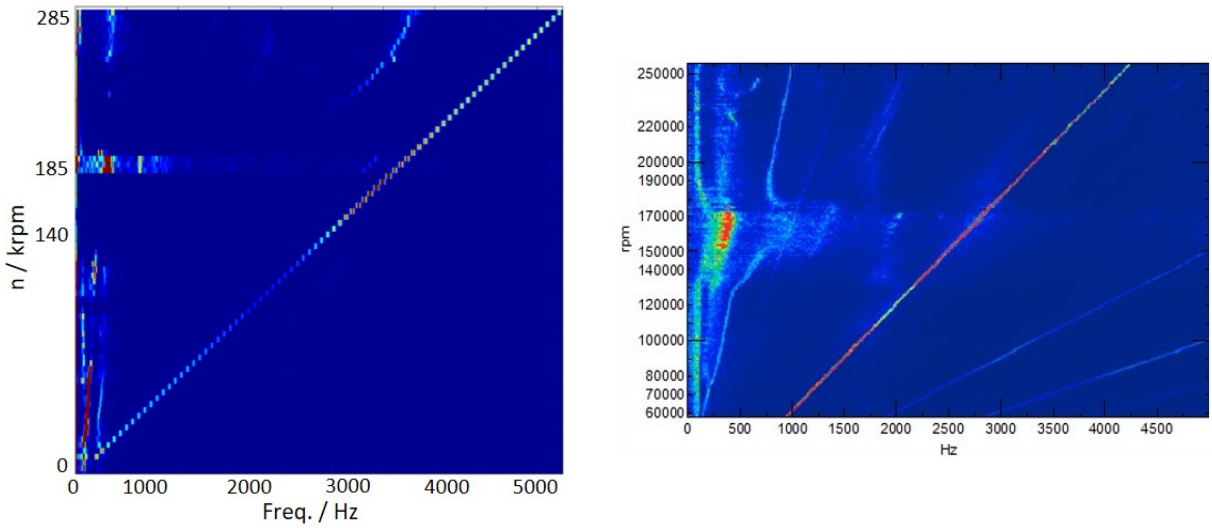

(a) Simulated waterfall plot.

(b) Measured waterfall plot.

Figure 9: Frequency analysis of shaft-nut deflections as a function of rotational speed.

model is deduced, implemented in a commercial simulation software and investigated. The model combines and couples a flexible rotor model, a non-linear ball bearing model together with a non-linear hydrodynamic model for the squeeze film dampers. All equations of motion are solved simultaneously within time domain, usually as linear run-up simulations. An analysis of the shaft-nut deflections within the frequency domain shows synchronous and concurrent sub-synchronous vibrations. At certain shaft speeds, the later one are more dominant. Finally, the simulations results are compared with a measurement. An agreement of the dominating effects is a achieved.

References

[1] Ashtekar, A., and Sadeghi, F. (2011): Experimental and Analytical Investigation of High Speed Turbocharger Ball Bearings. *J. Eng. Gas Turbines Power*, 133(12): 122501. https://doi.org/10.1115/1.4004004

[2] Conley, B. and Sadeghi, F. (2022): Impact of Whirl and Axial Motion on Ball Bearing Turbocharger Dynamics. *Tribology Transactions*, 1–14,. DOI: 10.1080/10402004.2022.2153774

[3] Craig Jr, R. R. and Bampton, M. C. C. (1968): Coupling of substructures for dynamic analyses. *AIAA journal*, **6** Vol.7, pp. 1313–1319.

[4] Daniel, C. and Göbel, S. and Nitzschke, S. and Woschke, E. and Strackeljan, J. (2013): Numerical simulation of the dynamic behaviour of turbochargers under consideration of full-floating-ring bearings and ball bearings. In *11th international conference on vibration problems*. Lisboa, Portugal, Vol. 400.

[5] Eschmann, P. and Hasbargen, L. and Brändlein, J. (1978): *Die Wälzlagerpraxis*. Oldenburg Verlag.

[6] Liew, A. and Feng, N. and Hahn, E. J. (2002): Transient Rotordynamic Modeling of Rolling Element Bearing Systems. *J. Eng. Gas Turbines Power*, **124**(4), pp. 984–991.

[7] Hamrock B. J. (1994): *Fundamentals of fluid film lubrication*. McGraw-Hill.

[8] Harris, T. A. and Kotzalas, M. N. (2007): *Essential Concepts if Bearing Technology*. Taylor & Francis.

[9] Hertz, H. (1882): Über die Berührung fester elastischer Körper. *J. für die reine und angewandte Mathematik*, **92**, pp. 156–171.

[10] Hertz, H. (1882): Über die Berührung fester elastischer Körper und über die Härte. *Verhandlung des Vereins zur Beförderung des Gewerbefleißes*, pp. 449–463.

[11] Johnson K. L. (1985): *Contact Mechanics*. Cambridge University Press.

[12] Moes, H. (2000): *Lubrication and Beyond*. University of Twente - lecture notes code 115531.

[13] Reynolds, R. (1886): On the Theory of Lubrication and Its Application to Mr. Beauchamp Tower's Experiments, Including an Experimental Determination of the Viscosity of Olive Oil. *Proceedings of the Royal Society of London*, **40**242-245, pp. 191–203.

[14] A. Z. Szeri (2011): *Fluid Film Lubrication*. Cambridge University Press.

[15] Tanimoto, K. and Kajihara, K. and Yanai, K. (2000): Performance of hybrid ceramic ball bearing for turbochargers. *Koyo Eng. J. Engl. Ed.*, Vol.257, pp. 21–31.

[16] Wensing, J. A. (1998): *On the Dynamics of Ball Bearings*. Ph.D. Thesis, University of Twente, Twente.

[17] Zeppei, D. and Koch, S. and Rohi, A. (11-2016): Ball Bearing Technology for Passenger Car Turbochargers. *MTZ worldwide*, **Volume 77**, pp. 26–31.

15th SIRM – European Conference on Rotordynamics,
Darmstadt, Germany, 22nd – 24th February 2023

Application of the fuzzy number method for analysis of nonlinear vibration of rotor systems with uncertain parameters

Jaroslav Zapoměl [1,2], Petr Ferfecki [3,4], Michal Molčan [5], Jan Kozánek [6]

[1] Department of Applied Mechanics, VSB - Technical University of Ostrava,
708 00, Ostrava, Czech Republic, jaroslav.zapomel@vsb.cz
[2] Department of Dynamics and Vibration, Institute of Thermomechanics,
182 00, Prague, Czech Republic, zapomel@it.cas.cz
[3] IT4Innovations National Supercomputing Center, VSB - Technical University of Ostrava, 708 00, Ostrava,
Czech Republic, petr.ferfecki@vsb.cz
[4] Department of Applied Mechanics, VSB - Technical University of Ostrava,
708 00, Ostrava, Czech Republic, petr.ferfecki@vsb.cz
[5] IT4Innovations National Supercomputing Center, VSB - Technical University of Ostrava, 708 00, Ostrava,
Czech Republic, michal.molcan@vsb.cz
[6] Department of Dynamics and Vibration, Institute of Thermomechanics,
182 00, Prague, Czech Republic, kozanek@it.cas.cz

Abstract

The actual behaviour of real rotating machines is difficult to predict as it depends on a variety of geometrical, physical, and technological factors, the values of which are uncertain. It implies amplitude of their vibration or magnitudes of the transmitted forces can be estimated only with a certain degree of probability. Several methods have been developed for analysis of such systems. This paper deals with the approach utilizing the fuzzy numbers. Its application requires performing interval operations and the results are expressed also the fuzzy numbers. The usability of this method in the field of rotor dynamics was tested by employing computer simulations. The investigated rotor consisted of a shaft and one disc. The shaft was coupled with the stationary part by two hydrodynamic bearings and the disc by two elastically connected brushes. The rotor unbalance, the steady state speed of its rotation, and prestress of the brushes were regarded to be uncertain. The task was to determine the maximum radial displacement of the rotor disc. The advantage of the method based on the application of fuzzy numbers is that it does not require knowledge of the probability density function of the uncertain parameters, and the corresponding generators of random numbers, and makes it possible to assign a degree of credibility to the results. To perform the analysis, the sufficient experience of persons solving the problem and an adequately intensive knowledge database are needed. The originality and the new contribution of this paper consists in the utilization of analytical manipulations with fuzzy numbers in performing the interval operations.

1 Introduction

The actual behavior of real rotating machines depends on a variety of geometric, physical, and technological factors (e.g. stiffness or damping of the individual components or contact connections, speed of the rotation, material constants, parameters of the unbalance and applied loading, etc.), the values of which are uncertain because of different reasons. Several methods have been developed to solve such problems. The worst scenario method, the probabilistic approaches like the Monte Carlo method, the fuzzy number approach, or the sensitivity approaches are among them.

The method based on utilization of the fuzzy numbers assumes that the value of each uncertain quantity is a real number from a certain interval and that the degree of membership, the magnitude of which runs between 0 and 1, is assigned to each value from this interval. This assignment requires adequate experience from persons involved in the solution of the problem and on the data gathered in sufficiently extensive knowledge databases. The degree of membership approaching one indicates a higher probability of the uncertain quantity value while

the degree of membership approaching zero means that the probability of the corresponding value is low. The fuzzy numbers method requires performing interval analyses for chosen membership levels, the same for all uncertain quantities, which makes it possible to construct corresponding intervals and membership functions of the results.

More details on fuzzy sets and fuzzy numbers can be found in [1] or [2]. Some rules and recommendations on how to determine the membership function are given in [3]. The fuzzy number approach was used in different fields of mechanics. Moens et al. [4] reported on the application of this method for the construction of the frequency-response function of damped structures. Sága et al. used the fuzzy number approach for the vibration analysis of vehicles [5]. Vaško at al. applied this method for damage prediction of mechanical structures [6]. Zapoměl et al. used the fuzzy numbers approach in the field of rotor dynamics [7], [8].

The individual methods for solving the problems with uncertain input parameters mutually differ. The possibility of application of each of them depends on the extent of the data and the computational (hardware and software) tools that are to the disposal to persons solving the problem. It implies each method is applicable only for certain cases. The methods also differ in the character and interpretation of the results.

The worst scenario method is based on searching for the worst case. It uses maximum extents of possible values of the uncertain parameters or such their values that lead to the worst solution from the point of view of the solved problem. The results are on the side of safety but they do not contain any information on the probability of occurrence of the worst case.

The fuzzy numbers approach requires to specify the possible extents of values of the individual uncertain parameters. Consequently, these extents are divided into sub-intervals, the elements of which have the same probability or frequency of occurrence defined by the ill-specified quantifiers (e.g. this value of the uncertain parameter is very frequent, frequent, low frequent, the frequency is marginal, etc.), to which the degree of membership from the interval between 0 and 1 is assigned. Then utilizing the approximation, the continuous membership function is constructed over all sub-intervals. Consequently, the interval analysis for the chosen values of the membership function is performed, which means finding the corresponding minimum and maximum values of each output parameter. This can be done either by solving the problem for the specified combinations of values of the uncertain parameters or by application of the rules for arithmetic operations with the fuzzy numbers if possible. The values of the output parameters are fuzzy numbers, the membership function of which gives the idea on their probability. The fuzzy numbers approach has a great advantage because the sub-intervals of the values of uncertain parameters can be determined by experienced engineers or workers. In addition, no statistic computational tools and no statistic treatment performed in advance are needed.

Application of the Monte - Carlo method requires assigning the probability density function to each uncertain parameter. The actual procedure consists in performing a vast number of simulations for randomly generated values of all uncertain parameters in accordance with their probability density function. This requires having to the disposal the corresponding generators of random numbers. The calculated results are stochastic quantities, the most probable value of which can be determined from their probability density function.

In this paper, the fuzzy numbers approach was applied to analyze non-linear steady state vibrations of a rotor by means of computer simulations. The studied rotor was rigid. Its shaft was supported by two hydrodynamic bearings and its disc was connected to the stationary part by two flexible brushes. Values of the rotor unbalance, the steady state speed of its rotation, and prestress of the brush springs were considered uncertain. The trigonometric collocation method was applied to determine the rotor steady state response. The goal of the analysis was determination of the rotor maximum radial displacement.

The originality and the contribution of this paper to the development of the fuzzy numbers method consists in the utilization of analytical manipulations with fuzzy numbers in performing the interval operations and their combination with the computational procedure and introduction of the parameter for evaluation of the credibility of the results (degree of credibility).

2 The equations of motion of the investigated rotor

The investigated rotor and its stationary part are rigid (Fig. 1). The rotor consists of a shaft and of one disc. At both ends, the shaft is coupled with the stationary part by hydrodynamic bearings. The disc is connected to the frame by two pre-stressed flexibly supported brushes (Fig. 2). The rotor rotates at constant angular speed, is loaded by its weight, and excited by the disc unbalance. The whole system can be considered symmetric relative to the disc middle plane.

The task was to determine maximum radial displacement of the disc.

In the computational model the rotor and the stationary part were considered absolute rigid and stiffness of the springs pushing the brushes to the disc constant and the mass of the springs negligible. The design and geometric parameters of the hydrodynamic bearings made it possible to model them as bearings of finite length. The pressure distribution in the bearing gap is determined by solving the Reynolds equation. Pressure in the

cavitation areas was considered constant. Components of the hydraulic forces were obtained by integration of the pressure distribution around the circumference and along the length of the bearing considering different pressure profiles in cavitation and non-cavitated regions. Damping caused by the environment was regarded as linear.

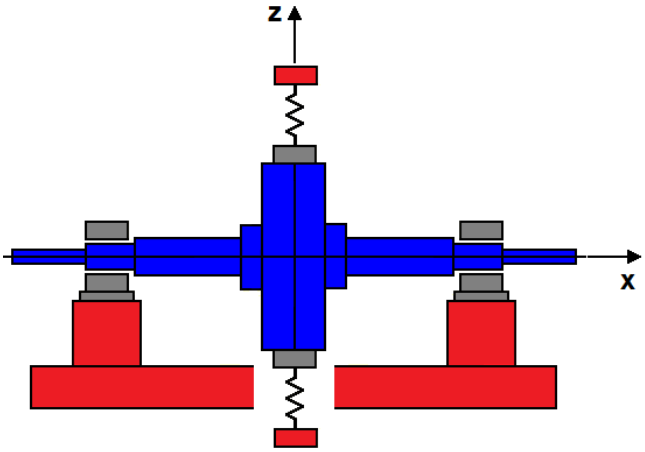

Figure 1: The investigated rotor system.

The equations of motion were set up by means of Lagrange equations of the second order.

$$m\ddot{y} + b_P\dot{y} = me_T\omega^2\cos(\omega t) + 2F_{hy} \tag{1}$$

$$m\ddot{z} + b_P\dot{z} + 2kz = me_T\omega^2\sin(\omega t) - mg + k(s_1 - s_2) + 2F_{hz} \tag{2}$$

m is the rotor mass, k is the stiffness of one brush spring (Fig. 2), b_P is the coefficient of the linear rotor damping caused by the environment, e_T is the eccentricity of the rotor center of gravity, ω is the angular speed of the rotor rotation, t is the time, g is the gravity acceleration, F_{hy}, F_{hz} are the horizontal and vertical components of the hydraulic force, s_1, s_2 are displacements prestressing the brush springs (Fig. 2), y, z are horizontal and vertical displacements of the rotor, respectively, and $(\dot{})$, $(\ddot{})$ denote the first and second derivatives with respect to time.

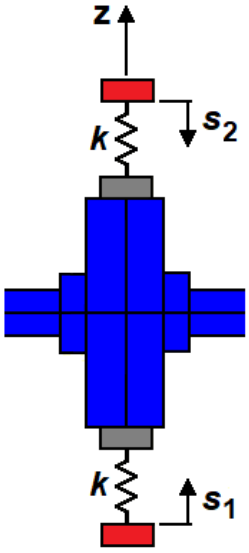

Figure 2: Prestress of the brush springs.

The steady state solution of the equations of motion was obtained by application of the trigonometric collocation method.

3 Fuzzy analysis of the rotor steady state oscillations

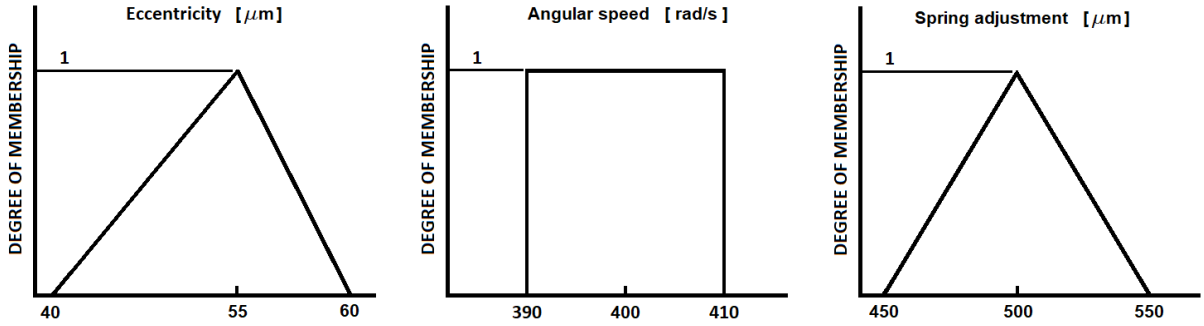

Figure 3: Membership functions of the uncertain parameters.

The principal technical parameters of the rotor and its bearings are: mass of the rotor 325 kg, rated angular speed of the rotor rotation 400 rad/s, stiffness of each brush spring 5 MNm, rated pre-compression of each brush spring 500 μm, coefficient of linear damping caused by the environment 1.3 kNs/m, the bearings length/diameter 100 mm/100 mm, and dynamic viscosity of the oil 0.008 Pas.

The rotor eccentricity, speed of rotor rotation, and pre-compression of the brush springs are uncertain parameters. Their values are expressed by fuzzy numbers. The magnitude of eccentricity of the rotor center of gravity ranges from 40 to 60 μm, the angular velocity runs between 390 and 410 rad/s, and the pre-compression of each brush spring varies from 450 to 550 μm. The corresponding membership functions are depicted in Fig. 3.

The pre-compression displacements s_1 and s_2 of the ends of the springs, by which the springs are attached to the rotor casing, occur in the equations of motion separately from other uncertain parameters in the form of their difference. This makes it possible to use the analytical relation for manipulation with the fuzzy numbers. It holds

$$\overline{s} = \overline{s}_1 - \overline{s}_2, \tag{3}$$

$$\Delta s = \Delta s_1 + \Delta s_2 \tag{4}$$

where

$$s_1 = \overline{s}_1 \pm \Delta s_1, \tag{5}$$

$$s_2 = \overline{s}_2 \pm \Delta s_2, \tag{6}$$

$$s = \overline{s} \pm \Delta s. \tag{7}$$

s is a new auxiliary parameter replacing displacements s_1 and s_2 in the equations of motion. The bar denotes the mean value of the displacements and Δs, Δs_1, Δs_2 are deviations from the mean values of parameters s, s_1, s_2, respectively. This holds for all membership levels (only the deviations differ). The performed modification reduces the number of uncertain parameters from four to three.

The membership function for values of the auxiliary parameter s is drawn in Fig. 4.

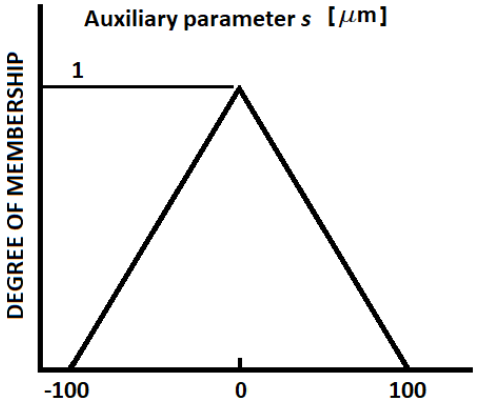

Figure 4: Membership function of the auxiliary parameter s.

The actual interval manipulations are done for three uncertain quantities, speed of the rotor rotation, eccentricity of the rotor centre of gravity, and the auxiliary parameter *s*.

4 Results of the simulations

The frequency response characteristic constructed for the rated or most probable values of uncertain parameters is depicted in Fig. 5. The figure shows the double amplitude of the rotor steady state vibration in the horizontal and vertical directions for angular velocity up to 1000 rad/s.

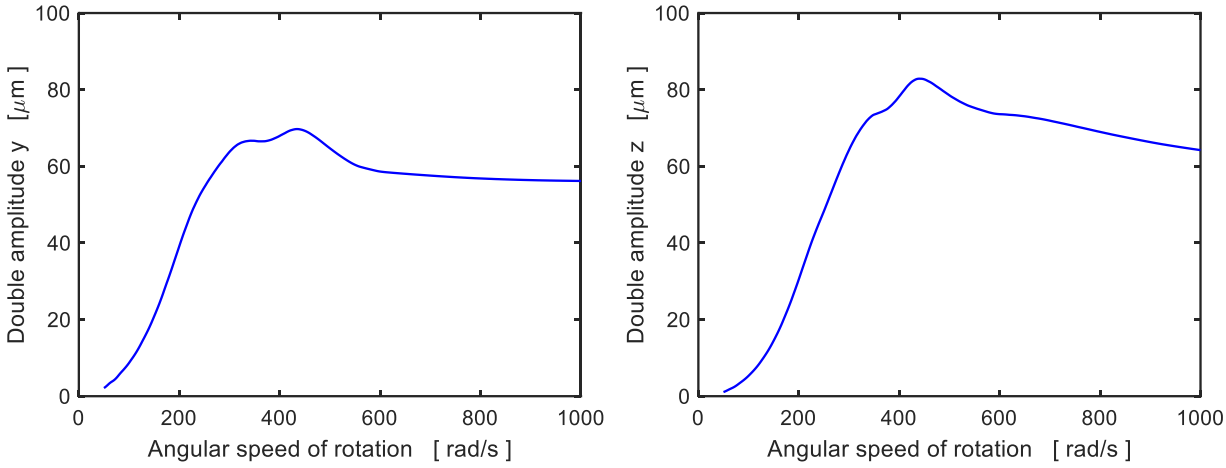

Figure 5: Frequency response characteristic.

The frequency responses show that the rated angular speed is near to the resonance area. It implies even a small deviation of angular velocity can significantly affect the vibration amplitude.

Fig. 6 shows the steady state orbit of the rotor journal center in the hydrodynamic bearing for the rated velocity of the rotor rotation (400 rad/s), rated pre-compression of each brush spring (0.5 mm) and for the most probable value of the rotor eccentricity (55 μm).

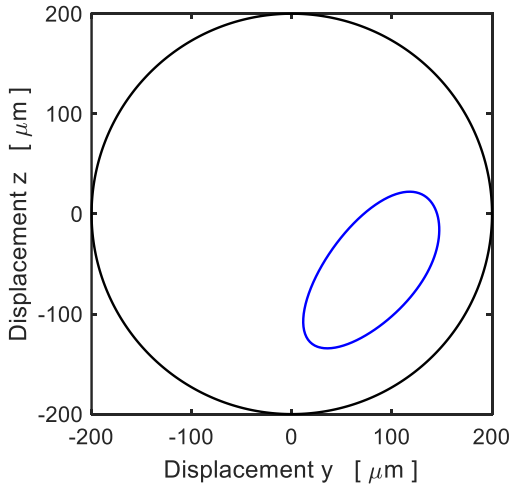

Figure 6: Steady state orbit of the rotor journal center (degree of membership 0.5).

To perform analysis of the rotor steady state vibration considering uncertain values of some parameters, the individual levels of the membership function were specified (0.0, 0.2, 0.4, 0.6, 0.8, 1.0). Consequently, the steady state response of the rotor was calculated for all combinations of specified values of the uncertain parameters and the results were sorted according to the individual levels of the membership function.

Fig. 7 shows the steady state trajectory of the rotor journal in the gap of the hydrodynamic bearing, which corresponds to the worst case (degree of membership 0.0). The steady state orbit is uncertain and has a fuzzy character.

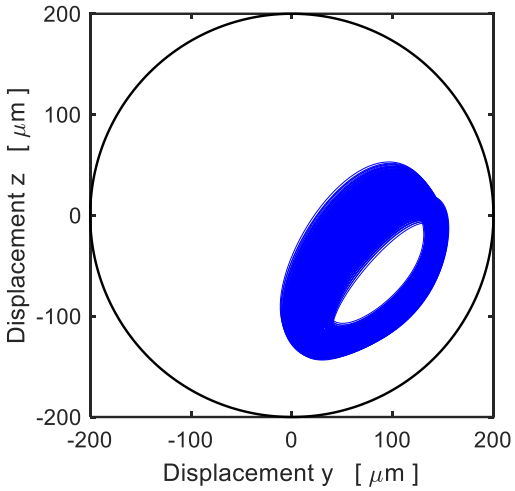

Figure 7: Steady state orbit of the rotor journal center (worst case).

Fig. 8 shows the membership function of the maximum radial displacement of the rotor disc. It is evident that its value ranges from 133 to 157 µm.

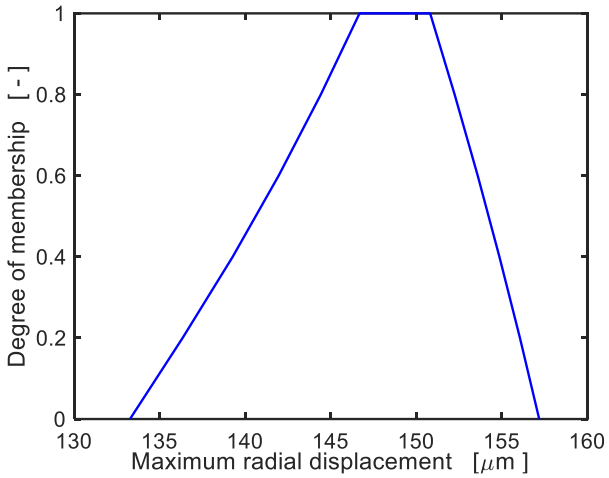

Figure 8: Membership function of the rotor radial displacement.

The interval related to the degree of membership of 0 corresponds to the worst case. The ratio of the lengths of intervals corresponding to the chosen degree of membership and the degree of membership of 0 can be considered as the degree of credibility, with which the results were obtained (Table 1).

Table 1: Degree of credibility

	Degree of membership	Extent [µm]	Degree of credibility [%]
1	1.0	147 - 151	16.7 %
2	0.8	144 - 152	33.3 %
3	0.6	142 - 154	50.0 %
4	0.4	139 - 155	66.7 %
5	0.2	136 - 156	83.3 %
6	0.0	133 - 157	100.0 %

5 Conclusion

The made simulations proved that the approach based on the application of fuzzy numbers can be applied to the analysis of systems with uncertain parameters in the field of rotor dynamics. The results are not single values, but they are fuzzy numbers. It implies the results are expressed by intervals and by the degree of credibility assigned to each of them.

The fuzzy number approach has some advantages. It does not require knowledge of the probability density function of the individual uncertain parameters and corresponding generators of random numbers. If the number of uncertain parameters is not too large, the number of performed simulations can be considerably lower than those if the Monte Carlo method were applied. The number of simulations can be significantly reduced if it is possible to combine the computational interval operations with the analytical solution. Nevertheless, the correct application of the fuzzy number method requires the persons solving the problem to be adequately experienced or persons having a sufficiently extensive knowledge database to their disposal.

The combination of the computational and analytical manipulations with fuzzy numbers to perform the interval operations and introduction of the degree of credibility are original and represent the principal contributions to the development of the procedures for analysis of machine systems with uncertain parameters in the field of rotor dynamics.

Acknowledgement

The research work has been supported by projects RVO: 61388998 and CZ.02.2.69/0.0./0.0/19_073/0016945 (DGS/TEAM/2020-033). The support is highly acknowledged.

References

[1] Zimmermann, H.-J. (1996): *Fuzzy Sets Theory and Its Application*. Kluwer Academic Publishers, Boston, Dordrecht, London.

[2] Gupta, M. M. and Yamakawa, T. (1998): *Fuzzy computing: Theory, hardware and applications*, North-Holland, Amsterdam.

[3] Novák, V. (1990): *Fuzzy sets and their applications*, SNTL Praha (in Czech).

[4] Moens, D. and Vandepitte, D. (2005): A fuzzy finite element procedure for the calculation of uncertain frequency-response function of damped structures: Part 1 – Procedure. *Journal of Sound and Vibration*, 288(3), pp. 431-462.

[5] Sága, M., Letrich, M. and Kocúr, R. (2005): An analysis of vehicle vibration with uncertain system parameters. *Komunikácie*, 7(1), pp. 16-21.

[6] Vaško, M. and Sága, M. (2013): Application of Fuzzy Structural Analysis for Damage Prediction Considering Uncertain S/N Curve. *Applied Mechanics and Materials*, 4(20), pp. 21-29.

[7] Zapoměl, J., Ferfecki, P. and Molčan, M. (2021): The fuzzy approach for investigation of the steady-state response of rotors excited by loading effects of uncertain magnitude. In *Proc. Computational Mechanics 2021*. Srní, Czech Republic, Nov. 8-10, pp. 1-4.

[8] Zapoměl, J., Ferfecki, P., Molčan, M. and Kozánek, J. (2022): Analysis of vibration of rotors with a thick rigid disc on the overhanging end supported by hydrodynamic bearings and loaded by uncertain unbalance effects. In *Proc. Engineering Mechanics 2022*. Milovy, Czech Republic, May 9-12, pp. 1-4.

15th SIRM – European Conference on Rotordynamics,
Darmstadt, Germany, 22nd – 24th February 2023

Reduced Order Models of Rotating Machines Considering Nonlinear Effects

Arthur Mereles [1], **Diogo Stuani Alves**[2], **Katia Cavalca**[1]

[1] Laboratory of Rotating Machinery, School of Mechanical Engineering, University of Campinas, 13083-860, Campinas, Brazil, arthur_guilherme_mereles@hotmail.com
[2] Department of Mechanical Engineering, University of Bath, BA2 7AY, Bath, UK.

Abstract

The complexity and intricate dynamics of rotating machines generally requires models with a high number of Degrees of Freedom (DOFs). In this way, any model must come with some reduction method, that reduces the dimensionality of the system while retaining the major dynamic characteristic of it. The existence of nonlinear effects often complicates even more the analysis, and they are often neglected in the model reduction by, for example, relying on linearized models. Taking this into account, this paper presents a nonlinear model reduction method to obtain Reduced Order Models (ROMs) to study rotating machines under nonlinear forces. The method is based on the idea of Nonlinear Normal Modes (NNMs) and the existence of Invariant Manifolds (IMs). These manifolds can be seen as an extension of the linear eigenspaces commonly used in modal analysis to reduce the dimensionality of dynamical systems. The basis of the method is the obtention of the manifolds, allowing the reduction of the model to a single nonlinear mode, thus essentially reducing the problem to integrating a single pair of equations. In addition, the method is applied on a rotor-bearing systems with two kinds of nonlinearities: a cubic nonlinearity and a hydrodynamic bearing.

1 Introduction

A common way of reducing the number of equations in dynamical systems is the projection of the equations onto a lower-order subspace (Figure 1). In structural mechanics, a natural subspace is the space spanned by the vibrating modes of the system, often called the eigenspace. An important characteristic of this space is the invariance property, which states that any motion that starts on the eigenspace, remains on it as time tends to infinity. This means that when the initial conditions is set to a single mode, no energy will be transferred to the remaining modes, and they can thus be neglected in the dynamic analysis of the system. This, however, is not true for nonlinear systems, where energy does not remains at a single mode, but is transferred back and forth between them. In terms of the 3D system depicted in Fig. 1, this means that the projection of the trajectory $q(t)$ will poorly represent the full system trajectory $\mathbf{x}(t)$.

The main idea in the Invariant Manifold Method (IMM) [22, 17], is the obtention of nonlinear eigenspaces, that take into account the interaction between the modes that occur in nonlinear systems. These spaces are manifolds that are tangent to the linear eigenspaces near the equilibrium. In this way, the invariance property is regained, and a single mode can be used to describe nonlinear systems. As defined in [22], the motion that occurs on these manifolds gives the Nonlinear Normal Modes (NMMs) of the system. This is not, however, the only definition

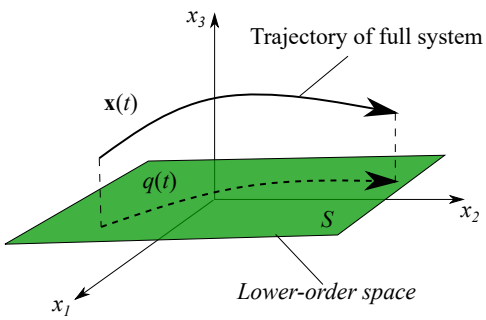

Figure 1: Reduction of a 3 dimensional system to a 2 dimensional one by a projection onto a lower-order space.

for NNM, as the literature is vast on this topic, and one can find more information in the reviews [18, 1, 3]. An important point about the above mentioned manifolds is that they may not be unique, specially for highly nonlinear systems, as explored in [9]. In addition, more than one nonlinear mode is required in cases of internal resonance, where there is a strong interaction between vibrating modes [13]. In [21], one can find several methods that have been developed to obtain the manifolds in nonlinear systems. Further applications of the IMM and alike can be seen in [12, 7, 2, 20].

This paper presents an application of the IMM in rotor-bearing systems. The rotor is modeled by means of the Finite Element Method (FEM). The approach can be used to reduce the equations of motion to a single pair of differential equations, allowing a fast obtention of forced solutions. Also, a wide variety of nonlinear forces can be incorporated in the approach. The method is presented for a rotor-bearing system considering two nonlinear bearing forces: a bearing with cubic nonlinearity, and a hydrodynamic bearing.

2 Theoretical Background

2.1 Rotordynamic model

The rotordynamic model considered in this paper is obtained through the discretization of the domain by the FEM, which leads to the following differential equation,

$$\mathbf{M}\ddot{\bar{\mathbf{x}}}(t) + (\mathbf{C_s} + \mathbf{C_b} + \Omega\mathbf{G})\dot{\bar{\mathbf{x}}}(t) + (\mathbf{K_s} + \mathbf{K_b})\bar{\mathbf{x}}(t) = \mathbf{f_{nl}}(\bar{\mathbf{x}}, \dot{\bar{\mathbf{x}}}) + \mathbf{f_h}(t) + \mathbf{f_g} \tag{1}$$

where $\bar{\mathbf{x}}(t)$ are the nodal displacements and rotations, $\mathbf{M}$ is the mass matrix, $\mathbf{G}$ is the gyroscopic matrix, Ω is the rotation speed, $\mathbf{K_s}$ and $\mathbf{C_s}$ are the stiffness and damping matrices of the shaft, and $\mathbf{K_b}$ and $\mathbf{C_b}$ are the stiffness and damping of the bearings, which come from a linearization procedure. The nonlinear force $\mathbf{f_{nl}}$, is the remaining component after the linearization. Also, $\mathbf{f_h}$ and $\mathbf{f_g}$, are the unbalance and the gravity force, respectively. The vector $\bar{\mathbf{x}}(t)$ is given as,

$$\bar{\mathbf{x}}(t) = \left\{\bar{\mathbf{x}}^1(t)\ \ \bar{\mathbf{x}}^2(t)\ \cdots\ \bar{\mathbf{x}}^N(t)\right\}^T, \quad \bar{\mathbf{x}}^i(t) = \left\{\bar{u}_y^i\ \ \bar{u}_z^i\ \ \bar{\theta}_y^i\ \ \bar{\theta}_z^i\right\}^T,\ \ i = 1, 2, \ldots, N \tag{2}$$

being N the number of nodes in the mesh and $\mathbf{x}^i(t)$ the displacements of the ith node; $\bar{u}_y^i$ and $\bar{u}_z^i$ are the ith nodal displacements and $\bar{\theta}_y^i$ and $\bar{\theta}_z^i$ the rotations. Figure 2 shows the coordinate system adopted. Since there are 4 Degrees of Freedom (DOFs) per node, the system in Eq. (1) has a total of $4N$ DOFs. The shape functions used to construct the physical matrices for the shaft takes into account rotary inertia and shear deformation (Timoshenko beam). One is referred to [11] or [6] on how to obtain the matrices. In addition to the shaft properties, the matrices also have the contribution of rigid disks, which are added at their corresponding nodal points. The disks are considered rigid masses with rotary inertia.

In order to apply the method proposed, Eq. (1) must be written with respect to the equilibrium position. This can be done by a change of variables as, $\mathbf{x}(t) = \bar{\mathbf{x}}(t) - \mathbf{x_e}$, being $\mathbf{x_e}$ the equilibrium position. which is obtained by setting $\ddot{\bar{\mathbf{x}}}(t) = \dot{\bar{\mathbf{x}}}(t) = \mathbf{f_h} = \mathbf{0}$ in the equations of motion. Equation (1) is rewritten in terms of $\mathbf{x}(t)$ as,

$$\mathbf{M}\ddot{\mathbf{x}}(t) + \mathbf{D}\dot{\mathbf{x}}(t) + \mathbf{K}\mathbf{x}(t) = \mathbf{f}(\mathbf{x}, \dot{\mathbf{x}}, t) \tag{3}$$

where,

$$\mathbf{D} = \mathbf{C_s} + \mathbf{C_b} + \Omega\mathbf{G}, \quad \mathbf{K} = \mathbf{K_s} + \mathbf{K_b}, \quad \mathbf{f}(\mathbf{x}, \dot{\mathbf{x}}, t) = \mathbf{f_{nl}}(\mathbf{x} + \mathbf{x_e}, \dot{\mathbf{x}}) + \mathbf{f_h}(t) + \mathbf{f_g} - (\mathbf{K_s} + \mathbf{K_b})\mathbf{x_e} \tag{4}$$

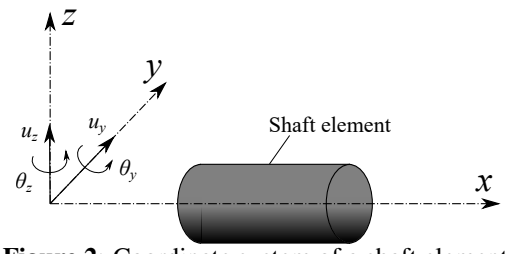

Figure 2: Coordinate system of a shaft element.

Equation (3) is the equation of motion for the rotor system written in terms of the equilibrium position. This equation is used in the following analysis.

2.2 The Invariant Manifold Method

Before the aplication of the IMM, Eq. (3) needs to be transformed in the modal space. It is worth mentioning that this step is not mandatory, since the IMM can be applied in the physical space as well (as first presented by [22], for example). However, this transformation is applied for two reasons: first, the number of degrees of freedom may be large in Eq. (3), which strongly affects the numerical cost in the IMM. Second, by transforming the equations in the modal space, a interpretation of the manifolds as curved spaces tangent to the linear eigenspaces can be made.

Since the system is damped and with gyroscopic effect, a complex modal analysis is necessary to fully decouple the equations [19]. Firstly, one rewrites the equations in state-space form, that is,

$$\dot{\mathbf{w}}(t) = \mathbf{A}\mathbf{w}(t) + \mathbf{G}(\mathbf{w}, t) \tag{5}$$

where,

$$\mathbf{A} = \begin{bmatrix} \mathbf{0} & \mathbf{I} \\ \mathbf{M}^{-1}\mathbf{K} & \mathbf{M}^{-1}\mathbf{D} \end{bmatrix}, \quad \mathbf{w}(t) = \left\{\mathbf{x}(t)\ \dot{\mathbf{x}}(t)\right\}^T \quad \mathbf{G}(\mathbf{w}, t) = \left\{\mathbf{0}\ \mathbf{M}^{-1}\mathbf{f}(\mathbf{w}, t))\right\}^T \tag{6}$$

here, $\mathbf{0}$ is a matrix of zeros and $\mathbf{I}$ is identity matrix, both with size $4N \times 4N$. To reduce the dynamical system, the state vector is approximated in terms of the eigenvectors of the matrix $\mathbf{A}$ as follows,

$$\mathbf{w}(t) \approx \sum_{i=1}^{n} \left(\boldsymbol{\phi}^i q_i(t) + \boldsymbol{\phi}^{i*} q_i^*(t) \right) \tag{7}$$

where $n \ll 4N$ are the number of modes retained, $\boldsymbol{\phi}^i$ are the eigenvectors, $q_i(t)$ are the modal (generalized) coordinates, and * denotes complex conjugation. The appearance of the complex conjugates comes from the fact that the modes in rotating machines are in general underdamped [8]. The eigenvectors and adjoints are the solution of,

$$\mathbf{A}\boldsymbol{\phi}^i = \lambda_i \boldsymbol{\phi}^i \quad \mathbf{A}^H \boldsymbol{\psi}^i = \lambda_i^* \boldsymbol{\psi}^i \quad \text{for } i = 1, 2, \ldots, 2n \tag{8}$$

being λ_i the eigenvalues, which are generally complex conjugate pairs, $\boldsymbol{\psi}^i$ the ith adjoint eigenvector, and H denote the hermitian (complex conjugate) transpose. The adjoint eigenvectors are the complex conjugate of the left eigenvectors, and they are necessary here due to the non-symmetric nature of $\mathbf{A}$, which in turn is due to the gyroscopic effect and possibly anisotropy of the bearings [6]. By substituting the expansion (7) in the equation of motion (5), and multiplying by the adjoint eigenvectors $\boldsymbol{\psi}$, one may have,

$$\begin{aligned} \dot{q}_i(t) &= \lambda_i q_i(t) + (\boldsymbol{\psi}^i)^T \mathbf{G}(\mathbf{q}, t) \\ \dot{q}_i^*(t) &= \lambda_i^* q_i^*(t) + (\boldsymbol{\psi}^i)^H \mathbf{G}(\mathbf{q}, t) \end{aligned} \quad \text{for } i = 1, 2, \ldots, n \tag{9}$$

which are $2n$, first-order, complex equations coupled by the nonlinearity. In order to apply the invariant manifold method, one needs to obtain the generalized coordinates q_i as real instead of complex as above. By separating the modal coordinates into its real and imaginary parts as $q_i = p_{2i-1} + jp_{2i}$, with $j = \sqrt{-1}$, Eq. (9) can be written as,

$$\begin{aligned} \dot{p}_{2i-1}(t) &= \sigma_i p_{2i-1}(t) - \omega_i p_{2i}(t) + \text{Re}\left\{(\boldsymbol{\psi}^i)^T \mathbf{G}(\mathbf{q}, t)\right\} \\ \dot{p}_{2i}(t) &= \sigma_i p_{2i}(t) + \omega_i p_{2i-1}(t) + \text{Im}\left\{(\boldsymbol{\psi}^i)^T \mathbf{G}(\mathbf{q}, t)\right\} \end{aligned} \quad \text{for } i = 1, 2, \ldots, n \tag{10}$$

with $\sigma_i = \text{Re}\{\lambda_i\}$ and $\omega_i = \text{Im}\{\lambda_i\}$. Eq. (10) is completely equivalent to (9), and either can be solved for the physical displacement $\mathbf{w}$.

The first step in the IMM is to select two generalized coordinates from the n modes used in the model reduction, say $u = p_{2k-1}$ and $v = p_{2k}$, to serve as "master" coordinates. These are then used as a basis to describe the remaining $2n-2$ "slave" modes of the system. The relation between the remaining modes with the master coordinates can be expressed as,

$$p_{2i-1} = P_i(u, v, \theta), \quad p_{2i} = Q_i(u, v, \theta), \quad \text{for } i = 1, 2, \ldots, n;\ i \neq k \tag{11}$$

where P_i and Q_i can be seen as the coordinates that compose the manifold, and $\theta = \Omega t$ is the phase of the unbalance excitation and its introduction is made to write the non-autonomous system as if it were an autonomous one (see [14]). Since P_i and Q_i depend on three quantities, one can think of the manifold as a 2D surface with time-varying coordinates due the the external excitation. To obtain these coordinates, one differentiates Eq. (11) with respect to time and substitutes the equations of motions of the slave modes, leading to the manifold equations,

$$\begin{aligned}
\sigma_i P_i - \omega_i Q_i + g_{2i-1} = \frac{\partial P_i}{\partial u}\Big(\sigma_k u - \omega_k v + g_{2k-1}\Big) + \frac{\partial P_i}{\partial \theta}\Omega \\
+ \frac{\partial P_i}{\partial v}\Big(\sigma_k v + \omega_k u + g_{2k}\Big) \\
\sigma_i Q_i + \omega_i P_i + g_{2i} = \frac{\partial Q_i}{\partial u}\Big(\sigma_k u - \omega_k v + g_{2k-1}\Big) + \frac{\partial Q_i}{\partial \theta}\Omega \\
+ \frac{\partial Q_i}{\partial v}\Big(\sigma_k v + \omega_k u + g_{2k}\Big)
\end{aligned} \quad \text{for } i = 1, 2, \ldots, n;\ i \neq k \tag{12}$$

where $g_{2i-1} = \text{Re}\left\{(\boldsymbol{\psi}^i)^T \mathbf{G}(u, v, \theta)\right\}$ and $g_{2i} = \text{Im}\left\{(\boldsymbol{\psi}^i)^T \mathbf{G}(u, v, \theta)\right\}$. The functional relationship with (u, v, θ) has been avoided for better clarity. The above equations are partial differential equations (PDEs) and independent of time. Their solution gives the coordinates of the invariant manifold P_i and Q_i, for the ith mode. The problem now consists in solving these equations and obtain the geometry of the invariant manifolds. After obtaining the coordinates P_i and Q_i, the first-order differential equations for the master coordinates need to be solved. They are given by,

$$\begin{aligned}
\dot{u}(t) &= \sigma_k u(t) - \omega_k v(t) + \text{Re}\left\{(\boldsymbol{\psi}^i)^T \mathbf{G}(u, v, \Omega t)\right\} \\
\dot{v}(t) &= \sigma_k v(t) + \omega_k u(t) + \text{Im}\left\{(\boldsymbol{\psi}^i)^T \mathbf{G}(u, v, \Omega t)\right\}
\end{aligned} \tag{13}$$

It is important to note that the contribution of the slave modes in Eq. (13) will be given by the functional relations $P_i(u, v, \theta)$ and $Q_i(u, v, \theta)$. These functional relations account for the coupling between the generalized coordinates due to the nonlinearity. Provided these functions are accurate, there is minimal lost of information comparing Eq. (13) and (10). Thus, the problem of integrating $2n$ nonlinear equations, given by Eq. (10), is substituted by the solution of $2n-2$ nonlinear partial differential equations for the geometry of the manifolds, Eq. (12), and an integration of 2 nonlinear equations for the master coordinates, Eq. (13). If one has an efficient way to solve the manifold equations, the approach reduces the solution to a single pair of nonlinear differential equations.

To solve Eq. (12), the coordinates are assumed as,

$$\begin{aligned}
P_i(u, v, \theta) &= \sum_{l=1}^{N_u}\sum_{m=1}^{N_v}\sum_{r=1}^{N_\theta} C_i^{lmr} T_{l,m}(u, v) F_r(\theta) \\
Q_i(u, v, \theta) &= \sum_{l=1}^{N_u}\sum_{m=1}^{N_v}\sum_{r=1}^{N_\theta} D_i^{lmr} U_{l,m}(u, v) F_r(\theta)
\end{aligned} \quad \text{for } i = 1, 2, \ldots, n;\ i \neq k \tag{14}$$

Being C_i^{lmr} and D_i^{lmr} the unknown coefficients, $T_{l,m}$, $U_{l,m}$ and F_r known shape functions, and N_u, N_v and N_θ the number of shape functions assumed. For the expansion in u and v, the shape functions were assumed standard Chebyshev polynomials, which are known to be very accurate in a wide range of applications [4, 5]. In this case, the 2D shape functions are obtained by means of the tensor product of two 1D polynomials in the u and v directions. For the expansion in θ, a Fourier series expansion was performed, taking advantage of the periodicity of this coordinate [14].

The coefficients are obtained from a Weighted Residual Method, namely the Galerkin method. In this manner, the form assumed in Eq. (14) are substituted in (12), and a Galerkin projection is carried out in the residue, resulting in a total of $N_u N_v N_\theta (2n-2)$ integro-algebraic equations that need to be solved for the coefficients C_i^{lmr} and D_i^{lmr}. With the functions P_i and Q_i, for $i = 1, 2, \ldots, n$, at hand, the equations of motion for the master coordinates, Eq. (13), can be solved. The physical displacements and velocities are then obtained by,

$$\begin{aligned}\mathbf{w}(t) &= \sum_{i=1}^{n} \Big(\mathrm{Re}\{\boldsymbol{\phi}^i\} p_{2i-1}(t) + \mathrm{Im}\{\boldsymbol{\phi}^i\} p_{2i}(t) \Big) \\ &= \mathrm{Re}\{\boldsymbol{\phi}^k\} u(t) + \mathrm{Im}\{\boldsymbol{\phi}^k\} v(t) + \sum_{i=1, i\neq k}^{n} \Big(\mathrm{Re}\{\boldsymbol{\phi}^i\} P_i(u, v, \Omega t) + \mathrm{Im}\{\boldsymbol{\phi}^i\} Q_i(u, v, \Omega t) \Big)\end{aligned} \tag{15}$$

To summarize the proposed method: the rotordynamics problem given by Eq. (3), of size $4N$, is first reduced by linear modal analysis, leading to $2n$ equations, Eq. (9), with $n \ll 4N$. Then, by means of the IMM, the integration of the $2n$ equations is reduced to a sigle pair of equations for the master mode only, together with $2n-2$ PDEs for the remaining modes.

3 Results and Discussion

The rotor system studied in this work is depicted in Fig. 3. It consist of a steel shaft of diameter $d = 12$ mm and length of $L = 600$ mm. The Young's modulus and Poisson ratio considered were $E = 210$ GPa and $\nu = 0.3$, respectively. A rigid steel disk is positioned at $L/3$ from the left free end, with diameter of $D = 95$ mm and thickness of $h = 45$ mm. In addition, two identical bearings are positioned at 50 mm from the free ends. The shaft is modeled by the FEM, with 12 elements of equal length, giving a total of 48 DOFs. In all the subsequent simulations, a personal computer with an Intel(R) Core(TM) i7-7500U CPU @ 2.90 GHz processor and the software MATLAB$^{\text{TM}}$ were used. The equations were integrated using the `ode45` integrator with standard options and zero initial conditions. The manifold equations were solved by means of the `fsolve` function.

3.1 Rotor with nonlinear bearing

In the first example, the bearings are considered to have a cubic nonlinearity. The horizontal and vertical components of the bearing force are given as,

$$F_y = c_1 \dot{\bar{u}}_y + k_1 \bar{u}_y + \beta_1 \bar{u}_y (\bar{u}_y^2 + \bar{u}_z^2), \quad F_z = c_2 \dot{\bar{u}}_z + k_2 \bar{u}_z + \beta_2 \bar{u}_z (\bar{u}_y^2 + \bar{u}_z^2) \tag{16}$$

being c_i and k_i the linear damping and stiffness coefficients, and β_i the cubic coefficients ($i = 1, 2$). The coefficients are assumed to be constants. This model is suited to represent rolling-element bearings [10, 24, 8]. Note that Eq. (16) is not written with respect to the equilibrium position (as denoted by the bars). The values considered for the bearings were $c_1 = 10$ Ns/m, $c_2 = c_1$, $k_1 = 10^5$ N/m, $k_2 = 0.9k_1$, and $\beta_1 = \beta_2 = \beta = 5 \times 10^9$ N/m^3. Figure 4 presents the frequency response of the system near the first two critical speeds for an unbalance moment of 0.07 kg·mm. The first forward and backward critical speeds are found to be $\omega_1^F = 1516$ rpm and $\omega_1^B = 1482$ rpm, respectively. The nonlinearity is clearly noticed by the bending of the resonance peaks, which is characteristic of hardening-type spring. It is noted that the linear model is very accurate up until very close to the critical speeds.

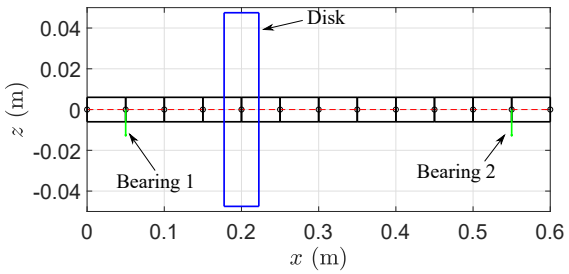

Figure 3: Rotor system studied.

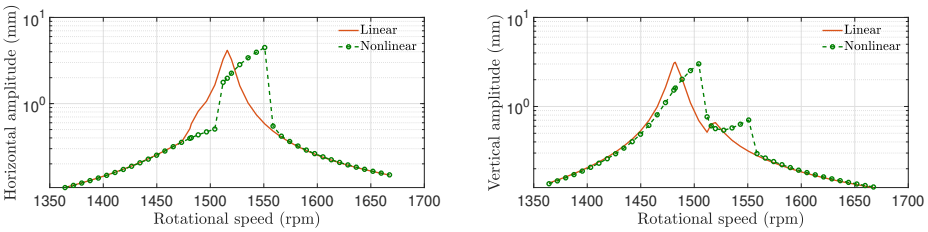

Figure 4: Frequency response of the rotor with cubic nonlinearity at the disk: horizontal (a) and vertical displacement (b).

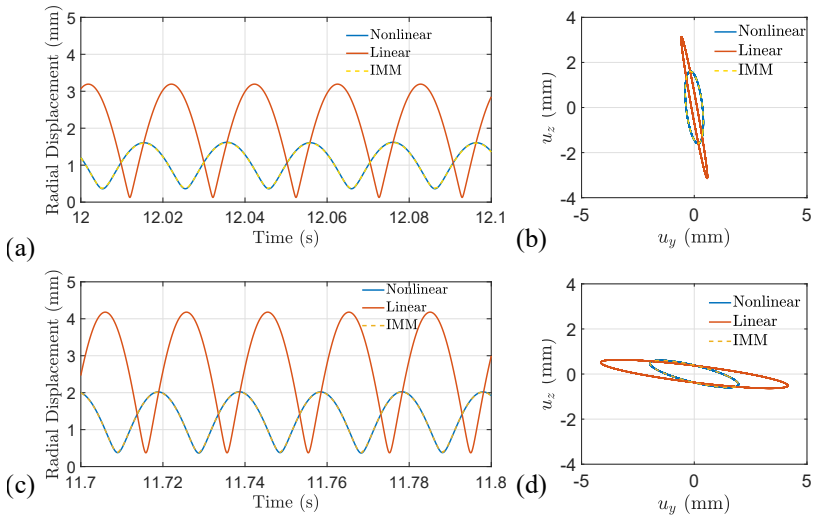

Figure 5: Radial displacements and orbits at the disk: for $\Omega = \omega_1^B$ (a) and (b), and for $\Omega = \omega_1^F$ (c) and (d).

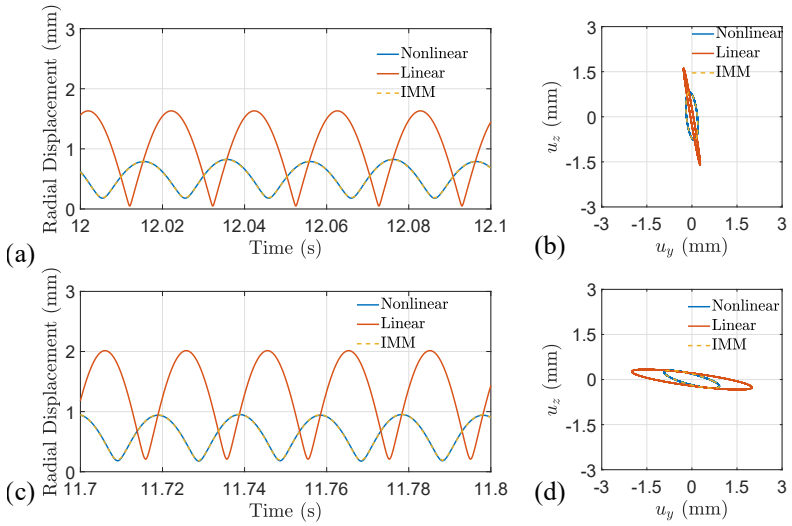

Figure 6: Radial displacements and orbits at bearing 1: for $\Omega = \omega_1^B$ (a) and (b), and for $\Omega = \omega_1^F$ (c) and (d).

Table 1: Computation time comparison for the rotor with cubic bearing. In the IMM, the parenthesis shows the computation time to obtain the manifolds.

Case	Full nonlinear	Linear	Reduced nonlinear	IMM
$\Omega = \omega_1^B$	531 s	158 s	5.99 s	2.40 s (82.0 s)
$\Omega = \omega_1^F$	527 s	151 s	6.97 s	2.05 s (84.4 s)

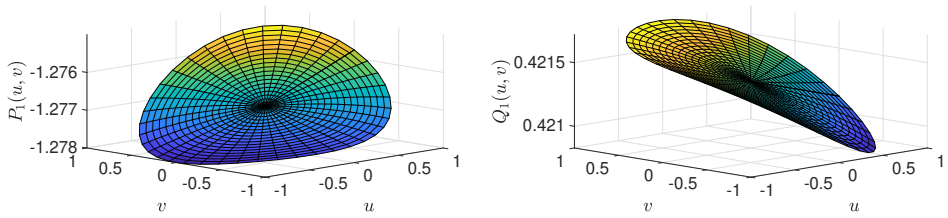

(a) (b)

Figure 7: Manifold for the first forward mode (rotor with cubic bearing): P_1 (a) and Q_1 (b).

In order to apply the IMM, the system is first reduced by modal analysis. The number of retained modes were $n = 6$, being half forward and half backward modes. Next, one of these modes must be selected to be used as a master mode. There is no clear procedure to follow here, and a test with several modes is required in general. In the present system, the weakest excited mode proved to be a good choice. The reason for this is that multiple solutions exist when the master mode posses high nonlinearity (see [7] for example). Not only this, but when the selected master mode is weakly excited, the solution of the manifold equations has a much faster convergence. Thus, the master mode selected was the second backward mode. In addition, the number of shape functions in the expansion (14) were $N_u = N_v = 2$, which correspond to a bilinear base and $N_\theta = 5$, which correspond to 4 harmonics plus the constant term. These numbers provided fast and accurate solutions for the system at hand.

Figures 5 and 6 show the time response of the system at the disk and bearing 1 for the first two critical speeds. The nonlinear and linear responses are obtained by integrating the full equations, that is, with no modal reduction. At first sight, the major difference between the linear and nonlinear system is clear, as the amplitudes of the latter are smaller. This occurs due to the "bending" of the resonance peak as shown in Fig. 4. The response by the IMM is also shown, and a great agreement, at both speeds considered, between it and the full solution of the nonlinear system is seen. The IMM needs much less numerical cost as compared to solving the full equations numerically, as only 2 equations are solved. The full system, on the other hand, has 96 equations (which is double the number of DOFs, as the equations need to be written in state-space form). Table 1 presents some comparison between the mean values several computation runs. The time to solve the manifold equations is also shown in parenthesis. It is worth mentioning that the obtention of the manifolds is an "off-line" cost, which means that they are obtained prior to the actual solution of the system. Even if one is to integrate the reduced system, that is, the $2n$ modal equations, the IMM has some advantages. If one chooses the master mode as the weakest excited mode, the solution of the manifold equations is very fast, and thus one needs to integrate only a pair of equations. Also, depending on the master mode, the solution of the IMM gives only the steady state solutions, that is, with no transients. For a weakly damped rotor, these transients may take long to die out, making the time integration process very costly if one is interested in the steady state solutions only.

Figure 7 shows the manifolds of the first forward mode with respect to the master mode for $\theta = 0$. One notes that they are curved surfaces due to the nonlinearity. Also, the manifolds are not still, and have a combined motion of rotation and translation [14]. It is this motion and the curvature of these surfaces that allows an effective model reduction and a good agreement between the single mode solution and the full solution of the nonlinear system.

3.2 Rotor with hydrodynamic bearings

In the second example, a more challenging nonlinearity is tested. The force considered comes from the solution of the Reynolds equation based on short bearing theory with half-Sommerfeld boundary conditions, of a fluid with constant viscosity. The forces in the vertical and horizontal direction can be obtained by [23, 15, 16].

$$F_y = f_\varepsilon \sin\phi + f_\phi \cos\phi, \quad F_z = f_\phi \sin\phi - f_\varepsilon \cos\phi, \quad \begin{cases} f_\varepsilon = -\dfrac{\mu R L_b^3}{2C^2}\left[\dfrac{2\varepsilon^2(\Omega - 2\dot{\phi})}{(1-\varepsilon^2)^2} + \dfrac{\pi(1+2\varepsilon^2)\dot{\varepsilon}}{(1-\varepsilon^2)^{5/2}}\right] \\ f_\phi = \dfrac{\mu R L_b^3}{2C^2}\left[\dfrac{\pi(\Omega - 2\dot{\phi})\varepsilon}{2(1-\varepsilon^2)^{3/2}} + \dfrac{4\varepsilon\dot{\varepsilon}}{(1-\varepsilon^2)^2}\right] \end{cases} \tag{17}$$

where ε is the dimensionless journal eccentricity, ϕ is the journal angular position relative to the negative vertical axis, R the journal's radius, μ is the fluid viscosity, L_b the bearing length and C the radial clearance. The linearization of these forces can be obtained by a first-order Taylor expansion relative to the equilibrium position (see

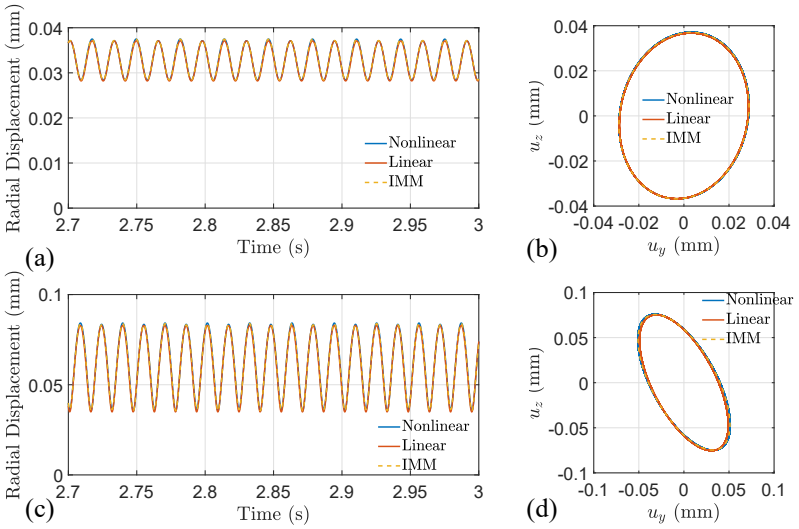

Figure 8: Radial displacements and orbits at the disk: for $\Omega = 0.96\omega_1^F$ (a) and (b), and for $\Omega = \omega_1^F$ (c) and (d).

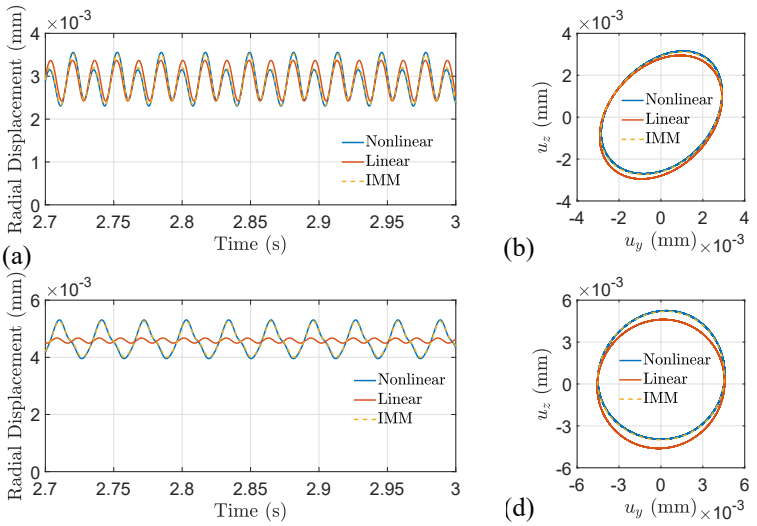

Figure 9: Radial displacements and orbits at bearing 1: for $\Omega = 0.96\omega_1^F$ (a) and (b), and for $\Omega = \omega_1^F$ (c) and (d).

Table 2: Computation time comparison for the rotor with hydrodynamic bearing.

Case	Full nonlinear	Linear	Reduced nonlinear	IMM
$\Omega = 0.96\omega_1^F$	192 s	23.2 s	127 s	4.05 s (135 s)
$\Omega = \omega_1^F$	175 s	22.7 s	129 s	4.01 s (136 s)

[16]). The following parameters were adopted for both bearings: $L_b = 20$ mm, $R = 15.5$ mm, $C = 90$ μm, and $\mu = 0.028$ Pa·s. In addition, an unbalance moment of 0.01 kg·mm is placed at the disk.

Prior to applying the IMM, the system must be reduced by means of modal analysis. Four highly overdamped modes were found in the studied system. Although these are fast-decaying, non-vibrating modes, they must be considered to correctly describe the full nonlinear system. The number of modes considered in the modal analysis was $n = 10$, being four overdamped modes, and six vibrating modes with half forward and half backward characteristics. The master mode was chosen to be the third forward mode for the same reasons discussed in the previous example. In addition, the number of shape functions in the expansion (14) were $N_u = N_v = 2$ and $N_\theta = 5$.

Figures 8 and 9 show the radial displacements and orbits at the disk and bearing 1 (the leftmost bearing in Fig. 3) for $\Omega = 0.96\omega_1^F$ and $\Omega = \omega_1^F$, with $\omega_1^F = 1939.7$ rpm. The effect of the nonlinearity appears as an distortion of the rotor's orbit, which is simply an ellipse in the linear case. Also, the nonlinear effect appears more severe at the bearing then at the disk, where the linear and nonlinear solutions are very similar. Comparing the

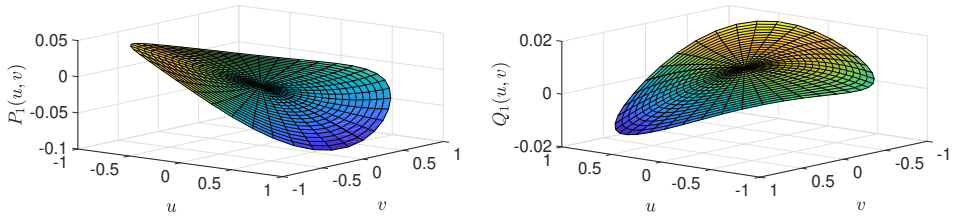

(a) (b)

Figure 10: Manifold for the first forward mode (rotor with hydrodynamic bearing): P_1 (a) and Q_1 (b).

results of the IMM with the full nonlinear solution, one sees a good agreement. Thus, the single pair of equations given by the IMM is able to capture the full rotor system with a highly nonlinear force. Table 2 shows some numeric values corresponding to the mean values of the computation runs. It is also shown in parenthesis the time for the obtention of the manifolds. One can observe the large computation time reduction that the IMM provides. It is worth mentioning that the computation time of the reduced nonlinear model is strongly affected by the overdamped modes, which makes the equations numerically stiff. If they are neglected, one gets much faster results but with higher errors compared with the full solution. The manifolds of the first forward mode are shown in Fig. 10, for $\theta = 0$. Again, these surfaces are not quite still, but move about according to the phase of the unbalance θ.

4 Conclusion

This work presented an aplication of the IMM in rotor-bearing systems with nonlinear forces. The basis of the IMM is the obtention of manifolds, which are curved spaces tangent to the eigenspace of the linearized system. With these manifolds, the method allows the obtention of forced responses of large DOFs systems by the integration of a single pair of equations. The method was validated by two examples: a rotor with a cubic force nonlinearity, and a rotor with hydrodynamic bearings. In both cases, the IMM proved accurate and fast for the obtention of the solutions.

Although the examples were based on a simple rotor, the method has capabilities to be applied in high-dimensional rotor systems modeled by the FEM. The main drawback of the IMM lies in the solution of the manifold equations (12), which are highly nonlinear partial differential equations and might posses multiple solutions. The best approach found was to select a weakly excited mode as the master mode. This makes the obtention of the manifold easier, and provide fast and accurate solutions. With the manifolds at hand, the single pair of equations can be integrated, and the response of the full system approximated with good accuracy.

Acknowledgment

The authors would like to thank CNPq (Grants #307941/2019-1 and #140275/2021-5) for the financial support to this research.

References

[1] Albu-Schäffer, A. and Della Santina, C., (2020): A review on nonlinear modes in conservative mechanical systems. Annual Reviews in Control, **50**, pp.49-71.

[2] Avramov, K.V. and Borysiuk, O., (2012): Nonlinear dynamics of one disk asymmetrical rotor supported by two journal bearings. Nonlinear Dynamics, **67**(2), pp.1201-1219.

[3] Avramov, K.V. and Mikhlin, Y.V., (2013): Review of applications of nonlinear normal modes for vibrating mechanical systems. Applied Mechanics Reviews, **65**(2).

[4] Boyd, J.P., (2001): *Chebyshev and Fourier spectral methods*. Dover Publications, Mineola NY.

[5] Fletcher, C.A., (1984): Computational galerkin methods. Springer, Berlin.

[6] Friswell, M.I., Penny, J.E., Garvey, S.D. and Lees, A.W., (2010): *Dynamics of rotating machines*. Cambridge university press, New York.

[7] Gabale, A.P. and Sinha, S.C., (2011): Model reduction of nonlinear systems with external periodic excitations via construction of invariant manifolds. Journal of Sound and Vibration, **330**(11), pp.2596-2607.

[8] Genta, G., (2005): *Dynamics of rotating systems*. Springer Science & Business Media, New York.

[9] Haller, G. and Ponsioen, S., (2016): Nonlinear normal modes and spectral submanifolds: existence, uniqueness and use in model reduction. Nonlinear dynamics, **86**(3), pp.1493-1534.

[10] Ishida, Y. and Inoue, T., (2004): Internal resonance phenomena of the Jeffcott rotor with nonlinear spring characteristics. J. Vib. Acoust., **126**(4), pp.476-484.

[11] Ishida, Y. and Yamamoto, T., (2013): *Linear And Nonlinear Rotordynamics: a modern treatment with applications*. Wiley-VCH, Weinheim.

[12] Jain, S. and Haller, G., (2022): How to compute invariant manifolds and their reduced dynamics in high-dimensional finite element models. Nonlinear dynamics, **107**(2), pp.1417-1450.

[13] Jiang, D., Pierre, C. and Shaw, S.W., (2005): The construction of non-linear normal modes for systems with internal resonance. International Journal of Non-Linear Mechanics, **40**(5), pp.729-746.

[14] Jiang, D., Pierre, C. and Shaw, S.W., (2005): Nonlinear normal modes for vibratory systems under harmonic excitation. Journal of sound and vibration, **288**(4-5), pp.791-812.

[15] Khonsari, M., (1993): Stability Boundary of Non-Linear Orbits with in Clearance Circle of Journal Bearings. Journal of Vibration and Acoustics, **115**(3), pp.303-307.

[16] Krämer, E., (2013): *Dynamics of rotors and foundations*. Springer-Verlag Berlin Heidelberg GmbH, New York.

[17] Legrand, M., Jiang, D., Pierre, C. and Shaw, S.W., (2004): Nonlinear normal modes of a rotating shaft based on the invariant manifold method. International Journal of Rotating Machinery, **10**(4), pp.319-335.

[18] Mazzilli, C.E., Gonçalves, P.B. and Franzini, G.R., (2022): Reduced-order modelling based on non-linear modes. International Journal of Mechanical Sciences, **214**, p.106915.

[19] Meirovitch, L., (1980): *Computational methods in structural dynamics*. Sjithoff & Noordhoff International Publishers, Rockville.

[20] Pesheck, E., Pierre, C. and Shaw, S.W., (2002): A new Galerkin-based approach for accurate non-linear normal modes through invariant manifolds. Journal of sound and vibration, **249**(5), pp.971-993.

[21] Renson, L., Kerschen, G. and Cochelin, B., (2016): Numerical computation of nonlinear normal modes in mechanical engineering. Journal of Sound and Vibration, **364**, pp.177-206.

[22] Shaw, S.W. and Pierre, C., (1993): Normal modes for non-linear vibratory systems. Journal of sound and vibration, **164**(1), pp.85-124.

[23] Wang, J.K. and Khonsari, M.M., (2006): Bifurcation analysis of a flexible rotor supported by two fluid-film journal bearings. Journal of tribology, **128**(3), pp.594-603.

[24] Yabuno, H., Kashimura, T., Inoue, T. and Ishida, Y., (2011): Nonlinear normal modes and primary resonance of horizontally supported Jeffcott rotor. Nonlinear Dynamics, **66**(3), pp.377-387.

Authors

Proposed for publication in the following journals:

*[1] BPASTS – Bulletin of the Polish Academy of Sciences: Technical Sciences - PAS journals,

*[2] ACM – Applied and Computational Mechanics, an open access international journal